

NUCLEI Experiment

Synthesis of $^{292}116$ in the $^{248}\text{Cm} + ^{48}\text{Ca}$ Reaction*

Yu. Ts. Oganessian, V. K. Utyonkov, and K. J. Moody¹⁾

Joint Institute for Nuclear Research, Dubna, Moscow oblast, 141980 Russia

Received February 28, 2001

Abstract—We report on the observation of the first decay event of the new nuclide $^{292}116$ produced in an experiment devoted to the synthesis of $Z = 116$ nuclei in the $^{248}\text{Cm} + ^{48}\text{Ca}$ reaction. The implantation of a heavy recoil in the focal-plane detector was followed in 46.9 ms by an α particle with $E_\alpha = 10.56$ MeV. The energies and decay times of the descendant nuclei are in agreement with those observed in the decay chains of the even–even isotope $^{288}114$, previously produced in the $^{244}\text{Pu} + ^{48}\text{Ca}$ reaction. Thus, the first α decay should be attributed to the parent nuclide $^{292}116$ produced via the evaporation of four neutrons in the complete fusion of ^{248}Cm and ^{48}Ca . The experiment is in progress at Flerov Laboratory for Nuclear Reactions (FLNR, JINR, Dubna). © 2001 MAIK “Nauka/Interperiodica”.

1. INTRODUCTION

In the reactions of actinide targets with ^{48}Ca projectiles, the first convincing piece of evidence for the synthesis of superheavy nuclei around the theoretically predicted spherical shell closures with $Z \geq 114$ and $N \geq 172$ was presented over the last two years [1–5].

These reports included the results of our experiments where a ^{244}Pu target was bombarded with 1.5×10^{19} ^{48}Ca ions throughout September–December 1998 and June–October 1999 and where the Dubna Gas-Filled Recoil Separator was employed. We observed two identical decay sequences of genetically linked events, each consisting of an implanted heavy atom, two subsequent α decays, and spontaneous fission (SF) as a final step [1, 2]. The measured α energies and the corresponding half-lives of the sequential chain members were $E_{\alpha 1} = 9.84$ MeV ($T_{1/2} = 1.9$ s) and $E_{\alpha 2} = 9.17$ MeV ($T_{1/2} = 9.8$ s); for spontaneous fission, $T_{1/2} = 7.5$ s. The decay properties of the synthesized nuclei are consistent with theoretical expectations for consecutive α decays originating from the parent even–even nucleus $^{288}114$ produced in the $4n$ -evaporation channel. We also observed a decay sequence consisting of an implanted nucleus, three subsequent α decays ($E_\alpha = 9.71, 8.67,$ and 8.83 MeV), and spontaneous fission [2, 3]. The most reasonable explanation for this decay chain is consecutive α decays starting

from the parent nucleus $^{289}114$ produced in the $3n$ -evaporation channel.

In March–April 1999, a ^{242}Pu target was bombarded with 7.5×10^{18} ^{48}Ca ions at the separator VASSILISSA. Two decay chains were assigned to the α decay of the parent nucleus $^{287}114$, with $T_{1/2} = 5.5$ s and $E_\alpha = 10.29$ MeV [4]. Both decay chains were terminated after the first α decays by the spontaneous fission of the daughter nucleus $^{283}112$, a nuclide previously observed in the $^{238}\text{U} + ^{48}\text{Ca}$ reaction [5].

On June 14, 2000, we started an experiment aimed at the synthesis of superheavy nuclei with $Z = 116$ in the vicinity of predicted spherical nuclear shells in the complete fusion of ^{248}Cm and ^{48}Ca [6].

In the reaction of ^{248}Cm with ^{48}Ca ions at an energy close to the Coulomb barrier, $^{296}116$ compound nuclei could be expected to deexcite via the emission of three or four neutrons. According to the macroscopic–microscopic Yukawa-plus-exponential model with Woods–Saxon single-particle potentials (YPE + WS) by Smolańczuk *et al.*, who adequately reproduced the radioactive properties (α decay and spontaneous fission) of the known heavy nuclei [7, 8], the even–even isotope $^{292}116$ is expected to have a partial α -decay half-life of $T_\alpha \approx 5$ ms. Its predicted spontaneous fission half-life is considerably longer: $T_{SF} \approx 2$ d. For the odd isotope $^{293}116$, the predictions are less definitive. The odd neutron can lead to hindrance of α decay and especially spontaneous fission. The macroscopic–microscopic finite-range droplet model with folded Yukawa single-particle potentials (FRDM + FY) by Möller *et al.* [9] gives a value of $T_\alpha \approx 0.3$ s for $^{293}116$. The alpha decays of the

*This article was submitted by the authors in English.

¹⁾University of California, Lawrence Livermore National Laboratory, Livermore, CA 94551 USA.

nuclides $^{292,293}_{116}$ lead to the isotopes of the element 114 that were produced in our recent experiments via the reactions $^{244}\text{Pu} (^{48}\text{Ca}, 3 - 4n)^{288,289}_{114}$ [1–3]. Their chains of sequential decays should be observed following α -particle emission from the parent nuclei with $Z = 116$.

2. EXPERIMENTAL TECHNIQUE

A beam of $^{48}\text{Ca}^{+5}$ ions was delivered by the U400 cyclotron at FLNR, JINR, operated with the ECR-4M ion source in a continuous mode. The average beam intensity at the target was $0.7 \mu\text{A}$ at the ^{48}Ca -material-consumption rate of about 0.3 mg/h . The beam energy was determined with a precision of about 1 MeV by measuring the energies of scattered ions and by the time-of-flight technique. The target material was provided by RIAR, Dimitrovgrad. A 32-cm^2 rotating target consisted of the enriched isotope ^{248}Cm (96.3%) in the form of CmO_2 deposited onto $1.5\text{-}\mu\text{m}$ Ti foils to a thickness of about 0.32 mg cm^{-2} , so that heavy recoil atoms would be knocked out of the target layer and transported through the separator to the detectors.

The evaporation residues (EVRs) recoiling from the target were separated in flight from the ^{48}Ca primary beam ions, scattered target and beam particles, and various transfer-reaction products by the Dubna Gas-Filled Recoil Separator [10]. Subsequently, the EVRs passed through a time-of-flight (TOF) system and were finally implanted in the detector array installed in the focal plane of the separator. The average charge state of recoil $Z = 116$ atoms in hydrogen filling the volume of the separator was estimated at 5.7 [11]. The collection efficiency of the separator was estimated from the results of test experiments and the ANAMARY code [12] developed for simulating the EVRs trajectories in the separator, the corresponding spatial distributions, and the resulting collection efficiencies. About 35% of the recoiling $Z = 116$ nuclei formed in the ^{248}Cm target were implanted in the focal-plane detector.

The focal-plane detector consisted of a $4 \times 12\text{-cm}^2$ semiconductor detector array with twelve vertical position-sensitive strips. This detector in turn was surrounded by eight $4 \times 4\text{-cm}^2$ side detectors without position sensitivity, forming a box of detectors open from the front side. The detection efficiency for α decays of implanted nuclei was 87% of 4π . The detection system was tested by recording the recoil nuclei and α and SF decays of the known isotopes of No produced in the reactions $^{204,206-208}\text{Pb} (^{48}\text{Ca}, xn)$ [10]. The energy resolution for the detection of α particles in the focal-plane detector was about 55 keV. For α

particles escaping from the focal-plane detector at different angles and absorbed in the side detectors, the energy resolution of the summed signals was about 190 keV because of energy losses in the entrance windows and dead layers of both detectors. We determined the position resolution of the signals of correlated decays of nuclei implanted in the detectors: for correlated EVR- α signals, the FWHM position resolution was 0.8 mm, while, for correlated EVR-SF signals, it was 0.6 mm. According to the measured position resolutions, more than 95% of genetically linked signals in the focal-plane detector appear in a position window of $\Delta y = 1.4 \text{ mm}$.

Fission fragments from ^{252}No implants produced in the $^{206}\text{Pb} + ^{48}\text{Ca}$ reaction were used for a fission-energy calibration. The measured fragment energies were not corrected for the pulse-height defect of the detectors. The energies of fragments recorded by the side detectors were not corrected for energy loss in the detectors' entrance windows, dead layers, or the pentane gas filling the detection system. The mean total energy loss of both fission fragments for ^{252}No was about 20 MeV; for fission fragments escaping from the focal-plane detector at a small angle, this value could be higher.

For the bombarding energy of ^{48}Ca ions, we chose the value of 240 MeV in the middle of the target. With an approximately 1.5-MeV beam energy resolution, a variation of the beam energy during irradiation within $\pm 0.9 \text{ MeV}$, and energy losses in the target of about 2.8 MeV, we expected the resulting compound nucleus $^{296}_{116}$ to have an excitation energy between 30.4 and 35.8 MeV. Thus, the compound nuclei should deexcite most probably through the evaporation of three or four neutrons and γ rays, producing the isotopes of the element 116 with neutron numbers of $N = 176$ and 177.

To improve background conditions for detecting long-time decay sequences, a special measurement mode was employed [10]. The beam was switched off after a recoil signal was detected with the parameters of the implantation energy and TOF expected for $Z = 116$ EVRs, followed by an α -like signal with an energy E_α between 10.25 and 11.5 MeV in the same strip within a position window of $\Delta y = 2 \text{ mm}$ and a time interval of 1 s. The duration of the pause was determined from the observed pattern of out-of-beam α decays and varied from 5 to 60 min. Thus, all the expected sequential decays of the daughter nuclides with $Z \leq 114$ could be observed in the absence of beam-associated background. With the full beam intensity on the target, the average rate of counting such “EVR $\rightarrow \alpha$ ” events in the detector system was less than one per three hours. The total counting rate for α particles with $E_\alpha > 8 \text{ MeV}$ in the entire

detector array over beam-off pauses was about 2 h^{-1} . The energy spectrum of α particles recorded by the focal-plane detector throughout beam-off pauses and off-line measurements is shown in Fig. 1a. The majority of $E_\alpha > 8\text{ MeV}$ events are caused by the α decays of short-lived isotopes ^{212}Po ($T_{1/2} = 0.3\ \mu\text{s}$, $E_\alpha = 8.784\text{ MeV}$) and ^{213}Po ($T_{1/2} = 4.2\ \mu\text{s}$, $E_\alpha = 8.376\text{ MeV}$) detected in coincidence with β^- decays of their precursors ^{212}Bi and ^{213}Bi , the descendant nuclei of long-lived isotopes ^{224}Ra , ^{225}Ac , or even $^{228,229}\text{Th}$ produced in transfer reactions with ^{244}Pu [1–3] and ^{248}Cm [6] targets.

3. EXPERIMENTAL RESULTS

The experiments were performed in June and July and in November and December 2000. A total of 1.6×10^{19} ^{48}Ca projectiles were delivered to the target. On the 35th day of irradiation, when the accumulated beam dose reached 6.6×10^{18} ions, the first event sequence was observed that can be attributed to the implantation and decay of the isotope of element 116 with mass number 292 (see Fig. 2a). The implantation of a heavy recoil in strip 4 of the focal-plane detector was followed in 46.9 ms by an α particle with $E_\alpha = 10.56\text{ MeV}$. This sequence switched the ion beam off, and further decays were detected under lower-background conditions. A second α particle with $E_\alpha = 9.81\text{ MeV}$ was observed 2.42 s later. After 53.87 s, a third α decay with an energy of 8.63 MeV was recorded by a side detector only. The energy deposited by this α particle in the focal-plane detector was not recorded because it was lower than the detection threshold of 0.92 MeV. However, the probability that the third α particle appeared in the chain ($\Delta t \sim 1\text{ min}$) as a random event can be estimated only at about 1%; for this reason, we attribute it to the decay of the same implanted nucleus. Thus its total energy is determined with a larger uncertainty: $E_\alpha = 9.09 \pm 0.46\text{ MeV}$.

Finally, 6.93 s after the last α decay, two coincident fission fragments, with a total energy of 197 MeV, were recorded by both the focal-plane and the side detectors. In this event, the low energy of the fission fragment measured by the side detector implies that a large amount of energy was lost by this fragment in the dead layers of the detectors.

The positions of four events whose signals were recorded in the focal-plane detectors (EVR, α_1, α_2 , and SF) were measured to be within a window of 0.5 mm, and all the events appeared within a time interval of 63.26 s, which suggests a strong probability of correlation between them. Over beam-off pauses, the counting rate for α particles with $E_\alpha > 8\text{ MeV}$ in the focal-plane detector was about $6 \times 10^{-5}\text{ min}^{-1}$

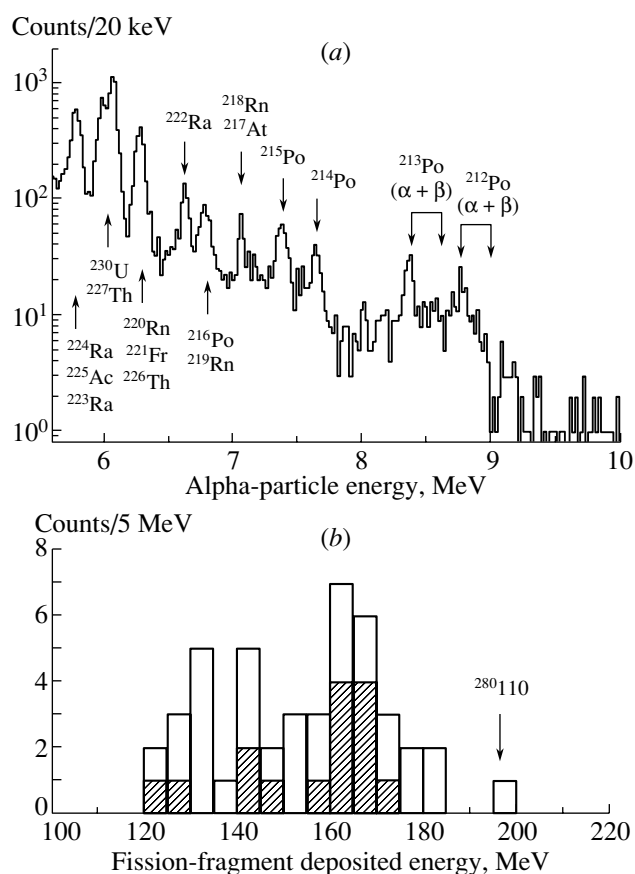


Fig. 1. (a) Energy spectrum of α particles recorded by the focal-plane detector over beam-off pauses and off-line measurements (85 days); (b) total spectrum of the entire amount of deposited energies of fission fragments of implanted nuclei recorded by both focal-plane and side detectors throughout the experiment and off-line measurements (open histogram). The dashed histogram shows the deposited energies of SF events detected throughout off-line measurements. The arrow shows the total measured deposited energy of a fission event preceded by the α -decay chain, assigned to $^{280}_{110}$ produced in the $^{248}\text{Cm} + ^{48}\text{Ca}$ reaction.

per pixel $\Delta y = 1.4\text{ mm}$. In the course of the 91-day bombardment of the ^{248}Cm target by ^{48}Ca projectiles, we observed 30 SF events and 15 events over the subsequent 83-day off-line measurement. The origin of these SF events could be spontaneous fission of $^{252,254}\text{Cf}$ and, to a lesser degree, ^{256}Fm long-lived products of transfer reactions with the ^{248}Cm target [13]. Using the measured production yields of heavy actinides from the interactions of ^{248}Cm with ^{48}Ca [13] and results of our bombardments at the same ^{48}Ca energy, we estimated the suppression factor at about 3×10^5 for such transfer-reaction products by the gas-filled separator, in good agreement with results for other reactions [10]. The spectra of to-

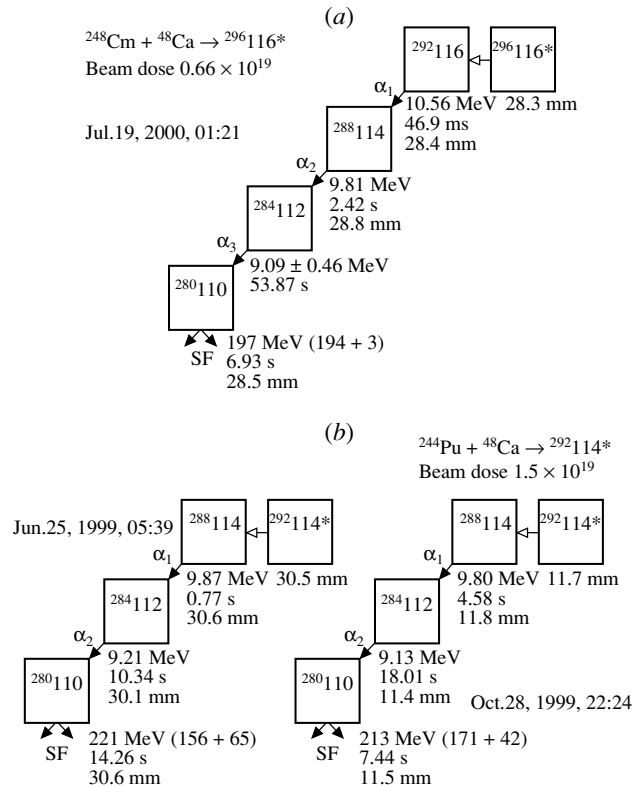


Fig. 2. (a) Time sequence in the observed decay chain; (b) two decay sequences of $^{288}114$ observed in the $^{244}\text{Pu} + ^{48}\text{Ca}$ reaction. Vertical positions of the observed events are given with respect to the top of the strip. Values in parentheses are fission energies measured by the focal-plane and side detectors.

tal deposited energies of fission fragments of implanted nuclei recorded by both the focal-plane and the side detectors are shown in Fig. 1b. Only one of these spontaneous-fission events was recorded after position-correlated signals from implanted heavy recoil and a subsequent α -decay chain. The total deposited energy of this SF event is shown in Fig. 1b by an arrow. For a position-correlation window $\Delta y = 1.4$ mm, the signals from SF events were observed with an average frequency of $7 \times 10^{-7} \text{ min}^{-1}$. By applying a Monte Carlo technique [14] and the procedures described in [15, 16], we have calculated the probabilities that this decay sequence was caused by the chance correlations of unrelated events at any position of the detector array and at the positions in which the candidate events occurred. The probability that the observed event is totally of a random origin is negligible.

All the decays following the first 10.56-MeV α particle agree well with the decay chains of $^{288}114$, which were previously observed in the $^{244}\text{Pu} + ^{48}\text{Ca}$ reaction [1, 2] (see Fig. 2b). Thus, it is reasonable to assign the observed decay to the nuclide $^{292}116$, produced via the evaporation of four neutrons in the complete fusion of ^{248}Cm and ^{48}Ca . All the de-

cay chain members follow the Geiger–Nuttall Q_α vs. T_α relationship for even–even nuclei. Substituting the values ($E_\alpha = 9.83 \pm 0.05$ MeV and $T_\alpha = 1.8_{-0.6}^{+2.1}$ s) measured in the $^{244}\text{Pu} + ^{48}\text{Ca}$ reaction (parent nuclide) and $^{248}\text{Cm} + ^{48}\text{Ca}$ (daughter nuclide) into the Viola–Seaborg formula with parameters fitted to data on all known $Z > 82$, $N > 126$ even–even nuclides [7], we obtain the atomic number of $Z = 114.3_{-0.8}^{+1.2}$.

Further experiments are in progress.

4. DISCUSSION

The newly observed nuclide $^{292}116$ is the heaviest of the known α -decaying even–even nuclides, following the production of $^{260,266}\text{Sg}$ ($Z = 106$) [17, 18], $^{264,266}\text{Hs}$ ($Z = 108$) [19, 20], $^{270}110$ [20], and two recently observed superheavy nuclei $^{288}114$ and $^{284}112$ [1, 2]. The decay energy of the $^{292}116$ and the half-life estimated from one event are $Q_\alpha = 10.71$ MeV and $T_\alpha = 33_{-15}^{+155}$ ms.

The radioactive decay properties of $^{292}116$ are in qualitative agreement with macroscopic–microscopic nuclear theory [7, 8], which predicts both α -decay

Experimental and calculated Q_α values for the α -decay chain of $^{292}116$

Z	A	Q_{expt} , MeV	Q_{theor} , MeV				
			YPE + WS	FRDM + FY	SHFB	RMF	TFM
110	280	≤ 9.4 (SF)*	9.84	9.05	9.8	8.98	9.245
112	284	9.30 ± 0.05	9.80	8.69	9.4	9.30	8.885
114	288	9.98 ± 0.05	10.32	9.16	9.4	9.83	9.385
116	292	10.71 ± 0.06	11.07	10.82	10.43	11.647	11.025

Note: YPE + WS, FRDM + FY, SHFB, RMF, and TFM stand for, respectively, the macroscopic–microscopic Yukawa-plus-exponential model with Woods–Saxon single-particle potentials [7, 8], the macroscopic–microscopic finite-range droplet model with folded Yukawa single-particle potentials [9], the self-consistent Skyrme–Hartree–Fock–Bogolyubov model with pairing [28], the self-consistent relativistic mean-field model [29], and the Thomas–Fermi model [27].

* The Q_α limit was calculated from the experimental $T_{1/2}$ value by using the Viola–Seaborg formula with parameters [7].

and spontaneous-fission properties of heavy nuclei. The alpha-decay energies of the synthesized nuclide and those of previously known isotopes of even- Z elements with $Z \geq 100$, together with theoretical Q_α values [7, 8] for even–even isotopes of $Z = 100 - 116$ elements, are shown in Fig. 3. It can be seen that the α -decay energy of the new even–even nuclide $^{292}116$, as well as those of other heaviest even–even nuclei with $Z = 112$ and 114 , are 0.35–0.5 MeV less than the corresponding predicted values. Such a decrease in Q_α values leads to an order of magnitude increase in the partial α -decay lifetimes. Thus, a comparison of the measured decay properties of the superheavy nuclide $^{292}116$ with theoretical predictions [7, 8] confirms the assumption [1, 2] that nuclei in the vicinity of spherical-shell closures with $Z = 114$ and $N = 184$ could show higher stability than what is predicted by the theory.

The α -decay properties of the synthesized nucleus can also be compared with the predictions of other theoretical models—for example, the Thomas–Fermi model (TFM) [27], calculations performed in the Hartree–Fock–Bogolyubov approach with different Skyrme forces (SHFB) [28], and relativistic mean-field calculations (RMF) [29]. The alpha-decay energies of the synthesized isotopes, together with theoretical Q_α values [7–9, 27–29], are shown in the table. A comparison of the present data with the results of calculations shows that the experimental results agree with theoretical predictions and confirm theoretical expectations for the existence of enhanced stability in the region of superheavy elements.

Some theoretical calculations using macroscopic–microscopic models [7–9] or the self-consistent Skyrme–Hartree–Fock–Bogolyubov model [28] predict $N = 184$ to be the next magic neutron number; however, the relativistic mean-field model [29] gives preference to the spherical $N = 172$ and deformed $N = 174$ shell closures. The relativistic mean-field model perfectly reproduces the measured

Q_α values for the even–even nuclei $^{284}112$ and $^{288}114$, suggesting the influence of the deformed $Z = 114$ and $N = 174$ shell closures, but it predicts that the α -decay energy for the heavier nuclide $^{292}116$ ($N = 176$) is higher by about 0.9 MeV. If, however, the effects of ground-state correlations are taken into account, this model leads to better agreement with experimental data [30].

Thus, the decay properties of $^{292}116$ and descen-

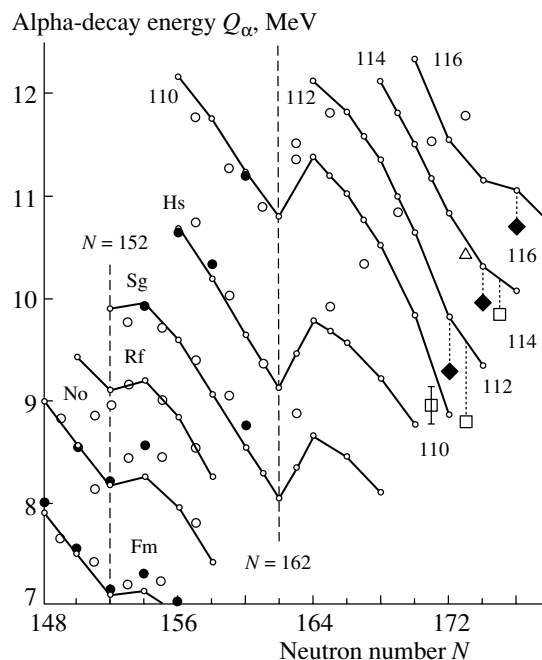


Fig. 3. Alpha-decay energy vs. neutron number for isotopes of even- Z elements with $Z \geq 100$ (solid circles show even–even isotopes, while open circles show even–odd isotopes) [17–26]. The triangle represents data from [4], while squares and diamonds correspond to data from [1–3, 6] and from the present study. Small open circles connected by solid lines show theoretical Q_α values [7, 8] for even–even $Z = 100–116$ isotopes.

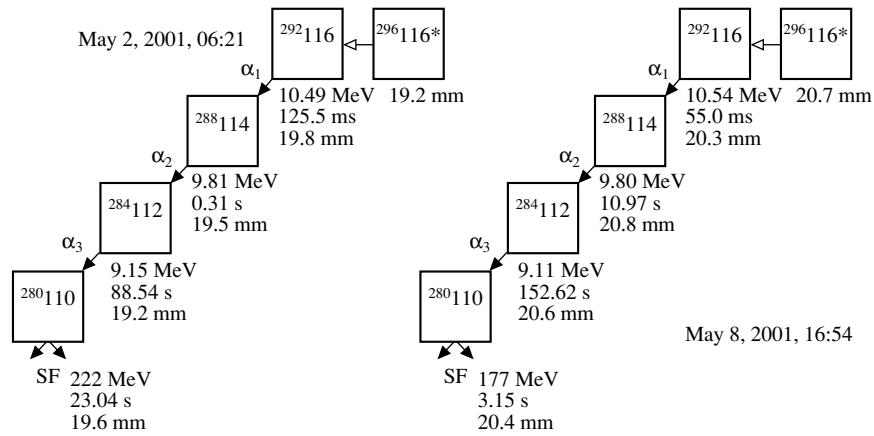


Fig. 4. Time sequence in the decay chains observed in the $^{248}\text{Cm} + ^{48}\text{Ca}$ reaction.

dant nuclei agree with the theoretical predictions of the stability island in the domain of superheavy elements around $Z = 114$ and $N = 184$.

ACKNOWLEDGMENTS

This paper presents the results obtained by a large group of physicists. We are indebted to Yu.V. Lobanov, F.Sh. Abdullin, A.N. Polyakov, I.V. Shirokovsky, Yu.S. Tsyganov, G.G. Gulbekian, S.L. Bogomolov, B.N. Gikal, A.N. Mezentsev, S. Iliev, V.G. Subbotin, A.M. Sukhov, O.V. Ivanov, G.V. Buklanov, K. Subotic, M.G. Itkis, J.F. Wild, N.J. Stoyer, M.A. Stoyer, R.W. Loughheed, C.A. Laue, Ye.A. Karelin, and A.N. Tatarinov.

We are grateful to the JINR Directorate—in particular to Prof. V.G. Kadyshesky, Prof. Ts. Vylov, and Prof. A.N. Sissakian—for the help and support we got during all stages of the experiment. The help of V.B. Galinsky, G.N. Ivanov, V.I. Krashonkin, V.I. Tomin, A.V. Rykhlyuk, A.M. Zubareva, and A.N. Shamanin in preparing and carrying out the experiment is gratefully acknowledged. Thanks are also due to I.V. Kalagin and the personnel of the U400 cyclotron and the associates of the ion-source group for obtaining an intense ^{48}Ca beam.

This work was supported by INTAS (grant no. 991-1344) and by the Russian Foundation for Basic Research (project no. 01-02-16486). Much support was provided through a special investment of the Russian Ministry for Atomic Energy. The ^{248}Cm target material was provided by the RIAR, Dimitrovgrad. Much of the support for the LLNL experimenters was provided by the US DOE under contract no. W-7405-Eng-48 with the University of California. These studies were performed in the framework of the Russian Federation—US Joint Coordinating Committee for Research on the Fundamental Properties of Matter.

Note added in proof. On April 20, 2001, we continued the experiment aimed at the synthesis of $Z = 116$ nuclei in the $^{248}\text{Cm} + ^{48}\text{Ca}$ reaction. The majority of the details of the experiment were similar to those described in this paper. On the 12th and 18th days of irradiation, after an integrated beam dose of 3.0×10^{18} , we observed two other decay chains of the even–even isotope $^{292}\text{116}$ that are shown in Fig. 4. The energies and the decay times of the parent and descendant nuclei are in agreement with those observed on July 19, 2000 (see Fig. 2a); the decay properties of the descendant nuclei are also in agreement with those observed in the decay chains of the isotope $^{288}\text{114}$ produced in the $^{244}\text{Pu} + ^{48}\text{Ca}$ reaction (see Fig. 2b).

Thus, from three decay events of the element $^{292}\text{116}$ and five decays of the elements $^{288}\text{114}$, $^{284}\text{112}$, and $^{280}\text{110}$ one can estimate the decay energies and half-lives of the even–even superheavy nuclei $^{292}\text{116}$ ($Q_\alpha = 10.68 \pm 0.06$ MeV, $T_{1/2} = 53_{-19}^{+63}$ ms), $^{288}\text{114}$ ($Q_\alpha = 9.96 \pm 0.06$ MeV, $T_{1/2} = 2.6_{-0.8}^{+2.0}$ s), $^{284}\text{112}$ ($Q_\alpha = 9.28 \pm 0.06$ MeV, $T_{1/2} = 45_{-14}^{+34}$ s), and $^{280}\text{110}$ ($T_{1/2} = 7.6_{-2.3}^{+5.8}$ s).

The experiments are now in progress.

REFERENCES

1. Yu. Ts. Oganessian *et al.*, Phys. Rev. C **62**, 041604(R) (2000).
2. Yu. Ts. Oganessian *et al.*, Yad. Fiz. **63**, 1769 (2000) [Phys. At. Nucl. **63**, 1679 (2000)].
3. Yu. Ts. Oganessian *et al.*, Phys. Rev. Lett. **83**, 3154 (1999).
4. Yu. Ts. Oganessian *et al.*, Nature **400**, 242 (1999).
5. Yu. Ts. Oganessian *et al.*, Eur. Phys. J. A **5**, 63 (1999).

6. Yu. Ts. Oganessian *et al.*, Phys. Rev. C **63**, 011301(R) (2001).
7. R. Smolańczuk, J. Skalski, and A. Sobiczewski, in *Proceedings of International Workshop XXIV on Gross Properties of Nuclei and Nuclear Excitations "Extremes of Nuclear Structure," Hirschegg, Austria, 1996* (GSI, Darmstadt, 1996), p. 35.
8. R. Smolańczuk, Phys. Rev. C **56**, 812 (1997).
9. P. Möller, J. R. Nix, and K.-L. Kratz, At. Data Nucl. Data Tables **66**, 131 (1997).
10. Yu. Ts. Oganessian *et al.*, in *Proceedings of 4th International Conference on Dynamical Aspects of Nuclear Fission, Častá-Papiernička, Slovak Republic, 1998* (World Sci., Singapore, 2000), p. 334; Yu. A. Lazarev *et al.*, in *Proceedings of International School—Seminar on Heavy Ion Physics, Dubna, Russia, 1993*, JINR Report E7-93-274 (Dubna, 1993), Vol. II, p. 497.
11. Yu. A. Lazarev *et al.*, JINR FLNR Scientific Report 1995/1996, E7-97-206 (Dubna, 1997), p. 30; Yu. Ts. Oganessian *et al.*, submitted to publication in Rhys. Rev. C.
12. K. Subotic *et al.*, Nucl. Instrum. Methods Phys. Res. A (to be published).
13. D. C. Hoffman *et al.*, Phys. Rev. C **31**, 1763 (1985).
14. N. J. Stoyer *et al.*, Nucl. Instrum. Methods Phys. Res. A **455**, 433 (2000).
15. V. B. Zlokazov, Eur. Phys. J. A **8**, 81 (2000).
16. K.-H. Schmidt *et al.*, Z. Phys. A **316**, 19 (1984).
17. A. G. Demin *et al.*, Z. Phys. A **315**, 197 (1984); G. Münzenberg *et al.*, Z. Phys. A **322**, 227 (1985).
18. Yu. A. Lazarev *et al.*, Phys. Rev. Lett. **73**, 624 (1994).
19. Yu. Ts. Oganessian *et al.*, Z. Phys. A **319**, 215 (1984); G. Münzenberg *et al.*, Z. Phys. A **324**, 489 (1986); F. P. Heßberger *et al.*, in *Proceedings of Tours Symposium on Nuclear Physics III, Tours, France, 1997* (AIP, New York, 1998), p. 3.
20. S. Hofmann *et al.*, Eur. Phys. J. A **10**, 5 (2001).
21. *Table of Isotopes*, Ed. by R. B. Firestone and V. S. Shirley (Wiley, New York, 1996, 8th ed.).
22. Yu. A. Lazarev *et al.*, Phys. Rev. Lett. **75**, 1903 (1995); Phys. Rev. C **54**, 620 (1996).
23. S. Hofmann *et al.*, Z. Phys. A **350**, 277 (1995); GSI Nachrichten GSI 02-95 (1995), p. 4; Z. Phys. A **350**, 281 (1995); **354**, 229 (1996).
24. A. Ghiorso *et al.*, Phys. Rev. C **51**, R2293 (1995).
25. V. Ninov *et al.*, Phys. Rev. Lett. **83**, 1104 (1999).
26. S. Hofmann and G. Münzenberg, Rev. Mod. Phys. **72**, 733 (2000).
27. W. D. Myers and W. J. Swiatecki, Nucl. Phys. A **601**, 141 (1996).
28. S. Ćwiok, W. Nazarewicz, and P. H. Heenen, Phys. Rev. Lett. **83**, 1108 (1999).
29. M. Bender, Phys. Rev. C **61**, 031302(R) (2000).
30. P.-G. Reinhard *et al.*, in *Proceedings of Tours Symposium on Nuclear Physics IV, Tours, France, 2000* (AIP, New York, 2001), p. 377.

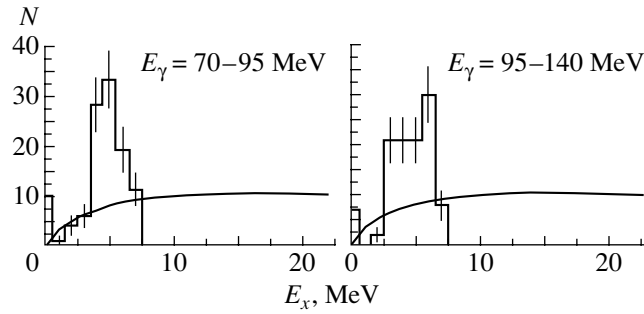


Fig. 1. Excitation-energy distribution of ^8Be intermediate nuclei. The histogram corresponds to experimental data. The solid curve represents the phase-space dependence [11].

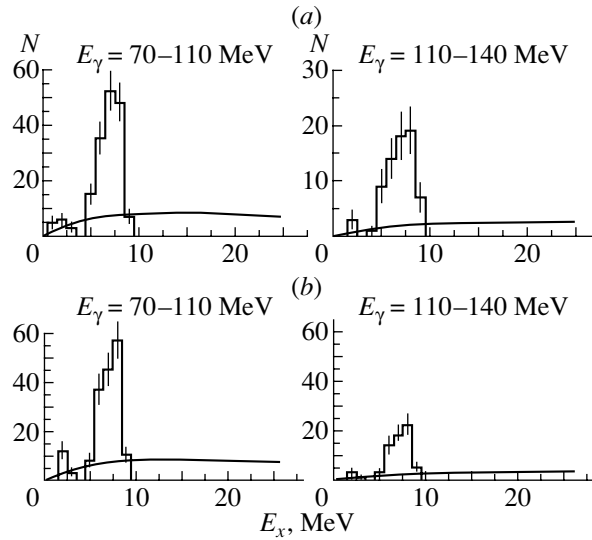


Fig. 2. Excitation-energy distribution of ^7Be intermediate nuclei under the assumption of the reaction channel (2): (a) the case where ^3He is the particle of highest energy and (b) the case where ^3He is the particle of lowest energy. The solid curve represents the phase-space dependence [11].

alpha particles and ^3He nuclei originating from the decay of ^{11}C intermediate nuclei will have the highest possible energy with respect to the same species of particles produced in the decay of ^7Be and ^8Be nuclei. Since the tracks of alpha particles and ^3He nuclei are virtually indistinguishable, there arises the problem of identifying these reaction channels. The results presented below are based on the statistics of 2466 events.

3. EXPERIMENTAL RESULTS

First, we plotted the excitation-energy distributions of ^8Be intermediate nuclei produced in the reaction channel (3) for two photon energy intervals. The excitation energy was defined as

$$E_x = E_0 - m_0, \quad (4)$$

where E_0 is the total reaction energy and m_0 is the rest mass of the nucleus.

In plotting the distributions, we assumed that ^3He is the particle of highest energy in the decay of ^{11}C intermediate nuclei. However, events of the reaction channel (2) can be a background in this case. In processing the total sample of events, we therefore assumed the reaction to proceed through channel (2) and eliminated events from the distributions that fall within following regions of ^7Be excitation energies: $E_x = 1-1.5$ MeV and $E_x > 5$ MeV. Figure 1 shows the results that we obtained, along with the phase-space dependences [11]

$$\frac{dN}{dE_x} = (E_x - E_x^{\min})^{\frac{3}{2}k - \frac{5}{2}} (E_x^{\max} - E_x)^{\frac{3}{2}(n-k) - 1}, \quad (5)$$

where n is the number of the particles in the final reaction state; k is the number of the particles used to plot the distributions; and E_x^{\min} and E_x^{\max} are, respectively, the minimum and the maximum value of the excitation energy. The phase-space dependences

were normalized to the area of the experimental distributions. From Fig. 1, we can see that the shape of the experimental distributions differs substantially from that of the phase-space dependences. However, the experimental distributions exhibit some maxima that can be identified with known ^8Be states [12].

Similarly, all selected events were analyzed under the assumption that the reaction under study proceeds through channel (2) involving the formation of a ^7Be intermediate nucleus in an excited state. In processing these events, we assumed that the alpha particle produced in the decay of a ^{11}C intermediate nucleus is one of the most energetic particles, and that ^3He and alpha particles produced in the decay of the ^7Be nucleus have the lowest energies. Further, the experimental excitation-energy distributions of ^7Be intermediate nuclei were plotted for the case where the ^3He nucleus is produced with an energy higher than that of the alpha particle and for the inverse case. A considerable contribution comes from events where the excitation energies of ^7Be nuclei are close to zero, indicating a background contribution of the reaction channel (3).

As in the preceding case, events that can correspond to ^8Be excitation energies in the regions $E_x = 0-1$ MeV and $E_x = 1.5-5$ MeV were therefore eliminated from the distributions. Figure 2 demonstrates the results that we obtained along with the phase-space dependences. In either case, the experimental distributions differ significantly in shape from the phase-space dependences. The maximum of the distributions occurs predominantly in the region $E_x > 5$ MeV; this complies with known data on the excited states of the ^7Be nucleus [12].

4. DISCUSSION OF THE RESULTS

The above data processing has revealed that the channels of the reaction being studied that involve the production of ^7Be and ^8Be intermediate nuclei can in principle be realized; that is, the mechanism of quasidirect interaction with ^{12}C nucleons is possible. Approximately equal numbers of events (about 240) associated with the reaction channels (2) and (3) were singled out from the total data sample featuring 2466 events.

For the reaction channel (2), the sampling of possible energy values of ^3He and alpha particles produced in ^7Be decay have demonstrated that the corresponding versions can hardly be discriminated because of the experimental errors and because of the

phase space. Nevertheless, qualitative isolation of the relevant reaction channel has been achieved.

That the reaction channels involving the production of ^{11}C intermediate nuclei and neutron emission are suppressed to a considerable extent in relation to the similar channels of the reaction $^{12}\text{C}(\gamma, pt)2\alpha$ suggests a substantial role of multiparticle correlations in the mechanism of the reaction under study. The same yield from the reaction channels (2) and (3) is also an indirect indication of this fact. Thus, our results and the previous experiments that studied the reaction $^{12}\text{C}(\gamma, pt)2\alpha$ furnish evidence for a possible contribution from the mechanism of quasidirect interaction with the S -shell nucleons of the carbon nucleus at high photon energies.

REFERENCES

1. V. N. Maïkov, Zh. Éksp. Teor. Fiz. **34**, 1406 (1958) [Sov. Phys. JETP **7**, 973 (1958)].
2. G. G. Taran, Yad. Fiz. **7**, 478 (1968) [Sov. J. Nucl. Phys. **7**, 301 (1968)].
3. V. I. Voloshchuk, I. V. Dogyust, V. V. Kirichenko, and A. F. Khodyachikh, Yad. Fiz. **49**, 916 (1989) [Sov. J. Nucl. Phys. **49**, 569 (1989)].
4. I. V. Dogyust, V. A. Zolenko, and V. V. Kirichenko, Yad. Fiz. **51**, 913 (1990) [Sov. J. Nucl. Phys. **51**, 583 (1990)].
5. V. G. Neudatchin, in *Proceedings of the VI Seminar on Electromagnetic Interactions at Low and Intermediate Energies, Moscow, 1985*, p. 109.
6. V. G. Neudatchin, and V. N. Orlin, Nucl. Phys. **31**, 338 (1962).
7. V. G. Neudatchin *et al.*, Phys. Lett. **10**, 180 (1964).
8. V. G. Neudatchin and Yu. F. Smirnov, *Nucleon Clusters in Light Nuclei* (Nauka, Moscow, 1969).
9. V. V. Balashov and V. N. Fetisov, Nucl. Phys. **27**, 337 (1961).
10. R. A. Golubev *et al.*, Preprint No. 92-30, KhFTI (Kharkov Institute for Physics and Technology, Kharkov, 1992).
11. A. M. Baldin *et al.*, *Kinematics of Nuclear Reactions* (Atomizdat, Moscow, 1968).
12. F. Aizenberg-Selove and T. Lauritsen, Nucl. Phys. A **227**, 1 (1974).

Translated by E. Kozlovskii

Logarithmic Corrections in m_1/m_2 to the Fine Shift of the S -Wave Energy Levels in the Muonium Atom

N. A. Boikova, S. V. Kleshchevskaya, Yu. N. Tyukhtyaev, and R. N. Faustov¹⁾,*

Saratov State University, Astrakhanskaya ul. 83, Saratov, 410071 Russia

Received May 25, 2000

Abstract—A $\alpha^5 \mu^3 (m_1 m_2)^{-1} (m_1/m_2) \ln (m_1/m_2)$ correction stemming from a consecutive exchange of a Coulomb and a transverse photon between the muon and the electron of the muonium atom is revealed and calculated (μ is the reduced mass of the system). Additional contributions of order $\alpha^6 \mu^3 (m_1 m_2)^{-1} \ln (m_1/m_2)$ due to one-photon exchange in the muonium atom are taken into account.
© 2001 MAIK “Nauka/Interperiodica”.

In recent years, much attention has been given to studying the spectra of hydrogen-like atoms. To a considerable extent, these studies have been motivated by the preparation and implementation of an experiment devoted to precisely measuring the $1S$ – $2S$ energy interval in the muonium atom. The current experimental value of this quantity is [1]

$$\Delta\nu_{1S2S}(\text{exp.}) = 2455528941.0(9.8) \text{ MHz.} \quad (1)$$

The relevant theoretical studies are comprehensively discussed in [2–4]. That the problem of calculating the spectrum of a hydrogen atom presents a real challenge is highlighted by long debates on the $\alpha^6 \ln \alpha$ logarithmic contribution to the fine shift of the S -wave levels in the muonium atom [2, 5–9]. It was found eventually that such corrections vanish. However, it is highly probable that there is a correction involving the logarithm of the parameter $\beta = m_1/m_2$. Contributions of order $\alpha^6 \mu^3 (m_1 m_2)^{-1} \beta \ln^2 \beta$ to the fine shift of the S -wave levels in the muonium atom were obtained in [10]. In further studying one-photon interaction, it was also demonstrated that there exist corrections exceeding this quantity by a factor of about β^{-1} .

Logarithmic corrections to the energy levels in the electron-to-muon mass ratio are essentially relativistic. According to [11], it is necessary, first of all, to analyze interactions whose contributions to the shift of energy levels is of order α^4 and higher. It is precisely the problem that is addressed in the present study.

In the quasipotential approach, the total logarithmic correction under investigation is determined by the expression

$$\begin{aligned} \Delta E_{nS} = & \langle \psi'_{nS} | (K_T)_{0F}^+ | \psi'_{nS} \rangle \\ & + \left\langle \psi'_{nS} \left| \left(K_C \overline{G_0 K_T} + \overline{K_T G_0} K_C \right)_{0F}^+ \right| \psi'_{nS} \right\rangle \quad (2) \\ & - \langle \psi'_{nS} | (K_T)_{0F}^+ F v_C | \psi_{nS} \rangle \\ & - \langle \psi_{nS} | v_C F (K_T)_{0F}^+ | \psi'_{nS} \rangle. \end{aligned}$$

where $v_C(p, q) = e_1 e_2 / (p - q)^2$ is the Coulomb potential and ψ_{nS} are eigenfunctions corresponding to S -wave states and satisfying the Schrödinger equation with the Coulomb potential,

$$\begin{aligned} \left(p^2 + \frac{\alpha^2 \mu^2}{n^2} \right) \psi_{nS}(p) &= \frac{\alpha \mu}{\pi^2} \int \frac{d^3 q}{(p - q)^2} \psi_{nS}(q), \\ \psi'_{nS}(p) &= \Omega_p \psi_{nS}(p), \\ \mu &= m_1 m_2 / (m_1 + m_2), \\ \Omega_p &= \frac{(\varepsilon_{1p} + m_1)(\varepsilon_{2p} + m_2)}{2\mu(\varepsilon_{1p} + \varepsilon_{2p} + m_1 + m_2)}, \quad (3) \\ \varepsilon_{ip} &= \sqrt{p^2 + m_i^2}, \quad i = 1, 2. \end{aligned}$$

Unless otherwise stated, the symbols p and q everywhere denote 3-vectors. We also use the following notation: K_C and K_T stand for the interactions associated with the exchange of a Coulomb and a transverse photon, respectively; G_0 is the free-particle Green's function of a free particle; the symbol $[\dots]^+$ is spelled out as $[\dots]^+ = u_1^* u_2^* [\dots] \gamma_{10} \gamma_{20} u_1 u_2$, where u_i is the Dirac bispinor corresponding to the i th particle; and

$$\overline{G}(p, q, E) = (2\pi)^{-2} \int G(p_0, q_0, p, q, E) dp_0 dq_0,$$

¹⁾Scientific Council for the Interdisciplinary Problem Cybernetics, Russian Academy of Sciences, ul. Vavilova 40, Moscow, 117967 Russia.

*e-mail: faustov@theory.npi.msu.su

$$F = \left(\overline{G_0^+} \right)^{-1}.$$

To the terms of order α^4 , the total energy of the system, E , is given by

$$E = E_1 + E_2 = m_1 + m_2 - \frac{\mu\alpha^2}{2n^2},$$

$$m_i^2 - E_i^2 = \frac{\mu^2\alpha^2}{n^2}, \quad E_i = m_i - \frac{\mu^2\alpha^2}{2m_i n^2}, \quad (4)$$

$$i = 1, 2.$$

Each term in expression (2) involves contributions to the energy-level shift that are proportional to α^4 . However, the corresponding contributions from two-photon exchanges and iteration terms cancel each other. This, however, does not imply that all possible corrections to α^4 terms vanish.

The logarithmic corrections in β that follow from expression (2) can be represented in the form

$$\Delta E_{\ln} = \frac{\alpha^5 \mu^3}{m_1 m_2} \quad (5)$$

$$\times (C_0 \beta \ln \beta^{-1} + C_1 \alpha \ln \beta^{-1} + C_2 \alpha \ln^2 \beta^{-1}).$$

Equations (3) and (4) allow one to reduce, with the required accuracy, the iteration terms from expression (2) to a quasipotential that describes one-photon exchange. To this accuracy, the quantity Ω_p can be written as

$$\Omega_p \approx \frac{p^2 + \alpha^2 \mu^2 / n^2}{2\mu (\varepsilon_{1p} - E_1 + \varepsilon_{2p} - E_2)}, \quad (6)$$

whence we obtain

$$\langle \psi_{nS} | v_C F (K_T)_{0F}^+ | \psi'_{nS} \rangle \quad (7)$$

$$= \langle \psi'_{nS} | (K_T)_{0F}^+ | \psi'_{nS} \rangle.$$

Proceeding to analyze the one-photon interaction in the muonium atom, we emphasize that, in the lowest orders of perturbation theory, some complicated integrals can be calculated by means of simple algebraic transformations.

In the general expression for the shift of the 1S level, we isolate two integrals

$$Q_1 = \alpha^6 \mu^3 \int \frac{d^3 p (\varepsilon_{1p} + m_1) (\varepsilon_{2p} + m_2)}{(\varepsilon_{1p} + \varepsilon_{2p} + m_1 + m_2) (p^2 + \omega^2)^2} \sqrt{\frac{\varepsilon_{1p} + m_1}{\varepsilon_{1p}}} \sqrt{\frac{\varepsilon_{2p} + m_2}{\varepsilon_{2p}}} \int \frac{d^3 q}{(q^2 + \omega^2)^2}$$

$$\times \frac{(\varepsilon_{1q} + m_1) (\varepsilon_{2q} + m_2)}{\varepsilon_{1q} + \varepsilon_{2q} + m_1 + m_2} \sqrt{\frac{\varepsilon_{1q} + m_1}{\varepsilon_{1q}}} \sqrt{\frac{\varepsilon_{2q} + m_2}{\varepsilon_{2q}}} \frac{1}{(\varepsilon_{1q} + m_1) (\varepsilon_{2q} + m_2)}$$

$$\times \left(1 - \frac{(p^2 - q^2)^2 p^4}{(p - q)^4 (\varepsilon_{1p} + \varepsilon_{1q}) (\varepsilon_{2p} + \varepsilon_{2q}) (\varepsilon_{1p} + m_1) (\varepsilon_{2p} + m_2)} \right), \quad (8)$$

$$Q_2 = \alpha^6 \mu^3 \int \frac{d^3 p (\varepsilon_{1p} + m_1) (\varepsilon_{2p} + m_2)}{(\varepsilon_{1p} + \varepsilon_{2p} + m_1 + m_2) (p^2 + \omega^2)^2}$$

$$\times \sqrt{\frac{\varepsilon_{1p} + m_1}{\varepsilon_{1p}}} \sqrt{\frac{\varepsilon_{2p} + m_2}{\varepsilon_{2p}}} \int \frac{d^3 q}{(q^2 + \omega^2)^2} \quad (9)$$

$$\times \frac{(\varepsilon_{1q} + m_1) (\varepsilon_{2q} + m_2)}{\varepsilon_{1q} + \varepsilon_{2q} + m_1 + m_2} \sqrt{\frac{\varepsilon_{1q} + m_1}{\varepsilon_{1q}}}$$

$$\times \sqrt{\frac{\varepsilon_{2q} + m_2}{\varepsilon_{2q}}} \frac{1}{(\varepsilon_{1q} + m_1) (\varepsilon_{2q} + m_2)},$$

where $\omega = \alpha\mu$.

The integral Q_1 converges owing to the parenthetical expression in the integrand. Each of these two integrals makes a contribution of order α^4 and involves, in addition, $\alpha^5 \mu^3 (m_1 m_2)^{-1} \ln \beta^{-1}$ logarithmic terms. These logarithmic terms could in principle substantially distort the basic result of Salpeter [12]. But in fact, it is necessary to calculate

the difference $Q_1 - Q_2$, which, upon integration with respect to the angular components of the vectors p and q , takes the form

$$Q_1 - Q_2 = (4\pi)^2 \alpha^6 \mu^3 \int_0^\infty \frac{p^2 dp}{(p^2 + \omega^2)^2}$$

$$\times \sqrt{\frac{(\varepsilon_{1p} + m_1) (\varepsilon_{2p} + m_2)}{\varepsilon_{1p} \varepsilon_{2p}}} \frac{1}{\varepsilon_{1p} + \varepsilon_{2p} + m_1 + m_2}$$

$$\times \int_0^\infty \frac{q^2 dq}{(q^2 + \omega^2)^2} \{ (\varepsilon_{1p} + m_1) (\varepsilon_{2p} + m_2)$$

$$- \frac{p^4}{(\varepsilon_{1p} + \varepsilon_{1q}) (\varepsilon_{2p} + \varepsilon_{2q})}$$

$$- (\varepsilon_{1p} + m_1) (\varepsilon_{2q} + m_2) \}$$

$$\times \sqrt{\frac{(\varepsilon_{1q} + m_1) (\varepsilon_{2q} + m_2)}{\varepsilon_{1q} \varepsilon_{2q}}} \frac{1}{\varepsilon_{1q} + \varepsilon_{2q} + m_1 + m_2}. \quad (10)$$

We now use the relation

$$\begin{aligned} & (\varepsilon_{1p} + m_1)(\varepsilon_{2p} + m_2) - (\varepsilon_{1p} + m_1)(\varepsilon_{2q} + m_2) \\ &= \left(2m_1 + \frac{p^2}{\varepsilon_{1p} + m_1}\right) \left(2m_2 + \frac{p^2}{\varepsilon_{2p} + m_2}\right) \quad (11) \\ & - \left(2m_1 + \frac{p^2}{\varepsilon_{1p} + m_1}\right) \left(2m_2 + \frac{q^2}{\varepsilon_{2q} + m_2}\right) \end{aligned}$$

and find that the p^4 or p^2q^2 terms in the integrand on the right-hand side of (10) yield, upon integration, a contribution of order α^6 and that the α^4 and $\alpha^5\mu^3(m_1m_2)^{-1}\ln\beta^{-1}$ contributions are canceled. As a consequence, one can proceed to compute integrals of higher orders in α .

Detailed calculations demonstrate that, in the muonium atom, one-photon exchange does not contribute in the order $\alpha^5\mu^3(m_1m_2)^{-1}\beta\ln\beta^{-1}$. However, contributions of this order may come from two-photon processes.

Let us consider the leading part of the correction from the consecutive exchange of a Coulomb and a transverse photon. We have

$$\begin{aligned} \Delta E &= \frac{\alpha^7\mu^5}{4\pi^6} \int \frac{d^3p}{(p^2 + \omega^2)^2} \int \frac{d^3q}{(q^2 + \omega^2)^2} \quad (12) \\ & \times \int \frac{d^3k}{(p-k)^2} F(k) \frac{1}{(k-q)^2} \frac{k^2}{\varepsilon_{1k}\varepsilon_{2k}}, \end{aligned}$$

where

$$\begin{aligned} F(k) &= \Omega_k f(k) = \frac{1}{\varepsilon_{1k} + \varepsilon_{2k} - E} \\ &= \frac{(\varepsilon_{1k} + m_1)(\varepsilon_{2k} + m_2)}{(k^2 + \alpha^2\mu^2)(\varepsilon_{1k} + \varepsilon_{2k} + m_1 + m_2)} \quad (13) \\ &= \frac{(\varepsilon_{1k} + m_1)(\varepsilon_{2k} + m_2)}{2(m_1 + m_2)(k^2 + \alpha^2\mu^2)} \\ & \quad - \frac{k^2}{2(m_1 + m_2)(k^2 + \alpha^2\mu^2)} \end{aligned}$$

is the free Green's function for the quasipotential equation; it appears to be a relativistic generalization of the analogous function associated with the Schrödinger equation and describes an intermediate virtual state of the two-particle system.

Having performed integration with respect to the angular components of the vectors p , q , and k in expression (12), we arrive at

$$\begin{aligned} \Delta E &= \frac{\alpha^5\mu^3}{\pi} \int_0^\infty \frac{dkk^4}{(k^2 + \alpha^2\mu^2)\varepsilon_{1k}\varepsilon_{2k}} \\ & \times \left[\frac{(\varepsilon_{1k} + m_1)(\varepsilon_{2k} + m_2)}{2(m_1 + m_2)(k^2 + \alpha^2\mu^2)} \quad (14) \right. \\ & \quad \left. - \frac{k^2}{2(m_1 + m_2)(k^2 + \alpha^2\mu^2)} \right]. \end{aligned}$$

The first term in the bracketed expression on the right-hand side of (14) involves the nonrelativistic part of the propagator and makes an α^4 contribution to the shift of $1S$ level. The second term is a relativistic correction, its contribution to the shift of the level being as follows:

$$\begin{aligned} \Delta E_R &= -\frac{1}{2\pi} \frac{\alpha^5\mu^3}{m_1 + m_2} \int_0^\infty \frac{dkk^6}{(k^2 + \alpha^2\mu^2)^3} \frac{1}{\varepsilon_{1k}\varepsilon_{2k}} \\ & \approx \frac{\alpha^5\mu^3}{m_1m_2} \frac{\beta}{1 + \beta} \ln\beta. \quad (15) \end{aligned}$$

Thus, the $\alpha^5\mu^3(m_1m_2)^{-1}\beta\ln\beta^{-1}$ contributions to the shifts appear as relativistic corrections to the leading contributions of order α^4 . We have shown that the leading contributions from the consecutive exchange of two transverse photons or from diagrams with intersecting photon lines are of order α^5 .

Contributions of order $\alpha^6\mu^3(m_1m_2)^{-1}\ln\beta^{-1}$ arise from the consecutive exchange of a Coulomb and a transverse photon. Here, we present a qualitative analysis of a typical expression that shows evidence for the existence of such a contribution. Let us consider the form

$$\begin{aligned} \Delta E_{\ln} &= \alpha^7\mu^3 \int \frac{d^3p}{(p^2 + \omega^2)^2} \frac{(\varepsilon_{1p} + m_1)(\varepsilon_{2p} + m_2)}{\varepsilon_{1p} + \varepsilon_{2p} + m_1 + m_2} \\ & \times \int \frac{d^3q}{(q^2 + \omega^2)^2} \frac{(\varepsilon_{2q} + m_2)}{\varepsilon_{1q} + \varepsilon_{2q} + m_1 + m_2} \quad (16) \\ & \times \int \frac{d^3k}{\varepsilon_{1k}\varepsilon_{2k}} \frac{(\varepsilon_{1k} + m_1)(\varepsilon_{2k} + m_2)^2}{\varepsilon_{1k} + \varepsilon_{2k} + m_1 + m_2} \\ & \times \frac{(kq)}{(k^2 + \alpha^2\mu^2)(\varepsilon_{2k} + \varepsilon_{2q})(\varepsilon_{1k} + \varepsilon_{1q})} \\ & \quad \times \frac{1}{(p-k)^2} \frac{(k^2 - q^2)^2}{(k-q)^4}. \end{aligned}$$

Without violating the convergence of the integral with respect to p , we can set

$$\frac{(\varepsilon_{1p} + m_1)(\varepsilon_{2p} + m_2)}{\varepsilon_{1p} + \varepsilon_{2p} + m_1 + m_2} \approx 2\mu \quad (17)$$

and perform integration:

$$\int \frac{d^3p}{(p^2 + \omega^2)^2} \frac{1}{(p-k)^2} = \frac{\pi^2}{\alpha\mu} \frac{1}{k^2 + \alpha^2\mu^2}. \quad (18)$$

A feature peculiar to integrals proportional to $\ln\beta^{-1}$ is that, because of divergences, one cannot get rid of the radicals depending on the heavy mass. Let us consider the integrals

$$i_1 = \int_0^\infty \frac{dpp}{(p^2 + m_1^2)\sqrt{p^2 + m_2^2}},$$

$$i_2 = \int_0^\infty \frac{dp}{(p^2 + m_1^2) \sqrt{p^2 + m_2^2}}. \quad (19)$$

The first integral involves $\ln \beta^{-1}$ terms, whereas the second does not involve such terms. The reason is that $\varepsilon_{2p}^{-1} = (p^2 + m_2^2)^{-1/2}$ cannot be replaced by m_2^{-1} in the first integral, but this can be done in the second.

In particular, it is possible to eliminate the radicals ε_{2p} , ε_{2q} , and ε_{2k} from the original expression (16) and recast the integral into the form

$$\Delta E_{\text{ln}} \approx \frac{\alpha^6 \mu^3}{m_1 m_2} \int \frac{d^3 k}{(k^2 + \delta^2)^2} \quad (20)$$

$$\times \int \frac{d^3 q (kq) (k^2 - q^2)^2}{(q^2 + \delta^2)^2 (\sqrt{k^2 + 1} + \sqrt{q^2 + 1}) (k - q)^4},$$

where $\delta = \alpha / (1 + \beta)$. Thus, we see that the original integral (16) does not involve contributions proportional to $\alpha^5 \mu^3 (m_1 m_2)^{-1} \ln \beta^{-1}$. Pursuing our analysis further, we test, for convergence, that part of the integral which involves the factor q^2 using the relation $2kq = q^2 + k^2 - (k - q)^2$. We have

$$\Delta E'_{\text{ln}} = 2\pi^2 \alpha^6 \mu^3 \int \frac{d^3 k}{(k^2 + \alpha^2 \mu^2)^2} \frac{1}{\varepsilon_{1k} \varepsilon_{2k}}$$

$$\times \frac{\varepsilon_{2k} + m_2}{\varepsilon_{1k} + \varepsilon_{2k} + m_1 + m_2} \int \frac{d^3 q q^2}{(q^2 + \alpha^2 \mu^2)^2}$$

$$\times \frac{\varepsilon_{2q} + m_2}{\varepsilon_{1q} + \varepsilon_{2q} + m_1 + m_2} \quad (21)$$

$$\times \frac{\varepsilon_{1k} + m_1}{\varepsilon_{1k} + \varepsilon_{1q}} \frac{\varepsilon_{2k} + m_2}{\varepsilon_{2k} + \varepsilon_{2q}} \frac{(k^2 - q^2)^2}{(k - q)^4}.$$

Without violating the convergence, we can set

$$\frac{\varepsilon_{2k} + m_2}{\varepsilon_{1k} + \varepsilon_{2k} + m_1 + m_2} \approx 1, \quad (22)$$

$$\frac{\varepsilon_{2q} + m_2}{\varepsilon_{2k} + \varepsilon_{2q}} \approx 1, \quad \frac{\varepsilon_{2k} + m_2}{\varepsilon_{2k}} \approx 2.$$

Since the integral with respect to the angular components of the 3-vector q is given by

$$\int \frac{d\Omega}{(k - q)^4} (k^2 - q^2)^2 = 4\pi, \quad (23)$$

we obtain

$$\Delta E'_{\text{ln}} \approx \frac{\alpha^6 \mu^3}{m_1 m_2} \beta \quad m_2^2 \int_0^\infty \frac{dq q^4}{(q^2 + \alpha^2 \mu^2)^2} \quad (24)$$

$$\times \frac{1}{\varepsilon_{1q} + \varepsilon_{2q} + m_1 + m_2}$$

$$\times \int_0^\infty \frac{dk k^2}{\varepsilon_{1k} (k^2 + \alpha^2 \mu^2)^2} \frac{\varepsilon_{1k} + m_1}{\varepsilon_{1k} + \varepsilon_{1q}}$$

$$\approx \frac{\alpha^6 \mu^3}{m_1 m_2} \beta \quad m_2^2 \int_0^\infty \frac{dq}{\varepsilon_{2q}} \int_0^\infty \frac{dk}{\varepsilon_{1k} + \varepsilon_{2q}} \frac{1}{k^2 + \alpha^2 \mu^2}.$$

The simple transformation

$$\frac{1}{(k^2 + \alpha^2 \mu^2) (\varepsilon_{1k} + \varepsilon_{1q})} \quad (25)$$

$$= \frac{1}{(k^2 + \alpha^2 \mu^2) (\varepsilon_{1q} + E_1)}$$

$$- \frac{1}{(\varepsilon_{1k} + E_1) (\varepsilon_{1q} + E_1) (\varepsilon_{1k} + \varepsilon_{1q})}$$

shows that expression (2) can be represented as the difference of the integrals

$$j_1 = \frac{\alpha^6 \mu^3}{m_1 m_2} \beta m_2^2 \int_0^\infty \frac{dq}{\varepsilon_{1q} \varepsilon_{2q}} \int_0^\infty \frac{dk}{k^2 + \alpha^2 \mu^2}, \quad (26)$$

$$j_2 = \frac{\alpha^6 \mu^3}{m_1 m_2} \beta m_2^2 \int_0^\infty \frac{dq}{\varepsilon_{1q} \varepsilon_{2q}} \int_0^\infty \frac{dk}{\varepsilon_{1k}^2}.$$

The first integral is of no interest because it makes a $\alpha^5 \mu^3 (m_1 m_2)^{-1} \ln \beta^{-1}$ contribution, which, as was shown above, is to be canceled by other terms in the resulting expression (16). Upon the substitutions $q = q' m_2$ and $k = k' m_2$, the second integral can be reduced to the form

$$j_2 = \frac{\alpha^6 \mu^3}{m_1 m_2} \beta \int_0^\infty \frac{dq}{\sqrt{q^2 + \beta^2} \sqrt{q^2 + 1}} \quad (27)$$

$$\times \int_0^\infty \frac{dk}{k^2 + \beta^2} \approx \frac{\alpha^6 \mu^3}{m_1 m_2} \ln \beta^{-1}.$$

Taking into account the above preliminary considerations, we can proceed to perform more detailed calculations. For the coefficients in expression (5) for the 1S and 2S levels, the results are

$$C_0 = \frac{1}{2\pi},$$

$$C_1 = \frac{1}{2\pi^2} \left(9 + \ln 2 - 4\sqrt{2} \ln \left(1 + \sqrt{2} \right) \right) \quad (28)$$

$$C_2 = 0$$

for 1S and

$$C'_{0,1,2} = \frac{1}{8} C_{0,1,2}$$

for 2S.

The integrals proportional to $\alpha^6 \mu^3 (m_1 m_2)^{-1} \times \ln^2 \beta^{-1}$ are presented in the Appendix.

With allowance for (28), the numerical value of the correction in (5) is

$$\Delta\nu_{1S2S} = 140.95 \text{ kHz.} \quad (29)$$

Thus, the contribution that we obtained is smaller than the experimental error in (1).

ACKNOWLEDGMENTS

We are grateful to S.N. Bagaev, V.I. Savrin, and O.A. Khrustalev for their interest in our study.

APPENDIX

Integrals proportional to $\alpha^6\mu^3(m_1m_2)^{-1}\ln^2\beta^{-1}$ (contributions of higher orders in α and β are omitted) are given by

$$\begin{aligned}
 I_1 &= \frac{\alpha^6\mu^3}{m_1} \int \frac{d^3q}{\varepsilon_{1q}(q^2 + \alpha^2\mu^2)} \\
 &\times \int \frac{d^3p}{\varepsilon_{1p}\varepsilon_{2p}} \frac{1}{(p-q)^2} = \frac{\alpha^6\mu^3}{m_1m_2} 2\pi^2 \ln^2\beta, \\
 I_2 &= \frac{\alpha^6\mu^3}{m_1} m_2 \int \frac{d^3q}{\varepsilon_{1q}(q^2 + \alpha^2\mu^2)} \\
 &\times \int \frac{d^3p}{\varepsilon_{1p}\varepsilon_{2p}(\varepsilon_{2p} + m_2)} \frac{1}{(p-q)^2} = \frac{\alpha^6\mu^3}{m_1m_2} 4\pi^2 \ln^2\beta, \\
 I_3 &= \frac{\alpha^6\mu^3}{m_1} \int \frac{d^3q}{\varepsilon_{1q}(\varepsilon_{1q} + m_1)} \frac{1}{(\varepsilon_{1q} + m_1)^2} \\
 &\times \int \frac{d^3p}{\varepsilon_{2p}(\varepsilon_{1p} + m_1)} \frac{1}{(p-q)^2} = \frac{\alpha^6\mu^3}{m_1m_2} 2\pi^2 \ln^2\beta, \\
 I_4 &= \frac{\alpha^6\mu^3}{m_1} \int \frac{d^3q}{\varepsilon_{1q}(\varepsilon_{1q} + m_1)} \frac{1}{(\varepsilon_{1q} + m_1)^2} \\
 &\times \int \frac{d^3p}{\varepsilon_{1p}\varepsilon_{2p}} \frac{1}{(p-q)^2} = \frac{\alpha^6\mu^3}{m_1m_2} 2\pi^2 \ln^2\beta,
 \end{aligned}$$

$$\begin{aligned}
 I_5 &= \frac{\alpha^6\mu^3}{m_1} m_2 \int \frac{d^3q}{\varepsilon_{1q}\varepsilon_{2q}(q^2 + \alpha^2\mu^2)} \\
 &\times \int \frac{d^3p}{\varepsilon_{2p}(\varepsilon_{1p} + \varepsilon_{1q})(p-q)^2} = \frac{\alpha^6\mu^3}{m_1m_2} 2\pi^2 \ln^2\beta.
 \end{aligned}$$

REFERENCES

1. V. Meyer, S. N. Bagaev, *et al.*, hep-ex/9907013.
2. K. Pachucki and H. Grotch, Phys. Rev. A **51**, 1854 (1995).
3. M. Eides, H. Grotch, and V. A. Shelyuto, hep-ph/0002158.
4. V. M. Shabaev, A. N. Artemyev, T. Beier, and G. Soff, J. Phys. B **31**, L337 (1998).
5. M. Doncheski, H. Grotch, and G. W. Erickson, Phys. Rev. A **43**, 2152 (1991).
6. I. B. Khriplovich and A. S. Yelkhovskiy, Phys. Lett. B **246**, 520 (1990).
7. R. N. Fell, Phys. Rev. Lett. **68**, 25 (1992).
8. R. N. Fell, I. B. Khriplovich, A. I. Milstein, and A. S. Yelkhovskiy, Phys. Lett. A **181**, 172 (1993).
9. A. S. Yelkhovskiy, Zh. Éksp. Teor. Fiz. **113**, 865 (1998) [JETP **86**, 472 (1998)].
10. N. A. Boikova, Yu. N. Tyukhtyaev, and R. N. Faustov, Yad. Fiz. **61**, 866 (1998) [Phys. At. Nucl. **61**, 781 (1998)].
11. Yu. N. Tyukhtyaev and R. N. Faustov, Soobshch. Ob'edin. Inst. Yad. Issled., Dubna, R2-86-281 (1986).
12. E. E. Salpeter, Phys. Rev. **87**, 328 (1952); G. W. Erickson, J. Phys. Chem. Ref. Data **6**, 833 (1977).

Translated by R. Rogalyov

Adiabatic Hyperspherical Approach to Describing Low-Energy Mesic-Atom Scattering*

D. I. Abramov¹⁾, V. V. Gusev²⁾, and L. I. Ponomarev

Russian Research Centre Kurchatov Institute, pl. Kurchatova 1, Moscow, 123182 Russia

Received April 7, 2000; in final form, July 17, 2000

Abstract—The adiabatic hyperspherical approach developed previously is used to describe the asymmetric mesic-atom scattering $a\mu + b \rightarrow a\mu + b$, $a + b\mu$ ($a, b = p, d, t$) in the collision-energy range $10^{-3} \leq \varepsilon \leq 10^2$ eV. Boundary conditions for $J \neq 0$ scattering states are formulated, and partial cross sections for $J = 0-3$ are calculated. Effective numerical codes are developed, and a fast convergence of the adiabatic hyperspherical approach is demonstrated: to achieve a precision of about 1% in the calculated cross sections, it is sufficient to use a basis of not more than ten adiabatic hyperspherical functions. The results that we obtained are compared with the previous ones. © 2001 MAIK “Nauka/Interperiodica”.

1. INTRODUCTION

In order to describe theoretically the kinetics of muon catalysis [1], it is necessary to know the cross sections of the mesic-hydrogen-isotope collision processes

$$a\mu + b \rightarrow a\mu + b, \quad (1a)$$

$$a\mu + b \rightarrow a + b\mu, \quad (1b)$$

where $a, b = p, d, t$. Some of the cross sections were calculated in the different approaches, including the approach based on Faddeev equations [2], the coupled-rearrangement-channel approach [3], the improved adiabatic approach [4], and the hyperspherical coupled-channel approach [5]. The most extensive and systematic calculations were performed in the adiabatic approach [6], which is based on the expansion of the wave function of the Coulomb three-body system in solutions of the two-center problem [7–9]. However, this expansion converges slowly because the asymptotic behavior of the two-center functions does not fit the boundary conditions at large internuclear distances. The continuous spectrum of the two-center problem contributes additional difficulties, especially for low-energy scattering.

The most promising method free from these disadvantages is the adiabatic hyperspherical approach (AHS), which was first proposed for describing the autoionizing states of He [10]. The underlying idea of this approach is the same as that of the adiabatic one,

but, in the AHS, the hyperradius $\rho \in [0, \infty)$ plays the role of a slow adiabatic variable. The methods based on the AHS are widely used at present in atomic and mesic-atomic physics (see, for example, [5, 11–16] and references therein). Its significant advantage for describing $2 \rightarrow 2$ scattering processes in the Coulomb three-body problem is a correct behavior of AHS basis functions at large distances between colliding fragments [17]. The original version of the AHS deals with the expansion of the three-body wave function in the AHS basis with coefficients that are continuous functions of ρ . In practical calculations, it is applied very rarely because of difficulties associated with numerous quasicrossings of AHS energy terms, where the nonadiabatic couplings have sharp extrema or jumps. One way to overcome these difficulties is the diabatic-by-sector (DBS) method [5, 13, 15] based on partitioning the entire region of ρ into a large number of small sectors. To improve the convergence of the DBS method, the hybrid scheme of AHS and DBS expansions was used, for example, in [5, 15].

We use the original version of the AHS (with a continuous ρ dependence) and demonstrate its efficiency. The algorithm developed here successfully overcomes difficulties associated with a slow decrease of the nonadiabatic matrix elements for $\rho \rightarrow \infty$, long-range nondiagonal couplings being taken into account [17]. Problems stemming from the quasicrossings of terms are solved by the variational approach to calculating AHS basis functions, nonadiabatic couplings, and hyperradial functions [11]. For nonzero angular momenta J , we use the reduced AHS (RAHS) basis [12, 18, 19], which allows one to simplify calculations and which coincides with the

*This article was submitted by the authors in English.

¹⁾St. Petersburg State University, Universitetskaya nab. 7/9, St. Petersburg, 199034 Russia.

²⁾Institute for High Energy Physics, Protvino, Moscow oblast, 142284 Russia.

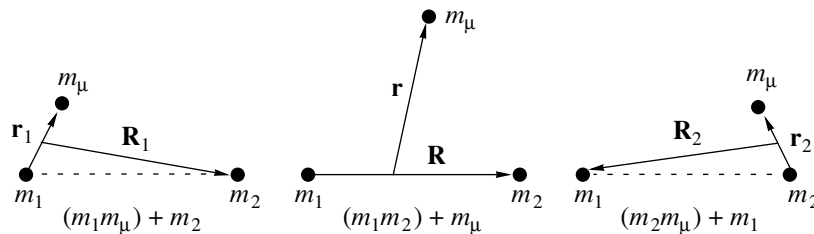


Fig. 1. Three pairs of Jacobi coordinates.

traditional AHS basis at $J = 0$. Basic points of our algorithm are described in [11, 12, 17]. It was successfully applied to calculating the energies and local characteristics of the bound [14, 19] and quasistationary [20, 21] states of muonic molecules; it was also used to perform preliminary calculations of the scattering cross sections in the $d\mu t$ system at $J = 0$ [22].

The objective of the present study is to calculate systematically partial-wave ($J = 0, 1, 2, 3$) and total cross sections for elastic-scattering and charge-exchange processes in asymmetric mesic atomic systems $d\mu t$, $p\mu t$, and $p\mu d$ at collision energies in the range $10^{-3} \leq \varepsilon \leq 10^2$ eV.

The results obtained demonstrate a fast convergence of the cross sections with increasing number of RAHS basis functions used and good agreement with the results of other studies. We present a systematic comparison of our results with the results from [6], which were obtained in the standard adiabatic approach [8]. A comparison with other results for the $d\mu t$ system is presented in [16].

2. FORMULATION OF THE PROBLEM IN THE RAHS APPROACH

In the Jacobi coordinates $\{\mathbf{R}, \mathbf{r}\}$ (see Fig. 1), the Hamiltonian for the system of three particles with charges $Z_1 = Z_2 = -Z_3 = 1$ and masses m_1, m_2 , and m_3 ($m_1 \geq m_2$) has the form

$$H = -\frac{1}{2M}\Delta_R - \frac{1}{2\mu}\Delta_r + V, \tag{2}$$

$$V = \frac{1}{R} - \frac{1}{r_1} - \frac{1}{r_2},$$

$$M^{-1} = m_1^{-1} + m_2^{-1}, \quad \mu^{-1} = 1 + (m_1 + m_2)^{-1},$$

where use is made of the mesic atomic units ($\hbar = e = m_\mu \equiv m_3 = 1$). Going over to the hyperspherical coordinates $\rho \in [0, \infty)$, $\chi \in [0, \pi]$, and $\vartheta \in [0, \pi]$,

$$\rho = (2MR^2 + 2\mu r^2)^{1/2},$$

$$\tan(\chi/2) = (\mu/M)^{1/2}r/R,$$

$$\cos \vartheta = (\mathbf{R}, \mathbf{r})/Rr,$$

and the Euler angles Φ, Θ , and φ , we obtain [12]

$$H = -\frac{1}{\rho^5} \frac{\partial}{\partial \rho} \rho^5 \frac{\partial}{\partial \rho} + \frac{\mathbf{J}^2 - 2(\mathbf{l}, \mathbf{J})}{\rho^2 \cos^2(\chi/2)} + h^R, \tag{3}$$

where h^R is the reduced AHS (RAHS) Hamiltonian

$$h^R = -\frac{4}{\rho^2 \sin^2 \chi} \left(\frac{\partial}{\partial \chi} \sin^2 \chi \frac{\partial}{\partial \chi} - \mathbf{l}^2 \right) + V(\rho, \chi), \tag{4a}$$

with \mathbf{l} and \mathbf{J} being, respectively, the muon angular momentum and the total angular momentum:

$$\mathbf{l} = -i[\mathbf{r}, \nabla_r], \quad \mathbf{J} = \mathbf{l} - i[\mathbf{R}, \nabla_R],$$

$$\mathbf{l}^2 = -\frac{1}{\sin \vartheta} \frac{\partial}{\partial \vartheta} \sin \vartheta \frac{\partial}{\partial \vartheta} - \frac{1}{\sin^2 \vartheta} \frac{\partial^2}{\partial \varphi^2}.$$

The RAHS Hamiltonian h^R differs (at $J \neq 0$) from the traditional AHS Hamiltonian h [10–13], which includes the Coriolis term:

$$h = h^R + \frac{\mathbf{J}^2 - 2(\mathbf{l}, \mathbf{J})}{\rho^2 \cos^2(\chi/2)}. \tag{4b}$$

We prefer the reduced version (4a), since the calculation of basis functions for $J \neq 0$ is simplified in this case [12].

The RAHS basis is defined as the set of functions $\Phi_{jm}^{JK\lambda}(\rho|\chi, \vartheta, \Phi, \Theta, \varphi)$, eigenfunctions of five operators $h^R, \mathbf{J}^2, J_3, J_3'^2$, and P simultaneously (J_3 and J_3' are the projections of \mathbf{J} onto the third axes of space-fixed and rotating frames, respectively, and P is the inversion of all coordinates). Every RAHS basis function depends on the hyperradius ρ parametrically and can be represented in the form

$$\begin{aligned} &\Phi_{jm}^{JK\lambda}(\rho|\chi, \vartheta, \Phi, \Theta, \varphi) \\ &= \varphi_{jm}(\rho|\chi, \vartheta) D_{Km}^{J\lambda}(\Phi, \Theta, \varphi), \end{aligned} \tag{5}$$

where $D_{Km}^{J\lambda}(\Phi, \Theta, \varphi)$ is a symmetrized Wigner D function; the indices $J = 0, 1, 2, \dots, K = 0, \pm 1, \dots, \pm J$, and $\lambda = \pm 1$ correspond to the integrals of the motion \mathbf{J}^2, J_3 , and P ; and $m^2 = 0, 1, \dots, J^2$ is the eigenvalue of $J_3'^2$. The functions $\varphi_{jm}(\rho|\chi, \vartheta)$ are solutions to the eigenvalue problem

$$h_m \varphi_{jm}(\rho|\chi, \vartheta) = E_{jm}(\rho) \varphi_{jm}(\rho|\chi, \vartheta),$$

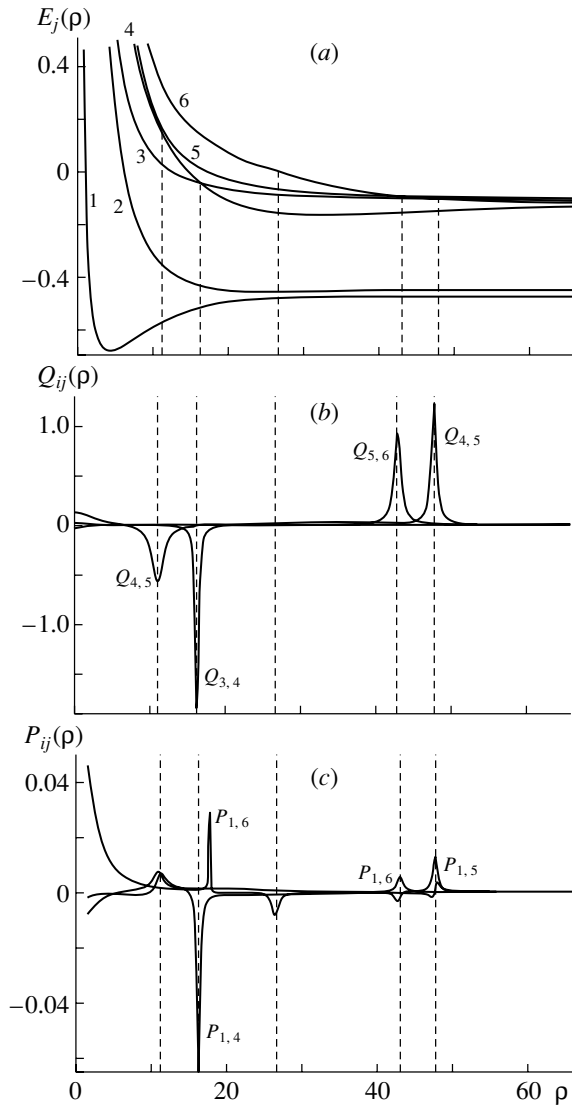


Fig. 2. (a) RAHS terms $E_j(\rho) \equiv E_{j0}(\rho)$ and matrix elements (b) $Q_{ij}(\rho) \equiv Q_{i0,j0}(\rho)$ and (c) $P_{ij}(\rho) \equiv P_{i0,j0}(\rho)$ for the $pd\mu$ system ($i, j = 1-6$). Avoided crossings look like exact crossings on the figure scale.

$$\begin{aligned}
 h_m &= h^R \left(-\frac{\partial^2}{\partial \varphi^2} \rightarrow m^2 \right) \\
 &= -\frac{4}{\rho^2 \sin^2 \chi} \left(\frac{\partial}{\partial \chi} \sin^2 \chi \frac{\partial}{\partial \chi} \right. \\
 &\quad \left. + \frac{1}{\sin \vartheta} \frac{\partial}{\partial \vartheta} \sin \vartheta \frac{\partial}{\partial \vartheta} - \frac{m^2}{\sin^2 \vartheta} \right) + V,
 \end{aligned} \quad (6)$$

where $E_{jm}(\rho)$ is the corresponding eigenvalue (RAHS energy term).

In our method, we construct the three-particle wave function with given quantum numbers J, K , and λ in the form of the decomposition in the RAHS basis:

$$\Psi^{JK\lambda}(\mathbf{r}, \mathbf{R}) = \rho^{-5/2} \quad (7)$$

$$\times \sum_{j=1}^{\infty} \sum_{m=0}^J f_{jm}^{J\lambda}(\rho) \Phi_{jm}^{JK\lambda}(\rho | \chi, \vartheta, \Phi, \Theta, \varphi).$$

The substitution of the expansion in (7) into the Schrödinger equation

$$(H - E) \Psi^{JK\lambda} = 0 \quad (8)$$

leads to a set of coupled differential equations for the hyperradial functions $f_{im}(\rho)$ [12]:

$$\begin{aligned}
 &\left(-\frac{\partial^2}{\partial \rho^2} + E_{im}(\rho) - E + \frac{15}{4\rho^2} \right) f_{im}(\rho) \\
 &+ \sum_{j=1}^{\infty} \sum_{m'=0}^J \left[P_{im,jm'}(\rho) + \frac{\partial}{\partial \rho} Q_{im,jm'}(\rho) \right. \\
 &\quad \left. + Q_{im,jm'}(\rho) \frac{\partial}{\partial \rho} + \frac{1}{\rho^2} R_{im,jm'}^J(\rho) \right] f_{jm'}(\rho) = 0.
 \end{aligned} \quad (9)$$

The nonadiabatic couplings $P_{im,jm'}(\rho)$, $Q_{im,jm'}(\rho)$, and $R_{im,jm'}^J(\rho)$ are integrals over the (χ, ϑ) plane that are defined and calculated in [12] (see Fig. 2).

To calculate the reaction matrix $K_{ij} = K_{ji}$ for the $2 \rightarrow 2$ process with n open channels (we label them with one index $i \equiv im, j \equiv jm'$), one has to obtain n linearly independent solutions ($i = 1, \dots, n$) corresponding to n input channels. The boundary conditions for these solutions are the following (index $j = 1, 2, \dots, \infty$ labels solution components):

$$\begin{aligned}
 f_j^i(\rho) &\underset{\rho \rightarrow 0}{=} 0, \quad j = 1, 2, \dots, \infty; \\
 f_j^i(\rho) &\underset{\rho \rightarrow \infty}{=} 0, \quad j = n+1, n+2, \dots, \infty;
 \end{aligned} \quad (10)$$

$$f_j^i(\rho) \underset{\rho \rightarrow \infty}{=} \delta_{ij} \sin(q_j \rho - \pi J/2)$$

$$+ (q_i/q_j)^{1/2} K_{ij} \cos(q_j \rho - \pi J/2), \quad j = 1, 2, \dots, n.$$

Here, $q_i^2 = \varepsilon_i$ is the kinetic energy of separated fragments in channel i :

$$q_i^2 \equiv \varepsilon_i = E - E_i(\infty). \quad (11)$$

The total cross sections for elastic ($i = j$) and inelastic ($i \neq j$) collisions are expressed in terms of K_{ij} . In the case of two open channels, we have [23]

$$\sigma_{ij} = \sum_{J=0}^{\infty} \sigma_{ij}^J = \frac{4\pi}{k_i^2} \sum_{J=0}^{\infty} (2J+1) \frac{\delta_{ij} (D^J)^2 + (K_{ij}^J)^2}{(1 - D^J)^2 + (F^J)^2}, \quad (12)$$

$$i, j = 1, 2,$$

where

$$D^J = K_{11}^J K_{22}^J - K_{12}^J K_{21}^J, \quad F^J = K_{11}^J + K_{22}^J,$$

$$k_i = (2\mu_i)^{1/2} q_i, \quad \mu_1^{-1} = (m_1 + 1)^{-1} + m_2^{-1},$$

$$\mu_2^{-1} = (m_2 + 1)^{-1} + m_1^{-1}.$$

Formula (12) is valid for one open channel as well. In this case, one has to substitute $K_{12}^J = K_{21}^J = K_{22}^J = 0$ and $K_{11}^J = \tan \delta^J$, δ^J being the phase shift.

The boundary conditions (10) are valid for the infinite system (9). In numerical calculations with a finite number N of Eq. (9), they must be modified.

3. BOUNDARY CONDITIONS AND NUMERICAL ALGORITHM

For $\rho \rightarrow \infty$, it is convenient to use the pairs of Jacobi coordinates $\{\mathbf{R}_\alpha, \mathbf{r}_\alpha\}$ labeled with the index of the corresponding nucleus $\alpha = 1, 2$ (see Fig. 1) and the reduced masses M_α and μ_α of the systems (m_α, m_μ) and $(m_\alpha, m_\mu) + m_\beta$ ($m_\beta = 1$):

$$\begin{aligned} M_\alpha^{-1} &= 1 + m_\alpha^{-1}, \\ \mu_\alpha^{-1} &= (m_\alpha + 1)^{-1} + m_\beta^{-1}, \quad (\alpha, \beta) = 1, 2. \end{aligned} \tag{13}$$

For $\rho \rightarrow \infty$, the two lowest terms $E_i(\rho), i = 1, 2$, tend to the energies of the ground state of isolated mesic atoms $(m_\alpha m_\mu), \alpha = 1, 2$.

The main advantage of the AHSA (RAHSA) for collision processes is that, for $\rho \rightarrow \infty$, each term of the decomposition in (7) reduces to the wave function of one specific channel with the correct reduced mass M_α of the bound pair $(m_\alpha m_\mu)$, the correct reduced mass μ_α of colliding fragments $(m_\alpha m_\mu) + m_\beta$, and the correct momentum k_α of relative motion of these fragments [17]. By way of example, we indicate that, for the $(m_\alpha, m_\mu) + m_\beta$ channel, we have, for $R_\alpha \rightarrow \infty, r_\alpha \ll R_\alpha$,

$$\begin{aligned} \rho &= (2MR^2 + 2\mu r^2)^{1/2} = (2M_\alpha r_\alpha^2 + 2\mu_\alpha R_\alpha^2)^{1/2} \\ &= (2\mu_\alpha)^{1/2} R_\alpha + O(R_\alpha^{-1}), \end{aligned} \tag{14}$$

$$\begin{aligned} E_\alpha(\infty) &= -\frac{M_\alpha}{2}, \quad \varepsilon_\alpha = E - E_\alpha(\infty), \\ q_\alpha \rho &= (2\mu_\alpha \varepsilon_\alpha)^{1/2} R_\alpha = k_\alpha R_\alpha. \end{aligned}$$

A numerical realization of the RAHSA involves calculating a finite number N of the basis functions $\varphi_{jm}(\rho|\chi, \vartheta)$ (5) and the matrix elements $P_{im,jm'}(\rho), Q_{im,jm'}(\rho)$, and $R_{im,jm'}^J(\rho)$ and solving the truncated set (9). Basis functions and matrix elements are calculated by the algorithm described in [11, 12]. Figure 2 illustrates special features of the calculated matrix elements caused by the quasicrossings of RAHS energy terms. Problems associated with these quasicrossings were successfully solved within the variational approach to calculating $\varphi_{jm}(\rho|\chi, \vartheta), P_{im,jm'}(\rho), Q_{im,jm'}(\rho), R_{im,jm'}(\rho)$, and $f_{im}(\rho)$ [11, 12].

Additional difficulties in numerically solving the set of Eq. (9) stem from a long-range character of the

nonadiabatic couplings $R_{im,jm'}(\rho)$ and from the need for modifying the boundary conditions (10) for finite N . This is especially important for calculating the K matrix at low collision energies, where it strongly depends on the behavior of the coupling matrix elements for $\rho \rightarrow \infty$. In what follows, we will consider only the scattering processes in the ground state. In this case, two channels only corresponding to mesic atoms $(m_\alpha, m_\mu), \alpha = 1, 2$, are open. The asymptotic expressions for the diagonal matrix elements corresponding to these channels are given by [17]

$$\begin{aligned} E_\alpha(\rho) &\underset{\rho \rightarrow \infty}{=} -\frac{M_\alpha}{2} - \frac{9}{2\rho^2}, \\ P_{\alpha\alpha}(\rho) &\underset{\rho \rightarrow \infty}{=} \frac{3}{4\rho^2}, \\ R_{\alpha\alpha}^J(\rho) &\underset{\rho \rightarrow \infty}{=} J(J+1) \frac{\mu}{M_\alpha}. \end{aligned} \tag{15}$$

Taking into account these relations and the asymptotic behavior of the nondiagonal matrix elements P_{ij}, Q_{ij} , and R_{ij} [17] and retaining only the leading terms in (9), we obtain the asymptotic form of the truncated set (9) for $\rho \rightarrow \infty$

$$\begin{aligned} \left(\frac{\partial^2}{\partial \rho^2} + \varepsilon_\alpha - \frac{J(J+1)}{\rho^2} \frac{\mu}{M_\alpha} \right) f_\alpha(\rho) \\ = \frac{1}{\rho^2} \sum_{j \neq \alpha, m}^N R_{\alpha 0, jm}^J(\rho) f_{jm}(\rho). \end{aligned} \tag{16}$$

We see that, at $J \neq 0$, the centrifugal potential $J(J+1)\mu/M_\alpha\rho^2$ differs from the correct form $J(J+1)/\rho^2$. This is a consequence of eliminating the Coriolis term from the RAHS Hamiltonian h^R (4a). As was shown in [17], the correct centrifugal term is reconstructed at $N \rightarrow \infty$ if the nondiagonal couplings $R_{ij} \sim \rho$ are taken into account near the threshold ($\sqrt{\varepsilon_\alpha} \rho \sim 1$). In this case, other couplings can be neglected and the set of Eqs. (16) can be diagonalized with a controlled precision of about m_α^{-3} [17]:

$$\begin{aligned} \left(\frac{\partial^2}{\partial \rho^2} + \varepsilon_\alpha - \frac{J(J+1)}{\rho^2} \frac{\mu}{M_\alpha} \right. \\ \left. + \frac{1}{\rho^4} \sum_{j \neq \alpha, m}^N \frac{|R_{\alpha 0, jm}^J(\rho)|^2}{E_j(\infty) - E_\alpha(\infty)} \right) f_\alpha(\rho) = 0. \end{aligned} \tag{17}$$

A further transformation can be performed by using the asymptotic behavior of $R_{\alpha 0, jm}(\rho)$ for $\rho \rightarrow \infty$ [17]. Specifically, we have

$$R_{\alpha 0, jm}^J \underset{\rho \rightarrow \infty}{=} \rho [J(J+1)(\mu - M_\alpha)]^{1/2} D_{\alpha 0, jm}, \tag{18}$$

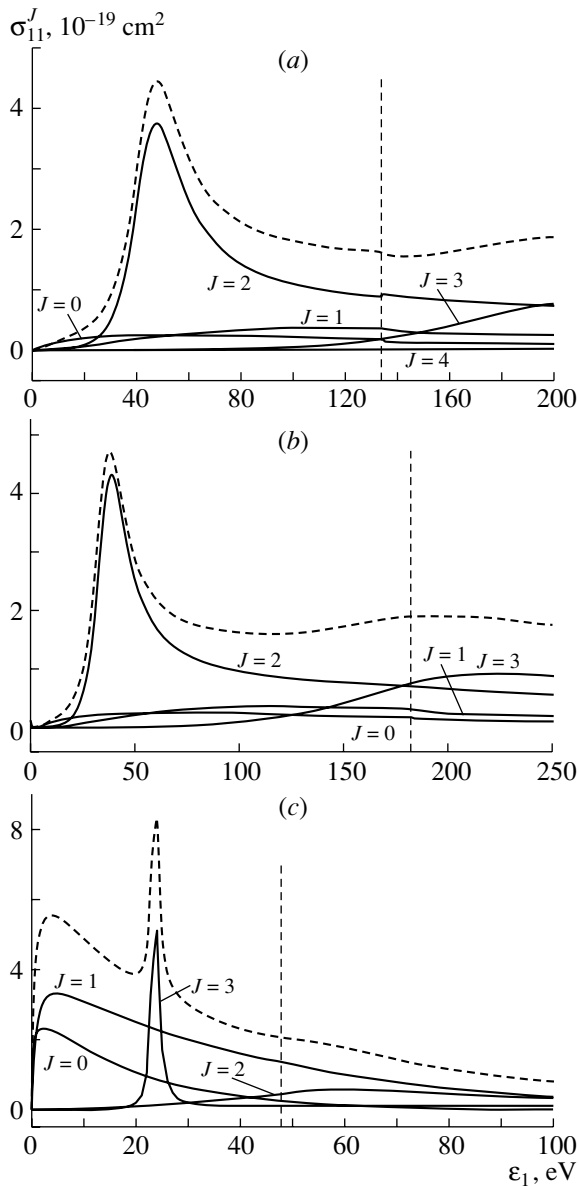


Fig. 3. Partial-wave $\sigma_{11}^J(\varepsilon_1)$ (solid curves) and total $\sigma_{11}(\varepsilon_1)$ (dashed curves) cross sections for the elastic-scattering processes (a) $d\mu + p \rightarrow d\mu + p$, (b) $t\mu + p \rightarrow t\mu + p$, and (c) $t\mu + d \rightarrow t\mu + d$. The vertical dashed lines indicate the inelastic-scattering threshold.

where $D_{\alpha 0, jm}$ is the matrix element of the derivative along the direction orthogonal to \mathbf{R}_α between two-dimensional (without azimuth variable) wave functions of atom α :

$$D_{\alpha 0, jm} = \frac{1}{M_\alpha} \langle \alpha 0 | \partial / \partial \tau | jm \rangle, \\ \tau_\alpha = r_\alpha \sin \vartheta_\alpha.$$

After the substitution of expression (18) into Eq. (17),

we have

$$\left[\frac{\partial^2}{\partial \rho^2} + \varepsilon_\alpha - \frac{J(J+1)}{\rho^2} \left(\frac{\mu}{M_\alpha} \right. \right. \\ \left. \left. + \left(1 - \frac{\mu}{M_\alpha} \right) \sum_{j \neq \alpha, m}^N \frac{2n_j^2 D_{\alpha 0, jm}^2}{n_j^2 - 1} \right) \right] f_\alpha(\rho) = 0, \quad (19)$$

where n_j is the principal quantum number of the corresponding atomic shell in the channel j . One can see now that, in the limit $N \rightarrow \infty$, the centrifugal potential takes the standard form $J(J+1)/\rho^2$, since the matrix elements $D_{\alpha 0, jm}$ satisfy the sum rule [17]

$$\Sigma_N = \sum_{j \neq \alpha, m}^N \frac{2n_j^2 D_{\alpha 0, jm}^2}{n_j^2 - 1} \underset{N \rightarrow \infty}{=} 1. \quad (20)$$

At finite N , the effective centrifugal potential can be written in terms of the effective angular momentum \tilde{J}_α defined by the relation

$$\frac{\tilde{J}_\alpha(\tilde{J}_\alpha + 1)}{\rho^2} \equiv \frac{J(J+1)}{\rho^2} \\ \times \left[1 + \left(\frac{\mu}{M_\alpha} - 1 \right) (1 - \Sigma_N) \right], \quad (21)$$

$$\tilde{J}_\alpha \underset{N \rightarrow \infty}{=} J.$$

At $N = 2$ and $n_j = n_\alpha = 1$, the disregard of higher states $n_j > 1$ leads to $\Sigma_N = 0$,

$$\tilde{J}_\alpha(\tilde{J}_\alpha + 1) = J(J+1) \frac{\mu}{M_\alpha} \\ = J(J+1) (1 + O(m_\alpha^{-1})), \quad (22)$$

at $m_\alpha \gg 1$. The contribution of the $n_j = 2$ shell can be calculated analytically:

$$\tilde{J}_\alpha(\tilde{J}_\alpha + 1) \\ = J(J+1) \left[1 + \left(\frac{\mu}{M_\alpha} - 1 \right) (1 - 16(2/3)^9) \right]. \quad (23)$$

At any value of N , the sum Σ_N can be calculated numerically by using the asymptotic relation (18) and the calculated matrix elements $R_{\alpha 0, jm}(\rho)$.

For $J = 0$, the leading term in the effective potentials in Eq. (8) is the polarization potential [24]

$$V(\rho) = -\frac{A_\alpha}{\rho^4}, \quad A_\alpha = \frac{9\mu_\alpha^2}{M_\alpha^3}. \quad (24)$$

Using the asymptotic expressions (19), (21), and (24), we obtain the asymptotic form of Eq. (9) for $\rho \rightarrow \infty$:

$$\left[-\frac{\partial^2}{\partial \rho^2} - q_\alpha^2 + \frac{\tilde{J}_\alpha(\tilde{J}_\alpha + 1)}{\rho^2} - \frac{A_\alpha}{\rho^4} \right] u_\alpha(\rho) = 0. \quad (25)$$

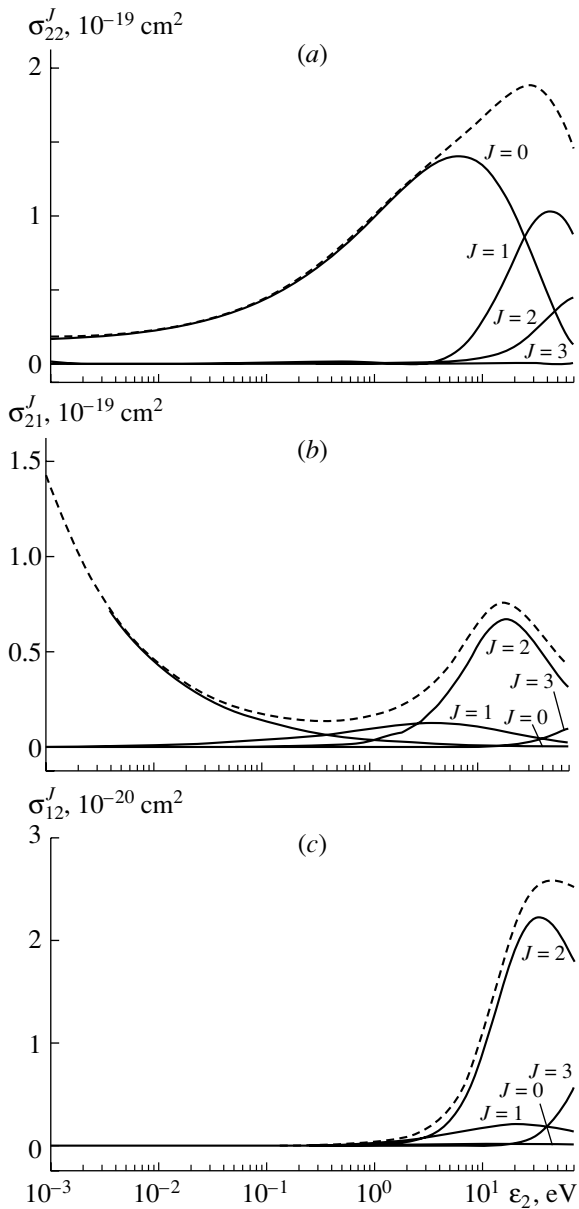


Fig. 4. (a) Partial-wave $\sigma_{22}^J(\varepsilon_2)$ (solid curves) and total $\sigma_{22}(\varepsilon_2)$ (dashed curves) cross sections for the elastic-scattering process $d\mu + t \rightarrow d\mu + t$, (b) cross sections $\sigma_{21}^J(\varepsilon_2)$ for the muon-transfer process $d\mu + t \rightarrow t\mu + d$, and (c) $\sigma_{12}^J(\varepsilon_2)$ for the reaction $t\mu + d \rightarrow d\mu + t$.

To solve the problem specified by Eqs. (9) and (10), we have developed a numerical algorithm based on the above analysis. By using a variable phase approach [25] and performing a numerical integration, we first construct, in the semi-interval $[\rho^*, \infty)$, $\rho^* \gg 1$, the reference functions $u_\alpha(\rho) = \{s_\alpha(\rho), c_\alpha(\rho)\}$ satisfying the boundary conditions

$$s_\alpha(\rho) \underset{\rho \rightarrow \infty}{=} \sin(q_\alpha \rho - \pi \tilde{J}_\alpha / 2), \quad (26)$$

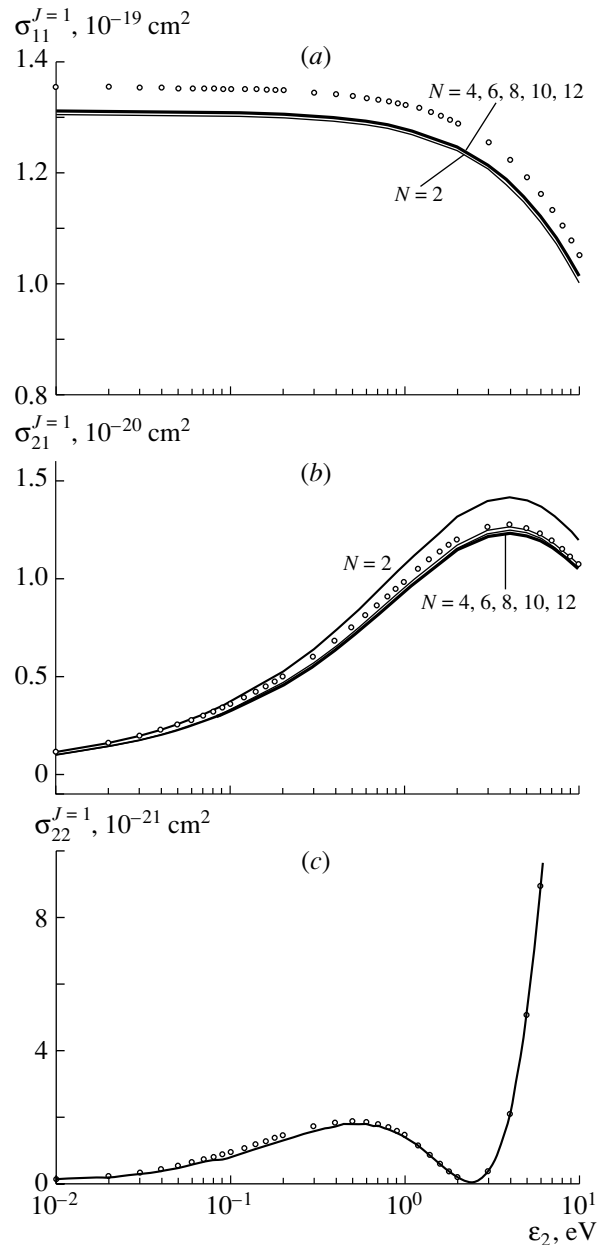


Fig. 5. Cross sections (a) $\sigma_{11}^{J=1}(\varepsilon_2)$ for the elastic-scattering process $t\mu + d \rightarrow t\mu + d$ and (b) $\sigma_{21}^{J=1}(\varepsilon_2)$ for the muon-transfer process $d\mu + t \rightarrow t\mu + d$ as calculated with different numbers N of RAHS basis functions; (c) cross section $\sigma_{22}^{J=1}(\varepsilon_2)$ for the elastic-scattering process $d\mu + t \rightarrow d\mu + t$ at $N = 12$. Circles represent the results from [6].

$$c_\alpha(\rho) \underset{\rho \rightarrow \infty}{=} \cos(q_\alpha \rho - \pi \tilde{J}_\alpha / 2).$$

The matrix $K_{\alpha\beta}$ and two linear independent solutions $f_i^\alpha(\rho)$ to the set of Eqs. (9) with two open channels ($\alpha = 1, 2$) are calculated with the boundary conditions at $\rho = 0$ and $\rho = \rho^* \gg 1$ (in practice $\rho^* =$

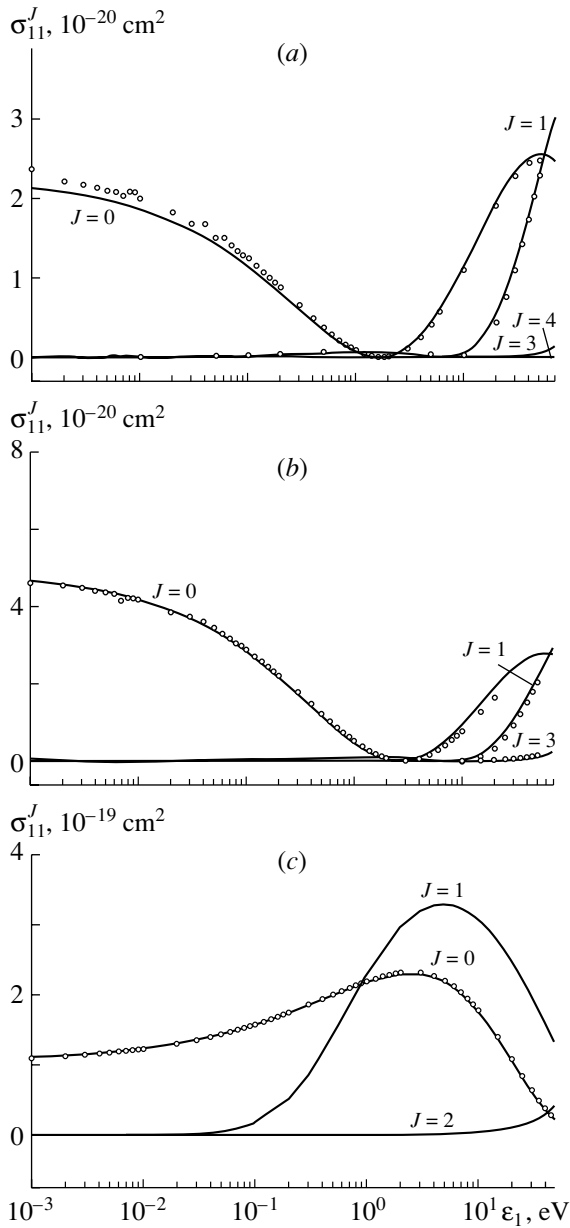


Fig. 6. Partial-wave cross sections $\sigma_{11}^J(\varepsilon_1)$ for the elastic-scattering processes (a) $d\mu + p \rightarrow d\mu + p$, (b) $t\mu + p \rightarrow t\mu + p$, and (c) $t\mu + d \rightarrow t\mu + d$. Circles represent the results from [6].

100):

$$f_i^\alpha(0) = 0, \quad i = 1, 2, \dots, N;$$

$$f_i^\alpha(\rho^*) = 0, \quad i = 3, 4, \dots, N;$$

$$f_\beta^\alpha(\rho^*) = \delta_{\alpha\beta} s_\beta(\rho^*) + (q_\alpha/q_\beta)^{1/2} K_{\alpha\beta} c_\beta(\rho^*), \quad (27)$$

$$(\alpha, \beta) = 1, 2.$$

The accuracy of the calculations was tested by fulfillment of the symmetry condition $K_{\alpha\beta} = K_{\beta\alpha}$, which follows from the unitarity of S matrix: $S = (1 +$

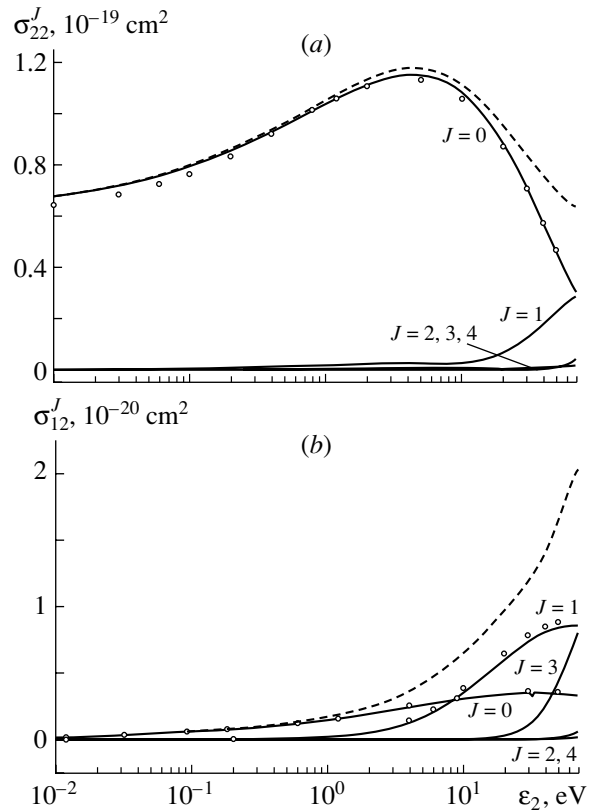


Fig. 7. (a) Partial-wave $\sigma_{22}^J(\varepsilon_2)$ (solid curves) and total $\sigma_{22}(\varepsilon_2)$ (dashed curves) cross sections for the elastic-scattering process $p\mu + d \rightarrow p\mu + d$ and (b) cross sections $\sigma_{12}^J(\varepsilon_2)$ for the muon-transfer process $d\mu + p \rightarrow p\mu + d$. Circles represent the results from [6].

$iK)(1 - iK)^{-1}$ (in our calculations $K_{\alpha\beta} - K_{\beta\alpha} \leq 10^{-4}$). The convergence is achieved by increasing ρ^* and N .

The disregard of the transformation $J \rightarrow \tilde{J}_\alpha$ in (27) would lead to the error $\Delta\delta^J = (J - \tilde{J}_\alpha)\pi/2 \approx \pi/2m_\alpha$ in the calculated phase shift δ^J . This correction is especially important in low-energy scattering, in which case $\delta \sim k^{2J+1}$ is very small, and in the region of the Ramsauer–Townsend effect.

4. RESULTS AND DISCUSSION

Figures 3–7 present the calculated partial-wave cross sections $\sigma_{\alpha\beta}^J$ ($\alpha, \beta = 1, 2$, $J = 0, 1, 2, 3$, solid curves) and total cross sections $\sigma_{\alpha\beta}$ (dashed curves) as functions of the scattering energy ε_α reckoned from the corresponding threshold $\varepsilon_\alpha \equiv q_\alpha^2$ (11). Traces of the threshold singularities are visible in Figs. 3a and 3b, but a correct analysis of the threshold behavior requires modifying the algorithm, but this is not the subject of the present study. Convergence of the results with increasing number N of basis functions

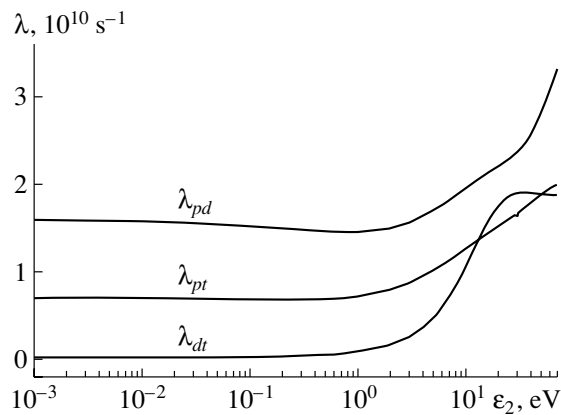


Fig. 8. Isotope-exchange rate $\lambda = \sigma_{21}vN_0$ (v is the relative velocity in the collision process, and $N_0 = 4.25 \times 10^{22} \text{ cm}^{-3}$ is the density of liquid hydrogen) for the processes $p\mu + d \rightarrow d\mu + p$ (λ_{pd}), $p\mu + t \rightarrow t\mu + p$ (λ_{pt}), and $d\mu + t \rightarrow t\mu + d$ (λ_{dt}).

used is demonstrated in Fig. 5. A comparison with the results presented in [6] (circles) is illustrated in Figs. 5–7; our values were obtained at $N = 12$. Figure 8 displays the calculated ε dependence of the isotope-exchange rate λ for all systems considered here. The values of λ calculated for the process $d\mu + t \rightarrow t\mu + d$ and the corresponding results of other calculations are compared in the table.

On the whole, our results are in good agreement with those from [6], where the standard adiabatic approach was used [7, 8], as well as with results from [16].

In the adiabatic representation based on two-center Coulomb functions, approximately 500 basis functions were required for obtaining a reasonable precision in calculating $\sigma_{ij}(\varepsilon)$ [6]. In the adiabatic hyperspherical approach, it is sufficient to use 6–10 basis functions (sometimes even 2) to achieve the same accuracy of the calculations (about 1%).

Isotope-exchange rate $\lambda = \sigma_{21}vN_0$ (in units of 10^8 s^{-1}) for the reaction $d\mu + t \rightarrow t\mu + d$

$\varepsilon_2, \text{ eV}$	[23]	[4]	[26]	[27]	[6]	Our study
0.001	–	–	–	2.7	2.26	2.35
0.01	–	–	2.6	2.7	2.31	2.38
0.04	1.9	3.5	2.7	2.9	2.46	2.50
0.1	–	–	2.7	3.2	2.78	2.77
0.4	–	–	–	5.0	4.58	4.37
1.0	–	–	–	8.9	8.69	8.09

The method developed here gives a regular way for describing low-energy scattering in other Coulomb three-body systems like $e^+e^-e^+$, $e^+\text{He}^+$, and $\bar{p}\text{He}^+$.

One of the significant results of this study is that we have been able to justify the calculation of Chiccoli *et al.* [6], who used the standard adiabatic approach. This is especially important because the atlas of mesic atomic cross sections [28] employed in all μCF -kinetics calculations is based on the results of the elaborate calculations from [6], which have never been confirmed systematically.

ACKNOWLEDGMENTS

We are deeply grateful to M.P. Faifman, S.S. Gersthein, V.I. Korobov, V.S. Melezhik, and O.I. Tolstikhin for stimulating discussions.

This work was supported by INTAS (grant no. 97-11032).

REFERENCES

- L. I. Ponomarev, *Contemp. Phys.* **31**, 219 (1990).
- A. A. Kvitsinsky, C. Y. Hu, and J. S. Cohen, *Phys. Rev. A* **53**, 255 (1996).
- Y. Kino and M. Kamimura, *Hyperfine Interact.* **82**, 45 (1993).
- J. S. Cohen and M. C. Struensee, *Phys. Rev. A* **43**, 3460 (1991).
- A. Igarashi, N. Toshima, and I. Shirai, *Phys. Rev. A* **50**, 4951 (1994).
- C. Chiccoli, V. I. Korobov, V. S. Melezhik, *et al.*, *Muon Catal. Fusion* **7**, 87 (1992).
- M. Born, *Nachr. Akad. Wiss. Göttingen* **1**, 1 (1951); M. Born and Huang Kun, *Dynamical Theory of Crystal Lattices* (Clarendon Press, Oxford, 1954).
- S. I. Vinitzky and L. I. Ponomarev, *Fiz. Élem. Chastits At. Yadra* **13**, 1336 (1982)[*Sov. J. Part. Nucl.* **13**, 557 (1982)].
- I. V. Komarov, L. I. Ponomarev, and S. Yu. Slavyanov, *Spheroidal and Coulomb Spheroidal Functions* (Nauka, Moscow, 1976).
- J. Macek, *J. Phys. B* **1**, 831 (1968).
- V. V. Gusev, V. I. Puzynin, V. V. Kostyrykin, *et al.*, *Few-Body Syst.* **9**, 137 (1990).
- D. I. Abramov, V. V. Gusev, and L. I. Ponomarev, *Yad. Fiz.* **60**, 1259 (1997) [*Phys. At. Nucl.* **60**, 1133 (1997)].
- C. D. Lin, *Phys. Rep.* **257**, 1 (1995).
- D. I. Abramov, L. N. Bogdanova, V. V. Gusev, and L. I. Ponomarev, *Hyperfine Interact.* **101/102**, 301 (1996); *Yad. Fiz.* **61**, 520 (1998) [*Phys. At. Nucl.* **61**, 457 (1998)].
- A. Igarashi, I. Shimamura, and N. Toshima, *Phys. Rev. A* **58**, 1166 (1998).
- O. Tolstikhin and C. Namba, *Phys. Rev. A* **60**, 5111 (1999).

17. D. I. Abramov, V. V. Gusev, and L. I. Ponomarev, Preprint No. IAE-6121/1 (Russian Research Centre Kurchatov Institute, Moscow, 1999).
18. D. I. Abramov, V. V. Gusev, and L. I. Ponomarev, in *Contributed Papers, 14th International Conference on Few-Body Problems in Physics, Williamsburg, 1994*, pp. 745, 749.
19. D. I. Abramov, V. V. Gusev, and L. I. Ponomarev, *Hyperfine Interact.* **101/102**, 375 (1996).
20. D. I. Abramov, V. V. Gusev, and L. I. Ponomarev, *Few-Body Syst., Suppl.* **10**, 57 (1999).
21. D. I. Abramov, V. V. Gusev, and L. I. Ponomarev, *Hyperfine Interact.* **119**, 127 (1999).
22. V. V. Gusev, L. I. Ponomarev, and E. A. Solov'ev, *Hyperfine Interact.* **82**, 53 (1993).
23. M. Bubak and M. P. Faifman, Preprint No. E4-87-464, OIYaI (Joint Institute for Nuclear Research, Dubna, 1987).
24. L. D. Landau and E. M. Lifshitz, *Quantum Mechanics: Non-Relativistic Theory* (Pergamon, Oxford, 1977).
25. V. V. Babikov, *Method of Phase Functions in Quantum Mechanics* (Nauka, Moscow, 1968).
26. V. S. Melezhik, *Muon Catal. Fusion* **2**, 117 (1988).
27. M. Kamimura, *Muon Catal. Fusion* **3**, 335 (1988).
28. A. Adamcak, M. P. Faifman, V. I. Korobov, *et al.*, *At. Data Nucl. Data Tables* **62**, 255 (1996).

Precision Neutrons in the Fission of ^{235}U and ^{252}Cf Nuclei

N. V. Kornilov*, A. B. Kagalenko, and F.-J. Hamsch¹⁾

Institute of Physics and Power Engineering, pl. Bondarenko 1, Obninsk, Kaluga oblast, 249020 Russia

Received November 2, 1999; in final form, September 12, 2000

Abstract—Experimental data obtained previously for the energy–angular distribution of neutrons originating from the fission of ^{252}Cf (spontaneous fission) and ^{235}U (thermal-neutron-induced fission) nuclei are analyzed, the angle being measured with respect to the direction of fission-fragment motion. A regularity common to all independent experiments is revealed: at an angle of about 90° , there exists an excess of neutrons (30% for ^{252}Cf and 60% for ^{235}U) that does not admit explanation within the model of neutron emission from fully accelerated fragments. Two possible explanations of this experimental fact—neutron emission during the acceleration process and the existence of an additional source of neutrons (predominantly, precision neutrons)—are considered. It is shown that the latter conjecture describes the observed features for both nuclei more adequately. The total yield of precision neutrons and their energy and angular distributions are determined. © 2001 MAIK “Nauka/Interperiodica”.

1. INTRODUCTION

Many experimental and theoretical studies were devoted to exploring neutron emission in the nuclear-fission process (for an overview, see, for example, [1]). Since the pioneering study of Bowman *et al.* [2], who demonstrated that there is a 10% excess of neutrons over the value ensured by the traditional mechanism of neutron emission from fully accelerated, excited fission fragments, the problem of contributions from various neutron-emission mechanisms and the problem of an extra source of neutrons have attracted the attention of researchers. In the theoretical analyses of Fuller [3] and Boneh and Fraenkel [4], the observed excess of neutrons was attributed to their emission occurring, because of a fast nonadiabatic change in the nuclear potential, as a fissile system descends from the saddle to the scission point, whence the commonly accepted term of precision neutrons for these particle species derives. It was shown in [4] that, for the emission of about 0.4 neutrons per fission event to occur, it is necessary that the descent time be about 1.5×10^{-21} s.

Over more than 30 years from the appearance of the study reported in [2], a vast body of relevant experimental data has been obtained, including both those that confirm a large contribution (10–15%) of precision neutrons for ^{252}Cf [5–8] and ^{235}U [9–11] and those that disprove its existence [12, 13]—more precisely, those that establish an upper limit on their contribution at a level of 1–3%. Later on, the

point of view of Butz-Jørgensen and Knitter [13] and of Brosa and Knitter [14], who argued that the fraction of precision neutrons is $1.1 \pm 0.3\%$ and that their mean energy is 0.39 ± 0.06 MeV, was adopted. This conclusion had a pronounced impact on the understanding of fission dynamics. Relying on data from experiments with heavy-ion reactions and on conclusions drawn in [13, 14] for low-energy fission, Hilscher and Fröbrich [15] deduced that fission is a rather slow process whose duration is 10^{-20} – 10^{-19} s.

In fact, experimental data from [13] do not exhibit glaring deviations from those in [5–8]; as was shown in [16], the conclusion that there are no precision neutrons, which was drawn at the stage of preliminary data processing [13], is insufficiently substantiated. A full realization of this fact provoked interest in this problem and gave us an incentive [17] to reanalyze the experimental data from [13].

A small fraction of precision neutrons and the absence of any spectacular features in the angular and energy distributions of neutrons hinder substantially the investigation of the aforementioned problems. Therefore, it is necessary above all to prove the very fact that extra neutrons exist and that the effect in question is not due to systematic experimental uncertainties and (or) an erroneous data analysis. Only following this would it be reasonable to develop models for explaining the effect.

The present study is devoted to solving precisely these problems. Here, we describe the results obtained from an analysis of the experimental angular

¹⁾IRMM, Retieseweg, Geel, Belgium

*e-mail: kornilov@ippe.rssi.ru

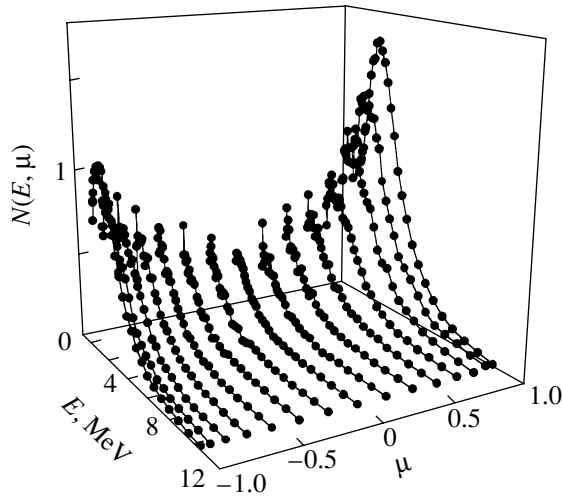


Fig. 1. Angular (with respect to the direction of fission-fragment motion) and energy distributions of neutrons [2].

and energy distributions of neutrons in the spontaneous fission of ^{252}Cf and the thermal-neutron-induced fission of ^{235}U , the angle in the angular distribution being measured with respect to the direction of fission-fragment motion.

The ensuing exposition is organized as follows. In Section 2, we demonstrate that there is indeed an excess of neutrons above the value predicted by the model of neutron emission from fully accelerated fragments. In Section 3, this excess is analyzed in terms of a model allowing for neutron emission prior to fragment acceleration. In Section 4, we perform an analysis and present its results for the case where it is assumed that there exists an extra source of neutrons. In the Conclusion, we summarize our results and give some recommendations.

2. EXPERIMENTAL CORROBORATION OF A NEUTRON EXCESS OVER THE PREDICTIONS OF THE TRADITIONAL MODEL

The experiments analyzed here measured the angular and energy distributions of neutrons, the angle in the former being reckoned from the direction of fission-fragment motion in the laboratory frame. A characteristic two-dimensional distribution is displayed in Fig. 1 (here and below, the light fragment travels in the positive direction of the cosine axis). If the assumptions underlying the model of neutron emission from fully accelerated fragments are valid, the number of neutrons for each specific fission fragment that are recorded at energy E_i and the cosine μ_i of the angle between the direction of motion of a given

fragment and the neutron-momentum direction in the laboratory frame, $N_{ij} = N(E_i, \mu_j)$, is given by

$$N_{ij} = \varphi(\mu_{ij}^c) \Phi(\varepsilon(E_i, \mu_j^l, E_v)) \frac{\sqrt{E_i}}{\sqrt{\varepsilon(E_i, \mu_j^l, E_v)}},$$

$$\varphi(\mu_{ij}^c) = (4\pi)^{-1} (1 + bP_2(\mu_{ij}^c)), \quad (1)$$

$$\mu_{ij}^c = \frac{\mu_j^l \sqrt{E_i} - \sqrt{E_v}}{\sqrt{\varepsilon(E_i, \mu_j^l, E_v)}},$$

$$\varepsilon = E_i + E_v - 2\mu_j^l \sqrt{E_i E_v},$$

where the indices l and c label relevant quantities referring to, respectively, the laboratory and the c.m. frame; E_v is the energy of a nucleon comoving with the c.m. frame; μ is the cosine of the angle between the direction of fission-fragment motion and the neutron momentum; ε is the neutron energy in the c.m. frame; $P_2(\mu)$ is a second-order Legendre polynomial; and $\Phi(\varepsilon)$ and $\varphi(\mu)$ are, respectively, the spectrum of neutrons and their angular distribution in the c.m. frame.

We define the function F_{ij} via the relation

$$F_{ij} = N_{ij} \frac{\sqrt{\varepsilon(E_i, \mu_j^l, E_v)}}{\varphi(\mu_{ij}^c) \sqrt{E_i}}. \quad (2)$$

If the parameters b and E_v are known, we can evaluate the spectrum of neutrons in the c.m. frame:

$$F_{ij} = \Phi(\varepsilon(E_i, \mu_j^l, E_v)). \quad (3)$$

It was shown in [18] that the angular anisotropy is small, $b \sim 2 \times 10^{-2}$; that is, neutron emission is virtually isotropic in the c.m. frame. Thus, we can see that, knowing the quantity E_v , we can calculate, on the basis of experimental data measured at any neutron-emission angle, the c.m. neutron spectrum as given by Eqs. (2) and (3) and, after that, reconstruct, with the aid of Eq. (1), the angular and energy distribution of neutrons in the laboratory frame. It should be emphasized that, in fact, nothing but the assumption that neutrons are emitted from fully accelerated fragments is invoked in doing this.

Relation (1) makes it possible to reveal easily the special features of the observed neutron distributions. The spectrum $\Phi(\varepsilon)$ is close to a Maxwell distribution characterized by a mean energy of $\langle \varepsilon \rangle \sim 1.3$ MeV, while $E_v \sim 0.7$ MeV. In order to obtain a neutron of preassigned energy E in the laboratory frame at an emission angle of 90° , it is therefore necessary to have a much higher c.m. emission energy than at zero angle. This feature and the fast decaying energy spectrum $\Phi(\varepsilon)$ explain the strong asymmetry of experimental data. The quantity E_v and the number of secondary neutrons are greater for a light fragment than for the complementary heavy one. These

distinctions are manifested in the asymmetry of the distribution shown in Fig. 1.

For a pair of fragments, a light and a heavy one, with masses A_l and A_h , we have $E_{vl} = \text{TKE} \frac{A_h}{A A_l}$ and $E_{vh} = \text{TKE} \frac{A_l}{A A_h}$, where $A = A_l + A_h$ and TKE is the total kinetic energy of fission fragments. The fission process results in the formation of a large set of fragments distributed with respect to masses and kinetic energies. The shape of the neutron spectrum in the c.m. frame and the number of neutrons depend on the fragment mass and on the TKE. For ^{252}Cf , it was shown in [17] that a transition from actual distributions to the model of two fragments, a light and a heavy one, with mean values of E_v , has but a slight effect on the angular and energy distribution of neutrons and on the results of the analysis; this can be taken into account by reducing E_v by about one to two percent. In the following, we therefore use the two-fragment model with the parameters set to the following values: $A_l = 109$, $A_h = 143$, $\text{TKE} = 184.1$ MeV [19], $E_{vl} = 0.951$ MeV, and $E_{vh} = 0.542$ MeV for ^{252}Cf (a correction for the transition to the two-fragment model was taken into account here) and $A_l = 96$, $A_h = 140$, $\text{TKE} = 168.6$ MeV [20], $E_{vl} = 1.042$ MeV, and $E_{vh} = 0.490$ MeV for ^{235}U (no correction was introduced here).

For our analysis, we made use of the data from [2, 8, 13] on ^{252}Cf and the data from [9] on ^{235}U . Data from other studies were not available in a numerical form that is appropriate for our analysis. In [2, 8, 9], the authors argued that it is necessary to include precission neutrons in the fission-process model, while, in [13], Butz-Jørgensen and Knitter advocated the opposite point of view.

Let us consider basic features of the experiments being discussed and of the analysis of data from these experiments. In [2, 9, 13], the neutron spectra were measured by the time-of-flight method; in [8], a single-crystal spectrometer for neutrons on the basis of an organic scintillator was used for this purpose. Schemes for suppressing photons were employed in [8, 13], in contrast to [2, 9]. In [2, 8, 9], the efficiency of the neutron detectors used was determined with respect to the integrated spectra of neutrons, while, in [13], this was done by invoking the dependence calculated by the Monte Carlo method. In [2, 8, 9], the angle between the direction of fragment motion and the neutron momentum was specified by the position of the neutron detector with respect to the fission-fragment detectors. In [13], this angle was established on the basis of the momentum analysis in a double fission chamber equipped with grids. A

detailed measurement of the angle and the statistical-accuracy level achieved there (factor of 2π) single out that study among all others.

In [2], the spectra of neutrons emitted by fission fragments following their acceleration were described by a superposition of evaporation spectra whose parameters were chosen by fitting experimental data. Within this approach, however, the authors of [2] were unable to remove the discrepancies between the calculated and measured angular distributions. On this basis, they concluded that there is a 10% contribution of precission neutrons whose mean energy was estimated at about 2.6 MeV. A similar approach was applied in [9], so that the conclusion about the yield of precission neutrons was model-dependent there.

The procedure used to analyze experimental angular and energy distributions [13] in the laboratory frame consisted in calculating the experimental angular distribution in the laboratory frame, $r_{\text{exp}}(E) = N(E, 90^\circ) / N(E, 0^\circ)$, and in comparing it with the model function $r_{\text{cal}}(E)$. In doing this, the authors of that study assumed that the spectra of neutrons from fully accelerated fragments in the c.m. frame are described by a Maxwell distribution with the parameter values from the study of Terrel of 1962 ($T_l = T_h = 0.94$ MeV and $E_{vl} = E_{vh} = 0.74$ MeV; see references in [13, 16]). As a check on this, we repeated anew the calculations of the angular anisotropy. Figure 2 displays experimental data taken from Fig. 6 of [13] and the results of our calculations with this parameter set (solid curve). Our results proved to be in agreement with the dependence obtained in the original study and confirmed the obvious conclusion of the authors that the contribution of precission neutrons is small and can be disregarded in data analysis. Upon drawing this conclusion, the authors of [13] recast all the recorded events into the c.m. frame and analyzed them in terms of the model of neutron emission from fully accelerated fragments.

However, the parameter values obtained in [16] on the basis of experimental data from [13] differ substantially from the old Terrell set ($T_l = 0.947$ MeV, $T_h = 0.850$ MeV, $E_{vl} = 0.979$ MeV, $E_{vh} = 0.569$ MeV). The calculation of the anisotropy with these values is illustrated by the dotted curve in Fig. 2. If the authors of [13] had performed such a calculation and obtained the same dependence, they would have undoubtedly arrived at a totally different conclusion about the presence of precission neutrons and would have used a different approach to processing experimental results. Moreover, they did not study the effect associated with the choice of a Maxwell distribution. As a matter of fact, it was assumed a priori in [13] that there are no extra neutrons.

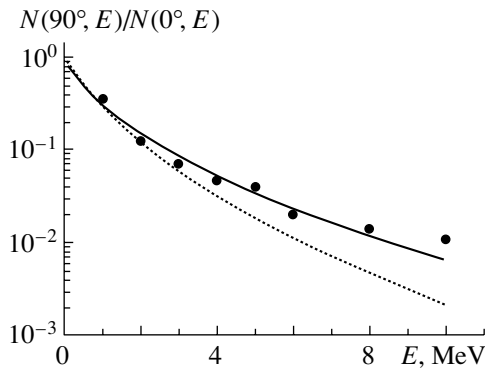


Fig. 2. Anisotropy of the neutron yield as a function of the laboratory neutron energy. Points represent experimental data from [13]. Theoretical results were obtained on the basis of calculations within the model of neutron emission from fully accelerated fragments with the parameters (solid curve) set to values from the Terrell systematics and (dotted curve) obtained from an analysis of the data from [13].

Seregina [8] employed a more consistent method for data analysis. Without specifying the shape of the spectrum of neutrons from fission fragments, she employed the spectrum of neutrons at small angles and relations (1)–(3) to compute the spectra of neutrons corresponding to the dominant mechanism of neutron emission at an angle of 90° and determined the total yield and spectra of prescission neutrons as the difference of the experimental and the calculated spectrum at 90° . Since the spectra were measured in [8] only for two angles in the laboratory frame, an isotropic distribution of prescission neutrons was assumed there.

In our analysis, we have used here a method similar to that adopted in [8], since it is free from restrictive assumptions and is therefore the most reliable.

In order to remove systematic experimental uncertainties associated with a determination of the efficiency of neutron detectors, a distortion of the spectra due to the spectrometer resolution, and other neutron-energy-dependent factors, we introduced an additional correction. The experimental distributions were integrated with respect to the angles, and the correcting function by which we divided experimental

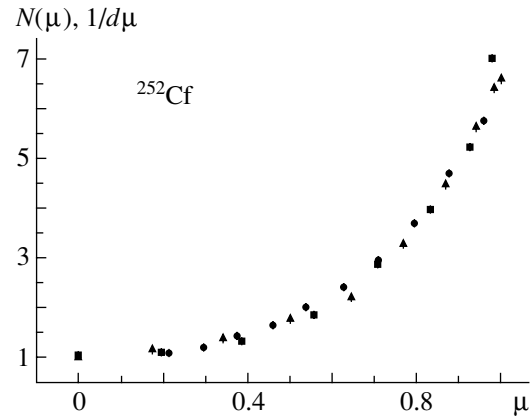


Fig. 3. Angular distribution of neutrons (in terms of the cosine of the angle) that is integrated from 1 to 5 MeV in the laboratory frame. The results represented by boxes, triangles, and circles correspond to data from [2], [8], and [13], respectively.

values was calculated on the basis of the relation

$$\zeta(E) = \frac{\int_{-1}^1 N(E, \mu) d\mu}{\nu S_{\text{st}}(E)}, \quad (4)$$

where $\nu^{\text{Cf}} = 3.766$, $\nu^{\text{U}} = 2.347$ [21], and $S_{\text{st}}(E)$ stands for the standard spectra of prompt fission neutrons for ^{252}Cf [22] and ^{235}U [23]. Moreover, the original data from [13] were corrected for neutron scattering in the material of the fission chamber used to record fission fragments.

A quantitative comparison of data represented as two-dimensional distributions is difficult; therefore, these distributions were integrated with respect to energy over the most reliable interval (from 1 to 5 MeV) and were recast into the form used by Seregina [8], who fixed only the direction of fission-fragment motion without a separation in mass. The angular distributions for ^{252}Cf that were obtained in this way are shown in Fig. 3. Although the scatter of data exceeds uncertainties, the results of different studies are in reasonably good agreement. The degree of agreement was quantified as follows. We had described the experimental data from [8] in terms of Legendre polynomials up to the fourth degree, whereupon we calculated the mean values of the ratios of the experimental data to the selected dependence (R_1) and the root-mean-square scatter of these ratios (dR_1) for each experiment being discussed. The resulting values are quoted in the first column of Table 1.

Thus, we can conclude that the data from three independent experiments performed by different methods yield consistent, to within 5%, angular distributions of neutrons with respect to the fixed direction of fission-fragment motion.

Table 1. Ratios R_1 and R_2

$R_1 \pm dR_1$	$R_2 \pm dR_2$	References
1.023 ± 0.036	0.244 ± 0.004	[13]
0.997 ± 0.045	0.213 ± 0.017	[2]
1.001 ± 0.035	0.242 ± 0.008	[8]

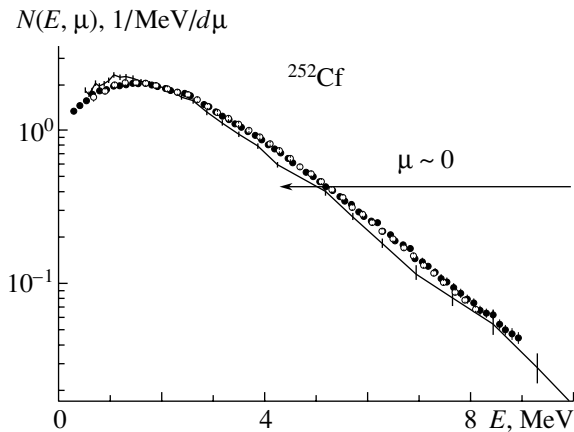


Fig. 4. Neutron spectrum at $\mu = 0.924$. The arrow restricts the energy interval corresponding to 1–5 MeV for $\mu \sim 0$. The solid curve, open circles, and closed circles correspond to data from [2], [8], and [13], respectively.

As a rule, $|\mu| \sim 1$ data (reference spectra), for which the contribution of neutrons from a pair fragment is small, are used to calculate the neutron distribution on the basis of relations (1)–(3). In order to assess the degree of reliability of such calculations, it is therefore necessary to determine the accuracy with which we know the reference spectra. Considering that the shape of the spectrum depends strongly on the angle (Fig. 1), we have interpolated the experimental data to the same angle of $\mu \sim 0.924$. The results that we obtained are displayed in Fig. 4. According to Eqs. (1)–(3), the region of energies in excess of 4 MeV for $\mu \sim 1$ corresponds to the energy range 1–5 MeV in the laboratory frame for angles close to $\mu \sim 0$. By comparing the integrals of the spectrum for $\mu \sim 0.924$ from 1 to 5 MeV with the analogous integral from 4 to 8 MeV, we can therefore determine quantitatively the accuracy to which the neutron spectrum is computed within the model of neutron emission from fully accelerated fragments. The ratio of the integrals $R_2 = \int_1^5 N(E, 0.924) dE / \int_4^8 N(E, 0.924) dE$ and the statistical uncertainty dR_2 are quoted in the second column of Table 1. The error in the mean-weighted value $\langle R_2 \rangle = 0.243 \pm 0.006$ (2.6%) makes it possible to conclude that the angular distribution of neutrons for ^{252}Cf can be calculated to within 3%.

Since the data from [8] and [13] comply well, those from [13] with the reference spectra at $\mu = \pm 0.958$ were used here to compute the angular distribution of neutrons for ^{252}Cf within the model of neutron emission from fully accelerated fragments. Figure 5 displays the ratio $R(\mu) = \int_1^5 N_{\text{exp}}(E, \mu) dE / \int_1^5 N_{\text{cal}}(E, \mu) dE$ for ^{252}Cf and ^{235}U (data from [9]) with the reference spectra at

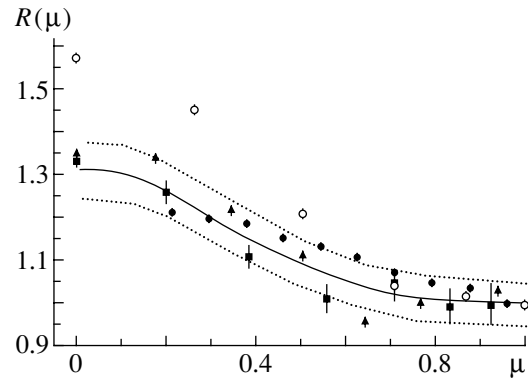


Fig. 5. Ratio of the experimental integrals of the spectrum (1–5 MeV) to the results of the calculations performed within the model of neutron emission from fully accelerated fragments. The results corresponding to data from [2], [8], [9], and [13] are represented by squares, triangles, open circles, and closed circles, respectively. The solid curve is an eyeball fit to data for ^{252}Cf . The dotted curves show $\pm 5\%$ deviations.

$\mu = \pm 1$). For ^{235}U , we used only data from [9]; therefore, we cannot assess definitively the accuracy of the calculations. One fact is beyond any doubt, however—all experimental data show that there is a neutron excess at angles $\mu \sim 0$, which is $(30 \pm 5)\%$ for ^{252}Cf and 58% for ^{235}U and which cannot be explained by neutron emission from fully accelerated fragments.

In addition to the aforementioned studies, we would also like to mention those that are reported in [12, 24], where it was concluded that there is no additional source of neutrons for ^{252}Cf . In [24], the analysis was based on a comparison of experimental data with the calculations within the model of neutron emission from fully accelerated fragments. The authors of that study indicated that they obtained a fairly accurate description of the angular and energy distribution of neutrons. For different values of the neutron emission angle and energy, the distinctions amounted to 10–20% and were commensurate with the uncertainties in the model parameters. Thus, we can see that, within that approach, it is impossible to establish the existence of an extra neutron source whose intensity is as low as 10% of the dominant component.

Batenkov *et al.* [12] also recorded an excess of neutrons in the spectrum at an angle of 90° , but it was as low as some 7%. Those authors state that recoil neutrons significantly affect a comparison of the spectra at 0° and 90° , but they do not discuss a method for taking this effect into account and do not present basic relations. Their experimental data are unavailable, and the description of the experiment is

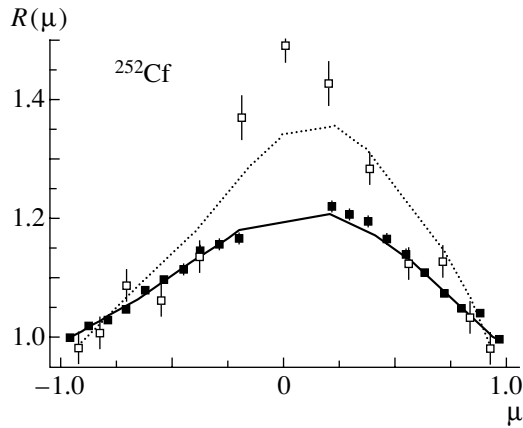


Fig. 6. Ratio of the experimental integrals of the spectra (1–5 MeV) (closed squares and open squares correspond to data from [2] and [13], respectively) and the quantities calculated with the chosen parameters E_v [model of neutron emission prior to the acceleration of fragments for data from [13] (solid curve) and [2] (dotted curve)] to the quantities predicted in the model of neutron emission from fully accelerated fragments. The calculations were performed separately for the reference spectra from [13] and from [2].

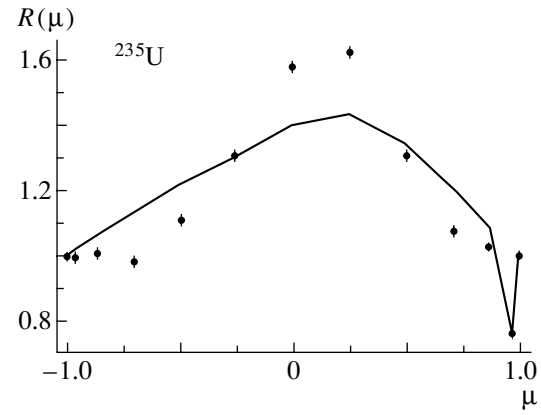


Fig. 7. As in Fig. 6, but for ^{235}U [9].

$$\begin{aligned}
 &= \sum_{j=1, i=1}^{j=m, i=n_j} w_{ij} \left[N_{ij} - F_{i0} \frac{\varphi(\mu_{ij}^c) \sqrt{E_i}}{\sqrt{\varepsilon}(E_i, \mu_j^l, E_v)} \right]^2 \\
 &= \sum_{j=1, i=1}^{j=m, i=n_j} w_{ij} [N_{ij} - S_{ij}(\mathbf{p})]^2, \\
 &w_{ij} = \frac{1}{\sigma_{ij}^2},
 \end{aligned}$$

very concise; therefore, it is impossible to confirm or disprove their conclusions.

Thus, it can be stated that a neutron excess over the prediction of the model of neutron emission from fully accelerated fragments was observed in all experimental studies or that, at least, we can indicate the reasons (in all cases with the exception of that of [12]) why it was overlooked.

3. DISCUSSION OF THE RESULTS

Two possibilities can be proposed for explaining the excess of neutrons at angles around 90° . These are neutron emission during the acceleration process (without changing the character of the angular and energy distributions of neutrons in the laboratory frame, this leads to an increase in their yield at angles around 90°) and a radically different source of neutrons. Let us investigate in detail each of these two possibilities.

3.1. Neutron Emission in the Process of Fragment Acceleration

If the parameters E_v in Eqs. (1)–(3) are unknown, we can then construct, on the basis of these relations, an algorithm for its search by minimizing the functional

$$M(b, E_v) \quad (5)$$

where σ_{ij} are the errors in the experimental values N_{ij} , F_{i0} are calculated on the basis of Eq. (3) for the reference spectrum at angle μ_0^l , and \mathbf{p} stands for the vector of parameters b and E_v . The method, whose efficiency was demonstrated in [25], was successfully used in [18] to analyze experimental data from [13]. The ratios of integrals in Figs. 6 and 7 are similar to the data in Fig. 5. The fitted parameters in the form of the ratio $\alpha = E_v/E_{v0}$ (E_v is a fitted parameter, E_{v0} is the value for the fully accelerated fragments, and $b = 0$) are quoted in Table 2 for a light and for the complementary heavy fragment.

The following special features in Figs. 6 and 7 attract attention. The angular dependence with the fitted parameters E_v is in good agreement with experimental data from [13] for ^{252}Cf , but it significantly deviates from them for ^{235}U . The data from [13] and [2] in the region $|\mu| < 0.5$ markedly differ as well. That, in the high-energy region, the spectrum for $\mu = 0.924$ (see Fig. 3 and Table 1), which was used as a reference one, was underestimated according to

Table 2. Values of the parameter α for ^{252}Cf and ^{235}U

	^{252}Cf [2]	^{252}Cf [13]	^{235}U [9]
Light fragment	0.83	0.90	0.89
Heavy fragment	0.89	0.89	0.81

the data from [2] may account for a factor of 1.15 in this deviation (a part of it, as a matter of fact). Since the results from [8] and [2] for $\mu = 0$ are consistent, we can conclude that, for $|\mu| < 0.5$, there was a systematic error in [13]. From other studies, that which was reported in [13] differs by the procedure for determining the cosine of the emission angle (it was deduced there from an analysis of momentum values in the ionization chamber equipped with a grid). Because of a partial loss of fragments, we restricted our analysis to the region of small angles ($|\mu| > 0.2$). In all probability, there are, however, some problems in this region ($0.2 < |\mu| < 0.5$) as well.

According to the calculations from [1, 16], the kinetic energy reaches about 0.9 of the TKE value at infinity over a time of about 10^{-20} s. As a matter of fact, this value determines the neutron lifetime in an excited fragment with respect to emission in the acceleration process. By using the calculated dependence $\alpha(t)$ and by assuming an exponential law with a neutron-emission lifetime τ , we can determine the expectation value $\langle\alpha(\tau)\rangle$ as

$$\langle\alpha(\tau)\rangle = \tau^{-1} \int_0^{\infty} \exp(-t/\tau) \alpha(t) dt. \quad (6)$$

By comparing $\langle\alpha(\tau)\rangle$ for various values of the lifetime τ with the experimental values of α , we can estimate that neutron lifetime in an excited fragment which corresponds to observed α . In doing this, it is necessary to consider that only first-chance neutrons can be emitted in the acceleration process. After their emission, the excitation energy decreases, which leads to the growth of the lifetime, and $\alpha = 1$ for subsequent cascade neutrons. Thus, we have

$$\alpha_{\text{expt}} = (\langle\alpha(\tau)\rangle + (\nu - 1)) / \nu, \quad (7)$$

where ν is the number of second-chance neutrons from a light or the complementary heavy fragment. In [16, 18], it was concluded that, for $\langle\alpha_{\text{expt}}\rangle \sim 0.9$ to be ensured, it is necessary that all first-chance neutrons be emitted within a characteristic time of $\tau \sim (1-2) \times 10^{-20}$ s. For the neutron lifetime in the Mo–Ba and Tc–Cs isotopes formed in ^{252}Cf fission, the statistical calculations from [16] show that the lifetime is $\tau \sim 2 \times 10^{-20}$ s for about 60% of fragments and $\tau \sim 1 \times 10^{-19}$ s for about 40% of fragments. In order to determine the lifetime, we use the approximate Moretto formula [26] with the level density in the Fermi gas model and the density parameter $a = A/10$. A more realistic dependence of the level density from [27] (superfluid model featuring a collective enhancement) leads to a lifetime longer by a factor of about 7. The total excitation energy for ^{235}U is approximately two-thirds as great as that for ^{252}Cf , with the result that the lifetime is longer for the former

by a factor of about 5, which obviously contradicts the observed values of $\langle\alpha_{\text{expt}}\rangle$.

Thus, the assumption of neutron emission during the acceleration of fragments can explain only partly the regularities for ^{252}Cf that are discussed here. Taking into account the different forms of the angular distribution (Fig. 6) and a noticeably greater neutron lifetime in fission fragments, we can see that the model of neutron emission during the acceleration of fragments is not applicable to ^{235}U .

3.2. Neutron Emission from an Extra Source

Even in the pioneering study of Bowman *et al.* [2], it was conjectured that an increase in the yield of neutrons at angles around 90° is associated with the existence of an extra source of fission neutrons, presumably with precission neutrons. All studies that explored precission neutrons relied on the assumption that they are isotropically distributed in the laboratory frame, but even the results from [2] showed some pieces of evidence that this is not so. Skarsvag and Bergheim [9] assumed that the precission-neutron spectrum is similar in shape to that for evaporation ($\approx E_{\text{exp}}(-E/T)$) and that a Maxwell distribution ($\approx \sqrt{E_{\text{exp}}}(-E/T)$) can be used to describe the neutron spectra in the c.m. frame. The parameters specifying the shape of the spectra were determined from a least squares fit. Thus, the conclusion on the number of precission neutrons and on their angular and energy distributions depend greatly on the input assumptions. For ^{252}Cf , it was first proven in [8] (and confirmed by investigations reported in [17]) that the precission-neutron spectrum involves two components (a soft and a hard one). In just the same way as in [8, 17], we used here an iterative procedure. However, the analysis performed in [17] was supplemented with an additional step that made it possible to investigate the angular distribution of precission neutrons in further detail.

The processing procedure consisted of the following steps:

(i) First, it was assumed that the reference spectra are free from the precission-neutron contribution. On the basis of the reference spectra, the energy and angular distributions were calculated within the model of neutron emission from fully accelerated fragments, whereupon the resulting distributions were subtracted from experimental data. The yield of the precission neutrons determined at this stage is shown by the open squares in Fig. 8.

(ii) The experimental spectra of precission neutrons were integrated over the angular region that is the most distant from the reference ones and were

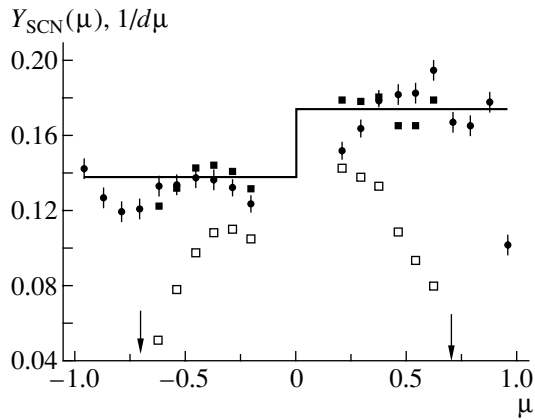


Fig. 8. Yield of precission neutrons as a function of the emission angle [13]. The symbols correspond to various steps of our analysis: (open squares) first step, (closed squares) second step, and (closed circles) third step; the line shows the resulting distribution for the calculation of the spectrum in the c.m. frame. The distributions were integrated with respect to energy from 0.5 to 6 MeV. The arrows indicate the positions of the reference spectra.

described, separately for positive and for negative cosines, by the expression

$$N(E) = \nu \left[\omega_1 \frac{E^{\lambda_1}}{\Gamma(\lambda_1 + 1) T_1^{\lambda_1 + 1}} \exp\left(-\frac{E}{T_1}\right) + (1 - \omega_1) \frac{E^{\lambda_2}}{\Gamma(\lambda_2 + 1) T_2^{\lambda_2 + 1}} \exp\left(-\frac{E}{T_2}\right) \right], \quad (8)$$

where $\Gamma(\lambda)$ is the complete gamma function. It is assumed that $\lambda_1 = \lambda_2 = 1$; the remaining parameters were calculated by the least squares method.

The precission-neutron spectra determined in this way were subtracted from the reference spectra, whereupon the second step of the iterative procedure was repeated again. In Fig. 8, the yield of precission neutrons after the second step of the iterative process is shown by closed squares. Upon integrating the angular distribution of precission neutrons over the total interval of angles under investigation, including the reference one, the parameters of the spectra of precission neutrons were selected and it was assumed that their yield is constant for $\mu < 0$ and for $\mu > 0$ (solid curve in Fig. 8). Further, we proceeded to implement the third step.

(iii) The precission-neutron angular and energy distributions calculated in this way were subtracted from experimental data. Within the model of neutron emission from fully accelerated fragments, the difference was transformed into the c.m. frame and the spectrum of neutrons in this frame was determined for the light and the heavy group of fragments. The neutron spectra in the c.m. frame were described by

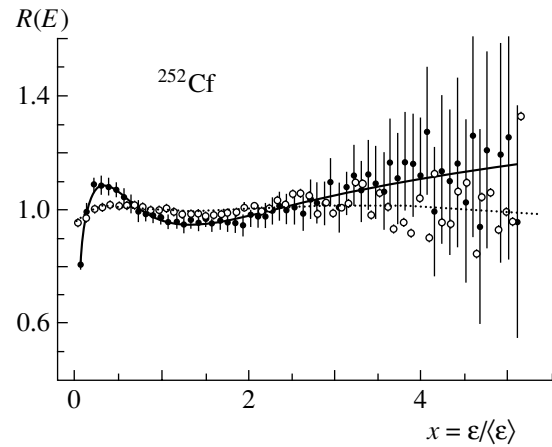


Fig. 9. Spectra of neutrons from (closed circles) a light and (open circles) the complementary heavy fission fragment in the c.m. frame as represented in the form of the ratio to the Maxwell distribution. Curves correspond to the description by formula (8) with the parameters determined by the least squares method.

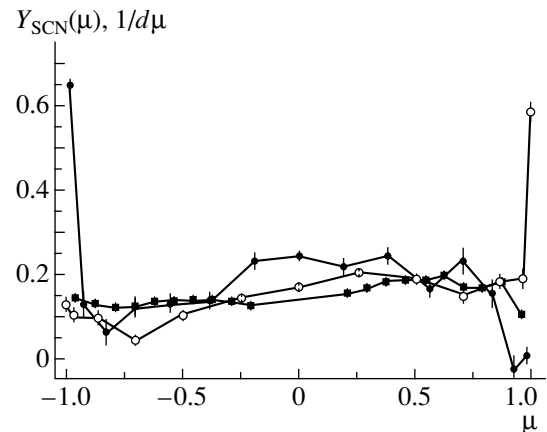


Fig. 10. Precission-neutron angular distributions integrated with respect to energy in the interval from 0.5 to 6 MeV. The results corresponding to the data from [13], [9], and [2] are represented by, respectively, closed squares, open circles, and closed circles (the points were connected in order to obtain a more instructive picture).

the function in (8) with one fixed parameter, $\lambda_1 = 1$. Without attaching any physical meaning to the parameters and to the function in (8) itself, we used this relation only in order to simplify the ensuing calculations. From Fig. 9, which displays the neutron spectra in the c.m. frame, it can be seen that the function in (8) makes it possible to describe in detail the shape of the spectrum. What is also worthy of note is that the shape of the spectrum deviates significantly from the Maxwellian one.

Knowing the shape of the spectrum in the c.m. frame and the absolute number of neutrons emitted

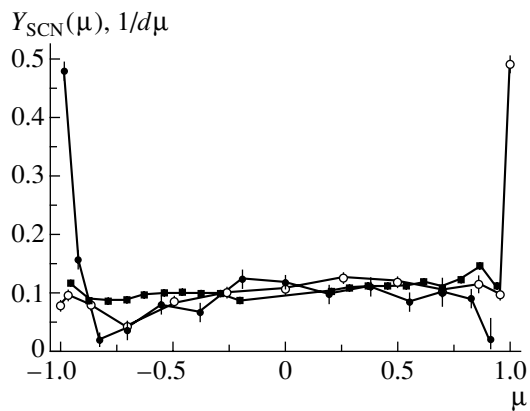


Fig. 11. As in Fig. 10, but for the energy interval 0.5–2 MeV. The results corresponding to the data from [13], [9], and [2] are represented by, respectively, closed squares, open circles, and closed circles.

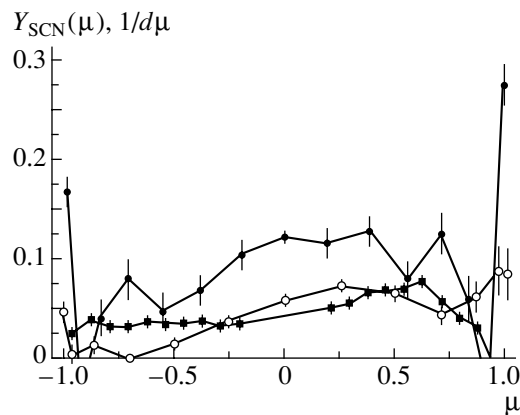


Fig. 12. As in Fig. 10, but for the energy interval 2–6 MeV. The results corresponding to the data from [13], [9], and [2] are represented by, respectively, closed squares, open circles, and closed circles.

from the light and the heavy group of fragments, we can calculate the angular and energy distributions of neutrons within the model of neutron emission from fully accelerated fragments and determine the eventual precission-neutron distribution as the difference between of experimental and calculated data (closed circles in Fig. 8). For precission neutrons, Figs. 10–12 demonstrate the angular distributions integrated over various energy intervals.

The precission-neutron energy spectra integrated with respect to all angles in the laboratory frame and their description on the basis of expression (8) are illustrated in Fig. 13. The parameter values determined from a least squares fit are quoted in Table 3.

The following features are worthy of special note:

(i) The number of precission neutrons emitted into the angular region $\mu > 0$ is greater than that for $\mu < 0$. For the ratio of the yields, the results are 1.73 [9], 1.26 [13], and 1.03 (1.24 without the point $\mu = -0.981$) [2].

(ii) The yield of the high-energy component into the angular region $\mu < 0$ is significantly smaller for ^{235}U than for ^{252}Cf .

(iii) A sharp increase in the multiplicity of low-energy precission neutrons is observed at small angles with respect to the direction of fission-fragment motion (axial neutrons). Their yield is associated with light fragments for ^{235}U and with heavy fragments for ^{252}Cf . The fractions of these neutrons are about 3% [9] and 8% [2] with respect to the total yield of precission neutrons. By using the parameters of the setup used, which are quoted in [9], we have calculated the angular resolution of this experiment. The result is about 5° for $\mu = 1$ at an angular step of 15° , whence it follows that the feature could be

reliably resolved at small angles. At $\mu \sim -1$, there is a trace of axial neutrons according to [13] as well (see also [18]), but their presence is not very spectacular because of low angular resolution at small angles, $d\mu \sim 0.07$.

(iv) The energy spectrum of precission neutrons involves two components at mean energies between 0.7 and 0.98 MeV and between 2.7 and 3.5 MeV. According to data from [13], the yields of precission neutrons and the parameters of their spectra for ^{252}Cf and ^{235}U agree within the errors of their determination.

On the basis of data presented in Figs. 10–13 and in Table 3, which quantify the properties of precission neutrons, it is possible to explain the features illustrated in Figs. 5 and 7. According to [9, 13], the yield

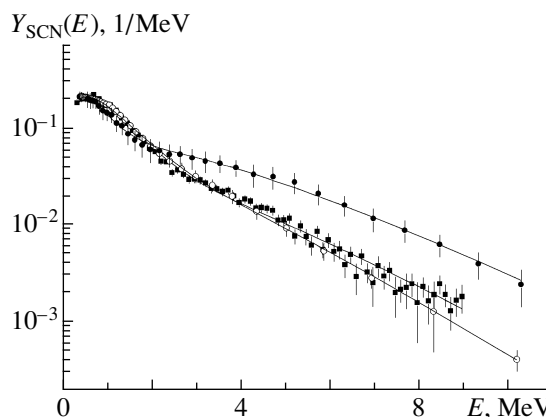


Fig. 13. Precission-neutron spectra integrated with respect to angles. Curves represent a description on the basis of expression (8) with the fitted parameter values (Table 3). The notation for the points is identical to that in Fig. 10.

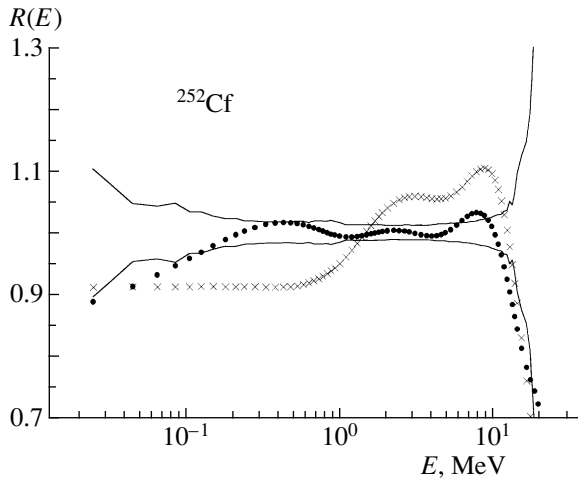


Fig. 14. Ratio of the reconstructed spectrum of neutrons in the laboratory frame to the reference spectrum of prompt fission neutrons that is used to normalize experimental data. The results obtained with and without allowance for the emission of precission neutrons are represented by, respectively, closed circles ($\chi^2 = 0.6$) and crosses ($\chi^2 = 13$) [13]. The curves indicate the relative error in the reference spectrum.

of precission neutrons takes the same value for ^{235}U and for ^{252}Cf , but the total number of second-chance neutrons is smaller for ^{235}U by a factor of about 1.5. The mean neutron energy in the c.m. frame is also lower, whereas the energy E_{vl} is higher. All this enhances kinematical collimation and increases the fraction of precission neutrons for ^{235}U at an angle of 90° by a factor of about 2.

In calculating the angular distribution for ^{235}U in the model of neutron emission from fully accelerated fragments, the spectra at $\mu = \pm 1$ were taken for a reference. The spectrum at $\mu = 1$ exhibits a sharp increase in the yield of neutrons with energies below 2 MeV (Fig. 10), but no such effect is observed for other angles, including the neighboring value of $\mu = 0.966$ (15°). Because of this, the calculated value is overestimated and there arises a dip in the ratio of the yields (Fig. 7). At large angles, use is made of a higher energy in the reference spectrum, where there is no contribution from axial neutrons.

We began to process experimental data by normalizing them to the standard spectrum of fission neutrons. Our analysis was performed either under the assumption that the model of neutron emission from fully accelerated fragments is valid for all neutrons or under the assumption that this model holds only for some part of them. In each case, we determined the spectrum of neutrons in the c.m. frame of moving fission fragments; hence, we could calculate the spectrum of prompt fission neutrons that is integrated with

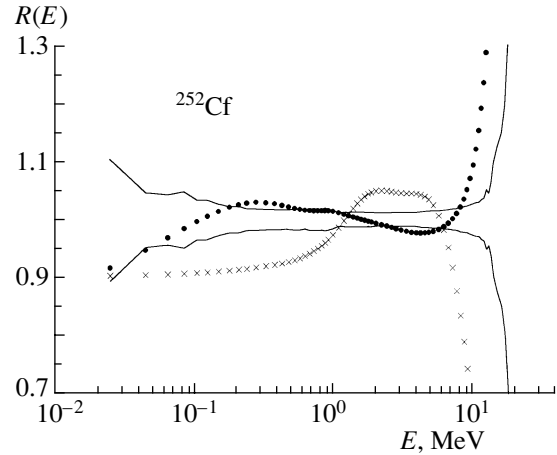


Fig. 15. As in Fig. 14, but for data from [2]: (closed circles) $\chi^2 = 13$ and (crosses) $\chi^2 = 18$.

respect to angles. A comparison of the calculated and the original spectrum is an important step in testing the self-consistency of the analysis and the validity of the assumptions made.

In order to calculate the neutron spectrum integrated with respect to angles, we have taken advantage of the description of the spectrum in the c.m. frame by means of expression (8). It was shown in [14]—and independently in [28]—that, if the spectrum of neutrons in the c.m. frame is described in the form $E^\lambda \exp(-E/T)$, then the spectrum of prompt fission neutrons in the laboratory frame can be expressed in terms of special functions convenient for practical calculations and the parameters of the spectra in the c.m. frame. The resulting form is

$$S(E) = \sum_{i=1,2} \nu_i [\omega_{1i} K(E, \lambda_{1i}, T_{1i}, E_{vi}) + (1 - \omega_{1i}) K(E, \lambda_{2i}, T_{2i}, E_{vi})] + \nu_{\text{SCN}} Y_{\text{SCN}}(E), \quad (9)$$

$$K(E, \lambda, T, E_v) = \frac{\Gamma(\lambda + 0.5, x_1) - \Gamma(\lambda + 0.5, x_2)}{4\Gamma(\lambda + 1) T y_v},$$

$$x_1 = (y + y_v)^2, \quad x_2 = (y - y_v)^2,$$

$$y = \sqrt{\frac{E}{T}}, \quad y_v = \sqrt{\frac{E_v}{T}},$$

where $\Gamma(\lambda)$ and $\Gamma(\lambda, x)$ are, respectively, the complete and the incomplete Euler gamma function; the index $i = 1(2)$ labels quantities referring to a light (heavy) fragment; ν_i is the number of neutrons from a light or the complementary heavy fragment; ν_{SCN} is the number of precission neutrons; and $Y_{\text{SCN}}(E)$ is the spectrum of precission neutrons in the form (8) with the parameter values from Table 3. The rest of the notation is clear from the structure of expression (8). Figures 14–16 show the deviations of the

Table 3. Parameters of the prescission-neutron spectrum (uncertainties in these values correspond to the accuracy of their determination from a least squares fit under the assumption that the experimental errors are independent)

Parameter	²⁵² Cf [2]	²⁵² Cf [13]	²³⁵ U [9]
ν , per fission event	0.46 ± 0.02	0.382 ± 0.003	0.378 ± 0.006
ω_1	0.41 ± 0.03	0.679 ± 0.012	0.657 ± 0.041
T_1 , MeV	0.35 ± 0.04	0.478 ± 0.008	0.49 ± 0.02
T_2 , MeV	1.77 ± 0.07	1.54 ± 0.04	1.37 ± 0.07
$\langle E \rangle$, MeV	2.38 ± 0.13	1.64 ± 0.04	1.58 ± 0.09

calculated spectra from the values used to normalize experimental data. As can be seen from the figures, only upon the introduction of an extra source of neutrons is the agreement with the input values ensured, whereby it is confirmed once again that such an extra source is necessary in describing the nuclear-fission process. The values in Figs. 14–16 for the sums of the squares of deviations per point, χ^2 , were determined for energies below 10 MeV. The deviations of the reconstructed spectra at higher energies (in excess of 10 MeV) are likely to be due to the model simplifications used [two fragments, extrapolation of expression (8) to the region of high energies, etc.] and can hardly be a serious argument against the above conclusion.

The original reference spectrum of ²⁵²Cf is described more poorly with the parameters of the neutron spectrum in the c.m. frame and $Y_{SCN}(E)$ from [2] than with the analogous data from [13]. However, this distinction is not so radical that, on its basis, one could reject the results presented in [2] and conclude that the yield of prescission neutrons and the shape of the energy spectrum are identical for ²³⁵U and ²⁵²Cf, as follows from the data reported in [9, 13]. As was noted above, there is every reason to believe that, in [13], a determination of the angles between the direction of fission-fragment motion and the neutron momenta could suffer from systematic errors.

The assumption that additional neutrons are emitted during the descent of the system from the saddle to the scission point owing to a fast (nonadiabatic) change in the nuclear potential makes it possible to understand qualitatively the emergence of anisotropy in the laboratory frame. It was shown in [29] that, because of nonadiabaticity of the process, alpha particles from ternary fission are emitted from three sources, the neck connecting fission fragments and the polar regions. One can assume that the same regions appear to be sources of neutrons. Because of shadowing by nearby fragments, neutrons are then emitted into bounded angular regions. The shadowing effect, which depends on the fragment dimensions and deformations, and the difference in the yields from three different regions may lead to an anisotropic distribution in the laboratory frame.

The coupling of single-particle degrees of freedom to the process of fragment acceleration and the impact of these nonadiabatic effects on neutron emission were considered in [30], where it was shown that the fission of ²⁵²Cf can be accompanied by the emission of about 2% of neutrons that move along the direction of fragment motion. Probably, this is the phenomenon that is responsible for the emergence of axial neutrons that we observed.

Experimental data on the properties of prescission neutrons are scanty and contradictory. It was shown in [8] (the relevant data are quoted in [17]) that their energy spectrum involves two components whose parameters take values close to those in Table 3. The yield of the high-energy component is weakly dependent on the fragment masses, whereas the yield of low-energy neutrons is approximately six times less for symmetric than for asymmetric fission. The maximum yield of prescission neutrons was observed at low kinetic energies (TKE ~ 160 MeV). The yield is much less at TKE ~ 180 MeV, but, as the energy increases up to TKE ~ 210 MeV, it grows to a lesser extent.

In [10], it was shown that the thermal-neutron-induced fission of ²³⁵U is accompanied by the emission of 0.25 ± 0.05 neutrons. This cannot be ex-

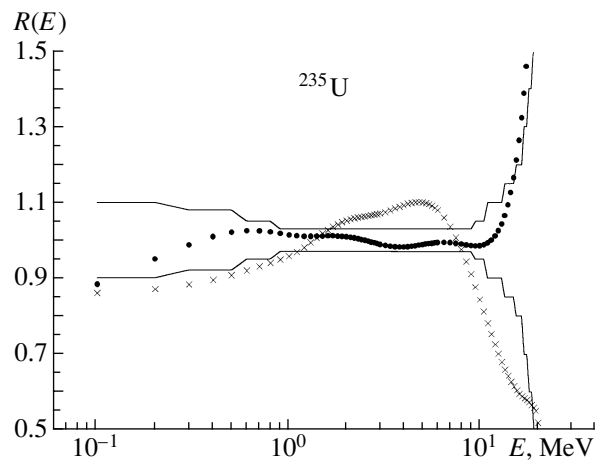


Fig. 16. As in Fig. 14, but for data from [9]: (closed circles) $\chi^2 = 0.2$ and (crosses) $\chi^2 = 4.7$.

plained within the model of neutron emission from fully accelerated fragments. The authors of [10] did not determine the energy distribution, but they established that the yield of prescission neutrons is weakly dependent on the fragment mass and that they are observed only at high kinetic energies (160–190 MeV).

CONCLUSION

The data analysis proposed in the present study has revealed that an excess of neutrons at an angle of 90° in relation to the predictions of the model of neutron emission from fully accelerated fragments is observed in the fission of ^{252}Cf and ^{235}U nuclei.

In order to explain this fact, it seems the most reasonable to assume that 10–15% of neutrons are emitted not from excited fragments following the disintegration of the nucleus but from some other source. In the present study, we have made use of the term “prescission neutrons,” relying on theoretical studies that support the possibility of this process and preserving the commonly accepted terminology. A definitive conclusion on the nature of these extra neutrons can be drawn only upon developing a theoretical model that would describe experimental facts and demonstrating the effect of prescission-neutron emission on the observed distributions of fission fragments.

Information about the properties of prescission neutrons is scanty and contradictory. On the basis of four independent experiments, it has been established that they are characterized by a two-component spectrum and by an anisotropic distribution in the laboratory frame. There are still some open questions: How do their properties change upon going over from the spontaneous fission of ^{252}Cf to the induced fission of ^{235}U ? What are their angular and energy distributions like? How do their properties depend on the fragment masses and the total kinetic energy? Are alternative explanations of the neutron excess possible? What is the nature of axial neutrons? What are masses and total kinetic energies that are responsible for their emergence?

Investigation of prescission neutrons is of paramount importance for understanding the dynamics of fission and for determining the time it takes for the system to descend from the saddle to the scission point. If the mechanism responsible for their emission is analogous to the mechanism of charge-particle emission in ternary fission, the character of the angular and energy distributions of prescission neutrons will furnish direct information about the properties of nuclear matter at the instant of scission, since their

characteristics are not distorted by Coulomb repulsion. Moreover, information about prescission neutrons is necessary in assessing the spectra of fission neutrons for practical applications.

In the present study, we have considered virtually the entire body of information accumulated previously. Therefore, it is desirable to perform new experiments aimed at exploring this small effect for various fissile systems. Investigation of ^{235}U , for which the maximum relative yield of prescission neutrons is observed and for which there is little doubt about the treatment of the results, seems very promising.

REFERENCES

1. H.-H. Knitter, U. Brosa, and C. Budtz-Jørgensen, in *The Nuclear Fission Process*, Ed. by C. Wagemans (CRC Press, Boca Raton, 1991), p. 497.
2. H. R. Bowman, J. C. D. Milton, *et al.*, *Phys. Rev.* **126**, 2120 (1962).
3. R. W. Fuller, *Phys. Rev.* **126** (2), 684 (1962).
4. Y. Boneh and Z. Fraenkel, *Phys. Rev. C* **10**, 893 (1974).
5. P. Riehs, *Acta Phys. Austriaca* **53**, 271 (1981).
6. V. M. Piksaikin, P. P. D'yachenko, and L. S. Kutsaeva, *Yad. Fiz.* **25**, 723 (1977) [*Sov. J. Nucl. Phys.* **25**, 385 (1977)].
7. E. A. Seregina and P. P. D'yachenko, *Yad. Fiz.* **42**, 1337 (1985) [*Sov. J. Nucl. Phys.* **42**, 845 (1985)].
8. E. A. Seregina, *Measurements and Analysis of Angular-Energy Distribution for $^{252}\text{Cf}(SF)$ Neutrons*, PhD Thesis (Obninsk, 1985).
9. K. Skarsvag and K. Bergheim, *Nucl. Phys.* **45**, 72 (1963).
10. M. S. Samant, R. P. Anand, *et al.*, *Phys. Rev. C* **51**, 3127 (1995).
11. S. S. Kapoor, R. Ramanna, and P. N. Rama Rao, *Phys. Rev.* **131**, 283 (1963).
12. O. I. Batenkov, A. B. Blinov, *et al.*, in *Proceedings of IAEA Consulting Meeting, Vienna, 1989*, INDS(NDS)-220, p. 207.
13. C. Budtz-Jørgensen and H.-H. Knitter, *Nucl. Phys. A* **490**, 307 (1988).
14. U. Brosa and H.-H. Knitter, *Z. Phys. A* **343**, 39 (1992).
15. D. Hilscher and P. Fröbrich, *Ann. Phys. (Paris)* **6**, 472 (1993).
16. N. V. Kornilov and A. B. Kagalenko, *ISINN-2* (Dubna, 1994), p. 116.
17. N. V. Kornilov, A. B. Kagalenko, and F.-J. Hamsch, Preprint IPPE-2763 (Obninsk, 1999); Report for ISINN-7 (Dubna, 1999), p. 241.
18. N. V. Kornilov, A. B. Kagalenko, and F.-J. Hamsch, in *Proceedings of International Conference on Nuclear Data for Science and Technology, Trieste, 1997*, Ed. by G. Reffo, A. Ventura, and C. Grandi (Italian Physical Society, Bologna, 1997), Vol. 1, p. 179.

19. F. Gonnwein, in *The Nuclear Fission Process*, Ed. by C. Wagemans (CRC Press, Boca Raton, 1991), p. 287.
20. V. V. Malinovskii, *Vopr. At. Nauki Tekh., Ser.: Yad. Konst.*, No. 2, 25 (1987).
21. *Nuclear Data Standards for Nuclear Measurements*, Ed. by H. Conder, NEANDC-311U, INDC(SEC)-101 (1992).
22. W. Manhart, TECDOC-410, IAEA (Vienna, 1987), p. 158.
23. N. V. Kornilov, A. B. Kagalenko, *et al.*, ISINN-6 (Dubna, 1998), p. 242.
24. H. Marten, D. Richter, *et al.*, in *Proceedings of IAEA Consulting Meeting, Vienna, 1989*, INDC(NDS)-220, pp. 161, 245.
25. N. V. Kornilov and A. B. Kagalenko, ISINN-3 (Dubna, 1995), p. 213.
26. L. G. Moretto, *Nucl. Phys. A* **180**, 337 (1972).
27. A. V. Ignatyuk, *Statistical Properties of Excited Nuclei* (Énergoatomizdat, Moscow, 1983).
28. N. V. Kornilov and A. B. Kagalenko, *Yad. Fiz.* **57**, 1240 (1994) [*Phys. At. Nucl.* **57**, 1172 (1994)].
29. O. Serot, C. Wagemans, *et al.*, in *Proceedings of International Conference on Nuclear Data for Science and Technology, Triest, 1997*, Ed. by G. Reffo, A. Ventura, and C. Grandi (Italian Physical Society, Bologna, 1997), Vol. 1, p. 476.
30. B. R. Milek, R. Reif, and J. Revai, *Phys. Rev. C* **37**, 1077 (1988).

Translated by A. Isaakyan

Induced Nuclear Fission Accompanied by Pion Emission

A. S. Iljinov and M. V. Mebel

*Institute for Nuclear Research, Russian Academy of Sciences,
pr. Shestidesyatiletiya Oktyabrya 7a, Moscow, 117312 Russia*

Received June 2, 2000

Abstract—Basic features of the nuclear-fission process induced by protons of incident energy in the range $150 < E_p < 600$ MeV and accompanied by pion emission are predicted on the basis of the cascade–evaporation–fission model. Specific calculations are performed for the total cross section; and the angular and double-differential distributions of pions; excitation-energy, mass number, and charge-number distributions of compound nuclei; and the mass–energy distributions of fission fragments. Various lines of possible experimental investigations into this fission channel are discussed, including searches for the pionic channel of nuclear decay induced by protons of energy close to the meson-production threshold, advancements to the energy region $E_p < 100$ MeV in order to study of new mechanisms of pion production in nuclear fission, and an extension of investigations to the case of nuclear fission accompanied by kaon emission. © 2001 MAIK “Nauka/Interperiodica”.

1. INTRODUCTION

It is well known that neutrons, photons, protons, and extremely light nuclei (d, t, α) are emitted in nuclear fission [1]. At the same time, energy released in nuclear fission (about 200 MeV) is sufficient for pion production. That pions can be emitted in the spontaneous fission of heavy transuranic elements was predicted in [2]. Since the mechanism of pion production in spontaneous fission is not known, it is hardly possible to obtain a realistic estimate of the branching ratio for the pionic channel.¹⁾ Only an upper limit on the ratio of the probability of the pionic channel to the total probability of spontaneous fission was established in subsequent experiments ($w_{\pi f}/w_{SF} < 10^{-11}$) [3].

Obviously, the probability of the pionic channel in induced fission can be many orders of magnitude larger than that in spontaneous nuclear fission. Both from the experimental and from the theoretical point of view, it is therefore reasonable to begin investigating the pionic channel from a region close to the pion-production threshold, where the mechanism of pion production is well understood.

In the present study, we predict the properties of the pionic channel of nuclear fission induced by protons of energy in the range $150 < E_p < 600$ MeV.

¹⁾For the sake of brevity, nuclear fission accompanied by pion emission will henceforth be referred to as pionic fission; the corresponding fission channel will accordingly be called a pionic channel.

In doing this, we rely on the cascade–evaporation–fission (CEF) model developed in our previous studies. On its basis, it was possible to describe successfully a vast body of experimental data on the mass–energy distributions of fission fragments; the spectra of emitted nucleons; and the yields of isotopes produced in the experiments with intermediate-energy beams of protons [4], neutrons [5], and antiprotons [6].

2. CASCADE–EVAPORATION–FISSION MODEL

The inelastic interaction of an intermediate-energy proton with a heavy nucleus—in particular, it can induce nuclear fission—proceeds in a few stages. At the first stage, the incident proton generates, within the target nucleus, a cascade of sequential NN and πN collisions. As a result, particles of the continuous spectrum that are produced in these elementary collisions escape the nucleus. The stage of the intranuclear cascade proceeds very fast (a typical time is $\tau_{cas} \sim \tau_0$, where $\tau_0 \sim 10^{-22}$ s is the time it takes for a fast particle to traverse the nucleus). This stage is described on the basis of the intranuclear-cascade model [7, 8], which implements a numerical method for solving the kinetic equation for the multiparticle distribution function [8, 9]. The model makes it possible to take correctly into account fluctuations of the cascade shower and to determine not only the spectra of outgoing particles but also the yield of excited residual nuclei, $Y(A, Z, E^*, \mathbf{P}, \mathbf{I})$; here, A and Z are, respectively, the number of nucleons and the

number of protons in the residual nucleus, while E^* , \mathbf{P} , and \mathbf{I} are its excitation energy, linear momentum, and angular momentum. Model parameters are fixed by fitting a vast body of data from experiments that studied the interaction of intermediate-energy particles with nuclei [7, 8]. A detailed description of the model can be found in [7, 8].

Upon the completion of the intranuclear cascade, thermodynamic equilibrium is fast established in the residual nucleus ($\tau_{\text{eq}} \sim 5\tau_0 - 10\tau_0$) [8, 9]. At the subsequent slow ($\tau_{\text{eq}} \gg \tau_0$) stage, the compound nucleus evaporates particles or undergoes fission. The fission process is accompanied by the most pronounced rearrangement of the nuclear structure and therefore proceeds much more slowly than particle emission.

The deexcitation of the compound nucleus is described on the basis of the evaporation model [10], where the weights of channels in each link of the evaporation chain are determined by the particle-emission widths Γ_i ($i = n, p, d, t, {}^3\text{He}, \alpha, \gamma$) and the fission width Γ_f , which are calculated by means of the well-known Weisskopf and Bohr–Wheeler equations, respectively. For the nuclear-level density $\rho(E^*)$, the most important ingredient of the evaporation model, use is made of the Fermi gas expression, which takes into account collective and pairing effects and the heat damping of shell effects. The parameters of the evaporation model are fixed by fitting a wide set of data on the level densities in compound nuclei and their decay widths and lifetimes [10]. The details of the calculations of the evaporation cascade can be found in [8, 10].

The evaporation cascade is completed when evaporated particles entirely carry away the excitation energy E^* of the compound nucleus or when fission occurs. At high excitations ($E^* \geq 50$ MeV), nuclei are characterized by the potential-energy surface identical to that of a liquid drop, because shell effects vanish, and there is only one fission valley. Therefore, fission is symmetric in this case. The descent of a highly excited fissile nucleus from the saddle to the scission point is described within the diffusion model based on the Fokker–Planck equation [11]. This model takes into account a dissipative nature of this dynamical process and thermodynamic quantum fluctuations of collective nuclear variables. The model explains a wide set of data on the mass–energy distributions of fragments produced in the fission of highly excited compound nuclei [11].

Shell effects play a significant role in the fission of highly excited ($E^* < 50$ MeV) nuclei, leading, in particular, to the existence of two (or even more) fission valleys on the potential-energy surface. It

follows that, at low excitation energies of a compound nucleus, a symmetric fission mode coexists with one mode of asymmetric fission or with a few of such modes [12]. Contemporary fission models cannot qualitatively describe thermal damping of shell effects in the mass–energy distributions of nuclear fragments in the excitation-energy region $7 < E^* < 50$ MeV. Therefore, our calculations of low-energy fission will be by empirically approximating this distribution with allowance for the coexistence of a symmetric fission mode and two modes of asymmetric fission [4].

We recall that, if fission occurs in one of the links of the evaporation chain, the mass (A_f) and charge (Z_f) numbers, the kinetic energy (E_f), and the excitation energy (U_f) of each fission fragment are determined on the basis of the diffusion model or on the basis of empirical approximation. For each excited fission fragment, we then calculate the evaporation cascade. The details of the calculation of fission can be found in [4].

Thus, the CEF model describes the evolution of a nuclear system over a wide time scale from 10^{-23} to 10^{-13} s, taking correctly into account all reaction stages (intranuclear cascade, particle evaporation from an excited residual nucleus, its fission, and particle evaporation from fission fragments). The model provides an exclusive description of a nuclear reaction, enabling one to evaluate the features of all product particles (including pions), light nuclear fragments, and fission fragments. Our CEF model faithfully reproduces available data on pion production on nuclei [8] and on nuclear fission induced by intermediate-energy particles [4–6]; on this basis, we can hope that its predictions for the properties of the pionic fission channel will be highly reliable. In the CEF model, pion emission and fission are well separated in time, occurring within very distinct time-scale regions ($\tau_\pi \sim 10^{-23} - 10^{-22}$ s, $\tau_f \sim 10^{-18} - 10^{-13}$ s).

3. BASIC PROPERTIES OF THE PIONIC CHANNEL OF PROTON-INDUCED NUCLEAR FISSION

On the basis of the CEF model, we have performed calculations for ${}^{238}\text{U}$ fission induced by protons of energy from 150 to 600 MeV. For the pionic fission channel, we have evaluated the total cross section $\sigma(p, \pi f)$, the angular distribution $d\sigma/d\Omega_\pi$ and the differential distribution $d^2\sigma/d\Omega_\pi dE_\pi$ for pions emitted with different charges, the distributions of compound nuclei with respect to the excitation energy E^* and the mass (A) and the charge (Z) number, and the mass and kinetic-energy distributions of fission fragments.

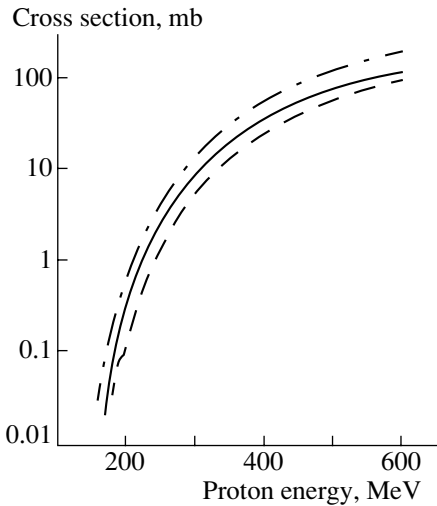


Fig. 1. Cross section for ^{238}U fission induced by protons and accompanied by the emission of a pion in a given charge state as a function of the incident-proton energy. The solid, the dashed, and the dash-dotted curves correspond to the π^+ , the π^- , and the π^0 channel, respectively.

Figure 1 presents the total cross section for the reaction $^{238}\text{U}(p, \pi f)$ as a function of energy. The cross section decreases very fast with decreasing initial energy, especially in the energy region below the pion-production threshold in NN collisions for $E_p < 290$ MeV. Even in the subthreshold region, however, the cross sections for the pionic channels are quite large. By way of example, we indicate that, at $E_p = 250$ MeV, the cross sections amount to a few mb—namely, $\sigma(p, \pi^+ f) = 2.7$ mb, $\sigma(p, \pi^- f) = 1.4$ mb, and $\sigma(p, \pi^0 f) = 4.5$ mb. The ratio of the pionic-channel cross section $\sigma(p, \pi f)$ to the total fission cross section σ_f also decreases very fast with decreasing incident energy: it is 8×10^{-2} at $E_p = 400$ MeV, 6×10^{-3} at $E_p = 250$ MeV, and 2×10^{-5} at $E_p = 160$ MeV (see table). Thus, it is advisable to begin experimental searches for the pionic channel at proton energies above the pion-production threshold ($E_p > 300$ MeV). In doing this, it should be borne in mind, however, that the cross section for the reaction $\sigma(p, \pi^0 f)$ is approximately twice as large as the cross section $\sigma(p, \pi^+ f)$ and that the cross section $\sigma(p, \pi^- f)$ is approximately one-half as large as the cross section $\sigma(p, \pi^+ f)$ (see table).

The angular distributions $d\sigma/d\Omega_\pi$ of pions emitted in the reaction $\text{U}(p, \pi f)$ at $E_p = 250$ MeV is presented in Fig. 2. The angular distributions of π^0 and π^+ mesons have a sharp maximum at $\theta_\pi = 0^\circ$; at the same time, the majority of π^- mesons are emitted at the angle $\theta_\pi = 180^\circ$. This difference in the shapes of the angular distributions is due to the fact

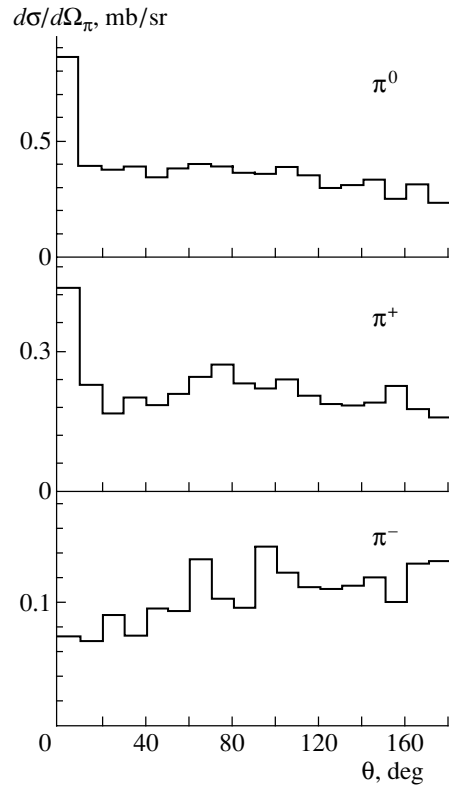


Fig. 2. Angular distribution $d\sigma/d\Omega_\pi$ of π^0 , π^+ , and π^- mesons emitted in the reaction $\text{U}(p, \pi f)$ induced by 250-MeV protons.

that both π^+ and π^0 mesons can be produced in the first collisions of the incident proton with intranuclear nucleons, while π^- mesons can be produced only in subsequent collisions of cascade neutrons with intranuclear nucleons.

Figure 3 shows the spectra of pions emitted into the angular intervals $0^\circ \leq \theta_\pi \leq 15^\circ$, $60^\circ \leq \theta_\pi \leq 90^\circ$,

Cross sections for ^{238}U fission induced by protons and accompanied by the emission of a pion in a given charge state and the fraction of the pionic channels in the total fission cross section, $w_{\pi f} = \sigma(p, \pi f)/\sigma_f$

E_p , MeV	$\sigma(p, \pi^+ f)$, mb	$\sigma(p, \pi^- f)$, mb	$\sigma(p, \pi^0 f)$, mb	$w_{\pi f}$
600	119.0	97.5	196.4	0.28
500	77.3	59.8	124.6	0.18
400	36.2	25.9	57.0	8.4×10^{-2}
350	19.6	3.2	31.1	4.5×10^{-2}
300	8.87	5.41	13.9	2.0×10^{-2}
250	2.72	1.38	4.53	6.2×10^{-3}
200	0.33	0.11	0.66	7.7×10^{-4}
180	0.08	0.03	0.20	2.2×10^{-4}
170	0.02	—	0.07	6.2×10^{-5}
160	—	—	0.03	2.0×10^{-5}

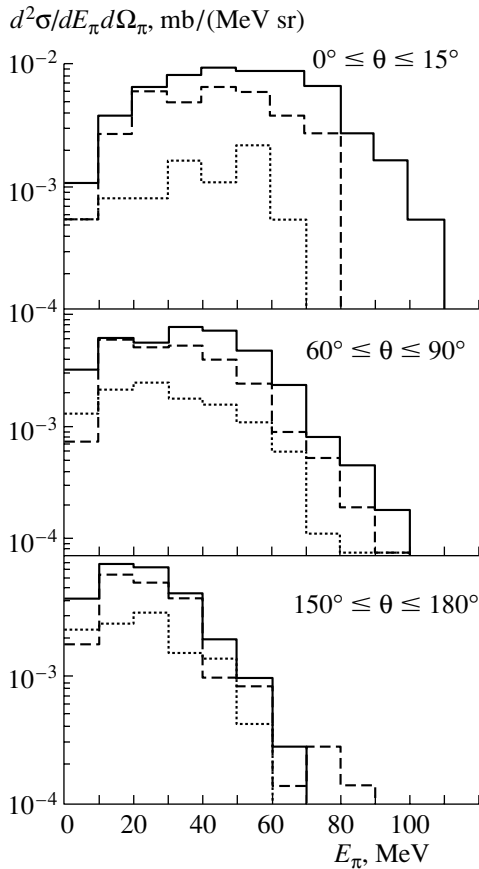


Fig. 3. Double differential distribution $d^2\sigma/dE_\pi d\Omega_\pi$ of pions emitted into the angular intervals $0^\circ \leq \theta_\pi \leq 15^\circ$, $60^\circ \leq \theta_\pi \leq 90^\circ$, and $150^\circ \leq \theta_\pi \leq 180^\circ$ in the reaction $U(p, \pi f)$ at $E_p = 250$ MeV. Solid, dashed, and dotted histograms correspond to π^0 , π^+ , and π^- mesons, respectively.

and $150^\circ \leq \theta_\pi \leq 180^\circ$ in the reaction $U(p, \pi f)$ at $E_p = 250$ MeV. Even in the subthreshold energy region, the pion spectrum extends to $E_\pi = 100$ MeV. Naturally, the spectrum of pions emitted into the forward hemisphere is harder than that of pions emitted into the backward hemisphere.

At $E_p = 250$ MeV, compound nuclei produced in the pionic channels have a narrow distribution with respect to the nucleonic composition (see Fig. 4). The shape of the mass distribution is virtually independent of the charge of the emitted pion, and the maximum of the charge-number distribution is shifted by unity upon a transition from the π^+ channel to the π^0 channel and then to the π^- channel. Therefore, the $(p, \pi^+ f)$ channel mostly produces Pa and U isotopes; the $(p, \pi^0 f)$ channel produces U and Np isotopes; and the $(p, \pi^- f)$ channel produces Np and Pu isotopes with mass numbers $A = 237, 238, \text{ and } 239$.

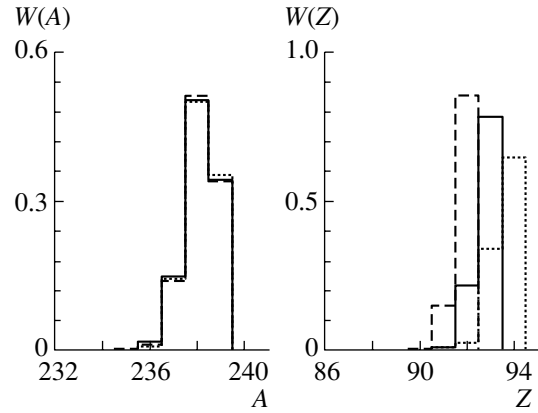


Fig. 4. Mass-number (A) and charge-number (Z) distributions of compound nuclei (normalized to unity) produced in the reaction $U(p, \pi f)$ at $E_p = 250$ MeV. Solid, dashed, and dotted histograms correspond to π^0 , π^+ , and π^- channels, respectively.

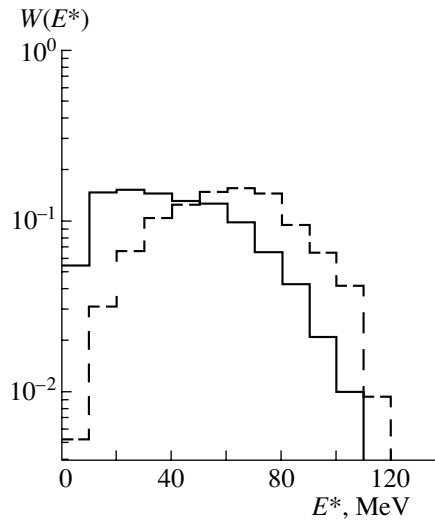


Fig. 5. Excitation-energy (E^*) distributions (normalized to unity) of compound nuclei produced in the collisions of 250-MeV protons with ^{238}U nuclei (solid histogram) through the pionic channels and (dashed histogram) through other fission channels.

The excitation energy E^* of compound nuclei is significantly lower in the pionic channels than in other fission channels (see Fig. 5). Therefore, shell effects play a more important role in the pionic channels, and the asymmetric-fission contribution to the mass distribution of fission fragments is quite large (see Fig. 6). In the $(p, \pi f)$ channel, fission is closer to the symmetric case, because, for producing a π^- meson, incident protons must undergo a greater number of rescatterings and charge exchanges, in which case a

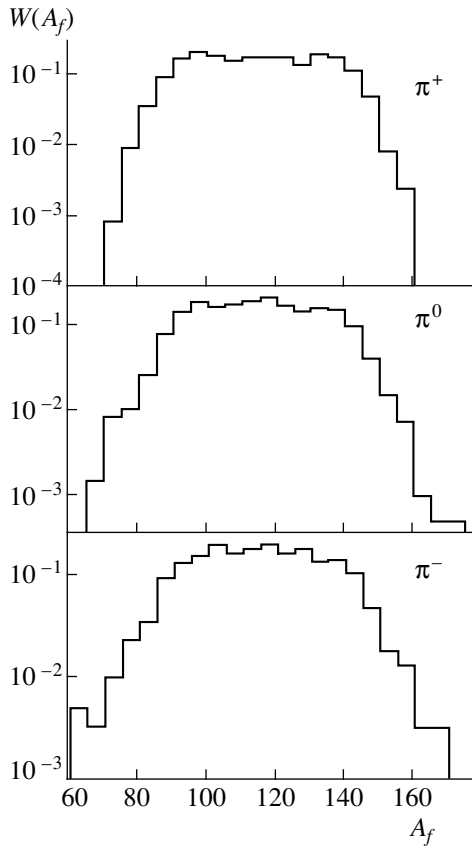


Fig. 6. Mass distribution (normalized to unity) of fission fragments produced in the reaction $U(p, \pi f)$ at $E_p = 250$ MeV.

compound nucleus is excited to energy higher than those in π^+ and π^0 production.

4. CONCLUSION

The simplest pionic-fission mechanism, which is dominant in the energy region close to and above the pion-production threshold has been examined. It is reasonable to begin seeking pionic fission in this energy region, where its cross section is rather large (about 10–100 mb) and where theoretical predictions are quite reliable. Of greatest interest for future investigations is the advancement to the energy region $E_p < 140$ MeV (that is, the region below the threshold of pion production on an infinitely heavy nucleus), where the mechanism considered here is not valid. Obviously, the probability of induced pionic fission at $E_p = 100$ MeV must be a few orders of magnitude greater than the probability of spontaneous pionic fission for which the current experimental limit is 10^{-11} [3]. It is worth noting that the experiments that studied pion production by heavy ions of energy 20–30 MeV per nucleon [13] suggest the existence

of other pion-production mechanisms that may play a significant role in the $(p, \pi f)$ reaction at this energy.

It is also of considerable interest to extend these investigations to the case of induced nuclear fission accompanied by kaon emission, since it is a Λ hypernucleus that undergoes fission here. On the basis of CEF model, it was found in [14] for the reaction $U(\pi^+, K^+ f)$ that the cross section for K fission is about 1 mb at the optimum incident energy of $E_\pi = 0.9$ GeV. According to [15], the cross section for the reaction $U(p, K^+ f)$ at $E_p = 1.5$ GeV is 0.1 mb. In [14], it was indicated that, by measuring, at a specific angle, the energy spectrum of all kaons in coincidence with fission fragments, one can then obtain, from the ratio of these spectra, the probability P_f of hypernucleus fission as a function of its excitation energy E^* . An analysis of the energy dependence of $P_f(E^*)$ will furnish information about the height of the fission barrier and about the level density in heavy hypernuclei.

At present, an experimental facility aimed at searches for pionic fission in a proton beam of the Moscow meson factory is being constructed on the basis of the predictions presented here. The advent of highly intense pion beams of momentum 1 GeV/c both at the existing (for example, GSI in Germany) and at the planned (for example, JHF in Japan) accelerators creates favorable preconditions for experimentally investigating the production and properties of Λ hypernuclei in the reaction $(\pi^+, K^+ f)$.

ACKNOWLEDGMENTS

We are grateful to A.B. Kurepin, V.M. Lobashev, M.G. Itkis, V.G. Nedorezov, A.I. Reshetin, and Yu.V. Ryabov for discussions on the possibility of performing, at the Moscow Meson Factory, an experiment devoted to searches for nuclear fission induced by protons and accompanied by pion emission and to Ye.S. Golubeva and I.A. Pshenisnov for discussions on the theoretical aspects of the problem.

This work was supported in part by the Russian Foundation for Basic Research (project no. 98-02-17171).

REFERENCES

1. R. Vandenbosch and J. R. Huizenga, *Nuclear Fission* (Academic, New York, 1973).
2. D. B. Ion *et al.*, *Ann. Phys. (N.Y.)* **171**, 237 (1986); *Rev. Roum. Phys.* **31**, 205, 209, 551 (1986); **32**, 1037 (1987); **33**, 239, 1071 (1988); **34**, 261, 359 (1989).
3. J. R. Beene *et al.*, *Phys. Rev. C* **38**, 569 (1988); C. Cerruti *et al.*, *Z. Phys. A* **329**, 383 (1988); Yu. V. Adamchuk *et al.*, *Yad. Fiz.* **49**, 232 (1989) [*Sov. J. Nucl. Phys.* **49**, 579 (1989)]; S. Stanislaus *et al.*, *Phys. Rev. C* **39**, 295 (1989); J. R. Knudson *et al.*, *Phys. Rev. C* **44**, 2869 (1991).

4. G. D. Adeev *et al.*, Preprint IYAI-816/93 (Institute for Nuclear Research, Moscow, 1993).
5. C. M. Zoller *et al.*, Report IKDA 95/25 (Darmstadt, 1995).
6. P. Hoffmann *et al.*, Phys. Rev. C **49**, 2555 (1994).
7. V. S. Barashenkov and V. D. Toneev, *Interactions of High-Energy Particles and Nuclei with Nuclei* (Atomizdat, Moscow, 1972).
8. A. S. Iljinov, M. V. Kazarnovsky, and E. Ya. Paryev, *Intermediate-Energy Nuclear Physics* (CRC Press, Boca Raton, 1994).
9. V. E. Bunakov, Fiz. Élem. Chastits At. Yadra **11**, 1285 (1980) [Sov. J. Part. Nucl. **11**, 507 (1980)]; V. E. Bunakov and G. V. Matvejev, Z. Phys. A **322**, 511 (1985).
10. A. S. Iljinov *et al.*, Nucl. Phys. A **543**, 517 (1992).
11. G. D. Adeev *et al.*, Fiz. Élem. Chastits At. Yadra **19**, 1229 (1988) [Sov. J. Part. Nucl. **19**, 529 (1988)].
12. M. G. Itkis *et al.*, Fiz. Élem. Chastits At. Yadra **19**, 701 (1988) [Sov. J. Part. Nucl. **19**, 301 (1988)].
13. P. Braun-Munzinger *et al.*, Phys. Rev. Lett. **52**, 255 (1984); M. Waters *et al.*, Nucl. Phys. A **564**, 565 (1993).
14. Ye. S. Golubeva and A. S. Iljinov, Yad. Fiz. **63**, 365 (2000) [Phys. At. Nucl. **63**, 303 (2000)].
15. Z. Rudy *et al.*, Z. Phys. A **351**, 217 (1995); **354**, 445 (1996).

Translated by S. Slabospitsky

Polarization Phenomena in $NN \leftrightarrow D\pi$ Reactions

A. Yu. Illarionov and G. I. Lykasov

Joint Institute for Nuclear Research, Dubna, Moscow oblast, 141980 Russia

Received January 28, 2000; in final form, August 14, 2000

Abstract—On the basis of a relativistic approach, $NN \leftrightarrow D\pi$ reactions are analyzed in detail. The coherent sum of one-nucleon-exchange and pion-rescattering diagrams is calculated. It is shown that polarization observables are highly sensitive to off-mass-shell effects within the deuteron and that some of these observables can change sign upon taking these effects into account. The effect of the deuteron P wave is also investigated. The results obtained by calculating a full set of observables are compared with experimental data on the reaction $pp \rightarrow D\pi^+$. © 2001 MAIK “Nauka/Interperiodica”.

1. INTRODUCTION

Investigation of the πNN system is one of the most important problems in intermediate-energy physics. This may provide deeper insights into nucleon–nucleon interaction at energies above the pion-production threshold. In addition, such an investigation will furnish a basis for calculating more involved processes that occur in multinucleon systems. This is due to an intermediate position that phenomena occurring in pion–deuteron interaction occupy, in what is concerned with complexity, between phenomena characteristic of pion–nucleon interactions and those peculiar to pion–nuclear reactions. Since the deuteron possesses a low binding energy and a large dimension, so that the constituent proton and neutron are offset by a large distance, it can be expected that the amplitude of pion–deuteron scattering is dominated by the contribution from coherent scattering on two single nucleons; however, it is necessary, in this pattern, to introduce kinematical corrections for the motion of the nucleons and corrections for the binding energy. By way of example, we indicate that, by comparing the total cross section for elastic pion–deuteron scattering at a primary-pion energy ω , $\sigma_{\pi D}(\omega)$, with the sum of the relevant cross sections, $\sigma_{\pi p}(\omega) + \sigma_{\pi n}(\omega)$, for scattering on free nucleons, one can see that this approximation, the simplest possible one indeed, yields an astonishingly accurate result over the entire range of laboratory pion energies from the threshold to 1 GeV. In general, additional terms stemming from rescattering on two nucleons are small, provided that leading terms are not suppressed.

This is not so only for pion-production and pion-absorption processes, for which it is not obvious that the description in terms of pion–nucleon amplitudes would be sufficient. Among these, we would like

to mention the pion-absorption process proceeding through the channel $\pi D \rightarrow NN$, which is related to the inverse reaction $NN \rightarrow D\pi$ by the detailed-balance principle. All these processes can be considered as prototypes of pion production and absorption in nuclei and, for this reason alone, have been the subject of keen interest both for experimentalists and theorists over the last five decades. The point is that the structure of the deuteron has been well understood, whence it follows that the pion–deuteron system is an ideal laboratory for studying the mechanisms of pion–nucleus interactions under controllable conditions. What is of importance in pion absorption on nuclei is its kinematics that is indeed unusual on the nuclear scale: the energy transfer from the incident pion to the nucleus involved is low, while the corresponding momentum transfer is high. By way of example, we indicate that, in the absorption of a pion at rest, its mass μ is shared among the final nucleons in equal fractions; therefore, the kinetic energy of each of these nucleons in the deuteron laboratory frame is equal to half the pion mass ($T = \mu/2$). Hence, the relative momentum of the nucleons is $p = \sqrt{m\mu} = 360 \text{ MeV}/c$, which corresponds to intradeuteron distances of about $1/\sqrt{m\mu} \simeq 0.6 \text{ fm}$. This is a large quantity in relation to the characteristic scale that the binding energy e_D specifies for the intradeuteron-nucleon momentum: $\alpha_D = \sqrt{me_D} \approx 45 \text{ MeV}/c$. Although the absorption process is allowed, the required relative momentum differs significantly from momenta easily accessible in the deuteron. Such a distinction is peculiar to pion absorption or production both in the deuteron and in more complex nuclei. The requirement that the momentum transfer between the two nucleons involved be high renders the pion-absorption process highly sensitive to the dynamics of the πNN system at relatively small distances.

Because of unusual pion-production kinematics, high momentum transfers must occur in the NN system. Therefore, it is necessary to introduce mechanisms that optimize the momentum transfer between the nucleons immediately prior to and after a pion-production event. The simplest approach consists in assuming that a pion is produced on a single nucleon, in which case the characteristic absolute value of the momentum carried away must be selected in the momentum distribution of the deuteron nucleon involved. Herein lies the reason behind the smallness of the amplitude in the impulse approximation: it is impossible to compensate effectively for so large a difference in momentum only owing to the momentum distribution in the deuteron. As a result, the one-nucleon-exchange mechanism is suppressed, so that there must exist a mechanism that ensures better balance. Obviously, the next step consists in exploring rescattering processes where a pion is produced on one nucleon and is then scattered on the second one.

From the first observation of the reaction being discussed [1] to the present day, there has been a torrent of experimental investigations and theoretical calculations. According to the first investigations [2–4], it is the excitation of a delta isobar that is the main point in explaining the energy dependence of the reaction cross section. Many analyses were based on the multichannel Schrödinger equation with a separable or a local potential [5–9]—that is, they relied on the nonrelativistic approach. The first attempts at constructing a relativistic description were made in [10–13], where the calculations took into account not only the one-nucleon-exchange pole diagram but also the rescattering diagram. For example, it was demonstrated in [13] that the cross section for the reaction being discussed is dominated by the contribution of the rescattering diagram. However, the calculations there were performed under very restrictive assumptions—in particular, the relevant matrix elements were factorized and the recoil effect was disregarded. A more accurate calculation for the reaction $pp \rightarrow D\pi^+$ revealed [14–17] that, in order to achieve agreement with experimental data, it is necessary to take into account diagrams of still higher orders. Nonetheless, a successful description of all polarization observables was not obtained in those studies either. Thus, we can conclude that, although basic bare mechanisms of pion production on a deuteron have been well understood, there are still open questions in what is concerned with detailed qualitative features.

As a matter of fact, an analysis of $NN \rightarrow D\pi$ reactions always entails the problem of nucleon off-mass-shell effects within the deuteron. In the present study, we focus primarily on the role of these effects and on the contribution of the P -wave component

of the deuteron wave function [18, 19]. The problem of an off-mass-shell extrapolation of meson–nucleon vertex functions will be an important point of this discussion, since $NN \rightarrow D\pi$ processes provide a sensitive test for such questions. We also explore the sensitivity of polarization observables to these effects and prove that some observables can even change sign.

The ensuing exposition is organized as follows. In Section 2, we discuss in detail the principles underlying our procedure for constructing relativistically invariant amplitudes for $NN \rightarrow D\pi$ reactions. Here, we also introduce helicity amplitudes, which are then expanded in terms of partial-wave amplitudes; it is by using these partial-wave amplitudes that we further analyze the reaction being studied. In Section 3, we consider the pole diagram and the rescattering diagram. In Sections 4 and 5, we discuss our results and compare them with available experimental data. The conclusions are formulated in Section 6.

2. GENERAL FORMALISM

2.1. Relativistically Invariant Expansion for the Reaction Amplitude

We begin by considering a basic point of our analysis, a relativistic construction of the $NN \rightarrow D\pi$ amplitude with allowance for the requirements of covariance. In general, the \mathcal{S} -matrix element for the reactions in question, $\mathcal{S}_{\sigma_2\sigma_1}^\beta = \langle \pi D, \text{out} | p_1 p_2, \text{in} \rangle$, is related to the corresponding \mathcal{M} -matrix element by the equation

$$\mathcal{S}_{\sigma_2\sigma_1}^\beta = \frac{1}{(2\pi)^2} \frac{m}{\sqrt{E_1 E_2 2\omega 2E_D}} \quad (1)$$

$$\times \delta^{(4)}(\pi + D - p_1 - p_2) \mathcal{M}_{\sigma_2\sigma_1}^\beta,$$

where π and D are, respectively, the pion and the deuteron momentum, while the indices β , σ_1 , and σ_2 label the polarization of the deuteron involved and the projections of primary-nucleon spins. The general form of the reaction amplitude is

$$\mathcal{M}_{\sigma_2, \sigma_1}^\beta(s, t, u) \quad (2)$$

$$= [\bar{v}_{\sigma_2}^{r_2}(p_2) \chi_{r_2 r_1}^\mu(s, t, u) u_{\sigma_1}^{r_1}(p_1)] \xi_\mu^{(\beta)}(D) \varphi_\pi,$$

where $u_{\sigma_1}^{r_1}(p_1) \equiv u_1$ and $\bar{v}_{\sigma_2}^{r_2}(p_2) \equiv \bar{v}_2$ are, respectively, the spinor and the antispinor of primary nucleons having the spin projections σ_1 and σ_2 and the

Dirac indices r_1 and r_2 [20]; $\xi_\mu(D)$ is the deuteron polarization vector; φ_π is the pion field; and s , t , and u are the invariant Mandelstam variables that are given by

$$s = (p_1 + p_2)^2, \quad t = (D - p_2)^2, \quad (3)$$

$$u = (D - p_1)^2$$

and which are related by the condition $s + t + u = M^2 + 2m^2 + \mu^2 = h$.

Because of the Pauli exclusion principle, this amplitude must be symmetrized with respect to initial nucleon states, whereupon it assumes the form

$$\bar{\mathcal{M}}_{\sigma_2, \sigma_1}^\beta = \frac{1}{\sqrt{2}} \left[\mathcal{M}_{\sigma_2, \sigma_1}^\beta(s, t, u) \right. \\ \left. + (-1)^\beta \mathcal{M}_{\sigma_1, \sigma_2}^\beta(s, u, t) \right]. \quad (4)$$

The second term on the right-hand side of Eq. (4) corresponds to the interchange of two identical nucleons or, equivalently, to the interchange of t and u .

By using the formulas that describe the transformations of wave functions, one can find that, under a Lorentz transformation of all 4-vectors, $p' = \Lambda(\mathcal{A})p$, the relativistic invariance of the spinor amplitude is ensured by the condition

$$\chi_{\alpha\beta}^\mu(p_1, p_2; D, \pi) \quad (5)$$

$$= \mathcal{S}_{\alpha'}^{\alpha'}(\mathcal{A}) \chi_{\alpha'\beta'}^{\mu'}(p'_1, p'_2; D', \pi') \mathcal{S}_{\beta'}^{\beta'}(\mathcal{A}^{-1}) \Lambda_{\mu'}^\mu(\mathcal{A}^{-1}).$$

In the spinor indices α and β , this equation has the form of the condition of invariance for the Dirac matrix of momenta, $\mathcal{S}(\mathcal{A})\hat{p}'\mathcal{S}(\mathcal{A}^{-1}) = \hat{p}$, while, in the vector index μ , it merely describes a Lorentz transformation of a vector. In particular, a product of the type $p^\mu(\hat{p})_{\alpha\beta}$ satisfies condition (5).

The requirement of \mathcal{P} invariance leads to the constraint

$$\chi^\mu(\mathbf{p}_1, \mathbf{p}_2; \mathbf{D}, \pi) \quad (6)$$

$$= \eta_P \gamma_0 \chi^\mu(-\mathbf{p}_1, -\mathbf{p}_2; -\mathbf{D}, -\pi) \gamma_0 g^{\mu\mu},$$

where $\eta_P = \frac{\eta_1 \eta_2}{\eta_\pi \eta_D} (-1)^{s_D - s_1 - s_2} = -1$, η_i and s_i being, respectively, the intrinsic parities and the intrinsic spins of the particles involved.

From previous experience, it is known that invariance under time reversal and under the charge-conjugation operation holds for processes induced by strong interaction. This leads to relationships between various processes and their amplitudes, but no constraints on the structure of the amplitude $\chi_{\alpha\beta}^\mu(\mathbf{p}_1, \mathbf{p}_2; \mathbf{D}, \pi)$ arise.

Time reversal changes the sign of the particle momentum \mathbf{p} , transforming the initial to the final state. Thus, the \mathcal{T} transformation leads to

$$\chi_{\alpha\beta}^\mu(\mathbf{p}_1, \mathbf{p}_2; \mathbf{D}, \pi) \quad (7)$$

$$= \eta_T \mathcal{T}_{\alpha\alpha'}^{-1} \chi_{\mu}^{\alpha'\beta'}(-\mathbf{D}, -\pi; -\mathbf{p}_1, -\mathbf{p}_2) \mathcal{T}_{\beta'\beta} g^{\mu\mu},$$

where the time-reversal matrix has the form $\mathcal{T} = \gamma^0 \gamma^1 \gamma^3$.

Charge conjugation relates the spinor amplitude χ for the process $NN \rightarrow D\pi$ to the spinor amplitude χ_C for the charge-conjugate process $\bar{N}\bar{N} \rightarrow \bar{D}\pi$ ($\mathcal{C} = i\gamma^0 \gamma^2$):

$$\chi(\mathbf{p}_1, \mathbf{p}_2; \mathbf{D}, \pi) = \eta_C \mathcal{C} \chi_C^t(\mathbf{p}_1, \mathbf{p}_2; \mathbf{D}, \pi) \mathcal{C}^{-1}. \quad (8)$$

Upon taking into account the \mathcal{P} invariance of the reaction being considered, the amplitude χ_μ for the production of two particles of spin 1 and 0 in the interaction of two spin-1/2 particles generally involves six relativistic structures (covariants), provided that all the particles involved are on their mass shells. It is convenient to choose the general form of six independent covariants in such a way as to ensure fulfillment of the above properties for each of these covariants. For this purpose, it is advisable to introduce the t -channel set of variables:

$$P = p_1 + p_2, \quad p = (p_1 - p_2)/2, \quad (9)$$

$$p' = (D - \pi)/2.$$

The amplitude χ_μ for the reaction $NN \rightarrow D\pi$ can then be represented in the form

$$\chi_\mu = \gamma_5 \left(X_1 \gamma_\mu + X_2 \frac{p_\mu}{m} + X_3 \frac{p'_\mu}{m} \right. \quad (10)$$

$$\left. + X_4 \frac{p_\mu \hat{p}'}{m} + X_5 \left(\gamma_\mu \frac{\hat{p}'}{m} - \frac{\hat{p}'}{m} \gamma_\mu \right) + X_6 \frac{p'_\mu \hat{p}'}{m} \right).$$

2.2. Helicity Amplitudes

In calculating observables, we will make use of the method that Bourrely, Leader, and Soffer [21] proposed for constructing the helicity amplitudes for the reaction in question. As will be shown in Section 4, it is in terms of the helicity amplitudes that observables assume the simplest and the most convenient form. We first denote by μ_1 and μ_2 the helicities of primary nucleons and by λ the helicity of the final deuteron; following [14], we refer to a function $\bar{\mathcal{M}}_{\mu_2, \mu_1}^\lambda(W, \vartheta)$ depending on the initial energy W in the NN c.m. frame and on the angle ϑ as a helicity amplitude for the reaction being studied. This amplitude corresponds to the transition of our NN system from a state characterized by the helicities μ_1 and $\mu_2 = \pm 1/2$ to the $\lambda = \pm 1, 0$ state.

However, all helicity amplitudes for this process are not independent—they are related by equations following from invariance under space inversion [see Eq. (6)]. For example, parity conservation in the reaction leads to the relation [21]

$$\mathcal{M}_{\mu_2 \mu_1}^\lambda = \eta_P (-1)^{(\mu_2 - \mu_1) - \lambda} \mathcal{M}_{-\mu_2 - \mu_1}^{-\lambda} \quad (11)$$

$$= (-1)^{\mu_2 + \mu_1 + \lambda} \mathcal{M}_{-\mu_2 - \mu_1}^{-\lambda}.$$

Invariance under time reversal relates them to the helicity amplitudes for the inverse reaction; that is,

$$\mathcal{M}_{\mu_2 \mu_1}^\lambda = (-1)^{(\mu_2 - \mu_1) - \lambda} \mathcal{M}_\lambda^{\mu_2 \mu_1}. \quad (12)$$

On the other hand, the Pauli exclusion principle imposes additional symmetry on the amplitudes,

$$\mathcal{M}_{\mu_2 \mu_1}^\lambda(W, \vartheta) = (-1)^\lambda \mathcal{M}_\lambda^{\mu_1 \mu_2}(W, \pi - \vartheta), \quad (13)$$

which makes it possible to restrict the calculation of any observable to the scattering-angle range $0 < \vartheta < \pi/2$.

From Eq. (11), it follows that there are six independent helicity amplitudes. For these, we choose [14]

$$\Phi_1 = \bar{\mathcal{M}}_{++}^\pm; \quad \Phi_2 = \bar{\mathcal{M}}_{+\pm}^0; \quad \Phi_4 = \bar{\mathcal{M}}_{+-}^\pm, \quad (14)$$

which satisfy the symmetry conditions (13):

$$\Phi_1(\vartheta) = -\Phi_1(\pi - \vartheta); \quad \Phi_2(\vartheta) = \Phi_2(\pi - \vartheta); \quad (15)$$

$$\Phi_4(\vartheta) = \Phi_4(\pi - \vartheta).$$

Since some of the amplitudes $\bar{\mathcal{M}}_{\mu_2 \mu_1}^\lambda(W, \vartheta)$ vanish at limiting values of the forward and backward angles, it is preferable to use the reduced amplitudes introduced in [21] as

$$\begin{aligned} & \bar{\mathcal{M}}_{\mu_2 \mu_1}^\lambda(W, \vartheta) \\ &= \left(\sin \frac{\vartheta}{2} \right)^{|\mu + \lambda|} \left(\cos \frac{\vartheta}{2} \right)^{|\mu - \lambda|} \tilde{\mathcal{M}}_{\mu_2 \mu_1}^\lambda(W, \vartheta), \end{aligned} \quad (16)$$

where $\mu = \mu_1 - \mu_2$ and where $\tilde{\mathcal{M}}_{\mu_2 \mu_1}^\lambda(W, \vartheta)$ are free from the aforementioned singularities at $\vartheta = 0$ and $\vartheta = \pi$.

The six helicity amplitudes Φ_i can easily be related to the invariant functions X_i by using the covariant-calculation method described in [22]. We choose the z axis along the direction of the nucleon momentum $\mathbf{p}_1 \equiv \mathbf{p}$. The basic idea is that the amplitude in Eq. (2) can be reduced to the form

$$\mathcal{M}_{\mu_2 \mu_1}^\lambda = \text{tr} [\Lambda_{\mu_2 \mu_1}(p) \chi^\mu] \xi_\mu^{(\lambda)}(D) \varphi_\pi, \quad (17)$$

$$\Lambda_{\mu' \mu}(p) = u_\mu(\mathbf{p}) \otimes \bar{v}_{-\mu'}(-\mathbf{p}).$$

In order to represent this expression in a covariant form, we make use of the identity $\bar{v}_{-\mu}(-\mathbf{p}) = \bar{u}_{-\mu}^*(\mathbf{p}) \mathcal{C}$; substituting it into Eq. (17), we obtain

$$\Lambda_{\mu, \mu}(p) = -\gamma_5 \frac{\hat{n}^{(\mu)}}{2} \frac{\hat{p} + m}{2m} \mathcal{C}; \quad (18)$$

$$\Lambda_{\mu, -\mu}(p) = \frac{1}{2} \left(1 + 2\mu\gamma_5 \hat{n}^{(3)} \right) \frac{\hat{p} + m}{2m} \mathcal{C},$$

where $n^{(\mu)} = (0; 1, 2\mu i, 0)$ and $n^{(3)} = (|\mathbf{p}|/m; 0, 0, E/m)$.

With the aid of the expansion in (10), we find from (17) that

$$\begin{aligned} \tilde{\Phi}_1 = \pm \sqrt{2} \left\{ \frac{p}{m} \left(\frac{E}{m} X_2^a + \frac{E_D - E}{m} X_4^a \right) \right. \\ \left. - 2 \frac{p(E_D - E) \mp kE}{m^2} X_5^a \right\}, \end{aligned}$$

$$\begin{aligned} \tilde{\Phi}_2 = -\frac{k}{M} \left\{ X_1^s - \frac{E}{m} \left(\frac{E}{m} X_3^s + \frac{E_D - E}{m} X_6^s \right) \right\} \\ - \frac{p}{m} \left\{ \frac{E_D}{M} \left(\frac{E}{m} X_2^a + \frac{E_D - E}{m} X_4^a \right) \right. \\ \left. + 2 \frac{EE_D - M^2}{Mm} X_5^a \right\} \cos \vartheta, \end{aligned} \quad (19)$$

$$\begin{aligned} \tilde{\Phi}_4 = \sqrt{2} \left\{ \left(\frac{p}{m} X_1^s \mp 2 \frac{k}{m} X_5^a \right) \right. \\ \left. \mp 2 \frac{p^2 k}{m^3} \left(\frac{\sin^2(\vartheta/2)}{\cos^2(\vartheta/2)} \right) X_4^a \right\}, \end{aligned}$$

$$\begin{aligned} \tilde{\Phi}_5 = 2 \frac{p}{m} \left\{ \frac{E_D}{M} \left(X_1^s + \frac{pk}{m^2} X_4^a \cos \vartheta \right) \right. \\ \left. - \frac{Ek^2}{Mm^2} X_6^s \right\}, \end{aligned}$$

where $X_i^{\{s\}}(s, t, u)$ are the symmetric and the antisymmetric combinations of the relevant functions: $X_i^{\{s\}} = (X_i(\vartheta) \pm X_i(\pi - \vartheta))/\sqrt{2}$. We can see that all the amplitudes in question possess the symmetry properties (15).

In the c.m. frame, the amplitude of the reaction $NN \rightarrow G\pi$ is often parametrized in terms of the Pauli matrices. The relationship between the invariant and helicity amplitudes [Eqs. (10) and (19), respectively], on one hand, and the corresponding Pauli amplitudes (A.2), on the other hand, is given in Appendix 1.

2.3. Expansion of Helicity Amplitudes in Partial Waves

In just the same way as the scalar functions X_i , the helicity amplitudes $\bar{\mathcal{M}}_{\mu_2 \mu_1}^\lambda(W, \vartheta)$ depend on angular and energy variables. Therefore, there arises the problem of separating the angular and energy variables for each helicity amplitude. This problem can be solved with the aid of the equation (see [14])

$$\begin{aligned} & \bar{\mathcal{M}}_{\mu_2 \mu_1}^\lambda(W, \vartheta) \\ &= \sum_J \frac{2J+1}{2} (\mathcal{M}^J(W))_{\mu_2 \mu_1}^\lambda d_{\mu, -\lambda}^J(x), \end{aligned} \quad (20)$$

where $x = \cos \vartheta$, the azimuthal scattering angle φ is set to zero, J is the total angular momentum

of the system, $(\mathcal{M}^J(W))_{\mu_2\mu_1}^\lambda$ is the helicity partial-wave amplitude describing transitions between states characterized by specific values of the helicities and parity, and $d_{\mu,\lambda}^J(x)$ is a function dependent only on the angle.

By employing the orthogonality of the d functions, we can find the inverse relation

$$(\mathcal{M}^J(W))_{\mu_2\mu_1}^\lambda = \int_{-1}^1 d_{\mu,-\lambda}^J(x) \bar{\mathcal{M}}_{\mu_2\mu_1}^\lambda(W, \vartheta) dx. \quad (21)$$

Considering that the d functions possess the properties

$$d_{\mu\nu}^J(x) = d_{-\nu-\mu}^J(x) = (-1)^{\mu-\nu} d_{-\mu-\nu}^J(x) \quad (22)$$

and using parity conservation and the Pauli exclusion principle, we arrive at the relations

$$(\mathcal{M}^J(W))_{\mu_2\mu_1}^\lambda = (\mathcal{M}^J(W))_{-\mu_2-\mu_1}^{-\lambda}; \quad (23)$$

$$(\mathcal{M}^J(W))_{\mu_2\mu_1}^\lambda = (-1)^{J+(\mu_2-\mu_1)} (\mathcal{M}^J(W))_{\mu_1\mu_2}^\lambda.$$

For example, we have $\Phi_4^J = (-1)^{J+1} \Phi_4^J$.

It is common practice to introduce the LS partial-wave amplitudes $\mathcal{M}_{L^{pp}S_{pp};L^\pi}^J(W)$ corresponding to specific ${}^{2S_{pp}+1}L_J^{pp}$ initial states of the NN system involved and a spin-parity L^π of the $D\pi$ state. The helicity partial-wave amplitudes $(\mathcal{M}^J(W))_{\mu_2\mu_1}^\lambda$ are related to the LS partial wave amplitudes $\mathcal{M}_{L^{pp}S_{pp};L^\pi}^J(W)$ by the equations

$$\begin{aligned} \Phi_i^J(W) &= (\mathcal{M}^J(W))_{\mu_2\mu_1}^\lambda \quad (24) \\ &= \sum_{L^{pp}S_{pp};L^\pi} \frac{\sqrt{(2L^{pp}+1)(2L^\pi+1)}}{2J+1} \\ &\times \langle \frac{1}{2}\mu_1 \frac{1}{2} - \mu_2 | S_{pp}\mu \rangle \langle L^{pp}0 S_{pp}\mu | J\mu \rangle \\ &\times \langle L^\pi 0 1 - \lambda | J - \lambda \rangle \mathcal{M}_{L^{pp}S_{pp};L^\pi}^J(W). \end{aligned}$$

In what is concerned with the amplitudes being discussed, we notice the following: Φ_2 is of a purely singlet character; Φ_4 and Φ_5 are purely triplet amplitudes; and Φ_1 mixes singlet and triplet states in such a way that the combination $(\Phi_1 + \Phi_3)$ is a pure singlet, while $(\Phi_1 - \Phi_3)$ is a pure triplet. By applying the Pauli exclusion principle and the parity-conservation rule to the amplitude $\mathcal{M}_{L^{pp}S_{pp};L^\pi}^J(W)$, we obtain the well-known relations

$$\mathcal{M}_{L^{pp}S_{pp};L^\pi}^J = -(-1)^{L^{pp}+L^\pi} \mathcal{M}_{L^{pp}S_{pp};L^\pi}^J, \quad (25)$$

$$\mathcal{M}_{L^{pp}S_{pp};L^\pi}^J = 0 \quad \text{for} \quad (-1)^{L^{pp}+S_{pp}} = -1, \quad (26)$$

where the minus sign in (25) reflects a negative parity of the pion. The last two formulas describe all possible transitions in the $NN \leftrightarrow D\pi$ system and play the role of selection rules imposed by angular-momentum conservation. They are especially spectacular in considering the absorption channel $\pi D \rightarrow NN$. Near the threshold, this process is determined by the S wave of πD interaction ($L^\pi = 0$). Therefore, the final nucleon pair has the total angular momentum of $J = 1$, a negative parity, and the isospin of $I = 1$. This singles out the unique final state of nucleons, that which is specified by 3P_1 . With increasing energy, the P wave of πD interaction ($L^\pi = 1$) comes into play. As before, the two nucleons have the isospin of unity; however, the parity is now positive, and the states characterized the total-angular-momentum values of $J = 0, 1$, and 2 are allowed. Therefore, the final nucleons must be in a singlet state, and only the 1S_0 and 1D_2 states are possible. The S - and the P -wave contribution are dominant up to the region of delta-resonance excitation in the πN channel.

For LS partial waves, it is common practice to use the symbols ${}^{2S_{pp}+1}L_J^{pp}L^\pi$ numbered as a_0, a_1, a_2, \dots according to the value of L^π [23, 24]. The relationship between the initial (NN), the intermediate ($N\Delta$), and the final ($D\pi$) state and all conventions are given in Table 1. In order to fix arbitrariness in the choice of the phases, the phase of the ${}^3P_1S \equiv a_0$ wave, which shows but a weak energy dependence, is set to zero (all waves are multiplied by $a_0^*/|a_0|$) in accordance with the convention in [25].

In order to obtain the first qualitative insights into the dynamics of these amplitudes, we recall that the delta resonance is of importance at intermediate energies. It is therefore natural to explore those channels of $NN \leftrightarrow D\pi$ where the delta resonance is operative in intermediate states. We will study the quantum numbers of the $N\Delta$ pair produced in the relative S state—that is, the coupling of the spin-isospin of the delta $(3/2, 3/2)^+$ state to the nucleon $(1/2, 1/2)^+$ state. The parity of possible spin-isospin states that are characterized by $I = 1$ or 2 and $J = 1$ or 2 is positive. From the data in Table 1, we find that only the 1D_2 state (that is, the amplitude a_2) can involve a delta resonance. Hence, the assumption of dominance naturally entails the conclusion that the amplitude a_2 must be a leading one—in particular, it must be much greater than the amplitude a_0 , which is characterized by the quantum numbers 1S_0 and which arises in the $L^\pi = 1$ state as well.

In the approximation of the first three waves, where $\tilde{a}_0 = \sqrt{3}a_0$, $\tilde{a}_1 = a_1$, and $\tilde{a}_2 = \sqrt{5}a_2$, we have

$$\tilde{\Phi}_3(W, \vartheta) \approx \mp 5 \sqrt{\frac{3}{2}} x \Phi_3^2(W) + \dots \quad (27)$$

$$= \mp \frac{3x}{2\sqrt{2}} \tilde{a}_2 + \dots,$$

$$\tilde{\Phi}_2(W, \vartheta) \approx \frac{1}{2} \Phi_2^0(W) \quad (28)$$

$$+ \frac{5}{4} (3x^2 - 1) \Phi_2^2(W) + \dots$$

$$= -\frac{1}{2} \left[\frac{\tilde{a}_1}{\sqrt{2}} - \frac{3x^2 - 1}{2} \tilde{a}_2 \right] + \dots,$$

$$\tilde{\Phi}_4(W, \vartheta) \approx \frac{3}{2} \Phi_4^1(W) \quad (29)$$

$$+ \frac{5}{2} (2x \mp 1) \Phi_4^2(W) + \dots = \frac{\tilde{a}_0}{2\sqrt{2}} + \dots,$$

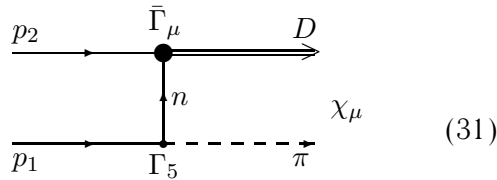
$$\tilde{\Phi}_5(W, \vartheta) \approx \frac{3}{\sqrt{2}} \Phi_5^1(W) + \dots = -\frac{\tilde{a}_0}{2} + \dots \quad (30)$$

We note that, in this approximation, the helicity amplitudes $\tilde{\Phi}_3$ satisfy the relation $\tilde{\Phi}_1 \approx -\tilde{\Phi}_3$, while $\tilde{\Phi}_4$ and $\tilde{\Phi}_5$ involve no angular dependence; we also have $\tilde{\Phi}_4 \approx \tilde{\Phi}_6 \approx -\tilde{\Phi}_5/\sqrt{2}$.

3. REACTION MECHANISM

3.1. One-Nucleon-Exchange and πNN Vertex

Within the one-nucleon-exchange model, the amplitude χ_μ has the simple form



$$\quad (31)$$

$$= g^+ \bar{\Gamma}_\mu(D) \mathcal{S}_F(n) \Gamma_5,$$

where the quantity $\bar{\Gamma}_\mu(D)$ describes the $pn \rightarrow D$ deuteron vertex involving one off-mass-shell nucleon, $\mathcal{S}_F(n) = (\hat{n} - m + i0)^{-1}$ is the fermion propagator, $g^+ = \sqrt{2}g^0 = \sqrt{2}g$ is the meson coupling constant ($g^2/4\pi = 14.7$), and $n^2 = (D - p_2)^2 = t$. The vertex $\bar{\Gamma}_\mu(D)$ can be related to the deuteron wave function by using the equation [26]

$$\bar{\Psi}_\mu = \frac{\bar{\Gamma}_\mu}{m^2 - n^2 + i0} = \varphi_1(t) \gamma_\mu + \varphi_2(t) \frac{n_\mu}{m} \quad (32)$$

$$+ \left(\varphi_3(t) \gamma_\mu + \varphi_4(t) \frac{n_\mu}{m} \right) \frac{\hat{n} - m}{m}.$$

The form factors $\varphi_i(t)$ are related to two large components u and w of the deuteron wave function, which correspond to the 3S_1 and 3D_1 deuteron states, and to two small components v_t and v_s , which correspond to the 3P_1 and 1P_1 states.

In a theoretical analysis of intermediate-energy processes, the structure of hadrons is often described by multiplying pointlike operators by corresponding form factors. It is usually implied that the vertices involved have the same structure both for free mass-shell hadrons and for off-mass-shell hadrons. But in the present case, the off-mass-shell pion vertex possesses a far richer structure: there are many independent operators, while the form factors involved may depend on more than one variable. The situation is similar to that in constructing an off-mass-shell electromagnetic vertex [27, 28]. It is usually assumed that off-mass-shell effects can be ignored because of their smallness, and use is made of free vertices. In studying delicate issues, such as searches for quark-gluon degrees of freedom or investigation of contributions from small wave-function components, it is necessary, however, to check in detail assumptions like that mentioned immediately above. Let us discuss the form of the πNN vertex Γ_5 on the basis of only the requirements of \mathcal{P} invariance and covariance. In the (most general) case where all particles involved in the vertex are off their mass shells, this vertex can be decomposed into four covariants as [29]

$$\Gamma_5(p_f, p_i) = \gamma_5 G_1 + \frac{\hat{p}_f - m}{m} \gamma_5 G_2 \quad (33)$$

$$+ \gamma_5 \frac{\hat{p}_i - m}{m} G_3 + \frac{\hat{p}_f - m}{m} \gamma_5 \frac{\hat{p}_i - m}{m} G_4,$$

where $G_i(t; p_i^2, p_f^2)$ are functions dependent on the invariant momentum transfer squared $t = (p_i - p_f)^2$ and on the nucleon masses $p_{i,f}^2$ (these are so-called pion form factors).

In our case, where $p_f = n$ and only one nucleon is off the mass shell, only the first two terms in decomposition (33) survive, since the third and the fourth term vanish by virtue of the Dirac equation for a free fermion. Therefore, expression (33) can be rewritten in the form of a linear combination of a pseudoscalar and a pseudovector component:

$$\Gamma_5(t) = \gamma_5 \left(G_1(t) + G_2(t) \frac{\hat{n} + m}{m} \right) \quad (34)$$

$$= G^{\text{PS}}(t) \gamma_5 + G^{\text{PV}}(t) \frac{\hat{n}}{2m} \gamma_5.$$

For the mass-shell neutron ($n^2 = m^2$) and a virtual pion, we arrive at the free πNN vertex $\Gamma_5 = G_1(t, m^2, m^2) \gamma_5$.

By making use of Eqs. (10) and (31) ($n = p' + p$), we eventually find explicit expressions for the invariant amplitudes $\{X_i\}_{i=1}^6$ in the one-nucleon-exchange model. The results are

$$X_1 = -g^+ \{G^{\text{PV}} \varphi_1 + 2G^{\text{PS}} \varphi_3\} \frac{m^2 - t}{2m}, \quad (35)$$

Table 1. LS partial-wave amplitudes $\mathcal{M}_{L^{pp}S_{pp};L^\pi}^J(W)$ for $NN \leftrightarrow D\pi$ reactions (the results are presented for $L^\pi \leq 6$, $L^\pi = 0, 1$ amplitudes being dominant)

J^P	${}^{2S_{pp}+1}L_J^{pp}L^\pi$	Notation	$\mathcal{M}_{L^{pp}S_{pp};L^\pi}^J$	Formula (24)	$L_{N\Delta}$
0^+	1S_0P	a_1	$\mathcal{M}_{00;1}^0$	$-\sqrt{2}\Phi_2^0$	D
1^-	3P_1S	a_0	$\mathcal{M}_{11;0}^1$	$\sqrt{2/3}(2\Phi_4^1 - \Phi_5^1)$	P
1^-	3P_1D	a_3	$\mathcal{M}_{11;2}^1$	$2/\sqrt{3}(\Phi_4^1 + \Phi_5^1)$	P
2^+	1D_2P	a_2	$\mathcal{M}_{20;1}^2$	$1/\sqrt{5}(\sqrt{3}[\Phi_1^2 + \Phi_3^2] + 2\Phi_2^2)$	S
2^+	1D_2F	a_7	$\mathcal{M}_{20;3}^2$	$\sqrt{2/5}([\Phi_1^2 + \Phi_3^2] - \sqrt{3}\Phi_2^2)$	S
2^-	3P_2D	a_4	$\mathcal{M}_{11;2}^2$	$\sqrt{2/5}([\Phi_1^2 - \Phi_3^2] + \sqrt{6}\Phi_4^2)$	P
2^-	3F_2D	a_5	$\mathcal{M}_{31;2}^2$	$-1/\sqrt{5}(\sqrt{3}[\Phi_1^2 - \Phi_3^2] - 2\sqrt{2}\Phi_4^2)$	P
3^-	3F_3D	a_6	$\mathcal{M}_{31;2}^3$	$1/\sqrt{7}(4\Phi_4^3 - \sqrt{6}\Phi_5^3)$	P
3^-	3F_3G	a_9	$\mathcal{M}_{31;4}^3$	$2/\sqrt{7}(\sqrt{3}\Phi_4^3 + \sqrt{2}\Phi_5^3)$	P
4^+	1G_4F	a_8	$\mathcal{M}_{40;3}^4$	$1/3(\sqrt{5}[\Phi_1^4 + \Phi_3^4] + 2\sqrt{2}\Phi_2^4)$	D
4^+	1G_4H	a_{13}	$\mathcal{M}_{40;5}^4$	$1/3(2[\Phi_1^4 + \Phi_3^4] - \sqrt{10}\Phi_2^4)$	D
4^-	3F_4G	a_{10}	$\mathcal{M}_{31;4}^4$	$2/3([\Phi_1^4 - \Phi_3^4] + \sqrt{5}\Phi_4^4)$	F
4^-	3H_4G	a_{11}	$\mathcal{M}_{51;4}^4$	$-1/3(\sqrt{5}[\Phi_1^4 - \Phi_3^4] - 4\Phi_4^4)$	F
5^-	3H_5G	a_{12}	$\mathcal{M}_{51;4}^5$	$1/\sqrt{11}(2\sqrt{6}\Phi_4^5 - \sqrt{10}\Phi_5^5)$	F
5^-	3H_5I	a_{14}	$\mathcal{M}_{51;6}^5$	$2/\sqrt{11}(\sqrt{5}\Phi_4^5 + \sqrt{3}\Phi_5^5)$	F

$$X_2 = -g^+ m \left[(G^{\text{PS}} + G^{\text{PV}})(\varphi_1 + \varphi_2) - \{G^{\text{PV}}(\varphi_2 + \varphi_3 + \varphi_4) + 2G^{\text{PS}}\varphi_4\} \frac{m^2 - t}{2m^2} \right],$$

$$X_3 = -g^+ m \left[(G^{\text{PS}} + G^{\text{PV}})(2\varphi_1 + \varphi_2) - \{G^{\text{PV}}(\varphi_2 + 2\varphi_3 + \varphi_4) + 2G^{\text{PS}}\varphi_4\} \frac{m^2 - t}{2m^2} \right],$$

$$X_4 = X_6$$

$$= g^+ m \left\{ (G^{\text{PS}} + G^{\text{PV}})\varphi_2 - G^{\text{PV}} \frac{m^2 - t}{2m^2} \varphi_4 \right\},$$

$$X_5 = -g^+ \frac{m}{2} \left\{ (G^{\text{PS}} + G^{\text{PV}})\varphi_1 - G^{\text{PV}} \frac{m^2 - t}{2m^2} \varphi_3 \right\}.$$

It should be noted that the amplitudes X_i satisfy the equations $X_2 - X_3 + 2X_5 = 0$ and $X_4 = X_6$.

For the first time, a DNN vertex of this type was studied by Buck and Gross [18] on the basis of the Gross equation for nucleon–nucleon scattering. Those authors used the one-boson-exchange model and included the exchanges of pions, rho mesons, omega mesons, and sigma mesons in their consideration. In addition, they assumed that the form factors G^{PS} and G^{PV} possess the same t structure, $G^{\text{PS}}(t) = \lambda h_N(t)$ and $G^{\text{PV}}(t) = (1 - \lambda)h_N(t)$, and

involve the so-called mixing parameter λ , for which they used the values of $\lambda = 0.0, 0.2, 0.4, 0.6, 0.8$, and 1.0 . In each of those cases, the parameters of the one-boson-exchange model were selected in such a way as to reproduce the static properties of the deuteron. Buck and Gross found that the weight of the small components in the deuteron wave function, $P_{\text{small}} = \int_0^\infty p^2 dp [v_t^2(p) + v_s^2(p)]$, grows monotonically with increasing λ from approximately 0.03% at $\lambda = 0$ to 1.5% at $\lambda = 1$.

The function $h_N(t)$ is a nucleon form factor that is associated with an off-mass-shell nucleon and which can be taken, in just the same way as in [30, 14], in a resonance form of the Breit–Wigner type,

$$h_N(t) = \frac{m - E_R}{\sqrt{t - E_R + i\Gamma(t)/2}}, \tag{36}$$

$$\Gamma(t) = 2\bar{\alpha}\Theta(\sqrt{t} - m - \mu) \exp \left\{ -\frac{\bar{\beta}}{\sqrt{t} - m - \mu} \right\},$$

with $\bar{\alpha} = 0.26$ GeV, $\bar{\beta} = 0.40$ GeV, and $E_R = 1.42$ GeV.

3.2. Rescattering Diagram

Let us now consider the second-order diagram describing virtual-pion rescattering on a primary nucleon. A similar mechanism of $NN \rightarrow D\pi$ reactions was analyzed by many authors (see, for example, [13,

Table 2. Kinematical limits at $T_p = 0.578$ GeV for $s_{\pi N}$ (GeV²), $t_{\pi N}$ (GeV²), $x = q^2/\mu^2$, and $x_N = k^2/m^2$ (the last two quantities are dimensionless) in the coplanar approximation ($\vartheta_\eta = \pi - \vartheta$, $\varphi_\eta = \pi$) versus the absolute value of the loop 3-momentum, $|\boldsymbol{\eta}|$, and the scattering angle ϑ

$ \boldsymbol{\eta} $	Independent of ϑ		$\vartheta = 0$		$\vartheta = \pi/2$		$\vartheta = \pi$	
	$s_{\pi N}$	x_N	x	$t_{\pi N}$	x	$t_{\pi N}$	x	$t_{\pi N}$
0.0	1.459	0.969	-13.9	-0.529	-13.9	-0.303	-13.9	-0.077
$\eta_m/2$	1.383	0.983	-5.5	-0.287	-16.0	-0.252	-26.5	-0.218
η_m	1.162	0.853	-1.1	-0.100	-22.1	-0.257	-43.0	-0.413

Note: In the coplanar approximation, $s_{\pi N}$ and x_N are independent of ϑ . The limits on the loop 3-momentum are specified by the physical region of the πN energy, $0.0 \leq |\boldsymbol{\eta}| \leq \eta_m$ with $\eta_m \approx 0.366$ GeV/ c .

14]). That the scattered pion possesses a high momentum ($q \sim \sqrt{m\omega}$, where ω is the final-pion energy) and low energy ($q_0 \sim \omega/2$)—that is, it is essentially an off-mass-shell particle—is an important feature of this mechanism. For this reason, the results of the calculations are highly sensitive to the choice of procedure for an off-mass-shell extrapolation of the elastic πN vertex; on the other hand, a high degree of spacelike off-mass-shellness of the 4-momentum of the rescattered pion leads to a strong dependence on the form of the πNN form factor, with the result that there arise constraints on the cutoff parameter Λ in this form factor.

Our procedure for constructing helicity amplitudes corresponding to the triangle diagram is similar to that reported in [14]; for this reason, we only briefly dwell on the points in the relevant derivation that are basically dissimilar to those in [14]. In dealing with the rescattering diagram, we make use of the relativistic impulse approximation; that is, we restrict our consideration to the contribution of the spectator nucleon with a momentum η . Specifically, this contribution arises from the integration of the spectator propagator with respect to the loop energy variable η_0 . Here, the spectator nucleon is on its mass shell; that is, $\eta^2 = m^2$. As in [17], we disregard corrections to the spectator contribution that emerge in taking the loop integral of the residue of the pion propagator, where the pion is on its mass shell as an antiparticle and where the two other intermediate nucleons are off the mass shell. As was shown in [14], the pion-residue contribution to the reaction amplitude is small (not greater than 10%). The contribution that comes from the residue of the second nucleon propagator (which corresponds to the nucleon k in the rescattering diagram) is also very small (see [14]). Therefore, we disregard this small correction as well. The spectator contribution can be

represented as

$$= \frac{g^+}{(2\pi)^3} \int h_\pi(q^2) \frac{\mathcal{F}_\mu(\eta, \eta_0 = \sqrt{\eta^2 + m^2}) d^3\eta}{q^2 - \mu^2} \frac{1}{2\eta_0}, \quad (37)$$

where $h_\pi(q^2)$ is a form factor that corresponds to an off-mass-shell pion and which, according to [13, 31], was chosen in the monopole form $h_\pi(q^2) = (\Lambda^2 - \mu^2)/(\Lambda^2 - q^2)$, with Λ being the relevant cutoff parameter. In general, \mathcal{F}_μ can be represented as

$$\mathcal{F}_\mu = \Gamma_5(\hat{\eta} - m)\bar{\Psi}_\mu(D)\left(\hat{k} + m\right)\mathcal{T}_{\pi N}, \quad (38)$$

where the deuteron wave function $\bar{\Psi}_\mu(D)$ is related to the deuteron vertex $\bar{\Gamma}_\mu(D)$ by Eq. (32) and where $\mathcal{T}_{\pi N}$ is the amplitude of elastic pion–nucleon scattering for the case where there is one off-mass-shell nucleon ($k^2 \neq m^2$). The energy $s_{\pi N}$, the momentum transfer $u_{\pi N}$, and the virtual-pion mass q^2 are independent of the azimuthal angle φ_η :

$$\begin{aligned} s_{\pi N} &= (p_1 + q)^2 = s - 2\sqrt{s}\eta_0 + m^2, \\ u_{\pi N} &= (p_1 - q)^2 = t, \\ q^2 &= 2(m^2 - E\eta_0 - p\eta_3). \end{aligned} \quad (39)$$

The physical region of πN energies, $m + \mu < \sqrt{s_{\pi N}} < \sqrt{s} - m = 2T_p + m$, determines the limits of integration with respect to η (for $T_p = 0.578$ GeV):

$$\eta_m^0 = \frac{s - (m + \mu)^2 + m^2}{2\sqrt{s}}, \quad (40)$$

$$\eta_m = \sqrt{(\eta_m^0)^2 - m^2} \approx 0.366 \text{ GeV}/c.$$

For calculating the contribution of the two-nucleon pion-absorption mechanism to $NN \rightarrow D\pi$ reactions,

it is of importance that the rescattered pion and the rescattered nucleon are off-mass-shell particles. By way of example, Table 2 displays the virtualities for the meson ($x = q^2/\mu^2$) and for the nucleon ($x_N = k^2/m^2$) in the delta-resonance region.

Hence, we need information about the behavior of the pion–nucleon amplitude for the case where colliding particles are off their mass shells. We propose to make use of the following scheme for constructing a continuation of the elastic pion–nucleon amplitude to the off-mass-shell region.

Let us consider the most general case of pion–nucleon scattering, that in which the initial and final nucleon momenta (denoted by p_i and p_f) and the pion momenta (q_i and q_f) are constrained only the conservation of the energy–momentum tensor in the reaction. In the case observed experimentally, all the particles involved are on their mass shells ($p_i^2 = p_f^2 = m^2$ and $q_i^2 = q_f^2 = \mu^2$), but we lift this constraint in order to obtain the off-mass-shell $\mathcal{T}_{\pi N}$ amplitude. The general requirements of invariance result in that the amplitude can be decomposed into eight covariants, and not into two, as in the case where all particles are on their mass shells. Specifically, the off-mass-shell amplitude can be represented in the form

$$\begin{aligned} \mathcal{T}_{\pi N}^{(I)} = & T_1^{(I)} + T_2^{(I)} \hat{Q} + \frac{\hat{p}_f - m}{m} \left(T_3^{(I)} + T_4^{(I)} \hat{Q} \right) \\ & + \left(T_5^{(I)} + T_6^{(I)} \hat{Q} \right) \frac{\hat{p}_i - m}{m} + \frac{\hat{p}_f - m}{m} \\ & \times \left(T_7^{(I)} + T_8^{(I)} \hat{Q} \right) \frac{\hat{p}_i - m}{m}, \end{aligned} \quad (41)$$

where $Q = (q_i + q_f)/2$ and $T_i^{(I)}(s_{\pi N}, t_{\pi N}, u_{\pi N}; p_i^2, q_i^2; p_f^2, q_f^2)$ are eight scalar amplitudes, which are generally dependent on the Mandelstam variables of the process and on the squares of the particle masses. In the case where one of the nucleons is on its mass shell—for example, $p_i^2 = m^2$ —we have only four terms in the decomposition given by (41). The remaining terms vanish by virtue of the Dirac equation $(\hat{p}_i - m)u(p_i) = 0$. Therefore, expression (41) can be rewritten in the form

$$\mathcal{T}_{\pi N}^{(I)} = \tilde{T}_1^{(I)} + \tilde{T}_2^{(I)} \hat{q}_f + \frac{\hat{p}_f - m}{m} \left(\tilde{T}_3^{(I)} + \tilde{T}_4^{(I)} \hat{q}_f \right). \quad (42)$$

We calculate $\tilde{T}_{1-4}^{(I)}$ on the basis of the on-mass-shell πN partial-wave amplitudes $\mathcal{T}_{l\pm}^{\text{on}}(s_{\pi N})$ under the assumption that

$$\mathcal{T}_{l\pm}(s_{\pi N}, t_{\pi N}, u_{\pi N}) \approx \mathcal{T}_{l\pm}^{\text{on}}(s_{\pi N}), \quad (43)$$

where the quantities $\mathcal{T}_{l\pm}^{\text{on}}(s_{\pi N})$ are taken from the Karlsruhe–Helsinki partial-wave analysis [32].

In expanding the invariant amplitudes for pion–nucleon scattering in partial waves, we took entirely into account the off-mass-shell kinematics of the operators projecting the angular momentum. Models like this have some bearing on popular resonance models that were constructed to describe such pion–nucleon amplitudes [33], which comply well with current algebras and with the hypothesis of a partial conservation of the axial current, and which were used quite successfully to describe many reactions [34]. Since the inclusion of higher partial waves leads to only small corrections in the total amplitude, we restrict our consideration to the four lowest waves, which are of greatest importance. For higher partial waves, use is made of conventional on-mass-shell relations between the invariant functions and partial waves. Exact expressions for the invariant amplitudes $\tilde{T}_{1-4}^{(I)}$ are presented in Appendix 2.

The triple integral in (37) with respect to the azimuthal angle φ_η , the polar angle ϑ_η , and the absolute value η of the 3-momentum is calculated numerically according to the procedure described in Appendix 3. In summary, six triple integrals featuring complex-valued integrands are computed for each value of the collision angle.

4. OBSERVABLES

By using the formalism of helicity amplitudes that was developed in Section 2, we can easily calculate any observables, such as the differential cross sections and asymmetries.

It is common practice to specify the parameters $(\alpha\beta | LM)$ of $NN \rightarrow D\pi$ reactions as [21, 35]

$$\begin{aligned} (\alpha\beta | LM)^{\text{Mad}} = & \varepsilon_\beta (-1)^M \\ & \times \text{tr} \left[\sigma_\alpha \sigma_\beta \overset{+}{\mathcal{M}}_{\mu_2\mu_1}^\lambda T_M^L(s_D) \mathcal{M}_{\mu_2\mu_1}^\lambda \right] \Sigma^{-1}, \end{aligned} \quad (44)$$

where $\varepsilon_0 = \varepsilon_x = 1$ and $\varepsilon_y = \varepsilon_z = -1$; σ_α and σ_β ($\alpha, \beta = 0, x, y, z$) are the Pauli spin operators for primary nucleons; and $T_M^L(s_D)$ is a spin-1 tensor of rank $L \leq 2$. The observables in question are normalized by the condition $(00 | 00) = 1$. Therefore, the differential cross section for the reaction in question is related to the quantity Σ by the equation

$$\Sigma = 2 \sum_1^6 |\Phi_i|^2 = 4 \frac{p}{k} \left(\frac{m}{4\pi\sqrt{s}} \right)^{-2} \frac{d\sigma}{d\Omega} = \frac{1}{\sigma_0} \frac{d\sigma}{d\Omega}, \quad (45)$$

where p and k are the c.m. momenta of the primary proton and the final deuteron. In all, there are $4 \times 4 \times 9 = 144$ parameters of the reaction. Since there are six independent amplitudes, there remain only

36 linearly independent bilinear observables. They possess the following symmetry properties:

$$(\alpha\beta | LM) - \begin{cases} \text{real} \\ \text{imag.} \end{cases},$$

$$\text{if } n_0 + n_y + L - \begin{cases} \text{even} \\ \text{odd} \end{cases},$$

$n_{0,y}$ is the number of $\sigma_{0,y}$;

$$(\alpha\beta | LM)_\vartheta = (-1)^M (\beta\alpha | LM)_{\pi-\vartheta}, \quad (46)$$

$$(\alpha\beta | LM) = \zeta_\alpha \zeta_\beta (-1)^{L+M} (\alpha\beta | L-M),$$

$$\zeta_0 = \zeta_y = 1, \quad \zeta_x = \zeta_z = -1.$$

We now present expressions for various spin observables in terms of Φ_i :

$$A_{y0} = 4 \text{Im}(\Phi_1\Phi_4^* + \Phi_2\Phi_5^* + \Phi_3\Phi_6^*)\Sigma^{-1}, \quad (47)$$

$$A_{0y}(\vartheta) = A_{y0}(\pi - \vartheta),$$

$$A_{xz} = -4 \text{Re}(\Phi_1\Phi_4^* + \Phi_2\Phi_5^* + \Phi_3\Phi_6^*)\Sigma^{-1}, \quad (48)$$

$$A_{zx}(\vartheta) = A_{xz}(\pi - \vartheta),$$

$$A_{zz} = -1 + 4(|\Phi_4|^2 + |\Phi_5|^2 + |\Phi_6|^2)\Sigma^{-1}, \quad (49)$$

$$A_{yy} = -1 + 2(|\Phi_1 + \Phi_3|^2 + |\Phi_4 + \Phi_6|^2)\Sigma^{-1}, \quad (50)$$

$$A_{xx} = A_{zz} + 2(|\Phi_1 + \Phi_3|^2 - |\Phi_4 + \Phi_6|^2)\Sigma^{-1}. \quad (51)$$

The analogous expressions for the components of the deuteron polarization tensor are

$$iT_{11} = -\sqrt{6} \text{Im}[(\Phi_1^* - \Phi_3^*)\Phi_2 + (\Phi_4^* - \Phi_6^*)\Phi_5]\Sigma^{-1}, \quad (52)$$

$$T_{20} = [1 - 6(|\Phi_2|^2 + |\Phi_5|^2)\Sigma^{-1}]/\sqrt{2}, \quad (53)$$

$$T_{21} = \sqrt{6} \text{Re}[(\Phi_1^* - \Phi_3^*)\Phi_2 + (\Phi_4^* - \Phi_6^*)\Phi_5]\Sigma^{-1}, \quad (54)$$

$$T_{22} = 2\sqrt{3} \text{Re}(\Phi_1^*\Phi_3 + \Phi_4^*\Phi_6)\Sigma^{-1} \\ = (1 + 3A_{yy} - \sqrt{2}T_{20})/(2\sqrt{3}). \quad (55)$$

The angular distributions for $NN \rightarrow D\pi$ processes have a form that is expected from S - and P -wave dominance. The S -wave cross section is isotropic, whereas the sum of the S - and the P -wave cross section has the characteristic form $A + B \cos^2 \vartheta$. Therefore, the differential cross section is usually expanded in a series in Legendre polynomials:

$$2\pi \frac{d\sigma}{d\Omega} = \sum_j \alpha_{2j} \mathcal{P}_{2j}(\cos \vartheta) \quad (56)$$

$$= \alpha_0 + \alpha_2 \mathcal{P}_2(\cos \vartheta) + \dots$$

It is convenient to express the expansion coefficients in terms of the partial S wave \tilde{a}_0 and the partial P waves \tilde{a}_1 and \tilde{a}_2 , which are defined in Table 1:

$$\sigma_{\text{tot}} = \frac{1}{2} \int d\Omega \frac{d\sigma}{d\Omega} = \alpha_0 = \frac{\sigma_0}{4} \sum_i |\tilde{a}_i|^2, \quad (57)$$

$$\alpha_2 = \frac{\sigma_0}{4} (|\tilde{a}_2|^2 - 2\sqrt{2} \text{Re}(\tilde{a}_1\tilde{a}_2^*)).$$

In the total cross section, the factor of 1/2 reflects the fact that identical protons should not be doubly counted in performing integration with respect to the angles. As a matter of fact, it is quite surprising that the total reaction cross section α_0 and the coefficient α_2 of the second-order Legendre polynomial in the resonance region are nearly identical both in shape and in magnitude. To within 10%, the ratio α_2/α_0 is equal to unity at energies in the range $30 < T_\pi < 165$ MeV. This value is natural for $NN \leftrightarrow D\pi$ processes, which are determined by the intermediate $N\Delta$ state of zero relative angular momentum. In any such model, the amplitudes a_0 and a_1 are negligible; hence, we have $\alpha_0 \approx \alpha_2$. The isotropic S -wave is dominant at very low energies. The contributions from higher partial waves manifest themselves at higher energies.

The remaining observables can also be expressed in terms of these three waves. The results are

$$\Sigma A_{y0} \approx \frac{\sin \vartheta}{4} \text{Im}[(\sqrt{2}\tilde{a}_1 - \tilde{a}_2) - 4\tilde{a}_2 \mathcal{P}_2(x)] \tilde{a}_0^* + \dots, \quad (58)$$

$$\sigma A_{xz} \approx -\frac{\sin \vartheta}{4} \text{Re}[(\sqrt{2}\tilde{a}_1 - \tilde{a}_2) - 4\tilde{a}_2 \mathcal{P}_2(x)] \tilde{a}_0^* + \dots, \quad (59)$$

$$A_{zz} \approx -1 + \frac{|\tilde{a}_0|^2}{2\Sigma} + \dots, \quad (60)$$

$$A_{yy} \approx -1 + \frac{|\tilde{a}_0|^2}{4\Sigma} + \dots \approx A_{xx},$$

$$\Sigma iT_{11} \approx -\left(\frac{3}{2}\right)^{3/2} \text{Im}(\tilde{a}_1\tilde{a}_2^*) \frac{\sin \vartheta}{2} + \dots, \quad (61)$$

$$\sqrt{2}T_{20} \approx -2 + \frac{1}{4\Sigma} \quad (62)$$

$$\times \left[(2 + \mathcal{P}_2(x)) |\tilde{a}_0|^2 + \frac{27}{8} |\tilde{a}_2|^2 \sin^2 2\vartheta + \dots \right],$$

$$\Sigma T_{21} \approx -\frac{\sqrt{3}}{16} \left[(|\tilde{a}_0|^2 - 3\sqrt{2} \text{Re}(\tilde{a}_1\tilde{a}_2^*)) + 6|\tilde{a}_2|^2 \mathcal{P}_2(x) + \dots \right] \sin 2\vartheta, \quad (63)$$

$$\Sigma T_{22} \approx \frac{\sqrt{3}}{16} \left[(|\tilde{a}_0|^2 - 3|\tilde{a}_2|^2) - 6|\tilde{a}_2|^2 \mathcal{P}_2(x) + \dots \right] \sin^2 \vartheta. \quad (64)$$

We note that, in the approximation being considered, the observables A_{zz} and $A_{yy} \approx A_{xx}$ are independent

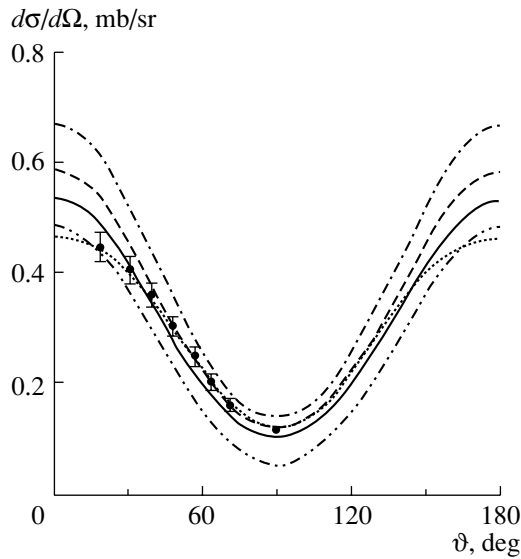


Fig. 1. Differential cross section $d\sigma/d\Omega$ for scattering in the process $pp \rightarrow D\pi^+$ as a function of the collision angle at the incident-proton kinetic energy of $T_p = 578$ MeV. The cutoff parameter Λ and the mixing parameter λ were varied both in the deuteron wave function and in the πNN vertex. The dashed ($\lambda = 0.6, \Lambda = 1$), the solid ($\lambda = 0.8, \Lambda = 0.6$), and the dash-dotted ($\lambda = 1, \Lambda = 0.6$) curve were computed on the basis of the Buck–Gross model [18] for the deuteron wave function. The result of the calculation with the deuteron wave function taken in the Locher model [17] is represented by the dash-and-double-dot curve ($\lambda = 1, \Lambda = 1$). The dotted curve corresponds to the data of the partial-wave analysis from [25]. Experimental data were borrowed from [15, 16, 25]. All the observables are presented according to the Madison convention [36].

of the collision angle—they are determined by the initial reaction energy.

5. RESULTS AND DISCUSSION

With reference to studying the small components of the deuteron wave function, we have calculated the differential cross section $d\sigma/d\Omega$ (45) for the reaction $pp \rightarrow D\pi^+$ and its polarization features as given by (47)–(55) versus the collision angle, the kinetic energy of the incident proton being fixed at $T_p = 578$ MeV. All the calculated quantities are presented in accordance with the Madison convention [36] and are compared both with existing experimental data [15, 25] and with the results of the partial-wave analysis from [37] (these results are shown by the dotted curves in the figures). For various values of the mixing parameter λ , the cutoff parameter Λ corresponding to the πNN vertex was chosen in such a way as to ensure the best fit of the theoretical curves to the experimental cross section $d\sigma/d\Omega$ (see Fig. 1). It should be noted that a variation of the cutoff parameter Λ at a

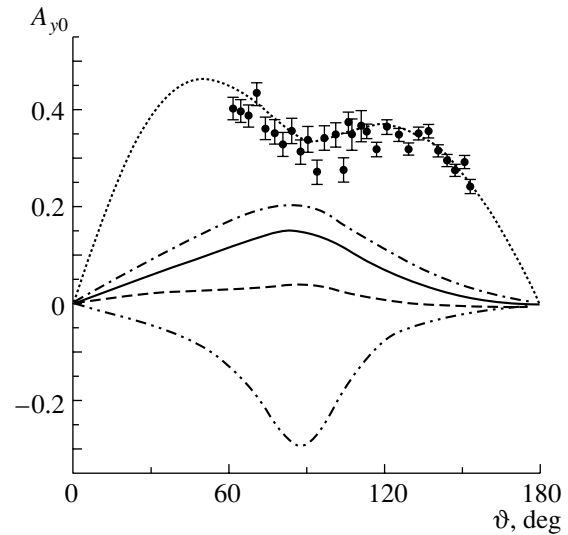


Fig. 2. Asymmetry A_{y0} . The notation is identical to that in Fig. 1.

fixed value of the mixing parameter λ has virtually no effect on the shape of the polarization curves, but that it affects the absolute cross-section value.

At intermediate energies, the contribution of the rescattering diagram is very large since the cross section for elastic pion–nucleon scattering is very large owing to possible delta-isobar production at these energies. It should be noted that, with the nonrelativistic deuteron wave function [15], it is impossible to reproduce the magnitude of the differential cross section over the entire range of the collision angle ϑ . By using the Buck–Gross model for the deuteron wave function, a fairly accurate description of the differential cross section $d\sigma/d\Omega$ for $\lambda = 0.6 - 0.8$ can be obtained.

Proceeding to consider polarization features, we find a high sensitivity of the result to the contribution of the small components of the deuteron wave function. The observables A_{y0} (Fig. 2) and iT_{11} (Fig. 3) can even change sign when the mixing parameter λ is varied, which corresponds to an increase in the content of the P wave in the deuteron wave function. As can be seen from the structure of these observables [see Eqs. (47)–(52)], they correspond to the mixing of all helicity amplitudes and are therefore sensitive to changes in their phases. The results obtained by calculating A_{y0} and iT_{11} with the nonrelativistic deuteron wave function have a wrong sign. By inspecting iT_{11} more closely, we can notice that the first term in (52), $(\Phi_1^* - \Phi_3^*)\Phi_2$, is a leading one. This is because the delta-resonance contribution is dominant at intermediate energies. Because of the dominance of the 1D_2 wave (that is, of the amplitude a_2), the amplitudes $\Phi_{1,2,3}$ are large, but they have

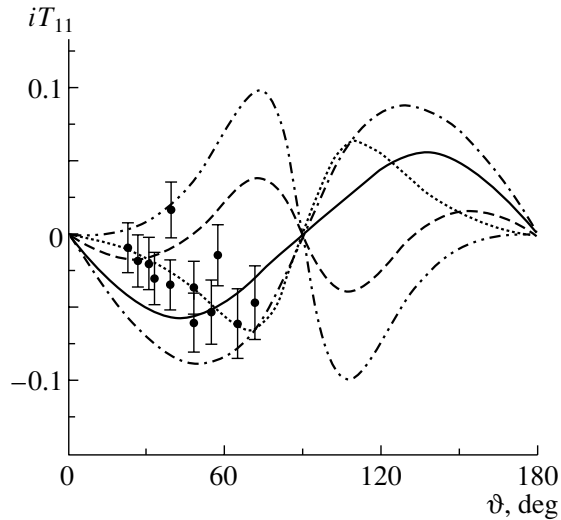


Fig. 3. Vector polarization iT_{11} . The notation is identical to that in Fig. 1.

identical weights in $\Phi_1^{J=2}$ and in $\Phi_3^{J=2}$. Since the corresponding Wigner d functions are of opposite signs, we arrive at the relation $\Phi_1 \approx -\Phi_3$ (27), which explains the leading character of the first term in iT_{11} . Further, it follows from the proportionality of iT_{11} and $\Phi_2 A$ that the phase Φ_2 (more precisely, the phase $\Phi_2^{J=0}$ of the 1S_0 partial wave) determines the sign of iT_{11} , since the contribution of the amplitudes $\Phi_{4,5,6}$ is small.

Within the Buck–Gross model, a correct behavior of the observables begins to manifest itself as the mixing parameter λ is increased, which corresponds to an increase in the contribution of the deuteron P waves. In the approximation of $v_t = v_s = 0$, all the curves nearly coincide with the result for the deuteron wave function from [17]. It should also be noted that the results of the calculations change only slightly in response to a variation of the parameter λ in the πNN vertex (34) at a fixed deuteron wave function.

The results obtained for the proton spin correlations A_{ii} are displayed in Figs. 4–6. We note that the data on A_{zz} measure the absolute values of the amplitude $\Phi_{4,5,6}$, since the deviation of A_{zz} from -1 is determined by these amplitudes [see Eq. (49)]. In accordance with a partial-wave expansion, the amplitudes Φ_4 and Φ_6 involve only triplet states in the NN channel (see Table 1). Thus, we arrive at the conclusion that the absolute values of the spin-triplet amplitudes are small. Proceeding to consider the observables A_{yy} (50) and A_{xx} (51), we note once again that terms proportional to $\Phi_1 + \Phi_3$ can be omitted owing to the phase relation $\Phi_1 \approx -\Phi_3$. Therefore, the deviation of A_{yy} and A_{xx} from -1 is again determined

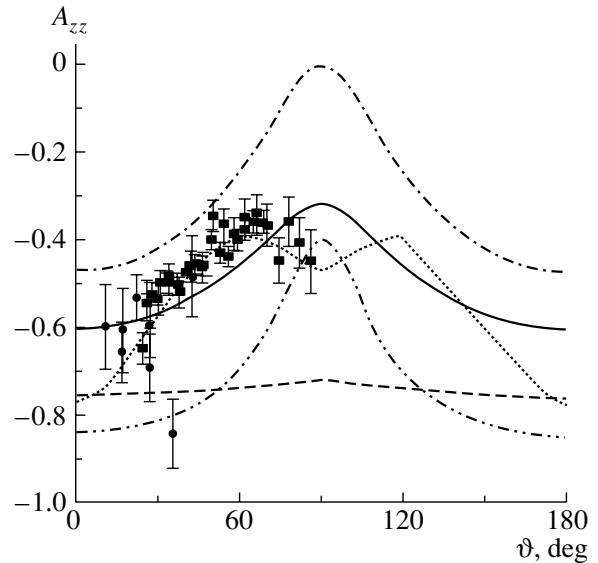


Fig. 4. Spin correlation A_{zz} . The notation is identical to that in Fig. 1.

by $\Phi_{4,6}$; at the same time, Φ_5 does not contribute to A_{yy} .

Inspecting the curves in Figs. 4–6, which display the results of our calculations for the correlations A_{ii} , we note once again the high sensitivity of these results to the choice of model for the deuteron wave function. To state this succinctly, the deuteron wave function in the Buck–Gross model [18] leads to a much better description of the observables than the wave function constructed on the basis of the model from [17], the latter actually corresponding to the nonrelativistic deuteron wave function.

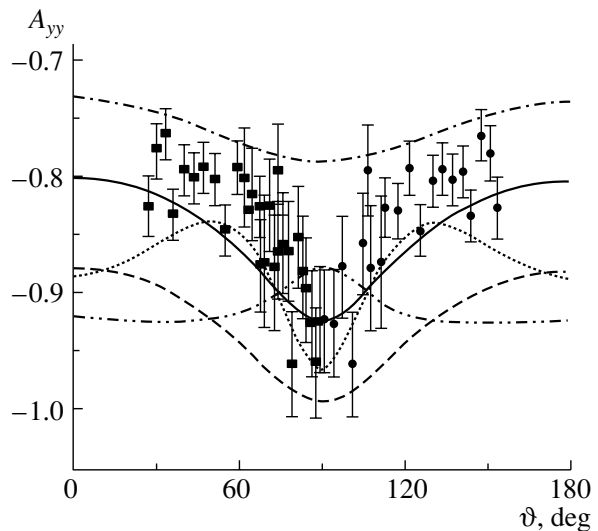


Fig. 5. Spin correlation A_{yy} . The notation is identical to that in Fig. 1.

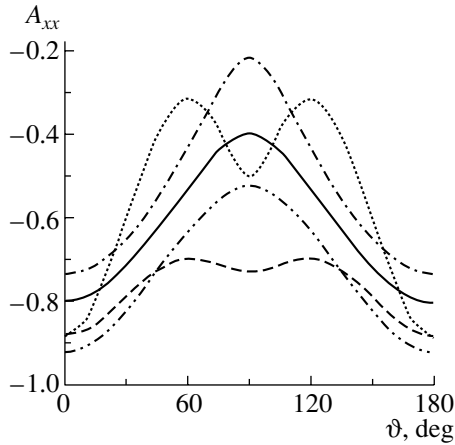


Fig. 6. Spin correlation A_{xx} . The notation is identical to that in Fig. 1.

6. CONCLUSION

We have considered in detail reactions of the $NN \leftrightarrow D\pi$ type, making use of two versions of the deuteron wave function, that from [15] and that from [18]. Previously, the former was employed by Grein *et al.* [14], who analyzed the reaction $pp \rightarrow D\pi^+$ and who also considered the mechanism of virtual-pion rescattering in the intermediate state. The distinctions between our approach and that in [14] are the following. We have analyzed the sensitivity of all observables to the form of the πNN current and to the choice of form for the relativistic deuteron wave function. From the results displayed in the figures, we can see that all observables, especially polarization features, are highly sensitive to the choice of form for the deuteron wave function. The inclusion of the P wave in the deuteron wave function within the Buck–Gross model [18] improves the description of experimental data both on the differential cross section for scattering and on the polarization observables. Yet another interesting result is associated with deriving new information about off-mass-shell effects in the presence of a virtual nucleon. By comparing the calculated observables with experimental data, one can test the approximation introduced in [19] to describe the possible form of the nucleon form factor. In doing this, we have found that it is incorrect to use the mixing-parameter value of $\lambda = 1$ (which was adopted in [15]).

A simple description of pion absorption and emission in terms of rescattering provides the necessary insight into these processes. Among other things, it ensures a physical mechanism for sidestepping the suppression associated with the momentum difference in the impulse approximation. The reason behind a slight discrepancy with experimental data is obviously that the contribution of this process is small

and is therefore sensitive to intermediate- and small-distance dynamics of the nucleon–nucleon interaction, but this dynamics is poorly understood. The corresponding uncertainty inevitably affects a detailed quantitative description in any such approach.

In a more general context, the approach based on rescattering could not be considered to be quite adequate even if the interaction were known in minute detail. Since the impulse approximation makes but a small contribution, the procedure used here consisted merely in the inclusion of rescattering as a next-order term in the absorption process. This approach has a solid physical basis; therefore, there naturally arises the problem of assessing the importance of rescattering terms in higher orders. If there is no small parameter in the expansion in rescattering, it cannot be guaranteed that such terms are negligibly small.

Finally, we note that, in principle, there are other approaches to studying the small-distance behavior of the deuteron wave function, which are based on considering nonnucleonic degrees of freedom [38–40]. However, the objective of the present study has been to reveal the role of conventional nucleonic degrees of freedom of the deuteron in $NN \leftrightarrow D\pi$ processes. For this reason, we have not analyzed here the applicability of various quark models to such processes.

APPENDIX 1

Pauli Representation for $NN \rightarrow D\pi$ Reactions

In the c.m. frame, the reaction amplitude can be expressed in terms of the Pauli matrices as

$$\mathcal{M}_{\sigma_2\sigma_1}^\beta(t, u) = w_{-\sigma_2}^+ (\boldsymbol{\chi} \cdot \boldsymbol{\xi}^{(\beta)}) w_{\sigma_1}. \quad (\text{A.1})$$

The reaction vector can be parametrized as

$$\begin{aligned} \boldsymbol{\chi} &= \sum_{i=1}^6 x_i (\mathbf{p}^2, \mathbf{n} \cdot \mathbf{p}) \mathbf{i} \\ &= x_1 \mathbf{e}_p + x_2 \mathbf{n} + ix_3 [\boldsymbol{\sigma} \times \mathbf{e}_p] \\ &\quad + ix_4 [\boldsymbol{\sigma} \times \mathbf{n}] + ix_5 (\boldsymbol{\sigma} \cdot \mathbf{n}) [\mathbf{n} \times \mathbf{e}_p] \\ &\quad + ix_6 (\boldsymbol{\sigma} \cdot \mathbf{e}_p) [\mathbf{n} \times \mathbf{e}_p], \end{aligned} \quad (\text{A.2})$$

where $\mathbf{e}_p = \mathbf{p}/|\mathbf{p}|$, $\mathbf{n} = -\mathbf{D}/|\mathbf{D}|$; $z = (\mathbf{n} \cdot \mathbf{e}_p)$.

Finally, the relation to the invariant expansion (10) is given by

$$\begin{aligned} x_1 &= -\frac{p}{m} \left(\frac{E}{m} X_2 + \frac{E_D - E}{m} (X_4 - 2X_5) \right), \\ x_2 &= -\frac{k}{M} \left(X_1 - \frac{E}{m} \left(\frac{E}{m} X_3 + \frac{E_D - E}{m} X_6 \right) \right) \\ &\quad - \frac{p}{m} \frac{E_D - M}{M} \left(\frac{E}{m} X_2 + \frac{E_D - E}{m} (X_4 - 2X_5) \right) \end{aligned}$$

$$+ 2 \frac{E_D + M}{m} X_5) z, \tag{A.3}$$

$$x_3 = \frac{p}{m} \left(\frac{E_D}{M} \left(X_1 + \frac{pk}{m^2} z X_4 \right) - \frac{Ek^2}{Mm^2} X_6 \right),$$

$$x_4 = -\frac{p}{m} \left(\frac{E_D - M}{M} \left(X_1 + \frac{pk}{m^2} z X_4 \right) - \frac{Ek^2}{Mm^2} X_6 \right) z - \frac{k}{m} \left(\frac{E^2}{m^2} X_4 - (X_4 - 2X_5) \right),$$

$$x_5 = -\frac{p}{m}$$

$$\times \left(\frac{E_D - M}{M} \left(X_1 + \frac{pk}{m^2} z X_4 \right) - \frac{Ek^2}{Mm^2} X_6 \right),$$

$$x_6 = -\frac{k}{m} \frac{E - m}{m} \left(\frac{E}{m} X_4 + (X_4 - 2X_5) \right).$$

The helicity amplitudes (14) are related to the corresponding Pauli amplitudes x_i (A.2) by the equations

$$\tilde{\Phi}_3 = \sqrt{2} (\mp x_1^a - x_4^a + x_5^s \cos \vartheta + x_6^a); \tag{A.4}$$

$$\tilde{\Phi}_2 = x_1^a \cos \vartheta + x_2^s;$$

$$\tilde{\Phi}_6 = \left\{ (x_3^s \pm x_4^a) + 2x_5^s \begin{pmatrix} \sin^2(\vartheta/2) \\ \cos^2(\vartheta/2) \end{pmatrix} \right\};$$

$$\tilde{\Phi}_5 = 2x_3^s \sin \vartheta.$$

APPENDIX 2

Off-Mass-Shell Amplitude for Pion-Nucleon Collisions

In order to calculate the contribution of the two-nucleon mechanism of pion absorption to $NN \rightarrow D\pi$ processes, it is important to consider that the scattered pion and nucleon are off their mass shells. Hence, information about the behavior of the pion-nucleon amplitude for the case where the particles involved in the collision process are off their mass shells is required.

At any isospin value, the off-mass-shell pion-nucleon amplitude can be written as ($P_S = p_i + q_i$)

$$\mathcal{T}_{\pi N} = \mathcal{N}_{0+} (\hat{P}_S + \sqrt{s}) \mathcal{T}_{0+} \tag{A.5}$$

$$+ \mathcal{N}_{1-} i\gamma_5 (\hat{P}_S + \sqrt{s}) i\gamma_5 \mathcal{T}_{1-}$$

$$+ \mathcal{N}_{1+} q_f^\mu \Delta_{\mu\nu} (P_S, \sqrt{s}) q_i^\nu \mathcal{T}_{1+}$$

$$+ \mathcal{N}_{2-} i\gamma_5 \left[q_f^\mu \Delta_{\mu\nu} (P_S, \sqrt{s}) q_i^\nu \right] i\gamma_5 \mathcal{T}_{2-} + \dots$$

It can be represented in the form of a decomposition in eight covariants [see Eq. (41)], and not in the form of an expansion in two covariants, which survive in the case where all particles are on their mass shells.

The projection operator for the case of a spin of 3/2 is defined as

$$\Delta_{\mu\nu}(p, m) = -(\hat{p} + m) \tag{A.6}$$

$$\times \left[g_{\mu\nu} - \frac{1}{3} \gamma_\mu \gamma_\nu - \frac{2}{3} \frac{p_\mu p_\nu}{m^2} + \frac{1}{3} \left(\frac{p_\mu}{m} \gamma_\nu - \gamma_\mu \frac{p_\nu}{m} \right) \right].$$

We are interested primarily in the case where only one nucleon is on its mass shell—for example, $p_i^2 = m^2$ —with the other particles being off their mass shells. The invariant pion-nucleon amplitude involves only four terms [see Eq. (42)]. With the aid of Eq. (A.5), one can express the invariant scalar functions \tilde{T}_{1-4} in terms of the partial-wave amplitudes $\mathcal{T}_{l\pm}$ as

$$\tilde{T}_1 = \frac{4\pi}{k^3} \left\{ (E - m) (\sqrt{s} + m) \mathcal{T}_{0+}^{\text{off}} - (E + m) (\sqrt{s} - m) \mathcal{T}_{1-}^{\text{off}} - \frac{1}{E + m} F_1^+ \mathcal{T}_{1+}^{\text{off}} + \frac{1}{E - m} F_1^- \mathcal{T}_{2-}^{\text{off}} \right\}$$

$$+ \frac{4\pi}{k^3} \sum_{l \geq 2} \mathcal{T}_{l+}^{\text{off}} [(E - m) (\sqrt{s} + m) \mathcal{P}'_{l+1}(z) + (E + m) (\sqrt{s} - m) \mathcal{P}'_l(z)]$$

$$- \frac{4\pi}{k^3} \sum_{l \geq 3} \mathcal{T}_{l-}^{\text{off}} [(E - m) (\sqrt{s} + m) \mathcal{P}'_{l-1}(z) + (E + m) (\sqrt{s} - m) \mathcal{P}'_l(z)], \tag{A.7}$$

$$\tilde{T}_2 = \frac{4\pi}{k^3} \left\{ (E - m) \mathcal{T}_{0+}^{\text{off}} + (E + m) \mathcal{T}_{1-}^{\text{off}} - \frac{1}{E + m} F_2^+ \mathcal{T}_{1+}^{\text{off}} + \frac{1}{E - m} F_2^- \mathcal{T}_{2-}^{\text{off}} \right\}$$

$$+ \frac{4\pi}{k^3} \sum_{l \geq 2} \mathcal{T}_{l+}^{\text{off}} [(E - m) \mathcal{P}'_{l+1}(z) - (E + m) \mathcal{P}'_l(z)]$$

$$- \frac{4\pi}{k^3} \sum_{l \geq 3} \mathcal{T}_{l-}^{\text{off}} [(E - m) \mathcal{P}'_{l-1}(z) - (E + m) \mathcal{P}'_l(z)],$$

$$\tilde{T}_3 = \frac{4\pi m}{k^3} \left\{ (E - m) \mathcal{T}_{0+}^{\text{off}} + (E + m) \mathcal{T}_{1-}^{\text{off}} + \frac{1}{E + m} F_3^+ \mathcal{T}_{1+}^{\text{off}} + \frac{1}{E - m} F_3^- \mathcal{T}_{2-}^{\text{off}} + \dots \right\},$$

$$\tilde{T}_4 = -\frac{4\pi m}{k^3} \left\{ \frac{1}{E + m} F_4^+ \mathcal{T}_{1+}^{\text{off}} - \frac{1}{E - m} F_4^- \mathcal{T}_{2-}^{\text{off}} + \dots \right\},$$

where $\mathcal{P}'_l(z)$ is the derivative of the l th Legendre polynomial,

$$z = \frac{s(t - u) + (p_i^2 - q_i^2)(p_f^2 - q_f^2)}{\lambda^{1/2}(s, p_i^2, q_i^2) \lambda^{1/2}(s, p_f^2, q_f^2)} \tag{A.8}$$

is the off-mass-shell cosine of the angle of a pion–nucleon collision in the c.m. frame, $k = |\mathbf{p}_f|$ is the absolute value of the final-state 3-momentum, and $E = \sqrt{k^2 + p_f^2}$ is the final-nucleon energy in the pion–nucleon c.m. frame. In expressions (A.7), we have used the notation

$$F_1^\pm = 3(\sqrt{s} \pm m) \chi - \frac{(\sqrt{s} \pm m)^2 (s - p_f^2) + q_i^2 q_f^2}{2\sqrt{s}},$$

$$F_2^\pm = \pm 3\chi + \left(1 \pm \frac{m}{\sqrt{s}}\right) \times \left\{ m(\sqrt{s} \pm m) \mp \frac{q_i^2 + q_f^2}{2} \pm \frac{p_f^2 - m^2}{2} \right\}, \quad (\text{A.9})$$

$$F_3^\pm = -3\chi + \frac{1}{2} \left(1 \pm \frac{m}{\sqrt{s}}\right) \{ (s - m^2) - p_f^2 + q_f^2 \},$$

$$F_4^\pm = \frac{(\sqrt{s} \pm m)^2 - q_i^2}{2\sqrt{s}},$$

where

$$\chi = -\frac{t}{2} - \frac{1}{6} \frac{(s - p_i^2 + q_i^2)(s - p_f^2 + q_f^2)}{s + \frac{q_i^2 + q_f^2}{2}} \quad (\text{A.10})$$

We note that all the variables used are determined by off-mass-shell kinematics.

APPENDIX 3

Here, we present explicit expressions for the helicity amplitudes (11) corresponding to the rescattering diagram. In the case being considered, the spin operator \mathcal{F}_μ (38),

$$\frac{1}{m^2} \mathcal{F}_\mu = \sum_{i=1}^{16} a_i \hat{\mathcal{T}}_\mu(i) \quad (\text{A.11})$$

$$= \Gamma_5 \frac{(\hat{\eta} - m)}{m} \bar{\Psi}_\mu(D) \frac{(\hat{k} + m)}{m} \mathcal{T}_{\pi N},$$

is a 4×4 matrix in spinor space and involves a deuteron-polarization index. The first six operators $\hat{\mathcal{T}}_\mu(i)$ are independent of the variable of integration:

$$\hat{\mathcal{T}}_\mu(1) = \gamma_5 \gamma_\mu, \quad \hat{\mathcal{T}}_\mu(2) = \gamma_5 \frac{p_\mu}{m}, \quad \hat{\mathcal{T}}_\mu(3) = \gamma_5 \frac{p'_\mu}{m}, \quad (\text{A.12})$$

$$\hat{\mathcal{T}}_\mu(4) = \gamma_5 \hat{\pi} \frac{p_\mu}{m}, \quad \hat{\mathcal{T}}_\mu(5) = \gamma_5 \hat{\pi} \frac{p'_\mu}{m}, \quad \hat{\mathcal{T}}_\mu(6) = \gamma_5 \gamma_\mu \hat{\pi}.$$

The second three, $\hat{\mathcal{T}}_\mu(i)$, depend only on η :

$$\hat{\mathcal{T}}_\mu(7) = \gamma_5 \frac{\eta_\mu}{m}, \quad \hat{\mathcal{T}}_\mu(8) = \gamma_5 \frac{\hat{\eta} \eta_\mu}{m^2}, \quad \hat{\mathcal{T}}_\mu(9) \quad (\text{A.13})$$

$$= \gamma_5 \left(\gamma_\mu \frac{\hat{\eta}}{m} - \frac{\hat{\eta}}{m} \gamma_\mu \right).$$

The remaining operators $\hat{\mathcal{T}}_\mu(i)$ are given by

$$\hat{\mathcal{T}}_\mu(10) = \gamma_5 \frac{\hat{\eta} p_\mu}{m^2}, \quad \hat{\mathcal{T}}_\mu(11) = \gamma_5 \frac{\hat{\eta} p'_\mu}{m}, \quad (\text{A.14})$$

$$\hat{\mathcal{T}}_\mu(12) = \gamma_5 \frac{\eta_\mu}{m} \hat{\pi},$$

$$\hat{\mathcal{T}}_\mu(13) = \gamma_5 \frac{\hat{\eta} p_\mu}{m^2} \hat{\pi}, \quad \hat{\mathcal{T}}_\mu(14) = \gamma_5 \frac{\hat{\eta} p'_\mu}{m^2} \hat{\pi},$$

$$\hat{\mathcal{T}}_\mu(15) = \gamma_5 \frac{\hat{\eta} \eta_\mu}{m^2} \hat{\pi} : \quad \hat{\mathcal{T}}_\mu(16) = \gamma_5 \gamma_\mu \frac{\hat{\eta}}{m} \hat{\pi}.$$

By using the algebra of gamma matrices, we obtain

$$a_1 = -T_1 \left(2 - \frac{q^2}{m^2} \right) \varphi_1 - T_2 \frac{m^2 - t}{m} \varphi_1 + \frac{m^2 - k^2}{m^2} \left\{ T_1 \varphi_3 + T_3 \left(\varphi_1 - \frac{q^2}{m^2} \varphi_3 \right) + T_4 \frac{m^2 - t}{m} \varphi_3 \right\},$$

$$a_2 = 2T_1 \varphi_1 - 2T_3 \frac{m^2 - k^2}{m^2} \varphi_3 = a_3,$$

$$a_4 = 2T_2 \varphi_1 - 2T_4 \frac{m^2 - k^2}{m^2} \varphi_4 = a_5,$$

$$a_6 = \frac{1}{m} T_1 \varphi_1 + T_2 \frac{q^2}{m^2} \varphi_1 + \frac{m^2 - k^2}{m^2}$$

$$\times \left\{ \left(T_2 - \frac{1}{m} T_3 \right) \varphi_3 + T_4 \varphi_1 - T_4 \left(2 + \frac{q^2}{m^2} \right) \varphi_3 \right\},$$

$$a_7 = 2T_1 (2\varphi_1 + \varphi_2) + T_1 \frac{q^2}{m^2} \varphi_2$$

$$+ T_2 \frac{m^2 - t}{m} (\varphi_1 + \varphi_2) - \frac{m^2 - k^2}{m^2}$$

$$\times \left\{ T_1 (\varphi_3 + \varphi_4) + T_3 \left(\varphi_1 + \varphi_2 + 2\varphi_3 + \frac{q^2}{m^2} \varphi_4 \right) \right.$$

$$\left. + T_4 \frac{m^2 - t}{m} (\varphi_3 + \varphi_4) \right\},$$

$$a_8 = -2T_1 (\varphi_1 + \varphi_2) - T_2 \frac{m^2 - t}{m} \varphi_2 + \frac{m^2 - k^2}{m^2}$$

$$\times \left\{ T_1 \varphi_4 + T_3 (\varphi_2 + 2\varphi_3) + T_4 \frac{m^2 - t}{m} \varphi_4 \right\}, \quad (\text{A.15})$$

$$a_9 = -T_1 \varphi_1 + T_2 \frac{m^2 - t}{2m} \varphi_1 + \frac{m^2 - k^2}{2m^2}$$

$$\times \left\{ T_1 \varphi_3 + T_3 \varphi_1 - T_4 \frac{m^2 - t}{m} \varphi_3 \right\},$$

$$a_{10} = -2T_1 \varphi_1 + 2T_3 \frac{m^2 - k^2}{m^2} \varphi_3 = a_{11},$$

$$\begin{aligned}
a_{12} &= -\frac{1}{m}T_1(2\varphi_1 + \varphi_2) + 2T_2\varphi_1 + T_2\frac{q^2}{m^2}\varphi_2 \\
&\quad - \frac{m^2 - k^2}{m^2} \\
&\times \left\{ \left(T_2 - \frac{1}{m}T_3 \right) (2\varphi_3 + \varphi_4) + T_4(2\varphi_1 + \varphi_2) \right. \\
&\quad \left. - 2T_4(\varphi_3 + \varphi_4) + T_4\frac{q^2}{m^2}\varphi_4 \right\}, \\
a_{13} &= -2T_2\varphi_1 + 2T_4\frac{m^2 - k^2}{m^2}\varphi_3 = a_{14}, \\
a_{15} &= -\frac{1}{m}T_1\varphi_2 - 2T_2\varphi_1 + \frac{m^2 - k^2}{m^2} \\
&\times \left\{ \left(T_2 - \frac{1}{m}T_3 \right) \varphi_4 + T_4\varphi_2 + 2T_4(\varphi_3 - \varphi_4) \right\}, \\
a_{16} &= \frac{1}{m}T_1\varphi_1 + \frac{m^2 - k^2}{m^2} \\
&\times \left\{ \left(T_2 - \frac{1}{m}T_3 \right) \varphi_3 + T_4(\varphi_1 - 2\varphi_3) \right\}.
\end{aligned}$$

For the helicity amplitudes corresponding to the rescattering diagram, a calculation of spinor matrix elements yields ($S = \sin \vartheta$; $C = \cos \vartheta$)

$$\begin{aligned}
\chi_3 &= \mathcal{M}_{++}^\pm = \mathcal{M}_{--}^\mp \quad (\text{A.16}) \\
&= \hat{\mathcal{I}} \left[\pm \left\{ \frac{p}{m} \left(\frac{E}{m}a_2 + \omega a_4 + \frac{\eta_0}{m}a_{10} \right) \right. \right. \\
&\quad \left. \left. - \frac{p\omega \pm kE}{m}a_6 \right\} \frac{S}{\sqrt{2}} \right. \\
&\quad \left. - \frac{(\xi_{\pm}\eta)}{m} \left\{ \frac{E}{m}a_7 + \frac{\eta_0}{m}a_8 + \omega a_{12} \right\} \right. \\
&\quad \left. - \sqrt{2} \frac{E(\eta_1 \pm i\eta_2 C) \pm p\eta_0 S}{m^2} a_9 \right. \\
&\quad \left. + \left\{ \eta_0 \frac{E\omega - pkC}{m^2} - \frac{kE}{m^2}(\eta_1 - i\eta_2)S \right. \right. \\
&\quad \left. \left. + \eta_3 \frac{p\omega - kEC}{m^2} \right\} \left\{ \pm \frac{p}{m}a_{13} \frac{S}{\sqrt{2}} - \frac{(\xi_{\pm}\eta)}{m}a_{15} \right\} \right. \\
&\quad \left. - \left\{ \frac{\omega}{m} \left[(\xi_{\pm}\eta) + \frac{\eta_1 \pm i\eta_2 C}{\sqrt{2}} \right] - \eta_0 \frac{k}{m} \frac{S}{\sqrt{2}} \right\} a_{16} \right], \\
\chi_2 &= \mathcal{M}_{++}^0 = -\mathcal{M}_{--}^0 \quad (\text{A.17}) \\
&= \hat{\mathcal{I}} \left[-\frac{k}{M} \left\{ a_1 - \frac{E}{m} \left(\frac{E}{m}(a_3 - 2ma_6) \right. \right. \right. \\
&\quad \left. \left. + \omega a_5 + \frac{\eta_0}{m}a_{11} \right) \right\} \right. \\
&\quad \left. - \frac{p}{m} \left\{ \frac{E_D}{M} \left(\frac{E}{m}a_2 + \omega a_4 + \frac{\eta_0}{m}a_{10} \right) \right. \right. \\
&\quad \left. \left. - \frac{2EE_D - M^2}{M}a_6 \right\} C \right]
\end{aligned}$$

$$\begin{aligned}
&\quad - \frac{(\xi_0\eta)}{m} \left\{ \frac{E}{m}a_7 + \frac{\eta_0}{m}a_8 + \omega a_{12} \right\} \\
&\quad + 2 \left\{ \frac{p}{m} \left(\frac{\eta_0 E_D}{mM}C + \frac{\eta_3 k}{mM} \right) - i \frac{\eta_2 E E_D}{m^2 M} S \right\} a_9 \\
&\quad - \left\{ \eta_0 \frac{E\omega - pkC}{m^2} - \frac{kE}{m^2}(\eta_1 - i\eta_2)S \right. \\
&\quad \left. + \eta_3 \frac{p\omega - kEC}{m^2} \right\} \left\{ \frac{pE_D}{mM}a_{13}C - \frac{kE}{mM}a_{14} \right. \\
&\quad \left. + \frac{(\xi_0\eta)}{m}a_{15} \right\} + 2 \frac{E_D - E}{m}(\xi_0\eta)a_{16} \\
&\quad - \left\{ i\eta_2 \frac{2EE_D - M^2}{mM}S + \frac{M}{m}(\eta_1 S + \eta_3 C) \right\} a_{16} \Big], \\
&\quad \chi_4 = \mathcal{M}_{+-}^\pm = -\mathcal{M}_{-+}^\mp \quad (\text{A.18}) \\
&= \hat{\mathcal{I}} \left[\sqrt{2} \begin{pmatrix} \cos^2(\vartheta/2) \\ \sin^2(\vartheta/2) \end{pmatrix} \left\{ \left(\frac{p}{m}a_1 \pm ka_6 \right) \right. \right. \\
&\quad \left. \left. \pm 2 \frac{p^2 k}{m^2} \begin{pmatrix} \sin^2(\vartheta/2) \\ \cos^2(\vartheta/2) \end{pmatrix} a_4 \right\} \right. \\
&\quad \left. - \frac{p}{m} \frac{(\xi_{\pm}\eta)}{m} \left\{ \frac{\eta_1 - i\eta_2}{m}a_8 + ka_{12}S \right\} \right. \\
&\quad \left. + 2\sqrt{2} \frac{\eta_3}{m} \begin{pmatrix} \cos^2(\vartheta/2) \\ \sin^2(\vartheta/2) \end{pmatrix} a_9 \pm \frac{\eta_1 - i\eta_2}{m} \right. \\
&\quad \left. \times \left(2a_9 + \frac{p^2}{m^2}a_{10} \right) \frac{S}{\sqrt{2}} + \frac{k}{m} \{ (\eta_1 - i\eta_2)C - \eta_3 S \} \right. \\
&\quad \left. \times \left\{ \pm \frac{p}{m}a_{13} \frac{S}{\sqrt{2}} - \frac{(\xi_{\pm}\eta)}{m}a_{15} \right\} \right. \\
&\quad \left. - 2 \frac{pk}{m^2}(\xi_{\pm}\eta)a_{16}S \pm \frac{\eta_1 - i\eta_2}{m} \left(E \frac{\omega}{m} \mp p \frac{k}{m} \right) \frac{S}{\sqrt{2}} a_{16} \right. \\
&\quad \left. + \sqrt{2} \begin{pmatrix} \cos^2 \vartheta/2 \\ \sin^2 \vartheta/2 \end{pmatrix} \left\{ \frac{E}{m} \left(\eta_3 \frac{\omega}{m} \mp \eta_0 \frac{k}{m} \right) \right. \right. \\
&\quad \left. \left. + \frac{p}{m} \left(\eta_0 \frac{\omega}{m} \mp \eta_3 \frac{k}{m} \right) \right\} a_{16} \right], \\
&\quad \chi_5 = \mathcal{M}_{+-}^0 = \mathcal{M}_{-+}^0 \quad (\text{A.19}) \\
&= \hat{\mathcal{I}} \left[\frac{p}{m} \left\{ \frac{E_D}{M} \left(a_1 - \frac{pk}{m}a_4 C \right) + \frac{Ek^2}{Mm}a_5 \right\} S \right. \\
&\quad \left. - \frac{p}{m} \frac{(\xi_0\eta)}{m} \left\{ \frac{\eta_1 - i\eta_2}{m}a_8 + ka_{12}S \right\} + 2 \frac{\eta_3 E_D}{mM}a_9 S \right. \\
&\quad \left. - \frac{\eta_1 - i\eta_2}{m} \left\{ \frac{E_D}{M} \left(2a_9 + \frac{p^2}{m^2}a_{10} \right) C - \frac{Epk}{m^2 M}a_{11} \right\} \right]
\end{aligned}$$

$$\begin{aligned}
& -\frac{k}{m} \{(\eta_1 - i\eta_2) C - \eta_3 S\} \left\{ \frac{pE_D}{mM} a_{13} C - \frac{Ek}{mM} a_{14} \right. \\
& \left. + \frac{(\xi_0 \eta)}{m} a_{15} \right\} - 2 \frac{pk}{m^2} (\xi_0 \eta) a_{16} S + \left\{ \frac{2EE_D - M^2}{mM} \right. \\
& \left. \times \left(\eta_0 \frac{p}{m} S - \frac{E}{m} \{(\eta_1 - i\eta_2) C - \eta_3 S\} \right) \right. \\
& \left. + 2 \frac{Epk}{m^2 M} (\eta_1 - i\eta_2) \right\} a_{16} \Big],
\end{aligned}$$

where

$$(\xi_{\pm} \eta) = \pm \frac{1}{\sqrt{2}} (\eta_1 C \pm i\eta_2 - \eta_3 S), \quad (\text{A.20})$$

$$(\xi_0 \eta) = \eta_0 \frac{k}{M} + \frac{E_D}{M} (\eta_1 S + \eta_3 C).$$

In the spectator case, we have to deal with the three-dimensional integral operator

$$\begin{aligned}
\hat{\mathcal{I}}^{sp} &= \frac{g^+}{(2\pi)^3} \int_0^{\eta_m} \frac{\eta^2 d\eta}{2\sqrt{\eta^2 + m^2}} \quad (\text{A.21}) \\
&\times \int_{-1}^1 \frac{h_\pi(q^2) d \cos \vartheta_\eta}{q^2 - \mu^2} \int_0^{2\pi} d\varphi_\eta.
\end{aligned}$$

REFERENCES

1. R. Durbin, H. Loer, and J. Steinberg, Phys. Rev. **83**, 646 (1951).
2. K. M. Watson and K. A. Bruckner, Phys. Rev. **83**, 1 (1951).
3. A. H. Rosenfeld, Phys. Rev. **96**, 139 (1954).
4. S. Mandelstam, Proc. R. Soc. London, Ser. A **244**, 491 (1958).
5. J. A. Niskanen, Nucl. Phys. A **298**, 417 (1978); Phys. Lett. B **71B**, 40 (1977); **79B**, 190 (1978).
6. A. M. Green and J. A. Niskanen, Nucl. Phys. B **271**, 503 (1976); A. M. Green and M. E. Sainio, J. Phys. G **4**, 1055 (1978).
7. T. Mizutani and D. Koltun, Ann. Phys. (N.Y.) **109**, 1 (1977).
8. A. S. Rinat, Nucl. Phys. A **287**, 399 (1977); A. S. Rinat, Y. Starkand, and E. Hammel, Nucl. Phys. A **364**, 486 (1981).
9. B. Blankleider and I. R. Afnan, Phys. Rev. C **24**, 1572 (1981).
10. T. Yao, Phys. Rev. B **134**, 454 (1964).
11. J. N. Chahoud, G. Russo, and F. Selleri, Nuovo Cimento **45**, 38 (1966).
12. D. Schiff and J. Tran Than Van, Nucl. Phys. B **5**, 529 (1968).
13. G. W. Barry, Ann. Phys. (N.Y.) **73**, 482 (1972).
14. W. Grein, A. König, P. Kroll, *et al.*, Ann. Phys. (N.Y.) **153**, 301 (1984).
15. M. P. Locher and A. Švarc, J. Phys. G **11**, 183 (1985).
16. M. P. Locher and A. Švarc, Few-Body Syst. **5**, 59 (1988).
17. M. P. Locher and A. Švarc, Z. Phys. A **316**, 55 (1984).
18. W. W. Buck and F. Gross, Phys. Rev. D **20**, 2361 (1979).
19. F. Gross, J. W. van Orden, and K. Holinde, Phys. Rev. C **45**, 2094 (1992).
20. C. Itzykson and J. B. Zuber, *Quantum Field Theory* (McGraw-Hill, New York, 1980).
21. C. Bourrely, E. Leader, and J. Soffer, Phys. Rep. **59**, 95 (1980).
22. R. Vega and J. Wudka, Phys. Rev. D **53**, 5286 (1996).
23. F. Mandl and T. Regge, Phys. Rev. **99**, 1478 (1955).
24. T. Ericson and W. Weise, *Pions and Nuclei* (Clarendon Press, Oxford, 1988).
25. R. A. Arndt, I. I. Strakovsky, R. L. Workman, and D. V. Bugg, Phys. Rev. C **48**, 1926 (1993); **49**, 1229 (1994).
26. J. Gunion and S. Brodsky, Phys. Rev. D **8**, 287 (1973); J. Gunion, Phys. Rev. D **10**, 242 (1974).
27. A. Bincer, Phys. Rev. **118**, 855 (1960); E. Nyman, Nucl. Phys. A **154**, 97 (1970); W. E. Fisher and P. Minkowski, Nucl. Phys. B **36**, 519 (1972); H. W. L. Naus and J. H. Koch, Phys. Rev. C **36**, 2459 (1987); P. C. Tiemeijer and J. A. Tjon, Phys. Rev. C **42**, 599 (1990); X. Song, J. Chen, and J. S. McCarthy, Z. Phys. A **341**, 275 (1992); J. W. Bos and J. H. Koch, Nucl. Phys. A **563**, 539 (1993).
28. R. M. Davidson and G. I. Poulis, nucl-th/9603031.
29. E. Kazes, Nuovo Cimento **13**, 1226 (1959).
30. W. T. Nutt and C. M. Shakin, Phys. Rev. C **16**, 1107 (1977); Phys. Lett. B **69B**, 290 (1977).
31. R. Machleidt, K. Holinde, and Ch. Elster, Phys. Rep. **149**, 1 (1987).
32. G. Höhler, F. Kaiser, and E. Pietarinen, Handbook of Pion-Nucleon Scattering **12**, 1 (1979).
33. F. Hachenberg and J. H. Pirner, Ann. Phys. (N.Y.) **112**, 401 (1978).
34. A. König and P. Kroll, Nucl. Phys. A **356**, 354 (1981).
35. F. Ferozghi, J. Phys. G **8**, 1345 (1982).
36. *Proceedings of International Symposium "Polarized Phenomena in Nuclear Reactions."* Ed. by H. H. Barschall and W. Haerberli (Univ. of Wisconsin Press, Madison, 1971), p. XXV.
37. Those with access to TELNET can run the SAID program with a link to <http://said.phys.vt.edu>.
38. G. I. Lykasov, Fiz. Élem. Chastits At. Yadra **24**, 140 (1993) [Phys. Part. Nucl. **24**, 59 (1993)].
39. L. Ya. Glzman, V. G. Neudatchin, and I. T. Obukhovskiy, Phys. Rev. C **48**, 389 (1993).
40. A. Kobushkin, J. Phys. G **19**, 1993 (1993).

Translated by A. Isaakyan

Neutron Halo in ${}^8\text{He}^*$

A. V. Nesterov, V. S. Vasilevsky, and O. F. Chernov

Bogolyubov Institute for Theoretical Physics, National Academy of Sciences of Ukraine, Metrologicheskaya ul. 14b, Kiev, 252143 Ukraine

Received April 5, 2000; in final form, August 24, 2000

Abstract—The structure of ${}^8\text{He}$ is investigated within a three-cluster microscopic model. The three-cluster configuration $\alpha + {}^2n + {}^2n$ is used to describe the properties of the ground state of this nucleus. The results obtained evidently indicate the existence of a neutron halo in ${}^8\text{He}$. © 2001 MAIK “Nauka/Interperiodica”.

1. INTRODUCTION

The development of experimental techniques made it possible to investigate light nuclei with large neutron excess—that is, nuclei for which the ratio $\eta = (N - Z)/A$ is significantly larger than that for common ones. Such nuclei lie near the drip line and are β -unstable. They live a short time and transform, by emitting electrons into nuclei, with approximately equal number of protons and neutrons. A number of unexpected properties were discovered in those nuclei—for instance, a neutron halo. It is natural that many attempts were undertaken to explain those properties within microscopic and semimicroscopic methods [1–8].

Our objective is to investigate the structure of the ${}^8\text{He}$ ground state. It is interesting that ${}^8\text{He}$ has the largest value of $\eta = 0.5$ among other nucleon-stable nuclei. Note that the average values of η is 0.4 for nuclei near the neutron drip line. As early as 1960, Zeldovich [9] and Goldansky [10] indicated that there can exist the ${}^8\text{He}$ isotope. This was experimentally confirmed [11] in the mid-1960s. A subsequent analysis revealed that the lowest threshold of ${}^8\text{He}$ decay is that for the ${}^6\text{He} + 2n$ mode and lies 2.1 MeV above the ground state and that the threshold energy for the $\alpha + 4n$ mode is 3.10 MeV (see, for instance, [12]).

A comprehensive body information about light nuclei featuring neutron excess can be obtained within a microscopic model. In this case, the problem is to solve the many-particle Schrödinger equation with a fixed (chosen) nucleon–nucleon interaction. The equation has to be solved by invoking some simplification based on one or another physical consideration. The resonating-group method [13] or its algebraic version [14, 15] is one of the methods that can be used for this.

In this study, we make use of the algebraic version of the resonating-group method where ${}^8\text{He}$ is considered as the three-cluster configuration $\alpha + {}^2n + {}^2n$. It is obvious that we make a priori some assumptions on the structure of the nucleus. First, the wave functions of each cluster are simulated by the shell-model functions. Second, valence neutrons are combined in dineutron clusters. To justify this assumption, we recall that the interaction between two neutrons may increase significantly in the presence of a third particle [16]. This can give rise to the formation of dineutron clusters on the surface of a nucleus. The chosen type of clustering allows us to consider an α -particle as a core, even though the lowest threshold of ${}^8\text{He}$ decay is that for ${}^6\text{He} + n + n$. Earlier, Ogloblin [17] highlighted the importance of the $\alpha + 4n$ cluster configuration. He indicated that the bound energy of two neutrons in ${}^8\text{He}$ is two times larger than that in ${}^6\text{He}$. This fact led him to the conclusion that ${}^6\text{He}$ cannot serve as a core and that the neutron halo in ${}^8\text{He}$ must consist of four neutrons.

The use of dineutron clusters is quite valid an approximation. For example, dineutron and diproton clusters were successfully used in [18] to describe the exit channels of the reactions ${}^3\text{H} + {}^3\text{H} \rightarrow {}^4\text{He} + n + n$ and ${}^3\text{He} + {}^3\text{He} \rightarrow {}^4\text{He} + p + p$, respectively. Moreover, basic features of ${}^{11}\text{Li}$ were reproduced in [19] on the basis of the ${}^9\text{Li} + {}^2n$ cluster configuration with a pointless dineutron.

2. DESCRIPTION OF THE METHOD

The present method for investigating the ${}^8\text{He}$ ground state is based on the algebraic version of the resonating-group method (AV RGM). For a long time, this version has been used to study the bound states of two-cluster systems, reactions involving a

*This article was submitted by the authors in English.

few open channels, the interaction of these channels with collective monopole and quadrupole modes, and also processes of full disintegration of light nuclei [20–22]. In recent years, the AV RGM was actively invoked to describe three-cluster systems [23–26].

The AV RGM is based on the use of an oscillator basis for solving bound-state problems and problems of continuous-spectrum states. This is achieved by expanding the wave function of intercluster motion in the oscillator basis. As a result, a trial three-cluster function takes the form

$$\Psi(A) = \sum_n C_n \hat{A} [\Phi_1(A_1) \Phi_2(A_2) \Phi_3(A_3) f_n(\mathbf{q}_1, \mathbf{q}_2)], \quad (1)$$

where \hat{A} is the antisymmetrization operator; $\Phi_i(A_i)$ are the internal functions of the cluster, which are selected in one or another form prior to solving the problem (for instance, in the form of many-particle oscillator shell functions, as in our case); and the set of coefficients C_n is nothing but a wave function in the oscillator representation. This function must be obtained from a system of linear equations

$$\sum_{n'} [\langle n | \hat{H} | n' \rangle - E \langle n | n' \rangle] C_{n'} = 0, \quad (2)$$

which is derived directly from the many-particle Schrödinger equation. The oscillator functions $f_n(\mathbf{q}_1, \mathbf{q}_2)$, where \mathbf{q}_1 and \mathbf{q}_2 are the Jacobi vectors fixing the positions of the clusters in space, are determined in the six-dimensional space and constitute the irreducible representation $[N00]$ of the unitary group $U(6)$. Thus, the composite index n consists of indices (six in total) of the irreducible representation of the $U(6)$ group and its subgroups.

The choice of one or another reduction of the $U(6)$ group is dictated by considerations of physical clarity and of the simplicity of numerical realizations as well. To consider the bound-state problem, it is convenient to use basis functions whose classification is associated with the following reduction of the $U(6)$ group:

$$U(6) \supset U(3) \otimes U(3) \implies |N_1, l_1, N_2, l_2; LM\rangle, \\ \cup \quad \cup \\ SO(3) \otimes SO(3) \supset SO(3)$$

$$U(6) \supset SU(3) \otimes U(2) \implies |(\lambda\mu)\nu; \omega LM\rangle. \\ \cup \quad \cup \\ SO(3) \quad O(3)$$

The first basis is usually referred to as the basis of two uncoupled oscillators or the bioscillator basis (BO). Each of the $U(3)$ groups that is associated with

one of the Jacobi vectors \mathbf{q}_1 and \mathbf{q}_2 generates the quantum numbers N_1, l_1 and N_2, l_2 . They are the principal quantum number (or the number of oscillator quanta) and partial angular momentum along the corresponding Jacobi vector:

$$|N_1, l_1, N_2, l_2; LM\rangle.$$

The second basis is an “ $SU(3)$ ” basis. The wave functions of this basis are classified in terms of the well-known Elliott indices (λ, μ) of the $SU(3)$ group, the multiplicity index ω arising in the reduction $SU(3) \supset SO(3)$, and the quantum number $\nu = \frac{1}{2}(N_1 - N_2)$ associated with oscillator quanta along the Jacobi vectors \mathbf{q}_1 and \mathbf{q}_2 :

$$|(\lambda\mu)\nu; \omega LM\rangle.$$

The total number of oscillator quanta is equal to $N = N_1 + N_2 = \lambda + 2\mu$ and defines an irreducible representation of the $U(6)$ group. For a given N —that is, for a fixed oscillator shell—functions of the two bases are related to each other through a unitary transformation, because these bases are formed by eigenfunctions of the same oscillator Hamiltonian in six-dimensional space. Thus, they are equivalent. Note that the unitary matrix relating these two bases consists of the Clebsch–Gordan coefficients of the $SU(3)$ group for the decomposition of the product $(N_1 0) \otimes (N_2 0) \Rightarrow (\lambda\mu)$. Thus, we have

$$|(\lambda\mu)\nu; \omega LM\rangle = \sum_{l_1, l_2} U(N_1, l_1, N_2, l_2; (\lambda\mu)\nu; \omega) \times |N_1, l_1, N_2, l_2; LM\rangle.$$

However, we make use of two bases. This is because the bioscillator basis has more natural quantum numbers. Meanwhile, the $SU(3)$ basis is more convenient for a numerical implementation—in particular, for eliminating Pauli-forbidden states. In addition, the use of two bases furnishes additional information about optimal subspaces that allow one to obtain reliable results with minimal effort.

Pauli-forbidden states are eliminated by diagonalizing the matrix of the antisymmetrization operator,

$$\|\langle n | n' \rangle\|, \quad (3)$$

between the basis functions f_n . Pauli-forbidden states correspond to those eigenfunctions of the matrix $\|\langle n | n' \rangle\| = \|\langle n | \hat{A} | n' \rangle\|$ that have zero eigenvalues. Pauli-allowed states represent a combination of original basis functions of a given oscillator shell that are eigenfunctions of the antisymmetrization operator. It should be noted that the matrix $\|\langle n | n' \rangle\|$ has a block structure. Nonzero matrix elements correspond to overlapping basis functions of the same oscillator shell—that is, those oscillator functions that obey

the condition $N = N'$. To solve the Schrödinger equation in a matrix form, one has to eliminate Pauli-forbidden states. Let e_α and $\{U_n^\alpha\}$ be, respectively, an eigenvalue and the corresponding eigenfunction of the antisymmetrization operator. The system of Eq. (2) must be transformed into the representation of Pauli-allowed states,

$$\sum_{\alpha'} \left[\langle \alpha | \hat{H} | \alpha' \rangle - E \delta_{\alpha, \alpha'} \right] C_{\alpha'} = 0, \quad (4)$$

where $\|\langle \alpha | \hat{H} | \alpha' \rangle\|$ is the matrix of the Hamiltonian between Pauli-allowed states; it is related to the matrix $\|\langle n | \hat{H} | n' \rangle\|$ by the equation

$$\langle \alpha | \hat{H} | \alpha' \rangle = \sum_{n, n'} U_n^\alpha \langle n | \hat{H} | n' \rangle U_{n'}^{\alpha'}$$

In this connection, the original scheme of classification totally changes for the bioscillator basis, but the quantum numbers $(\lambda\mu)$ are preserved for the $SU(3)$ basis, because the matrix $\|\langle n | n' \rangle\|$ is off-diagonal only with respect to the quantum number ν .

We omit all details of the calculation of the matrix element of the microscopic Hamiltonian and anti-symmetrization operator, referring the reader to [27], where one can find basic formulas and recurrence relations for matrix elements of operators of physical importance between bioscillator functions.

3. RESULTS

Results presented in this section were obtained with the Volkov potential [28]. The only free parameter, the oscillator radius r_0 , was chosen in such a way as to minimize the threshold energy of ^8He decay into ^4He and two dineutrons. It proved to be 1.51 fm. Under such conditions, the energy of the $^4\text{He} + ^2n + ^2n$ threshold is -22.15 MeV and the bound-state energy of an α particle is -26.84 MeV. Coulomb interaction was neglected because it shifts the bound-state energy and the threshold energy by the same value.

In what follows, we use two different trees of Jacobi vectors. In the first tree that we call a T tree, the vector \mathbf{q}_1 specifies the distance between two dineutrons and the vector \mathbf{q}_2 fixes the distance between the center of mass of two dineutrons and the α particle. The second tree is called Y tree. In this tree, the first vector \mathbf{q}_1 determines the distance between the α particle and one of the dineutrons, while the second vector \mathbf{q}_2 is associated with the distance between the second dineutron and the center of mass of the first dineutron and the α particle.

Since we consider only the ground state, we must use the wave function of the S state. In this case, the oscillator basis is reduced significantly. For instance, the bioscillator basis involves oscillator functions with

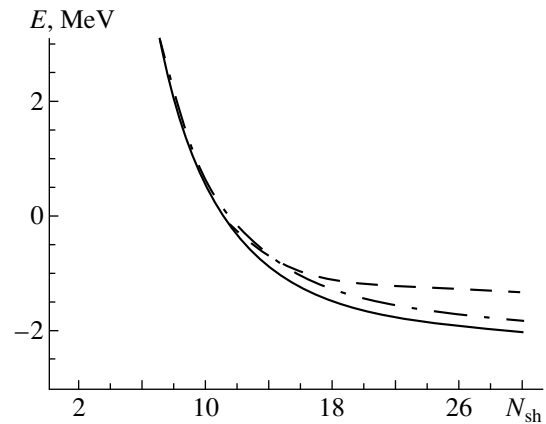


Fig. 1. Ground-state energy of ^8He as a function of the number N of oscillator shells involved in the calculation. Solid, dashed, and dash-dotted curves represent the energy obtained, respectively, with the total oscillator basis, with the $SU(3)$ basis ($\mu_{\text{max}} = 4$), and with the bioscillator basis ($l_{\text{max}} = 0$).

even values of N_1 and N_2 . In addition, the partial orbital angular momenta satisfy the condition $l_1 = l_2$. Actually, we need only three quantum numbers to classify basis functions with $L = 0$. These are $(N_1, N_2, l = l_1 = l_2)$ for the bioscillator basis and $(\lambda\mu, \nu)$ for the $SU(3)$ basis.

Bound-state energy and optimal subspaces.

The ground state of ^8He is considered with the basis that involves all oscillator functions of the 15 lowest oscillator shells—that is, the basis functions with even values of the principal quantum number N up to $N = 30$. The total number of original basis functions is equal to 815, and the total number of Pauli-allowed states reduces to 399 functions. This number of basis functions provides a fairly good convergence of the bound state energy, as is demonstrated in Fig. 1, which displays the ground-state energy as a function of the principal quantum number N . The energy is reckoned from the $\alpha + ^2n + ^2n$ threshold. Figure 1 also shows the ground-state energy obtained by using some subspaces of the total space of the oscillator basis used. In the BO basis, this subspace is defined by the maximal value of the partial orbital angular momentum $l = 0$, while, for the $SU(3)$ basis, this subspace involves basis functions with $\mu \leq 4$. The latter subspace, consisting of 274 functions, yields an energy that is noticeably different from that obtained with the total basis and sometimes referred to here as the “exact” value. But with the former subspace, including only 118 functions, we obtain an energy that is very close to the “exact” value. This is probably because the interaction between the clusters is the strongest in the S state.

Figure 2 displays the wave function of the ^8He

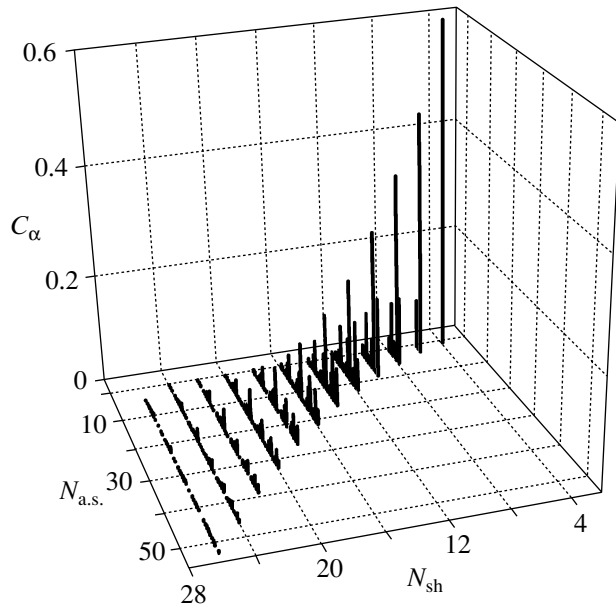


Fig. 2. Wave function of the ${}^8\text{He}$ ground state in the oscillator representation.

ground state—more precisely, the coefficients C_α in the expansion in Pauli-allowed states. Two labels N_{sh} and $N_{\text{a.s.}}$ are used to classify Pauli-allowed functions ($\alpha = \{N_{\text{sh}}, N_{\text{a.s.}}\}$). The first label N_{sh} numbers oscillator shells, and the second one, $N_{\text{a.s.}}$, numbers Pauli-allowed states in a given oscillator shell. The expansion coefficients C_α were determined in the $SU(3)$ basis, where the indices $(\lambda\mu)$ are good quantum numbers after eliminating Pauli-forbidden states. A detailed analysis shows that the main contribution (around 80%) to the wave function comes from the $\mu = 2$ basis states; the $\mu = 0$ basis states contribute only 9%. Note that the former states in

Table 1. ${}^8\text{He}$ ground-state energy reckoned from the ${}^4\text{He} + {}^2n + {}^2n$ threshold

Basis	Jacobi tree	Subspace	E , MeV	Number of functions
BO	T	Total	-2.065	399
		$l = 0$	-1.832	118
		$l \leq 2$	-2.047	219
		$l \leq 4$	-2.064	293
[-5pt] BO	Y	Total	-2.065	399
		$l = 0$	-1.839	118
		$l \leq 2$	-2.065	219
[-5pt] $SU(3)$	T	Total	-2.065	399
		$\mu = 0$	6.341	91
		$\mu \leq 2$	0.172	196
		$\mu \leq 4$	-1.335	274

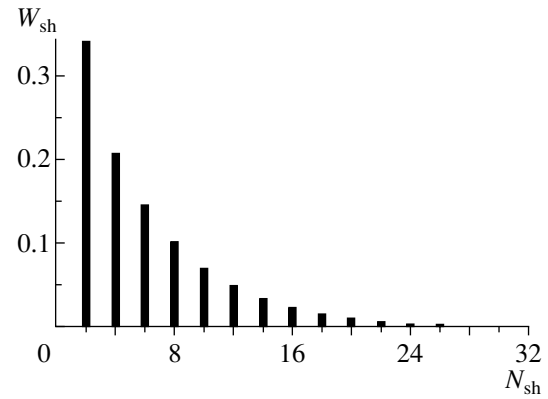


Fig. 3. Contribution of various oscillator shells N to the wave function of the ${}^8\text{He}$ ground state.

${}^6\text{He}$ (see [23, 24]) formed a dominant subspace whose contribution is more than 93%.

It can be seen from Fig. 2 and, more clearly, from Fig. 3 (where the weights of different oscillator shells are displayed) that the main contribution comes from the lowest oscillator shells; however, the contribution of large- N shells is also noticeable. This indicates a substantial clustering in the nuclei; that is, valence neutrons move predominantly far off the α particle, forming a neutron halo.

In order to obtain additional information about the role of different subspaces of the total space of oscillator functions, we impose various restrictions on the quantum numbers of basis states. For the bioscillator basis, we first took a subspace with the maximal value of partial orbital angular momenta ($l = l_1 = l_2$) $l = 0$, $l = 2$, and $l = 4$. This was done for both the Y and the T tree of Jacobi vectors. For the $SU(3)$ basis, we used only the T tree and the restriction was imposed on the maximal value of $\mu = 0, 2$, and 4 . The results of these calculations are presented in Table 1. One can see that the $l_1 = l_2 \leq 2$ subspace for the Y tree of the bioscillator basis is the most optimal part of the total basis, because 54% of the total basis (or 219 functions) make the ground-state energy very close to the “exact” value.

Effects of the Pauli exclusion principle. To understand the role of the Pauli exclusion principle in

Table 2. Root-mean-square radii for the ground state of ${}^8\text{He}$

RMS, fm	Theory	Experiment [29]	Experiment [30]
RMS_m	2.73	2.37 ± 0.18	2.52 ± 0.03
RMS_p	2.08	1.89 ± 0.17	2.15 ± 0.02
RMS_n	2.91	2.50 ± 0.19	2.64 ± 0.03
$\text{RMS}_n - \text{RMS}_p$	0.83	0.61	0.49

a three-cluster system, we investigate the contribution of different Pauli-allowed states to the ground-state wave function. Each of the Pauli-allowed states, which is an eigenfunction of the antisymmetrization operator, can be labeled (characterized) by the corresponding eigenvalue of this operator. As was mentioned above, the antisymmetrization operator overlaps only those functions that obey the relation $N_1 + N_2 = N'_1 + N'_2$ —that is, basis functions of the same oscillator shell. An analysis of the eigenfunctions shows that the diagonalization of the matrix $\|\langle n | \hat{A} | n' \rangle\|$ reveals states with specific eigenvalues of the antisymmetrization operator for a two-cluster subsystem. This means, in particular, that a Pauli-forbidden state of a three-cluster system is a state in which at least one pair of the clusters is in a Pauli-forbidden state. By way of example, we indicate that, for the two-cluster subsystem $\alpha + {}^2n$, the oscillator functions for which the numbers of oscillator quanta (along the intercluster coordinate) are $N = 0$ and $N = 1$ are Pauli-forbidden states. In the subsystem ${}^2n + {}^2n$, where symmetry of the subsystem allows only even functions, we have only one forbidden state, that for which $N = 0$. As to Pauli-allowed states for the three-cluster system, they describe the states in which all pairs of the two-cluster subsystems are out of the Pauli-forbidden region.

To prove these statements, we consider eigenvalues of the antisymmetrization operator (which we denote by λ_α) for Pauli-allowed states and the coefficients C_α in the expansion in these states for the $N_{\text{sh}} = 20$ oscillator shell. These quantities obtained in the $SU(3)$ basis are displayed in Fig. 4. The first seven functions correspond to the $SU(3)$ irreducible representation $(\lambda\mu) = (20, 0)$, the next eight functions belong to the $SU(3)$ irreducible representation $(\lambda\mu) = (16, 2)$, and so on. The last function has the $SU(3)$ symmetry $(\lambda\mu) = (0, 10)$. In this figure, the dashed horizontal lines represent the eigenvalues of the antisymmetrization operator for the two-cluster subsystem $\alpha + {}^2n$. Note that the corresponding values for the subsystem ${}^2n + {}^2n$ are equal to unity. Indeed, one can see that some eigenvalues of the operator \hat{A} for the three-cluster system coincide with the eigenvalues of this operator for the subsystem $\alpha + {}^2n$. Moreover, one notices that such states corresponding to the even oscillator quanta $N = 2$ and $N = 4$ in the $\alpha + {}^2n$ subsystem play a dominant role in the ground state of ^8He .

RMS radii. In Table 2, we compare the calculated mass, neutron, and proton root-mean-square (RMS) radii with the available experimental data. The theoretical values of RMS radii are somewhat larger than the experimental ones that we took from [29,

Table 3. Root-mean-square radii of ^8He that were obtained by different methods

RMS, fm	AV RGM	RRGM [1]	Shell Model [4]
RMS m	2.73	2.41	
RMS p	2.08	1.71	1.684
RMS n	2.91		

30]. This is perhaps because the calculated binding energy is slightly less than the experimental one. But the present model correctly reproduces the general picture of ^8He . One sees that the radius of neutron matter is larger than that of proton matter. The difference of these radii is 0.83 fm. These results also indicate the existence of a neutron halo in the nucleus.

In Table 3, we collected the mass, neutron, and proton RMS radii obtained by various theoretical methods: AV RGM (present calculations), the refined resonating-group method (RRGM)[1], and multi-configuration shell model [4].

Shape of the three-cluster system. Having calculated the coefficients C_n , the wave function in the oscillator representation, we thus obtain the wave function for the relative motion of the three-cluster

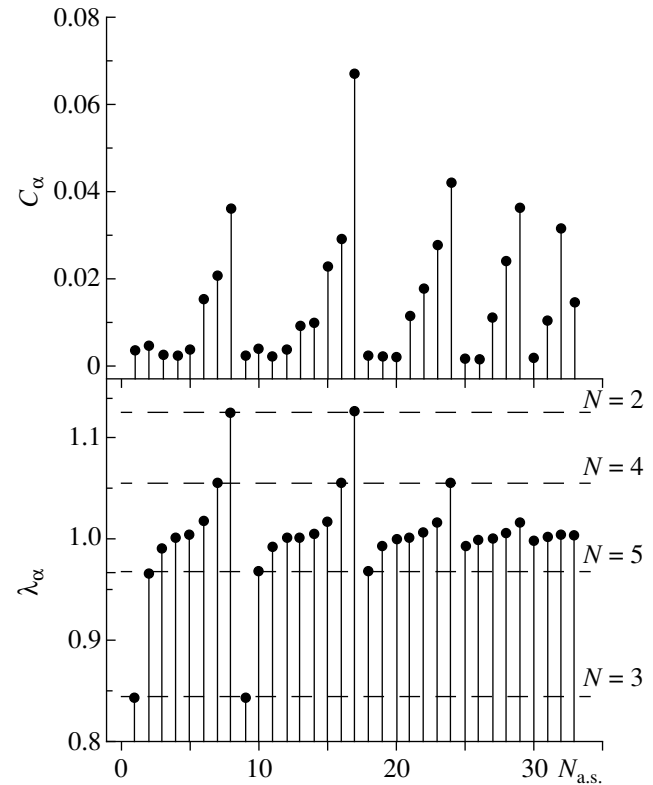


Fig. 4. Eigenvalues of the antisymmetrization operator λ_α and expansion coefficients C_α for the oscillator shell $N = 20$.

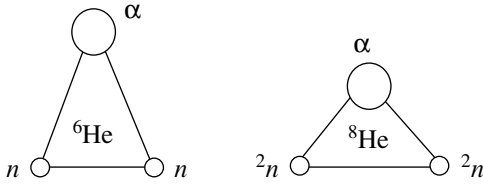


Fig. 5. Shape of the triangles formed by three clusters in ${}^8\text{He}$ and ${}^6\text{He}$.

system:

$$\Phi(\mathbf{q}_1, \mathbf{q}_2) = \sum_n C_n \phi_n(\mathbf{q}_1, \mathbf{q}_2). \quad (5)$$

By using (5), we can evaluate mean spacing between the clusters. For this purpose, one has to calculate the quantities

$$Q_1^2 = \int d\mathbf{q}_1 d\mathbf{q}_2 \Phi^*(\mathbf{q}_1, \mathbf{q}_2) \mathbf{q}_1^2 \Phi(\mathbf{q}_1, \mathbf{q}_2),$$

$$Q_2^2 = \int d\mathbf{q}_1 d\mathbf{q}_2 \Phi^*(\mathbf{q}_1, \mathbf{q}_2) \mathbf{q}_2^2 \Phi(\mathbf{q}_1, \mathbf{q}_2),$$

which, with allowance for the normalization of the wave function and the definition of Jacobi coordinates, specify the sought parameters. By way of example, we indicate that, for the T tree, the mean value of q_1 is related to the base of an isosceles triangle and the mean value of q_2 is related to its height.

The mean spacing between two dineutrons is 2.33 fm, while the mean spacing between the α particle and the center of mass of two dineutrons is 1.42 fm. Thus, the three clusters of ${}^8\text{He}$ form an isosceles, almost rectangular, triangle with the α particle at the vertex of the right angle.

In what is concerned with ${}^6\text{He}$, the situation is somewhat different. In this nucleus, the clusters appear at the vertices of an acute-angled triangle. Two valence neutrons in the presence of the α particle form a subsystem with the RMS radius equal to 2.52 fm, which is less than the RMS free-deuteron radius (2.69 fm) calculated with the same potential and the same number of basis functions. These triangles are displayed in Fig. 5.

The difference in the geometry of cluster disposition in ${}^6\text{He}$ and ${}^8\text{He}$ is more likely associated with the Pauli exclusion principle. There is an effective repulsion between two dineutrons, which arises from the Pauli exclusion principle and which strives to place dineutrons on the different sides of the α particle. In contrast to the case of ${}^8\text{He}$, the valence neutrons with opposite spin orientations may combine into a rather compact subsystem in ${}^6\text{He}$ (due to the presence of the α particle).

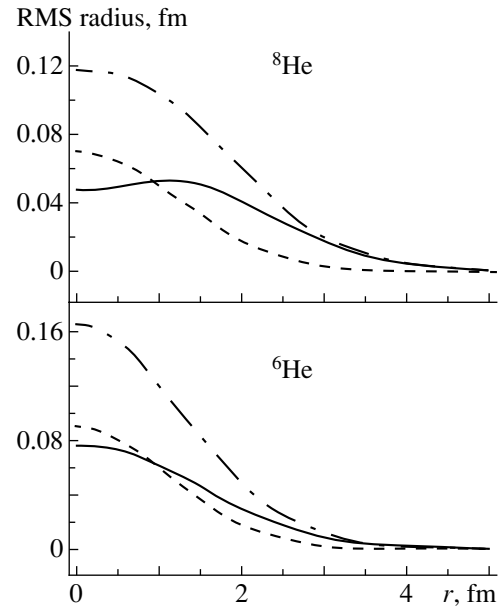


Fig. 6. Neutron (solid curve), proton (dashed curve) and mass (dash-dotted curve) density distributions in ${}^8\text{He}$ and ${}^6\text{He}$.

Density distributions. The proton-, the neutron-, and the mass-density distribution (they are defined as

$$R(\mathbf{r}) = \sum_i \langle \Psi | \delta(\mathbf{r}_i - \mathbf{r}) | \Psi \rangle$$

and are normalized by the conditions

$$\int d\mathbf{r} R(\mathbf{r}) = Z, N, \text{ or } A,$$

where Ψ is the wave function of a bound state and the sum in the expression for the above distributions is taken over protons, neutrons, or all nucleons for the first, the second, and the third case, respectively) also confirm the existence of a neutron halo in ${}^8\text{He}$. As can be seen from Fig. 6, where we display the proton-, the neutron-, and the mass-density distribution for both ${}^8\text{He}$ and ${}^6\text{He}$, the size of a neutron cloud is substantially larger than the size of a proton cloud. Moreover, the main part of neutrons in ${}^8\text{He}$ move at the surface of the nucleus. One sees a depression in the neutron-density distribution at small values of the coordinate r . This is due to the Pauli exclusion principle, which makes four neutrons (united in two dineutrons) move at a relatively large distance from the α particle.

4. CONCLUSION

We have investigated the ground-state properties of ${}^8\text{He}$ within the three-cluster microscopic model. The three-cluster configuration ${}^4\text{He} + {}^2n + {}^2n$ has

been used to simulate the dynamics of the eight-nucleon system. The proposed model describes reasonably well the parameters of the ground state, such as the binding energy, the mass, and the proton and neutron root-mean-square radii. The analysis of the system has shown that valence neutrons move at a large distance from the α particle, forming a neutron halo in ^8He .

REFERENCES

1. J. Wurzer and H. M. Hofmann, Phys. Rev. C **55**, 688 (1997).
2. Y. Suzuki, K. Varga, and R. G. Lovas, Nucl. Phys. A **571**, 447 (1994).
3. S. Karataglidis, P. J. Dortmans, K. Amos, and C. Bennhold, nucl-th/9811045.
4. P. Navratil and B. R. Barrett, Phys. Rev. C **57**, 3119 (1998).
5. M. V. Zhukov *et al.*, Phys. Rep. **231**, 151 (1993).
6. B. V. Danilin *et al.*, Phys. Rev. C **43**, 2835 (1991).
7. A. Csötó, Phys. Rev. C **48**, 165 (1993).
8. Y. Ohbayasi, K. Varga, and Y. Suzuki, Phys. Rev. C **50**, 189 (1994).
9. Ya. B. Zeldovich, Zh. Éksp. Teor. Fiz. **38**, 1123 (1960) [Sov. Phys. JETP **11**, 812 (1960)].
10. V. I. Goldansky, Zh. Éksp. Teor. Fiz. **38**, 1637 (1960) [Sov. Phys. JETP **11**, 1179 (1960)].
11. J. Cerny *et al.*, Phys. Rev. Lett. **16**, 469 (1966).
12. F. Ajzenberg-Selove, Nucl. Phys. A **490**, 1 (1988).
13. K. Wildermuth and Y. Tang, *A Unified Theory of the Nucleus* (Vieweg, Braunschweig, 1977).
14. G. F. Filippov and I. P. Okhrimenko, Yad. Fiz. **32**, 932 (1980) [Sov. J. Nucl. Phys. **32**, 480 (1980)].
15. G. F. Filippov, Yad. Fiz. **33**, 928 (1981) [Sov. J. Nucl. Phys. **33**, 488 (1981)].
16. A. B. Migdal, Yad. Fiz. **16**, 427 (1972) [Sov. J. Nucl. Phys. **16**, 238 (1972)].
17. A. A. Ogloblin, in *Proceedings of International Conference on Exotic Nuclei "Present Status of Exotic Lightest Nuclei," Foros, Crimea, 1991*, Ed. by Yu. E. Penionzhkevich and R. Kalpakchieva (World Sci., Singapore, 1991), p. 36.
18. V. S. Vasilevskiĭ and I. Yu. Rybkin, Yad. Fiz. **50**, 662 (1989) [Sov. J. Nucl. Phys. **50**, 411 (1989)].
19. B. Jonson and P. G. Hansen, Europhys. Lett. **4**, 409 (1987).
20. G. F. Filippov *et al.*, Yad. Fiz. **43**, 843 (1986) [Sov. J. Nucl. Phys. **43**, 536 (1986)].
21. G. F. Filippov, V. S. Vasilevsky, and A. V. Nesterov, Nucl. Phys. A **426**, 327 (1984).
22. G. F. Filippov, V. S. Vasilevskiĭ, and A. V. Nesterov, Yad. Fiz. **40**, 1418 (1984) [Sov. J. Nucl. Phys. **40**, 901 (1984)].
23. V. S. Vasilevsky, A. V. Nesterov, F. Arickx, and P. van Leuven, Preprint ITP-96-3E (1996).
24. V. S. Vasilevsky, A. V. Nesterov, F. Arickx, and P. van Leuven, Yad. Fiz. **60**, 413 (1997) [Phys. At. Nucl. **60**, 343 (1997)].
25. G. F. Filippov, A. D. Bazavov, and K. Katō, Yad. Fiz. **62**, 1763 (1999) [Phys. At. Nucl. **62**, 1642 (1999)].
26. S. V. Korennov, G. F. Filippov, I. Yu. Rybkin, and K. Kato, J. Math. Phys. **36**, 4571 (1995).
27. A. V. Nesterov, Yad. Fiz. **56** (10), 35 (1993) [Phys. At. Nucl. **56**, 1320 (1993)].
28. A. B. Volkov, Nucl. Phys. **74**, 33 (1965).
29. S. R. Neumaier, G. D. Alkhazov, and G. D. Andronenko, Scientific Report 1995, GSI 96-1 (Roether Druk, Darmstadt, 1996).
30. I. Tanihata *et al.*, Phys. Lett. B **206**, 592 (1988).

Simple Phenomenological Model of Neutron-Resonance Densities in $60 < A < 250$ Even–Even Compound Nuclei

L. L. Litvinsky

*State Scientific Engineering Center
of Control Systems and Emergency Response, Kiev, Ukraine*

Received March 16, 2000

Abstract—A simple relationship between the observed density of s -neutron resonances and the energy of the first 2^+ excited level of even–even compound nuclei is established. The corresponding phenomenological parameters are determined from an analysis of data on stable initial nuclei and are compared with available experimental data on β -unstable nuclei. © 2001 MAIK “Nauka/Interperiodica”.

1. INTRODUCTION

A series of fundamental and applied problems in neutron physics—such as those in astrophysics and reactor calculations—requires estimating neutron cross sections and their functionals over the region of neutron intermediate energies ($E_n < 0.5$ MeV) for nuclei far off the stability band, which have received virtually no experimental study.

Calculations within the R -matrix model that are based on the mean resonance nuclear parameters, such as the neutron strength functions S_{nl} , the mean radiative widths $\Gamma_{\gamma l}$, and the mean spacings D_J between the resonances at excitation energies close to the binding neutron energy $U \approx B_n$, are the most reliable method for estimating neutron cross sections in the intermediate-energy region [1, 2]. The quantities S_{nl} and $\Gamma_{\gamma l}$ exhibit a smooth mass dependence and, for unstable nuclei, can be easily extrapolated from the region of stability, where they are determined from abundant experimental data on the total and partial neutron cross sections in the region of resolved and unresolved resonances.

In the region of intermediate energies, the neutron cross sections show the lowest sensitivity to D_J of all the parameters listed above [1]. At the same time, experimental data on D_J are available in the limited energy region (that of resolved resonances) and the limited region of compound-nucleus spins J . For the majority of stable nuclei, only the observed values of D_0 averaged over resonances excited by the s -neutron wave ($l = 0$, $J = I_0 \pm 1/2$, where I_0 is the spin of the initial nucleus) can be assumed to be comparatively reliable [3].

In contrast to S_{nl} and $\Gamma_{\gamma l}$, D_0 and D_J change significantly from one nucleus to another, and it is

impossible to construct their model-independent extrapolation to the region of unstable nuclei.

The most popular parametrization of D_J is based on the Fermi gas model [4] with various phenomenological corrections [5]. The model approaches that are being developed currently rely on inputs that combine the parametrization of D_0 with spectroscopic data on the observed level densities in the region of low excitation energies ($U \ll B_n$). So far, the best results of this kind have been obtained within Ignatyuk’s model [6].

2. INFLUENCE OF COLLECTIVE EFFECTS

All previous systematics of the neutron-resonance density indicate that coherent effects of a collective nature are of importance [5]. These effects also determine the energy spectrum of low-lying states. For even–even nuclei, all theoretical approaches suggest a linear relationship between the energies E_i of the lowest excited states and the frequencies of the rotational and vibrational modes:

$$E_i \sim w_{i,v}. \quad (1)$$

For highly excited states, the density-enhancement coefficients are given by [7]

$$K_{r,v} \sim \exp(-\alpha w_{r,v}). \quad (2)$$

This has given us an incentive to seek a simple relationship between the observed mean spacing D_J and the energy E_1 of the first excited $J^\pi = 2^+$ level of even–even compound nuclei in the form

$$D_J \sim \exp(-aE_1). \quad (3)$$

3. SYSTEMATICS OF MEAN SPACINGS FOR STABLE NUCLEI

The experimental data compiled by Belanova *et al.* [5] for stable original nuclei were used here to analyze the mean spacings D_0 between s -neutron resonances. Figure 1 displays the mass dependence of $\ln D_0$ in the range $60 < A < 250$ for all even–even compound nuclei, with the exception of magic ones. A simple comparison with the mass dependence of E_1 (Fig. 2) confirms the validity of the assumption specified by Eq. (3).

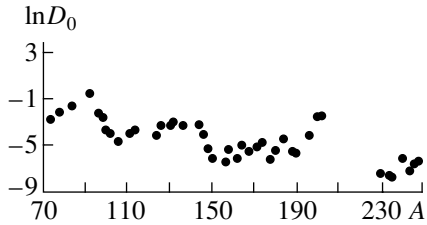


Fig. 1. Mass dependence of $\ln D_0$ for even–even compound nuclei.

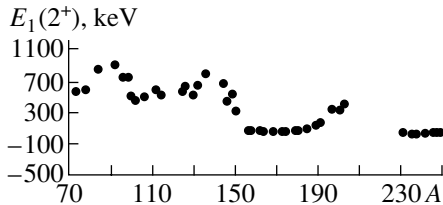


Fig. 2. Mass dependence of the energies E_1 of the first excited $J^\pi = 2^+$ level in even–even compound nuclei.

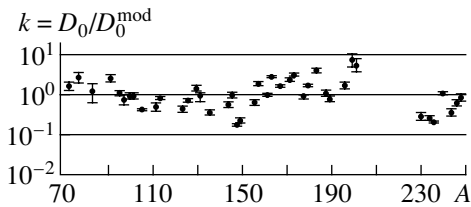


Fig. 3. Mass dependence of the quality of the approximation of the data on D_0 .

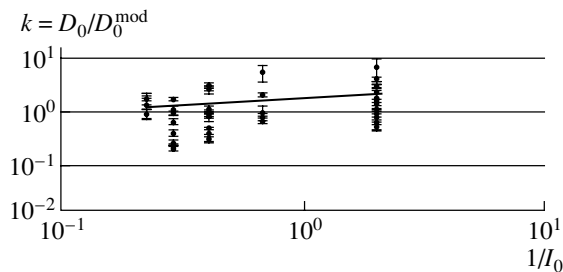


Fig. 4. Results of a data analysis performed to extract the systematic dependence $k(I_0)$.

For a first approximation, the experimental data were approximated by the linear expression

$$\ln D_0 = a + bE_1. \quad (4)$$

The model values of D_0^{mod} were determined as

$$D_0^{\text{mod}} = C \exp(bE_1), \quad C = \exp a. \quad (5)$$

Figure 3 shows the values of the coefficient

$$k = D_0/D_0^{\text{mod}}, \quad (6)$$

which demonstrates the quality of the approximation in (4).

To extract a possible systematic dependency on the spin I_0 of the original nucleus and on the neutron binding energy B_n , the k values were further analyzed for the entire set of nuclei. Figures 4 and 5 show the results of this analysis. The analysis of the dependence $k(I_0)$ yielded the expected result

$$k(I_0) = 0.49/I_0 + 1.0 \approx (2I_0 + 1)/2I_0, \quad (7)$$

which is in good agreement with the concepts of the Fermi gas model [4].

The analysis of the dependence $k(B_n)$ does not suggest any relationship with B_n in a wide range of mass numbers (Fig. 5). The reason is that variations in B_n are also determined by collective effects that have already been taken into account in the above approach in normalizing D_0 to E_1 .

Taking into account relation (7), we choose the eventual parametrization of the data on D_0 in the form

$$D_0^{\text{mod}} = C(2I_0 + 1)/2I_0 \exp(bE_1), \quad (8)$$

where the constants C and b estimated over a wide range of mass numbers are

$$C = 1.164 \times 10^{-3} \text{ keV}, \quad b = 5.156 \times 10^{-3} \text{ keV}. \quad (9)$$

Figure 6 displays the experimental values of D_0 along with its model estimates based on (8) and (9). It is obvious that the maximum distinction between D_0 and D_0^{mod} is within a factor of 3, which is typical of all currently available phenomenological systematics.

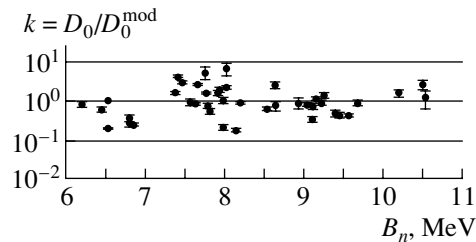


Fig. 5. Results of a data analysis performed to extract the systematic dependence $k(B_n)$.

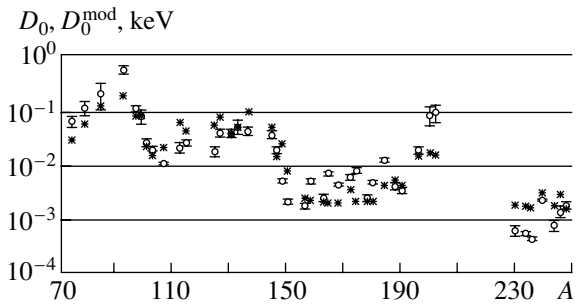


Fig. 6. Mass dependence of the mean spacing between s -neutron resonances in even–even compound nuclei: (open circles) experimental data and (asterisks) results of the model parametrization.

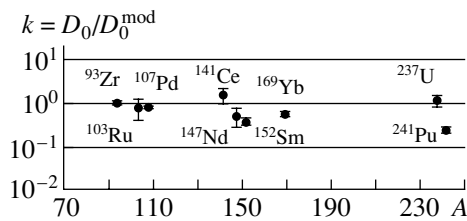


Fig. 7. Ratio D_0/D_0^{mod} for the β -unstable nuclei ^{93}Zr , ^{103}Ru , ^{107}Pd , ^{141}Ce , ^{147}Nd , ^{152}Sm , ^{169}Yb , ^{237}U , and ^{241}Pu .

4. ESTIMATING MEAN SPACINGS BETWEEN RESONANCES FOR UNSTABLE NUCLEI

The main advantage of the approach developed in this study is that it can be applied to a wide range of unstable nuclei, because the values of E_1 are well known from spectroscopic studies far beyond the boundaries of the stability band. This is supported by a comparison of the results of model calculations and experimental data on D_0 that are available for the β -unstable nuclei ^{93}Zr , ^{103}Ru , ^{107}Pd , ^{141}Ce , ^{147}Nd ,

^{152}Sm , ^{169}Yb , ^{237}U , and ^{241}Pu [5, 8] (see Fig. 7, which demonstrates that the model predictions are in good agreement with these experimental data; the maximum deviation, observed for ^{241}Pu , is within a factor of 3).

In summary, it should be noted that the approach proposed in this article can be most useful for estimating the averaged cross sections $\langle\sigma_\gamma\rangle$ for radiative neutron capture by unstable neutron-rich nuclei. These cross sections are necessary for deducing estimates relevant to s and r processes of stellar nucleosynthesis and for assessing resonance integrals that are characteristic of nuclear fission products and which are required for reactor calculations.

ACKNOWLEDGMENTS

This work was supported by International Atomic Energy Agency (IAEA) under the contract no. 9507/Regular Budget Fund.

REFERENCES

1. L. L. Litvinskii *et al.*, *Yad. Fiz.* **56** (1), 31 (1993) [*Phys. At. Nucl.* **56**, 17 (1993)].
2. L. L. Litvinskii *et al.*, *Yad. Fiz.* **58**, 1347 (1995) [*Phys. At. Nucl.* **58**, 1265 (1995)].
3. S. F. Mughabghab, *Neutron Cross Sections* (Academic, New York, 1984).
4. A. Gilbert and A. Cameron, *Can. J. Phys.* **43**, 1446 (1965).
5. T. S. Belanova *et al.*, *Radiative Neutron Capture* (Énergoatomizdat, Moscow, 1986).
6. A. V. Ignatyuk *et al.*, *Yad. Fiz.* **21**, 485 (1975) [*Sov. J. Nucl. Phys.* **21**, 255 (1975)].
7. A. Bohr and B. R. Mottelson, *Nuclear Structure, Vol. 2: Nuclear Deformations* (Benjamin, New York, 1975; Mir, Moscow, 1977).
8. V. A. Anufriev *et al.*, in *Neutron Physics* (TsNIIatominform, Moscow, 1980), Vol. 2, p. 137.

Translated by E. Kozlovskii

Parity Splitting in Nuclei Involving Octupole Correlations and the Alignment of the Angular Momentum

A. R. Safarov, R. Kh. Safarov, and A. S. Sitdikov¹⁾

*Kazan State Pedagogical University, ul. Levo-Bulachnaya 44, Kazan,
420021 Tatarstan, Russia*

Received February 4, 2000

Abstract—A rotational model based on a simultaneous analysis of parity splitting and the alignment of the angular momentum is developed to describe high-spin negative-parity states. A simple formula for the energy of these states is proposed. It is shown that negative-parity states exhibit alignment, provided that the ground-state band is aligned and that the two opposite-parity bands can be considered as a single alternating-parity band. © 2001 MAIK “Nauka/Interperiodica”.

1. INTRODUCTION

It has long been known [1] that strong octupole correlations between nucleons and the presence of low-lying negative-parity states, which form, together with the states of the ground-state rotational band, an alternating-parity band characterized by the spin-parity sequence $I^\pi = 0^+, 1^-, 2^+, \dots$, are typical of the shell structure of certain nuclei. In such a unified band, the energy gap in each doublet is referred to as parity splitting. Within the collective model of octupole motion, it was found [2, 3] that the parity splitting decreases exponentially with increasing angular momentum of the nucleus being considered. This regularity is noted in nuclei where the excitation energy of negative-parity states is low because of the collective nature of such states.

If excitation energies are sufficiently high, these states have a two-particle structure and, at a specific rate of rotation, their intrinsic angular momenta are aligned by Coriolis forces. In contrast to what occurs in the case mentioned immediately above, the difference of the energies of these states and the states of the ground-state rotational band, which is an analog of parity splitting in such nuclei, decreases linearly with increasing angular velocity of the core [4].

There are nuclei, however, in which the angular-momentum dependence of parity splitting differs from the two aforementioned patterns. Nuclei characterized by a manifest exponential dependence of parity splitting may exhibit a linear dependence at high angular momenta because of the alignment of the angular momentum. It follows that, for negative-parity

states, we need a theoretical description that would treat the two phenomena simultaneously. Here, we propose a combined rotational model for nuclei showing both exponentially decreasing parity splitting and the alignment of the angular momentum.

2. MODEL OF OCTUPOLE MOTION

If the chemical potential of a nucleus lies between two one-particle orbitals characterized by $\Delta l = 3$ and $\Delta j = 3$, then constituent nucleons develop strong octupole correlations, which may give rise to an axial deformation of the nucleus. From the requirement that the states of a nucleus be invariant under the reversal of the sign of an octupole deformation, it follows that the potential energy must have two minima separated by a potential barrier whose height depends on the angular momentum of the nucleus. The rate of tunneling between two states characterized by opposite signs of the deformation determines the energy gap between the two levels of the parity doublet. In the semiclassical approximation, the relevant problem was solved by Jolos and von Brentano [2] and by Jolos, von Brentano, and Donau [3], who found, for the parity-splitting energy, that

$$E_d^I = \Delta E \exp\left(\frac{-AI(I+1)}{1 + BE_{\text{rot}}^I}\right), \quad (1)$$

where ΔE is the splitting energy for $I = 0$, the parameter A is related to the moment of inertia, and B describes the change in the moment of inertia because of an increase in the rotational energy E_{rot}^I .

According to (1), the parity-splitting energy decreases exponentially with increasing spin. This formula agrees well with experimental data up to angular-momentum values at which positive- and

¹⁾Kazan State Power University, ul. Krasnosel'skaya 51, Kazan, Tatarstan, Russia.

negative-parity levels form a single band. In nuclei featuring a fully developed rotational band, there are, however, deviations from the exponential dependence at high spins, whence one can conclude that additional effects stemming from the high-velocity rotation of the nucleus must be taken into account. Of these effects, the Coriolis alignment of the angular momentum [4] is the most significant.

3. MODEL OF THE ROTATIONAL ALIGNMENT OF THE ANGULAR MOMENTUM OF NEGATIVE-PARITY STATES

In the high-spin approximation of the rotational model [5], two-particle negative-parity states are treated as those that are due to the effect of the quadrupole–quadrupole and the Coriolis interaction, which cause the splitting of a definite multiplet $(j_1, j_2)_{JM}$ of two nucleons from a spherical subshell.

Straightforward computations indicate that, with increasing velocity of rotation of the nucleus, the levels of the $K = 0$ rotational band characterized by the maximum possible value of the angular momentum J descend below the other rotational bands and become aligned.

With the proviso that the rotational energy of the core E_{rot}^I is subtracted, the energy of the levels of the rotational band under consideration is described by a simple linear dependence on the angular velocity ω_{rot} ; that is,

$$E_s^I = E^I - E_{\text{rot}}^I = E_{0s} - j_0 \omega_{\text{rot}}, \quad (2)$$

where E^I is the energy of negative-parity states, E_{0s} is the bandhead energy of the aligned band, j_0 is the value of the aligned angular momentum, and E_{rot}^I is the core rotational energy parametrized according to Harris [6] as

$$E_{\text{rot}}^I = \frac{1}{2} J_0 \omega_{\text{rot}}^2 + \frac{3}{4} J_1 \omega_{\text{rot}}^4, \quad (3)$$

$$\tilde{I} = J_0 \omega_{\text{rot}} + J_1 \omega_{\text{rot}}^3, \quad \tilde{I} = \sqrt{I(I+1)}. \quad (4)$$

The energies of the levels take this simple form as soon as the alignment of the angular momenta is completed—that is, for spin values of $I \geq j_0$.

4. COMBINED MODEL OF NUCLEUS INVOLVING PARITY SPLITTING AND THE ALIGNMENT OF THE ANGULAR MOMENTA

In order to describe high-spin negative-parity states, we propose a phenomenological model based on the Bohr–Mottelson Hamiltonian [1]. At $I \geq j_0$,

the Bohr–Mottelson Hamiltonian can be represented in the form [7]

$$\hat{H} = \hat{H}_0 - \omega_{\text{rot}} \hat{j}_x = \hat{H}_{\text{in}} + \hat{H}_{\text{rot}}(\hat{I}^2) - \omega_{\text{rot}} \hat{j}_x, \quad (5)$$

where \hat{H}_{in} describes internal excitations, $-\omega_{\text{rot}} \hat{j}_x$ is the Coriolis interaction, j_x is the projection of the intrinsic angular momentum onto the x axis, and $\hat{H}_{\text{rot}}(\hat{I}^2)$ is the Hamiltonian for rotational degrees of freedom of the core. The eigenvalues E_{rot}^I of the Hamiltonian $\hat{H}_{\text{rot}}(\hat{I}^2)$ are parametrized according to Harris [see Eqs. (3) and (4)].

Solutions to the Schrödinger equation $\hat{H}\Psi_n^I = E_n^I \Psi_n^I$ with Hamiltonian (5) are sought here in the form of an expansion in the basis of negative-parity states,

$$\Psi_n^I = a_d^I \varphi_d^I + a_s^I \varphi_s^I, \quad (6)$$

where the low-lying vibrational (phonon) d state and the aligned two-particle s state are described by the Bose operators $\varphi_d^I = \hat{b}_d^+ |I\rangle$ and $\varphi_s^I = \hat{b}_s^+ |I\rangle$, respectively, with $|I\rangle$ being the states of the rotating core.

We assume that these states satisfy the equations

$$\hat{H}_0 \varphi_d^I = (E_{\text{rot}}^I + E_d^I) \varphi_d^I, \quad (7)$$

$$\hat{H}_0 \varphi_s^I = (E_{\text{rot}}^I + E_s^I) \varphi_s^I, \quad (8)$$

where E_d^I , E_s^I , and E_{rot}^I are given by Eqs. (1), (2), and (3), respectively. The Coriolis interaction gives rise to the mixing of these states; as a result, the energy of the perturbed state assumes the form

$$E^I = E_{\text{rot}}^I + \varepsilon^I, \quad (9)$$

where

$$\varepsilon^I = \frac{1}{2} \left(E_d^I + E_s^I \pm \sqrt{(E_d^I - E_s^I)^2 + 4\omega_{\text{rot}}^2 j_{ds}^2} \right), \quad (10)$$

j_{ds} being the matrix elements of the Coriolis interaction between the d and s states. The solutions that we are going to compare with the experimental value of splitting energy are those with the lower sign in formula (10).

5. RESULTS OF THE CALCULATIONS AND DISCUSSION

Parity splitting in the $^{224-228}\text{Ra}$, $^{226-232}\text{Th}$, and $^{230-238}\text{U}$ nuclei, which are characterized by low-lying negative-parity states in their spectrum, has been computed within the combined model. The experimental values of the splitting energy are given by the formula

$$E_d^I = E_{\text{expt}}^I - E_{\text{rot}}^I, \quad (11)$$

where E_{expt}^I are the experimental values from [8, 9].

Table 1. Optimum values of the parameters of inertia J_0 and J_1 as determined from a fit to the energies of the ground-state-band levels up to the angular momentum I_m

Nucleus	J_0, MeV^{-1}	J_1, MeV^{-3}	I_m	E_4/E_2
^{224}Ra	32.45	1135.6	10^+	2.99
^{226}Ra	41.51	1164.5	10^+	3.32
^{228}Ra	45.48	794.6	6^+	3.21
^{226}Th	39.75	808.8	18^+	3.14
^{228}Th	50.89	732.7	14^+	3.32
^{230}Th	55.50	552.0	14^+	3.21
^{232}Th	59.90	586.6	12^+	3.28
^{230}U	57.31	575.8	16^+	3.28
^{232}U	61.43	616.7	20^+	3.33
^{234}U	69.09	575.6	12^+	3.26
^{236}U	67.75	595.4	10^+	3.31
^{238}U	67.75	629.4	10^+	3.30

At sufficiently high values of the angular momentum I , E_{rot}^I begins to deviate from a monotonic behavior, evincing the occurrence of some additional phenomena associated with rotation. This type of behavior of the ground-state rotational band is most conspicuous in the spectrum of $N = 90$ nuclei, which was described elsewhere [10] in terms of the alignment of the angular momentum. In determining the parameters of E_{rot}^I , we therefore used only that part of the ground-state band where there are no deviations from monotonicity—that is, levels whose angular momenta do not exceed I_m .

The optimum values of the parameters of inertia J_0 and J_1 , which describe the energy of rotation of the core, E_{rot}^I , were determined by means of the χ^2 goodness-of-fit test. The results are presented in Table 1. Also shown in Table 1 are I_m and the ratio E_{4^+}/E_{2^+} . We consider only those nuclei that satisfy the rigid-rotor condition $E_{4^+}/E_{2^+} = 3.3$ and which can be described by the Harris formula. Such nuclei are characterized by a large value of the moment of inertia J_0 and a comparatively small non-adiabaticity parameter J_1 . To parametrize E_{rot}^I , we used levels of the ground-state rotational band up to rather high angular-momentum $I_m = 20^+$ (^{232}U), $I_m = 18^+$ (^{226}Th), and $I_m = 16^+$ (^{230}Th , ^{230}U). This results in better agreement of E_{rot}^I with experimental values (deviations are not greater than $\delta E = 2\text{--}3$ keV).

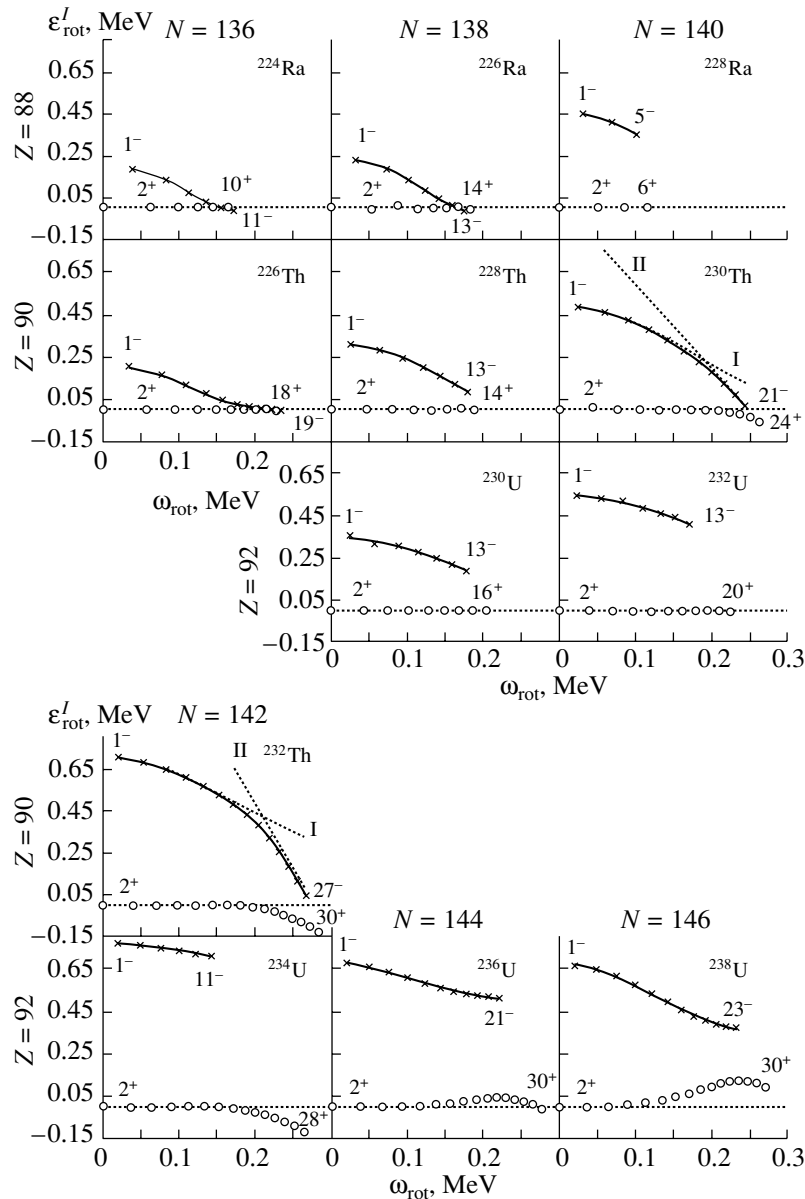
The experimental values of the splitting energies are determined on the basis of (11) by using the above

Table 2. Optimal values of the parameters describing parity splitting

Nucleus	$\Delta E, \text{MeV}$	A	B
^{224}Ra	0.209	0.030	-0.002
^{226}Ra	0.245	0.017	-0.015
^{228}Ra	0.462	0.010	0.639
^{226}Th	0.214	0.022	0.167
^{228}Th	0.311	0.008	0.131
^{230}Th	0.496	0.006	0.438
^{232}Th	0.702	0.003	0.466
^{230}U	0.346	0.004	0.264
^{232}U	0.550	0.003	0.452
^{234}U	0.774	0.001	1.090
^{236}U	0.681	0.004	1.649
^{238}U	0.672	0.004	0.780

parametrization of E_{rot}^I . These values are plotted in the figure versus the angular velocity ω_{rot} in order to give a graphical example of how one can isolate the rotational-band segment associated with the phenomenon of parity splitting and with the alignment of the angular momentum. The segments within which the exponential dependence goes over to a linear one were observed only in the spectra of the ^{230}Th and ^{232}Th nuclei. Negative-parity states of spin up to $I^\pi = 21^-$ ($I^\pi = 27^-$) were experimentally found in the spectrum of the former (latter) nucleus. For these nuclei, we have computed the energies of the negative-parity states on the basis of formulas (9) and (10), which describe the mixing of states. In our computations, we have used the optimum mixing-parameters values presented in Table 2 and the angular-momentum-alignment parameters E_{0s} and j_0 to be discussed below. The results of these calculations (solid curve in the figure) can be compared with the energies of the unperturbed s and d states. The calculated values and the experimental data comply well, which is clearly demonstrated in Table 3 for the ^{232}Th nucleus.

The spectra of the other nuclei studied here display only states associated with parity splitting. The energies of negative-parity states can readily be calculated by formula (1). It was noticed that the splitting energies ΔE at $I = 0$ behave in the same manner as the moment of inertia J_0 : as the product of the number of valence nucleons $N_p N_n$ increases up to the value corresponding to the ^{234}U nucleus, both J_0 and ΔE linearly increase but they remain constant at greater values of $N_p N_n$. Our values of ΔE agree with those



Experimental (crosses) and theoretical (solid curves) values of the parity-splitting energy versus the angular velocity ω_{rot} for the $^{224-228}\text{Ra}$, $^{226-232}\text{Th}$, and $^{230-238}\text{U}$ nuclei. The energies of the unperturbed (I) d states and (II) s states (dotted lines) and the energies of the positive-parity states (open circles) are reckoned from the core-rotation energy parametrized according to Harris (zero dotted line).

reported in [2] for the $^{224,226}\text{Ra}$ and ^{232}Th nuclei, the parameters A and B being redefined (see Table 2).

At high spins, the splitting energy in the ^{224}Ra nucleus takes negative values of about 10 keV in magnitude. In fitting these energies in terms of an exponential function, we have had to add this value to the experimental splitting energies and then to subtract it from the calculated energies.

Listed immediately below are the optimum values of the alignment parameters. In the ^{230}Th nucleus, the bandhead energy of the aligned band, $E_{0s} =$

0.812 MeV, is on the same order of magnitude as the splitting energy ΔE at $I = 0$, while the aligned angular momentum $j_0 = 3.11$ agrees with the momentum of the octupole vibrations; as to the matrix element of the interaction between s and d states, it is very small ($j_{ds} = -0.014$). The values of these parameters for the ^{232}Th nucleus are considerably greater than those for the collective state— $E_{0s} = 1.72$ MeV, $j_0 = 6.15$, and $j_{ds} = 0.26$ —whence we conclude that these states are predominantly of a two-particle nature, especially at high spins.

Table 3. Theoretical and experimental energy values E_{theor}^I and E_{expt}^I for the ^{232}Th nucleus ($\delta E = E_{\text{expt}}^I - E_{\text{theor}}^I$) (in MeV)

I^π	E_{expt}^I	E_{theor}^I	δE	I^π	E_{expt}^I	E_{theor}^I	δE
1 ⁻	0.714	0.715	-0.001	16 ⁺	1.858	1.856	0.002
2 ⁺	0.049	0.049	0	17 ⁻	2.445	2.450	-0.005
3 ⁻	0.774	0.774	0	18 ⁺	2.262	2.263	-0.001
4 ⁺	0.162	0.162	0	19 ⁻	2.813	2.816	-0.003
5 ⁻	0.884	0.884	0	20 ⁺	2.690	2.693	-0.003
6 ⁺	0.333	0.333	0	21 ⁻	3.203	3.201	0.002
7 ⁻	1.043	1.041	0.002	22 ⁺	3.143	3.145	-0.002
8 ⁺	0.557	0.556	0.001	23 ⁻	3.616	3.612	0.004
9 ⁻	1.249	1.244	0.005	24 ⁺	3.618	3.618	0
10 ⁺	0.827	0.824	0.003	25 ⁻	4.050	4.048	0.002
11 ⁻	1.498	1.492	0.006	26 ⁺	4.115	4.112	0.003
12 ⁺	1.137	1.133	0.004	27 ⁻	4.506	4.510	-0.004
13 ⁻	1.784	1.780	-0.004	28 ⁺	4.630	4.627	0.003
14 ⁺	1.482	1.479	0.003	29 ⁻			
15 ⁻	2.101	2.102	-0.001	30 ⁺	5.61	5.64	-0.003

In summary, the above analysis has revealed that the negative-parity band exhibits alignment of the angular momentum if the ground-state rotational

band is aligned at high spins. This suggests that the bands have the same nature and that they can be considered as a single alternating-parity band. We can also expect the alignment of the angular momentum in the negative-parity band extending beyond the $I^\pi = 11^-$ state in the spectrum of ^{234}U because the ground-state rotational band from $I^\pi = 12^+$ shows alignment.

REFERENCES

1. A. Bohr and B. R. Mottelson, *Nuclear Structure*, vol. 1: *Single-Particle Motion* (Benjamin, New York, 1969; Mir, Moscow, 1971).
2. R. V. Jolos and P. von Brentano, *Phys. Rev. C* **49**, R2301 (1994).
3. R. V. Jolos, P. von Brentano, and F. Donau, *J. Phys. G* **19**, L151 (1993).
4. F. S. Stephens, *Rev. Mod. Phys.* **47**, 43 (1975).
5. A. R. Safarov and R. Kh. Safarov, *Izv. Akad. Nauk, Ser. Fiz.* **62**, 949 (1998).
6. S. M. Harris, *Phys. Rev. Lett.* **13**, 663 (1964).
7. I. N. Mikhaïlov, R. Kh. Safarov, F. N. Usmanov, and Ch. Briançon, *Yad. Fiz.* **38**, 297 (1983) [*Sov. J. Nucl. Phys.* **38**, 177 (1983)].
8. P. C. Sood, D. M. Headly, and R. A. Sheline, *Nucl. Data Tables* **47**, 89 (1991).
9. P. C. Sood, D. M. Headly, and R. A. Sheline, *Nucl. Data Tables* **51**, 273 (1992).
10. R. Kh. Safarov and R. R. Safarov, *Yad. Fiz.* **56** (6), 30 (1993) [*Phys. At. Nucl.* **56**, 726 (1993)].

Translated by R. Rogalyov

Sign of P -Odd Observables in Neutron–Nucleus Interaction

L. M. Smotrisky

Petersburg Nuclear Physics Institute, Russian Academy of Sciences, Gatchina, 188350 Russia

Received May 17, 2000

Abstract—The signs of P -odd observables in neutron–nucleus interaction are analyzed on the basis of recent experiments. A simple formula describing these signs is derived. The proposed approach makes it possible to deduce information about the isospin structure of weak nucleon–nucleon interaction.

© 2001 MAIK “Nauka/Interperiodica”.

At present, it is well known from experiments that there is weak interaction between nucleons [1–3]. However, the isospin structure of this interaction has not yet received adequate study [4, 5]. For weak non-leptonic strangeness-conserving processes, including those that are induced by weak NN interaction, experimental data cannot be correctly compared with the predictions of the Standard Model of electroweak interaction because a transition from a description in terms of quarks to that in terms of nucleons and then in terms of nuclear degrees of freedom is a challenging theoretical problem [4, 5].

In view of this, investigation of parity-violation effects in neutron–nucleus interaction has hitherto been thought to be of little promise in what is concerned with deducing information about the isospin structure of weak NN interaction. Nevertheless, these effects have intensely been studied since their discovery in 1964 [1]. Investigations along these lines gained additional momentum upon the observation of P -odd effects in neutron optics [6, 7] and their resonance enhancement [3, 8]. It was found that P -odd observables, which were measured both for a wide range of nuclei (from ^{35}Cl to ^{238}U) and for a number of neutron resonances in a specific nucleus [9–11], may be as large as 10%.

Among experimental studies on the subject, it is worth highlighting those that revealed nonstatistical behavior of the signs of P -odd observables [9, 12–15]. Since a P -odd observable depends on the reaction amplitudes rather than on their squares, the sign dependence of an observable is very important because it opens new possibilities for interpreting experimental data and seeking the underlying theoretical mechanism.

Parity-violation effects in the integrated spectrum of (n, γ) reactions on various nuclei were first observed by Vesna *et al.* [12] and by Egorov *et al.* [13], who analyzed two observables: the P -odd angular

asymmetry A_γ in polarized-thermal-neutron capture by nuclei and the P -odd circular polarization P_γ in unpolarized-neutron capture. The observed magnitudes of the effect were at a level of 10^{-5} – 10^{-6} . Such small values were measured by an integrated detection method [2], which has no restrictions in input traffic. In view of the special feature of the procedure, the observation of nonzero effects was first very surprising. The spectrum of gamma rays from (n, γ) reactions is very complicated. Therefore, a P -odd observable is expected vanish upon averaging over a vast number of gamma transitions. But in fact, this does not occur, and a P -odd observable does not vanish upon averaging over output reaction channels.

The results of an experiment performed by the TRIPLE collaboration (Los Alamos) [9] are being extensively discussed now. In this experiment, the P -odd observable A_l in the total cross section was studied for several p -wave resonances in the ^{232}Th nucleus. It was surprising that, in all cases of p -wave resonances for which the P -odd observable was in excess of 2.4 standard deviations, it was positive. A sign correlation was observed for seven p -wave resonances at energies below 200 eV. In [16], the probability that this sign coincidence was accidental was estimated at 1.6%.

In [14, 15], the P -odd angular asymmetry was examined for some primary gamma transitions in the reaction $^{117}\text{Sn}(n, \gamma)$ induced by polarized neutrons. The very complicated spectrum of gamma rays from this reaction was detected by a Ge(Li) detector. Experimental data suggested a sign correlation in the output reaction channel: the sign of the P -odd observable for three 9.33-, 7.28-, and 6.42-MeV gamma transitions correlates with the sign of the corresponding spin factor. The spin factor characterizes a nuclear level to which a gamma transition proceeds and follows from the conservation of the total angular momentum [17]. The above correlation implies that

six electromagnetic amplitudes for three transitions are correlated in sign (the matrix element of weak interaction is assumed to take the same value for all three gamma transitions). We note that, as far back as 1972, Alberi *et al.* [18] observed a P -odd circular polarization in the reaction $^{113}\text{Cd}(n, \gamma)$ for two un-separated gamma transitions (9.04 and 8.48 MeV). In this case, the spin factor vanishes because the neutrons are unpolarized. The magnitude and sign of the observable can be matched with the result obtained for the same nucleus in [1], provided that the sign of the circular polarization is identical (negative) for 9.04- and 8.48-MeV gamma transitions. We note that the study reported in [18], along with that in [2], furnished the first independent piece of experimental evidence for the existence of weak NN interaction in the ^{114}Cd nucleus.

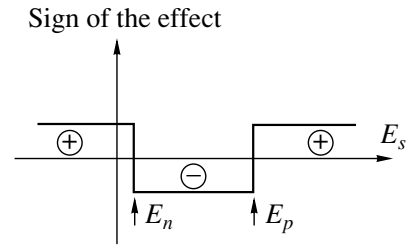
The aforementioned experimental results especially those presented in [14, 15] gave an incentive to more detailed studies.

Two classes of P -odd observables are usually examined in experiments. According to [19], the first class includes P -odd observables that arise when amplitudes interfere in the output reaction channel owing to weak interaction, the input channel being common. In this case, one can observe a P -odd (pseudoscalar) correlation of the $\sigma_n \cdot \mathbf{k}$ type, where σ_n is neutron spin and \mathbf{k} is the momentum of a final particle, a photon in the simplest case of (n, γ) reactions (considered below only this final-particle species). The class of observables in question includes the aforementioned quantities A_γ and P_γ . As was indicated above, P_γ differs from A_γ only by the absence of the spin factor. These observables vanish at the energy of a p -wave resonance. For this reason, they are usually analyzed at the thermal point far off the p -wave resonance.

The second class includes so-called P -odd observables in neutron optics [3, 6–11]. In this case, one observes a correlation of the $\sigma_n \cdot \mathbf{k}_n$ type, where \mathbf{k}_n is the neutron momentum. Among these observables, there are the P -odd longitudinal asymmetry A_l arising in the total cross section when longitudinally polarized neutrons with opposite helicities traverse a specimen and the rotation Φ_{pv} of the plane of polarization of transversely polarized neutrons. In this case, the amplitudes interfere in the input reaction channel, whereas the output channel is common.

Theoretical studies performed so far (see [20–22]) treat all P -odd effects as those that are due to the weak-interaction-induced mixing of s - and p -wave resonances, opposite-parity continuous-spectrum nuclear levels of identical spins. This mixing occurs at the compound-nucleus stage and makes the dominant contribution to the effect. For a specific nucleus and two mixed resonances, the same

^{35}Cl [12]	^{113}Cd [1, 18, 23]
^{56}Fe [13]	^{131}Xe [25]
^{117}Sn [3, 6, 7, 12, 14, 15, 26, 27]	^{232}Th [9]
^{139}La [3, 7, 12, 28, 29]	^{238}U [30]



Sign of a P -odd observable versus the energy of the s -wave resonance.

matrix element W_{sp} of weak interaction is responsible for all observables, with the result that the signs of different observables are related to one another. Only interfering amplitudes are different. For first-class P -odd observables, these are, for example, the amplitudes $\langle M1 \rangle$ and $\langle E1 \rangle$ for the electromagnetic decays of s - and p -wave resonances, respectively; for second-class observables, these are the amplitudes γ_s and γ_p for neutron capture to s - and p -wave resonances, respectively.

In a theoretical treatment, the problem of taking into account the phases (signs) of the amplitudes is a real challenge. According to [22], the phases arise in diagonalizing the Green's function of a compound state and can in principle be complex-valued.¹⁾ To calculate the phases, it is necessary to know the wave functions of neutron resonances, which are complex multiparticle states. It is emphasized in [20–22] that the phases must be taken into account, but they do not appear explicitly in the final formulas for the P -odd observables [23].

Let us now address experimental data. The figure, which was taken from [24] and which was plotted on the basis of an analysis of experimental data, shows the sign of the P -odd observable versus the relative position of the s - and p -wave resonances and the neutron energy. The data were reduced to the thermal point far off the p -wave resonance.

This consideration is more general because, in this case, we have three reference points: the neutron energy E_n and energies E_s and E_p of the s - and p -wave resonances, respectively. For resonance measurements, in which case the neutron energy coincides with the energy E_p , the pattern is incomplete. Nuclei that have an s -wave resonance at negative energies are quoted in the upper left column above the figure,

¹⁾For thermal neutrons, the potential phases can be ignored.

along with the references to the original studies where the relevant measurements were performed. For all these nuclei, the P -odd observable is positive. The central column contains nuclei that have an s -wave resonance between E_n and E_p and which are characterized by the negative sign of the observable. Finally, nuclei that are characterized by E_s greater than E_p and by a positive sign of the P -odd observable are quoted in the third column. For all these nuclei, a highly accurate description is provided by the two-resonance approximation, where the observable is determined by one s -wave resonance and one p -wave resonance exclusively; the contribution from other resonances can be ignored because they are located far off or have other spins. This is not so only for the ^{232}Th nucleus [9], which is a unique case where the multiresonance approximation is necessary. The target nucleus ^{232}Th has zero spin and positive parity ($J^\pi = 0^+$). When neutrons are captured to the s -wave resonance, only a $J^\pi = 1/2^+$ state arises. When neutrons are captured to the p -wave resonance, there arise the $J^\pi = 1/2^-$ or the $J^\pi = 3/2^-$ states. An observation of a P -odd effect for a specific p -wave resonance means that its spin is $J^\pi = 1/2^-$ because only such a resonance can be mixed with an s -wave resonance, whose spin-parity is $J^\pi = 1/2^+$. For a given p -wave resonance, one can therefore easily calculate the contributions (A_{ij} in the notation adopted in [9]) of all s -wave resonances located to the left and to the right of it. Such calculations revealed that, for each of the seven p -wave resonances for which the P -odd observable was nonzero, the contributions A_{ij} from all s -wave resonances located to the right of it are greater than the contributions from the resonances located to the left. It is this circumstance that explains a positive sign of the observable. The entire body of information necessary for the calculation was presented by Frankle *et al.* [9] for the 8.35-eV p -wave resonance. In that study, however, the result was obtained under the assumption of random contributions from all s -wave resonances.

Recently, the TRIPLE collaboration performed new investigations for the ^{232}Th [31] and ^{238}U [32] nuclei using a substantially upgraded experimental facility. For the ^{232}Th nucleus [31], nonzero P -odd effects were corroborated for six p -wave resonances, with the exception of that at 37.0 eV, and a nonzero effect was found for four other p -wave resonances. For all ten p -wave resonances, the sign correlation found previously was confirmed: the P -odd observables are positive for all resonances. All effects exceed three standard deviations. As was discussed above, a positive sign of the observable for the first seven p -wave resonances can be explained by taking into

account the contributions A_{ij} from all s -wave resonances in the region extending to 150–200 eV. For the remaining three p -wave resonances, this interval is insufficient. However, an analysis of spectroscopic data reveals that the region extending to 3 keV in ^{232}Th [33] does indeed involve a great number of s -wave resonances with anomalously large neutron widths (for example, $E_s = 1632$ eV, $g\Gamma_n = 552$ meV). To explain a positive sign of the observable for the resonances at $E_p = 196.2$ and 232 eV, it is sufficient to take into account all s -wave resonances in the region extending to 1500 eV; the contribution from all s -wave resonances in the region extending to 3.5 keV must be taken into account only for $E_p = 202.6$ eV.

Thus, the signs of P -odd observables for all ten p -wave resonances in the ^{232}Th nucleus are consistent with the data in the figure.

New measurements for ^{238}U [32] revealed statistically significant P -odd observables with either positive or negative signs for six p -wave resonances, whereas the previous study reported in [30] recorded only an effect for $E_p = 63.5$ eV. The ^{238}U nucleus is simple for interpretation because it, in just the same way as the ^{232}Th nucleus, has the spin-parity of $J^\pi = 0^+$. An analysis of the contributions from s -wave resonances occurring to the right (left) of a given p -wave resonance demonstrates that a larger contribution from the right (left) resonances corresponds to a positive (negative) sign of the P -odd observable. This is not so for the sign of the P -odd observable for the p -wave resonance at 89.2 eV. In [33], this resonance was assigned the spin-parity of $J^\pi = 3/2^-$, in which case the P -odd observable is expected to vanish for the $E_p = 89.2$ eV resonance. Here, further investigations are required.

So far, we have considered nuclei for which the two-resonance approximation yields highly accurate results or zero-spin nuclei for which a multiresonance analysis can easily be performed. We assumed that the matrix elements W_{sp} of weak interaction between a given p -wave resonance and different s -wave resonances are approximately identical. This assumption is compatible with available experimental data, which lead to a W_{sp} value at a level of a few millivolts over a wide range of nuclear masses [3, 14, 23].

The situation around nuclei whose spin is nonzero is much more complicated. When neutrons are captured, the spin-parity of s -wave resonances can then be $J^\pi = (I \pm 1/2)^\pi$, while the spin-parity of p -wave resonances can take values of $J^\pi = (I \pm 1/2)^{-\pi}$ or $J^\pi = (I \pm 3/2)^{-\pi}$. Therefore, a correct multiresonance analysis requires complete neutron-spectroscopic information about resonances in the energy range being considered. Moreover, two

capture amplitudes $\gamma_{p1/2}$ and $\gamma_{p3/2}$, which correspond to the values of $j = 1/2$ and $3/2$, respectively, for the total angular momenta of the captured neutron are operative in neutron capture to the p -wave resonance, but we have virtually no information at our disposal about these amplitudes.

Recently, P -odd observables were investigated for a number of resonances in the nuclei ^{107}Ag and ^{109}Ag [34], whose spin–parity is $J^\pi = 1/2^-$. Recall that the ground states of the nuclei that were considered above and which are presented in the figure have a positive parity. In this case, all p -wave resonances involved in neutron capture are of negative parity.

For the ^{107}Ag and ^{109}Ag nuclei, all p -wave resonances are of positive parity. In addition to studying P -odd observables, Lowie *et al.* [34] performed a dedicated investigation in order to determine the spins and neutron widths of the resonances. However, the pattern remained incomplete even upon this investigation. On the basis of the entire body of available information [33–35], an analysis of the contributions for three p -wave resonances in ^{107}Ag that yield a negative sign of the P -odd observable nevertheless revealed a reversed pattern: a negative sign of the observable corresponds to a larger total contribution from the s -wave resonances occurring to the right of a given resonance. For the remaining five resonances that lead to a positive observable, the situation is uncertain: the contributions from resonances located to the right of a given p -wave resonance are approximately equal to those from the resonances occurring to the left, whence it follows that we cannot draw a definitive conclusion in this case.

For the p -wave resonance in ^{109}Ag at 32.7 eV, the sign of the observable is positive, and a larger contribution comes from the s -wave resonances located to the left of this resonance. For the remaining two p -wave resonances, the situation is uncertain, in just the same way as for ^{107}Ag , and further investigations are required.

We emphasize once again that the signs of the P -odd observables for the 35.8-eV (^{107}Ag) and 32.7-eV (^{109}Ag) resonances are opposite to the signs of the observables in the figure. These p -wave resonances are the closest to the thermal point, lead to the greatest value of the P -odd observable (more than 1%), and admit a highly accurate description within the two-resonance approximation (the dominant contribution comes from $E_s = 41.6$ eV and $E_s = 30.6$ eV for the $E_p = 35.8$ eV and $E_p = 32.7$ eV resonances, respectively).

Thus, the sign of a P -odd observable for all aforementioned nuclei can be explained by taking into account properties of a strongly interacting system such as the positions of the resonances with respect

to the neutron energy, the spin factor, and the parity of the p -wave resonance. Since we consider a weak-interaction-induced process (a pseudoscalar correlation is observed), this means that the sign in question, which is determined by weak interaction, is identical for all the nuclei listed above. This conclusion, which follows from the experimental data discussed above, but which must be justified theoretically, is of paramount importance because, in principle, it allows one to determine the isospin structure of weak interaction from neutron data (only one isospin component or a specific mixture of the components contributes [15, 24, 36]). There are many arguments in favor of this conclusion both in weak-interaction physics and in nuclear theory [15, 36], but their discussion is beyond the scope of the present study.

What is of prime importance at the moment is the validity of the above simple description of the signs of P -odd observables in neutron-induced reactions, the more so as there are nuclei that do not fit in this pattern yet. These are predominantly the high-spin nuclei— ^{81}Br ($J^\pi = 3/2^-$) [3, 16, 37], ^{111}Cd ($J^\pi = 1/2^+$) [3], and ^{115}In ($J^\pi = 9/2^+$) [38]—for which the interpretation is not straightforward. As a rule, these elements have a number of isotopes. We emphasize once again that attributing resonances to certain isotopes and determining their spins, orbital angular momenta, and neutron widths are very important for interpreting the experimental results for multiisotope elements.

In this connection, investigation of P -odd effects is instructive even for the monoisotope element ^{133}Cs ($J^\pi = 7/2^+$). The ^{133}Cs nucleus has very interesting sequence of resonances: $E_s = -40.8$ eV ($J^\pi = 4^+$), $E_s = -15$ eV ($J^\pi = 3^+$), $E_s = 5.9$ eV ($J^\pi = 3^+$), $E = 9.5$ eV ($J = ?$), and $E_s = 22.5$ eV ($J^\pi = 3^+$) [33]. Neither the spin nor the orbital angular momentum of the 9.5-eV resonance is known. The following spin values are possible: $J^\pi = 2^-, 3^-, 4^-,$ or 5^- . An experiment with Cs and thermal neutrons was performed at the Petersburg Nuclear Physics Institute (PNPI, Gatchina), and a value of $P_\gamma = -(2.4 \pm 0.8) \times 10^{-6}$ [13] was determined for the P -odd integrated circular polarization. An observation of the effect means that there is a p -wave resonance near the thermal point. The possible candidate for this resonance is that at 9.5 eV because it has a small neutron width [33]. There are no direct gamma transitions from the capture state to the ground state in the ^{134}Cs nucleus [39]. For this reason, the sign of the P -odd observable does not provide direct information in this case, because this sign depends on the contribution of the secondary gamma transitions as well.

Recently, the TRIPLE collaboration investigated the P -odd effect directly at the 9.5-eV resonance

and obtained the value of $A_l = (2.4 \pm 0.2) \times 10^{-3}$ [40] for the longitudinal asymmetry. From the results of this experiment, it follows that the 9.5-eV state is indeed a p -wave resonance whose spin–parity is 3^- or 4^- . If the spin–parity of the p -wave resonance at 9.5 eV is 4^- , only the s -wave resonance at -40.8 eV can be mixed with the p -wave resonance by weak interaction. In this case, the sign that was measured for the P -odd observable [40] will be consistent with the data in the figure. In order to solve the problem considered here, it is therefore necessary to determine the spin of the p -wave resonance by other methods (for example, by the method used in [34]).

ACKNOWLEDGMENTS

I am grateful to the staff of the Neutron Research Department at the Petersburg Nuclear Physics Institute for numerous stimulating discussions and to Prof. J.D. Bowman (LANL) for the opportunity of participating in the investigation of P -odd observables with resonance neutrons.

Note added in proof. In [41], it is shown that, by introducing a resonance phase for two opposite-parity quasistationary states (s - and p -wave resonances) of the same spin, it is possible to match the theory with the observed sign dependence of P -odd effects (see figure) in neutron-induced reactions.

REFERENCES

1. Yu. G. Abov, P. A. Krupchitsky, and Yu. A. Oratovsky, *Phys. Lett.* **12**, 25 (1964); Yu. G. Abov *et al.*, *Usp. Fiz. Nauk* **118**, 141 (1976) [*Sov. Phys. Usp.* **19**, 75 (1976)].
2. V. M. Lobashev, V. A. Nazarenko, L. F. Saenko, *et al.*, *Yad. Fiz.* **13**, 555 (1971) [*Sov. J. Nucl. Phys.* **13**, 313 (1971)].
3. V. P. Alfimenkov, S. B. Borzakov, V. V. Thuan, *et al.*, *Nucl. Phys. A* **398**, 93 (1983).
4. E. G. Adelberger and W. C. Haxton, *Annu. Rev. Nucl. Part. Sci.* **35**, 501 (1985).
5. G. V. Lobov, *Nucl. Phys. A* **577**, 449 (1994).
6. M. Forte, B. R. Heckel, N. F. Ramsey, *et al.*, *Phys. Rev. Lett.* **45**, 2088 (1980).
7. E. A. Kolomensky, V. M. Lobashev, A. N. Pirozkov, *et al.*, *Phys. Lett. B* **107B**, 272 (1981).
8. J. D. Bowman, G. T. Garvey, M. B. Johnson, *et al.*, *Annu. Rev. Nucl. Part. Sci.* **43**, 829 (1993).
9. C. M. Frankle, J. D. Bowman, J. E. Bush, *et al.*, *Phys. Rev. C* **46**, 778 (1992).
10. E. I. Sharapov, J. D. Bowman, B. E. Crawford, *et al.*, in *Proceedings of the 6th International Seminar on Interaction of Neutron with Nuclei, Dubna, 1998*, E3-98-202, p. 19.
11. S. J. Seestrom, J. D. Bowman, B. E. Crawford, *et al.*, *Phys. Rev. C* **58**, 2977 (1998).
12. V. A. Vesna, É. A. Kolomenskiĭ, V. M. Lobashev, *et al.*, *Pis'ma Zh. Éksp. Teor. Fiz.* **36**, 169 (1982) [*JETP Lett.* **36**, 209 (1982)].
13. A. I. Egorov, É. A. Kolomenskiĭ, V. M. Lobashev, *et al.*, Preprint No. 1067, LIYaF (Leningrad Nuclear Physics Institute, Leningrad, 1985).
14. L. M. Smotritskiĭ and V. N. Dobrynin, Preprint No. 2041, PIYaF RAN (Petersburg Nuclear Physics Institute, Russian Academy of Sciences, Gatchina, 1995).
15. L. M. Smotritsky, Yu. E. Loginov, and P. A. Sushkov, in *Proceedings of the 9th International Symposium on Capture Gamma-Ray Spectroscopy and Related Topics*, Ed. by G. L. Molnar *et al.* (Springer-Verlag, Berlin, 1997), p. 628.
16. C. M. Frankle, J. D. Bowman, J. E. Bush, *et al.*, *Phys. Rev. C* **46**, 1542 (1992).
17. G. V. Lobov, *Izv. Akad. Nauk SSSR, Ser. Fiz.* **27**, 886 (1968).
18. J. L. Alberi, R. Wilson, and I. G. Schroder, *Phys. Rev. Lett.* **29**, 518 (1972).
19. Yu. G. Abov, O. N. Ermakov, I. L. Karpikhin, *et al.*, *Nucl. Instrum. Methods Phys. Res. A* **284**, 80 (1989).
20. O. P. Sushkov and V. V. Flambaum, *Usp. Fiz. Nauk* **136**, 3 (1982) [*Sov. Phys. Usp.* **25**, 1 (1982)].
21. V. E. Bunakov and V. P. Gudkov, *Nucl. Phys. A* **401**, 93 (1983).
22. V. V. Flambaum and O. P. Sushkov, *Nucl. Phys. A* **435**, 352 (1985).
23. V. P. Alfimenkov, Yu. D. Mareev, L. B. Pikel'ner, *et al.*, *Yad. Fiz.* **54**, 1489 (1991) [*Sov. J. Nucl. Phys.* **54**, 907 (1991)].
24. L. M. Smotritskiĭ, Preprint No. 2307, PIYaF RAN (Petersburg Nuclear Physics Institute, Russian Academy of Sciences, Gatchina, 1999), p. 14.
25. J. J. Szymanski, W. M. Snow, J. D. Bowman, *et al.*, *Phys. Rev. C* **53**, R2576 (1996).
26. H. Benkoula, J. C. Cavaignac, J. L. Charvet, *et al.*, *Phys. Lett. B* **71B**, 287 (1977).
27. G. V. Danilyan, *Usp. Fiz. Nauk* **131**, 329 (1980) [*Sov. Phys. Usp.* **23**, 323 (1980)].
28. V. W. Yuan, C. D. Bowman, J. D. Bowman, *et al.*, *Phys. Rev. C* **44**, 2187 (1991).
29. A. P. Serebrov, A. K. Petukhov, G. V. Val'skiĭ, *et al.*, *Pis'ma Zh. Éksp. Teor. Fiz.* **62**, 529 (1995) [*JETP Lett.* **62**, 545 (1995)].
30. X. Zhu, J. D. Bowman, C. D. Bowman, *et al.*, *Phys. Rev. C* **46**, 768 (1992).
31. S. L. Stephenson, J. D. Bowman, B. E. Crawford, *et al.*, *Phys. Rev. C* **58**, 1236 (1998).
32. B. E. Crawford, J. D. Bowman, P. P. J. Delheij, *et al.*, *Phys. Rev. C* **58**, 1225 (1998).
33. S. I. Sukhoruchkin, Z. N. Soroko, and V. V. Deriglazov, *Landolt-Bornstein New Series*, Vol. 1/16B: *Tables of Neutron Resonance Parameters* (Springer-Verlag, Berlin, 1998).
34. L. Y. Lowie, J. D. Bowman, F. Corvi, *et al.*, *Phys. Rev. C* **59**, 1119 (1999).

35. S. F. Mughabghab, M. Divadeenam, and N. E. Holden, *Neutron Cross Sections* (Academic, New York, 1981).
36. L. M. Smotrisky, in *Abstracts of Contributed Papers of the International Nuclear Physics Conference, Paris, 1998*, p. 733.
37. V. A. Vesna, É. A. Kolomenskiĭ, V. M. Lobashev, *et al.*, *Pis'ma Zh. Éksp. Teor. Fiz.* **35**, 351 (1982) [*JETP Lett.* **35**, 433 (1982)].
38. L. Y. Lowie, PhD Thesis (North Carolina State University, Raleigh, 1996).
39. *Nucl. Data Tables A* **5**, 57 (1968).
40. E. I. Sharapov, J. D. Bowman, B. E. Crawford, *et al.*, *Phys. Rev. C* **59**, 1772 (1999).
41. L. M. Smotrisky, *Pis'ma Zh. Éksp. Teor. Fiz.* **74**, 53 (2001) [*JETP Lett.* **74**, 51 (2001)].

Translated by R. Tyapaev

Pion Scattering on ${}^3\text{H}$ and ${}^3\text{He}$ Nuclei in the $\Delta_{33}(1232)$ Region

W. J. Briscoe¹), A. E. Kudryavtsev, I. I. Strakovsky¹), and V. E. Tarasov

Institute of Theoretical and Experimental Physics, Bol'shaya Cheremushkinskaya ul. 25, Moscow, 117259 Russia

Received June 1, 2000; in final form, August 17, 2000

Abstract—Elastic scattering of π^\pm mesons on ${}^3\text{H}$ and ${}^3\text{He}$ nuclei at energies around the $\Delta_{33}(1232)$ resonance is considered. The amplitudes for single and double scattering are calculated on the basis of the nonrelativistic diagram technique. The spin and isospin structure of pion–nucleon amplitudes is fully taken into account. The resulting theoretical predictions for the differential cross sections are compared with available experimental data. © 2001 MAIK “Nauka/Interperiodica”.

1. INTRODUCTION

The interaction of pions with extremely light nuclei belongs to the realms of pionic nuclear physics. In recent years, much attention has been given to mirror elastic reactions like $\pi^\pm d$, $\pi^\pm {}^3\text{H}$, and $\pi^\mp {}^3\text{He}$ scattering with special emphasis on studying issues associated with charge-symmetry violation in strong-interaction-induced processes (for an overview, see [1]). Usually, experimental data on charge-symmetry violation in reactions on ${}^3\text{He}$ and ${}^3\text{H}$ nuclei are represented in the form of the ratios $r_1 = [d\sigma/d\Omega(\pi^+{}^3\text{H})]/[d\sigma/d\Omega(\pi^-{}^3\text{He})]$ and $r_2 = [d\sigma/d\Omega(\pi^-{}^3\text{H})]/[d\sigma/d\Omega(\pi^+{}^3\text{He})]$ and in the form of the superratio $R = r_1 r_2$. In the case of charge-symmetry conservation, these quantities are equal to unity. In experiments that studied elastic pion scattering on ${}^3\text{H}$ and ${}^3\text{He}$ nuclei [2–4], it was found that, at energies in the region of the pion–nucleon resonance $\Delta_{33}(1232)$, the quantity R differs from unity and greatly depends on the scattering angle θ in the region $\theta \sim 60^\circ$ – 90° . Here, effects of charge-symmetry violation can arise for a number of reasons, including Coulomb interaction and the structural distinctions between the ${}^3\text{H}$ and the ${}^3\text{He}$ nucleus; in addition, there is charge-symmetry violation in strong-interaction pion–nucleon amplitudes that, at energies around the $\Delta_{33}(1232)$ resonance, is associated primarily with mass splitting in the Δ_{33} multiplet. At $\theta \sim 90^\circ$, the differential cross section $d\sigma/d\Omega$ has a minimum, which, in the impulse approximation (single scattering), is associated with the P -wave structure of the pion–nucleon amplitude around the Δ_{33} resonance. In the above region of angles, the angular distribution is therefore highly

sensitive to various details of the interaction. If factors that lead to charge-symmetry violation are put aside for the time being, multiple scattering and spin flip in pion–nucleon amplitude are worthy of note above all in this connection. It is clear that, in studying very subtle effects of charge-symmetry violation, one should generally rely on a model that would make it possible to describe differential cross sections over a wide interval of θ .

Processes of $\pi^3\text{H}$ and $\pi^3\text{He}$ scattering and allied effects of charge-symmetry violation were analyzed theoretically in a number of studies (see, for example, [5–7] and references therein). These analyses were based on a model that involves a first-order pion–nucleus optical potential. The relevant Born term in the scattering amplitude corresponds to the single-scattering amplitude. The resulting descriptions of the differential cross sections were quite accurate over broad regions of scattering angles ($\theta < 120^\circ$) and initial pion kinetic energies T_π (up to a few hundred MeV). At the same time, the predictions for the effects of charge-symmetry violation were qualitatively different in different studies. Experiments that explored backward $\pi^3\text{H}$ and $\pi^3\text{He}$ scattering [8] revealed a second minimum in the angular distributions at $\theta \sim 130^\circ$ – 140° in $\pi^+{}^3\text{He}$ and $\pi^-{}^3\text{H}$ scattering at $T_\pi = 180$ MeV and a growth of the differential cross sections for $\theta \rightarrow 180^\circ$. The existing predictions of the potential approach [5–7] do not reproduce this behavior of the differential cross sections. In order to describe the region of backward scattering, Collier and Gibbs [9] additionally took into account the amplitude involving a double spin flip—specifically, they considered that the spins of two intranuclear nucleons can be flipped. There is no such mechanism in a first-order optical potential, but it makes a sizable contribution to the cross section for $\pi^+{}^3\text{He}$ and $\pi^-{}^3\text{H}$ scattering at large angles. However, the authors of

¹Center of Nuclear Studies and Faculty of Physics, G. Washington University, Washington, DC 20052, USA.

[9] failed to reproduce the observed growth of the differential cross sections for the above reactions in the region $\theta > 140^\circ$ at $T_\pi = 180$ MeV. In our opinion, the approach used in [9] is not quite consistent: a part of the amplitude was taken into account there by one method (potential approximation), while the other part—the double-spin-flip contribution—was calculated by a different method (that of a direct evaluation of the double-scattering diagram). Wakamatsu [10] analyzed $\pi^-{}^3\text{He}$ scattering (both elastic and charge-exchange processes) on the basis of the optical-model potential that takes into account corrections for double pion–nucleon scattering and for the binding energy of the nucleons in the nucleus. In the case of elastic $\pi^-{}^3\text{He}$ scattering, the contribution of these corrections proved to be small. At energies around the pion–nucleon Δ_{33} resonance, the second-order correction (that which is due to double pion–nucleon scattering) to the optical potential is expected to be greater for $\pi^+{}^3\text{He}$ scattering, but there are no theoretical predictions for this case in [10].

In the present study, we calculate relevant differential cross sections on the basis of the nonrelativistic diagram technique, taking into account the diagrams of single and double scattering on intranuclear nucleons. Previously, a detailed calculation of single- and double-scattering diagrams in the Δ_{33} region with allowance for spin and isospin variables was performed in [11] in analyzing charge asymmetry for the case of $\pi^\pm d$ scattering. The calculation of double-scattering diagrams for scattering on three-nucleon systems becomes more involved. Here, we present detailed expressions for the relevant amplitudes and single out individual contributions corresponding to non-spin-flip (NSF), single-spin-flip (SSF), and double-spin-flip (DSF) processes, as well as processes in which the pion involved undergoes double intrinsic charge exchange (so-called DCX processes). The resulting theoretical predictions are compared with the experimental angular distributions $d\sigma/d\Omega$ for some values of the initial pion kinetic energy ($T_\pi = 142, 180, 220,$ and 256 MeV) in the region around the Δ_{33} isobar. We consider the region of not very small scattering angles, where Coulomb effects are immaterial, and disregard all effects violating isotopic invariance and leading to charge-symmetry violation. We are going to consider charge-symmetry-violation effects in subsequent publications.

In calculating nuclear-reaction amplitudes, it is necessary to take into account spin and isospin variables, but this usually leads to cumbersome expressions involving Clebsch–Gordan and $3j$ coefficients and some other similar quantities. Here, we make use of an alternative approach based on an invariant representation of spin vertex functions and elementary

amplitudes. The inclusion of spin (isospin) variables then reduces to evaluating expressions that involve products of σ (or τ) matrices. This approach is widely used to calculate reactions on a deuteron (see, for example [12–14]), where it is more economical. In our opinion, an attempt at calculating processes that involve three-nucleon nuclei is also of methodological interest.

2. AMPLITUDE FOR PION–NUCLEON SCATTERING AND WAVE FUNCTION FOR A THREE-NUCLEON SYSTEM

In the region around the $\Delta_{33}(1232)$ resonance, we take into account only the resonance part of the amplitude for pion–nucleon scattering. The amplitude $\hat{M}_{\pi N}$ then has the form ²⁾

$$\hat{M}_{\pi N} = 8\pi W_{\pi N} \hat{f}_{\pi N}, \quad \hat{f}_{\pi N} = f_{33} \hat{S} \hat{T}, \quad (1)$$

$$f_{33} = \frac{e^{2i\delta_{33}} - 1}{2ik_{\pi N}},$$

$$\hat{S} = 2(\hat{\mathbf{k}}_1 \cdot \hat{\mathbf{k}}_2) + i\boldsymbol{\sigma} \cdot [\hat{\mathbf{k}}_1 \times \hat{\mathbf{k}}_2],$$

$$\hat{T} = \frac{1}{3}(2 + \mathbf{t} \cdot \boldsymbol{\tau}),$$

where f_{33} is a scalar amplitude; δ_{33} is the resonance phase; $W_{\pi N}$ and $k_{\pi N}$ are, respectively, the invariant mass of the pion–nucleon system and the absolute value of the pion 3-momentum in the reaction c.m. frame (explicit expressions for these quantities are presented at the end of Section 3); $\hat{\mathbf{k}}_1$ and $\hat{\mathbf{k}}_2$ are unit vectors in the direction of the relative momentum of the pion and the nucleon prior to and after the scattering event respectively; \hat{S} and \hat{T} are the projection operators for the pion–nucleon state characterized by the total spin of $3/2$ and the isospin of $3/2$; \mathbf{t} and $\boldsymbol{\tau}/2$ are, respectively, the pion and the nucleon isospin operator; and $\boldsymbol{\sigma}$ and $\boldsymbol{\tau}$ are the Pauli matrices.

The wave function for the three-nucleon system can be represented as

$$\Phi = \Phi_{1(23)} + \Phi_{2(31)} + \Phi_{3(12)} = \sum_i \Phi_i, \quad (2)$$

$$\Phi_i \equiv \Phi_{i(jk)} = \sum_\nu \Phi_{i(jk)}^{(\nu)},$$

where $\Phi_{i(jk)}^{(\nu)}$ is a function that is asymmetric under the simultaneous interchange of configuration (coordinate or momentum), spin, and isospin variables of the j th and the k th nucleon, Φ (sum over cyclic

²⁾The quantity \hat{M} denotes the invariant amplitude, $\hat{M} = 8\pi\sqrt{s}\hat{f}$ (\sqrt{s} is the total energy in the reaction c.m. frame); in the case of unpolarized particles, the differential cross section then has the form $d\sigma/d\Omega = \frac{1}{2}\text{tr}\{\hat{f}^+\hat{f}\}$.

permutations of the indices ijk) is antisymmetric with respect to all three nucleons, and the function $\Phi_{i(jk)}$ is expanded in the components $\Phi_{i(jk)}^{(\nu)}$ characterized by a specific set (ν) of quantum-number values in the $i(jk)$ basis. For a three-nucleon system characterized by the total spin of $1/2$ and the isospin of $1/2$, such a set is usually specified by the quantities $(TSLJ)l(j)$, where T , S , L , and J are, respectively, the total isospin, the spin, the orbital angular momentum, and the total angular momentum of the (jk) nucleon pair; l is the orbital angular momentum of the relative motion of the i th nucleon and the jk pair; and j is the angular momentum composed of the orbital angular momentum l and the spin of the i th nucleon. The expression for the function $\Phi_{i(jk)}^{(\nu)}$ can be represented in the form

$$\Phi_{i(jk)}^{(\nu)} = \varphi^{(\nu)}(\mathbf{q}_i, \mathbf{Q}_i) X_i^{(\nu)} Y_i^{(\nu)}, \quad (3)$$

where $\varphi^{(\nu)}(\mathbf{q}_i, \mathbf{Q}_i)$ is a function of the relative momenta (Jacobi variables) $\mathbf{q}_i = (\mathbf{p}_j - \mathbf{p}_k)/2$ and $\mathbf{Q}_i = (\mathbf{p}_j + \mathbf{p}_k - 2\mathbf{p}_i)/3$ (\mathbf{p}_i is the 3-momentum of the i th intranuclear nucleon), while $X_i^{(\nu)}$ and $Y_i^{(\nu)}$ are, respectively, the spin-orbit and the isospin part of the wave function. In general, the quantities $X_i^{(\nu)}$ depend on the spin variables and the angles (that is, on the directions of the vectors \mathbf{q}_i and \mathbf{Q}_i), whereas the configuration functions $\varphi^{(\nu)}$ can be assumed to be dependent only on the absolute values $q_i = |\mathbf{q}_i|$ and $Q_i = |\mathbf{Q}_i|$. Hajdok *et al.* [15] constructed a parametrization of the ${}^3\text{H}$ wave function obtained by solving the Faddeev equations allowing for nucleon-nucleon interaction in the 1S_0 and 3S_1 - 3D_1 channels. The wave function then has five components ($\nu = 1, 2, 3, 4, 5$), the corresponding quantum-number sets being $(TSLJ)l(j) = (1000)0(1/2)$, $(0101)0(1/2)$, $(0121)0(1/2)$, $(0101)2(3/2)$, and $(0121)2(3/2)$ (see also [16]). Two types of expressions for $X_i^{(\nu)}$ and $Y_i^{(\nu)}$, with the total spin and the isospin of the jk pair taking the values of $S = 0$ and $T = 1$ for $\nu \equiv 1$ and $S = 1$ and $T = 0$ for $\nu \equiv 2$, correspond to the S -wave state of intranuclear nucleons ($L = l = 0$). These expressions can be represented as

$$X_i^{(1)} = \frac{1}{\sqrt{2}}(\chi_i^+ \chi)(\chi_j^+ \sigma_2 \chi_k^*), \quad (4)$$

$$Y_i^{(1)} = \frac{1}{\sqrt{6}}(\eta_i^+ \boldsymbol{\tau} \eta)(\eta_j^+ \boldsymbol{\tau} \tau_2 \eta_k^*),$$

$$X_i^{(2)} = \frac{1}{\sqrt{6}}(\chi_i^+ \boldsymbol{\sigma} \chi)(\chi_j^+ \boldsymbol{\sigma} \sigma_2 \chi_k^*), \quad (5)$$

$$Y_i^{(2)} = \frac{1}{\sqrt{2}}(\eta_i^+ \eta)(\eta_j^+ \tau_2 \eta_k^*),$$

where χ and η are, respectively, the spinor and the isospinor describing the ${}^3\text{H}$ or the ${}^3\text{He}$ nucleus, while χ_i , χ_j , and χ_k (η_i , η_j , and η_k) are the intranuclear-nucleon spinors (isospinors). The corresponding expressions for the other components ($\nu = 3, 4, 5$) are given in the Appendix (see Subsection A1).

The quantities $X_i^{(\nu)}$ and $Y_i^{(\nu)}$, which are presented in Eqs. (4) and (5) and in the Appendix (see Subsection A1), involve one of the nucleon spinors and isospinors in the charge-conjugate form of $\sigma_2 \chi_k^*$ and $\tau_2 \eta_k^*$. This representation does not require the use of Clebsch-Gordan coefficients and spherical functions; at the same time, expressions for $X_i^{(\nu)}$ and $Y_i^{(\nu)}$ are constructed in terms of the σ and τ matrices (in the case of nonzero orbital angular momenta, the vectors of the relative coordinates or momenta are also used in the expressions for $X_i^{(\nu)}$). From the identities $\chi_j^+ \sigma_2 \chi_k^* \equiv -\chi_k^+ \sigma_2 \chi_j^*$ and $\eta_j^+ \boldsymbol{\tau} \tau_2 \eta_k^* \equiv \eta_k^+ \boldsymbol{\tau} \tau_2 \eta_j^*$, it follows that the quantity $X_i^{(1)}$ ($Y_i^{(1)}$) is antisymmetric (symmetric) under the interchange of the spin (isospin) variables of the j th and the k th nucleon; this corresponds to $S = 0$ ($T = 1$).

In the present study, we make use of the wave function from [17]; it corresponds to the S -wave state of the nucleons ($L = l = 0$), which is characterized by a symmetric configuration dependence, its parametrization in the coordinate and in the momentum representation being given in the Appendix (see Subsection A2). There are then only two possible types of expressions for $X_i^{(\nu)}$ and $Y_i^{(\nu)}$, those in Eqs. (4) and (5). In the case of a symmetric configuration dependence, we have $\varphi^{(\nu)}(\mathbf{q}_i, \mathbf{Q}_i) \equiv \tilde{\varphi}(\mathbf{p}_1, \mathbf{p}_2, \mathbf{p}_3)$, where $\tilde{\varphi}(\mathbf{p}_1, \mathbf{p}_2, \mathbf{p}_3)$ is a symmetric function. The wave function then has the form

$$\begin{aligned} \Phi &= \tilde{\varphi}(\mathbf{p}_1, \mathbf{p}_2, \mathbf{p}_3) \sum_i X_i^{(\nu)} Y_i^{(\nu)} \\ &= \varphi^{(\nu)}(\mathbf{q}, \mathbf{Q}) \sum_i X_i^{(\nu)} Y_i^{(\nu)}, \end{aligned} \quad (6)$$

where $\varphi^{(\nu)}(\mathbf{q}, \mathbf{Q}) = \varphi^{(\nu)}(\mathbf{q}_i, \mathbf{Q}_i)$ is independent of the cyclic index i . By virtue of the equality

$$\sum_i X_i^{(\nu=1)} Y_i^{(\nu=1)} = - \sum_i X_i^{(\nu=2)} Y_i^{(\nu=2)}, \quad (7)$$

which is derived in the Appendix (see Subsection A3), the two versions of the wave function ($\nu = 1$ and $\nu = 2$) are then equivalent. In the following, we will therefore suppress the index ν .

3. SINGLE-SCATTERING AMPLITUDE

The amplitude \hat{M}_1 of single pion scattering on a ${}^3\text{H}$ (or ${}^3\text{He}$) nucleus is represented by the diagram in Fig. 1. The corresponding analytic expression is given by

$$\begin{aligned} & \langle A' | \hat{M}_1 | A \rangle \quad (8) \\ &= 3 \int \frac{d\varepsilon_2}{2\pi} \frac{d\varepsilon_3}{2\pi} \frac{d\mathbf{p}_2}{(2\pi)^3} \frac{d\mathbf{p}_3}{(2\pi)^3} \frac{\Gamma'_A \langle \hat{M}_{\pi N} \rangle_1 \Gamma_A}{D_1 D'_1 D_2 D_3}, \\ & D_i = 2m\varepsilon_i - p_i^2 + i0 \quad (i = 1, 2, 3), \\ & D'_1 = 2m\varepsilon'_1 - p_1'^2 + i0, \end{aligned}$$

where $|A\rangle$ ($|A'\rangle$) is the spin-isospin state of the initial (final) nucleus; \mathbf{p}_1 , \mathbf{p}_2 , \mathbf{p}_3 , and \mathbf{p}'_1 are the 3-momenta of intranuclear nucleons (see Fig. 1); ε_1 , ε_2 , ε_3 , and ε'_1 are the nonrelativistic energies of these nucleons; Γ_A and Γ'_A are the vertex functions for the breakup of, respectively, the initial and the final nucleus [their relation to the wave function is given by the general formula (A.13) in the Appendix]; the factor of 3 takes into account the presence of three equivalent diagrams that involve scattering on each intranuclear nucleon; and the quantity $\langle \hat{M}_{\pi N} \rangle_1$ is the amplitude of pion scattering on the first intranuclear nucleon. By calculating the integrals with respect to the energies ε_2 and ε_3 in expression (8), taking into account the relation of the vertices Γ_A and Γ'_A to the wave function, and going over to the variables $\mathbf{q} = (\mathbf{p}_2 - \mathbf{p}_3)/2$ and $\mathbf{Q} = (\mathbf{p}_2 + \mathbf{p}_3 - 2\mathbf{p}_1)/3$, we obtain

$$\begin{aligned} & \langle A' | \hat{M}_1 | A \rangle = 3 \cdot 3 \int \frac{d\mathbf{q}}{(2\pi)^3} \frac{d\mathbf{Q}}{(2\pi)^3} \quad (9) \\ & \times \Phi'^+(\mathbf{q}, \mathbf{Q}') \langle \hat{M}_{\pi N} \rangle_1 \Phi(\mathbf{q}, \mathbf{Q}), \end{aligned}$$

where Φ (Φ') is the wave function for the initial (final) nucleus and $\mathbf{Q}' = \mathbf{Q} - (2/3)\mathbf{\Delta}$, $\mathbf{\Delta}$ being the 3-momentum transfer to the nucleus. By using the same notation as in Eq. (1), we can write

$$\langle \hat{M}_{\pi N} \rangle_1 = 8\pi W'_{\pi N} f_{33} \cdot (\chi'^+_1 \hat{S} \chi_1) (\eta'^+_1 \hat{T} \eta_1), \quad (10)$$

where χ_1 and η_1 (χ'_1 and η'_1) are, respectively, the spinor and the isospinor describing the first nucleon prior to (after) the scattering event and $W'_{\pi N}$ is the effective mass of the pion-nucleon system. The quantities $\langle \hat{M}_{\pi N} \rangle_1$ and $\langle A' | \hat{M}_1 | A \rangle$ are matrices in the space spanned by the isospin of the initial and the final pion.

The quantity \hat{M}_1 is the transition matrix connecting the initial and the final state of the *pion + nucleus* system; for intermediate nucleons, it is assumed that, in expression (9), summation is performed over their spin and isospin variables, which are explicitly present

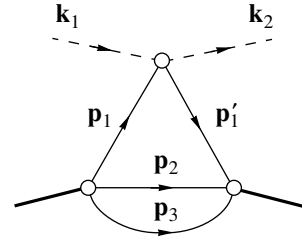


Fig. 1. Single-scattering diagram. The dashed, thin solid, and thick solid lines represent, respectively, the pions, the nucleons, and the initial and the final nucleus. The 3-momenta of the particles involved are indicated in the laboratory frame (rest frame of the initial nucleus).

in the quantities $\Phi'^+(\mathbf{q}, \mathbf{Q}')$, $\Phi(\mathbf{q}, \mathbf{Q})$, and $\langle \hat{M}_{\pi N} \rangle_1$. Further, we transform expression (9) by eliminating the spin and isospin variables of intranuclear nucleons from it. In doing this, we take into account the specific form of the wave function in (6) and go over to the conventional quantum-mechanical normalization (see Footnote 2). We then have

$$\begin{aligned} & \hat{F}_1 = \frac{\hat{M}_1}{8\pi W_{\pi A}} = \int \frac{d^3\mathbf{q}}{(2\pi)^3} \frac{d^3\mathbf{Q}}{(2\pi)^3} \quad (11) \\ & \times c_1 \varphi \left(\mathbf{q}, \mathbf{Q} - \frac{2}{3}\mathbf{\Delta} \right) \varphi(\mathbf{q}, \mathbf{Q}) f_{33} \sum_{ij} \hat{O}_{ij} \hat{\Pi}_{ij}, \\ & c_1 = \frac{3W'_{\pi N}}{W_{\pi A}}, \end{aligned}$$

where $W_{\pi A}$ is the total c.m. energy of the *pion + nucleus* system. The amplitude \hat{F}_1 (11) is a matrix in the space spanned by the spin and isospin variables of the pion and the nucleus in the initial and the final state. The structure of this matrix is determined by the expression $\sum_{ij} \hat{O}_{ij} \hat{\Pi}_{ij}$ (i and j are cyclic indices).

The quantities \hat{O}_{ij} and $\hat{\Pi}_{ij}$ are given by

$$\begin{aligned} & \chi'^+ \hat{O}_{ij} \chi = X'^+_i (\chi'^+_1 \hat{S} \chi_1) X_j, \quad (12) \\ & \eta'^+ \hat{\Pi}_{ij} \eta = Y'^+_i (\eta'^+_1 \hat{T} \eta_1) Y_j, \end{aligned}$$

where χ and η (χ' and η') are, respectively, the spinor and the isospinor describing the initial (final) nucleus. On the right-hand sides of Eqs. (12), it is implied that summation is performed over the spin (isospin) states of the nucleons involved—that is, the expression for \hat{O}_{ij} ($\hat{\Pi}_{ij}$) does not involve spinors χ'_1 , χ_1 , χ_2 , and χ_3 (isospinors η'_1 , η_1 , η_2 , and η_3). The quantities \hat{S} , \hat{T} , X_i , and Y_i were defined above [see Eqs. (1), (4)]. A prime denotes that X' (Y') involves the primed spinor χ'_1 (primed isospinor η'_1) corresponding to a nucleon after the scattering event. A feature peculiar to a calculation of \hat{O}_{ij} and $\hat{\Pi}_{ij}$ on the basis of relations (12) is that expressions for X_i and Y_i involve one

of the nucleon spinors and isospinors in the charge-conjugate form ($\sigma_2 \chi_k^*$ and $\tau_2 \eta_k^*$). In a more general case (for the triple-scattering amplitude), the expressions for \hat{O}_{ij} and $\hat{\Pi}_{ij}$ are presented in the Appendix (see Subsection A5); for the case of relations (12), the analogous expressions are given by (A.17) (see Subsection A6 in the Appendix).

If we write $\hat{S} = a + \hat{b}$, where $a = 2(\hat{\mathbf{k}}'_1 \cdot \hat{\mathbf{k}}'_2)$, $\hat{b} = (\mathbf{b} \cdot \boldsymbol{\sigma})$, and $\mathbf{b} = i[\hat{\mathbf{k}}'_1 \times \hat{\mathbf{k}}'_2]$ (a prime denotes that the corresponding variables are calculated in the c.m. frame of the pion–nucleon scattering subprocess), the operator part of the amplitude in (11) assumes the form

$$\begin{aligned} \hat{\Lambda}_1 &\equiv 3 \cdot \frac{2}{9} \sum_{ij} \hat{O}_{ij} \hat{\Pi}_{ij} & (13) \\ &= \frac{1}{3} [(6 + \mathbf{t} \cdot \boldsymbol{\tau})a + (2 - \mathbf{t} \cdot \boldsymbol{\tau})\hat{b}]. \end{aligned}$$

In expression (11), we take all factors of the pion–nucleon amplitude outside the integral sign, calculating them at a fixed nucleon momentum (at $\mathbf{p}_1 = 0$ in the simplest case). We then have

$$\hat{F}_1 = c_1 F(\boldsymbol{\Delta}) f_{33} \hat{\Lambda}_1, \quad (14)$$

where $F(\boldsymbol{\Delta})$ is the form factor given by (A.8). By taking the matrix elements of the operator $\hat{\Lambda}_1$ (13) over the spin variables for various reactions, we arrive at

$$\begin{aligned} \hat{\Lambda}_1^{\text{el}} &= \frac{1}{3}(7a + \hat{b}) \quad (\pi^{+3}\text{He}); \\ \hat{\Lambda}_1^{\text{el}} &= \frac{1}{3}(5a + 3\hat{b}) \quad (\pi^{-3}\text{He}); & (15) \\ \hat{\Lambda}_1^{\text{cex}} &= \frac{\sqrt{2}}{3}(a - \hat{b}). \end{aligned}$$

Here, the first, the second, and the third equality correspond to, respectively, elastic $\pi^{+3}\text{He}$ and $\pi^{-3}\text{H}$ scattering, elastic $\pi^{-3}\text{He}$ and $\pi^{+3}\text{H}$ scattering, and the charge-exchange reactions ${}^3\text{He}(\pi^{0,-}, \pi^{+,0}){}^3\text{H}$ and ${}^3\text{H}(\pi^{+,0}, \pi^{0,-}){}^3\text{He}$. For the purpose of the ensuing analysis, we represent the amplitude in (14) in the form

$$\hat{F}_1 = A_1 + iB_1(\boldsymbol{\sigma} \cdot [\hat{\mathbf{k}}'_1 \times \hat{\mathbf{k}}'_2]), \quad (16)$$

where the first and the second term represent, respectively, the amplitude of the processes without the flip of the nuclear spin (non-spin-flip, or NSF, amplitude) and the amplitude of the processes involving the flip of the nuclear spin (spin-flip, or SF, amplitude). The quantities A_1 and B_1 can easily be found from Eqs. (14) and (15). By way of example, we indicate that, for $\pi^{+3}\text{He}$ scattering, the results are

$$A_1 = c_1 F(\boldsymbol{\Delta}) f_{33} \cdot \frac{7}{3} a, \quad B_1 = c_1 F(\boldsymbol{\Delta}) f_{33} \cdot \frac{1}{3} \hat{b}.$$

In the unpolarized case, the differential cross section has the form

$$\begin{aligned} \frac{d\sigma}{d\Omega} &= c_1^2 F^2(\boldsymbol{\Delta}) |f_{33}|^2 \frac{1}{2} \text{tr}\{\hat{\Lambda}_1^+ \hat{\Lambda}_1\} & (17) \\ &= |A_1|^2 + |B_1|^2 (1 - z'^2). \end{aligned}$$

From expressions (15), we then obtain

$$\begin{aligned} \frac{1}{2} \text{tr}\{\hat{\Lambda}_1^+ \hat{\Lambda}_1\}^{\text{el}} &= \begin{cases} \frac{1}{9}(1 + 195z'^2) & (\pi^{+3}\text{He}), \\ \frac{1}{9}(9 + 91z'^2) & (\pi^{-3}\text{He}), \end{cases} \\ \frac{1}{2} \text{tr}\{\hat{\Lambda}_1^+ \hat{\Lambda}_1\}^{\text{cex}} &= \frac{2}{9}(1 + 3z'^2), \end{aligned}$$

where $z' = \cos \theta' = (\hat{\mathbf{k}}'_1 \cdot \hat{\mathbf{k}}'_2)$ and θ' is the scattering angle in the c.m. frame of the pion–nucleon scattering subprocess. Thus, we can see that, in the approximation of single scattering, the angular distribution for $\pi^{+3}\text{He}$ scattering differs from that for $\pi^{-3}\text{He}$ scattering (this was noticed by other authors as well—see, for example, [2]). At $z' = 0$, the angular distribution $d\sigma/d\Omega$ has a deeper minimum for $\pi^{+3}\text{He}$ scattering than for $\pi^{-3}\text{He}$ scattering. At the same time, the factor $\frac{1}{2} \text{tr}\{\hat{\Lambda}_1^+ \hat{\Lambda}_1\}^{\text{cex}}$ (for the charge-exchange reaction) has the same angular dependence as the differential cross section for P_{33} -wave pion–nucleon scattering in the Δ_{33} region.

Expressions (15) can be rewritten in the form

$$\begin{aligned} \hat{\Lambda}_1^{\text{el}} &= 2a^{\text{even}} + a^{\text{odd}} + \hat{b}^{\text{odd}}, & (18) \\ \hat{\Lambda}_1^{\text{cex}} &= a^{\text{odd}} - \hat{b}^{\text{odd}}, \end{aligned}$$

where the indices “even” and “odd” refer to the amplitudes for pion–nucleon scattering on, respectively, a pair intranuclear nucleon (a proton of ${}^3\text{He}$ and a neutron of ${}^3\text{H}$) and a nonpair one (the neutron of ${}^3\text{He}$ and the proton of ${}^3\text{H}$). Here, the isotopic factors of the P_{33} -wave pion–nucleon amplitudes (that is, 1 and $1/3$ for π^+p and π^+n scattering, $\sqrt{2}/3$ for charge-exchange processes, etc.) have already been taken into account. Thus, we have $a^{\text{even}} = a$, $\hat{b}^{\text{even}} = \hat{b}$, $a^{\text{odd}} = a/3$, and $\hat{b}^{\text{odd}} = \hat{b}/3$ for $\pi^{+3}\text{He}$ scattering; $a^{\text{even}} = a/3$, $\hat{b}^{\text{even}} = \hat{b}/3$, $a^{\text{odd}} = a$, and $\hat{b}^{\text{odd}} = \hat{b}$ for $\pi^{-3}\text{He}$ scattering; and $a^{\text{odd}} = (\sqrt{2}/3)a$ and $\hat{b}^{\text{odd}} = (\sqrt{2}/3)\hat{b}$ for charge-exchange reactions (cex). The spin-flip processes occur only on a nonpair nucleon, and this term (\hat{b}^{odd}) determines the contribution to the nuclear amplitude at $z' = 0$ (in which case $a^{\text{even}} = a^{\text{odd}} = 0$). Since the ratio of the amplitudes for the relevant reactions on nucleons is $\pi^+p/\pi^+n = 3$ in the Δ_{33} region, the ratio of the cross sections for

the reactions on the nuclei in question at the point of minimum (at $z' = 0$) is $d\sigma(\pi+^3\text{H})/d\sigma(\pi+^3\text{He}) = 9$.

Further, we disregard the distinction between the laboratory frame of the nucleus involved and the c.m. frame of the pion–nucleon scattering subprocess; that is, we set $\mathbf{k}'_{1,2} \equiv \mathbf{k}_{1,2}$, $z' \equiv z \equiv (\mathbf{k}_1 \cdot \mathbf{k}_2)$, and $k \equiv |\mathbf{k}_1| \equiv |\mathbf{k}_2|$, where k is the laboratory momentum of the initial pion (this corresponds to the static approximation). We took no account of off-mass-shell corrections to the pion–nucleon amplitude either. The aforementioned effects were considered by other authors (see, for example, [5, 7, 9, 10]) in the optical-potential approximation. We disregard these effects in the single- and the double-scattering amplitude, since their inclusion considerably complicates the calculation of the double-scattering amplitude and since the contributions of the two amplitudes are commensurate at $\theta \sim 90^\circ$ (in calculating the second-order optical potential, Wakamatsu [10] also disregarded corrections associated with the pion–nucleon c.m. frame). We will everywhere calculate the quantity $f_{33} = f_{33}(k_{\pi N})$ for the pion with the laboratory momentum k and the nucleon at rest. Concurrently, we have $k_{\pi N} = km/W_{\pi N} \approx km/(m + \omega)$ and $W_{\pi N} = m + \omega - k^2/2(m + \omega) \approx m + \omega$, where ω is the total pion momentum in the laboratory frame and m is the nucleon mass. The momentum transfer is $\Delta = 2k \sin(\theta/2) = k\sqrt{2(1 - z)}$.

4. DOUBLE-SCATTERING AMPLITUDE

The amplitude \hat{M}_2 for double pion scattering on ^3H (or ^3He) is represented by the diagram in Fig. 2. By evaluating the integrals with respect to the energies (that is, by taking the residues at the poles associated with nucleons of momenta \mathbf{p}'_1 , \mathbf{p}_2 , and \mathbf{p}_3 on the energy shell), we obtain

$$\langle A' | \hat{M}_2 | A \rangle = -\frac{3! \cdot 3}{2m} \int \frac{d\mathbf{q}}{(2\pi)^3} \frac{d\mathbf{Q}}{(2\pi)^3} \frac{d\mathbf{Q}'}{(2\pi)^3} \quad (19)$$

$$\times \Phi'^+(\mathbf{q}', \mathbf{Q}') \langle \hat{M}_{\pi N} \rangle_2 G_\pi \langle \hat{M}_{\pi N} \rangle_1 \Phi(\mathbf{q}, \mathbf{Q}),$$

where the factor of $3!$ takes into account the number of equivalent diagrams; $\langle M_{\pi N} \rangle_1$ and $\langle M_{\pi N} \rangle_2$ are the amplitudes for pion scattering on, respectively, the first and the second nucleon [see Eq. (10)]; and G_π is the propagator for the intermediate pion with a 3-momentum \mathbf{s} in the laboratory frame. We have also changed the variables of integration as $d\mathbf{p}'_1 d\mathbf{p}_2 d\mathbf{p}_3 \rightarrow d\mathbf{q} d\mathbf{Q} d\mathbf{Q}'$, where $\mathbf{q} = (\mathbf{p}_2 - \mathbf{p}_3)/2$, $\mathbf{Q} = (\mathbf{p}_2 + \mathbf{p}_3 - \mathbf{p}_1)/3$, and $\mathbf{Q}' = (\mathbf{p}'_2 + \mathbf{p}_3 - \mathbf{p}'_1)/3$. The propagator G_π as calculated without allowing for terms corresponding to the kinetic energy of the nucleons and the

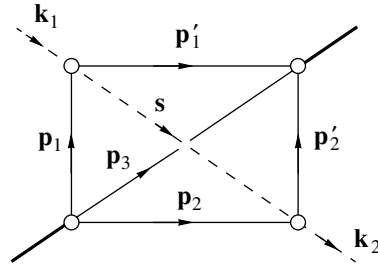


Fig. 2. Double-scattering diagram. The notation is identical to that in Fig. 1.

momenta \mathbf{q}' and \mathbf{s} are given by

$$G_\pi = \frac{1}{k_1^2 - s^2 + i0}, \quad (20)$$

$$\mathbf{q}' = \mathbf{q} - \frac{1}{2}\mathbf{Q} + \frac{1}{2}\mathbf{Q}' + \frac{1}{3}\Delta,$$

$$\mathbf{s} = \mathbf{k}_1 - \mathbf{Q} + \mathbf{Q}' - \frac{1}{3}\Delta.$$

The rest of the notation is identical to that in Eq. (9). Under a conventional normalization condition ($\hat{F}_2 = \hat{M}_2/8\pi W_{\pi A}$) with a wave function of the type in (6), the amplitude in (19) can be represented in the form

$$\hat{F}_2 = 4\pi \frac{9}{2} \int \frac{d\mathbf{q}}{(2\pi)^3} \frac{d\mathbf{Q}}{(2\pi)^3} \frac{d\mathbf{Q}'}{(2\pi)^3} \quad (21)$$

$$\times c_2 \varphi(\mathbf{q}', \mathbf{Q}') \varphi(\mathbf{q}, \mathbf{Q}) G_\pi f_{33}^2 \hat{\Lambda}_2, \quad c_2 = \frac{3W_{\pi N}^2}{mW_{\pi A}},$$

where f_{33} is the scalar amplitude for pion–nucleon scattering subprocess and

$$\hat{\Lambda}_2 = 3! \frac{2}{9} \sum_{ij} \hat{O}_{ij} \hat{\Pi}_{ij} = \hat{\Lambda}_2^{\text{el}} + \hat{\Lambda}_2^{\text{cex}} \quad (22)$$

is the relevant spin–isospin operator, which is represented as the sum of the terms $\hat{\Lambda}_2^{\text{el}}$ and $\hat{\Lambda}_2^{\text{cex}}$ describing, respectively, elastic-scattering and charge-exchange processes (it is of course the nucleus that undergoes charge exchange here). In turn, we have

$$\hat{\Lambda}_2^{\text{el}} = \hat{\Lambda}_2^{\text{ee}} + \hat{\Lambda}_2^{\text{cc}}; \quad (23)$$

that is, there are contributions in the former that come from successive elastic pion rescatterings on the intranuclear nucleons ($\hat{\Lambda}_2^{\text{ee}}$) and from double charge exchange ($\hat{\Lambda}_2^{\text{cc}}$). The operators \hat{O}_{ij} and $\hat{\Pi}_{ij}$ from Eq. (22) [their meaning is similar to that of expressions (12)] are given in the Appendix [Eqs. (A.18) and (A.19) in Subsection A7], where we use the notation

$$a_{1,2} = 2(\hat{\mathbf{k}}_{1,2} \cdot \hat{\mathbf{s}}), \quad \hat{b}_{1,2} = (\mathbf{b}_{1,2} \cdot \boldsymbol{\sigma}), \quad (24)$$

$$\mathbf{b}_1 = i[\hat{\mathbf{k}}_1 \times \hat{\mathbf{s}}], \quad \mathbf{b}_2 = i[\hat{\mathbf{s}} \times \hat{\mathbf{k}}_2],$$

with $\hat{\mathbf{s}} = \mathbf{s}/s$ being a unit vector in the direction of the momentum \mathbf{s} . The equalities in (24) correspond to the

static approximation, which was mentioned at the end of Section 3. By using the expressions for \hat{O}_{ij} and $\hat{\Pi}_{ij}$ from Subsection A7 in the Appendix and the notation in (24), we obtain

$$\hat{\Lambda}_2 = \frac{4}{9}(5 + \mathbf{t} \cdot \boldsymbol{\tau})a_1a_2 + \frac{4}{9}(a_1\hat{b}_2 + a_2\hat{b}_1) - \frac{1}{9}(6 + 3\mathbf{t} \cdot \boldsymbol{\tau})\hat{b}_1\hat{b}_2 - \frac{1}{9}(6 + 5\mathbf{t} \cdot \boldsymbol{\tau})\hat{b}_2\hat{b}_1, \quad (25)$$

$$\hat{\Lambda}_2^{\text{ee}} = \frac{2}{9}(12 + 4t_3\tau_3 - t_3^2)a_1a_2 + \frac{2}{9}(4 - t_3^2) \times (a_1\hat{b}_2 + a_2\hat{b}_1) - \frac{2}{9}(4 + 4t_3\tau_3 + t_3^2)(\mathbf{b}_1 \cdot \mathbf{b}_2)$$

[the expression for $\hat{\Lambda}^{\text{ee}}$ follows Eqs. (A.18) and (A.20) in the Appendix]. The quantity $\hat{\Lambda}_2^{\text{el}}$ is obtained from $\hat{\Lambda}_2$ by means of the substitution $\mathbf{t} \cdot \boldsymbol{\tau} \rightarrow t_3\tau_3$, and we also have $\hat{\Lambda}_2^{\text{cc}} = \hat{\Lambda}_2^{\text{el}} - \hat{\Lambda}_2^{\text{ee}}$. Taking the matrix elements of $\hat{\Lambda}_2^{\text{ee}}$, $\hat{\Lambda}_2^{\text{cc}}$, $\hat{\Lambda}_2^{\text{el}}$, and $\hat{\Lambda}_2^{\text{cex}}$ over isospin variables for the various reactions, we obtain (we make use of the uniform notation; that is, the quantities $\hat{\Lambda}^{\text{ee}}$, $\hat{\Lambda}^{\text{cc}}$, etc., nowhere below feature isospin matrices, only appearing to be matrices in the spin space of the initial and the final nucleus)

$$\begin{aligned} \hat{\Lambda}_2^{\text{ee}} &= 2 \left[(a_1^{\text{even}}a_2^{\text{even}} - (\mathbf{b}_1^{\text{even}} \cdot \mathbf{b}_2^{\text{even}})) \right. \\ &\quad \left. + a_1^{\text{even}}(a_2 + \hat{b}_2)^{\text{odd}} + a_2^{\text{even}}(a_1 + \hat{b}_1)^{\text{odd}} \right]; \\ \hat{\Lambda}_2^{\text{cc}} &= -(a_2 + \hat{b}_2)^{\text{even}}(a_1 + \hat{b}_1)^{\text{odd}} \quad (\pi^+{}^3\text{He}, \pi^-{}^3\text{H}); \\ \hat{\Lambda}_2^{\text{cc}} &= -(a_1 + \hat{b}_1)^{\text{even}}(a_2 + \hat{b}_2)^{\text{odd}} \quad (\pi^+{}^3\text{H}, \pi^-{}^3\text{He}); \\ \hat{\Lambda}_2^{\text{cc}} &= -(a_1 + \hat{b}_1)^{\text{even}}(a_2 + \hat{b}_2)^{\text{odd}} \\ &\quad - (a_2 + \hat{b}_2)^{\text{even}}(a_1 + \hat{b}_1)^{\text{odd}} \quad (\pi^0{}^3\text{H}, \pi^0{}^3\text{He}); \\ \hat{\Lambda}_2^{\text{el}} &= \hat{\Lambda}_2^{\text{ee}} + \hat{\Lambda}_2^{\text{cc}}; \\ \hat{\Lambda}_2^{\text{cex}} &= \frac{\sqrt{2}}{9}(8a_1a_2 - 3\hat{b}_1\hat{b}_2 - 5\hat{b}_2\hat{b}_1), \end{aligned} \quad (26)$$

where the quantities $a_{1,2}$ and $\hat{b}_{1,2}$ (and expressions $a + \hat{b}$) equipped with the indices “even” or “odd” already involve the isotopic factors corresponding to pion scattering on a specific (pair or nonpair) nucleon in the P_{33} wave [see the explanation in the text after Eqs. (18)], while the quantities $\hat{\Lambda}_2^{\text{cc}}$ are different for different elastic-scattering processes (indicated in parentheses) and are quoted separately.

Let us now discuss the structure of Eqs. (26). The quantity $\hat{\Lambda}_2^{\text{ee}}$ is the sum of three terms. Of these, the first corresponds to rescatterings on pair nucleons (pp for ${}^3\text{He}$ and nn for ${}^3\text{H}$) forming a spinless system. It contributes only to the amplitude for processes not involving nuclear-spin flip and contains both a term generated by processes in which the nucleon spins

are not flipped (NSF) and a term associated with the flip of the two spins (DSF). The second and the third term are due to rescatterings on a pair and a single nucleon. They involve a term stemming from the flip of a single-nucleon spin (single spin flip, or SSF) and contributing to the amplitude for nuclear-spin flip. The combinatorial factor of $3!$ —that is, the number of equivalent double-scattering diagrams—is recovered with allowance for the common factor of 2 in $\hat{\Lambda}_2^{\text{ee}}$. The expression for $\hat{\Lambda}_2^{\text{cc}}$ is responsible for the contribution of double charge exchange to the elastic-scattering nuclear amplitude and involves pion–nucleon charge exchange on a pair and on a single nucleon. Here, the spin-flip terms (\hat{b}) of both pion–nucleon amplitudes are operative. The reason why the expressions for $\hat{\Lambda}_2^{\text{cc}}$ are different for $\pi^+{}^3\text{He}$ and for $\pi^+{}^3\text{H}$ interactions can be understood from the following argument. The spin of the nucleus being considered and the spin of the relevant single nucleon (n in ${}^3\text{He}$ and p in ${}^3\text{H}$) coincide in direction. In the expression for $\hat{\Lambda}_2^{\text{cc}}$, the spin operator in the amplitude for pion–nucleon charge exchange on a single nucleon appears on the right, since it acts on the spinor of the initial nucleus. At the same time, the charge-exchange process first proceeds on a neutron ($\pi^+n \rightarrow \pi^0p$) and then on a proton ($\pi^0p \rightarrow \pi^+n$), but the status of these particles as a pair nucleon or a single one is different in ${}^3\text{H}$ and in ${}^3\text{He}$. In the expressions for $\hat{\Lambda}_2^{\text{cc}}$, there is no factor of 2 present in $\hat{\Lambda}_2^{\text{ee}}$. For the example of $\pi^+{}^3\text{H}$ scattering, this means that, because of spin asymmetry in the nn pair, π^+n charge exchange occurs only on one of the neutrons (specifically, on that whose spin has the same direction as the spin of the neutron that arises in the ensuing π^0p charge exchange). For reactions in which the nucleus undergoes charge exchange, expression (26) for $\hat{\Lambda}_2^{\text{cex}}$ can be represented in a more instructive form. Let us consider the reaction $\pi^+{}^3\text{H} \rightarrow \pi^0{}^3\text{He}$ and write down the relevant isotopic factors explicitly. We have

$$\begin{aligned} \hat{\Lambda}_2^{\text{cex}} &= \frac{\sqrt{2}}{3}(a_2 - \hat{b}_2)(a_1 + \hat{b}_1) + \frac{1}{3}(a_1 + \hat{b}_1)\frac{\sqrt{2}}{3} \\ &\quad \times (a_2 - \hat{b}_2) + \frac{\sqrt{2}}{3}(a_1 - \hat{b}_1)\frac{2}{3}(a_2 + \hat{b}_2) \\ &\quad + \frac{2}{3}(a_2 + \hat{b}_2)\frac{\sqrt{2}}{3}(a_1 - \hat{b}_1), \end{aligned}$$

where the first and the second (the third and the fourth) term are generated by, respectively, π^+ -meson rescattering (charge-exchange process $\pi^+n \rightarrow \pi^0p$) on the first nucleon and the charge-exchange process $\pi^+n \rightarrow \pi^0p$ (π^0 -meson rescattering) on the second nucleon. In the first and the third (the second and the

fourth) term, allowances are made for elastic rescattering on the single (pair) nucleon of the initial nucleus, and the relevant spin operator $a_i + \hat{b}_i$ appears as a left (right) factor. The expression for $\hat{\Lambda}_2^{\text{ex}}$ (in just the same way as the expression for $\hat{\Lambda}_1^{\text{ex}}$ in the single-scattering amplitude) involves pion–nucleon charge exchange where the sign of the spin operator is reversed—that is, $a_i - \hat{b}_i$.

In calculating the integral in the amplitude \hat{F}_2 (21), it is convenient to set

$$\hat{\Lambda}_2 = \hat{\Lambda}_{2,ij} \hat{s}_i \hat{s}_j, \quad (27)$$

where $\hat{\Lambda}_{2,ij}$ is a tensor independent of the variables of integration, and to denote

$$I_{ij} = 4\pi \frac{9}{2} \int \frac{d\mathbf{q}}{(2\pi)^3} \frac{d\mathbf{Q}}{(2\pi)^3} \frac{d\mathbf{Q}'}{(2\pi)^3} \quad (28)$$

$$\times \varphi(\mathbf{q}', \mathbf{Q}') \varphi(\mathbf{q}, \mathbf{Q}) \frac{\hat{s}_i \hat{s}_j}{k_1^2 - s^2 - i0}.$$

Taking the factors c_2 and f_{33} outside the integral sign, we obtain

$$\hat{F}_2 = c_2 f_{33}^2 \hat{\Lambda}_{2,ij} I_{ij}. \quad (29)$$

It is convenient to calculate the integral I_{ij} (28) in the coordinate representation by using the relations [18]

$$\frac{\hat{s}_i \hat{s}_j}{k^2 - s^2 - i0} = \frac{1}{4\pi} \int \exp(i\mathbf{s} \cdot \mathbf{r}) H_{ij}(\mathbf{r}) d\mathbf{r}, \quad (30)$$

$$H_{ij}(\mathbf{r}) = h_1(r) \hat{r}_i \hat{r}_j + h_2(r) \delta_{ij},$$

$$h_1(r) = \frac{e^{ikr}}{r} + \frac{3ie^{ikr}}{kr^2} - \frac{3e^{ikr}}{k^2 r^3} + \frac{3}{k^2 r^3},$$

$$h_2(r) = \frac{e^{ikr}}{k^2 r^3} - \frac{1}{k^2 r^3} - \frac{ie^{ikr}}{kr^2},$$

where $\hat{\mathbf{r}} = \mathbf{r}/r$. We then arrive at

$$I_{ij} = \frac{9}{2} \int d\rho d\mathbf{r} \psi^2(\boldsymbol{\rho}, \mathbf{R}) H_{ij}(\mathbf{r}) \quad (31)$$

$$\times \exp \left[i \left(\mathbf{k}_1 - \frac{\boldsymbol{\Delta}}{3} \right) \cdot \mathbf{r} + i \frac{\boldsymbol{\Delta} \cdot \boldsymbol{\rho}}{3} \right],$$

$$\mathbf{R} = \mathbf{r} + \frac{1}{2}\boldsymbol{\rho},$$

where $\psi(\boldsymbol{\rho}, \mathbf{R})$ is the S -wave nuclear wave function. For the function $\psi(\boldsymbol{\rho}, \mathbf{R})$ parametrized in terms of Gaussian terms [see Eqs. (A.4) in the Appendix], the integral in (31) reduces to a one-dimensional one. The result has the form

$$I_{ij} = J_1 \hat{\kappa}_i \hat{\kappa}_j + J_2 \delta_{ij}, \quad \hat{\kappa} = \boldsymbol{\kappa}/\kappa, \quad (32)$$

$$\boldsymbol{\kappa} = (\mathbf{k}_1 + \mathbf{k}_2)/2,$$

where J_1 and J_2 are functions that are dependent on the initial pion momentum k , the momentum transfer Δ , and the nuclear wave function. Explicit expressions for this function are presented in the Appendix (see Subsection A8).

In calculating the quantity $\hat{\Lambda}_{2,ij} I_{ij}$ appearing in the expression for the amplitude \hat{F}_2 (29), we represent $\hat{\Lambda}_2$ in the form of the sum

$$\hat{\Lambda}_2 \equiv \hat{\Lambda}_{2,ij} \hat{s}_i \hat{s}_j = C_0 a_1 a_2 + C_1 a_1 \hat{b}_2 \quad (33)$$

$$+ C_2 a_2 \hat{b}_1 + C_3 \hat{b}_1 \hat{b}_2 + C_4 \hat{b}_2 \hat{b}_1,$$

where the coefficients $C_{0,1,2,3,4}$ can easily be found for specific types of $\hat{\Lambda}_2$ ($\hat{\Lambda}_2^{\text{ee}}$, $\hat{\Lambda}_2^{\text{cc}}$, etc.) on the basis of (25) or (26). We then obtain

$$\hat{\Lambda}_{2,ij} I_{ij} = C_0 \hat{K}_0 + C_1 \hat{K}_1 + C_2 \hat{K}_2 \quad (34)$$

$$+ C_3 \hat{K}_3 + C_4 \hat{K}_4.$$

The calculations yield

$$\hat{K}_0 = 2(1+z)J_1 + 4zJ_2,$$

$$\hat{K}_1 = \hat{K}_2 = i(J_1 + 2J_2)(\mathbf{n} \cdot \boldsymbol{\sigma}), \quad (35)$$

$$\hat{K}_{3,4} = \frac{1}{2}(z-1)J_1 + 2zJ_2 \pm iJ_2(\mathbf{n} \cdot \boldsymbol{\sigma}),$$

$$z = (\mathbf{k}_1 \cdot \mathbf{k}_2), \quad \mathbf{n} = [\mathbf{k}_1 \times \mathbf{k}_2].$$

For the amplitude corresponding to the double-rescattering diagram, we eventually obtain

$$\hat{F}_2 = A_2 + iB_2(\mathbf{n} \cdot \boldsymbol{\sigma}), \quad (36)$$

where $A_2 = A^{\text{ee}} + A^{\text{cc}}$ and $B_2 = B^{\text{ee}} + B^{\text{cc}}$ for elastic scattering not accompanied by processes in which the nucleus undergoes charge exchange and $A_2 = A^{\text{cex}}$ and $B_2 = B^{\text{cex}}$ for the process where this charge exchange occurs. We also have

$$A^i = c_2 f_{33}^2 \left[C_0^i (2(1+z)J_1 + 4zJ_2) \right. \quad (37)$$

$$\left. + (C_3^i + C_4^i) \left(\frac{1}{2}(z-1)J_1 + 2zJ_2 \right) \right],$$

$$B^i = c_2 f_{33}^2 \left[(C_1^i + C_2^i)(J_1 + 2J_2) \right. \quad (38)$$

$$\left. + (C_3^i - C_4^i)J_2 \right] \quad (i = \text{ee, cc, cex}),$$

where $C_{0,1,2,3,4}^i$ are the coefficients in expressions of the type in (33) for $\hat{\Lambda}^i$. The results for these coefficients are

$$C_0^{\text{ee}} = 2(1+2/3) = 10/3, \quad C_{1,2}^{\text{ee}} = 2/3, \quad (38)$$

$$C_{3,4}^{\text{ee}} = -1, \quad C_{0,1,2,4}^{\text{cc}} = -2/9, \quad C_3^{\text{cc}} = 0$$

for elastic $\pi^+{}^3\text{He}$ and $\pi^-{}^3\text{H}$ scattering;

$$C_0^{\text{ee}} = 2\left(\frac{1}{3} \frac{1}{3} + \frac{2}{3}\right) = \frac{14}{9}, \quad C_{1,2}^{\text{ee}} = \frac{2}{3}, \quad (39)$$

$$C_{3,4}^{\text{ee}} = -\frac{1}{3} \frac{1}{3}, \quad C_{0,1,2,3}^{\text{cc}} = -\frac{2}{9}, \quad C_4^{\text{cc}} = 0$$

for elastic $\pi^+{}^3\text{H}$ and $\pi^-{}^3\text{He}$ scattering; and

$$C_0^{\text{cex}} = 8\sqrt{2}/9, \quad C_{1,2}^{\text{cex}} = 0, \quad (40)$$

$$C_3^{\text{cex}} = -3\sqrt{2}/9, \quad C_4^{\text{cex}} = -5\sqrt{2}/9$$

for charge-exchange reactions like $\pi^+{}^3\text{H} \rightarrow \pi^0{}^3\text{He}$.

The amplitudes for higher multiplicities (three or more) of rescatterings on intranuclear nucleons are given by more cumbersome formulas and are not considered here. That the first-order optical pion–nucleon potential is usually used in optical models (see Introduction), which provide a reasonably accurate description of the differential cross sections, is an argument in favor of this.

The differential cross section allowing for the contributions of single and double scattering (and of their interference) has the form

$$\frac{d\sigma}{d\Omega} = |A_1 + A_2|^2 + |B_1 + B_2|^2(1 - z^2), \quad (41)$$

where the quantities $A_{1,2}$ and $B_{1,2}$ were defined above. [Here, we additionally simplify the kinematical factors c_1 and c_2 presented in Eqs. (11) and (21). Since $W'_{\pi N} \approx m + \omega$ and $W'_{\pi A} \approx 3m + \omega$, we have $c_{1,2} \rightarrow 1$ for $\omega/m \rightarrow 0$. In the following, we set $c_1 = c_2 = 1$.] In our calculations, use is made of the scalar amplitude f_{33} as computed by formula (1) at the pion–nucleon phase shift δ_{33} [19] set to a value that corresponds to the initial pion kinetic energy (T_π) in the laboratory frame.

5. RESULTS OF THE CALCULATIONS AND COMPARISON WITH EXPERIMENTAL DATA

Figures 3, 4, 5, and 6 display the differential cross sections ($d\sigma/d\Omega$) for elastic $\pi^{\pm 3}\text{He}$ and $\pi^{\pm 3}\text{H}$ scattering at $T_\pi = 142, 180, 220,$ and 256 MeV. The curves in the figures represent the results of our theoretical calculations; the experimental data shown there were borrowed from [2–4, 8]. The closed (open) circles correspond to the scattering of positive (negative) pions. It should be emphasized that our calculations feature no free parameters—the results are expressed in terms of the nuclear wave function and the on-mass-shell pion–nucleon amplitudes. The dashed (dotted) curves were computed by using only the amplitude for single (double) scattering [recall that the diagrams representing these amplitudes are displayed in Fig. 1 (2)]. The results obtained with the total amplitude are shown by the solid curves. It should be indicated that the distinctions between the experimental cross sections for the mirror reactions (closed versus open circles) are much less than the distinctions between our theoretical predictions (where we disregarded the effects of charge-symmetry violation), on one hand, and the experimental data, on the other hand.

Single scattering (dashed curves). In the case of elastic $\pi^+{}^3\text{He}$ and $\pi^-{}^3\text{H}$ scattering, this contribution exhibits a sharp minimum near the point $\theta = 90^\circ$, at which the P -wave non-spin-flip amplitude

for pion–nucleon scattering vanishes. A nonzero value of $d\sigma/d\Omega$ at the point of minimum is due to the amplitude for spin-flip pion scattering on a single intranuclear nucleon. In the case of $\pi^+{}^3\text{H}$ - and $\pi^-{}^3\text{He}$ scattering, the value of $d\sigma/d\Omega$ at the point of minimum is nine times as great as that for the processes mentioned immediately above; as a result, the minimum in question is very shallow here. Owing to the nuclear form factor $F(\Delta)$, which decreases with increasing momentum transfer, the minimum in the theoretical distribution degenerates into a shoulder at $T_\pi = 180$ MeV (see Fig. 4*b*) and disappears with increasing energy (see Figs. 5*b*, 6*b*).

In addition to the minimum associated with the P -wave structure of the pion–nucleon amplitude, the angular distributions develop yet another minimum above some energy value (in Fig. 6, it occurs at $\theta \approx 130^\circ$). This minimum corresponds to a point at which the form factor $F(\Delta)$ vanishes. Formally, this “zero” arises because the wave function (A.3) is parametrized as the difference of two exponentials. The corresponding expression (A.9) leads to $F(\Delta) = 0$ at $\Delta \approx 670$ MeV—that is, at a value close to the position of the charge-form-factor minimum in more “realistic” wave functions.³⁾ With increasing (decreasing) initial energy, this minimum is obviously shifted toward the region of smaller (larger) scattering angles. At $T_\pi = 220$ MeV (see Fig. 5), it manifests itself as a sharp downfall of the dashed curve in the region of backward scattering. At lower values of T_π (see Figs. 3, 4), there is no such minimum. Obviously, the behavior of the cross sections near this, second, minimum may be poorly reproduced with the wave-function version used in the present study.

Double scattering (dotted curves). As can be seen from Figs. 3–6, the angular distribution corresponding to the double-scattering amplitude \hat{F}_2 shows but a slight shape variation with increasing energy and has a minimum whose position is slowly shifted to the right with increasing energy, remaining within the region $\theta \sim 110^\circ$ – 130° . The amplitude \hat{F}_2 is determined by the rather complicated formulas (36) and (37), and it cannot be expressed in terms of the form factor $F(\Delta)$. The distribution in question is insensitive to the position of the form-factor zero; that is, the contribution of the double-scattering diagram is less sensitive to details in the behavior of the wave function. We note that, in relation to the contribution of single scattering, the contribution to the cross section from the double-scattering amplitude

³⁾For the multicomponent wave function that was proposed in [15] and which was mentioned in Section 2, the position of the first minimum in the charge form factor is $\Delta^2 \approx 13.3 \text{ fm}^{-2}$, which corresponds to $\Delta \approx 720$ MeV.

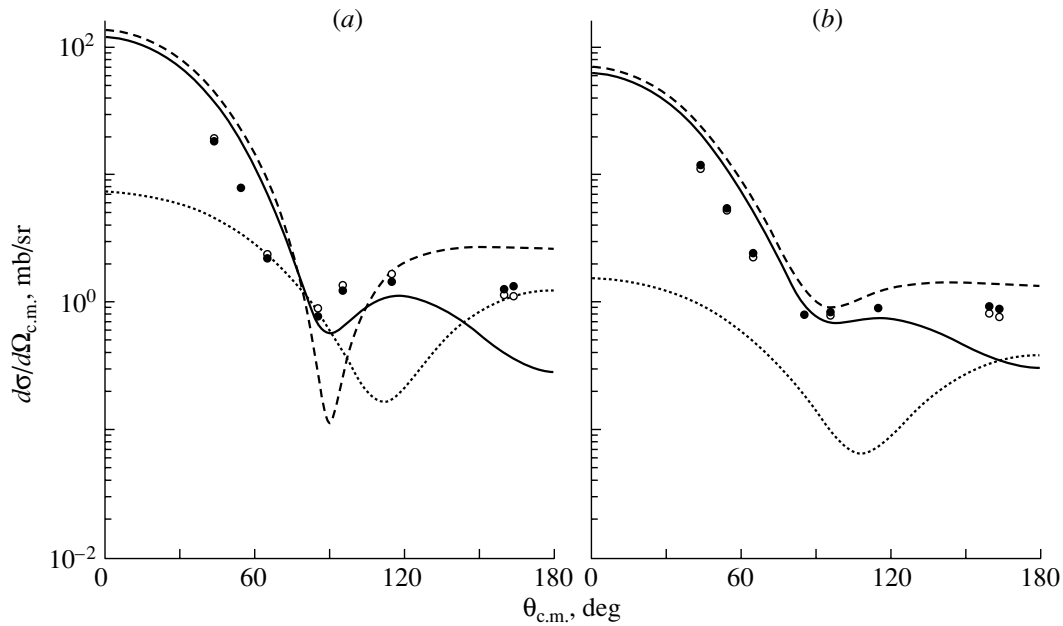


Fig. 3. Differential cross sections for elastic (a) $\pi^+{}^3\text{He}(\pi^-{}^3\text{H})$ and (b) $\pi^+{}^3\text{H}(\pi^-{}^3\text{He})$ scattering at $T_\pi = 142$ MeV. Closed (open) circles correspond to experimental values for the reactions induced by a π^+ (π^-) beam [2–4, 8]. Curves represent the results of our theoretical calculations employing (dashed curves) the single-scattering amplitude, (dotted curves) the double-scattering amplitude, and (solid curves) the total amplitude.

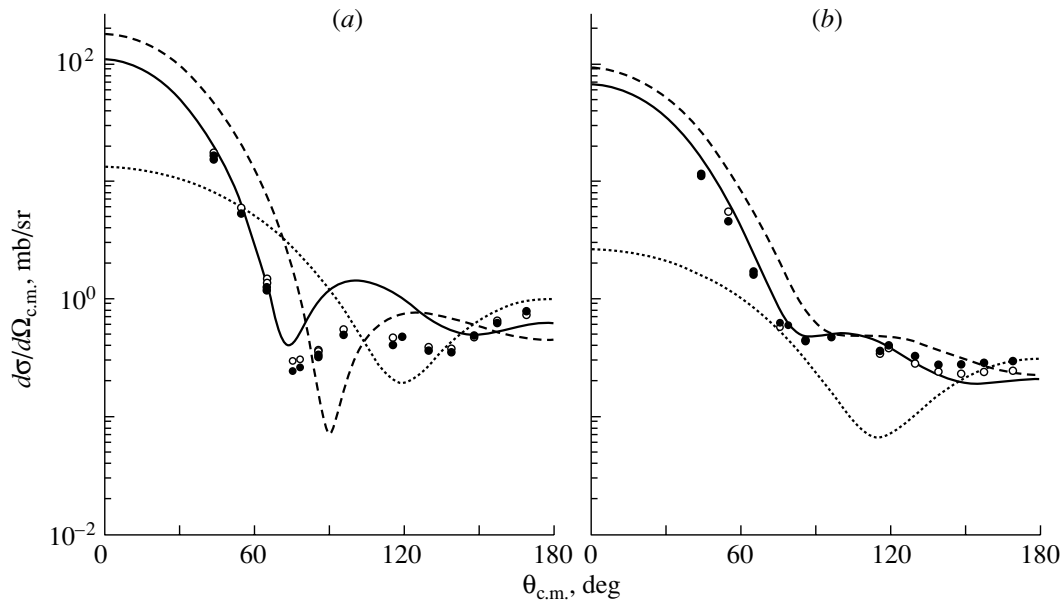


Fig. 4. Differential cross sections for elastic (a) $\pi^+{}^3\text{He}(\pi^-{}^3\text{H})$ and (b) $\pi^+{}^3\text{H}(\pi^-{}^3\text{He})$ scattering at $T_\pi = 180$ MeV. The notation is identical to that in Fig. 3.

is greater in elastic $\pi^+{}^3\text{He}$ and $\pi^-{}^3\text{H}$ scattering (see Figs. 3a, 4a, 5a, and 6a) than in elastic $\pi^+{}^3\text{H}$ and $\pi^-{}^3\text{He}$ scattering (see Figs. 3b, 4b, 5b, and 6b). This observation can easily be understood on the basis of isotopic relations.

Total contribution (solid curves). As can be

seen from Figs. 3a, 4a, 5a, and 6a ($\pi^+{}^3\text{He}$ and $\pi^-{}^3\text{H}$ scattering), the minimum in the cross section for single scattering at $\theta \approx 90^\circ$ is filled upon the inclusion of the double-scattering amplitude, becoming shallower in the total distributions. In Figs. 4a, 5a, and 6a, the positions of this minimum are shifted to

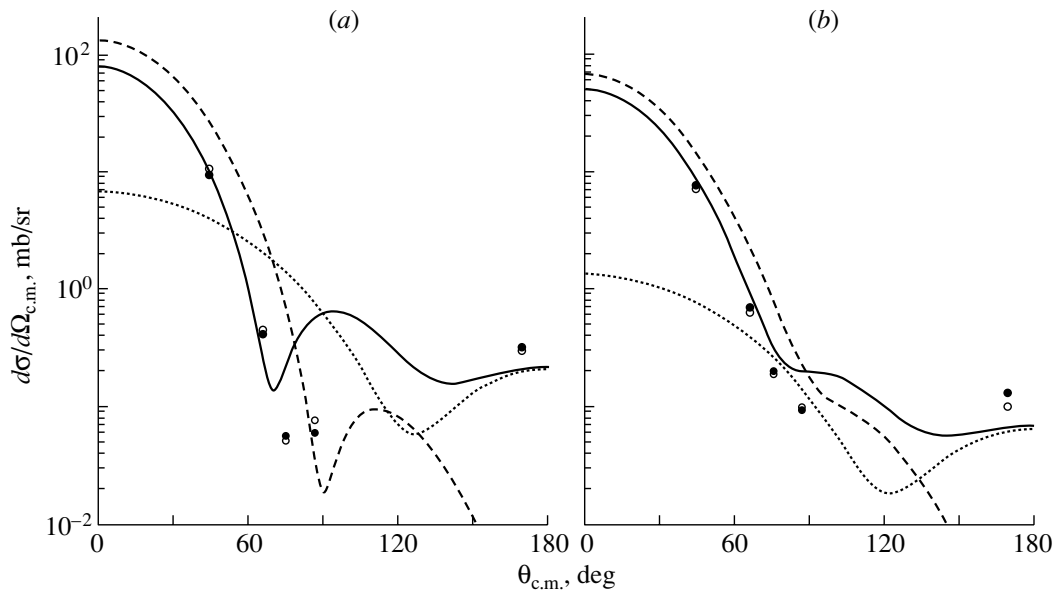


Fig. 5. Differential cross sections for elastic (a) $\pi^+{}^3\text{He}(\pi^-{}^3\text{H})$ and (b) $\pi^+{}^3\text{H}(\pi^-{}^3\text{He})$ scattering at $T_\pi = 220$ MeV. The notation is identical to that in Fig. 3.

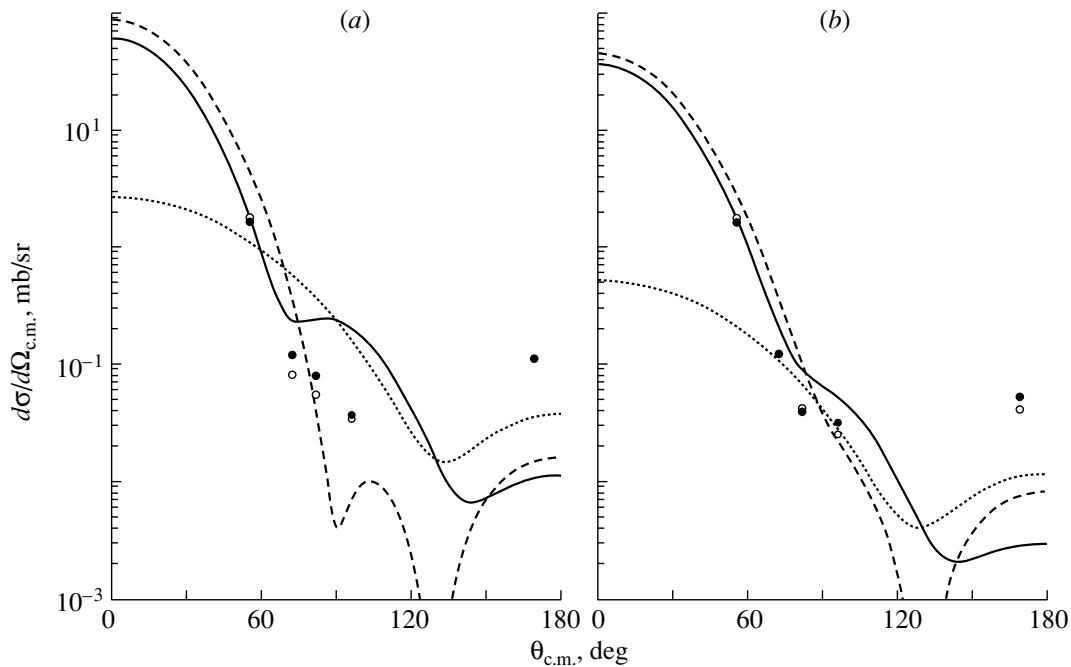


Fig. 6. Differential cross section for elastic (a) $\pi^+{}^3\text{He}(\pi^-{}^3\text{H})$ and (b) $\pi^+{}^3\text{H}(\pi^-{}^3\text{He})$ scattering at $T_\pi = 256$ MeV. The notation is identical to that in Fig. 3.

the left, toward θ values at which the contributions of the single- and the double-scattering amplitude become commensurate. Let us first consider our results for $T_\pi = 180$ MeV, an energy value closest to the position of the Δ_{33} resonance. As can be seen from Fig. 4, the curves fit the experimental cross sections fairly well everywhere, with the exception of

the region $\theta \sim 75^\circ\text{--}150^\circ$ in Fig. 4a, where the total curve lies noticeably higher than the experimental points. By and large, the theoretical distribution in Fig. 4a qualitatively reproduces the shape of the experimental distribution—in particular, it exhibits a second minimum near $\theta \sim 150^\circ$ and a rise in the region $\theta \sim 150^\circ\text{--}180^\circ$. In the case of elastic $\pi^+{}^3\text{H}$

and $\pi^{-3}\text{He}$ scattering (Fig. 4*b*), the agreement with the experimental data seems nearly perfect.

For higher energies (Figs. 5 and 6), the differential cross sections are still well described in the region $\theta < 70^\circ\text{--}80^\circ$. At larger values of θ , the curves pass above the experimental points. The paucity of data at $T_\pi = 220$ and 256 MeV (Figs. 5, 6) precludes a comparison in the interval $\theta \sim 100^\circ\text{--}170^\circ$. It should also be noted that, at these energy values, one can also observe the aforementioned effect of the form-factor zero. We expect that calculations on the basis of more “realistic” nuclear wave functions will show a higher sensitivity in this region to the inclusion of wave-function components other than the S -wave one.

At the lower energy of $T_\pi = 142$ MeV (Fig. 3), the theoretical curves lie much higher (lower) than the experimental points in the region $\theta < 90^\circ$ ($\theta > 90^\circ$). It is especially difficult to understand the reason behind the disagreement with experimental data at small scattering angles ($\theta < 90^\circ$), where the contribution of the diagram in Fig. 2 is relatively small and where the computed cross section is close to the result in the impulse approximation (proximity of solid and dashed curves). In this region, where the momentum transfer is low, the disagreement must not be due to the use of the simplified S -wave function in the calculation [17].

In an attempt at improving the description, we tried a few modifications to the single-scattering amplitude:

(i) In addition to the P_{33} wave, all the remaining partial S and P waves (that is, the S_{11} , S_{31} , P_{11} , P_{13} , and P_{31} waves) were included in the amplitude for pion–nucleon scattering with the relevant phases [19].⁴⁾ The inclusion of nonresonance waves significantly affects the behavior of the differential cross sections $d\sigma/d\Omega$ in the region of the minimum ($\theta \sim 70^\circ\text{--}90^\circ$), but the theoretical description of these distributions at $T_\pi = 142$ MeV is not improved as the result of this.

(ii) Using only the resonance P_{33} wave in the Breit–Wigner form (for the Δ_{33} mass and width, we have used the values of $M_\Delta = 1232$ MeV and $\Gamma_\Delta = 120$ MeV [20], respectively), we have taken into account the motion of the center of mass of the pion–nucleon system with respect to the nucleus and transformed accordingly the pion–nucleon scattering angle. In doing this, we have calculated all factors of the pion–nucleon amplitude using on-mass-shell nucleons and, as in (14), have taken these factors

⁴⁾We use here the notation $L_{2T,2J}$, where L , T , and J are, respectively, the orbital angular momentum, the total isospin, and the total angular momentum.

outside the integral sign in (11) at a fixed initial-nucleon momentum \mathbf{p}_1 (instead of $\mathbf{p}_1 = 0$ in the laboratory frame, we have used here the “mean” point $\mathbf{p} = -\Delta/3$, as in [5, 7]). However, these calculations yielded much poorer results.

(iii) Version (ii) was extended by considering that the resonance pion–nucleon amplitude is averaged owing to integration with respect to intranuclear-nucleon momenta. The Breit–Wigner factor $(W_{\pi N} - M_\Delta + i\Gamma_\Delta/2)^{-1}$ is retained under the integral sign in (11), while the remaining factors of the pion–nucleon amplitude (its angular dependence) are taken outside it, as in the preceding version. In relation to version (ii), the results changed only slightly, which indicates that the effect of averaging is small.

The above refinements on the single-scattering amplitude did not improve the description of experimental data. We will continue this discussion in the Conclusion. Among the contributions disregarded here, we can indicate pion absorption, which is usually taken into account phenomenologically in terms of the optical potential. It is conceivable that the cross section for small-angle scattering at $T_\pi = 142$ MeV is suppressed precisely because of this disregarded process.

NSF, SSF, DSF, and DCX contributions. The total nuclear amplitude contains various terms in which either the nucleon spins are not flipped [non-spin-flip (NSF) contribution], or the spin of one nucleon is flipped [single-spin-flip (SSF) contribution], or the spins of two nucleons are flipped [double-spin-flip (DSF) contribution]. The double-spin-flip contribution arises in the double-scattering amplitude⁵⁾ (\hat{F}_2), which involves double intrinsic charge exchange (DCX) as well. It is of interest to explore the effect of the above terms on the calculated differential cross sections. In Fig. 7, such cross sections are presented for $T_\pi = 180$ MeV. In this figure, the solid curves and circles represent, respectively, the results of the calculations with the total amplitude and experimental data (these are precisely the same values as in Fig. 4); the dashed curves correspond to eliminating the double-spin-flip contributions from the total amplitude; the dotted curves take into account only the non-spin-flip contributions; and the dash-dotted curves show the results of the calculations performed without including the contribution of double intrinsic

⁵⁾The double-spin-flip contribution is generated by $\hat{b}\hat{b}$ terms in the spin factors $\hat{\Lambda}$ [see Eq. (33)]. In the nuclear amplitude that takes into account only elastic rescatterings on nucleons, these terms do not lead to nuclear-spin flip. The inclusion of pion–nucleon charge-exchange processes in elastic-scattering reactions (DCX) and of simple charge-exchange processes (cex) results in that $\hat{b}\hat{b}$ terms begin to contribute to the nuclear-spin-flip amplitude.

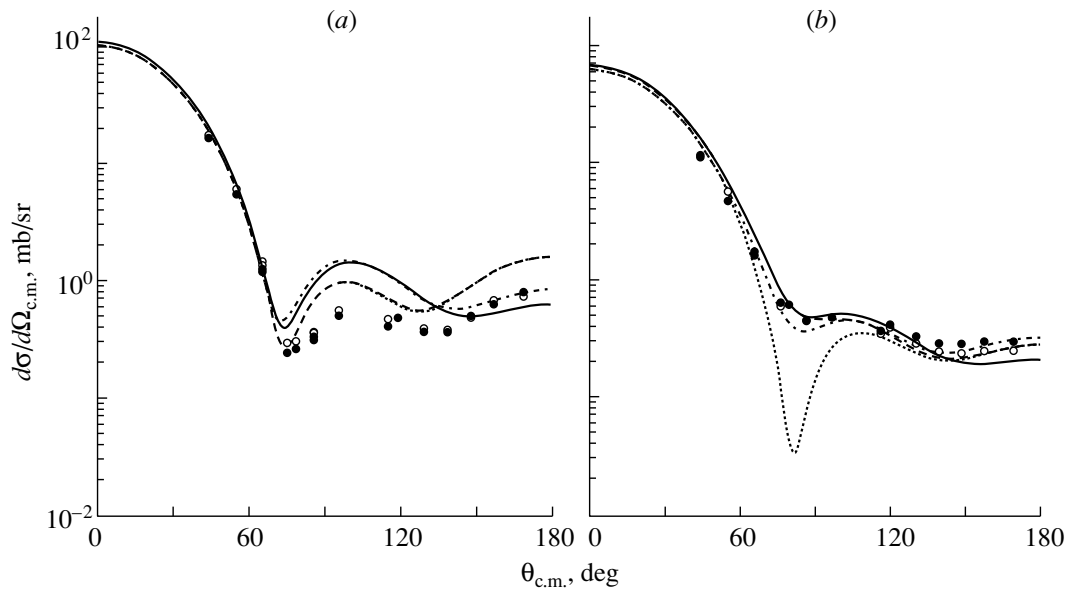


Fig. 7. Differential cross sections for elastic (a) $\pi^{+3}\text{He}(\pi^{-3}\text{H})$ and (b) $\pi^{+3}\text{H}(\pi^{-3}\text{He})$ scattering at $T_\pi = 180$ MeV. Here, experimental data [closed (open) circles for reactions induced by positive (negative) pions] and solid curves (results of the calculations with the total amplitude) are identical to those in Fig. 4. The dashed curves represent the results of the calculations in which the double-spin-flip contributions are eliminated from the total amplitude; the dotted curves correspond to taking into account only the non-spin-flip contributions; and the dash-dotted curves show the results computed without including the double-charge-exchange contribution to the total amplitude.

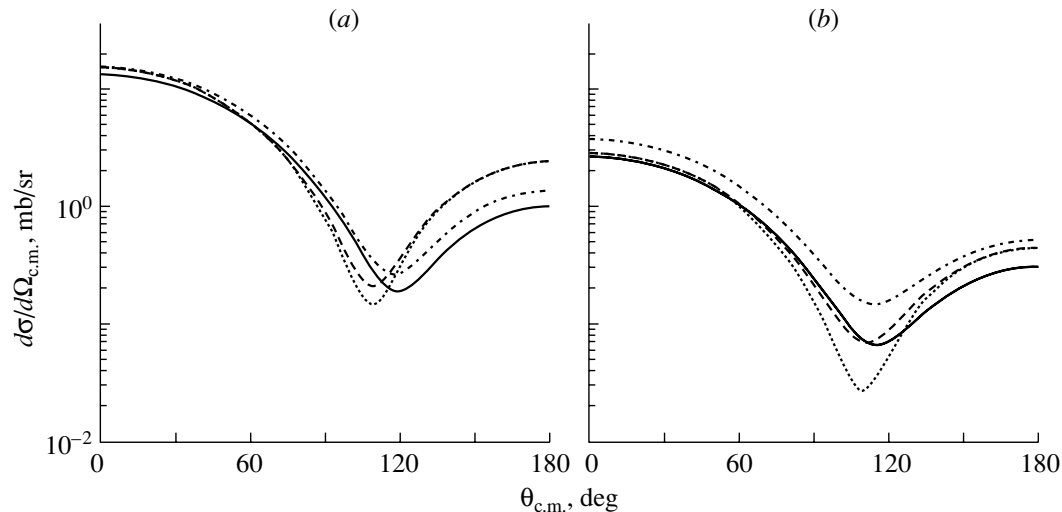


Fig. 8. Differential cross sections for elastic (a) $\pi^{+3}\text{He}(\pi^{-3}\text{H})$ and (b) $\pi^{+3}\text{H}(\pi^{-3}\text{He})$ scattering at $T_\pi = 180$ MeV according to the calculations that take into account only the double-scattering amplitude: (solid curves) results obtained with the total double-scattering amplitude, (dashed curves) results obtained without including the double-spin-flip contribution in the total amplitude, (dotted curves) results obtained by allowing only for the non-spin-flip contribution, and (dash-dotted curves) results obtained without including the contribution of double intrinsic charge exchange in the total amplitude.

charge exchange in the total amplitude. It can be seen that the minimum near the point $\theta = 90^\circ$ (it arises from the single-scattering diagram) in the distribution corresponding to the non-spin-flip contribution is less deep in Fig. 7a than in Fig. 7b. This minimum is filled by the non-spin-flip contribution

from the double-scattering diagram, the relative and the absolute value of this contribution being greater in the case of elastic $\pi^{+3}\text{He}$ and $\pi^{-3}\text{H}$ scattering.

It can be noticed that, in the region $\theta \sim 150^\circ - 180^\circ$, the dashed curves lie higher than the solid

curves; that is, the inclusion of the double-spin-flip contributions in the total amplitude reduces the differential cross sections. This is because of the destructive interference between the non-spin-flip and the double-spin-flip contribution to the double-scattering amplitude [this follows from the structure of the first term in expression (26) for $\hat{\Lambda}_2^{ee}$, provided that the addition in the double-spin-flip term from a small contribution of double intrinsic charge exchange is disregarded for the time being], which is dominant in the region being considered. Here ($\theta \sim 150^\circ\text{--}180^\circ$), one can also notice the effect of double intrinsic charge exchange. Its inclusion in the total amplitude reduces the cross sections (solid curves are below the dash-dotted ones).

Figure 8 displays the calculated differential cross sections that correspond to the double-scattering amplitude, where there arise the contributions of double spin flip and of double intrinsic charge exchange. The curves in Fig. 8 correspond to the same discrimination of the various contributions as those in Fig. 7, but the former were calculated without taking into account the contribution of the single-scattering diagram. From Figs. 7 and 8, it can be seen that the double-spin-flip contribution is relatively greater in $\pi^+{}^3\text{He}$ scattering (Figs. 7a, 8a) than in $\pi^+{}^3\text{H}$ scattering (Figs. 7b, 8b). If we disregard the process of double intrinsic charge exchange, the ratio of the double-spin-flip amplitudes for these two cases is $\pi^+{}^3\text{He}/\pi^+{}^3\text{H} = 9$ (since we have pion scattering in the P_{33} wave on the pp and on the nn system, respectively). On the contrary, the contribution of double intrinsic charge exchange is relatively enhanced in the case of $\pi^+{}^3\text{H}$ scattering. This can easily be understood if we disregard spin flip in the pion–nucleon amplitudes. The amplitudes for double intrinsic charge exchange are then equal in the two elastic processes ($\pi^+{}^3\text{He}$ and $\pi^+{}^3\text{H}$), but the total amplitude is greater in the case of $\pi^+{}^3\text{H}$ scattering.

6. CONCLUSION

We have considered the elastic scattering of charged pions on ^3H and ^3He nuclei at energies in the region of the Δ_{33} resonance. Our theoretical approach is based on calculating the single- and the double-scattering amplitude by using the nonrelativistic diagram technique with allowance for all spin and isospin effects. As inputs, we have used only the nuclear wave function and the phase shifts for pion–nucleon scattering; that is, our approximation features no free parameters. In order to simplify our analysis, we have adopted the static approximation,

taken into account only the P_{33} wave in the amplitudes for pion–nucleon scattering, disregarded off-mass-shell effects in pion–nucleon amplitudes, and used the nuclear wave function involving S -wave nucleons. Within the assumptions made here, we have obtained a qualitative description of experimental data at a few initial-energy values and a reasonable description at $T_\pi = 180$ MeV.

Comparing our approach with the popular model that was proposed in [5–7] and which employs a nuclear optical potential, we can notice the following distinctions. In the optical model, one takes into account iterations in the potential; that is, the scattering amplitude is unitarized in the intermediate *pion + nucleus* state. There is no such parametrization in our approach. At the same time, the double-scattering diagram included here features the contribution from the $\pi N N N$ intermediate state, which is absent from the aforementioned optical model. Thus, we can see that the two approaches are not equivalent.

In Section 5, we have indicated the flaws in our description of the experimental angular distributions at $T_\pi = 142$ MeV in the region $\theta < 90^\circ$. At small values of the scattering angle, the predictions of the optical model are in somewhat better agreement with experimental data (see, for example, the results obtained with the first-order optical potential and shown in Fig. 1 of [10] at $T_\pi = 135$ MeV). Usually, allowances are made in this context [5–7, 9, 10] for corrections associated with the motion of nucleons in the nucleus and with the off-mass-shell behavior of pion–nucleon amplitudes; in addition, a richer set of partial waves in pion–nucleon amplitudes are used and “realistic” multicomponent wave functions are considered [7]. Attempts at improving our results have revealed that the inclusion of the nonresonance S and P waves in the pion–nucleon amplitude (in addition to the resonance P_{33} wave) does not improve a theoretical description of experimental data and that the inclusion of nucleon motion impairs the agreement with these data. In our analysis, we disregarded off-mass-shell corrections to pion–nucleon amplitudes.

The following comment is in order here. Within the diagrammatic approach, nonadiabatic corrections associated with the motion and interaction of intranuclear nucleons and corrections for the off-mass-shell behavior of hadron–nucleon amplitudes were comprehensively studied for scattering on a deuteron (see, for example, [21]). These studies revealed that effects stemming from the inclusion of various corrections cancel to a considerable extent; therefore, the agreement between the theoretical predictions and experimental data is impaired if only part of the corrections are taken into account. We have not yet performed similar investigations for scattering on

three-nucleon nuclei (we note that it is rather difficult to take into account nucleon–nucleon interactions in three-nucleon systems). It can be conjectured that the situation here is analogous to that around the deuteron in the sense that the inclusion of part of the corrections would lead to inferior theoretical results.

From the results of our calculations, it follows that the contributions of the single- and the double-scattering amplitude to the differential cross section are commensurate at large scattering angles. Moreover, the contributions from the amplitudes for scattering of higher multiplicities may also prove to be significant. It can be hoped that the inclusion of these effects and of pion absorption would improve the description of data.

To summarize, we note that our theoretical predictions reproduce the basic features of the experimental angular distributions—in particular, around $\theta \sim 90^\circ$. It is worth noting that experimental effects of charge-symmetry violation are especially pronounced in this region of scattering angles (we mean here large scattering angles outside the Coulomb region). We hope to consider these effects in our subsequent studies.

7. ACKNOWLEDGMENTS

We are grateful to S. Kamalov and K. Dhuga for stimulating discussions.

This work was supported in part by the Russian Foundation for Basic Research (project nos. 98-02-17618 and 96-15-96578). The work of I.I. Strakovsky was supported by the US Department of Energy (grant nos. DE-FG02-99ER41110 and DE-AC05-84ER40150). W.J. Briscoe gratefully acknowledges partial support from the US Department of Energy (grant no. DE-FG02-95ER40901).

APPENDIX

A1. For various sets (ν) of $(TSLJ)l(j)$ values (see Section 2), we present here the spin–orbit ($X^{(\nu)}$) and isotopic ($Y^{(\nu)}$) parts for the components of the “realistic” wave function introduced in [15]. We denote by $\nu = 1, 2, 3, 4, 5$ the sets $(TSLJ)l(j) = (1000)0(1/2)$, $(0101)0(1/2)$, $(0121)0(1/2)$, $(0101)2(3/2)$, and $(0121)2(3/2)$, respectively. The cases of $\nu = 1$ and $\nu = 2$ were considered in Section 2 [Eqs. (4), (5)]. For the remaining components, we have $Y_i^{(3),(4),(5)} = Y_i^{(2)}$ and

$$X_i^{(3)} = \frac{1}{2\sqrt{3}}(\chi_i^+ \sigma \chi) \quad (\text{A.1})$$

$$\times \left(\chi_j^+ \left[\sigma - 3 \frac{\mathbf{Q}_i(\mathbf{Q}_i \cdot \sigma)}{Q_i^2} \right] \sigma_2 \chi_k^* \right),$$

$$X_i^{(4)} = \frac{1}{2\sqrt{3}}$$

$$\times \left(\chi_i^+ \left[\sigma - 3 \frac{\mathbf{Q}_i(\mathbf{Q}_i \cdot \sigma)}{Q_i^2} \right] \chi \right) (\chi_j^+ \sigma \sigma_2 \chi_k^*),$$

$$X_i^{(5)} = \frac{1}{2\sqrt{6}} \left(\chi_i^+ \left[\sigma - 3 \frac{\mathbf{Q}_i(\mathbf{Q}_i \cdot \sigma)}{Q_i^2} \right] \chi \right)$$

$$\times \left(\chi_j^+ \left[\sigma - 3 \frac{\mathbf{Q}_i(\mathbf{Q}_i \cdot \sigma)}{Q_i^2} \right] \sigma_2 \chi_k^* \right),$$

where \mathbf{q}_i and \mathbf{Q}_i are the relative 3-momenta. All the quantities $X_i^{(\nu)}$ and $Y_i^{(\nu)}$ are normalized by the conditions

$$(4\pi)^{-2} \int d\Omega(\mathbf{q}_i) d\Omega(\mathbf{Q}_i) \overline{X_i^{(\nu)+} X_i^{(\nu)}} = 1, \quad (\text{A.2})$$

$$\overline{Y_i^{(\nu)+} Y_i^{(\nu)}} = 1,$$

where $\int d\Omega(\mathbf{q}_i) d\Omega(\mathbf{Q}_i)$ is an integral over the directions of the 3-momenta \mathbf{q}_i and \mathbf{Q}_i and where an overbar denotes summation over the spin and the isospin states of the intranuclear nucleons.

A2. The wave function used in [17] can be parametrized as

$$\tilde{\psi}(\mathbf{r}_1, \mathbf{r}_2, \mathbf{r}_3) \quad (\text{A.3})$$

$$= N \sum_{m=1}^2 D_m \exp \left[-\frac{1}{2} \alpha_m \sum_{j=1}^3 (\mathbf{r}_j - \mathbf{R}_0)^2 \right],$$

$$D_1 = 1, \quad D_2 = -1.9,$$

$$\alpha_1 = 0.70 \text{ fm}^{-2}, \quad \alpha_2 = 2.24 \text{ fm}^{-2},$$

where N is a normalization factor and $\mathbf{R}_0 = \frac{1}{3} \sum_{j=1}^3 \mathbf{r}_j$ is the c.m. coordinate of the nucleus involved. Taking into account all spin and isospin variables, we can represent the wave function in the form

$$\Psi = \tilde{\psi}(\mathbf{r}_1, \mathbf{r}_2, \mathbf{r}_3) \sum_i X_i Y_i, \quad (\text{A.4})$$

$$\tilde{\psi} \equiv \psi(\boldsymbol{\rho}_i, \mathbf{R}_i)$$

$$= N \sum_{m=1}^2 D_m \exp \left[-\alpha_m \left(\frac{\boldsymbol{\rho}_i^2}{4} + \frac{\mathbf{R}_i^2}{3} \right) \right],$$

where the expressions for X_i and Y_i can be found in the main body of the text [see Eqs. (4)]. Here, the function $\tilde{\psi}$ (A.3) is rewritten as a function of the relative coordinates $\boldsymbol{\rho}_i = \mathbf{r}_j - \mathbf{r}_k$ and $\mathbf{R}_i = (\mathbf{r}_j + \mathbf{r}_k)/2 - \mathbf{r}_i$ and is independent of the choice of the basis $i(jk)$. From the normalization conditions

$$\int d\rho d\mathbf{R} \Psi^+ \Psi = 1, \quad (\text{A.5})$$

$$\overline{X_i^+ X_j} = \overline{Y_i^+ Y_j} = \begin{cases} 1, & i = j, \\ -1/2, & i \neq j \end{cases}$$

[here, the overbar has the same meaning as in Eq. (A.2)], we obtain

$$\int d\rho d\mathbf{R} \psi^2(\rho, \mathbf{R}) = \frac{2}{9}, \quad (\text{A.6})$$

$$N^{-2} = \frac{9}{2} (\pi\sqrt{12})^3 \sum_{mn} \frac{D_m D_n}{(\alpha_m + \alpha_n)^3}.$$

Let us derive expression (A.5) for $\overline{X_i^+ X_j}$. At $i = j$, it obviously coincides with (A.2), since we consider an S -wave state. Suppose that $i \neq j$. By using Eq. (4) for X_i , we obtain

$$\begin{aligned} \overline{X_i^+ X_j} &= \frac{1}{2} (\chi^+ \chi_i) (\chi_k^T \sigma_2 \chi_j) (\chi_j^+ \chi) (\chi_k^+ \sigma_2 \chi_i^*) \\ &= \frac{1}{2} (\chi^+ \chi_i) (\chi_i^+ \sigma_2^T \chi_k^*) (\chi_k^T \sigma_2 \chi_j) (\chi_j^+ \chi) \\ &= \frac{1}{2} (\chi^+ \sigma_2^T \sigma_2 \chi) = -\frac{1}{2}, \end{aligned}$$

where the superscript T labels the transposed matrix. Here, we have also used invariance under cyclic permutations of the indices ijk ($ijk = 123, 231$, or 312) and the identity $\chi_k^+ \sigma_2 \chi_i^* \equiv \chi_i^+ \sigma_2^T \chi_k^*$ and performed summation over the spin states of the nucleons. The case of $i = j$ can be considered in a similar way. The quantities $\overline{X_i^+ X_j}$ can also be obtained directly from the equality $\overline{X_i^+ X_j} = \chi^+ \hat{O}_{ij} \chi$, where \hat{O}_{ij} are determined by Eqs. (A.16) below at $\hat{S}_1 = \hat{S}_2 = \hat{S}_3 = \hat{1}$ ($\hat{1}$ is an identity 2×2 matrix). By using a similar procedure, one can also calculate the quantities $\overline{Y_i^+ Y_j}$.

In the momentum representation, we have

$$\begin{aligned} \Phi &= \varphi(\mathbf{q}, \mathbf{Q}) \sum_i X_i Y_i, \quad \varphi(\mathbf{q}, \mathbf{Q}) \quad (\text{A.7}) \\ &= \int d\rho d\mathbf{R} \psi(\rho, \mathbf{R}) \exp(-i\mathbf{q} \cdot \rho - i\mathbf{Q} \cdot \mathbf{R}) \\ &= N (\pi\sqrt{12})^3 \sum_m \frac{D_m}{\alpha_m^3} \exp\left(-\frac{q^2}{\alpha_m} - \frac{3Q^2}{4\alpha_m}\right), \end{aligned}$$

where $\mathbf{q} = \mathbf{q}_i = (\mathbf{p}_j - \mathbf{p}_k)/2$ and $\mathbf{Q} = \mathbf{Q}_i = (\mathbf{p}_j + \mathbf{p}_k - 2\mathbf{p}_i)/3$ are the relative momenta conjugate to the variables ρ and \mathbf{R} in the same $i(jk)$ basis (\mathbf{p}_i , \mathbf{p}_j , and \mathbf{p}_k are the 3-momenta of intranuclear nucleons). The function $\varphi(\mathbf{q}, \mathbf{Q})$ is also independent of the choice of the $i(jk)$ basis.

The elastic-scattering form factor for the wave function in (A.3) is given by

$$F(\Delta) = \frac{9}{2} \frac{d\mathbf{q}}{(2\pi)^3} \frac{d\mathbf{Q}}{(2\pi)^3} \varphi\left(\mathbf{q}, \mathbf{Q} - \frac{2}{3}\Delta\right) \varphi(\mathbf{q}, \mathbf{Q}), \quad (\text{A.8})$$

$$F(0) = 1,$$

where Δ is the 3-momentum transfer; that is,

$$\begin{aligned} F(\Delta) &= N_0^{-1} \quad (\text{A.9}) \\ &\times \sum_{mn} \frac{D_m D_n}{(\alpha_m + \alpha_n)^3} \exp\left[\frac{-\Delta^2}{3(\alpha_m + \alpha_n)}\right], \\ N_0 &= \sum_{mn} \frac{D_m D_n}{(\alpha_m + \alpha_n)^3}. \end{aligned}$$

A3. Let us derive the equality in (7). We begin by transforming expressions $X_i^{(1)}$ (4) and $X_i^{(2)}$ (5). For this, we represent the quantity $\chi\chi_j^+$ (which is a 2×2 matrix) in the general form $\chi\chi_j^+ = a + \hat{b}$, where $\hat{b} = (\mathbf{b} \cdot \boldsymbol{\sigma})$. Further, we make use of the relations $2a = \text{tr}\{\chi\chi_j^+\} = \chi_j^+ \chi$, $\boldsymbol{\sigma}(a + \hat{b})\boldsymbol{\sigma} = 3a - \hat{b}$, and $\sigma_2 \hat{b}^T = -\hat{b} \sigma_2$. We then obtain the following chain of equalities:

$$X_i^{(2)} = (\chi_i^+ \boldsymbol{\sigma} \chi) (\chi_j^+ \boldsymbol{\sigma} \sigma_2 \chi_k^*) \quad (\text{A.10})$$

$$\begin{aligned} &= \chi_i^+ \boldsymbol{\sigma} (\chi\chi_j^+) \boldsymbol{\sigma} \sigma_2 \chi_k^* = \chi_i^+ (3a - \hat{b}) \sigma_2 \chi_k^* \\ &= \chi_i^+ (4a - (a + \hat{b})) \sigma_2 \chi_k^* = 2(\chi_j^+ \chi) (\chi_i^+ \sigma_2 \chi_k^*) \\ &\quad - (\chi_i^+ \chi) (\chi_j^+ \sigma_2 \chi_k^*) = -2X_j^{(1)} - X_i^{(1)} \end{aligned}$$

and

$$\begin{aligned} X_i^{(1)} &= (\chi_i^+ \chi) (\chi_j^+ \sigma_2 \chi_k^*) = \chi_i^+ (a + \hat{b}) \sigma_2 \chi_k^* \quad (\text{A.11}) \\ &= \chi_k^+ \sigma_2^T (a + \hat{b}^T) \chi_i^* = \chi_i^+ (-a + \hat{b}) \sigma_2 \chi_k^* \\ &= \chi_i^+ (-2a + (a + \hat{b})) \sigma_2 \chi_k^* = -X_k^{(1)} - X_j^{(1)}. \end{aligned}$$

In the eventual expressions, we took here into account the equality $(\chi_i^+ \sigma_2 \chi_k^*) = -(\chi_k^+ \sigma_2 \chi_i^*)$ and invariance under the cyclic permutation of the indices ijk . By using (A.10) and (A.11), we obtain

$$X_i^{(2)} = X_k^{(1)} - X_j^{(1)}, \quad (\text{A.12})$$

$$X_i^{(1)} = \frac{1}{3} (X_j^{(2)} - X_k^{(2)}).$$

The analogous relations for the isospin components (Y) of the wave function follow from (A.12) upon the substitution $X^{(1),(2)} \rightarrow Y^{(2),(1)}$. With the aid of the resulting formulas, relation (7) can easily be verified.

A4. The vertex (Γ_A) for the breakup of the nucleus into nucleons has the form

$$\begin{aligned} \Gamma_A &= (A(2m)^{A-1})^{1/2} \left(\alpha^2 + \sum_{i=1}^A p_i^2 \right) \Phi \quad (\text{A.13}) \\ &\quad (\alpha^2 = 2m\varepsilon_A), \end{aligned}$$

where Φ is the nuclear wave function in the momentum representation, p_i are the nucleon momenta in

the c.m. frame of the nucleus, m is the nucleon mass, A is the number of nucleons in the nucleus, and ε_A is the binding energy of the nucleus. Relation (A.13) is usually obtained by equating the result obtained by calculating the form factor $F(\mathbf{\Delta})$ on the basis of the Feynman diagram to its expression in terms of the wave function (see, for example, [13]).

A5. In evaluating multiple-scattering amplitudes, it is necessary to compute the quantities \hat{O}_{ij} and $\hat{\Pi}_{ij}$ specified by the relations

$$\begin{aligned} & \chi'^+ \hat{O}_{ij} \chi & (A.14) \\ & = X_i'^+ (\chi_1'^+ \hat{S}_1 \chi_1) (\chi_2'^+ \hat{S}_2 \chi_2) (\chi_3'^+ \hat{S}_3 \chi_3) X_j, \\ & \quad \eta'^+ \hat{\Pi}_{ij} \eta \\ & = Y_i'^+ (\eta_1'^+ \hat{T}_1 \eta_1) (\eta_2'^+ \hat{T}_2 \eta_2) (\eta_3'^+ \hat{T}_3 \eta_3) Y_j, \end{aligned}$$

where summation over the spin ($\chi_{1,2,3}$ and $\chi'_{1,2,3}$) and isospin ($\eta_{1,2,3}$ and $\eta'_{1,2,3}$) nucleon states (the primed spinors and isospinors correspond to the nucleons after the scattering event and appear in expressions for X'_i and Y'_i , respectively) is implied and \hat{S}_i (\hat{T}_i) is the spin (isospin) operator in the amplitude of pion–nucleon scattering on the i th nucleon. The general expressions for X_i and $X_i'^+$ are

$$\begin{aligned} X_i &= (\chi_i'^+ \hat{U}_i^\alpha \chi) (\chi_j'^+ \hat{V}_i^\alpha \sigma_2 \chi_k^*), & (A.15) \\ X_i'^+ &= (\chi'^+ \hat{U}_i'^\alpha \chi_i) (\chi_k^T \sigma_2 \hat{V}_i'^\alpha \chi_j'), \end{aligned}$$

where \hat{U}_i^α and \hat{V}_i^α are Hermitian operators ($\hat{U}^+ = \hat{U}$, $\hat{V}^+ = \hat{V}$) whose form for specific expressions [Eqs. (4) and (5) or (A.1)] is clear; they can depend on the vectorial (α) and on the cyclic (i) index. The relevant calculations then yield

$$\begin{aligned} \hat{O}_{ii} &= \hat{U}_i'^\alpha \hat{S}_i \hat{U}_i^\beta \text{tr}\{\hat{V}_i'^\alpha \hat{S}_j \hat{V}_i^\beta \hat{S}_k^c\}, \\ \hat{O}_{ij} &= -\hat{U}_i'^\alpha \hat{S}_i (\hat{V}_j^\beta)^c \hat{S}_k^c \hat{V}_i'^\alpha \hat{S}_j \hat{U}_j^\beta, & (A.16) \\ \hat{O}_{ji} &= -\hat{U}_j'^\alpha \hat{S}_j \hat{V}_i^\beta \hat{S}_k^c (\hat{V}_j'^\alpha)^c \hat{S}_i \hat{U}_i^\beta, \end{aligned}$$

where $\text{tr}\{\dots\}$ is the trace of the matrix expression in braces. Use is also made of the operation $A^c \equiv \sigma_2 A^T \sigma_2$, where A is an arbitrary 2×2 matrix. All nine quantities \hat{O}_{ij} ($i, j = 1, 2, 3$) can be obtained from (A.16) by means of cyclic permutations of the indices ijk . By way of example, we now obtain an expression for \hat{O}_{ij} . With the aid of (A.14) and (A.15), we can derive the following chain of equalities:

$$\begin{aligned} \chi'^+ \hat{O}_{ij} \chi &= (\chi'^+ \hat{U}_i'^\alpha \chi_i) (\chi_k^T \sigma_2 \hat{V}_i'^\alpha \chi_j') \\ &\quad \times (\chi_i'^+ \hat{S}_i \chi_i) (\chi_j'^+ \hat{S}_j \chi_j) (\chi_k'^+ \hat{S}_k \chi_k) \\ &\quad \times (\chi_j'^+ \hat{U}_j^\alpha \chi) (\chi_k^+ \hat{V}_j^\alpha \sigma_2 \chi_i^*) = (\chi'^+ \hat{U}_i'^\alpha \chi_i) \\ &\quad \times (\chi_i'^+ \hat{S}_i \chi_i) (\chi_i^+ \sigma_2^T (\hat{V}_j^\alpha)^T \chi_k^*) \end{aligned}$$

$$\begin{aligned} &\times (\chi_k^T \hat{S}_k^T \chi_k^*) (\chi_k^T \sigma_2 \hat{V}_i'^\alpha \chi_j') (\chi_j'^+ \hat{S}_j \chi_j) (\chi_j^+ \hat{U}_j^\alpha \chi) \\ &= \chi'^+ \hat{U}_i'^\alpha \hat{S}_i \sigma_2^T (\hat{V}_j^\alpha)^T \hat{S}_k^T \sigma_2 \hat{V}_i'^\alpha \hat{S}_j \hat{U}_j^\alpha \chi \\ &= -\chi'^+ \hat{U}_i'^\alpha \hat{S}_i (\hat{V}_j^\alpha)^c \hat{S}_k^c \hat{V}_i'^\alpha \hat{S}_j \hat{U}_j^\alpha \chi. \end{aligned}$$

By rearranging factors, we have grouped here expressions of the types $\chi_i \chi_i^+$ and $\chi_k^* \chi_k^T$ and others that reduce to the identity matrix $\hat{1}$ upon summation over nucleon spins (in doing this, we have used identical transformations of the type $\chi_k^+ \hat{A} \chi_i = \chi_i^T \hat{A}^T \chi_k^*$, where \hat{A} is some matrix expression).

Expressions (A.16) can be used to compute the normalization factor of the wave function (at $\hat{S}_1 \equiv \hat{S}_2 \equiv \hat{S}_3 \equiv \hat{1}$) and the amplitudes for single (at $\hat{S}_2 \equiv \hat{S}_3 \equiv \hat{1}$), double (at $\hat{S}_3 \equiv \hat{1}$), and triple scattering. The expressions for the isotopic operators $\hat{\Pi}_{ij}$ are analogous to the formulas in (A.16). For example, we have

$$\begin{aligned} \hat{\Pi}_{13} &= -\hat{U}_1'^\alpha \hat{T}_1 \hat{V}_3^\beta \hat{T}_2^c (\hat{V}_1^\alpha)^c \hat{T}_3 \hat{U}_3^\beta \\ & (T^c = \tau_2 T^T \tau_2, \quad V^c = \tau_2 V^T \tau_2), \end{aligned}$$

where \hat{T}_i is the isospin operator in the amplitude for scattering on the i th nucleon and the quantities \hat{U} and \hat{V} specify here the form of the isospin parts (Y) of the nuclear wave function via expressions similar to those in (A.15). The order in which the operators \hat{T}_i appear in expressions $\hat{\Pi}_{ij}$ (and the same is true for the order of the operators \hat{S}_i in \hat{O}_{ij}) depends on the indices i and j and corresponds only to the order of arrangement of nucleon isospin matrices ($\boldsymbol{\tau}$) contained in \hat{T}_i . The pion isospin matrices (\mathbf{t}) contained in the operators \hat{T}_i are always arranged in the order inverse to the order in which the pion is scattered on intranuclear nucleons [that is, in the order of decrease of the number (i) of the nucleon on which the pion is rescattered]. By way of example, we indicate that, if $\hat{T}_i = \mathbf{t} \cdot \boldsymbol{\tau}$, then

$$\begin{aligned} \hat{T}_2 \hat{T}_1 &= t_\alpha t_\beta \tau_\alpha \tau_\beta = 2 - \mathbf{t} \cdot \boldsymbol{\tau}, \\ \hat{T}_1 \hat{T}_2 &= t_\alpha t_\beta \tau_\beta \tau_\alpha = 2 + \mathbf{t} \cdot \boldsymbol{\tau}, \end{aligned}$$

where α and β are vectorial indices.

A6. In calculating \hat{O}_{ij} and $\hat{\Pi}_{ij}$ for the case of single-scattering amplitude, we set $\hat{S}_1 = a + \hat{b}$, $\hat{S}_{2,3} = \hat{1}$, $\hat{T}_1 = (2 + \mathbf{t} \cdot \boldsymbol{\tau})/3$, and $\hat{T}_{2,3} = \hat{1}$. By using expressions (4) for X_i and Y_i and considering what was said in Subsection A5, we obtain

$$\begin{aligned} \hat{O}_{11} &= a + \hat{b}, \quad \hat{O}_{22,33} = a, & (A.17) \\ \hat{O}_{12,21,13,31} &= -(a + \hat{b})/2, \quad \hat{O}_{23,32} = -(a - \hat{b})/2, \\ \hat{\Pi}_{11} &= (6 - \mathbf{t} \cdot \boldsymbol{\tau})/9, \quad \hat{\Pi}_{22,33} = (6 + 2\mathbf{t} \cdot \boldsymbol{\tau})/9, \\ \hat{\Pi}_{12,21,13,31} &= -(6 + \mathbf{t} \cdot \boldsymbol{\tau})/18, \end{aligned}$$

$$\hat{\Pi}_{23,32} = -(6 + 5\mathbf{t} \cdot \boldsymbol{\tau})/18.$$

A7. In calculating \hat{O}_{ij} and $\hat{\Pi}_{ij}$ for double-scattering amplitude, we set $\hat{S}_{1,2} = a_{1,2} + \mathbf{b}_{1,2} \cdot \boldsymbol{\sigma}$, $\hat{S}_3 = \hat{1}$, $\hat{T}_{1,2} = (2 + \mathbf{t} \cdot \boldsymbol{\tau})/3$, and $\hat{T}_3 = \hat{1}$. By using expressions (4) for X_i and Y_i and following the procedure outlined in Subsection A5, we obtain

$$\begin{aligned} \hat{O}_{11} &= (a_1 + \hat{b}_1)a_2, \\ \hat{O}_{12} &= -\frac{1}{2}(a_1 + \hat{b}_1)(a_2 + \hat{b}_2), \\ \hat{O}_{13} &= -\frac{1}{2}(a_1 + \hat{b}_1)(a_2 - \hat{b}_2), \\ \hat{O}_{21} &= -\frac{1}{2}(a_2 + \hat{b}_2)(a_1 + \hat{b}_1), \\ \hat{O}_{22} &= (a_2 + \hat{b}_2)a_1, \\ \hat{O}_{23} &= -\frac{1}{2}(a_2 + \hat{b}_2)(a_1 - \hat{b}_1), \\ \hat{O}_{31} &= -\frac{1}{2}(a_2 - \hat{b}_2)(a_1 + \hat{b}_1), \\ \hat{O}_{32} &= -\frac{1}{2}(a_1 - \hat{b}_1)(a_2 + \hat{b}_2), \\ \hat{O}_{33} &= a_1a_2 - (\mathbf{b}_1 \cdot \mathbf{b}_2) \end{aligned} \quad (\text{A.18})$$

and

$$\begin{aligned} \hat{\Pi}_{11,22} &= \frac{2}{27}(4 + \mathbf{t} \cdot \boldsymbol{\tau}), \\ \hat{\Pi}_{33} &= \frac{2}{27}(7 + 4\mathbf{t} \cdot \boldsymbol{\tau}), \\ \hat{\Pi}_{12} &= \frac{1}{54}(-2 + \mathbf{t} \cdot \boldsymbol{\tau}), \\ \hat{\Pi}_{21} &= \frac{1}{54}(-2 + 7\mathbf{t} \cdot \boldsymbol{\tau}), \\ \hat{\Pi}_{13,32} &= \frac{-1}{54}(14 + 5\mathbf{t} \cdot \boldsymbol{\tau}), \\ \hat{\Pi}_{31,23} &= \frac{-1}{54}(14 + 11\mathbf{t} \cdot \boldsymbol{\tau}). \end{aligned} \quad (\text{A.19})$$

We can single out the contribution of elastic pion-nucleon rescatterings free from charge exchange processes. We then have $\hat{T}_{1,2} = (2 + t_3\tau_3)/3$ and, instead of (A.19), arrive at

$$\begin{aligned} \hat{\Pi}_{11,22} &= \frac{2}{27}(6 + t_3\tau_3 - t_3^2), \\ \hat{\Pi}_{33} &= \frac{2}{27}(6 + 4t_3\tau_3 + t_3^2), \\ \hat{\Pi}_{12,21} &= \frac{1}{54}(-12 + 4t_3\tau_3 + 5t_3^2), \\ \hat{\Pi}_{13,31,23,32} &= \frac{-1}{54}(12 + 8t_3\tau_3 + t_3^2). \end{aligned} \quad (\text{A.20})$$

A8. The integral I_{ij} (31) for the wave function in the form (A.4) can be factorized and reduced to the form (32), where the functions J_1 and J_2 are given by

$$\begin{aligned} J_{1,2} &= \frac{9}{2}N^2 \\ &\times \sum_{mn} D_m D_n \left(\frac{3\pi}{a_{mn}} \right)^{3/2} \exp\left(\frac{-\Delta^2}{12a_{mn}} \right) F_{1,2}(a_{mn}, \Delta), \\ a_{mn} &= \alpha_m + \alpha_n, \\ F_1(a, \theta) &= \pi \int_0^\infty r^2 \exp\left(\frac{-ar^2}{4} \right) \\ &\times (3E_2 - E_0)h_1(r)dr, \\ F_2(a, \theta) &= \pi \int_0^\infty r^2 \exp\left(\frac{-ar^2}{4} \right) \\ &\times [(E_0 - E_2)h_1(r) + 2E_0h_2(r)]dr, \\ E_n &= \int_{-1}^1 \exp(i\kappa rz)z^n dz, \quad \kappa = k \cos \frac{\theta}{2}, \\ \Delta &= 2k \sin \frac{\theta}{2}, \end{aligned} \quad (\text{A.21})$$

with the factor N having the form (A.6).

REFERENCES

1. G. A. Miller, B. M. K. Nefkens, and I. Slaus, Phys. Rep. **194**, 1 (1990).
2. B. M. K. Nefkens, W. J. Briscoe, A. D. Eichen, *et al.*, Phys. Rev. C **41**, 2770 (1990).
3. C. Pillai, D. B. Barlow, B. L. Berman, *et al.*, Phys. Rev. C **43**, 1838 (1991).
4. K. S. Dhuga, B. L. Berman, W. J. Briscoe, *et al.*, Phys. Rev. C **54**, 2823 (1996).
5. Kr. T. Kim, Y. E. Kim, and R. H. Landau, Phys. Rev. C **36**, 2155 (1987).
6. W. R. Gibbs and B. F. Gibson, Phys. Rev. C **43**, 1012 (1991).
7. S. S. Kamalov, L. Tiator, and C. Bennhold, Phys. Rev. C **47**, 941 (1993).
8. S. K. Matthews, W. J. Briscoe, C. Bennhold, *et al.*, Phys. Rev. C **51**, 2534 (1995).
9. S. L. Collier and W. R. Gibbs, nucl-th/9810046.
10. M. Wakamatsu, Nucl. Phys. A **340**, 289 (1980).
11. V. V. Baru, A. E. Kudryavtsev, V. E. Tarasov, *et al.*, nucl-th/9910011 (submitted to Phys. Rev. C.).
12. V. A. Karmanov and A. V. Smirnov, Nucl. Phys. A **575**, 520 (1994).
13. G. D. Alkhazov, V. V. Anisovich, and P. É. Volkovitskiĭ, in *Diffraction Interaction of Hadrons with Nuclei under High Energies* (Nauka, Leningrad, 1991), p. 163.
14. V. E. Tarasov, V. V. Baru, and A. E. Kudryavtsev, Yad. Fiz. **63**, 871 (2000) [Phys. At. Nucl. **63**, 801 (2000)].

15. Ch. Hajdok, A. M. Green, and M. E. Sainio, Nucl. Phys. A **337**, 13 (1980).
16. A. V. Blinov *et al.*, Nucl. Phys. A **451**, 701 (1986).
17. A. Foursat, E. Lyovshin, and K. Sailer, Nucl. Phys. A **392**, 399 (1983).
18. V. M. Kolybasov and A. E. Kudryavtsev, Yad. Fiz. **17**, 42 (1973) [Sov. J. Nucl. Phys. **17**, 22 (1973)].
19. R. A. Arndt, R. L. Workman, I. I. Strakovsky, and M. M. Pavan, nucl-th/9807087 (submitted to Phys. Rev. C); Phys. Rev. C **52**, 2120 (1995).
20. Review of Particle Physics (C. Caso *et al.*), Eur. Phys. J. C **3**, 1 (1998).
21. V. M. Kolybasov and V. G. Ksenzov, Zh. Éksp. Teor. Fiz. **71**, 13 (1976) [Sov. Phys. JETP **44**, 6 (1976)]; O. D. Dalkarov, V. M. Kolybasov, and V. G. Ksensov, Nucl. Phys. A **397**, 498 (1983); V. M. Kolybasov and L. A. Kondratyuk, Phys. Lett. B **39B**, 439 (1972).

Translated by A. Isaakyan

Elastic and Inelastic Scattering of π Mesons on ${}^7\text{Li}$ Nuclei

M. A. Zhusupov, E. T. Ibraeva*, and B. A. Prmantayeva

Institute of Experimental and Theoretical Physics, Al'Farabi Kazakh State University, ul. Timiryazeva 46, Almaty, 480121 Republic of Kazakhstan

Received December 10, 1999; in final form, July 28, 2000

Abstract—Within the diffraction theory of multiple scattering, the differential cross sections for elastic and inelastic pion scattering on a ${}^7\text{Li}$ nucleus are calculated for the case where the final nucleus is either in the ground or in the first excited state. The nuclear wave function is set to that in the αt cluster model. The sensitivity of the calculated observables to variations in the type of the wave functions for the alpha-particle and the triton cluster and for their relative motion is investigated. Various multiplicities of scattering and rescattering on the clusters constituting the ${}^7\text{Li}$ nucleus are taken into account, and their contributions to the cross section are revealed. The results of the calculations are compared with experimental data at $E_\pi = 143, 164,$ and 194 MeV. © 2001 MAIK “Nauka/Interperiodica”.

INTRODUCTION

The ${}^7\text{Li}$ nucleus possesses a nonzero spin and a sizable quadrupole deformation ($Q = -40.6$ mb); therefore, investigation of quadrupole effects in various nuclear processes involving this nuclear species is of particular interest. Sparrow [1] was among the first who studied pion scattering on a ${}^7\text{Li}$ nucleus within the shell model, focusing primarily on the quadrupole and spin effects of nuclear structure. Treating the ${}^7\text{Li}$ nucleus on the basis of the shell model with LS coupling, he considered elastic, inelastic, and charge-exchange scattering for energies in the range $E_\pi \simeq 80$ – 240 MeV. Unfortunately, there were no experimental data at that time on elastic scattering off ${}^7\text{Li}$ nuclei, so that the results of his calculations could not be subjected to experimental tests. It should be noted that the predicted cross sections proved to be very close to experimental values, at least at $E_\pi \simeq 160$ MeV (see below). A general conclusion that can be drawn from the results reported in [1] is the following: although the spin effects of the ${}^7\text{Li}$ structure are quite modest, negative-pion scattering is highly sensitive to the neutronic structure of the nucleus, especially in the region of large scattering angles ($\theta > 60^\circ$). Owing to this, the neutron distribution in the ${}^7\text{Li}$ nucleus can be probed in relevant pion-induced reactions.

Later on, the quadrupole-deformation effect was investigated in elastic and inelastic polarized-proton scattering [2], as well as in elastic and inelastic pion scattering [3]. Presently, the ${}^7\text{Li}$ nucleus has

been studied quite comprehensively—in particular, its wave functions were calculated within the shell and the cluster model (see [4, 5] and [6–8], respectively) and within the resonating-group method [9, 10]. The theoretical investigations that were devoted to the structure of the ${}^7\text{Li}$ nucleus and which were reported in [6, 8] revealed that the static and electromagnetic features of its ground and its first excited state can be faithfully reproduced on the basis of the cluster model assuming the dominance of the αt cluster configuration, which is thought to be that which is responsible for a sizable quadrupole deformation. Unkelbach and Hofmann [11] calculated the contribution of other configurations to electromagnetic form factors and showed that the αt component is dominant in the ground and the first excited state, other components contributing to higher excited states.

Experimental data on pion scattering were obtained at the meson factory of the Los Alamos National Laboratory (Los Alamos Meson Physics Facility, commonly known as LAMPF) [12] at $E_\pi = 143$ MeV and at the Paul Scherrer Institute (Villigen, Switzerland) [13] at $E_\pi = 164$ and 194 MeV. Calculations on the basis of these data were performed primarily within the optical model [3], the distorted-wave impulse approximation (DWIA) [12], and the coupled-channel method [13]. Oset and Strottman [14] calculated the features of elastic and inelastic scattering at $E_\pi = 160$ – 180 MeV on the basis of the Glauber diffraction theory of multiple scattering and showed that, in the region of the Δ_{33} resonance, this theory provides a description of scattering as adequate as that which is obtained with the aid of the generally recognized DWIA method. However, those

*e-mail: ibr@ietp.alma-ata.su

Table 1. Coefficients in the expansion of the wave function in a Gaussian basis and root-mean-square charge radius r_{ch} for the alpha-particle cluster (the names of the models are identical to those in [15])

Model	α_1, fm^{-2} C_1	α_2, fm^{-2} C_2	α_3, fm^{-2} C_3	$r_{\text{ch}}, \text{fm}^*$
D	0.4139 1.0	1.3514 3.79	2.5381 -4.694	1.664
B	0.5342 1.0	6.993 -1.0	0 0	1.646
EMQ	0.3022 1.0	0.964 12.04	1.6378 -13.04	1.673

*The experimental value is $r_{\text{ch}} = 1.673 \text{ fm}$ [16].

authors considered primarily scattering on ^{12}C , ^{16}O , and ^{24}Mg nuclei (for ^7Li , they addressed only the case of inelastic scattering), whose wave functions were taken within the shell model.

In the present study, the differential cross sections for elastic and inelastic pion scattering are calculated on the basis of diffraction theory. The polarization features of these reactions are not considered here, since they were measured with large uncertainties [13], so that the details of their behavior are not known at present. For the ^7Li wave functions, we take the results obtained within the αt cluster model by using various realistic potentials of αt interaction [6, 8]. As was shown in [11], the $n^6\text{Li}$ configuration, which is disregarded in our calculations, reduces the absolute value of the form factor C_2 only slightly. Glauber theory also makes it possible to estimate the effects induced by the collisions of a projectile with the clusters and nucleons of the target nucleus. Various multiplicities of scattering are considered, and their contributions to the relevant differential cross sections are revealed. For the wave functions of the alpha-particle and the triton cluster, we choose various models, thereby exploring the sensitivity of the calculated cross sections to these inputs. In order to highlight the distinction between cluster and oscillator wave functions, we have also calculated the differential cross sections with the oscillator ^7Li wave function [5].

DESCRIPTION OF THE FORMALISM

Within the αt cluster model, the wave function for the ^7Li nucleus can be represented in the form

$$\psi_{^7\text{Li}} = \langle LM_L SM_S | JM_j \rangle \Phi_\alpha \Phi_t \Phi_{\alpha t} \chi_{\frac{1}{2} M_S}. \quad (1)$$

The ground-state quantum numbers of the ^7Li nucleus are J^π , $T = 3/2^-$, $1/2$ and $L = 1$, while those

in its first excited state assume the values of J^π , $T = 1/2^-$, $1/2$ and $L = 1$. In Eq. (1), $\chi_{\frac{1}{2} M_S}$ is the spin function and Φ_α , Φ_t , and $\Phi_{\alpha t}$ are the wave functions that describe, respectively, the alpha-particle cluster, the triton cluster, and their relative motion and which are taken in the form of expansions in a Gaussian basis,

$$\Phi_\alpha = N_\alpha \sum_j C_j \exp(-\alpha_j R_\alpha^2), \quad (2)$$

$$\Phi_t = N_t \sum_k C_k \exp\left(-\frac{1}{2} \alpha_k \sum_{l=1}^3 (\mathbf{r}_l - \mathbf{R}_t)^2\right), \quad (3)$$

$$\Phi_{\alpha t} = \mathbf{R}^L Y_{LM}(\hat{\mathbf{R}}) N_{\alpha t} \sum_i C_i \exp(-\alpha_i R^2). \quad (4)$$

In the case being considered, the wave function for the alpha-particle cluster (in contrast to the triton-cluster wave function) depends only on the coordinates of its center of mass, since we assume the alpha particle to be a structureless object and, in the following, represent the operator of scattering on the alpha particle in accordance with this concept [see Eqs. (6), (7) below]. The alpha-particle wave functions were taken from [15], the coefficients being given in Table 1. For the the triton cluster and for the αt system, the wave functions were borrowed from [17–19] and from [6, 8], respectively, the coefficients for the former being quoted in Table 2. In Eqs. (2)–(4), \mathbf{R}_α and \mathbf{R}_t are the center-of-mass coordinates of, respectively, the alpha-particle and the triton cluster, while \mathbf{R} is their relative coordinate in the ^7Li nucleus.

The Glauber operator of multiple scattering can be represented in the form

$$\Omega = \Omega_\alpha + \Omega_t - \Omega_\alpha \Omega_t, \quad (5)$$

where Ω_α and Ω_t are the operators of scattering on, respectively, the alpha-particle and the triton cluster, while $\Omega_\alpha \Omega_t$ is the operator of multiple scattering on both clusters of the target nucleus.

It is well known that the operators Ω_i are expressed in terms of profile functions, which in turn involve elementary πN amplitudes. Our analysis of scattering on the alpha-particle cluster is performed under the assumption that it is structureless, so that the elementary $\pi\alpha$ amplitude, whose parameters are fitted to experimental data, is used instead of the elementary πN amplitude. Accordingly, we can write

$$\begin{aligned} \Omega_\alpha &= \omega_\alpha(\boldsymbol{\rho} - \boldsymbol{\rho}_\alpha) \quad (6) \\ &= \frac{1}{2\pi i k} \int d^2 \mathbf{q} \cdot \exp(-i \mathbf{q} \cdot (\boldsymbol{\rho} - \boldsymbol{\rho}_\alpha)) f_{\pi\alpha}(q). \end{aligned}$$

In [22], it was shown that, up to momentum-transfer-squared values of $q^2 \sim 0.8 \text{ (GeV}/c)^2$, the

Table 2. Coefficients in the expansion of the wave function in a Gaussian basis, binding energy E_{bind} , and root-mean-square charge radius r_{ch} for the triton cluster

Model	α_1, fm^{-2} C_1	α_2, fm^{-2} C_2	α_3, fm^{-2} C_3	$E_{\text{bind}}, \text{MeV}^*$	$r_{\text{ch}}, \text{fm}^{**}$
Model 1 [17]	0.2083 0.0173	0.6041 0.1137	1.4297 0.1300	8.471	1.691
Model 2 [19]	0.1720 1.0	0.5100 9.1100	1.3200 16.603	7.94	1.53
Model 3 [19]	0.2050 0.0206	0.6910 0.1370	4.2640 -0.0848	5.97	1.66
Model 4 [17]	0.1744 0.0236	1.3239 0.3779	0.5135 0.2090	7.937	1.686

*The experimental value of the binding energy is $E_{\text{bind}} = 8.48 \text{ MeV}$ [20]. **The experimental value of the charge radius is $r_{\text{ch}} = 1.68 \text{ fm}$ [21].

Table 3. Numerical values of α of the parameters of the $\pi\alpha$ amplitudes from [22]

E_π, GeV	$\sigma_{\pi\alpha}, \text{fm}^2$	$\varepsilon_{\pi\alpha}^c$	$\beta_{\pi\alpha}^c, \text{fm}^2$	t_1, fm^{-2}	t_2, fm^{-2}
0.15	31.98	0.148 ± 0.078	0.507	$20.86 + i0.392$	$6.116 - i1.515$
0.18	32.37	-0.028 ± 0.031	0.571	$2.569 + i0.279$	$5.841 - i1.339$
0.22	28.65	-0.019 ± 0.147	0.537	$3.405 + i0.094$	$6.856 - i0.954$

diffraction pattern of pion scattering on alpha particles at energies of about a few hundred MeV is well described by the following parametrization of the $\pi\alpha$ amplitude:

$$f_{\pi\alpha}^c(q) = \frac{k\sigma_{\pi\alpha}}{4\pi}(i + \varepsilon_{\pi\alpha}^c) \quad (7)$$

$$\times \left(1 - \frac{q^2}{t_1}\right) \left(1 - \frac{q^2}{t_2}\right) \exp(-\beta_{\pi\alpha}^c q^2/2).$$

The values used for the parameters of the $\pi\alpha$ amplitude are quoted in Table 3.

Scattering on the triton cluster will be considered as a process occurring on the three nucleons constituting this cluster. With allowance for all multiplicities of scattering, the Glauber operator Ω_t can be represented in the form

$$\Omega_t = \omega_1 + \omega_2 + \omega_3 - \omega_1\omega_2 - \omega_1\omega_3 - \omega_2\omega_3 + \omega_1\omega_2\omega_3. \quad (8)$$

The quantities ω_i can be written in a form similar to that in (6) with substitution of the πN amplitude for the $\pi\alpha$ amplitude, the former being represented in the standard form

$$f_{\pi N}^c = \frac{k\sigma_{\pi N}}{4\pi}(i + \varepsilon_{\pi N}^c) \exp(-\beta_{\pi N}^c q^2/2), \quad (9)$$

where the subscript $N = 1, 2$ labels quantities referring to p and n . The parameters of the πN amplitudes are set to values quoted in Table 4.

In the present calculation, we disregard charge-exchange effects, which are comparatively small, because charge-exchange processes contribute to the elastic-scattering channel only for collisions whose multiplicity is not lower than two—the maximum contribution to the cross section at small angles comes from single scattering.

Within multiple-scattering theory, the amplitude for hadron scattering on a ${}^7\text{Li}$ nucleus has the form

$$M_{if}(\mathbf{q}) = \frac{ik}{2\pi} \int d^2\rho \prod_{\nu=1}^4 d\mathbf{r}_\nu \exp(i\mathbf{q} \cdot \boldsymbol{\rho}) \quad (10)$$

$$\times \delta(\mathbf{R}_7) \langle \psi_{7\text{Li}} | \Omega | \psi_{7\text{Li}} \rangle,$$

where \mathbf{r}_ν are the single-particle coordinates of the nucleons and of the alpha-particle cluster in the target nucleus; $\boldsymbol{\rho}$ is the impact parameter; \mathbf{k} and \mathbf{k}' are the c.m. momenta of, respectively, the incident and the outgoing pion; $\mathbf{q} = \mathbf{k} - \mathbf{k}'$ is the momentum transfer; and \mathbf{R}_7 is the c.m. coordinate of the ${}^7\text{Li}$ nucleus. In the case of elastic scattering, we have $k = k'$ and $|\mathbf{q}| = 2k \sin(\theta/2)$, where θ is the scattering angle.

The differential cross section for scattering can easily be expressed in terms of the amplitude in (10) as

$$\frac{d\sigma}{d\Omega} = \frac{1}{2J+1} |M_{if}(\mathbf{q})|^2. \quad (11)$$

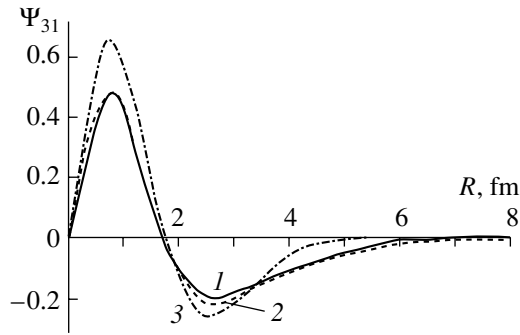


Fig. 1. Radial wave functions describing the relative motion of the alpha-particle and the triton cluster in the ${}^7\text{Li}$ nucleus within various models: (1, 2) results within the cluster model and (3) results within the oscillator model.

The procedure for calculating the Glauber amplitudes with the cluster wave function for the ${}^7\text{Li}$ nucleus is described in [25].

DISCUSSION OF THE RESULTS

We have calculated the differential cross sections for pion scattering on a ${}^7\text{Li}$ nucleus at a few incident-pion-energy values ($E_\pi = 143$ [12], 164 [13], and 194 [13] MeV) for which there are experimental data.

Figure 1 displays the radial wave functions that describe the relative motion of the alpha-particle and triton cluster in the ${}^7\text{Li}$ nucleus and which were calculated within the cluster (curves 1 and 2) and the oscillator (curve 3) model. In order to go over from the shell model to the cluster model, the radial function $\Psi_{31}(R)$ in the oscillator wave function $\Psi_{NLM}(\mathbf{R}) = \Psi_{31}(R)Y_{1M}(\mathbf{R})$ for relative motion is replaced by the cluster wave function $\Psi_{L=1}^{J=3/2}(R)$, which appears to be a solution to the Schrödinger equation for a deep optical potential involving forbidden states and allowing for spin-orbit splitting. Curves 1 and 2 were computed on the basis of potentials in a Woods-Saxon [6] and a Gaussian [8] form, respectively. Curve 3 represents the oscillator wave function $\Psi_{31}(R)$, this notation corresponding to the value of $N = 3$ for the principal quantum number and the value of $L = 1$ for the orbital angular momentum of relative motion. For

Table 4. Numerical values of the parameters of the πN amplitudes from [23, 24]

E_π , GeV		$\sigma_{\pi N}$, fm ²	$\varepsilon_{\pi N}^c$	$\beta_{\pi N}^c$, fm ²
0.15	πN	10.93	0.522	1.25
0.18	$\pi^- p$	6.0	0.18	0.570
	$\pi^- n$	17.6	-0.03	0.586
0.2	πN	11.90	-0.17	0.873

such potentials, the cluster wave function for the αt system in a bound state has a node at $R \approx 1.7$ fm, which coincides with the node of the oscillator wave function. Concurrently, a correct exponential asymptotic behavior is reproduced within the cluster model up to distances around $R = 12$ fm.

Figure 2 shows the differential cross sections in question for various ${}^7\text{Li}$ wave functions at three pion-energy values: $E_\pi = (a)$ 143, (b) 164, and (c) 194 MeV. Although all kinds of wave functions make it possible to reproduce faithfully the behavior of the cross sections, the curves calculated with the cluster wave functions (curves 1 and 2) are closer, by and large, to the experimental points than the curve calculated with the oscillator wave function (3). The distinctions between the results at small scattering angles, which correspond to low momentum transfers (at $E_\pi = 164$ MeV, $q = 0.089$ GeV/c for $\theta = 20^\circ$), are due to the fact that the different wave functions behave differently at large distances from the center of the nucleus (in the asymptotic region); at the same time, large scattering angles, which correspond to high transverse momenta (at $\theta = 80^\circ$, $q = 0.33$ GeV/c), determine the behavior of the wave function in the interior of the nucleus. We note that diffractive-scattering theory is inapplicable at large scattering angles, so that the agreement between the theoretical and experimental results for $\theta > 60^\circ$ is accidental rather than indicative of the validity of our approach.

From Fig. 1, it can be seen that the cluster wave functions differ from the oscillator wave function both in the interior of the nucleus and in the asymptotic region, but that the node occurs at the same point in all the cases being considered. The cluster wave functions are close to each other, and so are the corresponding cross sections (curves 1 and 2 in Figs. 2a and 2b). In Fig. 2b, curve 4 represents the results of Sparrow's calculation [1] with the shell-model wave function for the ${}^7\text{Li}$ nucleus. This calculation of 1977 was performed long before the emergence of experimental data [12, 13], but it provides a qualitatively correct description of the behavior of the cross section and reproduces its absolute value. This predictive power is undoubtedly an achievement of the theory.

Although only two points at $\theta = 50^\circ$ and 65° were measured in [13] at $E_\pi = 194$ MeV, we have also calculated the differential cross section at this incident-pion-energy value (see Fig. 2c). In general, our curves are compatible with these data; however, the paucity of the data precludes a true comparison of the theory with them. In particular, it is not clear whether the diffraction minimum that is seen in the computed curve will manifest itself sharply in the experimental cross section around $\theta \sim 50^\circ$, or whether it will be smoothed, as it is at lower energies ($E_\pi = 143$ and

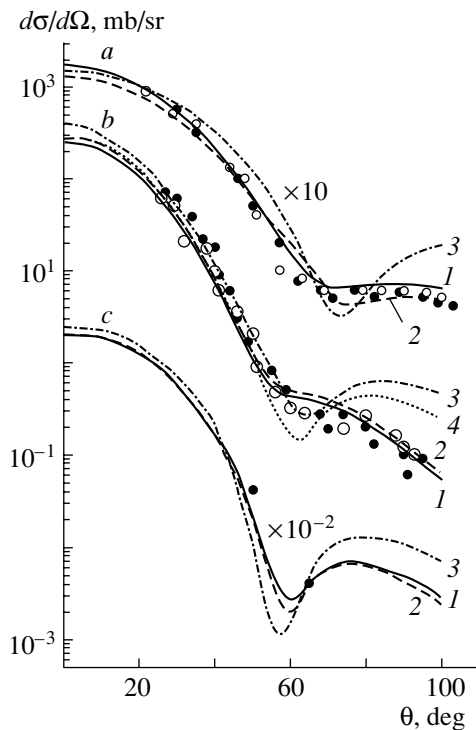


Fig. 2. Differential cross sections for various ${}^7\text{Li}$ wave functions at the incident-pion energies of $E_\pi =$ (a) 143, (b) 164, and (c) 194 MeV (in Figs. 2a and 2c, all theoretical and experimental values are multiplied by 10 and 10^{-2} , respectively, the scale being sometimes changed in this figure and in those that follow in order to avoid an overlap of data at different energy values): (1, 2) theoretical results obtained with the cluster wave functions for deep attractive potentials in, respectively, a Woods–Saxon [6] and a Gaussian [8] form; (3) theoretical results obtained with the oscillator wave function; and (4) results of the calculations from [1] with the shell-model wave function. Experimental data for the scattering of (open circles) negative and (closed circles) positive pions were borrowed from (a) [12] and (b, c) [13].

164 MeV). As was shown for proton scattering on a ${}^7\text{Li}$ nucleus [26], the diffraction minima in the differential cross sections are more pronounced at higher energies and are shifted toward the region of smaller scattering angles with increasing energy.

For inelastic pion scattering that leads to the excitation of the first excited level of the ${}^7\text{Li}$ nucleus ($J^\pi = 1/2^-, E^* = 0.48$ MeV), Fig. 3 shows the differential cross sections calculated at the incident-pion energies of $E_\pi =$ (a) 164 and (b) 143 MeV. These calculations were performed with the cluster wave function in the Woods–Saxon potential (solid curves) and with the oscillator wave function (dashed curves). It can be seen that the distinctions between the results obtained with the different wave functions are still greater here than for the ground state. It should be noted that, in this state, the weight of the component $\Psi_{31}(R)$ in the wave function for the ${}^7\text{Li}$

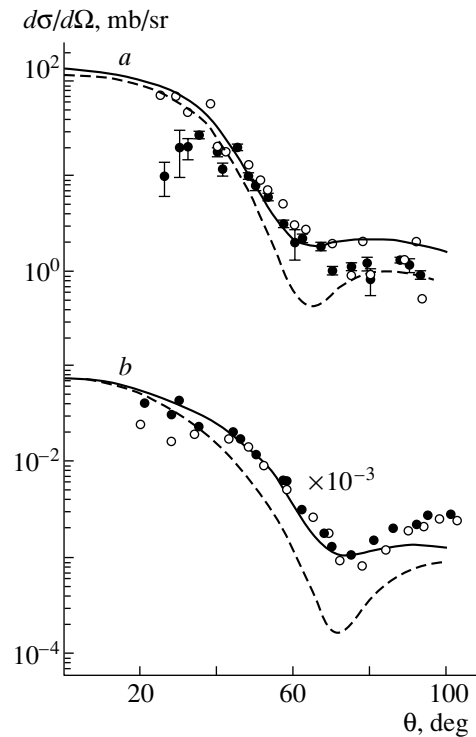


Fig. 3. Differential cross section for pion scattering on a ${}^7\text{Li}$ nucleus at the incident-pion energies of $E_\pi =$ (a) 164 and (b) 143 MeV: (solid curve) results of the calculations with the cluster wave function of the ${}^7\text{Li}$ nucleus and (dashed curve) results of the calculations with the oscillator wave function of the ${}^7\text{Li}$ nucleus. Experimental data on the scattering of (open circles) negative and (closed circles) positive pions were borrowed from (a) [13] and (b) [12].

nucleus is 98%—that is, the radial component of this wave function is identical to that in the ground state (the difference lies exclusively in the spin–orbit component); since these functions are not orthogonal, the differential cross section shows no minimum at $\theta = 0^\circ$ that would have been observed if the functions had been orthogonal.

For various models of the alpha-particle-cluster wave function, Fig. 4 shows the differential cross section in question at the incident-pion energies of $E_\pi =$ (a) 164 and (b) 143 MeV. The solid, dashed, and dotted curves represent the results obtained on the basis of the wave-function models EMQ, D, and B (see Table 1). The parameters of the ${}^4\text{He}$ wave function were borrowed from the article of Dakhno and Nikolaev [15], who studied the contribution of a 12-quark bag to the structure of a nucleus in diffractive proton and pion scattering on it at energies as high as a few hundred GeV. All wave functions computed in [15] faithfully reproduce the root-mean-square charge radius and, up to specific momentum-transfer values [$q \sim 0.4$ (GeV/c) 2] for the wave functions in model

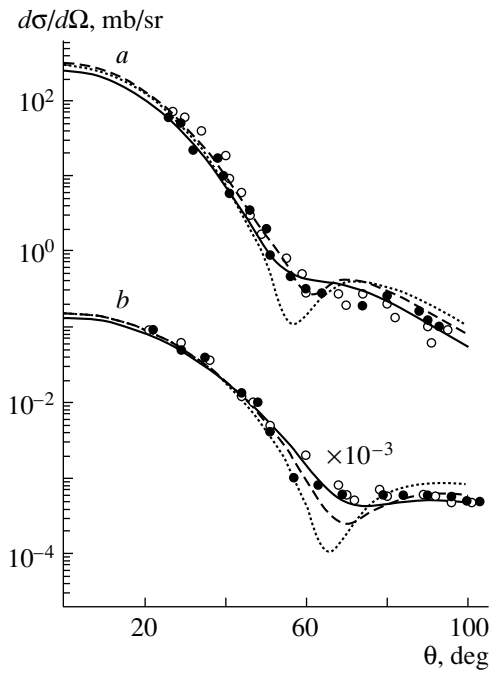


Fig. 4. Differential cross sections for various alpha-particle-cluster wave functions at the incident-pion energies of $E_\pi = (a)$ 164 and (b) 143 MeV. The solid, dashed, and dotted curves correspond to the wave functions in the EMQ, D, and B models.

B and $q^2 \sim 0.8$ (GeV/c)² for the wave functions in model D], charge form factors. Moreover, the wave function in model D takes into account short-range correlations, and its density in the central region of the nucleus decreases, assuming the shape of the bottle bottom. In [15], the wave function in model EMQ, where the contribution of the 12-quark bag is included, reproduces best of all charge form factors and elastic scattering (this is especially well seen at large scattering angles). At the energy values considered here, this is not very important; it can be seen from Fig. 4 that all wave functions describe the cross sections similarly, but they behave differently in the region of the minimum. The wave functions in model EMQ provide the best description of the cross section, its minimum being nearly unnoticeable—there is only an inflection point on the curve, in just the same way as in the experimental cross section. A similar result was obtained in [26] in calculating the differential cross section for proton scattering on a ⁷Li nucleus.

A different situation is observed for the differential cross section computed at $E_\pi =$ (Fig. 5a) 164 and (Fig. 5b) 143 MeV with various triton-cluster wave functions. The triton-cluster wave functions in models 1 and 4 from [17] and in model 2 from [18] (the values of their parameters are quoted in

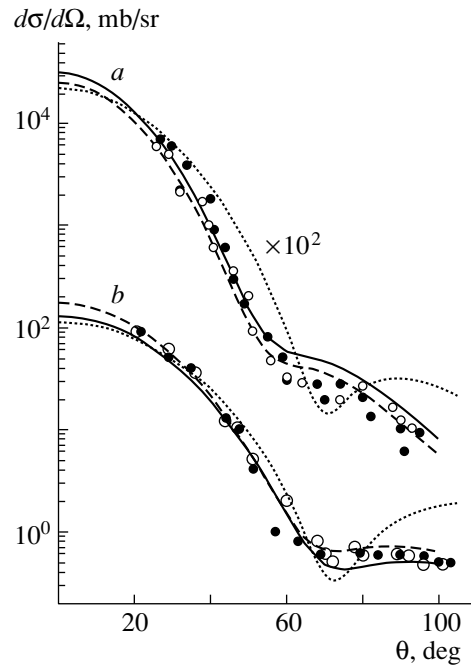


Fig. 5. Differential cross sections for pion scattering on a ⁷Li nucleus at the incident-pion energies of $E_\pi = (a)$ 164 and (b) 143 MeV for various models of the triton-cluster wave function. The solid, dashed, and dotted curves represent the results obtained on the basis of the wave-function models 1, 2, and 3.

Table 2) were calculated for attractive potentials that describe well electromagnetic form factors for elastic scattering and NN phase shifts at high energies. The wave function for model 3 from [19] (see Table 2) was calculated for a potential that involves a core and which also describes electromagnetic form factors, but which yields underestimated results for the radius and for the quadrupole moment. In Fig. 5, the solid, dashed, and dotted curves represent results obtained on the basis of the wave-function models 1, 2, and 3, respectively. The results of the calculations with the wave function in model 4 are not presented in this figure, since they are very close to those in model 1. All curves describe almost identically the cross section at small scattering angles, whence we conclude that all the wave functions being considered behave similarly at large distances. But at large scattering angles, the dotted curve, which was obtained with the wave function in model 3 on the basis of a nucleon–nucleon potential involving a core, begins to deviate strongly from the other curves. From Table 2, we can see that, within this model, the triton binding energy is approximately 2.5 MeV below the experimental value. As has already been mentioned in discussing the results displayed in Fig. 4, the difference in the behavior of the wave functions at small distances is manifested in the distinctions between the cal-

culated observables at large scattering angles, and vice versa—the difference in the behavior of the wave functions at large distances from the center of the nucleus is manifested in the distinctions between the observables at small scattering angles. From Fig. 5, we can see that the use of the wave-function model 3 leads to inadequate results for the central region of the triton cluster. It follows that the sensitivity of the differential cross section to the choice of cluster wave functions is sufficiently high, so that this can serve as a test for the relevant wave functions. For the cross sections being discussed, similar calculations were performed in [3], with the cluster radii being set to different values, and it was concluded that the effect in question does indeed occur, becoming more pronounced at high momentum transfers. These conclusions are compatible with our present results.

Let us now consider the contributions to the differential cross section in question that come from various multiplicities of scattering on the nucleons and clusters constituting the ${}^7\text{Li}$ nucleus and which can naturally be taken into account precisely within the diffraction theory, where the scattering operator is represented in the form of a multiple-scattering series [see Eqs. (5) and (8)]. The results of the calculations are illustrated in Fig. 6, which shows separately the contributions to the differential cross sections from various scattering multiplicities. These contributions are specified by Eq. (5): in Fig. 6, curves 1, 2, 3, and 4 represent, respectively, the contribution of the first term in (5) (scattering on the alpha-particle cluster), the contribution of the second term (scattering on the triton cluster), the contribution of the third term (rescattering on the two clusters), and the total contribution of all terms to the differential cross section:

$$\frac{d\sigma}{d\Omega} = \frac{1}{2J+1} |M_1(\Omega_\alpha) + M_2(\Omega_t) - M_3(\Omega_\alpha\Omega_t)|^2.$$

From Fig. 6, it can be seen that, in the region of small scattering angles, the main contribution to the differential cross section comes from scattering on the alpha-particle and the triton cluster, whereas the contribution from rescattering is nearly two orders of magnitude less at $\theta = 0^\circ$; however, the contribution of rescattering approaches, in absolute value, the first two at $\theta \approx 40^\circ$ and becomes dominant at large scattering angles. For the first time, this behavior of the amplitudes of various multiplicities was indicated by Glauber himself in [27] for proton–deuteron scattering; later on, it was confirmed in [28], where it was shown that, with increasing scattering multiplicity, the absolute values of the amplitudes decrease, but that, concurrently, the rate of their decrease becomes lower, so that higher multiplicities prove to be dominant over lower ones at high momentum transfers. The regions where the contributions of these multiplicities become commensurate are the regions of

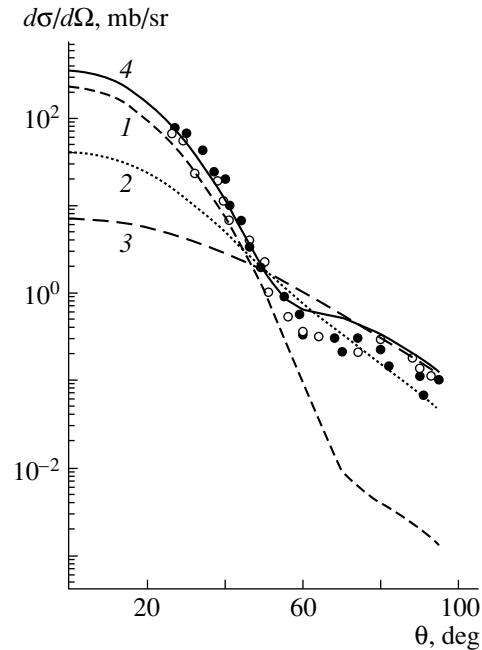


Fig. 6. Contributions to the differential cross sections from various scattering multiplicities at $E_\pi = 164$ MeV. Curves 1, 2, 3, and 4 represent the contributions from, respectively, scattering on the alpha-particle cluster, scattering on the triton cluster, rescattering on the two clusters, and the sum of all contributions.

interference minima, and this can clearly be seen in Fig. 6. Here, however, the minimum is smoothed since the cross section is the sum of three terms, each amplitude being a complex-valued quantity, with the result that the addition of the real and imaginary parts may lead to either constructive or destructive interference. In the case of the ${}^7\text{Li}$ nucleus, there is yet another reason for the smoothing of the minimum, a large quadrupole deformation in this nuclear species. Within the model used here for the wave function, we cannot isolate the quadrupole component and consider scattering on it, as was done, for example, in [2, 3], where it was shown that, while providing, by and large, a correct description of the behavior of the cross section in the regions around $\theta \approx 55^\circ$ and 95° , the monopole-scattering contribution has deep minima, which are filled by the quadrupole-scattering contribution. In our calculation based on the cluster model, it is the dominant αt configuration that corresponds to a large contribution of quadrupole scattering.

As can be seen from the theoretical results displayed in Fig. 6, the differential cross section cannot be described satisfactorily, in the majority of the cases, by taking into account only single (and even double) scattering. In order to obtain a correct description of the cross section over a sufficiently wide range of angles (and momentum transfers), it is necessary to

take into account all multiplicities of scattering on a nucleon cluster (triton in the present case) or to select a realistic πx amplitude for a structureless cluster (alpha particle in the present case).

REFERENCES

1. D. A. Sparrow, Nucl. Phys. A **276**, 365 (1977).
2. C. W. Glover, C. C. Foster, P. Schwandt, *et al.*, Phys. Rev. C **43**, 1664 (1991).
3. Naoko Nose, Kenji Kume, and Shinichiro Yamaguchi, Phys. Rev. C **50**, 321 (1994).
4. S. Cohen and D. Kurath, Nucl. Phys. **73**, 217 (1965); T.-S. Lee and D. Kurath, Phys. Rev. C **21**, 293 (1980).
5. A. N. Boyarkina, *Structure of 1p-Shell Nuclei* (Mosk. Gos. Univ., Moscow, 1973).
6. S. B. Dubovichenko and M. A. Zhusupov, Izv. Akad. Nauk Kaz. SSR, Ser. Fiz.-Mat., No. 4, 44 (1984).
7. B. Buck, R. A. Baldock, and A. Rubio, J. Phys. G **11**, 11 (1985); B. Buck and A. C. Merchant, J. Phys. G **14**, 211 (1988).
8. S. B. Dubovichenko and A. V. Dzhazairov-Kakhramanov, Yad. Fiz. **57**, 784 (1994) [Phys. At. Nucl. **57**, 733 (1994)].
9. H. Kanada, Q. K. K. Liu, and Y. C. Tang, Phys. Rev. C **22**, 813 (1980).
10. H. Walliser and T. Fliessbach, Phys. Rev. C **31**, 2242 (1985); H. Walliser, Q. K. K. Liu, H. Kanada, and Y. C. Tang, Phys. Rev. C **28**, 57 (1983).
11. M. Unkelbach and H. M. Hofmann, Phys. Lett. B **261**, 211 (1991).
12. E. F. Gibson, J. J. Kraushaar, T. G. Masterson, *et al.*, Nucl. Phys. A **377**, 389 (1982).
13. R. Meier, E. T. Boschitz, B. Brinkmoller, *et al.*, Phys. Rev. C **49**, 320 (1994); J. A. Zichy, PhD Thesis 6612 (ETH, Zurich, 1980).
14. E. Oset and D. Strottman, Nucl. Phys. A **377**, 297 (1982).
15. L. G. Dakhno and N. N. Nikolaev, Nucl. Phys. A **436**, 653 (1985).
16. E. Borie and G. A. Rinker, Phys. Rev. A **18**, 324 (1978).
17. S. B. Dubovichenko and M. A. Zhusupov, Izv. Akad. Nauk Kaz. SSR, Ser. Fiz.-Mat., No. 4, 64 (1987).
18. M. Le Mere and R. E. Brown, Phys. Rev. C **12**, 1140 (1975).
19. P. Shen *et al.*, Phys. Rev. C **33**, 1214 (1986).
20. H. Coelho *et al.*, Phys. Rev. C **28**, 1812 (1983).
21. D. Beck *et al.*, Phys. Rev. C **30**, 1403 (1984).
22. F. Binon, P. Duteil, and M. Gouanere, Nucl. Phys. A **298**, 499 (1978).
23. I. M. A. T. Eldin, E. H. Esmael, M. Y. M. Hassan, and M. N. H. Comsan, J. Phys. G **17**, 271 (1991); **16**, 1051 (1990).
24. H. Lesniak and L. Lesniak, Nucl. Phys. B **38**, 221 (1972).
25. M. A. Zhusupov, E. T. Ibraeva, and B. A. Prmantaeva, Available from KazGosINTI No. 8482-KA-98 (1998).
26. M. A. Zhusupov and E. T. Ibraeva, in *Proceedings of the 2nd International Conference "Nuclear and Radiation Physics," Almaty, 1999*, Vol. 1, p. 82; M. A. Zhusupov, E. T. Ibraeva, and B. A. Prmantaeva, in *Proceedings of the Third International Conference "Modern Problems of Nuclear Physics," Bukhara, 1999*, p. 67.
27. R. Glauber, Usp. Fiz. Nauk **103**, 641 (1971).
28. V. S. Barashenkov and V. D. Toneev, Usp. Fiz. Nauk **100**, 425 (1970) [Sov. Phys. Usp. **13**, 182 (1971)]; G. D. Alkhazov, V. V. Anisovich, and P. É. Volkovitskiĭ, *Diffraction Interactions of Hadrons with Nuclei under High Energies* (Nauka, Leningrad, 1991).

Translated by A. Isaakyan

Classical-like Description of Quantum States and Propagator for Particles in Time-Independent and Dispersing δ Potentials

V. I. Man'ko¹⁾ and A. S. Chikhachev²⁾

Received July 13, 2000

Abstract—Probability distributions that determine completely the bound state in the problem of a quantum particle in one or two delta-function wells are derived within the recently developed tomographic representation of quantum states, where a state is characterized by a positive probability distribution. The quantum propagator for the Schrödinger equation is obtained for the problem of two dispersing delta-function wells.
© 2001 MAIK “Nauka/Interperiodica”.

1. INTRODUCTION

Since the infancy of quantum mechanics and since the introduction of the wave function satisfying the Schrödinger equation [1], attempts have been made to develop a classical-like picture of quantum regularities. For example, Madelung [2], who isolated the phase and the amplitude of the wave function, showed that the set of equations for these two real-valued quantities is formally the set of equations of classical fluid dynamics. De Broglie associated the wave function with the pilot wave [3]. Bohm [4] introduced the concept of hidden variables. Moyal [5] showed that the evolution equation for the density matrix introduced by Landau [6] in the energy representation and by von Neumann [7] in a general formulation can be written in a form very similar to the form of a stochastic equation in classical kinetic theory. However, this equation was obtained for a function that is not a positive probability distribution, but this is necessary for a truly classical form of description of the dynamics of a fluctuating system. On the basis of the same idea—that of reducing a quantum description to a classical one, at least in form—Moyal used the function coincident with the functions introduced by Wigner in [8]. Functions like that of Wigner, which depend on points in phase space and which are not simultaneous distributions of the coordinate and momentum because of the uncertainty relation [9] are referred to as quasidistributions. The Glauber–Sudarshan function [10, 11] and the Husimi function [12], which belong to the s -parametric family of quasidistribution functions [13], were introduced for the same purpose. Attempts undertaken in [2–4, 10–12] did not result in

the desired classical description of quantum states in terms of probability distributions. Vogel and Risken [14], who studied the possibility of introducing a positive distribution function for a quantum system—a general procedure for constructing such a distribution on the basis of the known density matrix was given in [11]—showed that, for a specific choice of observable (so-called homodine observable or a point rotated in phase space through a given angle), it is possible to invert, with the aid of the Radon transformation, the formula for the distribution of the probabilities of this variable and to obtain thereby a Wigner function expressed only in terms of this distribution. This approach was used in introducing the optical-tomography method for measuring a quantum state [15]. In [16–18], the optical-tomography scheme was extended to the symplectic-tomography scheme, where the Fourier transformation is used instead of the Radon transformation. A distribution function was introduced that depends both on the variable coordinate and on two additional parameters; of these, one describes, in just the same way as in the optical-tomography scheme, a rotation in phase space, while the other describes the variations in scale there. Implicitly, the earlier analyses reported in [13–17] admitted the possibility for proposing new tomographic methods for classically interpreting a quantum state in terms of distribution functions. Explicitly, this was done in [19, 20]—in order to describe a quantum state, it was proposed there to employ, instead of a complex density matrix or a wave function, the classical probability distribution, which completely determines the density matrix itself. Analogs of the time-dependent [19, 20] and time-independent [21] Schrödinger equation were formulated in terms of the classical probability distribution. The evolution equation appeared to be similar to the Fokker–Planck

¹⁾Lebedev Institute of Physics, Russian Academy of Sciences, Leninskii pr. 53, Moscow, 117924 Russia.

²⁾Khrunichev State Research and Production Space Association, Moscow, Russia.

equation, but, for a general potential, the former involves higher derivatives up to an infinite order.

So far, the new formulation of quantum mechanics (it can be referred to as a classical formulation) has been invoked to consider the simplest problem characterized by a quadratic Hamiltonian. These include free motion, a harmonic oscillator, a damped oscillator [22], and a parametric oscillator [23]. In [24, 25], some nonstationary systems specified by a Hamiltonian that is quadratic in the coordinate and momentum operators were investigated within this new formulation of quantum mechanics. Probability distributions were used in [26–28] to formulate spin states and in [29] to describe rotor states. The general properties of the new description of quantum states in terms of probability distributions were discussed in [30]. At the same time, problems involving more complicated (nonquadratic) potentials—for example, delta-function potentials—are of great interest. Exact solutions to the Schrödinger equation for the time-dependent dispersing delta-function wells were obtained in [31–33].

The objective of the present study is to derive, in the problem of delta-function wells, exact expressions for distribution functions specifying quantum states. We consider both the case of a discrete energy spectrum and the case of scattering states. We also address the problem of constructing the propagator for the problem of dispersing delta-function wells.

The ensuing exposition is organized as follows. In Section 2, we present a general survey of the classical approach and of the relation between the Wigner function and the positive probability distribution specifying a quantum state. In Section 3, we consider the distribution function for the bound state of a particle in a delta-function well. In Section 4, we solve the problem for dispersing delta-function wells and discuss the propagator for the Schrödinger equation in this case.

2. WIGNER FUNCTION AND MARGINAL DISTRIBUTION

The Wigner function, which is determined by the equality (we use the system of units where the Planck constant \hbar is set to unity)

$$W(p, q, t) = \int_{-\infty}^{\infty} e^{ipu} du \psi^*(q+u/2, t) \psi(q-u/2, t), \tag{1}$$

where $\psi(q, t)$ is the particle wave function, possesses the properties of a phase density. In particular, the probability density in configuration space is

$$\rho(q, t) = (1/2\pi) \int_{-\infty}^{\infty} W(p, q, t) dp, \tag{2}$$

where $\rho(q, t) \geq 0$.

However, the Wigner function $W(p, q, t)$ cannot be interpreted as a probability density in phase space because the condition $W(p, q, t) \geq 0$ is not valid at all values of the momentum p and the coordinate q .

If a marginal distribution is further introduced via the equality

$$w(X, \mu, \nu, t) = \int e^{-ik(X-q\mu-p\nu)} W(p, q, t) dk dq dp / (2\pi)^2, \tag{3}$$

we can demonstrate that $w(X, \mu, \nu, t) = \int e^{-ikX} \chi(k) dk$, where $\chi(k) = \langle e^{ik\hat{X}} \rangle$, and that $w(X, \mu, \nu, t) \geq 0$; that is, the marginal distribution can be treated as a probability density:

$$w(X, \mu, \nu, t) = \langle X | \hat{S}^+ \hat{\rho} \hat{S} | X \rangle = \text{tr} \hat{S}^+ \hat{\rho} \hat{S} | X \rangle \langle X |,$$

where $\hat{S}^+ \hat{q} \hat{S} = \mu \hat{q} + \nu \hat{p} = \hat{X}$ and $\hat{\rho}$ is the density matrix. The marginal probability distribution, referred to as a tomographic distribution function [30], fully characterizes a quantum state because of invertibility of the integral transformation (3).

3. WIGNER FUNCTION AND MARGINAL DISTRIBUTION FOR DELTA-FUNCTION POTENTIALS

If $V(x) = \kappa \delta(x)$ ($m = \hbar = 1$), there exists the bound state

$$\psi_0(x, t) = \sqrt{\kappa} e^{-\kappa|x| + i\kappa^2 t/2}. \tag{4}$$

The Wigner function $W(p, q) \equiv W(p, q, t)$ describing this state has the form

$$W(p, q) = \kappa \int_{-\infty}^{\infty} \exp(-\kappa|q+u/2| - \kappa|q-u/2| - ipu) du = 2\kappa e^{-2\kappa|q|} \left\{ \frac{\sin 2p|q|}{p} - \frac{p \sin 2p|q|}{p^2 + \kappa^2} + \frac{\kappa \cos 2p|q|}{p^2 + \kappa^2} \right\}. \tag{5}$$

For a time-independent marginal distribution, we can obtain

$$w(X, \mu, \nu) = (1/2\pi) \int \delta(X - \mu q - \nu p) \times W(p, q) dp dq = \frac{\kappa}{\pi} \left\{ \Phi(X, \mu, \nu, \kappa) + \Phi^*(X, \mu, \nu, \kappa) \Phi(-X, \mu, \nu, \kappa) + \Phi^*(-X, \mu, \nu, \kappa) \right\}, \tag{6}$$

where

$$\Phi(X, \mu, \nu, \kappa)$$

$$= \int_0^\infty dq \exp\left[-2\kappa q + \frac{2iq}{\nu}(X - \mu\nu)\right] \quad (7)$$

$$\times \left\{ \frac{1}{i(X - \mu q)} + \frac{1}{\kappa\nu - i(X - \mu q)} \right\}.$$

For $w(X, \mu, \nu)$, we can additionally find from (1) and (3) that

$$w(X, \mu, \nu) = \frac{1}{2\pi|\nu|} \int_{-\infty}^\infty dy \psi(y) \exp\left(\frac{i\mu y^2}{2\nu} - \frac{iXy}{\nu}\right)$$

$$\times \int_{-\infty}^\infty \psi^*(y_1) dy_1 \exp\left(-\frac{i\mu y_1^2}{2\nu} + \frac{iXy_1}{\nu}\right). \quad (8)$$

If $\psi(y) = \sqrt{\kappa} e^{-\kappa|y|}$, then $w = \frac{\kappa}{2\pi|\nu|} |\Psi|^2$, where

$$\Psi = \sqrt{\frac{\pi\nu i}{2\mu}} \left\{ \exp\left[\frac{i}{2\nu\mu}(X - i\kappa y)^2\right] \operatorname{erfc}\left[\frac{X - i\kappa\nu}{\sqrt{2\mu\nu i}}\right] \right.$$

$$\left. + \exp\left[-\frac{i}{2\mu\nu}(X + i\kappa y)^2\right] \operatorname{erfc}\left[-\frac{X + i\kappa\nu}{\sqrt{2\mu\nu i}}\right] \right\},$$

$$\operatorname{erfc}\zeta = \frac{2}{\sqrt{\pi}} \int_\zeta^\infty e^{-y^2} dy.$$

It should be noted that the following normalization conditions are valid:

$$\int W(p, q) dp dq / (2\pi) = 1, \quad \int_{-\infty}^\infty dX w(X, \mu, \nu) = 1.$$

Further, we assume that there are two delta-function centers: $V = \kappa(\delta(x - a) + \delta(x + a))$. There then exist a symmetric and an antisymmetric solution to the Schrödinger equation, which correspond to bound states:

$$\psi(x) = C_1 e^{-\beta|x-a|} + C_2 e^{\beta|x+a|}. \quad (9)$$

At $C_1 = C_2$, we have $\kappa = \beta/(1 + e^{-2\beta a})$, and this (symmetric) solution always exists; at the same time, the antisymmetric ($C_1 = -C_2$) solution is characterized by the relation $\kappa = \beta/(1 - e^{-2\beta a})$ and exists if $\kappa > 1/(2a)$. We denote by C_+ and C_- the normalization constants for the symmetric and the antisymmetric state, respectively. These constants can be found from the condition $\int |\psi(x)|^2 dx = 1$, where $\psi(x)$ is determined by expression (9). For the symmetric solution, we can then find for the Wigner function W_+ that

$$W_+(p, q) = 2C_+^2 \left\{ e^{-2\kappa|q-a|} F(p, q-a) \right. \quad (10)$$

$$\left. + 2e^{-2|q|} F(p, q) \cos 2pa + e^{-2\kappa|q+a|} F(p, q+a) \right\},$$

where

$$F(p, q) = \frac{\sin 2p|q|}{p} - \frac{p \sin 2p|q|}{p^2 + \kappa^2} + \frac{\kappa \cos 2p|q|}{p^2 + \kappa^2}. \quad (11)$$

For the antisymmetric state, the Wigner function W_- can be found analogously. The marginal distributions for the symmetric and the antisymmetric state are also easily calculable. The results are

$$w_\pm(X, \mu, \nu)$$

$$= \frac{C_\pm}{\pi|\nu|} \int_0^\infty dq e^{-2\kappa q} \left\{ F\left(q, \frac{\mu q - (X + \mu a)}{\nu}\right) \right.$$

$$+ F\left(q, \frac{\mu q + X + \mu a}{\nu}\right) \pm 2 \cos\left(2a \frac{\mu q - X}{\nu}\right)$$

$$\times F\left(q, \frac{\mu q - X}{\nu}\right) \pm 2 \cos\left(2a \frac{\mu q + X}{\nu}\right)$$

$$\times F\left(q, \frac{\mu q + X}{\nu}\right) + F\left(q, \frac{\mu q - (X - \mu a)}{\nu}\right)$$

$$\left. + F\left(q, \frac{\mu q + X - \mu a}{\nu}\right) \right\},$$

where w_\pm are the functions for the symmetric and the antisymmetric state, respectively.

Let us now consider the problem of dispersing delta-function centers, where the potential has the form $V(x, t) = \kappa(\delta(x - vt) + \delta(x + vt))$. In contrast to the cases considered above, the bound-state wave function here explicitly depends on time, with the result that the Wigner function also proves to be time-dependent. For the even bound state, the wave function obtained by summing expressions quoted in [31] assumes the form

$$\psi(x, t) = \sqrt{i/2\pi t} e^{iv^2 t/2} \int_L ds e^{-is^2/2t + is\kappa}$$

$$\times \left\{ e^{-\kappa|z_-| + ivx} \exp\left[-\frac{\kappa}{2iv}(1 - e^{-2v(s+iz_-)})\right] \right. \quad (12)$$

$$\left. + e^{-\kappa z_+ - ivx} \exp\left[-\frac{\kappa}{2iv}(1 - e^{-2v(s+iz_+)})\right] \right\},$$

where $z_\pm = |x \pm vt|$ and where the contour L goes from $s = i\infty$ to $s = 0$ and further from zero to $s = \infty$. Substituting this relation into (1), we arrive at an expression for the Wigner function in the form of a threefold integral. This expression explicitly depends on time and cannot be simplified.

It is also of interest to derive the wave functions for states corresponding to the continuous spectrum of a delta-function center. It was shown in [34] that

$$\psi_s = \frac{1}{\sqrt{2\pi}} \left\{ e^{isx} + \frac{i\kappa}{|s| - i\kappa} e^{i|s||x|} \right\} e^{is^2 t/2},$$

where s is a momentum. The density matrix can be represented in the form

$$\begin{aligned} \rho(x, x') = & \frac{1}{2\pi} \left\{ e^{is(x-x')} \right. \\ & + \frac{i\kappa}{s^2 + \kappa^2} \left[(|s| + i\kappa) e^{i|s||x|-isx'} \right. \\ & \left. \left. - (|s| - i\kappa) e^{-i|s||x'|+isx} \right] + \frac{\kappa^2}{s^2 + \kappa^2} e^{i|s|(|x|-|x'|)} \right\}. \end{aligned} \quad (13)$$

The Wigner function corresponding to (13) can be represented as the sum of four terms (we omit here the argument of the Wigner function),

$$W = W_1 + W_2 + W_3 + W_4.$$

These terms are given by

$$W_1 = \frac{1}{2\pi} \int_{-\infty}^{+\infty} e^{-ipu+isu} du = \delta(s - p);$$

$$\begin{aligned} W_2 = & \frac{i\kappa(|s| + i\kappa)}{2\pi(s^2 + \kappa^2)} \left[e^{-2iqs\sigma(s)} \int_{-\infty}^{-2q} du e^{-ipu+ius\sigma(-s)} \right. \\ & \left. + e^{-2iqs\sigma(s)} \int_{-2q}^{\infty} du e^{-ipu+ius\sigma(s)} \right], \end{aligned}$$

where $\sigma(x) = 1$ for $x \geq 0$ and $\sigma(x) = 0$ for $x < 0$;

$$\begin{aligned} W_3 = & \frac{-i\kappa(|s| - i\kappa)}{2\pi(s^2 + \kappa^2)} \left[e^{2iqs\sigma(s)} \right. \\ & \times \int_{-\infty}^{2q} du e^{-ipu+ius\sigma(-s)} \\ & \left. + e^{2iqs\sigma(-s)} \int_{-2q}^{\infty} du e^{-ipu+ius\sigma(s)} \right]; \end{aligned}$$

$$\begin{aligned} W_4 = & \frac{\kappa^2}{2\pi(s^2 + \kappa^2)} \left\{ \int_{-\infty}^{-2q} du e^{-ipu-2i|s|q} \right. \\ & \left. + \int_{-2q}^{2q} du e^{-ipu+i|s|u} + \int_{-2q}^{\infty} du e^{-ipu+2i|s|q} \right\}. \end{aligned}$$

The marginal distribution can be calculated in a similar way (we omit its argument):

$$w = w_1 + w_2 + w_3 + w_4; \quad w_1 = 1/(2\pi|\mu|),$$

$$w_2 = \frac{i\kappa(|s| + i\kappa)}{2\pi(s^2 + \kappa^2)\sqrt{2\pi\mu i}} \int_0^{\infty} dq e^{iq|s|}$$

$$\begin{aligned} & \times \left(\exp \left[iqs + \frac{i}{2\mu\nu} (\nu s + \mu q - X)^2 \right] \right. \\ & \left. + \exp \left[-iqs - \frac{i}{2\mu\nu} (\nu s - \mu q - X)^2 \right] \right), \end{aligned}$$

$$w_3 = w_2^*,$$

$$w_4 = \frac{\kappa^2}{2\pi(s^2 + \kappa^2)} \left\{ \sqrt{\frac{2\pi\mu i}{\nu}} e^{\frac{2i|s|X}{\nu}} \right.$$

$$\times \int_0^{\infty} du \exp \left[-\frac{2\nu i}{\mu} \left(\frac{X}{\nu} + |s| + \frac{u\mu}{\nu} \right)^2 \right]$$

$$\left. + \sqrt{\frac{2\pi\mu}{\nu i}} e^{-\frac{2i|s|X}{\nu}} \right.$$

$$\times \int_0^{\infty} du \exp \left[\frac{2\nu i}{\mu} \left(\frac{X}{\nu} + |s| + \frac{u\mu}{\nu} \right)^2 \right]$$

$$\begin{aligned} & \left. + \frac{1}{|\mu|} \int_{-\infty}^{\infty} \frac{dp}{i(|s| - p)} \left(\exp \left[-\frac{2i(p - |s|)(X - p\nu)}{\mu} \right] \right. \right. \\ & \left. \left. - \exp \left[\frac{2i(p - |s|)(X - p\nu)}{\mu} \right] \right) \right\}. \end{aligned}$$

4. PROPAGATOR FOR A PARTICLE IN THE FIELD OF DISPERSING DELTA-FUNCTION CENTERS

The problem of the propagator in the field of dispersing delta-function wells belongs to the same class as the problems considered above.

The propagator for the Schrödinger equation satisfies the equation

$$\left\{ i \frac{\partial}{\partial t} + \frac{1}{2} \frac{\partial^2}{\partial x^2} + \alpha \delta(x - vt) + \beta \delta(x + vt) \right\} \quad (14)$$

$$\times G(x, x', t) = i\delta(x - x')\delta(t),$$

which must be supplemented with the boundary condition

$$G(x, x', t) \Big|_{t=0} = i\delta(x - x'). \quad (15)$$

In order to solve the problem specified by Eqs. (14) and (15), we represent the propagator G as the sum $G = G_0 + G_1$, where G_0 satisfies the equation

$$\left(i \frac{\partial}{\partial t} + \frac{1}{2} \frac{\partial^2}{\partial x^2} \right) G_0 = i\delta(x - x')\delta(t),$$

whence it follows that

$$G_0(x, x', t) = \frac{\sigma(t)}{\sqrt{2\pi i t}} e^{i \frac{(x-x')^2}{2t}}. \quad (16)$$

The equation for G_1 can be represented in the integral form

$$G_1 = i \int_{-\infty}^{\infty} d\xi \int_0^t \frac{d\tau}{\sqrt{2\pi i(t-\tau)}} e^{i\frac{(x-\xi)^2}{2(t-\tau)}} \times \left(\alpha\delta(\xi - v\tau) + \beta\delta(\xi + v\tau) \right) \times (G_0(\xi - x', \tau) + G_1(\xi, x', \tau)). \tag{17}$$

By introducing the notation

$$f_{1,2}(x', t) = \exp\left(-i\frac{v^2 t}{2} \pm ivx'\right) G_1(\pm vt, x', t), \tag{18}$$

we obtain the following set of equations from (17):

$$f_1(x', t) = i \int_0^t \frac{d\tau}{\sqrt{2\pi i(t-\tau)}} \times \left\{ \alpha \left(\frac{e^{ix'^2/2\tau}}{\sqrt{2\pi\tau}} + f_1(x', \tau) \right) + \beta \exp\left(\frac{2iv^2 t\tau}{t-\tau} + 2ivx'\right) \left(\frac{e^{ix'^2/2\tau}}{\sqrt{2\pi i\tau}} + f_2(x', \tau) \right) \right\}, \tag{19}$$

$$f_2(x', t) = i \int_0^t \frac{d\tau}{\sqrt{2\pi i(t-\tau)}} \times \left\{ \alpha \exp\left(\frac{2iv^2 t\tau}{t-\tau} - 2ivx'\right) \left(\frac{e^{ix'^2/2\tau}}{\sqrt{2\pi i\tau}} + f_1(x', \tau) \right) + \beta \left(\frac{e^{ix'^2/2\tau}}{\sqrt{2\pi i\tau}} + f_2(x', \tau) \right) \right\}. \tag{20}$$

In turn, the set of Eqs. (19) and (20) can be represented in a simpler form by using the following substitution for the required functions:

$$f_{1,2}(x', t) = \frac{1}{t^{3/2}} g_{1,2}(x', 1/t).$$

Setting $t = 1/\eta$ and $\tau = 1/\xi$, we then obtain the equations

$$\eta g_1(x', \eta) = S_1(x', \eta) + \frac{\alpha i}{\sqrt{2\pi i}} \int_{\eta}^{\infty} \frac{d\xi}{\sqrt{\xi - \eta}} g_1(x', \xi) + \frac{\beta i}{\sqrt{2\pi i}} e^{2ivx'} \int_{\eta}^{\infty} \frac{d\xi}{\sqrt{\xi - \eta}} g_2(x', \xi) e^{2iv^2/(\xi - \eta)}, \tag{21}$$

$$\eta g_2(x', \eta) = S_2(x', \eta) + \frac{\alpha i}{\sqrt{2\pi i}} e^{-2ivx'}$$

$$\times \int_{\eta}^{\infty} \frac{dxi}{\sqrt{\xi - \eta}} g_1(x', \xi) e^{2iv^2/(\xi - \eta)} + \frac{\beta i}{\sqrt{2\pi i}} \int_{\eta}^{\infty} \frac{d\xi}{\sqrt{\xi - \eta}} g_2(x', \xi), \tag{22}$$

where

$$S_1 = \frac{1}{2\pi} \int_{\eta}^{\infty} \frac{d\xi}{\xi\sqrt{\xi - \eta}} e^{ix'^2\xi/2} \times \left(\alpha + \beta \exp\left(\frac{2iv^2}{\xi - \eta} + 2ivx'\right) \right),$$

$$S_2 = \frac{1}{2\pi} \int_{\eta}^{\infty} \frac{d\xi}{\xi\sqrt{\xi - \eta}} e^{ix'^2\xi/2} \times \left(\alpha \exp\left(\frac{2iv^2}{\xi - \eta} - 2ivx'\right) + \beta \right).$$

The expressions for $S_{1,2}$ can be transformed by using the relation $1/\xi = \int_0^{\infty} dp e^{-p\xi}$ ($\xi > 0$). We then obtain

$$S_{1,2}(x', \eta) = \frac{1}{2\pi} \int_0^{\infty} dp \exp\left(-p\eta + \frac{ix'^2\eta}{2}\right) Q_{1,2}(p, x'),$$

where

$$Q_1(p, x') = \int_0^{\infty} \frac{d\xi}{\sqrt{\xi}} \exp\left(-p\xi + \frac{ix'^2\xi}{2}\right) \times \left(\alpha + \beta \exp\left(\frac{2iv^2}{\xi} + 2ivx'\right) \right),$$

$$Q_2(p, x') = \int_0^{\infty} \frac{d\xi}{\sqrt{\xi}} \exp\left(-p\xi + \frac{ix'^2\xi}{2}\right) \times \left(\alpha \exp\left(\frac{2iv^2}{\xi} - 2ivx'\right) + \beta \right).$$

In Eqs. (21) and (22), the kernels of the integral transformations depend on the difference $\xi - \eta$; it is this circumstance that eventually makes it possible to find an exact solution. For this, we substitute, into Eqs. (21) and (22), the sought functions $g_{1,2}$ in the form of the integral representations

$$g_{1,2}(x', \eta) = \frac{1}{\sqrt{2\pi i}} e^{ix'^2\eta/2} \int_0^{\infty} e^{-p\eta} h_{1,2}(x', p) dp.$$

Further, we consider that

$$\int_{\eta}^{\infty} \frac{d\xi}{\sqrt{\xi - \eta}} g_1(x', \xi)$$

$$\begin{aligned}
 &= \frac{e^{ix'^2\eta/2}}{\sqrt{2\pi i}} \int_0^\infty dp h_1(x', p) e^{-p\eta} a_1(p, x'), \\
 a_1 &= \int_0^\infty \frac{dy}{\sqrt{y}} \exp\left(-py + \frac{ix'^2 y}{2}\right) = \sqrt{\frac{2\pi i}{2pi + x'^2}}, \\
 &\int_0^\infty \frac{d\xi}{\sqrt{\xi - \eta}} g_1(x', \xi) e^{2iv^2/(\xi - \eta)} \\
 &= \frac{e^{ix'^2\eta/2}}{\sqrt{2\pi i}} \int_0^\infty dp h_1(x', p) e^{-p\eta} a_2(p, x'), \\
 a_2 &= \int_0^\infty \frac{dy}{\sqrt{y}} \exp\left(-py + \frac{ix'^2 y}{2} + \frac{2iv^2}{y}\right) \\
 &= \sqrt{\frac{2\pi i}{2pi + x'^2}} \exp\left(2iv\sqrt{2pi + x'^2}\right).
 \end{aligned}$$

In addition, we have

$$\begin{aligned}
 Q_1(p, x') &= \alpha a_1(p, x') + \beta a_2(p, x') e^{2ivx'}, \\
 Q_2(p, x') &= \alpha a_2(p, x') e^{-2ivx'} + \beta a_1(p, x').
 \end{aligned}$$

It can be shown that

$$\eta \int_0^\infty e^{-p\eta} h_1(x', p) dp = h_1(x', 0) + \int_0^\infty \frac{dh_1}{dp} e^{-p\eta} dp.$$

Further, we assume that $h_1(x', p)|_{p=0} = h_2(x', p)|_{p=0} = 0$. By using the above equalities, both the right- and the left-hand sides of Eqs. (21) and (22) can be represented in the form $\int_0^\infty dp e^{-p\eta} \Psi(\eta)$, where $\Psi(\eta)$ is a function of η . Equations (21) and (22) hold if the equalities for the integrands are satisfied. In this way, we can obtain

$$\frac{dh_1}{dp} = \frac{\alpha i}{\sqrt{2pi + x'^2}} + \frac{\beta i}{\sqrt{2pi + x'^2}} \quad (23)$$

$$\begin{aligned}
 &\times \exp\left(2iv\sqrt{2pi + x'^2} + 2ivx'\right) + \frac{\alpha i h_1}{\sqrt{2pi + x'^2}} \\
 &+ \frac{\beta i h_2}{\sqrt{2pi + x'^2}} \exp\left(2iv\sqrt{2pi + x'^2} + 2ivx'\right),
 \end{aligned}$$

$$\begin{aligned}
 \frac{dh_2}{dp} &= \frac{\alpha i}{\sqrt{2pi + x'^2}} \exp\left(2iv\sqrt{2pi + x'^2} - 2ivx'\right) \\
 &+ \frac{\beta i}{\sqrt{2pi + x'^2}} + \frac{\alpha i h_1}{\sqrt{2pi + x'^2}} \quad (24)
 \end{aligned}$$

$$\times \exp\left(2iv\sqrt{2pi + x'^2} - 2ivx'\right) + \frac{\beta i h_2}{\sqrt{2pi + x'^2}}.$$

In order to solve the set of Eqs. (23) and (24), it is convenient to introduce the independent variable $\theta = \exp[2iv\sqrt{2pi + x'^2}]$. Denoting $dh/d\theta \equiv \dot{h}$, we can obtain

$$-2v\theta \dot{h}_1 = \alpha i + \beta i \theta e^{2ivx'} + \alpha i h_1 + \beta i \theta h_2 e^{2ivx'}, \quad (25)$$

$$-2v\theta \dot{h}_2 = \alpha i \theta e^{-2ivx'} + \beta i + \alpha i \theta h_1 e^{-2ivx'} + \beta i h_2. \quad (26)$$

The set of Eqs. (25) and (26) is equivalent to the equations

$$\begin{aligned}
 \ddot{h}_1 - \frac{\alpha + \beta}{2iv\theta} \dot{h}_1 + h_1 \left(\frac{\alpha\beta}{4v^2} - \frac{\alpha\beta}{4v^2\theta^2} \right. \\
 \left. + \frac{\alpha}{2iv\theta^2} \right) &= -\frac{\alpha\beta}{4v^2} + \frac{\alpha\beta}{4v^2\theta^2} - \frac{\alpha}{2iv\theta^2}, \quad (27)
 \end{aligned}$$

$$\begin{aligned}
 \ddot{h}_2 - \frac{\alpha + \beta}{2iv\theta} \dot{h}_2 + h_2 \left(\frac{\alpha\beta}{4v^2} - \frac{\alpha\beta}{4v^2\theta^2} \right. \\
 \left. + \frac{\beta}{2iv\theta^2} \right) &= -\frac{\alpha\beta}{4v^2} + \frac{\alpha\beta}{4v^2\theta^2} - \frac{\beta}{2iv\theta^2}. \quad (28)
 \end{aligned}$$

Concurrently, the following conditions must hold:

$$\begin{aligned}
 h_1|_{\theta=\theta_0} = h_2|_{\theta=\theta_0} &= 0, \\
 -2v\theta_0 \dot{h}_1|_{\theta=\theta_0} &= \alpha i + \beta i \theta_0 e^{2ivx'}, \quad (29) \\
 -2v\theta_0 \dot{h}_2|_{\theta=\theta_0} &= \alpha i \theta_0 e^{-2ivx'} + \beta i, \quad \theta_0 = e^{2iv|x'|}.
 \end{aligned}$$

For the functions $h_1 + 1$ and $h_2 + 1$, Eqs. (27) and (28) appear to be homogeneous; a general solution can be represented as

$$h_1 + 1 = \theta^{\frac{1}{2} + \frac{\alpha + \beta}{4iv}} [C_1 J_m(z) + C_2 J_{-m}(z)], \quad (30)$$

$$h_2 + 1 = \theta^{\frac{1}{2} + \frac{\alpha + \beta}{4iv}} [C_3 J_n(z) + C_4 J_{-n}(z)], \quad (31)$$

where $J_s(z)$ are Bessel functions,

$$m = \frac{1}{2} \left(1 - \frac{\alpha - \beta}{2iv} \right), \quad n = \frac{1}{2} \left(1 + \frac{\alpha - \beta}{2iv} \right),$$

$$z = \frac{\sqrt{\alpha\beta}}{2v} \theta.$$

The constants C_1, C_2, C_3 , and C_4 can be determined from the boundary conditions (29) (see Appendix). By consecutively expressing the functions $g_{1,2}$ in terms of $h_{1,2}$ and by subsequently calculating the functions $f_{1,2}$, we can also derive an explicit expression for the propagator.

APPENDIX

We will now demonstrate that the expression derived in [35] for G_1 follows from our formulas (29), (30), and (31) at $\alpha = \beta$ and $v \rightarrow 0$. At $\alpha = \beta$, it does indeed follow from (30) and (31) that

$$C_{1,3} = \theta_0^{-\alpha/2iv} \left(\sin \frac{\alpha\theta_0}{2v} - i e^{\pm 2ivx'} \cos \frac{\alpha\theta_0}{2v} \right),$$

$$C_{2,4} = \theta_0^{-\alpha/2iv} \left(\cos \frac{\alpha\theta_0}{2v} + ie^{\pm 2ivx'} \sin \frac{\alpha\theta_0}{2v} \right),$$

$$h_{1,2} + 1 = \left(\frac{\theta}{\theta_0} \right)^{\alpha/2iv}$$

$$\times \left(\cos \frac{\alpha(\theta - \theta_0)}{2v} - ie^{\pm 2ivx'} \sin \frac{\alpha(\theta - \theta_0)}{2v} \right).$$

For the functions $g_{1,2}$, we then have

$$g_{1,2} = \frac{1}{\sqrt{2\pi i}} e^{ix'^2\eta/2} \int_0^\infty e^{-p\eta} h_{1,2}(x', p) dp,$$

whence, for the function G_1 , we further obtain

$$G_1(x, x', t) = \frac{2\alpha i}{2\pi i} \int_0^t \frac{d\tau \exp \left[\frac{ix'^2}{2\tau} + \frac{ix^2}{2(t-\tau)} \right]}{\tau^{3/2} \sqrt{t-\tau}}$$

$$\times \int_0^\infty dp e^{-p/\tau} \exp \left[\frac{\alpha}{2iv} (e^{2iv\sqrt{2pi+x'^2}} - e^{2iv|x'|}) \right].$$

After some simple algebra, we arrive at

$$G_1(x, x', t) = \frac{2\alpha i}{\sqrt{2\pi i}} \exp \left(-2\alpha|x'| + \frac{ix^2}{2t} + \frac{ix'^2}{2t} \right)$$

$$\times \int_0^\infty \frac{dp}{\sqrt{2pi+x'^2}}$$

$$\times \exp \left[-\frac{p}{t} + \left(2\alpha + i\frac{|x|}{t} \right) \sqrt{2pi+x'^2} \right].$$

By introducing the variable $s = \sqrt{2pi+x'^2} - |x'|$, we obtain

$$G_1(x, x', t) = \frac{2\alpha}{\sqrt{2\pi i}} \exp \left[\frac{i}{2t} (|x| + |x'|)^2 \right]$$

$$\times \int_0^{(1+i)\infty} ds \exp \left[\frac{is^2}{2t} + \frac{is}{t} (|x| + |x'|) + 2\alpha s \right].$$

The last relation can be recast into the form quoted in [35].

REFERENCES

1. E. Schrödinger, *Ann. Phys. (Leipzig)* **79**, 489 (1926).
2. E. Madelung, *Z. Phys.* **40**, 332 (1926).
3. L. De Broglie, *C. R. Hebd. Seances Acad. Sci.* **183**, 447 (1926); **184**, 273 (1927); **185**, 380 (1927).
4. D. Bohm, *Phys. Rev.* **85**, 166 (1952); **85**, 180 (1952).
5. J. E. Moyal, *Proc. Cambridge Philos. Soc.* **45**, 99 (1949).
6. L. D. Landau, *Z. Phys.* **45**, 430 (1927).
7. J. von Neuman, *Mathematische Grundlagen der Quantenmechanik* (Springer-Verlag, Berlin, 1932).

8. E. Wigner, *Phys. Rev.* **40**, 749 (1932).
9. W. Heisenberg, *Z. Phys.* **43**, 172 (1927).
10. R. Glauber, *Phys. Rev. Lett.* **10**, 84 (1963).
11. E. C. G. Sudarshan, *Phys. Rev. Lett.* **10**, 277 (1963).
12. K. Husimi, *Proc. Phys. Math. Soc. Jpn.* **23**, 264 (1940).
13. K. E. Cahill and R. J. Glauber, *Phys. Rev.* **177**, 1882 (1969).
14. K. Vogel and H. Risken, *Phys. Rev. A* **40**, 2847 (1989).
15. D. T. Smithey, M. Beck, M. G. Raymer, and A. Fardani, *Phys. Rev. Lett.* **70**, 1244 (1993).
16. S. Mancini, V. I. Manko, and P. Tombesi, *Quantum Semiclass. Opt.* **7**, 615 (1995).
17. Cr. M. D. Ariano, S. Mancini, V. I. Manko, and P. Tombesi, *Quantum Semiclass. Opt.* **8**, 1017 (1996).
18. S. Mancini, V. I. Manko, and P. Tombesi, *J. Mod. Opt.* **44**, 2281 (1997).
19. S. Mancini, V. I. Manko, and P. Tombesi, *Phys. Lett. A* **213**, 1 (1996).
20. S. Mancini, V. I. Manko, and P. Tombesi, *Found. Phys.* **27**, 801 (1997).
21. V. I. Manko, *J. Russ. Laser Res.* **17**, 579 (1996).
22. V. I. Man'ko and S. S. Safonov, *Teor. Mat. Fiz.* **112**, 1172 (1997).
23. O. V. Manko, *Phys. Lett. A* **228**, 29 (1997).
24. V. I. Manko, L. Rosa, and P. Vitale, *Phys. Rev. A* **57**, 3291 (1998).
25. V. I. Man'ko, M. Moshinsky, and A. Sharma, *Phys. Rev. A* **59** (3), 1809 (1999).
26. V. V. Dodonov and V. I. Manko, *Phys. Lett. A* **229**, 335 (1997).
27. V. I. Man'ko and O. V. Man'ko, *Zh. Éksp. Teor. Fiz.* **112**, 796 (1997) [*JETP* **85**, 430 (1997)].
28. V. A. Andreev and V. I. Man'ko, *Zh. Éksp. Teor. Fiz.* **114**, 437 (1998) [*JETP* **87**, 239 (1998)].
29. V. I. Man'ko and S. S. Safonov, *Yad. Fiz.* **61**, 658 (1998) [*Phys. At. Nucl.* **61**, 585 (1998)].
30. V. I. Man'ko, *Yad. Fiz.* **61**, 1791 (1998) [*Phys. At. Nucl.* **61**, 1674 (1998)].
31. S. K. Zhdanov and A. S. Chikhachev, *Dokl. Akad. Nauk SSSR* **218**, 1323 (1974) [*Sov. Phys. Dokl.* **19**, 696 (1974)].
32. A. S. Chikhachev, *Zh. Éksp. Teor. Fiz.* **107**, 1153 (1995) [*JETP* **80**, 641 (1995)].
33. V. I. Man'ko and A. S. Chikhachev, *Zh. Éksp. Teor. Fiz.* **113**, 606 (1998) [*JETP* **86**, 335 (1998)].
34. W. Damert, *Am. J. Phys.* **43**, 531 (1975).
35. N. M. Nussenzweig, in *Symmetries in Physics, Proceedings of the I International Symposium in Honour of Prof. M. Moshinsky, 1991*, Ed. by A. Frank and K. B. Wolf (Springer-Verlag, Berlin, 1992).

Translated by A. Isaakyan

ELEMENTARY PARTICLES AND FIELDS
Experiment

Experimental Observation of a Two-Phase State of Expanding Nuclear Matter at $E_p = 1$ GeV

Yu. A. Chestnov* and B. Yu. Sokolovsky

Petersburg Nuclear Physics Institute, Russian Academy of Sciences, Gatchina, 188350 Russia

Received March 29, 2000; in final form, August 9, 2000

Abstract—A double-arm time-of-flight spectrometer was used to study the thermal multifragmentation of ^{238}U , ^{232}Th , and ^{197}Au nuclei that is induced by 1-GeV protons. It is established that the pseudo-evaporation channel, where a single heavy fragment of mean mass in the range 80–90 amu is produced in association with approximately ten smaller clusters ($\langle M \rangle = 7\text{--}10$ amu) emitted anisotropically at low velocities, is dominant at this energy. The pseudoevaporation cross sections change from 10 ± 5 mb for ^{197}Au to 120 ± 40 μb for ^{238}U . For ^{238}U and ^{232}Th , it is found that, in the region $M < 8$ amu, the power law is violated, which is explained by the decay of part of small primary clusters in the course nucleon exchange through the “gas” phase within the expanding nucleus. © 2001 MAIK “Nauka/Interperiodica”.

1. INTRODUCTION

1.1. History of the Problem

In the late 1970s, a double-arm time-of-flight spectrometer intended for studying high-energy fission was constructed at the Leningrad Nuclear Physics Institute (LNPI, presently known as Petersburg Nuclear Physics Institute, or PNPI). Even the first experiments in a beam of 1-GeV protons revealed, in addition to the products studied at that time, some events whose kinematics differed substantially from fission kinematics.

In terms of the velocity–momentum ($V - P$) coordinates, a typical two-dimensional distribution of reaction products that were recorded by this spectrometer in the case where its arms were arranged collinearly in the direction orthogonal to the proton beam incident on a thin ^{238}U target is shown schematically in Fig. 1 for $V \geq 0.45$ cm/ns. The contour plot displays (i) binary-fission fragments (FF) having kinetic energies in the region $E_{\text{FF}} > 35$ MeV, masses in the region $M_{\text{FF}} > 40$ amu, and a mean momentum of 4 GeV/ c (in collinear geometry, the relevant events, which constitute about 85% of statistics, were analyzed in detail elsewhere [1]); (ii) coincident heavy fragments (CHF) that have the same threshold energy, somewhat smaller masses, and a mean momentum of 3 GeV/ c and which are grouped in a separate peak in the distribution with respect to the sum of the masses of binary heavy fragments (BHF = FF + CHF) (see Fig. 2), the cross section

σ_{CHF} for ^{238}U being $(0.8 \pm 0.1)\%$ of the fission cross section σ_f for this nucleus [2]; and (iii) single heavy fragments (SHF) satisfying the conditions $E_{\text{SHF}} < 35$ MeV and $M_{\text{SHF}} > 40$ amu [they were recorded in coincidence with one of the accompanying clusters (AC): $E_{\text{AC}} < 50$ MeV and $M_{\text{AC}} \leq 40$ amu].

Moreover, AC–AC and AC–BHF events were also recorded. The detection of a cluster in coincidence with one of the binary heavy fragments became possible when the other missed the spectrometer angular acceptance. Events where two reaction products were simultaneously detected in one of the spectrometer arms were rejected by the fast-selection trigger.

Kinematical features peculiar to nonfission events, which are characterized by a high multiplicity of accompanying clusters, allowed us to conclude that, at an incident proton energy of 1 GeV, there occurs a very specific nuclear reaction that we dubbed the explosion of nucleus [3–5]. Unfortunately, a major part of information about the explosion reaction has not yet been published.

In subsequent years, there have ever more often appeared theoretical and experimental studies exploring the multiparticle production of large fragments and yielding results that comply well with ours. This new nuclear-reaction mechanism was referred to as multifragmentation.

1.2. Multifragmentation Reaction

By multifragmentation, we mean the multiparticle production of large clusters in an explosive disintegration of a highly excited ($E^*/A > 3$ MeV/nucleon

*e-mail: chestnov@pnpi.spb.ru

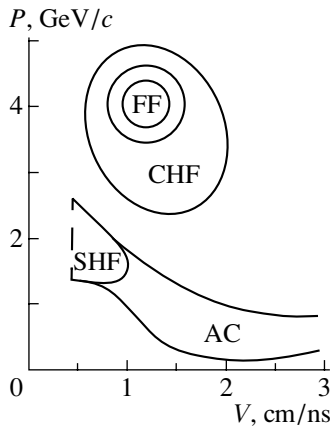


Fig. 1. Contour plot for the products of ^{238}U disintegration induced by 1-GeV protons: (FF) binary-fission fragments, (CHF) coincident heavy fragments, (SHF) single heavy fragments, and (AC) accompanying clusters (that is, clusters accompanying all types of heavy fragments).

[6]) expanding nucleus occurring in a two-phase state.

One of the first explanations of this phenomenon was proposed by the inventors of the statistical model [6]. According to this model, highly excited nuclei undergo disintegration via the spinodal breakup of expanding nuclear matter into two phases, a set of liquid clusters in a gaseous nucleon medium. An increase in the volume of a nucleus is due to a decrease in its surface tension and to a thermal motion of constituent nucleons upon the completion of the fast interaction stage, which proceeds through a cascade and which is accompanied by a high energy transfer from an incident particle. Since nascent clusters must develop a surface and since the thermal energy of the nucleus must partly be converted into the kinetic energy of the radial motion of its constituents, the decay process is moderated, which facilitates nucleon exchange between the clusters. As soon as a critical density, which is a few times smaller than the equilibrium density, is achieved, the clusters freeze out, whereupon their motion is accelerated under the effect of Coulomb forces. If the nuclear-matter density has not achieved the critical value, the process begins to develop in the inverse direction—that is, the residual nucleus returns into the equilibrium state, and the excitation energy is dissipated through the competing processes of particle evaporation and residual-nucleus fission (see, for example, [7–13] and references therein).

Such a multifragmentation process, which proceeds without a preliminary compression of nuclear matter, is referred to as thermal multifragmentation [7, 8]. In the threshold region of excitation energies, the reaction products are likely to feature one

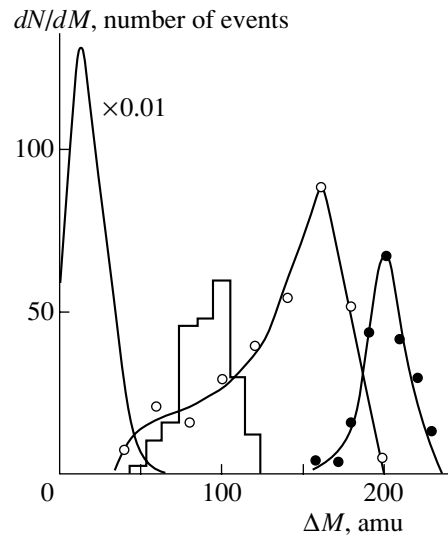


Fig. 2. Missing-mass distribution of basic forms of products that originate from ^{238}U disintegration induced by 1-GeV protons and which are recorded in coincidence. The left-hand curve, which was drawn through experimental points (whose errors are negligibly small, reduced by a factor of 100), correspond to binary-fission fragments. The histogram, open circles, and closed circles represent, respectively, coincident heavy fragments, AC–SHF events, and AC–AC events.

(pseudoevaporation), two (pseudofission), or more (cracking) heavy fragments [9]. That the volume of the nucleus increases considerably at the instant of cluster freeze-out is a feature that is peculiar to the multifragmentation reaction and which distinguishes it, at the fundamental level, from the traditional cascade–evaporation concepts. The dimensions of the region from which the multiparticle emission of large clusters occurs are determined experimentally by the correlation-function method [10]. If statistics are low, in which case this method cannot be used, information about the dimensions of the emitting source is deduced from the mean relative velocity of intermediate-mass fragments (IMF) taking mass values in the range $6 \leq M_{\text{IMF}} \leq 30$ amu and traveling in opposite directions [11, 12]. Light charged particles having masses not larger than 5 amu are thought to carry a lesser amount of relevant information, since they can be emitted at any reaction stage.

The appearance of the theoretical studies by Mishustin [7] and Shapiro [10] rekindled interest in experimental information that was obtained for the explosion nuclear reaction. For the explosion-reaction products, we therefore decided to perform a thorough analysis of the kinematical features that were obtained 15 years ago at the completing stage of treatment of fission events. This analysis has revealed that the explosion reaction has much in common with

Table 1. Mean masses of single heavy fragments and mean masses, velocities, and multiplicities of accompanying clusters (the quoted errors are purely statistical)

Target	$\langle M_{\text{SHF}} \rangle$, amu	$\langle M_{\text{AC}}^{(\text{SHF})} \rangle$, amu	$\langle V_{\text{AC}}^{(\text{SHF})} \rangle$, cm/ns	$\langle n_{\text{AC}}^{(\text{SHF})} \rangle$, clusters
^{238}U	92 ± 2	9.5 ± 0.4	2.06 ± 0.04	9.7 ± 0.7
^{232}Th	86 ± 2	10.0 ± 0.4	2.24 ± 0.04	9.4 ± 0.7
^{197}Au	77 ± 2	7.2 ± 0.4	3.18 ± 0.08	11.2 ± 1.1

the thermal multifragmentation of heavy nuclei at high projectile energies and made it possible to determine its cross section at the incident-proton energy of 1 GeV. It turned out that the values that we found for intermediate masses and the multiplicity of the products of this reaction are in qualitative agreement with the results of the calculations presented in [7, 10]. Moreover, our data contain new information about special features of multifragmentation in the threshold energy region.

The measurements were performed with ^{238}U , ^{232}Th , and ^{197}Au targets of thickness 80, 250, and $500 \mu\text{g}/\text{cm}^2$, respectively. The background of random coincidences was negligibly small in the experiment being discussed. The procedure of measurements was described elsewhere [1, 2, 14].

2. EXPERIMENTAL RESULTS

2.1. Missing-Mass Distributions

The sum of the masses of any two products not originating from the fission process differs considerably from the target-nucleus mass M_{targ} . By way of example, Fig. 2 shows the distribution in the missing mass $\Delta M = M_{\text{targ}} - (M_1 + M_2)$ amu for the various types of ^{238}U disintegration events induced by 1-GeV protons and classified as in Fig. 1. The overlap of the nonfission events mentioned immediately above forms tails in the integrated distributions with respect to the sum of the masses of nuclear-reaction products recorded in coincidence [2–4].

The expectation value for the mass distribution of coincident heavy fragments recorded in collinear geometry proved to be 73.5 ± 1.5 amu for ^{238}U . The mean missing mass for these fragments was 91 amu. There were 8 ± 1 charged particles accompanying them [15]. The mean mass of coincident heavy fragments corresponded to filled deformed shells [2, 5]. The mean relative velocity of these fragments, 3.0 ± 0.1 cm/ns, was consistent with that which touching spherical fragments of mass 74 amu would acquire as the result of mutual Coulomb acceleration if they had equal numbers of protons and neutrons. On the basis of these and some other indications, we identified coincident heavy fragments with those that were

formed in the pseudofission channel [2]. According to our data, the cross section for fissionlike multifragmentation for ^{238}U was 12 ± 2 mb at the incident-proton energy of 1 GeV.

2.2. Properties of the Products of the Reaction Leading to the Formation of Single Heavy Fragments

Our experiment recorded 300 to 500 AC–SHF events for each target nucleus. The energy, velocity, and mass distributions of reactions products in these events are presented in [16]; the mass distributions can also be found in [2]. The most probable values of the single-heavy-fragment masses are quoted in Table 1, along with the mean masses and velocities of the clusters accompanying these fragments.

For the actinide nuclei studied in our experiment, the properties of the velocity and mass distributions of single heavy fragments were somewhat distorted by the selection criterion $V_{\text{SHF}} \geq 0.45$ cm/ns, which rejected about 30% (15%) of such fragments for ^{238}U (^{232}Th). For ^{238}U and ^{232}Th , the values of $\langle V_{\text{SHF}} \rangle$ that correspond to the maxima of the velocity distributions of single heavy fragments are, respectively, 0.61 and 0.66 (± 0.02) cm/ns [16]. For ^{197}Au , the measured value of this quantity is $\langle V_{\text{SHF}} \rangle = 0.71 \pm 0.01$ cm/ns.

In a run that employed the zero-time detector in the charge-analyzer mode, we established that the mean charge of single heavy fragments is much greater than the mean charge of accompanying clusters [16].

Figure 3 shows $\langle M_{\text{AC}}^{(\text{SHF})} \rangle$ as a function of the single-heavy-fragment mass. In the region of small M_{SHF} , the following correlation is observed for the actinide targets: the smaller M_{SHF} , the larger the clusters that are emitted in the opposite direction. This effect may be due to the cracking of heavy nuclei into four fragments of comparable masses. The probability of this process with respect to binary fission is about 10^{-4} .

Probabilities of cluster detection in coincidence with heavy fragments. We define the probability of detecting AC–HF events as the ratio of their number $N_{\text{AC-HF}}$ to the total number

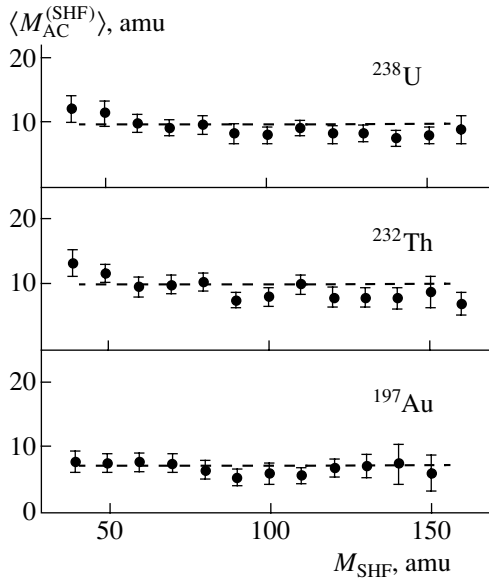


Fig. 3. The mean mass of accompanying clusters as a function of the single-heavy-fragment mass. The dashed lines represent the mean values $\langle M_{AC}^{(SHF)} \rangle$ for all AC-SHF events recorded in the present experiment.

of events featuring at least one heavy fragment (HF = BHF + SHF + heavy cracking products):

$$W_{AC-HF} = N_{AC-HF} / (N_{AC-HF} + N_{HF-HF}). \quad (1)$$

For two values of the kinetic-energy threshold ($E_{HF} > 8$ and > 35 MeV), the experimental values of the probability W_{AC-HF} are plotted in Fig. 4 versus the heavy-fragment momentum P_{HF} (at the latter kinetic-energy-threshold value, single heavy fragments were rejected). As P_{HF} is reduced, binary-fission fragments give way to coincident heavy fragments and then to single heavy fragments (see Fig. 1); concurrently, W_{AC-HF} increases considerably. The mean values $\langle W_{AC-HF} \rangle$ carry information about the multiplicity of accompanying clusters. However, the method that was proposed in [16] for determining the multiplicity of the clusters accompanying binary heavy fragments in terms of $\langle W_{AC-BHF} \rangle$ is inappropriate for events involving the production of single heavy fragments because there is no heavy partner in this case.

Estimating the mean multiplicity of clusters in terms of the mean values of the reaction-product masses. The results of the calculations performed in [7] for the multifragmentation of ^{197}Au nuclei revealed that, over a wide range of excitation energies, the number of neutrons released in this reaction is close to the neutron excess in the primary nucleus. Therefore, the nucleus breaks up into $N \approx Z$ fragments. Extrapolating this situation to case of actinides and disregarding the decrease in the nuclear

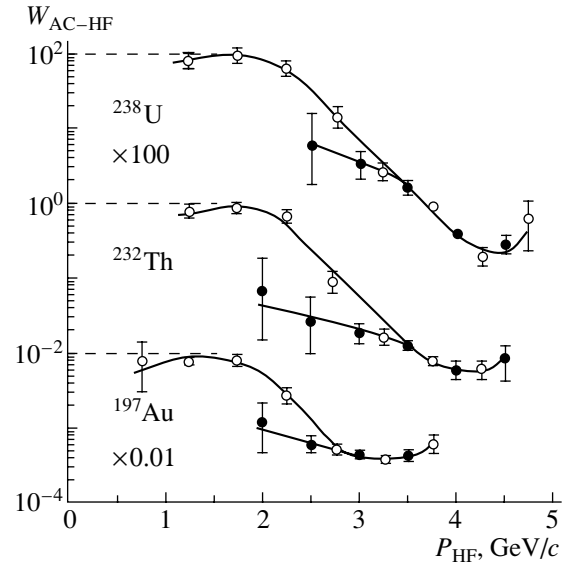


Fig. 4. Probability of cluster detection in coincidence with heavy fragments as a function of the momentum of these fragments: (open circles) for all heavy fragments and (closed fragments) without single heavy fragments. The curves connecting the experimental points were drawn as an eyeball fit. The dashed lines correspond to the value of $W_{AC-HF} = 1$ for each target nucleus.

charge at the cascade reaction stage, we can set, for a first approximation,

$$\langle n_{AC}^{(SHF)} \rangle = (2 \times Z_{\text{targ}} - \langle M_{SHF} \rangle) / \langle M_{AC}^{(SHF)} \rangle, \quad (2)$$

where $\langle n_{AC}^{(SHF)} \rangle$ is the mean number of clusters in events featuring single heavy fragments; Z_{targ} is the charge number of the target nucleus; and $\langle M_{SHF} \rangle$ and $\langle M_{AC}^{(SHF)} \rangle$ are the mean mass numbers of, respectively, single heavy fragments and accompanying clusters. The values of $\langle n_{AC}^{(SHF)} \rangle$ that were computed by formula (2) are quoted in Table 1.

The mean-multiplicity estimate based on the charge-balance equation for the nuclear reaction being studied exceeds the tabular values by about 15% [16]. On the other hand, an expansion of the time window could lead to an increase in $\langle M_{SHF} \rangle$ for actinides [14] and to the corresponding decrease in $\langle n_{AC}^{(SHF)} \rangle$. For a rough estimate, we can therefore use a value of $\langle n_{AC}^{(SHF)} \rangle \approx 10$ for the number of clusters in events of this type.

The results of Mishustin's calculations revealed [7] that the release of 11 charged products in ^{197}Au multifragmentation corresponds to an excitation energy of $E^* \approx 600$ MeV. At the same time, the value of $\langle M_{SHF} \rangle$ for ^{197}Au proved to be below its computed counterparts [7, 10] at this excitation energy.

Table 2. Features of the momentum distributions of reaction products for AC–SHF events (the quoted errors are purely statistical)

Target	$\langle P_{AC} \rangle$, MeV/c	$\sigma_{P(AC)}$, MeV/c	$\langle P_{SHF} \rangle$, MeV/c	$\sigma_{P(SHF)}$, MeV/c
^{238}U	500 ± 11	200 ± 13	1770 ± 20	355 ± 13
^{232}Th	532 ± 10	214 ± 11	1720 ± 20	350 ± 13
^{197}Au	373 ± 10	200 ± 9	1515 ± 25	480 ± 17

For the sake of comparison, we indicate that fragments originating from ^{238}U fission induced by 1-GeV protons are accompanied, on average, by 1.2 ± 0.2 clusters of mass 4.0 ± 0.2 amu that move at a velocity of 3.1 ± 0.1 cm/ns. When we go over to ^{197}Au , the mean mass of accompanying clusters in fission events undergoes virtually no changes, whereas their multiplicity and velocity increase to, respectively, 2.6 ± 0.4 clusters and 3.5 ± 0.1 cm/ns. This is due to an increase in the excitation energy [14, 16].

Momentum distributions of reaction products. Figure 5 displays the experimental momentum distributions of reaction products for AC–SHF events. For these distributions, the expectation values and standard deviations are quoted in Table 2.

It is well known that, with increasing statistics, the distribution of the projection of the sum of N

($N \geq 7$) vectors oriented at random in space onto a specific axis (for example, onto the double-arm-spectrometer axis, which is orthogonal to the proton beam) asymptotically tends to a normal distribution characterized by zero expectation value [17]. The momentum distributions of single heavy fragments in Fig. 5 differ basically from normal momentum distributions of fissile nuclei [1]. Therefore, the ensemble of accompanying clusters is grouped near the direction opposite to that of single-heavy-fragment emission; that is, the emission of accompanying clusters in events featuring single heavy fragments is anisotropic, and the breakup of nuclei is of an explosive character.

In contrast to fission, the emission of accompanying clusters in events involving coincident charged fragments is also anisotropic: for $n_{AC}^{(BHF)} \geq 7$, the clusters are grouped near the direction orthogonal to the line along which binary heavy fragments fly apart [18].

The assumptions that the moving nucleons of a residual nucleus having an invariable volume and a mass A are grouped at random into a cluster of mass M and that the Fermi motion of these nucleons make a decisive contribution to the scatter of cluster momenta lead to the well-known formula

$$\sigma^2 = \sigma_0^2 \frac{M(A-M)}{(A-1)}, \quad (3)$$

where σ^2 is the variance of the momentum distribution of the clusters and $\sigma_0^2 = P_F^2/5$ is a universal momentum parameter that is determined by the Fermi momentum P_F for a given nucleus [19].

The experimental values of the standard deviations σ_P in Table 2 are determined to a considerable extent by a strong mass dependence of the fragment momentum. Having found σ_P , we deduced that their values are approximately one-third as large as those computed by formula (3) for heavy nuclei of equilibrium density. This is due to the effect of three factors.

First of all, the variance of the momentum distribution of clusters in a given direction (say, the direction specified by the detector used) is always less than the variance of the projection of the 3-momentum distribution of the same clusters onto a specific axis.

It is natural to expect that, when a nucleus undergoes thermal expansion, spatially close nucleons

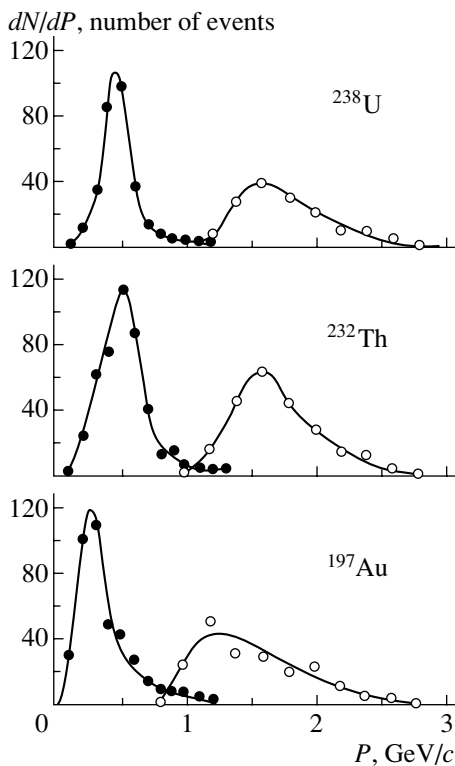


Fig. 5. Momentum distributions of reaction products in AC–SHF events for (closed circles) accompanying clusters and (open circles) single heavy fragments.

that have a common momentum component in the radial direction are combined into a cluster. It follows that, in each event featuring a single heavy fragment, the expectation value for the momentum distribution of accompanying clusters at the freeze-out instant is nonzero, which leads to a decrease in the variance of this distribution [16].

Finally, the Fermi momentum P_F decreases with decreasing nuclear-matter density.

Mean transverse velocity of the center of mass of the ensemble of accompanying particles in events featuring single heavy fragments. To within 0.5%, all velocities and momenta measured in collinear geometry can be considered to be transverse with respect to the beam. From the momentum-conservation law, it follows that, in each event, P_{SHF} is equal to the sum of the projections of the momenta of accompanying particles onto the spectrometer axis. The transverse velocity of the center of mass of these particles is given by

$$V_{\perp} = P_{\text{SHF}}/M_t, \quad (4)$$

where $M_t = M_{\text{targ}} + m_p - M_{\text{SHF}}$ (amu) is the total mass of all particles accompanying a single heavy fragment (including nucleons) and m_p is the proton mass.

Figure 6 displays the mean transverse velocity $\langle V_{\perp} \rangle$ as a function of M_t for events featuring a single heavy fragment and for nuclei undergoing fission. A feature peculiar to expression (4) for the fission process is that, instead of P_{SHF} , its numerator involves the absolute value of the vector sum of the projections of the measured fission-fragment momenta onto the spectrometer axis [1, 4]; in addition, we have $M_t = M_{\text{targ}} + m_p - (M_1 + M_2)$ (amu) in this case. The values of the mean transverse velocity of the center of mass of all particles accompanying single heavy fragments are quoted in Table 3.

By convention, particles accompanying single heavy fragments can be considered as products originating from the complete breakup of some source (multibaryon cluster) having the mass M_t and moving at the velocity V_{\perp} [4, 5]. This simple model makes it possible to estimate the anisotropy of the angular distribution of the ensemble of accompanying clusters in each event by using the values of $V_{\text{AC}}^{(\text{SHF})}$ in the laboratory frame and in the c.m. frame of the relevant multibaryon cluster. Specifically, we have

$$K = \frac{4\pi}{\Delta\Omega} \quad (5)$$

$$\times \int_{(\Delta\Omega)} N_{\text{AC-SHF}}(\theta, \varphi) d\Omega / \int_{(4\pi)} N_{\text{AC-SHF}}(\theta, \varphi) d\Omega,$$

where $\Delta\Omega = 15$ msr is the angular acceptance of one of the two equivalent spectrometer sensors.

Table 3. Mean transverse velocities of multibaryon clusters, anisotropy values, and cross sections for the production of single heavy fragments

Target	$\langle V_{\perp} \rangle$, cm/ns	K	σ_{SHF} , mb
^{238}U	0.47 ± 0.02	3.5 ± 0.3	120 ± 40
^{232}Th	0.46 ± 0.02	3.0 ± 0.2	110 ± 30
^{197}Au	0.52 ± 0.02	2.3 ± 0.2	10 ± 5

The longitudinal component V_{\parallel} of the multibaryon-cluster velocity can be estimated in terms of the mean momentum transfer to the residual nucleus from the incident proton in events involving a coincident heavy fragment [2] or in terms of the presumed value of the excitation energy of the residual nucleus. In either case, the longitudinal velocity V_{\parallel} is less than the transverse velocity V_{\perp} and affects the parameter K only slightly.

The values of the anisotropy K that were averaged over all events are quoted in Table 3. In the following, they will be used to determine the cross section σ_{SHF} . Large values of K partly result from the application of the selection criterion $V_{\text{SHF}} \geq 0.45$ cm/ns.

In [1, 4], it was shown that the mean transverse velocity of the ensemble of particles accompanying

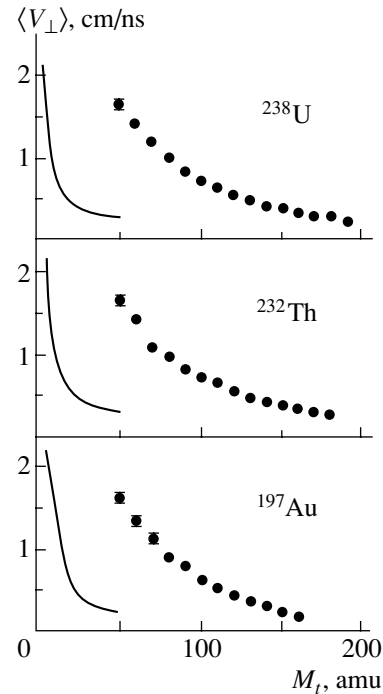


Fig. 6. Mean transverse velocity over the ensemble of particles accompanying (points) single heavy fragments and (curves, their statistical uncertainties being negligibly small) binary-fission fragments as a function of the total mass of these particles.

Table 4. Probabilities of the detection of AC–X events, X = BHF, SHF, or AC (in percent)

Target	W_{AC-BHF}	W_{AC-SHF}	W_{AC-AC}
^{238}U	18 ± 2	48 ± 5	34 ± 4
^{232}Th	18 ± 2	52 ± 4	30 ± 3
^{197}Au	26 ± 2	32 ± 2	42 ± 3

fission fragments as a function of their total mass M_t can be closely approximated by the formula

$$\langle V_{\perp} \rangle = \sqrt{2/\pi} [(\sigma_p^{\text{app}})^2 + Nq^2/3]^{1/2}/M_t, \quad (6)$$

where $(\sigma_p^{\text{app}})^2$ is the instrumental variance of the momentum distribution, N is the mass number corresponding to M_t , and q is the root-mean-square momentum of accompanying particles.

For all events characterized by large values of ΔM , the missing-mass dependences of $\langle V_{\perp} \rangle$ were presented in [4, 20–22]. Later on, it was established that the variances of the distributions of the disbalance of the coincident-heavy-fragment and the fission-fragment momenta are nearly identical [2]. Therefore, it is events involving a single heavy fragment that are primarily responsible for the emergence of a maximum around $\Delta M \approx 70$ amu in these dependences.

Although the dependences for fission fragments and single heavy fragments are qualitatively similar in Fig. 6, the latter cannot be approximated by formula (6), because the momentum distributions of single heavy fragments are not normal distributions with zero expectation value. Such an approximation would lead to a systematic overestimation of the root-mean-square momentum q .

Estimating cross sections for reactions leading to the production of single-heavy fragments.

By using the relative method for cross-section measurements, one can obtain an estimate of σ_{SHF} on the basis of the relevant formula from [16] and the values of σ_f [23]. Specifically, we have

$$\sigma_{\text{SHF}} = \frac{2\pi}{\Delta\Omega} \frac{\sigma_f G N_{AC-SHF}}{\langle n_{AC}^{(\text{SHF})} \rangle K N_{\text{FF-FF}}}, \quad (7)$$

where G is a geometric factor that is equal to the ratio of the number of fission events recorded in collinear geometry to their number that could be recorded with the aid of a double-arm spectrometer equipped with $\Delta\Omega$ and $(4\pi - \Delta\Omega)$ sensors [16].

The results are presented in Table 3. Thus, the nuclear reaction that we revealed can significantly contribute to the measured cross sections for nuclear fission induced by high-energy protons if the measurement procedure used gives no way to identify fission fragments in mass or in kinetic energy and if the detection threshold is overly low.

Table 5. Mean masses and velocities of intermediate-mass fragments in IMF–IMF events and exponents τ in power-law approximations of the mass distributions of intermediate-mass fragments in IMF–SHF events

Target	$\langle M_{\text{IMF}} \rangle$, amu	$\langle V_{\text{IMF}} \rangle$, cm/ns	τ
^{238}U	17 ± 1	1.61 ± 0.03	3.1 ± 0.5
^{232}Th	14 ± 1	1.74 ± 0.04	3.2 ± 0.5
^{197}Au	11 ± 1	1.80 ± 0.04	2.2 ± 0.4

Integrated probabilities of the detection of reaction products. In Table 4, we present the integrated probabilities of the detection of AC–X events,

$$W_{AC-X} \quad (8)$$

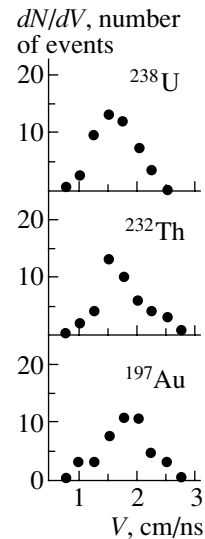
$$= N_{AC-X}/(N_{AC-BHF} + N_{AC-SHF} + N_{AC-AC}),$$

where X = BHF, SHF, or AC (BHF = FF + CHF).

For a ^{238}U target nucleus bombarded by 1-GeV protons, its binary fission induced by these protons is a dominant nuclear reaction (σ_f saturates 0.865 ± 0.036 of the total inelastic-interaction cross section σ_{in} [23]). According to our data, σ_{SHF} is $(0.07 \pm 0.02) \sigma_{\text{in}}$ for this target nucleus. Despite this, $W_{AC-SHF} > W_{AC-BHF}$. It can easily be shown that

$$\frac{W_{AC-SHF}}{W_{AC-BHF}} \approx \frac{\sigma_{\text{SHF}} \langle n_{AC}^{(\text{SHF})} \rangle}{\sigma_f \langle n_{AC}^{(\text{BHF})} \rangle} K. \quad (9)$$

Thus, high probabilities of the detection of AC–SHF events follow from a high multiplicity of accompanying clusters and from the anisotropy of their emission.

**Fig. 7.** Velocity distributions of intermediate-mass fragments recorded in coincidence at the incident-proton energy of 1 GeV.

2.3. Mean Velocities of Intermediate-Mass Fragments

In the thermal multifragmentation of heavy nuclei, the velocities of large clusters are less than those of single clusters having the same mass and originating from residual nuclei [11, 12, 24]. Our experiment recorded 42 (^{197}Au) to 49 (^{238}U) coincidences of intermediate mass fragments ($6 \leq M_{\text{IMF}} \leq 30$ amu) emitted in opposite directions. These statistics are insufficient for applying the method of correlation functions to data analysis. Figure 7 shows the velocity distribution of intermediate-mass fragments for such events. The mean values of the masses and velocities of intermediate-mass fragments are quoted in Table 5.

The velocity distributions of intermediate-mass fragments fall in between two natural reference values represented by the mean velocity of fission fragments and the mean velocity of clusters accompanying these fragments. That the reference values measured in our study for the ^{238}U target nucleus comply with data presented in [14] confirms the reliability of our experimental results.

For the ^{197}Au nucleus, the mean relative velocity of intermediate-mass fragments emitted in opposite directions, $\langle V_1 + V_2 \rangle = 3.6 \pm 0.1$ cm/ns, is compatible with the value of 3.8 cm/ns, which was measured for its multifragmentation induced by alpha particles of energy 800 MeV per nucleon [11]. For $E_\alpha = 1.0$ –3.6 GeV per nucleon, intermediate-mass fragments have somewhat higher velocities [12]. That the results of the measurements at the incident-proton energy of 1 GeV agree with those at incident-alpha-particle energies in the range 0.8–3.6 GeV per nucleon implies that, in both cases, the nuclear reactions in question are governed by the same mechanism.

The most probable kinetic energy (about 40 MeV) of single intermediate-mass fragments ($Z_{\text{IMF}} = 7$ charge units) emitted by ^{197}Au nuclei under the effect of 1-GeV protons [25] corresponds, at $\langle M_{\text{IMF}} \rangle \approx 15$ amu [24], to the root-mean-square velocity of 2.3 cm/ns. For the target-nucleus species mentioned immediately above and for $\langle M_{\text{IMF}} \rangle = 15$ amu, our experiment yielded the value of $\langle V_{\text{IMF}}^2 \rangle^{1/2} = 1.60 \pm 0.05$ cm/ns. Because of low velocities of recoil nuclei, single intermediate-mass fragments were not recorded by our double-arm spectrometer.

Within the errors, the M_{AC} dependences of the mean velocity and the mean kinetic energy of accompanying clusters are identical for AC–SHF and AC–AC events. Moreover, clusters in events of these two types display similar mass distributions distinguishing them from particles that accompany fission fragments [14]. At the incident-proton energy of 1 GeV,

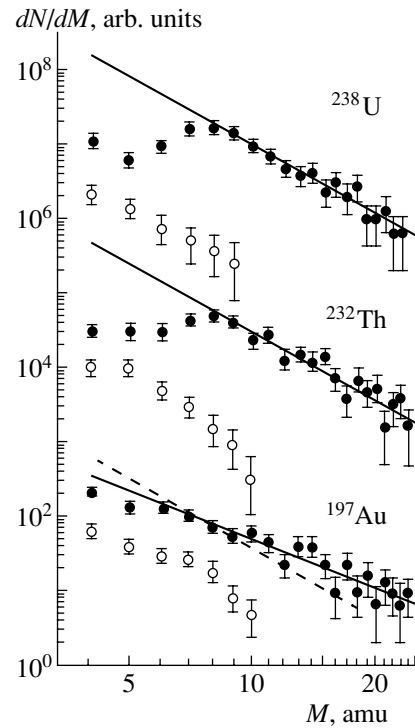


Fig. 8. Mass distributions of accompanying clusters in (closed circles) AC–SHF and (open circles) AC–FF events at the incident-proton energy of 1 GeV. The solid lines and the dashed line represent, respectively, power-law approximations of these mass distributions and the result from [25] for single intermediate-mass fragments.

reaction products accompanying two intermediate-mass fragments that are recorded in coincidence are therefore expected to include a single heavy fragment that missed the angular acceptance of the spectrometer.

2.4. Power-Law Approximation of the Mass Distributions of Clusters

The model of a spinodal disintegration of nuclei [6], as well as some other models not invoking the concept of a nuclear liquid, leads to a power-law dependence of the number of clusters on their mass:

$$N(M_{\text{AC}}) \propto M_{\text{AC}}^{-\tau}. \quad (10)$$

The validity of this power law for accompanying clusters that are formed in nuclear multifragmentation induced by relativistic particles has been confirmed in many studies. However, the mass distributions of actinide-multifragmentation products have not been studied so far in the threshold region of energies.

According to the results obtained in one run of our measurements, we plotted, in Fig. 8, the mass distributions of accompanying fragments in AC–FF

and in AC–SHF events. By using the method of least squares, the latter were fitted in terms of expression (10). The values of the exponent τ are quoted in Table 5.

The dependence of τ on the nuclear excitation energy is rather smooth and has a minimum around the value of 4 MeV per nucleon of the residual nucleus [8]. Therefore, the value of τ that we obtained for ^{197}Au can be used to estimate the excitation energy of the residual nucleus. For single intermediate-mass fragments emitted by ^{197}Au at the incident-proton energy of 1 GeV, the fitted value of the exponent is $\tau = 3.1 \pm 0.2$ and $E^* = 399 \pm 78$ MeV [25]. For the multiparticle emission of intermediate-mass fragments, the mean excitation energy of nuclei is expected to be higher than this value, but it must be lower than in the case where the multifragmentation of the same nuclear species is induced by ^{40}Ar ions of energy 30 MeV per nucleon ($\tau \approx 1.7 \pm 0.3$, $E^* \approx 640 \pm 90$ MeV [13]). The value of $\tau = 2.17 \pm 0.08$ ($E_p = 2.16$ GeV, $E^* \approx 540$ MeV) [8] is the closest to our results.

That Kotov *et al.* [25] failed to observe the multifragmentation of ^{197}Au at the incident-proton energy of 1 GeV is explained by a higher detection threshold in their experiment. Moreover, a comparison of the cross section for the nuclear reaction involving the emission of single intermediate-mass fragments [25] with the cross section that we determined for their multiparticle production (within the errors, it coincides with the value of σ_{SHF} in Table 3) shows that the latter process is much rarer at the energy value used. At greater length, this issue will be considered in the subsequent publication.

3. DISCUSSION OF THE RESULTS

3.1. Pseudoevaporation Channel

The detection of single heavy fragments in coincidence with reaction products accompanying them was first reported by Wilkins *et al.* [26]. In events characterized by copious alpha-particle emission, these authors observed single heavy fragments among products of ^{238}U disintegration induced by 11.5-GeV protons. The most probable mass of single heavy fragments recorded in their experiment also proved to be less than that of fission fragments, and the mean velocity of the former even exceeded the value of 0.6 cm/ns determined in our study. The reason is that, in a nucleus undergoing disintegration, the Coulomb repulsion from a single heavy fragment has a stronger effect than the interaction of accompanying clusters with one another, with the result that, at the freeze-out instant a single heavy fragment and the ensemble of accompanying clusters are at

opposite points of the nucleus [10]. This entails high momenta of single heavy fragments, the anisotropy of accompanying-cluster emission, a comparatively high velocity of their center of mass, and low relative velocities of intermediate-mass fragments.

On the basis of three signatures (a high multiplicity of accompanying clusters, low velocities of intermediate-mass fragments, and exponents in the power-law approximations of their mass distributions), events in which our experiment recorded single heavy fragments must be treated as evidence for the pseudoevaporation channel in the multifragmentation of heavy nuclei. For ^{238}U , the cross section for the pseudoevaporation channel at the incident-proton energy of 1 GeV proved to be one order of magnitude larger than the cross section for pseudofission (producing coincident heavy fragments).

The multifragmentation of ^{197}Au nuclei that is induced by 1-GeV protons proved to be a rare phenomenon: $\sigma_{\text{SHF}} < 1\% \sigma_{\text{in}}$; for actinides, however, we have $\sigma_{\text{SHF}} \approx 7\% \sigma_{\text{in}}$. In all probability, this is because actinide nuclei are rather loosely bound. Under the effect of a fast branched cascade, they readily break up into clusters as soon as this becomes allowed by the internal energy. In our opinion, this looseness is due to large nuclear charges and dimensions. A branched-cascade-induced short-term reduction of the binding energy and the impact heating of the nucleus involved lead to its disintegration under the concerted effect of Coulomb repulsion forces and the thermal motion of nucleons.

It should be noted that the non-steady-state process through which part of the thermal energy is converted into the energy of collective motion in a specific direction (explosion mechanism) can be responsible, in a somewhat reduced form, for the high-energy fission of nuclei as well [27].

3.2. Reason behind the Deviation of Mass Distributions of Clusters Emitted in the Multifragmentation of Heavy Target Nuclei from a Power-Law Approximation

For actinide nuclei, a feature peculiar to the mass distributions of accompanying clusters (see Fig. 8) is that there is a deviation from a power law in the region $M_{\text{AC}} < 8$ amu. This effect cannot be explained by methodological factors [14].

In [28], the charge distribution of intermediate-mass fragments, which has a maximum in the region of ^{12}C , was obtained in simulating the multifragmentation of ^{197}Au nuclei. A low multiplicity of light charged particles resulted from a suppression of high multiplicities in the condensation of dilute nuclear matter into clusters. For the initial condition in that

calculation, use was made, however, of the doubled density in the original nucleus, with the result that its breakup occurred through an intermediate form with an internal void. It is unlikely that this situation is realized at the initial-proton energy of 1 GeV.

At the same time, large clusters can grow at the expense of small ones owing to nucleon exchange through the gas phase [29, 30]. The tendency toward the growth of primary clusters is observed at temperatures considerably below the point of a liquid–gas phase transition. The degree to which this tendency has time to develop depends on the duration of the period over which the two phases coexist. The multifragmentation process, which proceeds at a lower rate in the threshold energy region [31], is expected to result in the reduction of the number of light charged particles, first of all, for ^{238}U . This is suggested by the mean velocities of accompanying clusters in events featuring single heavy fragments (see Table 1), by the values of τ (Table 5), and by the fact that deformed shells manifest themselves in the mass distribution of coincident heavy fragments.

In our opinion, the fact that, in the multifragmentation of actinide nuclei, the power law for small clusters is violated in the threshold energy region is yet another indication that expanding nuclear matter occurs in a two-phase state. In experiments with nuclei, this effect was observed for the first time.

4. CONCLUSION

The fission of heavy nuclei that is induced by 1-GeV protons has been studied with the aid of a double-arm spectrometer [1], and the reaction of thermal multifragmentation has been discovered. Among the products of this reaction, there are clusters emerging with a high multiplicity and accompanying the formation of one or, more rarely, two heavy fragments. The mean velocities of large accompanying clusters and the exponent in the power-law approximation of their mass distributions proved to be less than the corresponding quantities in the reaction leading to the emission of single accompanying clusters having the same mass.

The majority of the features of this reaction undergo no qualitative changes in response to the increase in the incident-particle energy to $E_p = 2.16\text{--}8.1$ GeV (protons) [8] or $E_\alpha = 0.8\text{--}3.6$ GeV/nucleon (alpha particles) [11, 12]. However, we were able to reveal two features unobserved so far in the experimental investigations into the multifragmentation of nuclei. First, there is a deviation from the power law in the region $M_{AC} < 8$ amu. We believe that this effect is of a threshold character and attribute it to the decay of some accompanying clusters whose radius is less than the critical one (this occurs via nucleon

exchange between the clusters within an expanding nucleus). Second, we found that, in events leading to the production of single heavy fragments, the emission of accompanying clusters is anisotropic, which is indicative of an explosive disintegration of nuclei here.

The reaction mechanism suggested by the present analysis of experimental information obtained in the threshold energy region is consistent with the concept of an evolutionary expanding emitted source [24]. A partial transformation of a chaotic thermal motion of nucleons into an ordered radial flow and the possible emission of neutrons and light charged particles at early stages of the expansion of the residual nucleus reduce the excitation energy of this nucleus to such an extent that large clusters begin to grow at the expense of the disappearance of smaller ones. This process ends up in the formation of one or two especially large fragments accompanied by a few clusters. In this case, the separation of coincident heavy fragments becomes possible under two conditions: not only must these fragments be near the ground state, but it is also required that their binding energy be maximal.

The cross section for the multifragmentation of ^{238}U , ^{232}Th , and ^{197}Au nuclei at the incident-proton energy of 1 GeV has been estimated here at 130 ± 40 (coincident heavy fragments being included), 110 ± 30 , and 10 ± 5 mb, respectively. That the cross section for the reaction being studied depends greatly on the charge of the target nucleus and that the emission of clusters is anisotropic suggest that Coulomb interaction plays an important role in the multifragmentation reaction. We deem that, in the threshold energy region, thermal multifragmentation proceeds through an explosion of nuclei rather than through their boiling.

ACKNOWLEDGMENTS

Our work was supported by an individual grant from the International Science Foundation.

REFERENCES

1. Yu. A. Chestnov *et al.*, *Yad. Fiz.* **45**, 19 (1987) [*Sov. J. Nucl. Phys.* **45**, 11 (1987)].
2. Yu. A. Chestnov and B. Yu. Sokolovsky, *Yad. Fiz.* **60**, 811 (1997) [*Phys. At. Nucl.* **60**, 720 (1997)].
3. B. L. Gorshkov *et al.*, *Pis'ma Zh. Éksp. Teor. Fiz.* **37**, 60 (1983) [*JETP Lett.* **37**, 72 (1983)].
4. Yu. A. Chestnov *et al.*, Preprint No. 941, LIYaF (Leningrad Nuclear Physics Institute, Leningrad, 1984).
5. Yu. A. Chestnov *et al.*, *Pis'ma Zh. Éksp. Teor. Fiz.* **40**, 490 (1984) [*JETP Lett.* **40**, 1326 (1984)].
6. J. P. Bondorf *et al.*, *Nucl. Phys. A* **443**, 321 (1985); **444**, 460 (1985).
7. I. N. Mishustin, *Nucl. Phys. A* **630**, 111c (1998).

8. V. A. Karnaukhov *et al.*, *Yad. Fiz.* **62**, 272 (1999) [*Phys. At. Nucl.* **62**, 237 (1999)].
9. D. H. E. Gross, *Rep. Prog. Phys.* **53**, 605 (1990).
10. O. Schapiro *et al.*, *Nucl. Phys. A* **568**, 333 (1994).
11. D. H. E. Gross *et al.*, *Phys. Lett. B* **224**, 29 (1989).
12. Bao-An Li *et al.*, *Phys. Lett. B* **335**, 1 (1994).
13. R. Trockel *et al.*, *Phys. Rev. C* **39**, 729 (1989).
14. Yu. A. Chestnov and B. Yu. Sokolovsky, Preprint No. 2314, PIYaF (Petersburg Nuclear Physics Institute, Gatchina, 1999).
15. A. I. Obukhov and G. E. Solyakin, *Pis'ma Zh. Éksp. Teor. Fiz.* **55**, 547 (1992) [*JETP Lett.* **55**, 568 (1992)].
16. Yu. A. Chestnov and B. Yu. Sokolovsky, Preprint No. 2350, PIYaF (Petersburg Nuclear Physics Institute, Gatchina, 2000).
17. A. A. Zhdanov *et al.*, Preprint No. 1693, LIYaF (Leningrad Nuclear Physics Institute, Leningrad, 1991).
18. N. P. Filatov *et al.*, Preprint No. 1683, LIYaF (Leningrad Nuclear Physics Institute, Leningrad, 1991).
19. A. S. Goldhaber, *Phys. Lett. B* **53B**, 306 (1974).
20. A. A. Zhdanov *et al.*, *Pis'ma Zh. Éksp. Teor. Fiz.* **54**, 311 (1991) [*JETP Lett.* **54**, 304 (1991)].
21. A. A. Zhdanov *et al.*, *Yad. Fiz.* **57**, 1210 (1994) [*Phys. At. Nucl.* **57**, 1143 (1994)].
22. G. E. Solyakin and A. V. Kravtsov, *Phys. Rev. C* **54**, 1798 (1996).
23. L. A. Vaishnene *et al.*, *Z. Phys. A* **302**, 143 (1981).
24. G. Wang *et al.*, *Phys. Rev. C* **60**, 014603 (1999).
25. A. A. Kotov *et al.*, *Nucl. Phys. A* **583**, 575c (1995).
26. B. D. Wilkins *et al.*, *Phys. Rev. C* **19**, 856 (1979).
27. S. A. Karamian and I. V. Kuznetsov, Preprint No. R7-10009, OIYaI (Joint Institute for Nuclear Research, Dubna, 1976).
28. A. Guarnera *et al.*, *Phys. Lett. B* **403**, 191 (1997).
29. V. G. Bořko *et al.*, *Fiz. Élem. Chastits At. Yadra* **22**, 675 (1991) [*Sov. J. Part. Nucl.* **22**, 326 (1991)].
30. L. V. Bravina and E. E. Zabrodin, *Phys. Rev. C* **54**, R464 (1996).
31. E. Bauge *et al.*, *Phys. Rev. Lett.* **70**, 3705 (1993).

Translated by A. Isaakyan

ELEMENTARY PARTICLES AND FIELDS
Theory

Weak and Magnetic Inelastic Scattering of Antineutrinos on Atomic Electrons*

S. A. Fayans[†], L. A. Mikaelyan, and V. V. Sinev

Russian Research Centre Kurchatov Institute, pl. Kurchatova 1, Moscow, 123082 Russia

Received April 5, 2000; in final form, July 12, 2000

Abstract—Neutrino scattering on electrons is considered as a tool for laboratory searches for the neutrino magnetic moment. Inelastic $\bar{\nu}_e e^-$ scattering on electrons bound in the germanium ($Z = 32$) and iodine ($Z = 53$) atoms is studied for antineutrinos generated in a nuclear reactor core and in ^{90}Sr – ^{90}Y and ^{147}Pm artificial sources. On the basis of the relativistic Hartree–Fock–Dirac model, both the magnetic- and weak-scattering cross sections are calculated for the recoil electron energy range between 1 and 100 keV, where a higher sensitivity to the neutrino magnetic moment could be achieved. Particular attention is paid to an approximate procedure that allows us to take into account the effects of atomic binding on the inelastic-scattering spectra in a simple way. © 2001 MAIK “Nauka/Interperiodica”.

1. INTRODUCTION

In the present paper, we consider some issues of low-energy neutrino physics that could be of importance for current and future experiments aimed at seeking a “large” neutrino magnetic moment. In [1], we studied the inelastic weak and magnetic scattering of reactor antineutrinos on the K - and L -shell electrons in the iodine atom. Here, we extend our calculations to the iodine M -shell electrons and present the results for the K - and L -shell electrons bound in a germanium atom. In addition to reactor $\bar{\nu}_e$'s, we also consider electron antineutrinos emitted by ^{90}Sr – ^{90}Y and ^{147}Pm artificial sources. The use of artificial $\bar{\nu}_e$ sources and semiconductor germanium detectors in experiments seeking the neutrino magnetic moment has been considered in [2, 3] (see also references therein).

For reactor $\bar{\nu}_e$'s, it was shown in [1] that free-scattering differential cross sections can be approximately converted into inelastic ones by means of a simple step-function transformation. Here, we investigate the accuracy of such a recipe in more detail, with different $\bar{\nu}_e$ energy spectra.

As an input, we use a standard power-law reactor $\bar{\nu}_e$ spectrum corrected for antineutrinos from beta emitters produced in a core in (n, γ) reactions [4]; for ^{90}Sr – ^{90}Y and ^{147}Pm sources, we use the spectra tabulated in [5]. The chosen input spectra are plotted in Fig. 1. The calculated recoil-electron energy spectra with these three sources for the case of free $\bar{\nu}_e e^-$ scattering are presented in Fig. 2. In

these calculations, use was made of Eqs. (2)–(4) from [1]. The free magnetic- and weak-scattering recoil spectra are denoted by S_{free}^M and S_{free}^W , respectively. All calculations in the present paper have been performed for the neutrino magnetic moment $\mu = 2 \times 10^{-11} \mu_B$ (μ_B is the Bohr magneton), the constants of electroweak interaction being the same as in [1].

We consider issues that can be of importance for current and future experiments aimed at seeking a “large” neutrino magnetic moment.

2. INELASTIC SCATTERING ON ATOMIC ELECTRONS

In this section, we consider the $\bar{\nu}_e$ scattering on electrons bound in iodine and germanium atoms. The energies and wave functions of discrete single-electron states are calculated within the relativistic self-consistent Hartree–Fock–Dirac (HF–D) approach, with a local exchange–correlation potential. The wave functions of outgoing electrons in the continuum were obtained by numerically integrating the Dirac equation in the HF–D mean field. The details of this approach can be found in [6]. The calculated energies of some electron subshells are listed in the table; they agree with spectroscopic data within a few percent.

For the iodine atom, the cross sections for weak and magnetic inelastic $\bar{\nu}_e e^-$ scattering have been calculated for K , L , and M shells, which contain, in total, 28 electrons, the remaining 25 electrons with binding energies less than 200 eV being considered to be free. For germanium, the atomic binding of K - and L -shell electrons has been taken into account,

*This article was submitted by the authors in English.

[†]Deceased.

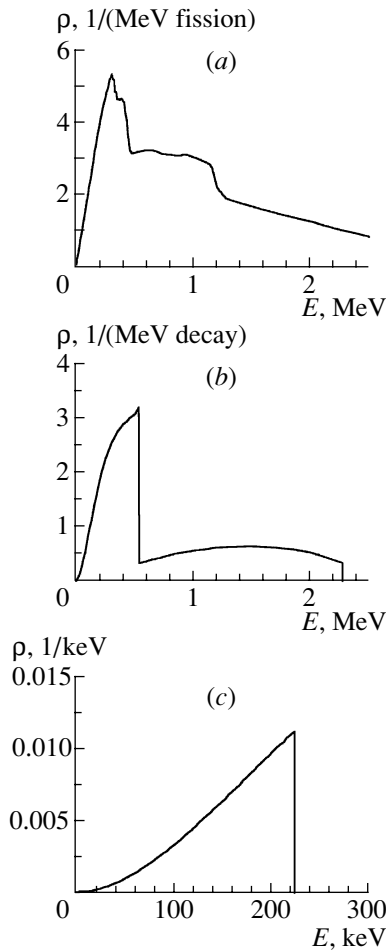


Fig. 1. Antineutrino energy spectra from three different sources: (a) reactor $\bar{\nu}_e$ (only the low-energy part is shown), (b) $\bar{\nu}_e$'s from ^{90}Sr – ^{90}Y source (two $\bar{\nu}_e$'s per sequential ^{90}Sr – ^{90}Y decay), and (c) $\bar{\nu}_e$ from a ^{147}Pm source.

all the other electrons being treated as free particles. We denote by S_{in}^M and S_{in}^W the inelastic-recoil energy spectra for electrons knocked out from an atom as the result of magnetic and weak interactions, respectively.

The results obtained by calculating the recoil

Calculated HF–D binding energies (in keV) of some electron shells in the iodine and germanium atoms

Atom	Shell									
	<i>K</i>	<i>L</i> _I	<i>L</i> _{II}	<i>L</i> _{III}	<i>M</i> _I	<i>M</i> _{II}	<i>M</i> _{III}	<i>M</i> _{IV}	<i>M</i> _V	
	1 <i>s</i> _{1/2}	2 <i>s</i> _{1/2}	2 <i>p</i> _{1/2}	2 <i>p</i> _{3/2}	3 <i>s</i> _{1/2}	3 <i>p</i> _{1/2}	3 <i>p</i> _{3/2}	3 <i>d</i> _{3/2}	3 <i>d</i> _{5/2}	
I	32.9	5.09	4.78	4.48	1.03	0.90	0.84	0.61	0.60	
Ge	10.9	1.35	1.22	1.18	0.18					

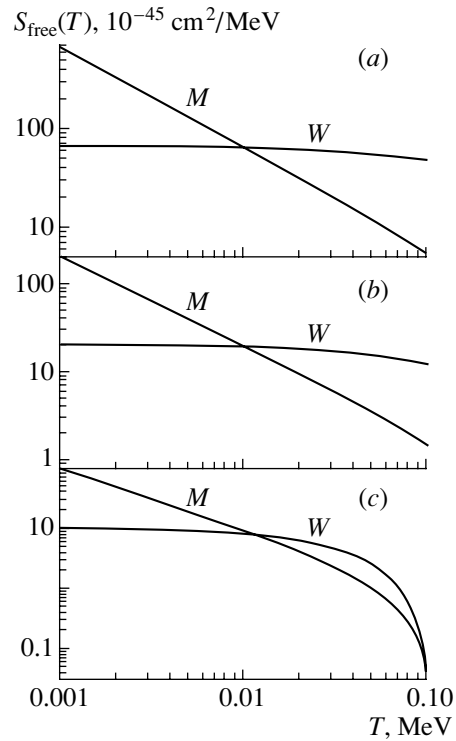


Fig. 2. Kinetic-energy spectra of recoil electrons for magnetic (*M*) and weak (*W*) $\bar{\nu}_e$ scattering on free electrons for (a) reactor, (b) ^{90}Sr – ^{90}Y , and (c) ^{147}Pm antineutrinos.

spectra S_{in}^M and S_{in}^W are shown in Figs. 3a and 4a, respectively, for electrons knocked out from different electronic subshells of an iodine atom by $\bar{\nu}_e$'s from a ^{90}Sr – ^{90}Y source. Their ratios to the corresponding free-recoil spectra are plotted in Figs. 3b and 4b. It can be seen that magnetic scattering is strongly suppressed by the atomic-binding effect for the *K*- and *L*-shell electrons; even for the *M* shell, with a lower binding energy, the effect of suppression is quite noticeable. Atomic electron binding affects the weak-scattering cross sections as well, but to a much weaker extent. This is unfavorable for the detectability of the neutrino magnetic moment.

As follows from our calculations, the ratios $S_{\text{in}}^{M,W}(T)/S_{\text{free}}^{M,W}(T)$ for other sources and target atoms are typically of the same character as those presented in Figs. 3 and 4.

Cross sections for weak and magnetic inelastic $\bar{\nu}_e e^-$ scattering were found for *K*, *L*, and *M* shells, which contain 28 of the 53 electrons of the iodine atom, the remaining 25 electrons, with binding energies less than 200 eV, being considered as free particles. For germanium, the atomic binding of *K* and *L* electrons was taken into account, the outer electrons being treated as free particles.

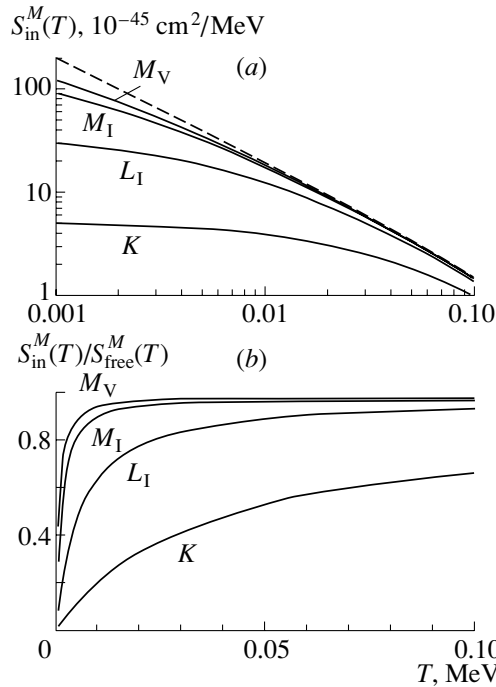


Fig. 3. Inelastic magnetic scattering of ^{90}Sr – ^{90}Y antineutrinos on iodine atomic electrons. The curves correspond to different subshells and are labeled in the same way as in the table: (a) electron-kinetic-energy spectra (the dashed curve represents results for scattering on free electrons) and (b) ratios of the inelastic spectra to the free spectrum.

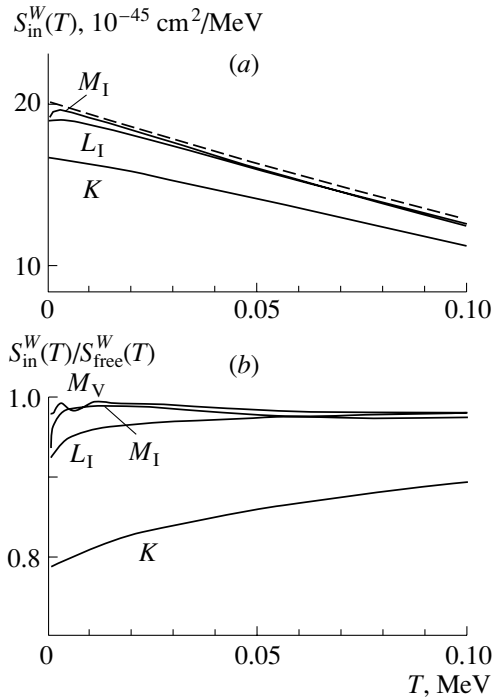


Fig. 4. As in Fig. 3, but for weak scattering.

Let us now introduce, instead of the electron kinetic energy T , the energy transfer q defined by

$$q = \Delta E = \epsilon_i + T, \quad (1)$$

where ΔE is the neutrino energy loss in the inelastic-scattering process and ϵ_i is the electron binding energy in the atomic shell being considered (nuclear recoil is neglected). For scattering on free electrons, one has $\epsilon = 0$ and $q = T$. In practice, for the majority of detectors, q is just the total energy that could be recorded as a visible energy of an event, since soft x rays and Auger electrons ejected to fill a vacancy in the shell are absorbed in the detector sensitive volume and their summed energy ϵ_i is added to the kinetic energy T of the recoil electron.

It was demonstrated in [1] that, for reactor antineutrinos, the inelastic-scattering spectrum $S_{in}^i(q)$ for electrons from the subshell i of the iodine atom can be obtained from the free-scattering spectrum $S_{free}(q)$ taken at the same visible energy q , provided that one introduces the response function $R^i(q, \epsilon_i)$ defined by the relation

$$S_{in}^i(q) = R^i(q, \epsilon_i) S_{free}(q), \quad (2)$$

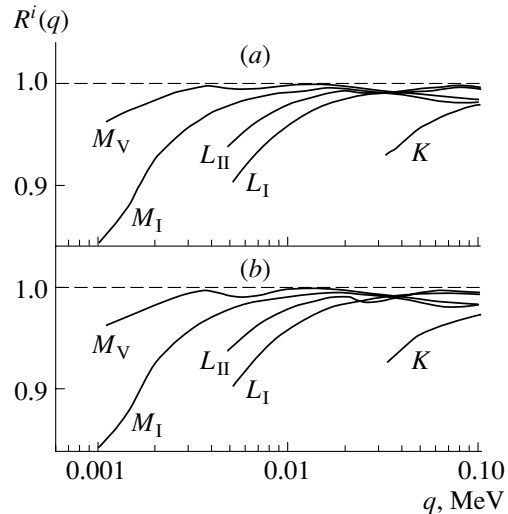


Fig. 5. “Exact” response functions $R^i(q, \epsilon_i) = S_{in}^i(q)/S_{free}(q)$ for inelastic magnetic $\bar{\nu}_e$ scattering on the K -, L -, and M -shell electrons of an iodine atom. The curves are labeled with the corresponding subshells as in the table: (a) results for reactor antineutrinos and (b) results for $\bar{\nu}_e$'s from a ^{90}Sr – ^{90}Y source.

where $R^i(q, \epsilon_i)$ is approximated by the Heaviside step function $\theta(q - \epsilon_i)$,

$$R^i(q, \epsilon_i) \approx \theta(q - \epsilon_i) = \begin{cases} 1 & \text{for } q > \epsilon_i \\ 0 & \text{for } q < \epsilon_i. \end{cases} \quad (3)$$

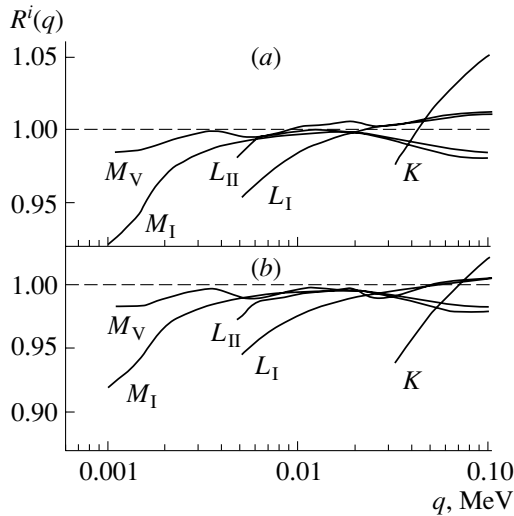


Fig. 6. As in Fig. 5, but for weak scattering.

In the following, this will be referred to as the zero (or step-function) approximation.

For each antineutrino source under consideration, we now calculate the “exact” spectra $S_{\text{in}}^i(q)$ of electrons knocked out from the iodine and germanium atomic subshells in magnetic and weak $\bar{\nu}_e e^-$ scattering, evaluate the “exact” partial response functions $R^i(q, \epsilon_i) \equiv S_{\text{in}}^i(q)/S_{\text{free}}(q)$, and analyze their deviations from the zero approximation of Eq. (3). The term “exact” means that the calculations are performed within the HF–D model. Some of the results that we obtained are discussed below.

It can be seen in Figs. 5 and 6 that, for the *L*- and *M*-shell electrons, the “exact” response functions for magnetic and weak inelastic scattering differ only slightly from each other. They, however, are close to

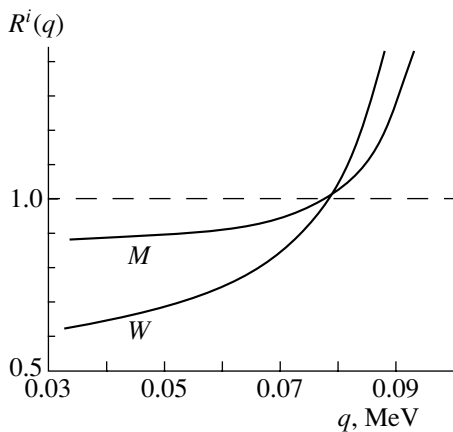


Fig. 7. “Exact” response functions for magnetic (*M*) and weak (*W*) $\bar{\nu}_e$ scattering on the iodine *K*-shell electrons for a ^{147}Pm source.

unity everywhere with the exception of rather narrow regions near the corresponding threshold energies $q = \epsilon_i$. In the case of magnetic scattering, the same is true for the *K*-shell electrons; on the other hand, the weak-scattering *K*-shell response function exceeds unity at sufficiently high energies. This reflects the effect of the atomic binding at relativistic energies [7], which leads to an enhancement of the weak inelastic cross section by a factor of $1 + O(\alpha^2 Z^2) \sim 1 + O(\epsilon_K/mc^2)$ (α is the fine-structure constant, m is the electron mass, and ϵ_K is the *K*-shell binding energy); this effect might be of relative importance only for the tightly bound *K*-shell electrons.

It can be seen in Figs. 7 and 8 that, for soft ^{147}Pm antineutrinos, the zero approximation does not provide a good fit for weak scattering on the *K*-shell electrons either in the iodine or in the germanium atom. We also note that the step-function approximation is strongly violated at energy transfers around the free-scattering upper limit $q^{\text{max}} = 2E^2/(2E + mc^2)$ (E is the incoming $\bar{\nu}_e$ energy). For $q > q^{\text{max}}$, the free-scattering cross sections are identically zero; the inelastic ones are small, but they are still finite in the “kinematically forbidden” region beyond q^{max} [6, 7]. This tendency can be clearly seen for all iodine and germanium subshells: for energy transfers in the region $q > 80$ keV, the ratios $S_{\text{in}}^i(q)/S_{\text{free}}(q)$ increase fast with q , as is demonstrated in Figs. 7–9.

3. ASSESSING THE APPROPRIATENESS OF THE STEP-FUNCTION APPROXIMATION

In order to obtain an “exact” visible-energy-transfer electron spectrum $S_{\text{in}}^Z(q)$ for a given atom,

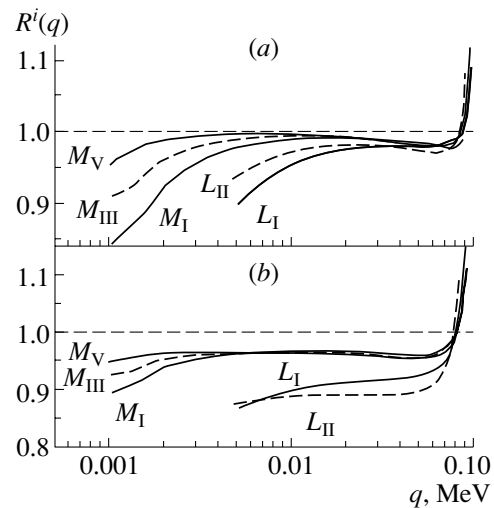


Fig. 8. “Exact” response functions for (a) magnetic and (b) weak $\bar{\nu}_e$ scattering on the iodine *L*- and *M*-shell electrons for a ^{147}Pm source. The curves are labeled with the corresponding subshells as in the table.

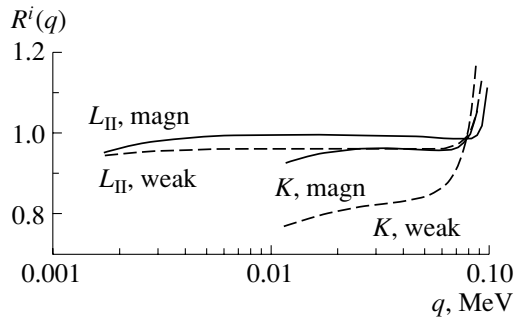


Fig. 9. “Exact” response functions for $\bar{\nu}_e$ scattering on the germanium K - and L -shell electrons for a ^{147}Pm source. The curves are labeled with the corresponding subshells as in the table.

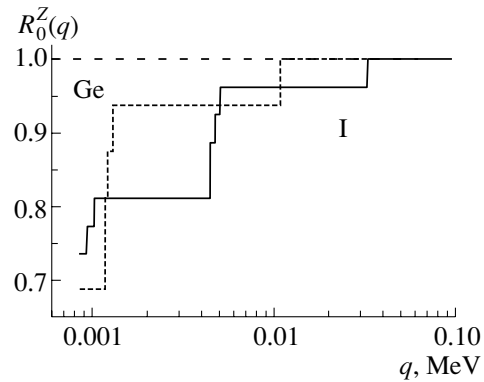


Fig. 10. Zero-approximation response functions calculated according to Eq. (6) for iodine and germanium atoms.

we have to sum all the partial contributions $S_{\text{in}}^i(q)$ from different subshells; that is,

$$\begin{aligned} S_{\text{in}}^Z(q) &= \sum (n_i/Z) S_{\text{in}}^i(q) \\ &= S_{\text{free}}(q) \sum (n_i/Z) R^i(q, \epsilon_i), \end{aligned} \quad (4)$$

where n_i is the number of electrons in the i th subshell, the spectrum being normalized to one electron. According to (4), the “exact” response function for the entire atom has the form

$$R^Z(q) \equiv S_{\text{in}}^Z(q)/S_{\text{free}}(q) = \sum (n_i/Z) R^i(q, \epsilon_i); \quad (5)$$

accordingly, the atomic response function in the zero approximation reads

$$R_0^Z(q) = \sum (n_i/Z) \theta(q - \epsilon_i). \quad (6)$$

One sees that R_0^Z is defined only by a set of the shell energies ϵ_i and the shell occupancies n_i of a particular atom. It takes the same value for magnetic and for weak scattering and is independent of the $\bar{\nu}_e$ source. For the iodine and germanium atoms, the functions R_0^Z are shown in Fig. 10.

To check the validity of the step-function approximation for the three $\bar{\nu}_e$ sources considered here, we have calculated the “exact” electron-energy spectra $S_{\text{in}}^Z(q)$ for weak and magnetic $\bar{\nu}_e$ scattering on these two atoms. We have obtained, in total, 12 different spectra. Twelve corresponding “exact” response functions (5) have then been evaluated and compared with those derived in the zero approximation of Eq. (6). The main output of this comparison can be summarized as follows: in the energy range $q = (1.5\text{--}100)$ keV for reactor and $^{90}\text{Sr}\text{--}^{90}\text{Y}$ $\bar{\nu}_e$ sources and in the range $q = (1.5\text{--}80)$ keV for a ^{147}Pm $\bar{\nu}_e$ source, the relative deviation $|R_0^Z - R^Z|/R_0^Z$ does not exceed 1.5–2%, with the exception of the case where ^{147}Pm $\bar{\nu}_e$'s undergo weak scattering on an iodine atom (there the deviation can reach 3–4%).

4. CONCLUSION

A simple prescription has been formulated for taking into account the effects of atomic-electron binding: to a good approximation, a visible-energy single-electron spectrum for the atomic inelastic $\bar{\nu}_e e^-$ scattering can be obtained by multiplying the free-electron spectrum by the “zero response function” $R_0^Z = \sum (n_i/Z) \theta(q - \epsilon_i)$. This step-function approximation can be safely used in the majority of current and future experiments aimed at searches for the neutrino magnetic moment.

We note, however, that this prescription is not universal. It can be used for some specific, though practically, important cases like those considered in the present paper. For much softer antineutrinos (e.g., those from a tritium source), direct accurate calculations of the cross sections for $\bar{\nu}_e e^-$ scattering on atomic electrons are needed.

ACKNOWLEDGMENTS

This work was supported in part by the Russian Foundation for Basic Research (project no. 00-15-96708).

REFERENCES

1. V. I. Kopeikin, L. A. Mikaelyan, V. V. Sinev, and S. A. Fayans, *Yad. Fiz.* **60**, 2032 (1997) [*Phys. At. Nucl.* **60**, 1859 (1997)].
2. V. N. Kornoukhov, *Yad. Fiz.* **61**, 1352 (1998) [*Phys. At. Nucl.* **61**, 1250 (1998)]; B. R. Bergelson *et al.*, *Yad. Fiz.* **61**, 1347 (1998) [*Phys. At. Nucl.* **61**, 1245 (1998)]; L. A. Mikaelyan, V. V. Sinev, and S. A. Fayans, *Pis'ma Zh. Éksp. Teor. Fiz.* **67**, 435 (1998) [*JETP Lett.* **67**, 453 (1998)].
3. A. G. Beda, E. V. Demidova, A. S. Starostin, and M. B. Voloshin, *Yad. Fiz.* **61**, 72 (1998) [*Phys. At. Nucl.* **61**, 66 (1998)].

4. A. M. Bakalyarov, V. I. Kopeikin, and L. A. Mikaelyan, *Yad. Fiz.* **59**, 1225 (1996) [*Phys. At. Nucl.* **59**, 1171 (1996)]; V. I. Kopeikin, L. A. Mikaelyan, and V. V. Sinev, *Yad. Fiz.* **60**, 230 (1997) [*Phys. At. Nucl.* **60**, 172 (1997)].
5. V. G. Aleksankin *et al.*, *Beta and Anti-Neutrino Nuclear Radiation: A Reference Book*, Ed. by P. M. Rubtsov (Énergoatomizdat, Moscow, 1989).
6. S. A. Fayans, V. Yu. Dobretsov, and A. B. Dobrotsvetov, *Phys. Lett. B* **291**, 1 (1992); V. Yu. Dobretsov, A. B. Dobrotsvetov, and S. A. Fayans, *Yad. Fiz.* **55**, 2126 (1992) [*Sov. J. Nucl. Phys.* **55**, 1180 (1992)].
7. S. A. Fayans, V. Yu. Dobretsov, and A. B. Dobrotsvetov, in *Proceedings of the III International Symposium on Weak and Electromagnetic Interactions in Nuclei (WEIN-92), Dubna, 1992*, Ed. by Ts. D. Vylov (World Sci., Singapore, 1992), p. 773.

ELEMENTARY PARTICLES AND FIELDS

Theory

Effectively Two-Dimensional Mechanism of Axion and Neutrino Bremsstrahlung in the Interaction of Electrons with Nuclei in a Magnetic Field

V. V. Skobelev*

Moscow State Industrial University, Moscow, 109280 Russia

Received March 20, 2000

Abstract—Axion and neutrino bremsstrahlung from electrons in the processes $e(Ze) \rightarrow e(Ze) a(\nu\bar{\nu})$ is considered within the proposed two-dimensional covariant method for calculating Feynman diagrams in an external magnetic field. General expressions for squared matrix elements, as well as for the probability and power of this radiation, are obtained for a nonrelativistic nondegenerate electron gas. The energy scale f_a characteristic of the violation of global Peccei–Quinn symmetry is constrained by comparing the contributions of the above processes to the emissivity of magnetic neutron stars. © 2001 MAIK “Nauka/Interperiodica”.

1. INTRODUCTION

Since the formulation of the Standard Model [1, 2], attempts have repeatedly been made to extend it by introducing hypothetical pseudoscalar particles emerging upon a spontaneous breakdown of global symmetries. The axion, whose possible existence is associated with $U(1)_{PQ}$ symmetry introduced by Peccei and Quinn [3], seems to be the most popular candidate for such particles. The axion hypothesis makes it possible to explain, in the most natural way, the exact CP invariance of strong interactions; in the astrophysical respect, the small dynamical axion mass m_a that arises owing to mixing with the neutral pion, could provide the bulk of cold dark matter in the Universe [4]. Astrophysical considerations make it possible to set rather stringent upper and lower limits on the possible values of the axion mass [5],

$$10^{-5} \lesssim m_a \lesssim 10^{-2} \text{ eV}, \quad (1)$$

and, hence, on the energy scale of f_a of $U(1)_{PQ}$ breakdown, because this scale and the axion mass are related as [6]

$$m_a \simeq 0.6 \times 10^{-3} (10^{10} \text{ GeV}/f_a) \text{ eV}. \quad (2)$$

It can be seen that f_a , in just the same way as f for different global symmetries, is extremely large, which entails the smallness of the interaction of pseudo-Goldstone bosons ϕ with unknown particles, which is described by the Lagrangian

$$\mathcal{L} = \frac{1}{f} \frac{\partial \phi}{\partial x^\mu} J^\mu, \quad (3)$$

where J^μ is the current of Standard Model particles. In particular, the Lagrangian for electron–axion interaction can be represented as

$$\mathcal{L}_{ae} = \frac{c_e}{2f_a} \frac{\partial \phi_a}{\partial x^\mu} (\bar{\Psi} \gamma^\mu \gamma^5 \Psi). \quad (4a)$$

In the case considered here, this Lagrangian is equivalent to the pseudoscalar-coupling Lagrangian

$$\mathcal{L}_{ae} = -i \frac{m c_e}{f_a} \phi_a (\bar{\Psi} \gamma^5 \Psi), \quad (4b)$$

where c_e is a model-dependent constant and m is the electron mass.

The bremsstrahlung process $e(Ze) \rightarrow e(Ze) a$ [7] (diagrams in Figs. 1a, 1b) is one of the basic mechanisms of axion generation in stars. Here, the contribution of the diagram in Fig. 1a comes from direct (aee) coupling, while the contribution of the diagram in Fig. 1b is due to effective ($a\gamma\gamma$) interaction (Primakoff effect), with the axion being coupled to heavy fermions according to Eq. (3). In the latter case, ($a\gamma\gamma$) coupling is induced by the triangle loop for which the effective interaction Lagrangian has the form [6] ($e^2 = 1/137$)

$$\mathcal{L}_{a\gamma} = \frac{g_\gamma}{16\pi} F^{\mu\nu} \tilde{F}_{\mu\nu} \phi_a, \quad g_\gamma = \frac{\alpha c_\gamma}{2\pi f_a}, \quad (5)$$

where $\tilde{F}_{\mu\nu}$ is the dual strength tensor and c_γ is the corresponding model-dependent constant. In the case considered here, axions interact with light fermions as well, so that the diagram in Fig. 1b is a radiative correction to the diagram in Fig. 1a and is disregarded in the following.

*e-mail: skobelev@mail.mfiu.ru

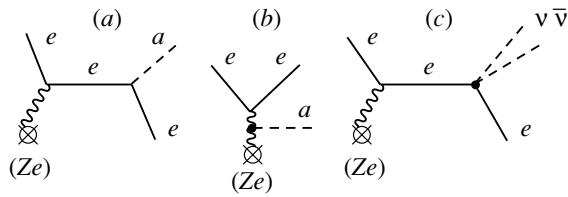


Fig. 1.

The choice of axion-parameter values is based on astrophysical estimates; therefore, it is necessary to take into account the presence of strong magnetic fields in collapsed objects like neutron stars. This results in the opening of new axion-generation channels [8, 9] and in noticeable modifications to the properties of processes that can proceed in the absence of a magnetic field [10, 11]. As far as we know, no attention has been given so far to the effect of external fields on the process of axion bremsstrahlung on nuclei. It should be noted, however, that, in a specific range of parameters that characterize magnetic neutron stars (see Section 4), a nondegenerate electron gas occupies the first Landau level, so that the effect of a magnetic field is decisive here [in the presence of degeneracy, the process $e(Ze) \rightarrow e(Ze)a$ is obviously suppressed].

A conventional method for estimating the axion mass m_a and the energy scale f_a then consists in comparing of the axion and the neutrino emissivity (the latter owes its existence to the diagram in Fig. 1c) of a neutron star in the processes of bremsstrahlung from electrons on nuclei. It is the program that is realized in the present study.

It should be noted that the process $e(Ze) \rightarrow e(Ze)\nu\bar{\nu}$ in a magnetic field was considered in [12]; however, the calculations there were performed in the simplest version of the four-fermion interaction ($C_V = C_A = 1$),¹⁾ and the use of a noncovariant procedure in the calculations resulted in unjustifiably cumbersome intermediate expressions.

The computations here are based on a two-dimensional covariant method developed in our study and intended for calculating the matrix elements of relevant Feynman diagrams. The foundations of the method were laid in [13].

The ensuing exposition is organized as follows. In Section 2, we give a brief account of the two-dimensional covariant mathematical formalism used. In Section 3, we derive relevant matrix elements and general expressions for the probabilities of the processes $e(Ze) \rightarrow e(Ze)a$ and $e(Ze) \rightarrow e(Ze)\nu\bar{\nu}$

and determine the probabilities of axion and neutrino bremsstrahlung and the power of this radiation for a nondegenerate nonrelativistic effectively two-dimensional electron gas. In Section 4, we discuss the astrophysical aspects of our results and the possible lower limit on the axion scale parameter f_a .

2. TWO-DIMENSIONAL REPRESENTATIONS OF THE ELECTRON WAVE AND GREEN'S FUNCTIONS IN A CONSTANT UNIFORM MAGNETIC FIELD

For the potential A_α of a constant uniform external magnetic field of induction B , we make use of the special gauge $A_\alpha = Bx_1g_{\alpha 2}$. In this case, a normalized solution to the Dirac equation has the form

$$\Psi = \frac{(\gamma/\pi)^{1/4}}{(2p_0L_2L_3)^{1/3}} \exp\left[-\frac{\xi^2}{2} + i(p_2x_2 + p_3x_3)\right] u_n, \tag{6}$$

where L_2 and L_3 are normalization lengths, $\gamma = |eB|$, p_2 is the quasimomentum along the second axis, and the energy $p_0 = (m^2 + 2\gamma n + p_3^2)^{1/2}$ depends on the momentum p_3 along the third axis and on the quantum number $n = 0, 1, 2, \dots$. The spinor u_n is expressed in terms of the Hermite polynomials of the argument

$$\xi = x_1\sqrt{\gamma} + p_2/\sqrt{\gamma}.$$

On the first Landau level ($n = 0$), it is independent of ξ , obeying the relations

$$\begin{cases} (\hat{p}_\parallel - m)u_0 = 0, & \Pi u_0 = u_0, \\ \bar{u}_0 u_0 = 2m, & u_0 \bar{u}_0 = \Pi(\hat{p}_\parallel + m), \end{cases} \tag{7}$$

where $\hat{p}_\parallel = p^0\gamma_0 + p^3\gamma_3$ and $\Pi = (1 - i\gamma_1\gamma_2)/2$ is the operator projecting the spin onto the direction antiparallel to the field.

Following the same line of reasoning, we can show that, if the momentum of the internal electron line in a magnetic field satisfies the condition

$$q_\parallel^2 - m^2 \ll \gamma, \quad q_\parallel^2 = q_0^2 - q_3^2, \tag{8}$$

which corresponds to a dominant contribution of the $n = 0$ intermediate state, the Green's function for the Dirac equation in a magnetic field can be represented in the form

$$G(x, y) = \frac{\gamma}{2\pi} f(x_\perp, y_\perp) \Pi \tilde{G}(x - y), \tag{9}$$

$$f(x_\perp, y_\perp) = \exp\left\{-\frac{i\gamma}{2}(x_1 + y_1)(x_2 - y_2) - \frac{\gamma}{4}[(x_1 + y_1)^2 + (x_2 - y_2)^2]\right\}, \tag{9a}$$

$$\tilde{G}(z) = \frac{1}{(2\pi)^2} \int d^2q_\parallel e^{-i(qz)_\parallel} G(q), \tag{9b}$$

¹⁾See the effective Standard Model Lagrangian in Section 3.

$$G(q) = \frac{\hat{q}_{\parallel} + m}{q_{\parallel}^2 - m^2}. \quad (9c)$$

Since the vertex factors in the matrix elements $\Pi(\gamma_{\alpha}, \gamma_{\alpha}\gamma^5)\Pi$ are nonzero only at $\alpha = 0, 3$ and since the role of the γ^5 matrix is played by $\bar{\gamma}^5 = \gamma^0\gamma^3$ (in view of the relation $\Pi\gamma^5\Pi = \Pi\bar{\gamma}^5$), Eqs. (7) and (9) actually lead to the reduction of the space of the mathematical formalism to (0, 3). Upon calculating the relevant integrals with respect to the coordinates, the matrix element assumes a form that is manifestly covariant in two dimensions and which involves scalar products and 2×2 matrices in the (0, 3) subspace, so that the projection operator Π can be omitted. The quantity u_0 then reduces to the two-component spinor $v(p)$, $p = (p_0, p_3)$, possessing the properties [see also (7)]

$$(\hat{p} - m)v = 0, \quad \bar{v}v = 2m, \quad v\bar{v} = \hat{p} + m. \quad (10)$$

Unless otherwise stated, all matrices and contractions are henceforth two-dimensional in the (0, 3) subspace. Analogously, the matrix elements will involve the two-dimensional propagator [see also (9c)]

$$G(q) = \frac{\hat{q} + m}{q^2 - m^2}. \quad (11)$$

We also present those properties of the matrices and tensors in (0, 3) subspace that are necessary for calculating the traces of the matrices involved. If we introduce the metric tensor $g^{\alpha\beta} = \text{diag}(1, -1)$ and the antisymmetric tensor $\varepsilon^{\alpha\beta}$ ($\varepsilon^{03} = -\varepsilon^{30} = 1$, $\varepsilon^{00} = \varepsilon^{33} = 0$), the basic reduction formula takes the form

$$\gamma^{\alpha}\gamma^{\beta} = g^{\alpha\beta} + \bar{\gamma}^5\varepsilon^{\alpha\beta}. \quad (12)$$

Considering that

$$\begin{cases} (\bar{\gamma}^5)^2 = 1, & \text{tr}(\bar{\gamma}^5) = \text{tr}(\bar{\gamma}^5\gamma^{\alpha}) = 0, \\ \varepsilon^{\alpha\beta}\varepsilon^{\rho\sigma} = g^{\alpha\rho}g^{\beta\sigma} - g^{\alpha\sigma}g^{\beta\rho}, \end{cases} \quad (13)$$

we can straightforwardly calculate the traces of any number of γ matrices. For example, we have

$$\frac{1}{2}\text{tr}(\gamma^{\alpha}\gamma^{\beta}\gamma^{\rho}\gamma^{\sigma}) = g^{\alpha\beta}g^{\rho\sigma} + g^{\alpha\rho}g^{\beta\sigma} - g^{\alpha\sigma}g^{\beta\rho},$$

$$\frac{1}{2}\text{tr}(\bar{\gamma}^5\gamma^{\alpha}\gamma^{\beta}\gamma^{\rho}\gamma^{\sigma}) = g^{\alpha\beta}\varepsilon^{\rho\sigma} + \varepsilon^{\alpha\beta}g^{\rho\sigma},$$

and so on. We also note that

$$\gamma^{\alpha}(\gamma_{\alpha_1} \dots \gamma_{\alpha_{2n+1}})\gamma_{\alpha} = 0. \quad (14)$$

The proof of this relation with the aid of the reduction formula (12) is obvious.

3. MATRIX ELEMENTS, PROBABILITIES, AND POWER OF AXION AND NEUTRINO BREMSSTRAHLUNG

1. In order to compute the matrix element for the axion-bremsstrahlung process $e(Ze) \rightarrow e(Ze)a$, we make use of the axion Lagrangian (4b) and of the electrodynamic-interaction Lagrangian

$$\mathcal{L}_e = e(\bar{\Psi}\gamma^{\alpha}\Psi)A_{\alpha}, \quad (15)$$

which features a four-dimensional contraction. If

$$|p_3| m, \quad p_3^2 \ll \gamma, \quad (16)$$

where p_3 is the primary-electron momentum, the conditions in (8), which constrain the applicability of the two-dimensional representation of the electron propagator as specified by Eqs. (9) and (11), also hold; after some algebra, we can obtain the relevant S -matrix element in the form

$$\langle f|S|i\rangle = \frac{\delta(p_0 - p'_0 - k_0)}{(2p_0 2p'_0 2k_0)^{1/2} L_2 L_3 V^{1/2}} \quad (17)$$

$$\times AJM \exp\left[\frac{i}{2\gamma}(p_2 + p'_2)k_1\right],$$

$$A = -\frac{4\pi(Ze^2)mc_e}{f_a}, \quad (17a)$$

$$J = \frac{\pi}{(\kappa_2^2 + \kappa_3^2)^{1/2}} \quad (17b)$$

$$\times \exp\left[-\frac{|p_2 + p'_2|}{2\gamma}(\kappa_2^2 + \kappa_3^2)^{1/2}\right],$$

$$M = \bar{v}(p') \quad (17c)$$

$$\begin{aligned} &\times \left[\bar{\gamma}^5 \frac{\hat{p}' + \hat{k} + m}{(p' + k)^2 - m^2} \gamma^0 \right. \\ &\left. + \gamma^0 \frac{\hat{p} - \hat{k} + m}{(p - k)^2 - m^2} \bar{\gamma}^5 \right] v(p), \end{aligned}$$

where V is a normalization volume; $p = (p_0, p_3)$ and $p' = (p'_0, p'_3)$ are the two-dimensional momenta of the initial and the final electron, respectively; p_2 and p'_2 are their quasimomenta; and k is the axion momentum. For the sake of brevity, we have also introduced the notation

$$\kappa_{2,3} = -(p - p' - k)_{2,3}. \quad (18)$$

In the expression for the probability, summation over final-electron states leads to the emergence of the factor

$$J_1 = \int_{-\infty}^{\infty} \frac{L_2 dp'_2}{2\pi} J^2. \quad (19)$$

Upon the subsequent summation over the ensemble of nuclei, there arises the factor

$$J_2 = N_0 \int_{-\infty}^{\infty} J_1 \frac{dX_1}{L_1}, \quad X_1 = \frac{p_2}{\gamma}, \quad (20)$$

where L_1 is the effective normalization length along the first axis and N_0 is the number of nuclei. After some simple calculations, we find, in the same approximation (16), that

$$J_2 = \frac{\pi n_0}{\kappa_3^2} L_2^2 L_3, \quad (21)$$

where n_0 is the concentration of nuclei. The probability of the axion bremsstrahlung from an electron per unit time is then independent of the normalization lengths and is given by

$$W_a = \frac{(Ze^2)^2 m^2 c_e^2 n_0}{(2\pi)^2 f_a^2 p_0} \times \int \frac{dp'_3}{2p'_0} \int \frac{d^3k}{2k_0} \frac{|M|^2}{\kappa_3^2} \delta(p_0 - p'_0 - k_0). \quad (22)$$

In order to preserve covariance in the (0, 3) sub-space in calculating $|M|^2$, we introduce the notation

$$\begin{cases} \bar{p} = (p_0, -p_3), \\ \bar{p}' = (p'_0, -p'_3), \\ \bar{k} = (k_0, -k_3). \end{cases} \quad (22a)$$

By using the rules for evaluating traces and the form (10) of the two-dimensional density matrix (10) (see Section 2), we can represent $|M|^2$ in the form

$$\begin{aligned} |M|^2 = & 1 + \frac{k^4}{\Delta\Delta'} + \frac{2(p\bar{k}) - k^2}{\Delta'} \\ & - \frac{2(p'\bar{k}) + k^2}{\Delta} - 2 \left[(p'\bar{p}) + m^2 \right] \left(\frac{k}{\Delta} - \frac{\bar{k}}{\Delta'} \right)^2 \\ & - 2k^2 \left(\frac{p\bar{k}}{\Delta^2} - \frac{p'\bar{k}}{\Delta'^2} \right) - \frac{4}{\Delta\Delta'} (p\bar{k})(p'\bar{k}), \end{aligned} \quad (23)$$

where $\Delta = -2(pk) + k^2$, $\Delta' = 2(p'k) + k^2$.

We were able to perform further calculations only for nonrelativistic electrons,

$$p_3^2 \ll m^2. \quad (24)$$

In this case, the expression for $|M|^2$ takes the simple form

$$|M|^2 = \frac{k^4}{m^2 k_0^4} (p_3 - p'_3)^2. \quad (25)$$

For the probability of axion bremsstrahlung, we then obtain

$$W_a \simeq \frac{4}{45\pi} \frac{(Ze^2)^2 c_e^2 n_0}{f_a^2} \left(\frac{|p_3|}{m} \right)^3. \quad (26)$$

In the case of a nondegenerate nonrelativistic electron gas, the power of axion emission from a unit volume is

$$S_a = n \int_{-\infty}^{\infty} dp_3 f_M(p_3) \int_{-|p_3|}^{|p_3|} dp'_3 \frac{dW_a}{dp'_3} k_0, \quad (27)$$

where

$$\frac{dW_a}{dp'_3} \simeq \frac{(Ze^2)^2 c_e^2 n_0}{15\pi f_a^2 m^3} (p_3^2 - p_3'^2), \quad k_0 \simeq \frac{p_3^2 - p_3'^2}{2m};$$

n is the electron concentration; and $f_M(p_3)$ is the one-dimensional Maxwell distribution with respect to p_3 ,

$$f_M(p_3) = (2\pi mT)^{-1/2} \exp\left(-\frac{p_3^2}{2mT}\right). \quad (28)$$

After simple algebra, we arrive at

$$S_a = \frac{256}{15^2 (2\pi)^{3/2}} \frac{(Ze^2)^2 c_e^2 n_0 n m}{f_a^2} \left(\frac{T}{m}\right)^{5/2}. \quad (29)$$

In accordance with expressions (16) and (24), the temperature must satisfy the constraints

$$(T/m) \ll 1, \quad (T/m) \ll (B/B_0)^2, \quad (30)$$

where $B_0 = m^2/|e| = 4.41 \times 10^{13}$ G is the characteristic Schwinger field.

2. Analogous features of the neutrino-bremsstrahlung process $e(Ze) \rightarrow e(Ze) \nu\bar{\nu}$ can be calculated on the basis of expression (4b) and the effective Standard Model Lagrangian

$$\begin{aligned} \mathcal{L} = & -\frac{G}{\sqrt{2}} (\bar{\Psi}_e \gamma^\mu (C_V + C_A \gamma^5) \Psi_e) \\ & \times (\bar{\Psi}_\nu \gamma_\mu (1 + \gamma^5) \Psi_\nu), \end{aligned} \quad (31)$$

where C_V and C_A are the relevant structure constants, their values being

$$C_V^{(e)} = \frac{1}{2} + \sin^2 \theta_W, \quad C_A^{(e)} = \frac{1}{2} \quad (32)$$

for the electron neutrino and $C^{(\mu,\tau)} = C^{(e)} - 1$ for the muon and the tau neutrino (θ_W is the Weinberg angle). For the probability, the calculation yields

$$\begin{aligned} W_\nu = & \frac{(Ze^2)^2 G^2 n_0}{2 (2\pi)^5 p_0} \int \frac{dp'_3}{2p'_0} \\ & \times \int \frac{d^3k}{2k_0} \int \frac{d^3k'}{2k'_0} \frac{|F^\beta M_\beta|^2}{\kappa_3^2} \delta(p_0 - p'_0 - q_0). \end{aligned} \quad (33)$$

This expression is similar to that in (22), where k and k' are, respectively, the neutrino and the antineutrino momentum; $q = k + k'$; $\kappa_3 = -(p_3 - p'_3 - q_3)$; the four-dimensional neutrino bracket is given by

$$F^\beta = \bar{u}_\nu(k) \gamma^\beta (1 + \gamma^5) u_\nu(-k'); \quad (33a)$$

and the form of M_β in the two-dimensional notation is

$$M_\beta = \bar{v}(p') \left[\gamma_\beta (C_V + C_A \bar{\gamma}^5) \frac{\hat{p}' + \hat{q} + m}{(p' + q)^2 - m^2} \gamma^0 + \gamma^0 \frac{\hat{p} - \hat{q} + m}{(p - q)^2 - m^2} \gamma_\beta (C_V + C_A \bar{\gamma}^5) \right] v(p). \quad (34)$$

Considering that

$$\int \delta^{(0,3)}(q - k - k') k_\alpha k'_\beta \frac{d^3 k}{2k_0} \frac{d^3 k'}{2k'_0} = \frac{\pi^2 q^2}{12} \left(q_\alpha q_\beta + \frac{q^2}{4} g_{\alpha\beta} \right),$$

we reduce W_ν to the form

$$W_\nu = \frac{(Ze^2)^2 G^2 n_0}{3(2\pi)^3 p_0} \int \frac{dp'_3}{2p'_0} \int \frac{dq_3 q^2}{(p_3 - p'_3 - q_3)^2} I, \quad (35)$$

$$I = \frac{1}{2} \left[|Mq|^2 - \frac{q^2}{2} (MM^*) \right], \quad q_0 = p_0 - p'_0. \quad (35a)$$

After some cumbersome transformations, we find that the quantity I can be represented in the form

$$\begin{aligned} I = & C_A^2 m^2 + 2C_V C_A ((q - p') \varepsilon \bar{p}) \\ & + \frac{1}{\Delta'} \{ 2C_A^2 m^2 (-q^2 + 2(\bar{p}q)) \\ & + 2C_V C_A [-2(q\varepsilon p')(\bar{p}(p' + q)) \\ & - q^2((q + p')\varepsilon \bar{p}) + 2m^2(q\varepsilon \bar{p})] \} - (C_V^2 + C_A^2) \\ & \times \frac{2}{\Delta'^2} m^2 q^2 [m^6 + (p'\bar{p}) + (\bar{p}q)] + \frac{m^2}{\Delta \Delta'} \quad (36) \\ & \times \left\{ 4C_A^2 \left[(q\bar{q})(m^2 + (p'\bar{p})) + \frac{q^4}{4} - (q\bar{p})(q\bar{p}') \right] \right. \\ & \left. - 2q^2 (C_V^2 - C_A^2) (p'(\bar{p}' + \bar{q} + p)) \right\} + (p \leftrightarrow p'), \\ & \Delta = -2(pq) + q^2, \quad \Delta' = 2(p'q) + q^2, \end{aligned}$$

where we have used the notation in (22a) once again and the symbolic representation

$$(a\varepsilon b) \equiv a^\alpha b^\beta \varepsilon_{\alpha\beta}.$$

Here, $\varepsilon_{\alpha\beta}$ is the antisymmetric tensor introduced in Section 2; we also have

$$(\bar{a}\varepsilon b) = -(a\varepsilon \bar{b}).$$

As before, we consider only the nonrelativistic approximation specified in (24), where expression (36) becomes

$$I \simeq (C_V^2 + C_A^2) \frac{q^4}{q_0^4} (p_3 - p'_3)^2. \quad (37)$$

The probability of neutrino-pair production via the bremsstrahlung mechanism is then given by

$$W_\nu \simeq \frac{8(C_V^2 + C_A^2)}{3 \times 35^2 \pi^3 m^5} (Ze^2)^2 G^2 n_0 |p_3|^7. \quad (38)$$

At $C_V = C_A = 1$, this result coincides with formula (19) from [12] if we consider that the factor 4π was omitted in that formula.

The power S_ν of neutrino emission from a unit volume is determined by expression (27) with the substitution $k_0 \rightarrow q_0$; in the same approximation specified by (30), it therefore has the form

$$S_\nu = \frac{2^{13} (C_V^2 + C_A^2)}{9 \times 35^2 \pi^3 (2\pi)^{1/2}} (Ze^2)^2 G^2 n_0 n m^3 \left(\frac{T}{m} \right)^{9/2}. \quad (39)$$

4. DISCUSSION

In magnetic neutron stars, the electron concentration is extremely high, $n \sim 10^{30-37} \text{ cm}^{-3}$; therefore, there arises yet another nontrivial constraint on our results (which are based on the use of the Maxwell distribution), $T \gg p_F^2/2m$, where p_F , the Fermi momentum in an effectively two-dimensional magnetized electron gas, is given by [14]

$$p_F = 2\pi^2 n / \gamma. \quad (40)$$

Thus, we see that, in addition to the inequalities in (30), it is necessary that

$$\left(\frac{T}{m} \right) \gg \left(\frac{B_0}{B} \right)^2 (n\lambda_c^3)^2 \times 10^2, \quad (41)$$

where λ_c is the electron Compton wavelength. The ranges of other parameters, $T \sim 10^{8-10} \text{ K}$ and $B \sim 10^{12-14} \text{ G}$, admit T , n , and B values that satisfy the inequalities in (30) and (41). By way of example, we set $n \sim 10^{30} \text{ cm}^{-3}$, $B \sim 10^{14} \text{ G}$, and $T \sim 10^8 \text{ K}$. If we adopt the condition that the currently prevalent concepts of the evolution of magnetic neutron stars must not change, then the inequality $S_\nu \gtrsim S_a$ must be valid; that is,

$$\frac{7.55c_e^2}{f_a^2 G^2 (C_V^2 + C_A^2) T^2} \leq 1. \quad (42)$$

At the above value of T , we can constrain the energy scale f_a from below as

$$f_a \gtrsim \left(\frac{c_e^2}{C_V^2 + C_A^2} \right)^{1/2} \times 2.1 \times 10^{10} \text{ GeV}. \quad (43)$$

This value of f_a falls within the range given by (1) and (2). It follows that, at the parameter values chosen here, the axion emissivity of stars that is due to the effectively two-dimensional bremsstrahlung mechanism can be close to their neutrino emissivity.

We also note that, for the parameters n and T within their intervals for magnetic neutron stars, the range of applicability of expressions (29) and (39) for S_a and S_ν , respectively, in these parameters broadens at magnetic-field-induction values greater than 10^{14} G, which cannot be ruled out in principle.

REFERENCES

1. S. Weinberg, Phys. Rev. Lett. **27**, 1688 (1971).
2. A. Salam, in *Elementary Particle Theory*, Ed. by N. Svartholm (Almqvist and Wiksell, Stockholm, 1968).
3. R. D. Peccei and H. R. Quinn, Phys. Rev. Lett. **38**, 1440 (1977).
4. J. Preskill, M. Wise, and F. Wilczek, Phys. Lett. B **120B**, 127 (1983).
5. G. Raffelt, *Stars as Laboratories for Fundamental Physics* (Univ. of Chicago Press, Chicago, 1996).
6. G. G. Raffelt, Phys. Rep. **198**, 1 (1990).
7. G. Raffelt and A. Weiss, Phys. Rev. D **51**, 1495 (1995).
8. V. V. Skobelev, Zh. Éksp. Teor. Fiz. **116**, 26 (1999) [JETP **89**, 13 (1999)].
9. A. V. Borisov and V. Yu. Grishina, Zh. Éksp. Teor. Fiz. **106**, 1553 (1994) [JETP **79**, 837 (1994)].
10. V. V. Skobelev, Yad. Fiz. **61**, 2236 (1998) [Phys. At. Nucl. **61**, 2123 (1998)].
11. A. V. Borisov and K. V. Zhukovskii, Yad. Fiz. **58**, 1298 (1995) [Phys. At. Nucl. **58**, 1218 (1995)].
12. Yu. M. Loskutov and V. V. Skobelev, Teor. Mat. Fiz. **29**, 65 (1976).
13. V. V. Skobelev, Zh. Éksp. Teor. Fiz. **71**, 1263 (1976) [Sov. Phys. JETP **44**, 660 (1976)]; **72**, 1298 (1977) [**45**, 682 (1977)]; Doctoral Dissertation in Mathematical Physics (Mosk. Gos. Univ., Moscow, 1982).
14. Yu. M. Loskutov and V. V. Skobelev, Yad. Fiz. **43**, 1495 (1986) [Sov. J. Nucl. Phys. **43**, 964 (1986)].

Translated by A. Isaakyan

ELEMENTARY PARTICLES AND FIELDS
Theory

Hard QCD Processes and Impact-Parameter Dependence of Parton Energy Losses in Ultrarelativistic Nuclear Collisions

I. P. Lokhtin and A. M. Snigirev

Institute of Nuclear Physics, Moscow State University, Vorob'evy gory, Moscow, 119899 Russia

Received February 29, 2000; in final form, September 7, 2000

Abstract—Special features of particle and jet production in hard QCD processes induced by ultrarelativistic heavy-ion collisions are investigated. The energy loss of partons produced in hard collisions that is due to their multiple scattering in dense quark–gluon matter is analyzed as a function of the impact parameter of a nucleus–nucleus collision. The possibility of experimentally observing effects that are expected in this connection and which include different impact-parameter dependences of radiative and collision hard-jet energy losses, a modification to the shape of the impact-parameter distribution of dijets, and the suppression of the yield of muon pairs having large invariant masses is discussed.

© 2001 MAIK “Nauka/Interperiodica”.

1. INTRODUCTION

Presently, great interest in studying the properties of superdense matter formed in ultrarelativistic nuclear collisions is generated by the possibility of reaching, under these conditions, the deconfinement of hadronic matter and the formation of quark–gluon plasma (QGP), where color interaction between partons is screened by virtue of collective effects (for an overview, see [1–6]). The use of “hard” tests—heavy quarkonia, hard hadrons and hadronic jets, and muon pairs of large invariant mass—seems very promising in future experiments at the RHIC and LHC colliders. Since hard QCD scattering processes occur at the earliest stage of a nucleus–nucleus collision, particles and parton jets produced in such processes do not belong to the thermalized system being considered and can carry information about the initial stages of its evolution.

In particular, the formation of quark–gluon plasma in heavy-ion collisions is expected to be accompanied by a strong suppression of the yield of massive vector mesons J/ψ and ψ' ($c\bar{c}$) and of Υ , Υ' , and Υ'' ($b\bar{b}$) particles [7]. An anomalous suppression of the yield of ψ resonances as observed by the NA50 experiment [8], which studied collisions of lead ions at the SPS accelerator (CERN), is an intriguing phenomenon that does not comply with absorption models in cold nuclear matter and hadronic gas, and we have yet to clarify its origin [9]. A similar suppression effect in superdense matter for heavier systems ($b\bar{b}$) is possible at temperatures that are higher than those for $c\bar{c}$ and which are expected to be achieved in central heavy-ion collisions at RHIC and LHC.

In addition to the suppression of heavy quarkonia, we would like to mention yet another hard test of the production of quark–gluon plasma, the propagation of hard jets of color-charged partons through it that are produced in pairs at the earliest stages of the collision process ($\tau_{\text{form}} \sim 1/p_T \lesssim 0.01 \text{ fm}/c$) in individual events of hard nucleon–nucleon (parton–parton) scattering. Such jets propagate through dense quark–gluon matter formed by the system of minijets over a large time scale ($\gtrsim 0.1 \text{ fm}/c$) and interact with matter constituents, with the result that their original properties are modified as the result of additional rescatterings. The inclusive cross section for the production of hard hadronic jets ($Q^2 \gg 1 \text{ (GeV}/c)^2$) is overly small at the SPS energies ($\sqrt{s} \simeq 20 \text{ GeV}$ per nucleon pair) for analyzing such events, but it grows fast with energy of colliding particles. Hard and semihard processes of parton–parton scattering will play an important role in the formation of the initial state in heavy-ion collisions at the energies of the RHIC ($\sqrt{s} = 200 \text{ GeV}$ per nucleon pair) and LHC ($\sqrt{s} = 5.5 \text{ TeV}$ per nucleon pair) colliders [10].

It is of paramount importance to investigate the mechanisms that can be responsible for hard-parton energy losses in dense QCD matter and which can be partitioned into (i) radiative losses associated with the emission of bremsstrahlung gluons [11–16] and (ii) collision losses associated with elastic rescattering on medium constituents [17, 18]. Since the rescattering intensity grows fast with temperature (energy density), the formation of superdense and hot parton matter in heavy-ion collisions (with the initial tem-

perature estimated at $T_0 \simeq 1$ GeV for LHC [10]) must lead to much greater hard-jet energy losses in relation to the case of cold nuclear matter or hadronic gas with $T \lesssim 0.2$ GeV.

It is expected that gluon bremsstrahlung is a much more effective mechanism of hard-parton energy losses in a QCD medium than the collision mechanism [12]. However, an increase in the energy of the radiating parton results in that the maximum in the angular distribution of emitted gluons is shifted toward the direction of its motion. This means that, if the jet energy is measured by summing the energies of all hadrons over a sufficiently large cone with an apex angle θ_0 , a major part of the initial-parton energy can be reconstructed. Hence, medium-induced radiation will predominantly soften the energy distribution of particles in a jet; increase the multiplicity of secondaries; and, to a lesser extent, affect the total jet energy. In this connection, it should be recalled that coherent effects play an important role for the radiation of energetic gluons with formation times that exceed the range of a hard parton in a medium and which lead to a substantial modification of the bremsstrahlung spectrum [13–15] in relation to that in the Bethe–Heitler mode of independent radiations (QCD analog of the Landau–Pomeranchuk–Migdal effect in QED [19]). In particular, coherent Landau–Pomeranchuk–Migdal radiation results in a strong dependence of the jet energy on the angular size θ_0 of its cone [20–22]. At the same time, thermal particles that have elastically interacted with a hard parton travel at sufficiently large angles with respect to the axis of a jet and do indeed reduce its energy. Thus, the relative contribution of collision losses can be quite sizable for jets of finite angular size $\theta_0 \simeq 15^\circ$ – 30° [20].

A number of processes have been proposed to perform experimental searches for hard-quark and gluon energy losses in dense QCD matter and a relevant analysis of the properties of the medium formed in ultrarelativistic nuclear collisions. These include

(i) the suppression of the yield of hard dijets [18, 23] and the enhancement of the yield of single jets [24, 25] produced in the initial processes of hard parton–parton scattering,

$$gg \rightarrow gg, \quad qg \rightarrow qg, \quad qq, gg \rightarrow qq;$$

(ii) a disbalance of transverse momenta in the production of a partonic jet and an unsuppressed particle (that is, a particle that has not suffered strong interaction and which leaves dense matter almost freely)—specifically, in the Z boson + jet [26] and photon + jet [27] produced in the processes

$$q + g \rightarrow q + Z (\rightarrow \mu^+ \mu^-), \quad q + g \rightarrow q + \gamma;$$

(iii) the suppression of the yield of muon pairs having large invariant masses and originating from

the semileptonic decays of B and D mesons [this effect is due to heavy-quark (b and c) energy losses] [28–30],

$$gq \rightarrow b\bar{b} (c\bar{c}) \rightarrow B\bar{B} (D\bar{D}) \rightarrow \mu^+ \mu^- X.$$

The aforementioned production processes can be investigated in heavy-ion collisions [31] at the compact-muon-solenoid (CMS) detector that is now being constructed at LHC and which can be optimized for a precise measurement of the features of energetic muons, photons, electrons, and hadronic jets [32].

It should be noted that $Z + jet$ and $\gamma + jet$ production channels are advantageous in that it is possible, in these processes, to observe directly mean jet energy losses as the difference of the mean value of the measured jet energy and the mean absolute value of the momentum (which is close to the jet initial energy) of a photon or a Z boson traveling in the opposite direction. In particular, the dependence of energy losses per unit length, dE/dx , on the total distance L traversed in dense matter is an interesting prediction, which is associated with the coherent nature of the radiation induced by a QCD medium [13, 14]. In the approximation of a strong Landau–Pomeranchuk–Migdal effect, the energy loss dE/dx is estimated to be proportional to L for a static medium [13] and shows a weaker L dependence for the case of expanding matter [14]. For nucleus–nucleus interactions, the L dependence of the energy loss can be experimentally investigated in various bins of the impact parameter, a quantity that determines the effective volume of the dense part of nuclear overlap. Another possibility consists in varying beams of colliding ions and in selecting the most central collisions.

The main objective of our study is to explore radiative and collision hard-parton energy losses in quark–gluon matter with allowance for actual nuclear geometry—in particular, to estimate the dependence of these losses on the impact parameter of a nucleus–nucleus collision. We apply our analysis to studying special features of hard QCD production processes (those that could be used as a test of the properties of a superdense medium formed in ultrarelativistic heavy-ion collisions) such as different L dependences of radiative and collision hard-jet energy losses, modifications to the shape of the impact-parameter distribution of the number of dijets, and a suppression of the yield of muon pairs having large invariant masses.

2. GEOMETRIC MODEL OF HARD-PARTON PRODUCTION IN NUCLEUS–NUCLEUS COLLISIONS

Let us consider a simple geometric model of the production of hard partons in symmetric ultrarela-

tivistic nucleus–nucleus collisions and the propagation of these partons through the dense matter formed. For two colliding nuclei (AA), Fig. 1 illustrates the problem in the impact-parameter plane. Here, the impact parameter b is defined as the transverse (with respect to the collision axis z , which is orthogonal to the plane of the figure) distance between the centers O_1 and O_2 of the nuclei involved, $OO_2 = -O_1O = b/2$. The jet-production (dijet-production) vertex is denoted by $B(r \cos \psi, r \sin \psi)$, where r is the distance from the z axis to the point B . The distance between the center of one of the nuclei (O_1 or O_2) and the vertex B is then given by

$$r_{1,2} = \sqrt{r^2 + \frac{b^2}{4} \pm rb \cos \psi}. \quad (1)$$

The distribution of jet-production vertex $B(r, \psi)$ at an impact parameter b has the form

$$P_{AA}(\mathbf{r}, b) = \frac{T_A(r_1)T_A(r_2)}{T_{AA}(b)}, \quad (2)$$

where

$$\begin{aligned} T_{AA}(b) &= \int d^2s T_A(\mathbf{s})T_A(\mathbf{b} - \mathbf{s}) \\ &= \int_0^{2\pi} d\psi \int_0^{r_{\max}} r dr T_A(r_1)T_A(r_2) \end{aligned} \quad (3)$$

is the nuclear-overlap function and $T_A(\mathbf{r}) = A \int_{-\infty}^{+\infty} \rho_A(\mathbf{r}, z) dz$ is the nuclear-thickness function for an intranuclear-nucleon density $\rho_A(\mathbf{r}, z)$. The maximum possible value of r in the nuclear-overlap region can be estimated on the basis of the equation

$$\max\{r_1(r = r_{\max}), r_2(r = r_{\max})\} = R_A \quad (4)$$

(R_A is the radius of nucleus A). On this basis, we obtain

$$\begin{aligned} r_{\max} &= \min \left\{ \sqrt{R_A^2 - \frac{b^2}{4} \sin^2 \psi} + \frac{b}{2} \cos \psi, \right. \\ &\quad \left. \sqrt{R_A^2 - \frac{b^2}{4} \sin^2 \psi} - \frac{b}{2} \cos \psi \right\}. \end{aligned} \quad (5)$$

In particular, the nuclear-overlap function is $T_A^{\text{un}}(r) = 3A\sqrt{R_A^2 - r^2}/(2\pi R_A^3)$ for a homogeneous distribution of intranuclear nucleons, $\rho_A^{\text{un}}(\mathbf{R}) = \rho_0 \Theta(R_A - |\mathbf{R}|)$.

For the distribution $P_{AA}^{\text{un}}(\mathbf{r}, b)$, we then have

$$P_{AA}^{\text{un}}(\mathbf{r}, b) \propto \sqrt{R_A^2 - r_1^2(r, \psi, b)} \sqrt{R_A^2 - r_2^2(r, \psi, b)}. \quad (6)$$

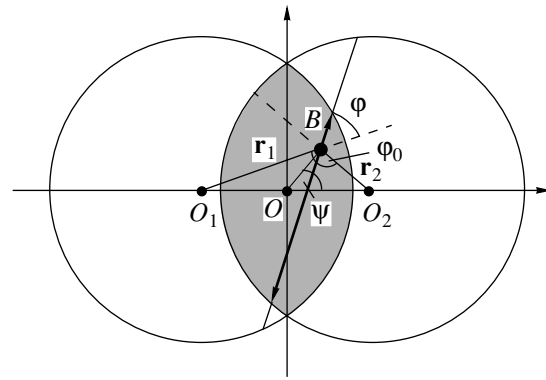


Fig. 1. Hard-parton (parton-pair) production in symmetric AA collisions in the impact-parameter \mathbf{b} plane, which is orthogonal to the collision axis z . Here, O_1 and O_2 are the centers of the nuclei involved, $OO_2 = -O_1O = b/2$; $B(r \cos \psi, r \sin \psi)$ is the parton-production vertex; r is the distance from the z axis to the vertex B ; r_1 and r_2 are the distances between the centers O_1 and O_2 of the nuclei and B ; φ is the azimuthal angle that determines the direction of parton motion; and φ_0 is the angle between the vectors \mathbf{r}_1 and \mathbf{r}_2 .

For central AA collisions ($b = 0, r_{\max} = R_A$), this result takes the form $P_{AA}^{\text{un}}(\mathbf{r}, b = 0) \propto (R_A^2 - r^2)$.

One can also easily estimate the proper time $\tau_L = L$ over which the jet resides within the dense region. The result is

$$\tau_L = \min \left\{ \sqrt{R_A^2 - r_1^2 \sin^2 \varphi} - r_1 \cos \varphi, \quad (7)$$

$$\sqrt{R_A^2 - r_2^2 \sin^2(\varphi - \varphi_0)} - r_2 \cos(\varphi - \varphi_0) \right\},$$

where φ is the azimuthal angle that determines the direction of jet motion in the impact-parameter plane and φ_0 is the angle between the vectors \mathbf{r}_1 and \mathbf{r}_2 . The expression for

$$\varphi_0 = \arccos \frac{r^2 - b^2/4}{r_1 r_2} \quad (8)$$

can be obtained from the condition

$$\begin{aligned} r_1 r_2 \cos \varphi_0 &= \mathbf{r}_1 \cdot \mathbf{r}_2 \\ &= (-b/2 - r \cos \psi)(b/2 - r \cos \psi) \\ &\quad + r^2 \sin^2 \psi = r^2 - b^2/4. \end{aligned} \quad (9)$$

Let us now proceed to estimate the impact-parameter (b) dependence of the initial energy density in the nuclear-overlap region. At collider energies, the system of minijets (semihard gluons, quarks, and antiquarks with $p_T \gtrsim p_0 \simeq 1\text{--}2$ GeV/ c) is formed in the central rapidity region at the earliest reaction stage, $\tau_0 \sim 1/p_T \lesssim 1/p_0 \simeq 0.1$ fm/ c , determining the initial conditions for a further evolution of the system [10]. In general, soft particle-production mechanisms (like color-field decay) may also contribute to

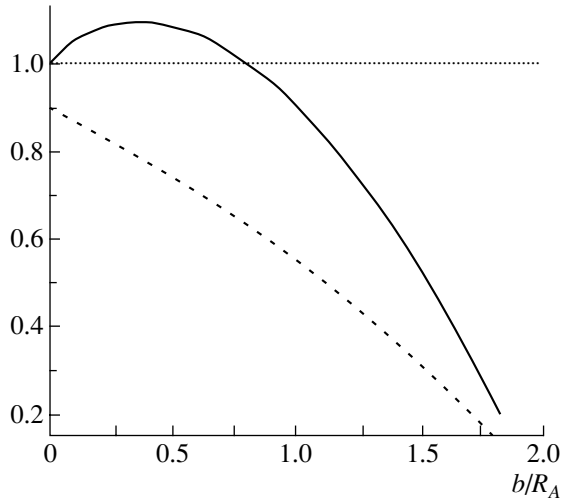


Fig. 2. Initial energy density $\varepsilon_0(b)/\varepsilon_0(b=0)$ in the nuclear-overlap region (solid curve) and mean proper time $\langle\tau_L\rangle/R_A$ of hard-parton escape from dense matter (dashed curve) versus the impact parameter of an AA collision.

the initial conditions in nuclear interactions, but the relative importance of this contribution decreases fast with increasing c.m. energy of the beams. By way of example, we indicate that, at the LHC energies [$\sqrt{s} = 7 \text{ TeV} \times (2Z/A)$ per nucleon pair], hard and semihard processes saturate more than 80% of the total transverse-energy release [10]. Moreover, soft processes characterized by low momentum transfers [$Q^2 \sim \Lambda_{\text{QCD}}^2 \simeq (200 \text{ MeV})^2 \ll p_0^2$] may be partly or fully suppressed because of the screening of color interaction in dense partonic matter formed earlier from the system of minijets [33]. At the LHC energies, we will therefore consider only the dominant contribution to the initial conditions from semihard partons.

The initial energy density within the comoving volume of longitudinal dimension $\Delta z = \tau_0 \times 2\Delta y$ can be estimated on the basis of the Bjorken formula [10, 34]

$$\varepsilon(\tau = \tau_0) \quad (10)$$

$$= \frac{\langle E_T^A(|y| < \Delta y) \rangle}{S(b)\Delta z} = \frac{\langle E_T^A(|y| < \Delta y) \rangle p_0}{S(b) \times 2\Delta y},$$

where

$$S_{AA}(b) = \int_0^{2\pi} d\psi \int_0^{r_{\max}} r dr \quad (11)$$

$$= \left(\pi - 2 \arcsin \frac{b}{2R_A} \right) R_A^2 - b \sqrt{R_A^2 - \frac{b^2}{4}}$$

is the effective transverse area of the nuclear-overlap region at an impact parameter b . The total initial transverse energy in the central rapidity region can be calculated as [10]

$$\langle E_T^A(b, \sqrt{s}, p_0, |y| < \Delta y) \rangle \quad (12)$$

$$= T_{AA}(b) \sigma_{NN}^{\text{jet}}(\sqrt{s}, p_0) \langle p_T \rangle,$$

where the first p_T moment $\sigma_{NN}^{\text{jet}} \langle p_T \rangle$ of the differential cross section for minijet production is determined by the dynamics of nucleon–nucleon interactions at the corresponding c.m. energy. The impact-parameter dependence of the initial-energy density ε_0 in the nuclear-overlap region then has the form

$$\varepsilon_0(b) \propto T_{AA}(b)/S_{AA}(b), \quad (13)$$

$$\varepsilon_0(b) = \varepsilon_0(b=0) \frac{T_{AA}(b)}{T_{AA}(b=0)} \frac{S_{AA}(b=0)}{S_{AA}(b)}.$$

For central AA collisions, we have $S_{AA}(b=0) = \pi R_A^2$ and $T_{AA}(b=0) = 9A^2/(8\pi R_A^2)$.

It is worth noting that, although the simple geometric model that we use to describe hard-parton production in AA interactions is formally applicable at the impact-parameter values in the region $b \leq 2R_A$, central and semicentral collisions characterized by $b \lesssim R_A$ are of prime importance for us here. The reasons for this are the following:

(i) Although such events are responsible for only a few percent of the total inelastic AA cross section [35], their contribution to the total number of product jets is dominant. By way of example, we indicate that, in PbPb interactions at the LHC energy, about 50% of dijets are produced in events where the impact parameter takes values in the region $b < 0.9R_{\text{Pb}} = 6 \text{ fm}$, the fraction of such events in the total cross section being only about 10% [31].

(ii) It is in central heavy-ion collisions that a maximal initial energy density is expected to be achieved within large (in relation to characteristic hadronic scales) volumes, so that the effect of the formation of quark–gluon plasma could be observed. For a homogeneous density of intranuclear nucleons, Fig. 2 shows the initial energy density ε_0 (13) in the nuclear-overlap region as a function of the impact parameter; it can be seen that ε_0 changes only slightly with b ($\delta\varepsilon_0 \lesssim 10\%$) up to $b \sim R_A$ and decreases fast for $b \gtrsim R_A$. At the same time, the quantity $\langle\tau_L\rangle$ obtained by averaging the time (7) of hard-parton escape from the dense region over all production vertices decreases nearly in inverse proportion to b (see dashed curve in Fig. 2). By varying the impact parameter b of a nucleus–nucleus collision (this parameter can be evaluated by using, for example, the measured value of the total-transverse-energy release in the calorimeter [36]) up to $b \sim R_A$, it is possible to study the energy loss and the hard-jet yield as functions of the distance traveled in a dense medium without significant changes in ε_0 .

Moreover, it can be seen that, for a weak b dependence of ε_0 , we have an advantage in relation to the case where use is made of beams of various ions at

a fixed impact parameter $b \sim 0$, with the result that a variation of the escape time is given by the simple formula $\langle \tau_L \rangle(b=0) \propto R_A \propto A^{1/3}$. Equation (13) yields $\varepsilon_0(b=0) \propto A^2/R_A^4$; that is, $\varepsilon_0(b=0) \propto A^{2/3}$. Figure 3 illustrates the variation of the initial energy density ε_0 and of the mean time $\langle \tau_L \rangle$ of propagation in the dense region in response to a variation of the impact parameter b (at fixed $A = \text{Pb} = 207$) and of the atomic number A (at fixed $b = 0$). For example, a reduction of $\langle \tau_L \rangle(\text{Pb}, b = 0) \simeq 6 \text{ fm}/c$ by a factor of about 1.7 can be achieved (a) by increasing b up to $b = 0.9R_{\text{Pb}} \simeq 6 \text{ fm}$ (at a simultaneous 10% reduction of ε_0) or (b) by reducing A down to $A = 40$ (Ca) (at the expense of reducing ε_0 by a factor of about 3).

(iii) It is well known that a homogeneous distribution of the intranuclear-nucleon density, $\rho_A^{\text{un}}(\mathbf{R}) = \rho_0 \Theta(R_A - |\mathbf{R}|)$, can serve as a good approximation for central and semicentral collisions¹⁾ (see Fig. 4, which displays the nuclear-overlap function for a homogeneous and for a Woods–Saxon distribution). However, we do not consider here edge effects near the nuclear surface, the impact-parameter dependence of intranuclear-nucleon structure functions [37], an early transverse expansion of the system, and some other phenomena that can in principle be important for peripheral ($b \sim 2R_A$) interactions.

3. PARTON ENERGY LOSSES AND IMPACT PARAMETER

The intensity of multiple scattering, as well as radiative and collision hard-parton energy losses, in dense QCD matter formed in the region of nuclear overlap is sensitive to the initial parameters of this matter (like the energy density and the formation time) and to its spacetime evolution [18]. For the ensuing analysis of the parton energy loss as a function of the impact parameter, we will describe the evolution of the medium in question on the basis of one-dimensional scaling (Lorentz invariant) fluid dynamics, where particles are produced on a hypersurface specified by the same value of the proper time $\tau = \sqrt{t^2 - z^2}$ [34]. We expect that, in the case of central and semicentral collisions, this approximation

¹⁾We note that, in this case, the expression for $T_{AA}(b)$ can be derived explicitly, $T_{AA}^{\text{un}}(b) = T_{AA}^{\text{un}}(b=0) \left[1 - \tilde{b} \left[1 + \left(1 - \frac{\tilde{b}}{4} \right) \ln \frac{1}{\tilde{b}} + 2 \left(1 - \frac{\tilde{b}}{4} \right) \times \left(\ln(1 + \sqrt{1 - \tilde{b}}) - \frac{\sqrt{1 - \tilde{b}}}{1 + \sqrt{1 - \tilde{b}}} \right) - \frac{\tilde{b}(1 - \tilde{b})}{2(1 + \sqrt{1 - \tilde{b}})^2} \right] \right]$, where $\tilde{b} = b^2/(4R_A^2)$; on this basis, it can be found analytically for $b \lesssim R_A$ that ε_0 is weakly dependent on b and that $\langle \tau_L \rangle(b)$ decreases almost linearly.

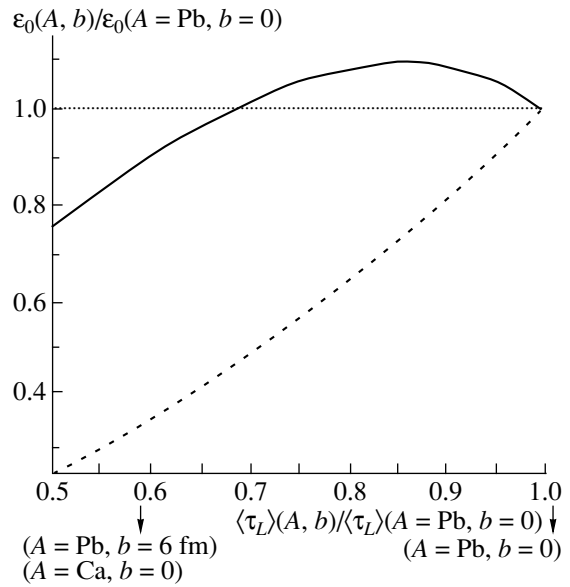


Fig. 3. Variation of $\varepsilon_0(A, b)/\varepsilon_0(A = \text{Pb}, b = 0)$ and $\langle \tau_L \rangle(A, b)/\langle \tau_L \rangle(A = \text{Pb}, b = 0)$ in response to a variation of A at fixed $b = 0$ (dashed curve) and in response to a variation of the impact parameter b at fixed $A = \text{Pb} = 207$ (solid curve).

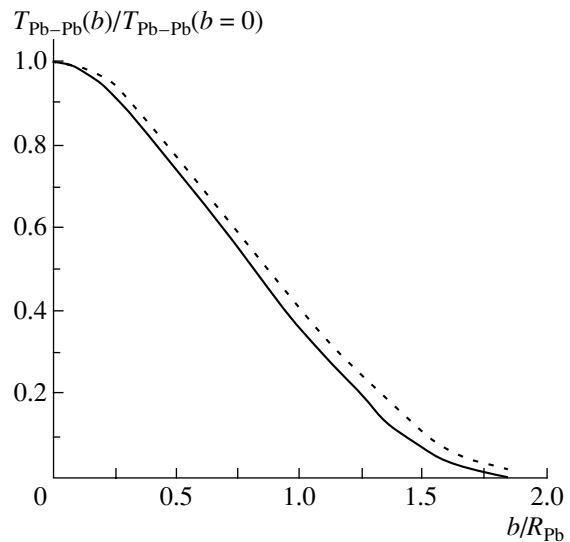


Fig. 4. Profile of the nuclear-overlap function for (solid curve) a homogeneous nucleon density and (dashed curve) a nucleon density in the form of a Woods–Saxon distribution.

is adequate to the purposes of our semiquantitative analysis.

Within our model, radiative and collision energy losses are associated with each scattering event in an expanding medium, the inclusion of interference effects in gluon bremsstrahlung being performed by modifying the bremsstrahlung spectrum as a function

of decreasing temperature, $dE/dx(T)$. It should be noted that, for a fast parton propagating through a QCD plasma that undergoes evolution in accordance with the Bjorken model [34], Baier *et al.* [14] expressed radiative energy losses in terms of the loss in a static medium as $dE/dx|_{\text{expan}} = cdE/dx|_{T_L}$, where c is a numerical factor that is approximately equal to 6 (2) for a parton produced outside (within) the medium being considered and T_L is the temperature of the medium at the place where the parton leaves it. We found that, in a numerical calculation of the energy loss, the use of reasonable values for the model parameters leads to close results in the two cases [20].

The total hard-parton energy losses in the transverse (with respect to the nuclear-collision axis) direction that are due to multiple rescattering in a medium appear to be the result of averaging over the production vertex $P_{AA}(\mathbf{r}, b)$ (2), over the momentum transfer squared t in a scattering event, and over the spacetime evolution. Specifically, we have

$$\begin{aligned} & \langle \Delta E_T(b) \rangle \\ &= \int_0^{2\pi} d\psi \int_0^{r_{\max}} r dr \frac{T_A(r_1)T_A(r_2)}{T_{AA}(b)} \int_0^{2\pi} \frac{d\varphi}{2\pi} \int_{\tau_0}^{\tau_L} d\tau \quad (14) \\ & \times \left(\frac{dE^{\text{rad}}}{dx}(\tau) + \sum_b \sigma_{ab}(\tau) \rho_b(\tau) \nu(\tau) \right), \end{aligned}$$

where τ_0 and τ_L (7) are, respectively, the proper time of medium formation and the proper time of jet escape from it; $\rho_b \propto T^3$ is the density of the b -type medium constituents at temperature T ; σ_{ab} is the cross section for the interaction of a parton from jet a with a constituent b moving at the same longitudinal rapidity y ; ν is the thermal expectation value of the parton energy loss per elastic-scattering event; and dE^{rad}/dx is the radiative energy loss per unit length.

If the hard-parton range λ in a medium is much greater than the Debye color-screening radius μ_D^{-1} ($\lambda \gg \mu_D^{-1}$), all scattering events can be considered to be independent [12]. The transverse distance between successive rescattering events, $\Delta r_i = (\tau_{i+1} - \tau_i)v_T = (\tau_{i+1} - \tau_i)p_T/E$, is determined in linear kinetic theory in accordance with the probability density

$$\begin{aligned} & \frac{dP}{d(\Delta r_i)} \quad (15) \\ &= \lambda^{-1}(\tau_{i+1}) \exp \left(- \int_0^{\Delta r_i} \lambda^{-1}(\tau_i + s) ds \right), \end{aligned}$$

where there appears the inverse range $\lambda_a^{-1}(\tau) = \sum_b \sigma_{ab}(\tau) \rho_b(\tau)$.

In a superdense system ($\rho^{1/3} \gg \Lambda_{\text{QCD}}$), where color interaction is screened as the result of collective effects, partons are asymptotically free. This makes it possible to determine, on the basis of perturbative QCD, the dominant contribution to the differential cross section $d\sigma/dt$ for the scattering of a hard parton of energy E by thermal partons of energy (effective mass) $m_0 \sim 3T \ll E$ at temperature T [12, 38]. The result is

$$\frac{d\sigma_{ab}}{dt} \simeq C_{ab} \frac{2\pi\alpha_s^2(t)}{t^2}, \quad (16)$$

where $C_{ab} = 9/4$, 1, and $4/9$ for gg , gq , and qq scattering processes, respectively;

$$\alpha_s = \frac{12\pi}{(33 - 2N_f) \ln(t/\Lambda_{\text{QCD}}^2)} \quad (17)$$

is the running QCD coupling constant for N_f active quark flavors; and Λ_{QCD} is the QCD scale factor, which is of order of the critical temperature T_c . The integrated cross section

$$\sigma_{ab} = \int_{\mu_D^2(\tau)}^{m_0(\tau)E/2} dt \frac{d\sigma_{ab}}{dt} \quad (18)$$

is regularized at the lower limit by the square of the Debye screening mass; in the high-temperature limit of perturbation theory [39], this mass squared is estimated as $\mu_D^2 \simeq 4\pi\alpha_s^* T^2(1 + N_f/6)$, where there appears the thermal coupling constant $\alpha_s^* = \alpha_s(16T^2)$.

The thermally averaged hard-parton energy loss per elastic-scattering event can be estimated as

$$\begin{aligned} & \nu = \left\langle \frac{t}{2m_0} \right\rangle \quad (19) \\ &= \frac{1}{2} \left\langle \frac{1}{m_0} \right\rangle \langle t \rangle \simeq \frac{1}{4T\sigma_{ab}} \int_{\mu_D^2}^{3TE/2} dt \frac{d\sigma_{ab}}{dt} t. \end{aligned}$$

The quantity ν is independent of the total distance traveled in a dense medium and, as a matter of fact, is determined exclusively by the temperature, $\nu \propto T$, if we disregard the weak t dependence of the coupling constant. The total collision energy loss (integral over the entire trajectory of a hard parton) can then be estimated as $\langle \Delta E_{\text{col}} \rangle \propto T_0^2 \propto \sqrt{\varepsilon_0}$; the τ_L dependence of ΔE_{col} is merely linear, $\Delta E_{\text{col}} \propto \tau_L$, for a static medium, but it can be much weaker for an expanding system. It should be recalled that we take no account here of the possibility of additional energy losses due to the soft interactions of hard partons with collective modes of quark–gluon plasma (so-called plasma polarization) [17], but the inclusion of these losses is not crucial for the effects considered in the present study.

The energy spectrum of medium-induced coherent gluon bremsstrahlung and the corresponding dominant part of radiative energy losses, dE/dx , were determined in [13, 14] from a Schrödinger type equation with a potential that is expressed in terms of the cross section for single hard-parton scattering in a medium. For the massless-quark case, the result has the form [14, 15]

$$\frac{dE^{\text{rad}}}{dx} \quad (20)$$

$$= \frac{2\alpha_s C_R}{\pi\tau_L} \int_{\omega_{\min}}^E d\omega \left[1 - y + \frac{y^2}{2} \right] \ln \left| \frac{\sin(\omega_1\tau_1)}{\omega_1\tau_1} \right|, \quad (21)$$

$$\omega_1 = \sqrt{i \left(1 - y + \frac{C_R}{3} y^2 \right) \bar{\kappa} \ln \frac{16}{\bar{\kappa}}}, \quad (21)$$

$$\bar{\kappa} = \frac{\mu_D^2 \lambda_g}{\omega(1-y)},$$

where $\tau_1 = \tau_L/(2\lambda_g)$, $y = \omega/E$ is the hard-parton-energy fraction carried away by the gluon, and $C_R = 4/3$ is the quark color factor. By setting $C_R = 3$ and by replacing the bracketed expression in Eq. (20) by the result obtained in [14] for gluons, one can obtain a similar expression for the gluon jet. Integration in (20) is performed with respect to the energy from the minimal gluon energy in the coherent Landau–Pomeranchuk–Migdal mode, $\omega_{\min} = E_{\text{LPM}} = \mu_D^2 \lambda_g$ (λ_g is the gluon range), to the maximum possible energy value equal to the initial hard-parton energy E . We were unable to single out the explicit functional τ_L and T dependences of dE^{rad}/dx because of the complicated form of Eq. (20). In the limiting case of a strong Landau–Pomeranchuk–Migdal effect, $\omega \gg \mu_D^2 \lambda_g$, one can find that, apart from a logarithmic factor, $dE/dx^{\text{rad}} \propto T^3$ and $dE/dx^{\text{rad}} \propto \tau_L$ [13, 14, 21]. The total radiative energy loss $\langle \Delta E_{\text{rad}} \rangle = \int d\tau dE^{\text{rad}}/dx$ can then be estimated as $\langle \Delta E_{\text{rad}} \rangle \propto T_0^3 \propto \varepsilon_0^{3/4}$ and $\Delta E_{\text{rad}} \propto \tau_L^\beta$, where $\beta \lesssim 2$ for an expanding medium ($\beta \sim 2$ for a static medium).

In order to simplify numerical calculations and to avoid introducing new parameters, we disregard here the transverse expansion of our quark–gluon fluid and effects associated with its viscosity; specifically, we make use of the well-known Bjorken scaling solution [34] for the temperature and density of quark–gluon plasma for $T > T_c \simeq 200$ MeV:

$$\varepsilon(\tau)\tau^{4/3} = \varepsilon_0\tau_0^{4/3}, \quad T(\tau)\tau^{1/3} = T_0\tau_0^{1/3}, \quad (22)$$

$$\rho(\tau)\tau = \rho_0\tau_0.$$

It should be noted, however, that a modification to hydrodynamics equations by introducing viscosity leads

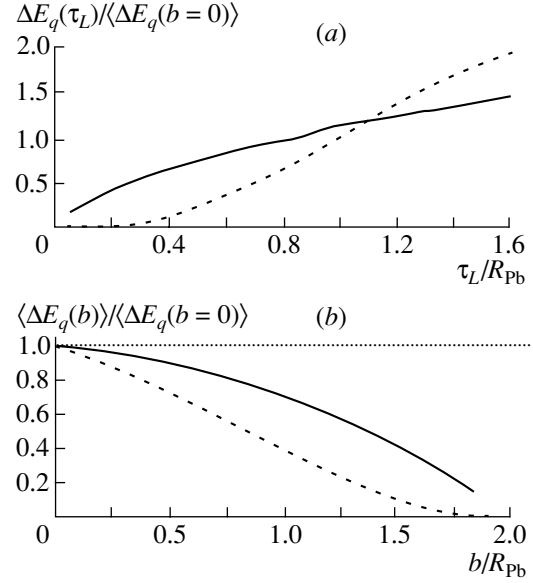


Fig. 5. (a) $\langle \tau_L \rangle$ and (b) b dependences of (dashed curves) radiative and (solid curves) collision energy losses experienced by a quark of initial energy $E_T^q = 100$ GeV. The results are normalized to the corresponding values at zero impact parameter ($b = 0$).

to a slower cooling of quark–gluon plasma, in which case a hard parton resides for a longer time in the hottest and densest regions of the medium, so that the rescattering intensity (which is a fast growing function of temperature) increases with increasing viscosity coefficient [18]; equivalently, the analogous result can be obtained by merely increasing the effective medium temperature. We do not consider the probability of hard-parton rescattering in nuclear matter either, since its intensity and the corresponding contribution to the total energy loss are not expected to be sizable because of much lower energy density in cold nuclear matter. For the sake of definiteness, we have used the initial conditions of the formation of gluon-rich plasma ($N_f \approx 0$, $\rho_g \approx 1.95T^3$) that are expected for PbPb central collisions at LHC [10]: $\tau_0 \approx 0.1$ fm/c and $T_0 \approx 1$ GeV. Needless to say, this estimate is quite rough and model-dependent—in particular, it depends on the uncertainty in the structure functions at small values of the Bjorken variable x .

For a hard quark of initial energy $E_T^q = 100$ GeV, Fig. 5a shows the calculated τ_L dependences of radiative (dominant medium-dependent coherent part) and collision energy losses. In order to obtain a more informative representation, the energy loss $\Delta E_T(\tau_L)$ is normalized to the corresponding mean values at zero impact parameter, in which case $\langle \Delta E_{T^{\text{rad}}}^q(b=0) \rangle \sim 16$ GeV and $\langle \Delta E_{T^{\text{col}}}^q(b=0) \rangle \sim 5$ GeV for the parameter values used here. It can be seen that the

radiative and the collision loss behave differently as functions of τ_L : $\Delta E_{\text{rad}}(\tau_L)$ grows somewhat faster than a linear function, whereas $\Delta E_{\text{col}}(\tau_L)$ seems to increase logarithmically. This leads to the corresponding difference in the impact-parameter dependence of the radiative and the collision energy loss, whose normalized profiles are displayed in Fig. 5b. By way of example, we indicate that, in response to an increase in the impact parameter from $b = 0$ to $b = R_{\text{pb}}$, the radiative and the collision loss decrease by about 60 and 30%, respectively. We have also found that the functional form of the b dependence of the collision loss is virtually insensitive to details of spacetime evolution (perfect versus viscous quark–gluon plasma), whereas the b dependence is more prone to respond to such effects.

It should be noted that the initial quark energy at the scale of $E_T^q \sim 100$ GeV corresponds to the threshold above which, in heavy-ion collisions at LHC, it becomes possible to single out hard QCD jets against the background of spurious jets (statistical fluctuations of the transverse-energy flux that are due to a formidable multiplicity of particles in an event) with a sufficiently high efficiency of reconstruction [31, 32, 40]. We hope that the contributions from the radiative and from the collision energy loss can be separated on the basis of the distinction between their angular distributions: the radiative component is dominant at comparatively small angular dimensions of the jet cone ($\theta_0 \rightarrow 0$), whereas the relative contribution of collision losses grows with increasing θ_0 .

4. IMPACT-PARAMETER DISTRIBUTION OF THE YIELD OF DIJETS

In the preceding section, we have analyzed the impact-parameter dependence of the parton-jet energy loss, which directly manifests itself as a P_T disbalance in hard QCD processes leading to the production of $Z + \text{jet}$ and $\gamma + \text{jet}$ systems. A suppression of the yield of hard jets in nucleus–nucleus interactions—this is due to jet–parton multiple scattering and energy losses in a dense medium—can be yet another observable effect. In this connection, we will estimate the impact-parameter distribution of the yield of such dijets. The number of $\{ij\}$ dijets having transverse momenta p_{T1} and p_{T2} and originating in initial hard scattering processes in AA interactions can be represented in the form

$$\frac{dN_{ij}^{\text{dijet}}}{dp_{T1}dp_{T2}} \quad (23)$$

$$= \int_0^\infty d^2b \frac{d^2\sigma_{\text{jet}}^0}{d^2b} \frac{dN_{ij}^{\text{dijet}}}{dp_{T1}dp_{T2}}(b) \bigg/ \int_0^\infty d^2b \frac{d^2\sigma_{\text{jet}}^0}{d^2b},$$

$$\frac{dN_{ij}^{\text{dijet}}}{dp_{T1}dp_{T2}}(b) = \int_0^{2\pi} d\psi$$

$$\times \int_0^{r_{\text{max}}} r dr T_A(r_1) T_A(r_2) \int_0^{2\pi} \frac{d\varphi}{2\pi} \quad (24)$$

$$\times \int dp_T^2 \frac{d\sigma_{ij}}{dp_T^2} \delta(p_{T1} - p_T + \Delta E_T^i(r, \psi, \varphi, b))$$

$$\times \delta(p_{T2} - p_T + \Delta E_T^j(r, \psi, \pi - \varphi, b)),$$

where $d\sigma_{ij}/dp_T^2$ is the cross section for hard parton–parton scattering in the c.m. frame. It is given by the expression

$$\frac{d\sigma_{ij}}{dp_T^2} = K \int dx_1 \int dx_2 \quad (25)$$

$$\times \int d\hat{t} f_i(x_1, p_T^2) f_j(x_2, p_T^2) \frac{d\hat{\sigma}_{ij}}{d\hat{t}} \delta(p_T^2 - \frac{\hat{t}\hat{u}}{\hat{s}}),$$

where $d\hat{\sigma}_{ij}/d\hat{t}$ is the differential parton–parton cross section as a function of the kinematical Mandelstam variables \hat{s} , \hat{t} , and \hat{u} ; $f_{i,j}$ are the structure functions for partons i and j ; x is the total-nucleon-momentum fraction carried away by a given parton; and the coefficient K takes into account higher order corrections in α_s . By using the procedure developed by Ellis *et al.* [41], we have verified that next-to-leading corrections in α_s are insignificant ($K \sim 1$) for jets having transverse momenta of $p_T \geq 50$ – 100 GeV/ c and typical angular cone dimensions of $R = 0.3$ – 0.5 in the (y, φ) plane (see also [42]). It should be emphasized that the effect of saturation for partonic structure functions characterizing an intranuclear nucleon (so-called nuclear shadowing)—it plays an important role at small values of the momentum fraction carried away by the parton ($x \ll 0.1$)—exerts virtually no influence on the yield of hard jets in the kinematical region of comparatively large $x_{1,2}$ considered here ($x_{1,2} \sim \sqrt{\hat{s}/s} \gtrsim 0.2$) [43]. For any case of AA collisions, the dijet yield integrated over some region above a threshold value p_T^{cut} and taken in relation to the yield from the corresponding pp collisions,

$$R_{AA}^{\text{dijet}}(p_{T1}, p_{T2} > p_T^{\text{cut}}) \quad (26)$$

$$= \int_{p_T^{\text{cut}}} dp_{T1} \int_{p_T^{\text{cut}}} dp_{T2} \sum_{i,j} \left(\frac{dN_{ij}^{\text{dijet}}}{dp_{T1}dp_{T2}} \right)_{AA},$$

can be normalized by using the known cross section that describes some unsuppressed process and which is proportional to the number of binary nucleon–nucleon collisions in the nucleus–nucleus interaction being studied. For such a process, we can consider the production of hard Drell–Yan muon pairs or (what

is more appropriate for the case of LHC [26]) the production of a $Z(\rightarrow \mu^+\mu^-)$ boson:

$$\begin{aligned} & R_{AA}^{\text{dijet}}/R_{pp}^{\text{dijet}} \quad (27) \\ & = \left(\sigma_{AA}^{\text{dijet}}/\sigma_{pp}^{\text{dijet}} \right) / \left(\sigma_{AA}^{\text{DY}(Z)}/\sigma_{pp}^{\text{DY}(Z)} \right). \end{aligned}$$

The initial impact-parameter distribution $d^2\sigma_{\text{jet}}^0/d^2b$ of the cross section for jet production in AA collisions has the form [31, 35]

$$\begin{aligned} & \frac{d^2\sigma_{\text{jet}}^0}{d^2b}(\mathbf{b}, \sqrt{s}) \quad (28) \\ & = T_{AA}(\mathbf{b})\sigma_{NN}^{\text{jet}}(\sqrt{s})\frac{d^2\sigma_{AA}^{\text{in}}}{d^2b}(\mathbf{b}, \sqrt{s}), \end{aligned}$$

where the relevant cross section for the hard process in a nucleon–nucleon collision, σ_{NN}^{jet} , was calculated on the basis of the PYTHIA model [44] used together with the STEQ2L parametrization of the structure function. The total inelastic cross section for AA interaction is calculated as

$$\begin{aligned} & \frac{d^2\sigma_{AA}^{\text{in}}}{d^2b}(\mathbf{b}, \sqrt{s}) \quad (29) \\ & = \left[1 - \left(1 - \frac{1}{A^2}T_{AA}(\mathbf{b})\sigma_{NN}^{\text{in}}(\sqrt{s}) \right)^{A^2} \right], \end{aligned}$$

where the cross section for nondiffractive inelastic nucleon–nucleon interaction is $\sigma_{NN}^{\text{in}}(\sqrt{s} = 5.5 \text{ TeV}) \simeq 60 \text{ mb}$.

For three cases where (i) there are no energy losses, (ii) only collision losses are included, and (iii) both radiative and collision losses are included, Fig. 6 displays the impact-parameter distribution of the jet yield, $\sigma_{AA}^{\text{in}}R_{AA}^{\text{dijet}}L$ ($E_T^{\text{jet}} > p_T^{\text{cut}} = 100 \text{ GeV}$, the rapidity acceptance being $|y^{\text{jet}}| < 2.5$). The jet yield is normalized to the expected number of events in PbPb collisions over two weeks ($1.2 \times 10^6 \text{ s}$) of LHC operation at the presumed luminosity of $L = 10^{27} \text{ cm}^{-2} \text{ s}^{-1}$ [32]. The initial number of jets produced with $E_T^{\text{jet}} > 100 \text{ GeV}$ is estimated at 1.1×10^7 (where approximately 60, 30, and 10 percent correspond to $gg \rightarrow gg$, $qg \rightarrow qg$, and $qq, gg \rightarrow qq$, respectively). As might have been expected, the suppression of the dijet yield is much more pronounced in central than in peripheral collisions. Observation of sizable changes in the impact-parameter dependence and in the absolute yield of dijets in heavy-ion collisions in relation to the analogous changes that are expected from the pattern of independent nucleon–nucleon interactions can furnish information about the intensity of parton rescattering in a medium.

As has already been mentioned, a correlation between the transverse-energy flux E_T^{tot} and the impact parameter b [36]—approximately, $\overline{E_T^{\text{tot}}}(b) \propto$

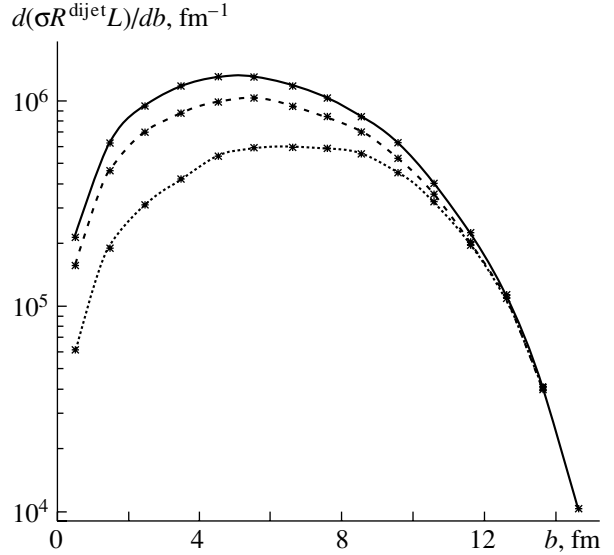


Fig. 6. Impact-parameter distribution of the yield of dijets with $E_T^{\text{jet}} > 100 \text{ GeV}$ and $|y^{\text{jet}}| < 2.5$ for three cases: (solid curve) without energy losses, (dashed curve) with allowance for only collision losses, and (dotted curve) with allowance for both radiative and collision losses. The yield of jets was normalized to the expected number of events in PbPb collisions over two weeks of LHC operation at the luminosity of $L = 10^{27} \text{ cm}^{-2} \text{ s}^{-1}$.

$T_{AA}(b)$ —can serve as an experimental criterion of the degree to which a given event is central. If the jet energy loss $\langle \Delta E_T^{\text{jet}} \rangle$ (14) or the dijet yield R^{dijet} as given by (26) and (27) changes as a function of E_T^{tot} , one can obtain a relation between the b and the E_T^{tot} dependences for $F = (\Delta E_T^{\text{jet}}, R^{\text{dijet}})$ by using the $E_T^{\text{tot}} - b$ correlation function C_{AA} :

$$F(E_T^{\text{tot}}) = \int d^2b F(b) C_{AA}(E_T^{\text{tot}}, b), \quad (30)$$

$$= \frac{1}{\sqrt{2\pi}\sigma_{E_T}(b)} \exp \left(-\frac{\left(E_T^{\text{tot}} - \overline{E_T^{\text{tot}}}(b) \right)^2}{2\sigma_{E_T}^2(b)} \right),$$

$$F(b) = \int dE_T^{\text{tot}} F(E_T^{\text{tot}}) C_{AA}(b, E_T^{\text{tot}}), \quad (31)$$

$$= \frac{1}{\sqrt{2\pi}\sigma_b(E_T^{\text{tot}})} \exp \left(-\frac{\left(b - \overline{b}(E_T^{\text{tot}}) \right)^2}{2\sigma_b^2(E_T^{\text{tot}})} \right).$$

For AA collisions at LHC, Zarubin *et al.* [45], who relied on the HIJING model [46], estimated the accuracy in determining the impact parameter at $\sigma_b(E_T^{\text{tot}}) \sim 1\text{--}2 \text{ fm}$, which seems sufficient for observing effects considered in the present study.

5. SPECTRUM OF $\mu^+\mu^-$ PAIRS OF LARGE INVARIANT MASSES

While the P_T disbalance in the $Z + jet$ and $\gamma + jet$ production processes is due to jet energy losses predominantly initiated by light u and d quarks and while the suppression of dijet yields carries information predominantly about gluon strings, the spectrum of muon pairs having large invariant masses is sensitive to the rescattering of heavy b and c quarks, whose pairs, $b\bar{b}$ and $c\bar{c}$, are produced at the earliest stages of a nucleus–nucleus collision in hard gluon–gluon interactions; after that, they move through a dense medium and, picking up, at the hadronization stage, a u or a d quark, form B and D mesons. After a lapse of some time of about their mean lifetime ($c\tau_{B^\pm} = 495 \mu\text{m}$, $c\tau_{B^0} = 468 \mu\text{m}$, $c\tau_{D^\pm} = 300 \mu\text{m}$, $c\tau_{D^0} = 124 \mu\text{m}$), these mesons in turn decay into hadrons and leptons. In particular, about 20% of B mesons and about 12% of D mesons produce muons, about one-half of muons from B mesons being generated through an intermediate D meson. At the LHC energy, the contribution of the pairs of oppositely charged muons, $\mu^+\mu^-$, from a semileptonic $b\bar{b}$ decay is dominant in the invariant-mass-spectrum region $M_{\mu^+\mu^-} = \sqrt{(E_{\mu^+} + E_{\mu^-})^2 - (\mathbf{p}_{\mu^+} + \mathbf{p}_{\mu^-})^2} = 20\text{--}50 \text{ GeV}/c^2$ [47], which is unaffected by the decays of heavy quarkonia ($M_{\mu^+\mu^-}^{\Upsilon} \simeq 10 \text{ GeV}/c^2$) and of the Z boson ($M_{\mu^+\mu^-}^Z \simeq 90 \text{ GeV}/c^2$). Here, the direct production of Drell–Yan muon pairs through the channel $q\bar{q} \rightarrow \mu^+\mu^-$ appears to be the main source of background. In addition, a contribution commensurate with the $b\bar{b}$ signal comes from the uncorrelated pion and kaon decays $\pi^\pm, K^\pm \rightarrow \mu^\pm\nu(\bar{\nu})$, as well as from muon pairs of a mixed type (for example, one muon from a hadronic decay and the other from $b \rightarrow B$). However, this uncorrelated part of the spectrum can be subtracted if use is made of pairs formed by likely charged muons:

$$\frac{dN_{\mu^+\mu^-}^{\text{uncor}}}{dM} = 2\sqrt{\frac{dN_{\mu^+\mu^+}}{dM} \frac{dN_{\mu^-\mu^-}}{dM}}. \quad (32)$$

We have performed a Monte Carlo simulation of the production, rescattering, and hadronization of b and c quarks in PbPb collisions at the LHC energy. The cross section for heavy-quark production (as well as the cross section for the production of Drell–Yan dimuons in nucleon–nucleon interactions at $\sqrt{s} = 5.5 \text{ TeV}$), their initial momentum spectra, and the schemes of the hadronization and fragmentation of B and D mesons were obtained with the aid of the PYTHIA-5.7 model [44]. The corresponding cross sections for PbPb collisions were normalized to the number of binary nucleon–nucleon collisions, and the initial impact-parameter distribution of the quark

yield was specified according to (28). We have also taken into account the modification of the nucleon structure function in the nucleus (nuclear shadowing) on the basis of the phenomenological parametrization introduced in [43]; in the mass region being considered, this has led to a slight decrease in the yield of $\mu^+\mu^-$ pairs in relation to the signal (by about 15%) and the Drell–Yan background (by about 25%).

The range of a heavy quark in a longitudinally expanding dense medium was simulated in accordance with the distribution in (15). In a specific i th collision with a medium constituent moving at the same longitudinal rapidity y and having an energy m_{0i} , a hard quark of mass M_q and energy E lost energy Δe_i and, accordingly, the transverse (with respect to the collision axis) energy Δe_i^T [see Eq. (19)] and changed the direction of its motion, acquiring an additional transverse momentum (in relation to the current momentum \mathbf{p}) $\Delta \tilde{\mathbf{k}}_{ti}$. In the case of relativistic kinematics, $E \gg m_0$, we have

$$\begin{aligned} \Delta e_i^T &= \frac{t_i}{2m_{0i}} = \frac{\Delta e_i}{\text{cosh}y} - \Delta \tilde{k}_{ti} \tanh y, \quad (33) \\ \Delta \tilde{k}_{ti}^2 &= \left(E - \frac{t_i}{2m_{0i}}\right)^2 \\ &- \left(p - \frac{E}{p} \frac{t_i}{2m_{0i}} - \frac{t_i}{2p}\right)^2 - M_q^2. \end{aligned}$$

For the b - and c -quark masses, we used the values of $M_b = 5 \text{ GeV}/c^2$ and $M_c = 1.35 \text{ GeV}/c^2$. The problem of correctly describing the coherent pattern of radiative heavy-quark energy loss has yet to be solved. There is every reason to believe that medium-induced gluon bremsstrahlung from slow quarks ($p_T \lesssim M_q$) is suppressed [38]. At the same time, the spectrum of gluon bremsstrahlung from a massless quark corresponds to the limiting ultrarelativistic case of $p_T \gg M_q$ [see Eq. (20)]. In our case, the main contribution to the invariant-mass region $M_{\mu^+\mu^-} = 20\text{--}50 \text{ GeV}/c^2$ comes from b quarks with intermediate momentum values in the range $p_T \gtrsim 5\text{--}10 \text{ GeV}/c$, but a reliable scheme for calculating their radiative energy losses has not yet been developed. In the calculations presented here, we have taken into account only collision energy losses, thereby deriving a lower bound on the sensitivity of the spectrum of $\mu^+\mu^-$ pairs to medium-induced heavy-quark rescattering.

In the case where a heavy quark lost so great an amount of energy that its transverse momentum upon some scattering event proved to be less than the mean transverse momentum of a thermal medium constituent at temperature T , this quark became a part of the thermalized system; its momentum

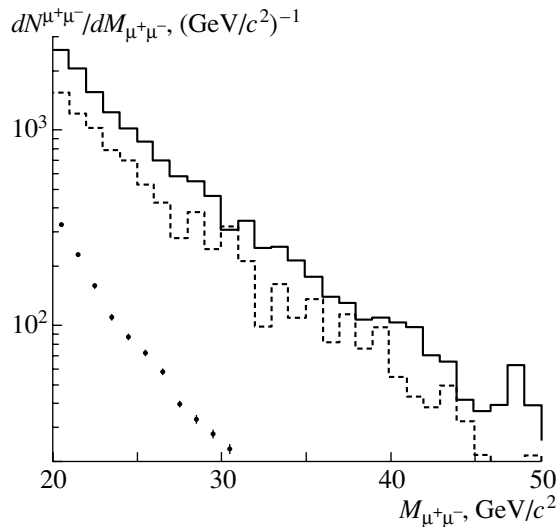


Fig. 7. Invariant-mass ($M_{\mu^+\mu^-}$) distribution of $\mu^+\mu^-$ pairs from $b\bar{b}$ (solid-line histogram) without rescattering and (dashed-line histogram) with allowance for rescattering and for collision energy losses and of (points) Drell–Yan dimuons. The data presented in this figure were obtained for $p_T^\mu > 5$ GeV/c, $|y^\mu| < 2.4$, and $p_T^{\mu^+} + p_T^{\mu^-} < 20$ GeV/c. The histograms are normalized to the number of events in PbPb collisions over two weeks of LHC operation at the luminosity of $L = 10^{27}$ cm $^{-2}$ s $^{-1}$.

was then generated in the rest frame of the comoving medium element from the distribution $dN/d^3p \propto \exp(-E/T)$, whereupon a Lorentz transformation to the c.m. frame of the nucleus–nucleus collision was performed.

In order to be consistent with the acceptance of the CMS experiment [32] at LHC, we selected only muons that had momentum and pseudorapidity values in the regions $p_T^\mu > 5$ GeV/c and $|\eta^\mu| < 2.4$, respectively. In addition, we imposed a constraint on the total transverse momentum of the dimuon, $p_T^{\mu^+} + p_T^{\mu^-} < 20$ GeV/c; owing to this, the relative contribution of the background (Drell–Yan pairs) from the unsuppressed $b\bar{b}$ signal in the mass region $M_{\mu^+\mu^-} = 20\text{--}50$ GeV/c 2 was reduced from 15 to 8%, with resulting decrease in total statistics being approximately twofold.²⁾ In the case free from rescattering, the number of $\mu^+\mu^-$ pairs from $c\bar{c}$ decays is approximately one-fifth as great as the $b\bar{b}$ signal and is commensurate with the number of background dimuons; in the following, only the dominant channel

²⁾The possibility of such a background discrimination is due to the distinctions between the p_T distributions of muons from $b\bar{b}$ decays and Drell–Yan muons: the harder spectrum of the latter results in that the contribution to the region of large invariant masses comes from high- p_T muons.

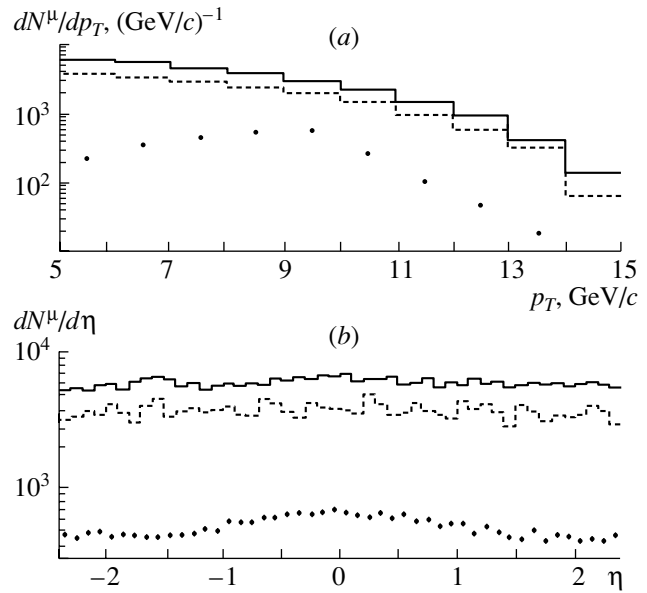


Fig. 8. (a) Transverse-momentum (p_T) and (b) pseudorapidity (η) distribution of muons in the region $M_{\mu^+\mu^-} = 20\text{--}50$ GeV/c 2 . The notation is identical to that in Fig. 7.

$b\bar{b} \rightarrow B\bar{B} \rightarrow \mu^+\mu^-X$ will therefore be considered as a signal.

Figures 7, 8a, and 8b show, respectively, the invariant-mass, transverse-momentum, and rapidity distributions of $\mu^+\mu^-$ pairs. In these figures, the histograms are normalized to the expected number of events in PbPb collisions over two weeks (1.2×10^6 s) of LHC operation at the luminosity of $L = 10^{27}$ cm $^{-2}$ s $^{-1}$. The total number of $\mu^+\mu^-$ pairs in the region $M_{\mu^+\mu^-} = 20\text{--}50$ GeV/c 2 is estimated at 1.4×10^4 for an unsuppressed $b\bar{b}$ signal and at 1.3×10^3 for the Drell–Yan background. The rescattering of b quarks in quark–gluon plasma and their collision energy losses reduce the integrated yield of $\mu^+\mu^-$ pairs by a factor of about 1.6, the effect, as might have been expected, being the most pronounced for muons with lower p_T and being weakened with increasing p_T . We have also found that the suppression of the yield of $\mu^+\mu^-$ by a factor of about 1.8 in central ($b \rightarrow 0$) collisions exceeds only slightly the effect summed over all events. This is due, in particular, to a relatively weak impact-parameter dependence of collision energy losses (see Fig. 5b): for example, a change in the impact-parameter value from $b = 0$ to $b = 0.9R_{\text{Pb}} \simeq 6$ fm (events in which $b \lesssim 6$ fm produce half of $b\bar{b}$ pairs) reduces collision losses only by about 25%. The inclusion of the b -quark collision energy loss can somewhat enhance the suppression of the

dimuon yield and, probably, render the effect more sensitive to variations in the impact parameter.

It should be noted that, to some extent, the cross sections for heavy-quark production that are estimated on the basis of PYTHIA and the corresponding spectra of $\mu^+\mu^-$ pairs in nucleon–nucleon collisions depend on the choice of structure functions, hadronization scheme, and B - and D -meson fragmentation functions. Moreover, it is necessary in general to take into account higher order corrections of perturbative QCD in α_s , but their effect is moderate in the region of p_T^μ and $M_{\mu^+\mu^-}$ values under study; in summary, we can expect (see [48]) correction-factor values of $K \sim 1.5$ for the $b\bar{b}$ signal and $K \sim 1$ for Drell–Yan $\mu^+\mu^-$ pairs. In any case, it is necessary to introduce a normalization to the corresponding spectra of $\mu^+\mu^-$ pairs of large invariant masses in pp collisions; measurement of the production cross section for such muon pairs would make it possible to refine our estimates for the yield of dimuons in AA interactions. If it is observed that, in relation to what is expected from the pattern of independent nucleon–nucleon interactions, the yield of $\mu^+\mu^-$ pairs in heavy-ion collisions is suppressed to an extent greater than that associated with nuclear shadowing, this will suggest that massive (predominantly, b) quarks undergo dense-medium-induced rescattering and lose energy.

6. CONCLUSION

In connection with experimental investigations into the properties of superdense QCD matter formed in ultrarelativistic heavy-ion collisions (in particular, at the LHC energy), it seems promising to make use of special features of particle and jet production in hard QCD processes. These features include a suppression of the hard-dijet yield, a transverse-momentum disbalance in the $Z + \text{jet}$ and $\gamma + \text{jet}$ processes, and a modification to the spectra of $\mu^+\mu^-$ pairs having large invariant masses and originating from the decays of B and D mesons. The rescattering of partons in a medium that were produced in hard processes at the early reaction stage leads to far-reaching consequences: these partons lose energy through collisions and radiation. The radiative and the collision energy loss show markedly different dependences on the impact parameter b of the nucleus–nucleus collisions in question. This distinction is associated with the coherent nature of the radiation induced by a QCD medium (the parton energy loss per unit length, dE/dx , depends on the total distance L traveled in dense matter). The radiative energy losses are more sensitive to variations in the impact parameter, which determines the effective volume

of the dense nuclear-overlap region, and to the spacetime evolution of the medium.

A direct observation of the jet energy losses initiated primarily by light u and d quarks is possible in analyzing the distributions of the P_T disbalance in the $Z + \text{jet}$ and $\gamma + \text{jet}$ processes. Since the mean distance $\langle L \rangle$ traveled by a hard parton in a dense medium decreases almost linearly with increasing b and since the initial energy density ε_0 in the dense region changes only slightly with increasing b ($\delta\varepsilon_0 \lesssim 10\%$) up to $b \sim R_A$, investigation of the energy loss as a function of L by varying the impact parameter (measured on the basis of the total energy release in the calorimeter) is preferable to the use of beams of different ions at a fixed $b \sim 0$ (in which case $\langle L \rangle \propto A^{1/3}$, but $\varepsilon_0 \propto A^{2/3}$). We hope that, for jets of a nonzero cone, the contributions from radiative and collision losses can be separated on the basis of the distinction between their angular distributions.

The yield of hard dijets is suppressed because of energy losses, primarily gluon-jet energy losses, and is much more pronounced in central collisions rather than in peripheral ones, with the result that the impact-parameter distribution of dijets can be noticeably modified. The spectra of $\mu^+\mu^-$ pairs of large invariant masses are of interest because of their sensitivity to rescattering induced by a dense QCD medium and to the energy lost by heavy b and c quarks.

ACKNOWLEDGMENTS

We are grateful to R. Vogt, Yu.L. Dokshitzer, and L.I. Sarycheva for stimulating discussions.

REFERENCES

1. H. Satz, Phys. Rep. **88**, 349 (1982).
2. I. L. Rozental' and Yu. A. Tarasov, Usp. Fiz. Nauk **163** (7), 29 (1993) [Phys. Usp. **36**, 572 (1993)].
3. M. I. Dremin and A. V. Leonidov, Usp. Fiz. Nauk **165**, 759 (1995) [Phys. Usp. **38**, 723 (1995)].
4. J. W. Harris and B. Muller, Annu. Rev. Nucl. Part. Sci. **46**, 71 (1996).
5. I. P. Lokhtin, L. I. Sarycheva, and A. M. Snigirev, Fiz. Élem. Chastits At. Yadra **30**, 660 (1999) [Phys. Part. Nucl. **30**, 279 (1999)].
6. S. A. Bass, M. Gyulassy, H. Stöcker, and W. Greiner, J. Phys. G **25**, R1 (1999).
7. T. Matsui and H. Satz, Phys. Lett. B **178**, 416 (1986); D. Kharzeev and H. Satz, Phys. Lett. B **334**, 155 (1994).
8. NA50 Collab. (M. C. Abreu *et al.*), Phys. Lett. B **410**, 337 (1997); **450**, 456 (1999).
9. R. Vogt, Phys. Rep. **310**, 197 (1999).

10. K. J. Eskola, K. Kajantie, and P. V. Ruuskanen, Phys. Lett. B **332**, 191 (1994); Eur. Phys. J. C **1**, 627 (1998); K. J. Eskola, Prog. Theor. Phys. Suppl. **129**, 1 (1997); Comments Nucl. Part. Phys. **22**, 185 (1998); K. J. Eskola and K. Tuominen, Preprint JYFL-1-00; hep-ph/0002008.
11. M. G. Ryskin, Yad. Fiz. **52**, 219 (1990) [Sov. J. Nucl. Phys. **52**, 139 (1990)].
12. M. Gyulassy and X.-N. Wang, Nucl. Phys. B **420**, 583 (1994); X.-N. Wang, M. Gyulassy, and M. Plumer, Phys. Rev. D **51**, 3436 (1995).
13. R. Baier, Yu. L. Dokshitzer, S. Peigne, and D. Schiff, Phys. Lett. B **345**, 277 (1995); R. Baier, Yu. L. Dokshitzer, A. H. Mueller, *et al.*, Nucl. Phys. B **483**, 291 (1997).
14. R. Baier, Yu. L. Dokshitzer, A. H. Mueller, and D. Schiff, Nucl. Phys. B **531**, 403 (1998); Phys. Rev. C **58**, 1706 (1998).
15. B. G. Zakharov, Pis'ma Zh. Éksp. Teor. Fiz. **65**, 615 (1997) [JETP Lett. **65**, 615 (1997)].
16. U. Wiedemann and M. Gyulassy, Nucl. Phys. B **560**, 345 (1999).
17. S. Mrowczynsky, Phys. Lett. B **269**, 383 (1991); M. H. Thoma, Phys. Lett. B **273**, 128 (1991).
18. I. P. Lokhtin and A. M. Snigirev, Yad. Fiz. **60**, 360 (1997) [Phys. At. Nucl. **60**, 295 (1997)].
19. B. G. Zakharov, Yad. Fiz. **61**, 924 (1998) [Phys. At. Nucl. **61**, 838 (1998)].
20. I. P. Lokhtin and A. M. Snigirev, Phys. Lett. B **440**, 163 (1998).
21. R. Baier, Yu. L. Dokshitzer, A. H. Mueller, and D. Schiff, Phys. Rev. C **60**, 064902 (1999).
22. B. G. Zakharov, Pis'ma Zh. Éksp. Teor. Fiz. **70**, 181 (1999) [JETP Lett. **70**, 176 (1999)].
23. M. Gyulassy and M. Plumer, Phys. Lett. B **243**, 432 (1990).
24. M. Gyulassy, M. Plumer, and X.-N. Wang, Nucl. Phys. A **590**, 511 (1995).
25. I. P. Lokhtin, L. I. Sarycheva, and A. M. Snigirev, Yad. Fiz. **62**, 1333 (1999) [Phys. At. Nucl. **62**, 1258 (1999)].
26. V. Kartvelishvili, R. Kvatadze, and R. Shanidze, Phys. Lett. B **356**, 589 (1995).
27. X.-N. Wang, Z. Huang, and I. Sarcevic, Phys. Rev. Lett. **77**, 231 (1996).
28. E. Shuryak, Phys. Rev. C **55**, 961 (1997).
29. Z. Lin, R. Vogt, and X.-N. Wang, Phys. Rev. C **57**, 899 (1998); Z. Lin and R. Vogt, Nucl. Phys. B **544**, 339 (1999).
30. B. Kampfer, O. P. Pavlenko, and K. Gallmeister, Phys. Lett. B **419**, 412 (1998).
31. M. Bedjidian, I. P. Lokhtin, *et al.*, CERN CMS NOTE 1999/016.
32. CMS Collab., Technical Proposal, CERN/LHCC 94-38.
33. K. J. Eskola, B. Müller, and X.-N. Wang, Phys. Lett. B **374**, 20 (1996).
34. J. D. Bjorken, Phys. Rev. D **27**, 140 (1983).
35. R. Vogt, Heavy Ion Phys. **9**, 339 (1999).
36. V. Kartvelishvili and R. Kvatadze, CERN CMS NOTE 1999/015.
37. I. Sarcevic, Nucl. Phys. A **638**, 531 (1998); V. Emel'yanov, A. Khodinov, S. R. Klein, and R. Vogt, Phys. Rev. C **59**, R1860 (1999).
38. M. G. Mustafa, D. Pal, D. K. Srivastava, and M. Thoma, Phys. Lett. B **428**, 234 (1998).
39. S. Nadkarni, Phys. Rev. D **33**, 3738 (1986).
40. N. A. Kruglov, I. P. Lokhtin, L. I. Sarycheva, and A. M. Snigirev, Z. Phys. C **76**, 99 (1997).
41. S. D. Ellis, Z. Kunszt, and D. E. Soper, Phys. Rev. Lett. **62**, 726 (1989); Phys. Rev. D **40**, 2188 (1989); Phys. Rev. Lett. **69**, 1496 (1992).
42. K. J. Eskola and X.-N. Wang, Int. J. Mod. Phys. A **10**, 3071 (1995).
43. K. J. Eskola, Nucl. Phys. B **400**, 240 (1993); K. J. Eskola, V. J. Kolhinen, and C. A. Salgado, Eur. Phys. J. C **9**, 61 (1999).
44. T. Sjostrand, Comput. Phys. Commun. **82**, 74 (1994).
45. P. I. Zarubin, M. V. Savina, N. V. Slavin, and S. V. Shmatov, Yad. Fiz. **62**, 2263 (1999) [Phys. At. Nucl. **62**, 2084 (1999)].
46. M. Gyulassy and X.-N. Wang, Comput. Phys. Commun. **83**, 307 (1994).
47. M. Bedjidian, V. Kartvelishvili, and R. Kvatadze, CERN CMS NOTE 1999/017.
48. S. Gavin *et al.*, Int. J. Mod. Phys. A **10**, 2961 (1995); P. L. McGaughey *et al.*, Int. J. Mod. Phys. A **10**, 2999 (1995); R. Vogt, Z. Phys. C **71**, 475 (1996).

Translated by A. Isaakyan

ELEMENTARY PARTICLES AND FIELDS
Theory

Running Coupling at Low Momenta, Renormalization Schemes, and Renormalons*

N. V. Krasnikov and A. A. Pivovarov

*Institute for Nuclear Research, Russian Academy of Sciences,
pr. Shestidesyatiletiya Oktyabrya 7a, Moscow, 117312 Russia*

Received April 4, 2000

Abstract—We propose a method for summing a perturbation-theory asymptotic series that is related to infrared (IR) renormalons in QCD using special renormalization schemes in which the running coupling constant can be integrated over the small momenta. For our method to work, we should consider higher order perturbation-theory corrections to the standard bubble-chain diagrams. High-order corrections allow one to choose a scheme in which the coupling-constant evolution can be smoothly extrapolated to low momenta. In these schemes, the sum of an (extended) IR-renormalon asymptotic series is defined as an integral of the running coupling constant over the IR region. We present explicit examples of renormalization schemes of QCD that can be used to sum IR-renormalon asymptotic series according to our definition. © 2001 MAIK “Nauka/Interperiodica”.

High-order behavior of perturbation-theory (PT) series in quantum field theory determines the analytic structure of amplitudes as functions of the coupling constant. This analytic structure encodes important information about the ultimate precision obtainable in finite-order PT analysis for physical observables. The general approach to analyzing high-order PT expansions is based on the saddle-point approximation for evaluating a path integral [1–3]. The leading asymptotic behavior of PT coefficients was investigated in some simplified models of quantum field theory, but there are still no exact results in realistic theories like QCD.

Another approach to the high-order behavior and to the determination of possible corrections to finite-order PT expressions is based on selecting numerically large contributions of some particular subclass of simple diagrams [4, 5]. In QED, such a set of diagrams is generated by inserting an infinite number of one-loop fermionic corrections in the photon propagator (so-called bubble-chain diagrams). In other gauge models (for instance, in QCD), the selection of relevant diagrams (or even only parts of them) is more involved because of the need for preserving gauge invariance. The properties of summability of the divergent series [6] emerging from a type of high-order behavior (bubble chains or renormalons) were studied in [7–9]. There are two kinds of renormalon contributions: ultraviolet (UV) and infrared (IR) ones. They are complementary: UV renormalons correspond to integration over large energies, while IR ones correspond to integration over small energies. Depending

on the model, renormalons lead to alternating (Borel-summable) or nonalternating (Borel-nonsummable) asymptotic series. It is generally assumed that the Borel sum gives the proper value for the asymptotic series, which means that the theory can cope with such type of singularities. The appearance of Borel-nonsummable series is usually considered as an indication of an inconsistency in the theory. In the leading-order approximation for the β function of QCD, IR renormalons provide an example of Borel-nonsummable series.

Recently, IR renormalons in QCD have drawn closer attention [10] in connection with possible theoretical nonperturbative corrections to some observables. Interest in such corrections is caused by a limitation on the accuracy of finite-order PT expressions and by a significant improvement in the precision of experimental data (see, for example, [11]). Usually non-PT corrections are taken into account within the operator-product expansion (OPE), which is a general method of quantum field theory [12]. However, OPE has been proven only within PT; its validity beyond PT has not yet been established rigorously, although it was studied in some models [13, 14]. In cases of quantities related to two-point correlation functions, nonperturbative terms can be represented semiphenomenologically as the vacuum expectation values of some local operators [15, 16]. Such an approach turned out to be quite successful in investigating the hadron properties in QCD [17]. In more complicated cases, however, there is no well-established technique to calculate nonperturbative contributions.

*This article was submitted by the authors in English.

In such cases, one can hope to find necessary non-perturbative terms by studying the structure of high orders of standard PT and by resumming the most divergent contributions. Infrared renormalons are proposed as proper candidates for such a summation.

Note that, in QED, a consideration of renormalon chains as dominant contributions becomes well-justified within a $1/N_F$ expansion [18]. As for QCD, no formal expansion in which renormalon chains would constitute dominant contributions has been constructed so far. Therefore, results based on considering renormalon chains are plausible, but they are not rigorous (see, for example, [19, 20]). The technical trick that is used as a theoretical basis for constructing renormalon contributions in a gauge-invariant way is the method of “naive non-Abelianization” [21, 22] that, in practice, is equivalent to substituting the leading-order running coupling constant into integrals over phase space. Thus, the simplicity of renormalon approximations, which makes them attractive from the practical point of view, is due to the fact that relevant diagrams are closely related to the running of the coupling constant within the renormalization-group analysis. Therefore, renormalon contributions in a given model of quantum field theory can be formally obtained in two ways: either by directly summing a selected set of diagrams or by integrating the running coupling constant over the phase space of the leading-order diagram, which serves as a source for bubble chain generation. Note that these two ways of looking at renormalon contributions (direct summation of a given subclass of diagrams or even only of their leading behavior vs. integration of the running coupling constant) are similar to two ways in which ultraviolet asymptotic behavior in quantum electrodynamics was historically obtained in high orders. The first way was a direct summation of diagrams in all orders [23], while the second was based on performing a one-loop calculation of the β function and solving the renormalization-group (RG) equation for the invariant charge [24, 25]. Note that the first way (direct summation) is very difficult to use in higher orders, while the second (solving the RG equations for higher order β function) is much more feasible. The same is true for renormalons: it is difficult to analyze corrections to the leading-order renormalon expressions within the direct-summation approach, but integration of the running coupling constant can be performed in any order of approximation for the evolution—one needs to calculate the β function of the model. The technique for calculating RG functions is well-advanced in renormalization schemes of the MS type (see, for example, [26]).

In the following, we will mainly discuss QCD as the most interesting model for a practical ap-

plication of renormalon-type estimates (see, for example, [27]). Ultraviolet renormalons correspond to integration over high energies, where the running coupling constant in OCD is regular (asymptotic freedom) and where the integral is well-defined, which solves the problem of summing ultraviolet-renormalon contributions. In the direct-summation technique, these types of contributions correspond to alternating asymptotic series, which are Borel-summable. They can also be obtained by a formal term-by-term integration of the expansion of the running coupling constant.

Infrared renormalons correspond to contributions of the infrared domain of phase space. Within the integration technique, one should integrate the running coupling constant over low energies, where it is singular in the leading order of PT (Landau pole). Therefore, the integral (and the contribution of IR renormalon) is not defined in the leading order of the evolution of the coupling constant. By expanding the running coupling constant in PT series under the integration sign and by integrating the resulting series term by term, one arrives at divergent series that are not Borel-summable. This corresponds to the direct-summation method. Thus, the problem of summing large contributions stemming from the infrared region (asymptotic series) can be reduced (at least at the computational level) to defining the integral of the running coupling constant over low momenta. If there is a singularity in this region (the standard situation in the leading order of PT in QCD, where there is the Landau pole), then it is necessary to interpret the integral. Therefore, one can identify, at the computational level, the set of contributions leading to singularities that are not summable by the Borel technique as that which emerges from the formal integral of the running coupling constant over the infrared region. A definition of the evolution in the IR region can then provide a recipe for a resummation of Borel-nonsummable asymptotic series. Note that, in this region, the evolution trajectory is not perturbative, which gives no way to obtain reliable results on the running at low momenta. The pole appears, however, in the leading order for the β function computed within perturbation theory. The pole can disappear in higher orders (infrared fixed point), or the kind of the singularity can change (it can become an integrable one, and the integration will lead to a physically acceptable result), or the singularity can be eliminated by summing an infinite subset of terms for the β function. In these cases, integration is possible, which defines the way of resummation of the asymptotic series generated by the IR renormalon; this means that higher order corrections stabilize the theory. In the direct-summation technique, this corresponds to the situation where higher order

corrections render the asymptotic series related to IR renormalon Borel-summable. Note that, technically, analysis of higher order corrections that is based on integration of the running coupling constant is easier. Therefore, we propose dealing with the problem of defining IR-renormalon contributions in the following way. We choose to generate the renormalon approximation from integration of the running coupling constant over the IR region. This is simpler, this can be written in a compact form, and this can easily be generalized to higher orders. In the leading order, this is equivalent to the naive-non-Abelianization trick. Then, the IR contribution is not defined in the leading order because of the singularity in the running coupling constant formally extrapolated to low momenta. However, the method of integration allows one to generalize the renormalon expressions to higher orders of coupling evolution. In higher orders, however, there is a freedom of choosing renormalization schemes for the coupling constant. One can always find renormalization schemes in which the running coupling constant is integrable in the IR region [28]. With such a coupling constant, we obtain a particular way of resummation of renormalon-type contributions.

This procedure can easily be understood in QED, though the UV and IR renormalons interchange. In QED, the leading-order coefficient of the beta function that governs the evolution of the coupling constant has the opposite sign in relation to the standard QCD (with three light flavors), and one can perform integration over the IR region, where there are no singularities in the running coupling constant. Therefore, IR-renormalon contributions in QED are well-defined. Ultraviolet renormalons in QED are ill-defined (in just the same way as IR renormalons in QCD) because of the Landau pole in the coupling constant. In this case, a generalization to higher orders means that one inserts not a one-loop bubble but the full single-particle-irreducible polarization function in the photon propagator. This is close in spirit to organizing the expansion in skeleton diagrams. In QCD, there is no possibility of identifying proper diagrams in the direct-summation technique, but the method still works if one generates renormalon chains from the running coupling constant.

To summarize, we note that a direct diagram-by-diagram analysis provides an asymptotic expansion (IR renormalons) which leads to Borel-nonsummable PT series. Within our approach, this nonsummability is reflected in the singularity of the running coupling constant along the contour of integration. In higher orders of PT for bubble insertions (when a bubble becomes a blob), the situation can be cured by going over to the renormalization scheme (RS) for the coupling constant, where integration is possible. We

explore some possibilities of defining the integral of the running coupling constant over the IR region by using the RS freedom in higher orders of the PT expansion, which corresponds to summing asymptotic series related to IR renormalons. Note that, for our method to work, we should consider higher order PT corrections to the standard bubble chain diagrams.

Before going into details, we note that an important practical consequence of Borel nonsummability of such contributions in the theory of heavy quarks is the arbitrariness of the pole mass of a heavy quark [29]. Because of the nonperturbative origin of this arbitrariness, it is difficult to obtain any strict numerical estimates for it. It is generally assumed in a high-precision analysis including heavy quarks that the arbitrariness is numerically small [30, 31].

Let us first consider a simple example of how higher order PT contributions can be used to give a (non-PT) regularization of IR-renormalon contributions. Let the β function of a theory in some particular renormalization scheme be summed into the expression

$$\beta(\alpha) = -\frac{\alpha^2}{1+k\alpha^2}, \quad k > 0, \quad (1)$$

with the standard asymptotic β function of the form $\beta^{\text{as}}(\alpha) = -\alpha^2 + \dots$. The renormalization-group equation for the running coupling constant $\alpha(z)$,

$$z \frac{\partial}{\partial z} \alpha(z) = \beta(\alpha), \quad (2)$$

has a solution

$$\alpha(z) = \frac{-L_z + \sqrt{L_z^2 + 4k}}{2k}, \quad L_z = \ln \frac{z}{\Lambda^2}. \quad (3)$$

The solution in (3) has no singularities at positive z . However, the asymptotic solution

$$\alpha^{\text{as}}(z) = \frac{1}{\ln(z/\Lambda^2)} \quad (4)$$

has a usual unphysical pole at $z = \Lambda^2$. Thus, the particular way of summing an infinite number of perturbative terms for the β function (1) can cure the Landau pole problem in a sense that the coupling constant becomes smooth in the infrared region and the integration of the evolution trajectory can be performed explicitly. Let us emphasize that there are no nonperturbative terms added, but that the freedom of choosing a renormalization scheme for an infinite series defining the running coupling constant was used instead. This is, however, beyond the formal framework of PT, where only finite-order polynomials in the coupling constant are considered for the β function. Note that the problem of the renormalization-scheme ambiguity in higher orders of PT was discussed in [32–35], where a few methods for reducing this ambiguity were proposed. In contrast to previous approaches, where the main criterion for a good scheme

was a weak dependence on the change in the scheme parameterization, we use here the renormalization-scheme freedom to find a scheme that allows one to perform integration over the IR region without encountering a singularity.

Equation (1) can be considered either as a pure PT result in some particular renormalization scheme after an infinite resummation or as a sort of Padé approximation of some exact β function (as obtained from a numerical study on a lattice, for instance) that might include nonperturbative terms as well. An important point for us here is that the running coupling constant obeying the renormalization-group equation with this β function has a smooth continuation of the evolution trajectory to the IR region. The running coupling constant given by (3) has a correct asymptotic behavior for $z \rightarrow \infty$. It is a good expansion parameter for physical observables that obey the dispersion relation because it has no Landau pole on the physical cut.

A generalization of (1) to QCD is now straightforward. Bearing in mind that the first two coefficients β_0 and β_1 of the QCD β function are renormalization-scheme-invariant and that they cannot be changed, one can propose a possible “improved” β function in the form

$$\beta(\alpha) = \frac{-\beta_0\alpha^2 - \beta_1\alpha^3}{1 + k(\beta_0\alpha^2 + \beta_1\alpha^3)}, \quad k > 0, \quad (5)$$

with the running coupling constant $\alpha(z)$ being implicitly determined by the equation

$$\begin{aligned} & \beta_0 \ln \frac{z}{\Lambda^2} \\ &= \frac{1}{\alpha(z)} - \frac{\beta_1}{\beta_0} \ln \left(\frac{\beta_0 + \beta_1\alpha(z)}{\beta_1\alpha(z)} \right) - k\beta_0\alpha(z), \end{aligned} \quad (6)$$

which reduces to Eq. (3) in the special (unrealistic) case of $\beta_1 = 0$ and $\beta_0 = 1$.

The β function given by (5) is bounded at large α and Eq. (6) has a solution for $\alpha(z)$ that is defined on the positive semiaxis and has no singularities. The absence of singularities (the Landau pole in the leading order, for instance) prevents us from directly applying the mathematical part of the reasoning about Borel nonsummability (or the dominance of leading-order contributions).

The solution in (6) can be rewritten in a more traditional form through some intermediate energy scale μ without using the parameter Λ (the parameter Λ has no special meaning as a position of the pole of the running coupling constant). Doing that for the leading-order expression (3) (only for the sake of simplicity), we obtain

$$\alpha(Q^2) \quad (7)$$

$$= \frac{2\alpha}{1 + \alpha L_Q - k\alpha^2 + \sqrt{(1 + \alpha L_Q - k\alpha^2)^2 + 4k\alpha^2}},$$

where $L_Q = \ln(Q^2/\mu^2)$ and $\alpha \equiv \alpha(\mu^2)$. It is clear that this form of the evolution of the coupling constant is a specific regularization of the Landau singularity. This regularization introduces no imaginary part [36].

Thus, we can see that, within pure perturbation theory, one can eliminate the Landau pole of the coupling constant by using the freedom in choosing a renormalization scheme in higher orders. The smooth coupling constant does not require, however, any nonperturbative effects to regularize integrals in which it appears.

Expression (5) for the β function has a somewhat unusual form. Yet, even for a two-loop β function, there can exist an IR fixed point that allows an extrapolation to low energies. Indeed, for n_f light flavors in QCD, the first two coefficients of the β function are given by

$$4\pi\beta_0 = 11 - \frac{2}{3}n_f, \quad (4\pi)^2\beta_1 = 102 - \frac{38}{3}n_f;$$

for

$$\frac{153}{19} < n_f < \frac{33}{2},$$

one has

$$\beta_0 > 0, \quad \beta_1 < 0.$$

Therefore, an infrared fixed point exists, say, for $n_f = 9$, and an extended IR-renormalon asymptotic series can be explicitly summed according to our prescription in the second-order approximation for the evolution of the coupling constant in QCD.

The coupling constant defined in a particular renormalization scheme is not an immediate physical quantity. However, one can easily write a formal definition of the effective coupling through some physical quantity. This definition can implicitly include nonperturbative terms. By way of example, we indicate that, by taking the expression for Adler’s function,

$$D_{e^+e^-}(Q^2) = Q^2 \int \frac{R_{e^+e^-}(s)ds}{(s + Q^2)^2},$$

one can define

$$d^{\text{as}}(Q^2) = (D_{e^+e^-}(Q^2) - 1)\pi\beta_0 = \left(\ln \frac{Q^2}{\Lambda^2} \right)^{-1}$$

and [37, 38]

$$\begin{aligned} r_{e^+e^-}^{\text{as}}(s) &= \frac{1}{\pi} \arctan \left(\frac{\pi}{\ln \frac{s}{\Lambda^2}} \right) \Theta(s) \\ &+ \Theta(s + \Lambda^2)\Theta(-s). \end{aligned}$$

The unphysical singularity (a cut along a part of the negative semiaxis) corresponds to the unphysical pole

in $D(Q^2)$. Subtracting this singularity in a minimal way, we arrive at the expression

$$d(Q^2) = \frac{1}{\ln(Q^2/\Lambda^2)} - \frac{\Lambda^2}{Q^2 - \Lambda^2}, \quad (8)$$

which is regular, but which seems nonperturbative in terms of the asymptotic charge

$$\begin{aligned} d^{\text{as}}(Q^2) &= (\ln(Q^2/\Lambda^2))^{-1}, \quad (9) \\ d(Q^2) &= d^{\text{as}}(Q^2) - \frac{1}{e^{\frac{1}{d^{\text{as}}(Q^2)}} - 1} \\ &= d^{\text{as}}(Q^2) - e^{-\frac{1}{d^{\text{as}}(Q^2)}} + \dots \end{aligned}$$

The corresponding β function written in terms of the asymptotic charge $d^{\text{as}} \equiv \xi$,

$$\begin{aligned} Q^2 \frac{\partial}{\partial Q^2} d(Q^2) &= \beta(d(Q^2)) \quad (10) \\ &= -\xi^2 + e^{-1/\xi} (1 - e^{-1/\xi})^{-2} \Big|_{\xi=d^{\text{as}}(Q^2)}, \end{aligned}$$

also has an explicit nonperturbative term, in contrast to expression (5). It is unclear whether the β function (10) can be rewritten in terms of the full charge $d(Q^2)$ from (8).

Thus, we have two possibilities of eliminating the pole and, hence, of interpreting the renormalon series as an integral of the running coupling constant over the IR region. One possibility, a purely perturbative one, is that where higher order corrections simply make the running well-defined up to $Q = 0$. This can be achieved either in a finite-order expression for the β function or through a resummation of an infinite number of terms for it. The other possibility is a nonperturbative one in which the running is made safe by some nonperturbative procedure. As for this nonperturbative possibility, vacuum condensates could provide a kind of subtraction made by hand in (8).

In order to define IR contributions, we do not need to know the evolution of the coupling constant in the IR domain pointwise. We only have to define some integral of it. This is a much less restrictive requirement that can be formulated in terms of distributions. In this way, we can see the role of the gluon condensate in defining the IR structure of the theory. The idea of our approach is to make the naive effective charge [computed with a polynomial β function (as in the \overline{MS} scheme in low orders)] integrable without explicitly using the renormalization-scheme freedom but by adding a nonperturbative parameter immanent to the field theory. One can also hope that this construction can recover the true behavior of the effective charge in the IR region.

The realization of this idea in the simplest approximation is achieved by using the simple regularization [principal value (PV) prescription] for the

naive coupling, which makes it integrable and which is assumed to be perturbative. However, this regularization is not unique. The arbitrariness in the regularization is compensated by the parameters A and B that play the part of nonperturbative terms and which ought to be fixed through a comparison with the full charge. Therefore, we write

$$\begin{aligned} &\beta_0 \alpha^{\text{eff}}(s) \quad (11) \\ &= \beta_0 \alpha_s(s) |_{\text{PV}} + A \Lambda^2 \delta(s) + B \Lambda^4 \delta'(s) + \dots \end{aligned}$$

Note that the normalization is chosen in such a way that, for large s ,

$$\alpha_s(s) = \frac{1}{\beta_0 \ln(s/\Lambda^2)}. \quad (12)$$

Equation (11) is understood in a sense of distributions, and $\alpha_s(s) |_{\text{PV}}$ is the charge in a scheme like \overline{MS} containing a pole regularized by taking the principal value. Such a distribution is a natural generalization of a classical solution to the renormalization-group equation with the asymptotic β function $\beta^{\text{as}}(x) = -\beta_0 x^2 + \dots$. The generalized solution (in the sense of distributions) is not unique and allows some arbitrariness at the point $s = \Lambda^2$. Therefore, this solution should be a series of a delta function and its derivatives. The PV-regularized running coupling constant is not positive definite, while A, B, \dots are nonperturbative parameters used to improve the IR behavior (in the sense of distribution theory). We have chosen the support of nonperturbative terms to lie at $s = 0$ instead of $s = \Lambda^2$, which does not make much difference in our approximation. Note that, strictly speaking, multiplication is not defined for distributions; therefore, all PT corrections are assumed to be included in the leading-order term.

We now consider a few models for $\alpha^{\text{eff}}(s)$ and compute numerical values of the parameters A and B . In the spirit of the operator-product expansion, $A = 0$ (there are no gauge-invariant operators of dimensionality two) and $B \sim \langle G^2 \rangle$, where $\langle G^2 \rangle$ is the gluon condensate. Within this model, the gluon condensate is related to the PT scale parameter Λ and depends on the pattern of extrapolation of the running coupling constant to the IR region. Note that quark condensates are related to chiral-symmetry breaking, and we do not treat them within our approach. On the contrary, the gluon condensate is associated with dilatation-symmetry violation, which is closely related to dimensional transmutation and to the emergence of the scale Λ . Therefore, one can relate these two parameters in a nonperturbative way.

Bearing in mind the process of e^+e^- annihilation, where the operator-product expansion is applicable, we can find a relation between the parameter B and

the gluon condensate. The expression for Adler's function at large Q^2 is

$$D_{e^+e^-}(Q^2) = 1 + \frac{\alpha_s^{e^+e^-}(Q)}{\pi} + \frac{\langle g_s^2 G^2 \rangle}{6Q^4}, \quad (13)$$

which leads to the spectral density in the form

$$R_{e^+e^-}(s) = 1 + \frac{\alpha_s^{e^+e^-}(s)}{\pi} + \frac{\langle g_s^2 G^2 \rangle}{12} \delta'(s), \quad (14)$$

where

$$\alpha_s^{e^+e^-}(s) = \frac{1}{\beta_0 \ln(s/\Lambda_{e^+e^-}^2)}. \quad (15)$$

Interpreting the expression in Eq. (15) as a distribution on the semiaxis $0 < s < \infty$ with a PV regularization, we can represent the asymptotic charge $\alpha_s^{e^+e^-}(s)$ as

$$\alpha_s^{\text{eff}}(s) = \alpha_s^{e^+e^-}(s)|_{\text{PV}} + \frac{\pi}{12} \langle g_s^2 G^2 \rangle \delta'(s). \quad (16)$$

This should be compared with Eq. (11). From Eqs. (11) and (14), we obtain

$$16B\Lambda_{e^+e^-}^4 = 3\langle g_s^2 G^2 \rangle,$$

which translates into the following expression for the scale parameter $\Lambda_{e^+e^-}$ through the gluon condensate:

$$\Lambda_{e^+e^-} = \frac{1}{2} \left(\frac{3\langle g_s^2 G^2 \rangle}{B} \right)^{1/4}.$$

For the canonical numerical value of $\langle g_s^2 G^2 \rangle = 0.47 \text{ GeV}^4$, we find that the scale parameter $\Lambda_{e^+e^-}$ takes the value

$$\Lambda_{e^+e^-} = \frac{546}{B^{1/4}} \text{ MeV},$$

which depends on the extrapolation of the coupling constant to the IR region through the parameter B [see Eq. (11)]. In the case of e^+e^- annihilation, the parameter $\Lambda_{e^+e^-}$ is an effective scale of the process [39, 40]. The use of the effective scale allows one to absorb the next-to-leading order PT correction into $\alpha_s^{e^+e^-}$. The numerical value of the effective scale is rather sensitive to the process and can characterize the scale where PT is violated and where non-PT terms are therefore important numerically [41, 42]. To relate this parameter to the standard $\Lambda_{\overline{MS}}$, we consider the first perturbative correction to the coupling constant $\alpha_s^{e^+e^-}$ in (13). We have

$$\frac{\alpha_s^{e^+e^-}}{\pi} = \frac{\alpha_{\overline{MS}}}{\pi} + k_1 \left(\frac{\alpha_{\overline{MS}}}{\pi} \right)^2 + O(\alpha_s^3), \quad (17)$$

where

$$k_1 = \frac{365}{24} - 11\zeta(3) + n_f \left(-\frac{11}{12} + \frac{2}{3}\zeta(3) \right).$$

Here, $\zeta(z)$ is a Riemann ζ function. For standard QCD with $n_f = 3$, we numerically obtain

$$\frac{\alpha_s^{e^+e^-}}{\pi} = \frac{\alpha_{\overline{MS}}}{\pi} + 1.64 \left(\frac{\alpha_{\overline{MS}}}{\pi} \right)^2 + O(\alpha_s^3), \quad (18)$$

which leads to

$$\Lambda_{e^+e^-} = 1.44\Lambda_{\overline{MS}}. \quad (19)$$

Using Eq. (19), one obtains the numerical prediction

$$\Lambda_{\overline{MS}} = 380B^{-1/4} \text{ MeV}. \quad (20)$$

One expects the numerical value of the parameter B to be on the order of unity, which implies that the prediction in (20) is rather close to the present experimental value extracted from the data on τ -lepton decay [43],

$$\Lambda_{\overline{MS}}^{\text{exp}} = 349 \pm 61 \text{ MeV}. \quad (21)$$

Below, we consider a few explicit models of extrapolation of the evolution of the coupling constant to the IR region that allow one to determine the parameter B . For the sake of technical simplicity, we do not use sophisticated expressions for the running coupling constant in the IR region that stem from redefining the RS. We limit ourselves to models where the IR behavior is expressible in simple analytical terms. These models preserve all features pertinent to a more accurate consideration, but they make a numerical analysis more transparent.

Model (i). Switching the interaction off completely at low momenta:

$$\alpha^{\text{eff}}(z) = \alpha_s(z)\Theta(z - a\Lambda^2).$$

The system of equations for determining A and B is [44]

$$\text{li}(a) + A = 0, \quad \text{li}(a^2) - B = 0,$$

where $\text{li}(a)$ is the special function

$$\text{li}(a) = \int_0^a \frac{dt}{\ln(t)}$$

with a PV prescription for the pole at $t = 1$ at real positive $a > 1$ [45]. The numerical solution to the system of equations with the additional constraint $A = 0$ reads $a = 1.45$ and $B = \text{li}(2.1) = 1.19$. We retain only three significant digits.

Model (ii). Freezing the running coupling at low momenta (see, for example, [46]):

$$\alpha^{\text{eff}}(s) = \alpha_s(a)\Theta(a\Lambda^2 - s) + \alpha_s(s)\Theta(s - a\Lambda^2).$$

The system of equations for determining A and B is

$$\frac{a}{\ln(a)} = \text{li}(a) + A, \quad \frac{a^2}{2\ln(a)} = \text{li}(a^2) - B.$$

The numerical solution with the constraint $A = 0$ reads $a = 3.85$ and $B = 2.6$.

Model (iii). Regularization of the low-energy behavior by the minimal subtraction of the singularity:

$$\beta_0 \alpha^{\text{eff}}(s) = \frac{1}{\ln(s/\Lambda^2)} - \frac{\Lambda^2}{s - \Lambda^2}.$$

The system of equations for determining the parameters A and B has the form

$$\begin{aligned} \text{li}(a) - \ln(a - 1) &= \text{li}(a) + A, \\ \text{li}(a^2) - a - \ln(a - 1) &= \text{li}(a^2) - B. \end{aligned}$$

The solution with $A = 0$ is $a = 2$ and $B = 2$. Note that this model received some attention in the past few years [47].

Model (iv). Renormalization-group modification of the β function and a smooth extrapolation of the evolution to low momenta. The model is given by the pattern of running presented in Eq. (3). The solution depends strongly on the numerical value of the parameter k appearing in expression (1) for the β function. For $k \sim 2$, the solution is close to that in models (ii) and (iii). For some other values of k , there may be no solution at all or a solution does not fit the requirement $A = 0$ and $B > 0$.

Thus, the models of reasonably soft extrapolation of the running to low momenta give B values close to unity. For numerical estimates, we use the results obtained within models (i), (ii) and (iii), where $B = 1.2$ – 2.6 . We find $B^{1/4} = 1.05$ – 1.27 . From (20), one obtains $\Lambda_{\overline{\text{MS}}} = 362$ – 300 MeV. Taken literally, this yields $\Lambda_{\overline{\text{MS}}} = 331 \pm 31$ MeV, which is in reasonable agreement with current data. Note that the present numerical value of the gluon condensate is slightly higher than its canonical value. This makes the agreement better. In general, our result means that the numerical values of the gluon condensate and of the parameter $\Lambda_{\overline{\text{MS}}}$ are compatible with each other, at least in the case of a smooth continuation to the infrared region. The gluon condensate is interpreted as a quantity that makes the leading-order running coupling constant well-defined at low momenta (in a sense of distributions). An analogous situation has been discovered in some models [48]. A practical consequence of this fact for heavy quarks would be that, when using the effective model of the coupling constant in sum rules for J/ψ (charmonium) states, one might find a numerical value for $\langle G^2 \rangle$ compatible with zero.

To conclude, we have exploited the renormalization-scheme freedom to show that some infinite subsets of diagrams that are represented as integrals over the IR region can explicitly be summed in a generalized way through a proper definition of the integral. The lack of any parameter or a sensible strict criterion for choosing a particular set of diagrams that dominate high-order behavior beyond the leading-order expression for the running constant allows one

to use the renormalization-scheme freedom for interpreting the renormalon singularities. If, in a particular renormalization scheme, there are no singularities of the running coupling constant at low momenta, this scheme provides a particular recipe for a resummation of the asymptotic series related to IR renormalons. As to phenomenological applications, models with some extrapolation of the running coupling constant into the IR region are used for practical calculations (usually under the integral sign). Our results show that, with an extrapolation chosen, one cannot freely add the standard contribution of the gluon condensate to take into account nonperturbative effects and “improve” the computation—this contribution must be coordinated with the continuation of the coupling constant.

REFERENCES

1. L. N. Lipatov, Zh. Éksp. Teor. Fiz. **72**, 411 (1977) [Sov. Phys. JETP **45**, 216 (1977)].
2. A. P. Bukhvostov and L. N. Lipatov, Zh. Éksp. Teor. Fiz. **73**, 1658 (1977) [Sov. Phys. JETP **46**, 871 (1977)].
3. J. Zinn-Justin, *Quantum Field Theory and Critical Phenomena* (Oxford Univ. Press, Oxford, 1996, 3rd ed.).
4. G. 't Hooft, in *Proceedings of the 15th International School on Subnuclear Physics “The Why’s of Subnuclear Physics,” Erice, Sicily, 1977*, Ed. by A. Zichichi (Plenum, New York, 1979), p. 943.
5. B. Lautrup, Phys. Lett. B **69B**, 109 (1977).
6. G. H. Hardy, *Divergent Series* (Clarendon, Oxford, 1973).
7. G. Parisi, Phys. Lett. B **76B**, 65 (1978); Nucl. Phys. B **150**, 163 (1979).
8. A. H. Mueller, Nucl. Phys. B **250**, 327 (1985).
9. I. I. Balitsky, Phys. Lett. B **273**, 282 (1991).
10. V. I. Zakharov, Nucl. Phys. B **385**, 452 (1992).
11. J. G. Korner, F. Krajewski, and A. A. Pivovarov, Eur. Phys. J. C **12**, 461 (2000); **14**, 123 (2000).
12. K. G. Wilson, Phys. Rev. **179**, 1399 (1969).
13. F. David, Nucl. Phys. B **209**, 433 (1982).
14. A. A. Pivovarov, A. N. Tavkhelidze, and V. F. Tokarev, Theor. Math. Phys. **60**, 765 (1985).
15. H. D. Politzer, Nucl. Phys. B **117**, 397 (1976).
16. A. I. Vainshtein, V. I. Zakharov, and M. A. Shifman, Pis'ma Zh. Éksp. Teor. Fiz. **27**, 65 (1978) [JETP Lett. **27**, 55 (1978)].
17. M. A. Shifman, A. I. Vainshtein, and V. I. Zakharov, Nucl. Phys. B **147**, 385 (1979).
18. R. Coquereaux, Phys. Rev. D **23**, 2276 (1981).
19. S. V. Faleev and P. G. Silvestrov, Nucl. Phys. B **507**, 379 (1997).
20. I. M. Suslov, Zh. Éksp. Teor. Fiz. **116**, 369 (1999) [JETP **89**, 197 (1999)].
21. D. J. Broadhurst and A. G. Grozin, Phys. Rev. D **52**, 4082 (1995); M. Beneke and V. Braun, Phys. Lett. B **348**, 513 (1995); C. N. Lovett-Turner and C. J. Maxwell, Nucl. Phys. B **452**, 188 (1995).

22. G. P. Korchemsky and G. Sterman, Nucl. Phys. B **437**, 415 (1995).
23. L. D. Landau, A. A. Abrikosov, and I. M. Khalatnikov, Dokl. Akad. Nauk SSSR **95**, 773 (1954).
24. M. Gell-Mann and F. E. Low, Phys. Rev. **95**, 1300 (1954).
25. N. N. Bogolyubov and D. V. Shirkov, Dokl. Akad. Nauk SSSR **103**, 391 (1955); Nuovo Cimento **3**, 845 (1956).
26. A. A. Vladimirov, Teor. Mat. Fiz. **43**, 210 (1980).
27. M. Beneke, Phys. Rep. **317**, 1 (1999).
28. N. V. Krasnikov and A. A. Pivovarov, Mod. Phys. Lett. A **11**, 835 (1996); hep-ph/9512213; hep-ph/9607247.
29. I. I. Bigi, M. A. Shifman, N. G. Uraltsev, and A. I. Vainshtein, Phys. Rev. D **50**, 2234 (1994).
30. A. Hoang *et al.*, Eur. Phys. J. C **3**, 1 (2000).
31. A. A. Penin and A. A. Pivovarov, Phys. Lett. B **435**, 413 (1998); Nucl. Phys. B **549**, 217 (1999); hep-ph/9904278.
32. P. M. Stevenson, Phys. Rev. D **23**, 2916 (1981).
33. J. Brodsky, G. P. Lepage, and P. B. Mackenzie, Phys. Rev. D **28**, 228 (1983).
34. A. Dhar and V. Gupta, Phys. Rev. D **29**, 2822 (1984).
35. A. C. Mattingly and P. M. Stevenson, Phys. Rev. D **49**, 437 (1994).
36. G. Grunberg, Phys. Lett. B **349**, 469 (1995).
37. N. V. Krasnikov and A. A. Pivovarov, Phys. Lett. B **116**, 168 (1982).
38. A. A. Pivovarov, Yad. Fiz. **54**, 1214 (1991) [Sov. J. Nucl. Phys. **54**, 676 (1991)]; Z. Phys. C **53**, 461 (1992); Nuovo Cimento A **105**, 813 (1992).
39. N. V. Krasnikov, Nucl. Phys. B **192**, 497 (1981).
40. G. Grunberg, Phys. Lett. B **90B**, 70 (1980).
41. A. L. Kataev, N. V. Krasnikov, and A. A. Pivovarov, Phys. Lett. B **107B**, 115 (1981); Nucl. Phys. B **198**, 508 (1982); **490**, 505 (1997).
42. A. A. Pivovarov and E. N. Popov, Phys. Lett. B **205**, 79 (1988); Yad. Fiz. **49**, 1118 (1989) [Sov. J. Nucl. Phys. **49**, 693 (1989)].
43. J. G. Korner, F. Krajewski and A. A. Pivovarov, hep-ph/0002166.
44. N. V. Krasnikov, A. A. Pivovarov, and N. N. Tavkhelidze, Pis'ma Zh. Éksp. Teor. Fiz. **36**, 272 (1982) [JETP Lett. **36**, 333 (1982)]; Z. Phys. C **19**, 301 (1983).
45. I. S. Gradshteyn and I. M. Ryzhik, *Tables of Integrals, Series, and Products* (Nauka, Moscow, 1971; Academic, New York, 1980).
46. N. V. Krasnikov and A. A. Pivovarov, Sov. Phys. J. **25**, 55 (1982).
47. D. V. Shirkov and I. L. Solovtsov, Phys. Rev. Lett. **79**, 1209 (1997).
48. A. A. Penin and A. A. Pivovarov, Phys. Lett. B **357**, 427 (1995); **367**, 342 (1996); **401**, 294 (1997); Yad. Fiz. **60**, 2239 (1997) [Phys. At. Nucl. **60**, 2056 (1997)].

ELEMENTARY PARTICLES AND FIELDS

Theory

Classical Pion Fields in the Presence of a Source

M. G. Ryskin* and A. G. Shuvaev**

Petersburg Nuclear Physics Institute, Russian Academy of Sciences, Gatchina, 188350 Russia

Received March 10, 2000; in final form, June 7, 2000

Abstract—A classical pion field that is similar to a disoriented chiral condensate is considered in the presence of an external source. The field is similar to the condensate in that the isotopic orientation of the field in the whole space is determined by a single vector. Within the nonlinear sigma model, classical solutions are considered both in the chiral limit, where the pions are massless, and in the case of a finite pion mass. In either case, the classical field is similar to the Coulomb field of a charged particle; however, the nonlinear pion interaction results in the existence of several solutions. In the massless case and in the case where the source is sufficiently small, there are a great number of classical solutions characterized by finite discrete energies. In the more realistic case of heavy ions, there are no stable solutions of this type; however, long-lived quasistationary states, which slowly decay, emitting very soft pions, can be formed. The structure and the energies of these solutions are studied numerically. © 2001 MAIK “Nauka/Interperiodica”.

1. INTRODUCTION

The low-energy interaction of soft pions is described by the effective Lagrangian

$$L_\pi = \frac{1}{2} [(\partial_\mu \sigma)^2 + (\partial_\mu \pi)^2], \quad (1)$$

which involves three isovector pion fields π_i , $i = 1, 2, 3$, and an auxiliary scalar field σ subjected to the condition

$$\sigma^2 + \pi^2 = f_\pi^2,$$

where $f_\pi = 92$ MeV is the pion decay constant.

The pion field is a chiral phase of a quark condensate; therefore, it is natural to represent it in the form of the unitary matrix

$$U = \frac{1}{f_\pi} (\sigma + i\boldsymbol{\pi} \cdot \boldsymbol{\tau}), \quad U^+ U = 1.$$

The Lagrangian in (1) then assumes the form

$$L_{\text{eff}} = \frac{f_\pi^2}{4} \text{tr} \partial_\mu U \partial_\mu U^+. \quad (2)$$

The Lagrangian in (2) includes nonlinear terms, which describe multipion interactions. Plane-wave-type solutions obtained by Anselm [1, 2] represent an important case of classical solutions associated with this Lagrangian. A disoriented chiral condensate is a special case of these solutions that corresponds to zero wave vector ($\mathbf{k} = 0$) [3–7].

High-energy particle (heavy-ion) collisions are accompanied by heating up to temperatures at which

chiral symmetry is restored. Upon cooling, this symmetry is spontaneously broken again, with the result that a scalar ($\langle \bar{q}q \rangle$) or a pseudoscalar ($\langle \bar{q}\gamma_5\tau_a q \rangle$) condensate with the quantum numbers of σ or π^a mesons is formed. All four directions in the isotopic $O(4)$ space (three pions and the σ meson) are equivalent, and the formation of the pion condensate ($\bar{q}\gamma_5\tau_a q$) in some spatial region means that a disoriented chiral condensate is generated.

Various scenarios of the formation of a classical pion field (disoriented chiral condensate) at high energies and its experimental manifestations are widely discussed in the literature [3–13].

A distribution of neutral and charged pions is one of the most spectacular indications of the formation of a disoriented chiral condensate.

The multiplicity distribution for independent meson production obeys the Poisson law; therefore, the fraction of π^0 mesons in high-multiplicity events is $1/3$ of the total number of mesons, and the distribution of the ratio $f = n^0/n_{\text{tot}}$ is close to $\delta(f - 1/3)$ (here, n^0 is the number of π^0 mesons and n_{tot} is the total number of mesons).

When a classical pion field is produced, the orientation of the isotopic vector \mathbf{A}^a , which determines the neutral-to-charge pion multiplicity ratio, takes the same value over the entire region where the field exists. As a result, the probability of events featuring an anomalously small number of neutral pions proves to be large [1, 3, 5, 6, 14],

$$\frac{dw}{df} = \frac{1}{2\sqrt{f}}. \quad (3)$$

* e-mail: ryskin@thd.pnpi.spb.ru

** e-mail: shuvaev@thd.pnpi.spb.ru

So far, attempts at detecting such events experimentally (in $p\bar{p}$ collisions at the FNAL collider [15] and in nucleus–nucleus collisions at CERN [16]) have been futile; however, the expectations for the appearance of a disoriented chiral condensate under these conditions are low. Heavy-ion collisions at new colliders like RHIC and LHC are more promising.

In this study, we consider a different possibility, classical pion fields that can arise and exist in the presence of an external source like nucleons (or quarks) of the projectile nucleus. In contrast to Skyrmion-type fields, for which the direction of the isotopic vector is strictly correlated with the spatial-point position (hedgehog ansatz), the isotopic direction in the case being considered is determined by a single vector \mathbf{A}^a in the whole space, in just the same way as for the Anselm solutions or a disoriented chiral condensate. Thus, the distribution in (3) for the neutral-to-charge particle multiplicity ratio remains valid for the fields under consideration.

These solutions are similar in structure and physical nature to the electromagnetic (Coulomb) field of a charged particle. However, the nonlinear form (2) of pion interaction results in the existence of several solutions characterized by different energies. A nucleon or a nucleus together with the surrounding pion field can be interpreted as an excited state or as a resonance.

Below, we consider spherically symmetric solutions first in the chiral limit, $m_\pi = 0$, and then with a mass added to the Lagrangian in (2).

The mass term appears as a source in the classical equations and makes a contribution of the form $m_\pi^2 \sin \varphi$, where $\varphi = |\pi|/f_\pi$. The contribution of the external source is opposite in sign with respect to the mass term. In weak fields ($\varphi \ll 1$), the source acts like an attractive potential, enabling the existence of stable solutions, bound states. In strong fields ($\varphi \sim 1$), a stationary state is possible for large sources. If such a state appears in a heavy-ion collision, it can live long and decay slowly through the emission of very soft pions (in the nucleus rest frame).

The ensuing exposition is organized as follows. In Section 2, we describe classical solutions for fields surrounding a nucleon and possible excitations (resonances) in this system. In Section 3, we consider the more interesting case of a large nucleus.

2. CLASSICAL SOLUTIONS IN THE CHIRAL LIMIT

The interaction of pions with fermions (quarks or nucleons) is described by the effective Lagrangian

$$L_f = \bar{q}i\gamma^\mu \partial_\mu q - g\bar{q}(\sigma + i\boldsymbol{\pi} \cdot \boldsymbol{\tau}\gamma_5)q. \quad (4)$$

Below, we consider it as an interaction with an external classical source represented by the isoscalar $[\rho(x) = \langle \bar{q}(x)q(x) \rangle]$ or isovector $[\rho_V(x) = \langle \bar{q}(x)\boldsymbol{\tau}\gamma_5 q(x) \rangle]$ density. For the sake of simplicity, we take a zero-isospin source, $\rho_V(x) = 0$, in which case the Lagrangian assumes the form

$$L = \frac{f_\pi^2}{4} \text{tr} \partial_\mu U \partial_\mu U^+ - \frac{1}{4} g f_\pi \rho \text{tr}(U + U^+ - 2). \quad (5)$$

By varying the Lagrangian with respect to the pion matrix U , we arrive at

$$\partial_\mu [U^+ \partial_\mu U] = \frac{g}{2f_\pi} \rho(x) [U^+ - U].$$

Below, we seek the matrix $U(x)$ in the class of exact solutions found in [1, 2]; that is, we set

$$U(x) = V^{-1} e^{i\tau_3 f(x)} V, \quad (6)$$

where V is an arbitrary unitary matrix and the function $f(x)$ satisfies the equation

$$\partial^2 f(t, x) = \frac{g}{f_\pi} \rho(x) \sin f(t, x).$$

We are interested in stationary solutions, for which

$$\Delta f(x) = \frac{g}{f_\pi} \rho(x) \sin f(x),$$

where $\Delta = -\partial_i^2$ is the Laplace operator. Assuming that the function $f(x)$ decreases at spatial infinity, we can recast this equation into the integral form

$$f(x) = \frac{1}{4\pi} \frac{g}{f_\pi} \int \frac{d^3 y \rho(y)}{|x - y|} \sin f(y). \quad (7)$$

The total energy of the pion field is finite:

$$E = g f_\pi \int d^3 x \rho(x) \left[\frac{1}{2} f \sin f + \cos f - 1 \right]. \quad (8)$$

We can distinguish two characteristic modes in Eq. (8), that of a small size and that of a large size of the source.

In the first case, the density is entirely concentrated in a small spatial region. Assuming that the solution in question is smooth, we can therefore set $\sin f(y) \approx \sin f(0)$ in the integrand on the right-hand side of (7). At a finite distance from the source, we then arrive at the Coulomb-type potential

$$f(x) = \frac{1}{4\pi} \frac{g}{f_\pi} \frac{1}{|x|} \sin f,$$

where the charge constant $f = f(0)$ satisfies the equation

$$f = \frac{1}{a} \sin f, \quad (9)$$

with the dimensionless parameter a , which is given by

$$\frac{1}{a} = \frac{g}{4\pi f_\pi} \int \frac{d^3 y \rho(y)}{|y|},$$

being proportional to the source size.

For $a \ll 1$, Eq. (9) has the set of solutions

$$\sin f_n \simeq \pi a n, \quad n = 0, \pm 1, \pm 2, \dots, \quad |n| \leq 1/(\pi a).$$

It follows that, despite the use of a purely classical approach, the pion energy (8) takes the quantized values

$$E_n = g f_\pi \left[\frac{1}{2} f_n \sin f_n + \cos f_n - 1 \right]. \quad (10)$$

As the effective dimensionless radius a of the source decreases, more energy levels appear. For $a \rightarrow 0$, the levels form two quasicontinuous bands for even and odd states. For not very large n , the energies of the levels are given by

$$E_n \simeq g f_\pi \left[(-1)^n - 1 + \frac{1}{2} \pi^2 n^2 a \right]. \quad (11)$$

A typical energy interval between the levels in each band is about $g \pi^2 f_\pi a$.

The energies of low levels in the odd band are negative. It is worth emphasizing that the values E_n stand for the energy of the pion field; the total energy must include the source energy as well—that is, the energy of quarks or nucleons. The lower the volume occupied by the source, the higher its energy. Under certain conditions, these two effects can result in the formation of a bound state.

In the second mode, there are no finite-energy solutions different from $f = 0$. In order to demonstrate this, we note that, in terms of the variables $\rho(x) = (1/r_0^3) \bar{\rho}(x/r_0)$ and $f(x) = \bar{f}(x/r_0)$, where r_0 is the characteristic size of the region where the source density is nonzero, Eq. (7) assumes the form

$$\bar{f}(z) = \frac{g}{4\pi f_\pi r_0} \int \frac{d^3 z' \bar{\rho}(z')}{|z - z'|} \sin \bar{f}(z'),$$

whence it does indeed follow that, at sufficiently large r_0 , only zero solution is possible.

Simple estimates show that the critical radius r_0 required for the existence of a nontrivial solution must be on the order of 1 fm. In this case, the energy E_1 at $r_0 \sim 1$ fm is on the same order of magnitude as the characteristic mass difference between the baryon resonances. Therefore, part of these could appear as excitations of the ‘‘Coulomb’’ pion field considered here.

3. LARGE SOURCE

The conclusion that there is no solution for a large source holds only for a fixed constant g . At the same time, $g = g_{\pi NN} A$ increases for heavy ions with increasing atomic number A faster than the characteristic radius $r_0 \propto A^{1/3}$. Let us discuss this case in more detail. We assume that the nucleon density is constant within the nucleus, $\rho = \text{const}$, and consider a finite pion mass. We then arrive at the equation

$$\Delta f(x) = \left(\frac{g}{f_\pi} \rho(x) - m_\pi^2 \right) \sin f(x), \quad (12)$$

where the density is $\rho(x) = \rho_0 \theta(R - |x|)$, R being the radius of the nucleus. For a normal nuclear density, the effective coupling constant for the interaction with the source is $G = \rho_0 g / f_\pi \simeq 4.7 \text{ fm}^{-2}$.

As a result, Eq. (12) takes the form of the static version of the sine-Gordon equation. For large values of the effective constant ($G > m_\pi^2$), however, the sign in front of the sine is opposite to the standard one. Within a very large nucleus, the vacuum value must therefore be $f = \pi$ rather than $f = 0$.¹⁾ On the other hand, the dimensions of actual nuclei are not very large, so that it is necessary, first of all, that the solution in question be stable at large distances ($|x| > R$). Therefore, we first consider the case of the weak fields ($f \ll 1$), which corresponds to an expansion around the point of the potential minimum outside the nucleus.

For weak fields, the equation is linearized, assuming the simple form

$$\Delta f(x) = (G - m_\pi^2) f(x). \quad (13)$$

It has the well-known spherically symmetric solution

$$\begin{aligned} f(r) &= B_1 \sin(rb)/r, \quad r = |x| < R, \\ f(r) &= B_2 \exp(-rm_\pi)/r, \quad r > R, \end{aligned} \quad (14)$$

where $b = \sqrt{G - m_\pi^2}$.

We choose the solution for which the function $xf(x)$ vanishes, $xf(x) \rightarrow 0$, for $x \rightarrow 0$. Otherwise, the pion field energy $E \propto \int d^3x |\nabla f(x)|^2$ diverges for $x \rightarrow 0$ in the linear approximation.

At the boundary $r = R$, the logarithmic derivative in the first expression must satisfy the matching condition

$$\left. \frac{d \ln(rf(r))}{dr} \right|_{r=|x|=R} = b \cot(Rb) = -m_\pi. \quad (15)$$

In order to satisfy Eq. (15), a fine tuning of the nuclear radius R is required, which of course seems

¹⁾The (new) $f = \pi$ ground state can be interpreted as the result of pion condensation [17]. The possibility of this phenomenon was previously discussed within Fermi liquid theory.

very unnatural. In the nonlinear case, however, the matching is ensured by appropriately choosing the value $f(0) \sim O(1)$ for sufficiently large b ($b > \pi/R$). We have found such solutions numerically for realistic ion-radius values of $R = 5.6\text{--}5.9$ fm and $f(0) \simeq 1\text{--}2$. The solid curves in the figure represent our results.

In a sense, the solution that we obtained is similar to a classical pion field whose value is determined by the source charge and size.

The pion-field energy calculated according to expression (8) with allowance for the mass term m_π^2 is very small, $E = -8$ MeV, at $f(0) = 0.96$ (which still corresponds to the weak-field limit); however, it is equal to $E = -280$ MeV at $f(0) = 2$.²⁾

The fields shown by the solid curves in the figure seem to have a form that results from pion condensation in heavy nuclei, which was studied long ago [17], predominantly within Fermi liquid theory. The possibility of observing pion condensation in heavy-ion collisions was discussed in [18].

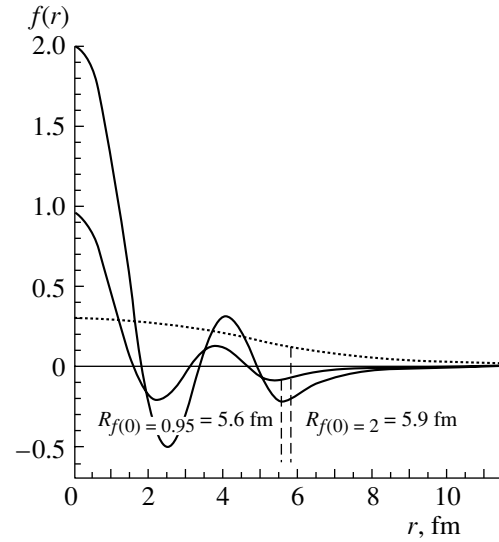
However, such a solution cannot be realized. At a normal nuclear density ρ_0 , pion condensation does not occur.

The reason is that the Lagrangian in (4) as written in terms of quarks and pions cannot be directly applied to the nucleon. In using the constant $g = g_{\pi NN}$, we assumed that the nucleon owes its mass entirely to interaction with the classical σ field, $\langle \sigma \rangle = f_\pi$. In terms of the effective Lagrangian specified by Eqs. (1) and (2), this leads to a very strong interaction of soft pions with nucleons. At the same time, the πN scattering amplitude is rather small. It is determined by the so-called σ term, whose value is less than the proton mass by a factor of 20 to 30.

For this reason, we took a smaller value of g (for example, $G = 0.18$ fm⁻²) that is in better agreement with the nucleon σ term. In this case, a heavy ion appears to be a rather weak source. For $G < 0.067$ fm⁻² and for a realistic ion size ($R \sim 6$ fm), the attractive potential is insufficiently strong for a bound state to emerge.

However, a quasistationary long-lived state can arise at $G = 0.18$ fm⁻². This state can decay only because of nonlinear effects. In the weak-field approximation, we can indeed seek a time-dependent solution $f(t, x) = \exp(iEt)f(x)$, where the function $f(x)$ satisfies Eq. (13), with the term $G - m_\pi^2$ being replaced by $G + E^2 - m_\pi^2$. We chose the energy

²⁾As a matter of fact, there is no boundary layer in the approximation used here [$\rho(r) = \rho_0\theta(R - r)$]. Despite this, the energy of the pion field is determined primarily by the matching condition at $r = R$ —that is, by the boundary region.



Amplitude of a classical pion field in the presence of a nucleon or a quark source of large size (heavy ion) as a function of the source size. The dashed lines indicate the ion radius R . The solid and dotted curves represent the cases of strong ($G = 4.7$ fm⁻²) and weak ($G = 0.18$ fm⁻²) coupling, respectively.

eigenvalue of $E \simeq 130$ MeV in order to ensure matching at $r = R$ and found the solution represented by the dotted curve in the figure (at $R = 5.9$ fm).

If such a state appears in a heavy-ion collision, it can live very long, decaying through the emission of very soft pions (in the rest frame of the nucleus), which occurs owing to the presence of nonlinear terms in Lagrangian (2). The lifetime of the solution increases with the field amplitude f , which determines the pion multiplicity n_π in the classical field. The dotted curve in the figure corresponds to $n_\pi = 2Ef_\pi^2 \int f^2(x)d^3x \simeq 12.3$.

The existence of such a solution can be of interest from the viewpoint of the appearance of breather classical pion fields [19]. Interaction with a source (nuclear matter) enhances the stability of these solutions and their lifetime. It is conceivable that the presence of the source can stabilize solutions of the pion-string type [20], which are characterized by a correlation between the direction of the isotopic vector A^a and the azimuthal angle in the xy coordinate plane.

The emergence of the classical fields that we considered at the beginning of the article (solid curves in the figure) in heavy-ion collisions cannot be completely ruled out either. If we assume that some kind of a quark bag (a large drop of quark plasma) is generated in a collision instead of a nucleus formed by nucleons, we can return to the quark-pion Lagrangian (4) with a large constant g and a corresponding value of $G \sim 3\text{--}5$ fm⁻². In this case, the interaction would

be sufficiently strong for a classical pion field (pion condensate) to be formed in the drop of quark matter.

ACKNOWLEDGMENTS

A.G. Shuvaev is grateful to Prof. K. Goeke for the hospitality extended to him and to Prof. L. McLerran for discussions.

The work was supported by a joint grant from Deutsche Forschungsgemeinschaft and the Russian Foundation for Basic Research (no. 436-M3/540) and by the Russian Foundation for Basic Research (project no. 98-02-17636).

REFERENCES

1. A. A. Anselm, Phys. Lett. B **217**, 169 (1989).
2. A. A. Ansel'm and M. Bander, Pis'ma Zh. Éksp. Teor. Fiz. **59**, 503 (1994) [JETP Lett. **59**, 503 (1994)].
3. J. D. Bjorken, Int. J. Mod. Phys. A **7**, 4189 (1992); Acta Phys. Pol. B **23**, 561 (1992).
4. J.-P. Blaizot and A. Krzywicki, Phys. Rev. D **46**, 246 (1992).
5. K. L. Kowalski and C. C. Taylor, CWRUTH-92-6; hep-ph/9211282.
6. J. D. Bjorken, K. L. Kowalski, and C. C. Taylor, SLAC-PUB-6109 (1993).
7. K. Rajagopal and F. Wilczek, Nucl. Phys. B **399**, 395 (1993).
8. J. D. Bjorken *et al.*, MiniMax: A Revised Proposal for T-864, Apr. 1993.
9. P. V. Ruuskanen, Z. Phys. C **38**, 219 (1988); Acta Phys. Pol. B **18**, 551 (1987).
10. S. Gavin, A. Gocksch, and R. D. Pisarski, Phys. Rev. Lett. **72**, 2143 (1994).
11. S. Gavin and B. Müller, Phys. Lett. B **329**, 486 (1994).
12. Ya. I. Kogan, Pis'ma Zh. Éksp. Teor. Fiz. **59**, 307 (1994) [JETP Lett. **59**, 307 (1994)].
13. A. A. Anselm, M. G. Ryskin, and A. G. Shuvaev, in *Proceedings of International Winter School on Theoretical High Energy Physics "Problems of High Energy Physics," St. Petersburg, 1995*; Z. Phys. A **354**, 333 (1996).
14. I. V. Andreev, Pis'ma Zh. Éksp. Teor. Fiz. **33**, 367 (1981) [JETP Lett. **33**, 367 (1981)].
15. MiniMax Collab. (T. C. Brooks *et al.*), hep-ex/9906026.
16. WA98 Collab. (M. M. Aggarwal *et al.*), Phys. Lett. B **420**, 169 (1998).
17. A. B. Migdal, Rev. Mod. Phys. **50**, 107 (1978); A. B. Migdal, E. E. Saperstein, M. A. Troitsky, and D. N. Voskresensky, Phys. Rep. **192**, 179 (1990).
18. H. J. Pirner and D. N. Voskresensky, Phys. Lett. B **343**, 25 (1995).
19. V. A. Gani, A. E. Kudryavtsev, and T. I. Belova, Yad. Fiz. **62**, 956 (1999) [Phys. At. Nucl. **62**, 895 (1999)].
20. X. Zhang, T. Huang, and R. H. Brandenberger, Phys. Rev. D **58**, 027702 (1998); hep-ph/9711452.

Translated by M. Kobrinsky

ELEMENTARY PARTICLES AND FIELDS

Theory

Renormalization of Parameters of a Soft Breakdown of Supersymmetry in the Regime of Strong Yukawa Coupling within a Nonminimal Supersymmetric Standard Model

R. B. Nevzorov and M. A. Trusov

*Institute of Theoretical and Experimental Physics, Bol'shaya
Cheremushkinskaya ul. 25, Moscow, 117259 Russia*

Received March 24, 2000; in final form, June 28, 2000

Abstract—Within a nonminimal supersymmetric (SuSy) model, the renormalization of trilinear coupling constants $A_i(t)$ for scalar fields and of specific combinations $\mathfrak{M}_i^2(t)$ of the scalar-particle masses is investigated in the regime of strong Yukawa coupling. The dependence of these parameters on their initial values at the Grand Unification scale disappears as solutions to the renormalization-group equations approach infrared quasifixed points with increasing $Y_i(0)$. In the vicinities of quasifixed points for $\tilde{\alpha}_{\text{GUT}} \ll Y_i(0) \ll 1$, all solutions $A_i(t)$ and $\mathfrak{M}_i^2(t)$ are concentrated near some straight lines or planes in the space of parameters of a soft breakdown of supersymmetry. This behavior of the solutions in question is explained by a sufficiently slow disappearance of the $A_i(0)$ and $\mathfrak{M}_i^2(0)$ dependence of the trilinear coupling constants and combinations of the scalar-particle masses. A method is proposed for deriving equations describing the aforementioned straight lines and planes, and the process of their formation is discussed by considering the example of exact and approximate solutions to the renormalization-group equations within a nonminimal supersymmetric standard model. © 2001 MAIK “Nauka/Interperiodica”.

1. INTRODUCTION

Parameters of a soft breakdown of supersymmetry play a key role in analyzing the particle spectra in supersymmetric (SuSy) models. The Bose–Fermi degeneracy of the spectrum is one of the most serious flaws in SuSy models. This means that the masses of observable particles and their superpartners coincide in the limit of exact supersymmetry, but this is in glaring contradiction with experimental data. Thus, supersymmetry must be broken, but its breakdown must not lead to the hierarchy problem [1]. Such a breakdown of supersymmetry is referred to as a soft breakdown. Supersymmetry breaking associated with supergravity (SuGra) effects is one of the most promising mechanisms for constructing a realistic model. Although the Lagrangian of ($N = 1$) SuGra models [2] is unrenormalizable, it can be shown that, in the low-energy region $E \ll M_{\text{Pl}}$, where $M_{\text{Pl}} = 2.4 \times 10^{18}$ GeV is the Planck mass, all unrenormalizable terms in the Lagrangian for observable fields are suppressed in a power-law way with respect to M_{Pl} , vanishing in the limit $M_{\text{Pl}} \rightarrow \infty$. In the case being considered, the Lagrangian for observable fields can be represented as the sum

$$L = L_{\text{SuSy}} + L_{\text{soft}}, \quad (1)$$

where L_{SuSy} is the Lagrangian corresponding to unbroken supersymmetry, while L_{soft} takes into account

terms that generate a soft breakdown of supersymmetry.

To a considerable extent, the form of the first term in Eq. (1) is determined by the superpotential of the SuSy model under study, this superpotential in turn being a function of chiral superfields. For a SuSy theory to be renormalizable, the superpotential must include only terms that are quadratic and cubic in chiral superfields S_α :

$$W(S_\alpha) = \frac{1}{2}\mu_{\alpha\beta}S_\alpha S_\beta + \frac{1}{6}h_{\alpha\beta\gamma}S_\alpha S_\beta S_\gamma. \quad (2)$$

When local supersymmetry is broken in SuGra models, parameters of a soft breakdown of supersymmetry are generated in the sector of observable fields [3, 4]. Since the explicit form of terms that violate supersymmetry, but which do not lead to the emergence of second-order divergences, is known [5], the Lagrangian for the case where supersymmetry is softly broken can be represented as

$$L_{\text{soft}} = \frac{1}{2}M_a \bar{\lambda}_a \lambda_a - m_\alpha^2 y_\alpha^* y_\alpha - \left(\frac{1}{6}A_{\alpha\beta\gamma} h_{\alpha\beta\gamma} y_\alpha y_\beta y_\gamma + \frac{1}{2}B_{\alpha\beta} \mu_{\alpha\beta} y_\alpha y_\beta + \text{h.c.} \right), \quad (3)$$

where y_α are the scalar components of the chiral superfields S_α and λ_a are gaugino fields. Usually, the parameters M_a , m_α^2 , $A_{\alpha\beta\gamma}$, and $B_{\alpha\beta}$ of a soft

breakdown of supersymmetry are defined at the scale of $M_X \approx 3 \times 10^{16}$ GeV. In minimal SuSy models, the values of all three gauge coupling constants g_i coincide at this scale: $g_i(M_X) = g_{\text{GUT}}$ [6]. This relationship between the gauge coupling constants arises within Grand Unified Theories [7]. In such theories, all observable gauge bosons and their superpartners (gaugino fields) belong to the same multiplet; therefore, the masses of all gauginos also coincide at the scale M_X . In the following, we everywhere set $M_a(M_X) = M_{1/2}$. The parameters $M_{1/2}, m_\alpha^2, A_{\alpha\beta\gamma}$, and $B_{\alpha\beta}$ defined in this way at the Grand Unification scale should be treated as boundary conditions for the set of renormalization-group equations that describes the evolution of the parameters of a soft breakdown of supersymmetry down to the electroweak scale.

Within the minimal SuSy Standard Model (MSSM), an exact analytic solution to the renormalization-group equations exists at $\tan\beta \sim 1$ [8], in which case the Yukawa coupling constants h_b and h_τ for the b quark and the τ lepton, respectively, are negligibly small. This solution makes it possible to analyze the evolution of the t -quark Yukawa coupling constant $h_t(t)$ and of the parameters of a soft breakdown of supersymmetry. For the coupling constant $h_t(t)$, this solution has the form

$$Y_t(t) = \frac{E_t(t)}{6F_t(t)} \left/ \left(1 + \frac{1}{6Y_t(0)F_t(t)} \right) \right., \quad (4)$$

where $Y_t(t) = h_t^2(t)/(4\pi)^2$ and $t = \ln(M_X^2/q^2)$. The explicit expressions for the functions $E_t(t)$ and $F_t(t)$ are presented in the Appendix [see Eq. (A.2)]. At low energies, the second term in the parentheses on the right-hand side of Eq. (4) is much less than unity at sufficiently large values of $h_t^2(0)$; as a result, all solutions (4) to the renormalization-group equations are focused in a narrow interval near the quasifixed point $Y_{\text{QFP}}(t) = E(t)/6F(t)$ [9]. Formally, a solution of this type can be obtained by making $Y_t(0)$ tend to infinity in Eq. (4).

Along with the Yukawa coupling constant for the t quark, solutions to the renormalization-group equations for the corresponding trilinear coupling constant A_t for scalar fields and the combination $\mathfrak{M}_t^2 = m_Q^2 + m_U^2 + m_2^2$ of the scalar-particle masses approach the infrared quasifixed point with increasing $h_t^2(0)$. An analytic solution for these parameters can be represented as

$$A_t(t) = A_t(0) \frac{\epsilon_t(t)}{E_t(t)} \quad (5)$$

$$+ M_{1/2} \left(t \frac{E'_t(t)}{E_t(t)} - \frac{tE_t(t) - F_t(t)}{F_t(t)} \left(1 - \frac{\epsilon_t(t)}{E_t(t)} \right) \right),$$

$$\mathfrak{M}_t^2(t) = (\mathfrak{M}_t^2(0) - A_t^2(0)) \frac{\epsilon_t(t)}{E_t(t)}$$

$$+ \left(A_t(0) \frac{\epsilon_t(t)}{E_t(t)} - M_{1/2} \frac{tE_t(t) - F_t(t)}{F_t(t)} \right. \\ \left. \times \left(1 - \frac{\epsilon_t(t)}{E_t(t)} \right) \right)^2$$

$$+ M_{1/2}^2 \left[\frac{d}{dt} \left(t^2 \frac{E'_t(t)}{E_t(t)} \right) - \frac{t^2 E'_t(t)}{F_t(t)} \left(1 - \frac{\epsilon_t(t)}{E_t(t)} \right) \right],$$

where $\epsilon_t(t) = Y_t(t)/Y_t(0)$. In the regime of strong Yukawa coupling, in which case $h_t^2(0) \gg g_{\text{GUT}}^2(0)$, the natural small parameter $\epsilon_t(t)$ arises in the theory being considered. In the infrared region, the dependence of the solutions in (4) and (5) on the boundary conditions at the Grand Unification scale disappears almost completely. Near the infrared fixed point, we have $Y_t(t_0) \approx Y_{\text{QFP}}(t_0)$, $A_t(t_0) \approx A_{\text{QFP}}(t_0)$, and $\mathfrak{M}_t^2(t_0) \approx \mathfrak{M}_{\text{QFP}}^2(t_0)$, where $A_{\text{QFP}}(t)$ and $\mathfrak{M}_{\text{QFP}}^2(t)$ are expressed in terms of only the gaugino mass at the scale M_X and $t_0 = 2 \ln(M_X/M_t^{\text{pole}})$, the pole t -quark mass M_t^{pole} being approximately equal to 175 GeV. The deviations from $Y_{\text{QFP}}(t)$, $A_{\text{QFP}}(t)$, and $\mathfrak{M}_{\text{QFP}}^2(t)$ are determined by the ratio $\epsilon_t(t)/E_t(t) \approx 1/(6F_t(t)Y_t(0))$, which is of order $1/(10h_t^2(0))$ at the electroweak scale. The properties of solutions to the renormalization-group equations within the MSSM and the spectrum of particles in the infrared-fixed-point regime at $\tan\beta \sim 1$ were investigated in [10–13].

At large values of $\tan\beta$ (about 50 to 60), the Yukawa coupling constants h_b and h_τ are of order h_t ; for this case, an exact analytic solution to the renormalization-group equations has not yet been found. Nonetheless, the detailed investigations performed in [1, 13, 14] revealed that, in this region of the parameter space, solutions to the set of nonlinear differential equations being studied also approach the infrared quasifixed point, the basic properties of the solutions remaining unchanged.

A reduction of the number of independent parameters in the vicinity of the infrared fixed point at $\tan\beta \sim 1$ made it possible to obtain, to a sufficiently high degree of precision, an upper limit on the mass of the lightest Higgs boson. In the case being considered, this upper limit does not exceed 94 ± 5 GeV [12, 13, 15], the constraints on the mass of the lightest Higgs boson from LEP II [16] being such that a considerable part of solutions approaching the quasifixed point at $\tan\beta \sim 1$ have already been ruled out by the existing experimental data. This gives an additional incentive to study the Higgs sector and the renormalization-group equations and their solutions within more involved SuSy models.

Of extensions of the MSSM, the simplest one that makes it possible to preserve the unification of the gauge coupling constants and which leads to a higher upper limit on the mass of the lightest Higgs boson is the nonminimal SuSy Standard Model (NMSSM) introduced in [17, 18]. The Higgs sector of this model contains an extra singlet superfield Y in addition to two doublets H_1 and H_2 . The upper limit on the mass of the lightest Higgs boson within the NMSSM attains a maximum value in the regime of strong Yukawa coupling, in which case the Yukawa coupling constants $Y_i(0)$ are much greater than the gauge coupling constant $\tilde{\alpha}_{\text{GUT}} = g_{\text{GUT}}^2/(4\pi)^2$. In the parameter-space region being considered, solutions to the renormalization-group equations within the NMSSM are attracted to quasifixed lines or surfaces in the space of Yukawa coupling constants. In the limit $Y_i(0) \rightarrow \infty$, all solutions to the set of differential equations in question are concentrated near quasifixed points [19], which arise as the result of intersections of Hill lines or surfaces with the invariant line connecting the stable fixed point at $Y_i \gg \tilde{\alpha}_i$ [20] with the stable infrared fixed point within the NMSSM [21].

For the parameters of a soft breakdown of supersymmetry, the behavior of solutions to the renormalization-group equations within the NMSSM is studied here near infrared quasifixed points. Approximate solutions for the trilinear coupling constants $A_i(t)$ and for the combinations $\mathfrak{M}_i^2(t)$ of the scalar-particle masses are presented in the Appendix. In the regime of strong Yukawa coupling, where $\tilde{\alpha}_{\text{GUT}} \ll Y_i(0) \ll 1$, $A_i(t)$ and $\mathfrak{M}_i^2(t)$ at the electroweak scale are concentrated near some straight lines or surfaces in the space of the parameters being considered. With increasing $Y_i(0)$, the dependence of the trilinear coupling constants and of the combinations of the scalar-particle masses on $A_i(0)$ and $\mathfrak{M}_i^2(0)$ becomes weaker; in the limit $Y_i(0) \rightarrow \infty$, solutions to the renormalization-group equations for the parameters of a soft breakdown of supersymmetry approach a quasifixed point.

2. RENORMALIZATION OF THE PARAMETERS OF A SOFT BREAKDOWN OF SUPERSYMMETRY IN THE CASE OF UNIVERSAL BOUNDARY CONDITIONS

The superpotential in the NMSSM involves a large number of Yukawa coupling constants. At $\tan\beta \sim 1$, however, all of these are small, with the exception of the t -quark Yukawa coupling constant h_t , the self-interaction constant κ for the neutral scalar field Y , and the constant λ characterizing the interaction of the field Y with the doublets H_1 and H_2 .

In the regime of strong Yukawa coupling, the aforementioned constants can be chosen in such a way that, at the scale M_X , the Yukawa coupling constant h_b for the b quark is equal to the Yukawa coupling constant h_τ for the τ lepton [19, 22]. This relationship between h_b and h_τ is usually realized in the minimal schemes of unification of gauge interactions [23].

Disregarding all Yukawa coupling constants, with the exception of h_t , λ , and κ , we can represent the total superpotential within the NMSSM in the form

$$W = \lambda Y(H_1 H_2) + \frac{\kappa}{3} Y^3 + h_t(H_2 Q)U_R^c. \quad (6)$$

By construction, the superpotential of the nonminimal SuSy model is invariant under the discrete transformations $y'_\alpha = e^{2i\pi/3} y_\alpha$ of the Z_3 group [18]. Second-order terms in superfields do not satisfy this condition; therefore, they have been eliminated from the superpotential (6). Upon a spontaneous breakdown of gauge symmetry, the field Y develops a nonzero vacuum expectation value ($\langle Y \rangle = y/\sqrt{2}$). For example, a mixing of the doublets H_1 and H_2 , which is necessary for the emergence of the vacuum expectation value v_1 of the H_1 doublet (without this vacuum expectation value, down quarks and charged leptons remain massless), is generated within the NMSSM.

That the extra superfield Y , which is a singlet with respect to $SU(2) \times U(1)$ gauge interactions, and the coupling constant λ are introduced in the superpotential (6) leads to an increase in the upper limit on the mass of the lightest Higgs boson in relation to that within the MSSM: in the NMSSM, it is 135 GeV [24], which is 7 to 10 GeV greater than the corresponding value in the minimal SuSy model, the largest value of the mass of the lightest Higgs boson being attained in the regime of strong Yukawa coupling.

Upon a soft breakdown of supersymmetry due to SuGra effects, scalar fields acquire masses m_i^2 ; in addition, a trilinear coupling constant A_i for the interaction of scalar fields is associated with each Yukawa coupling constant in the total Lagrangian of the theory. That the models being considered involve a large number of unknown parameters of a soft breakdown of supersymmetry is one of the main flaws in such models. The hypothesis of universality of these constants at the scale M_X makes it possible to reduce their number in the NMSSM to three (the mass m_0 of all scalar particles, the trilinear coupling constant A for the interaction of scalar fields, and the gaugino mass $M_{1/2}$), whereby the analysis of the spectrum of SuSy particles is significantly simplified. Naturally, the universal parameters of supersymmetry breaking arise in the minimal SuGra model (see [4, 25]) and in some string models [26]. Even in the

region of low energies, the hypothesis of universality of fundamental parameters makes it possible to avoid the emergence of flavor-changing neutral currents. Thus, the minimal set of the fundamental parameters in the NMSSM includes, in addition to the constants of the Standard Model, five unknown constants (λ , κ , A , m_0 , and $M_{1/2}$). Within the nonminimal SuSy model, the spectrum of the superpartners of observable particles and Higgs bosons for universal boundary conditions was studied in [27].

The full set of renormalization-group equations that describes the evolution of Yukawa coupling constants, the trilinear coupling constants $A_i(t)$, and the scalar-particle masses $m_i^2(t)$ within the nonminimal SuSy model from the Grand Unification scale down to the electroweak scale can be found in [28, 29] (see also Appendix). This set of equations is nonlinear even in the one-loop approximation; in view of this, its analytic solution has not yet been found. All equations that form the set being considered can be partitioned into two groups. The first includes equations that describe the evolution of gauge and Yukawa coupling constants. If their evolution is known, the remaining equations from the set of renormalization-group equations can be considered as a set of linear differential equations for the parameters of a soft breakdown of supersymmetry. In solving this set of equations, it is necessary to integrate, first of all, the equations for the gaugino masses and for the trilinear coupling constants for the interactions of scalar particles. A general solution to the set of linear differential equations

$$\frac{dy_i(t)}{dt} = S_{ij}(t)y_j(t) + F_i(t),$$

where the matrix $S_{ij}(t)$ and the column vector (non-homogeneous term) $F_i(t)$ are known, has the form

$$y_i(t) = \Phi_{ij}(t)y_j(0) + \Phi_{ik}(t) \int_0^t \Phi_{kj}^{-1}(t')F_j(t')dt', \quad (7)$$

where $\Phi_{ij}(t)$ is a solution to the homogeneous equation $d\Phi_{ij}(t)/dt = S_{ik}(t)\Phi_{kj}(t)$ with the boundary conditions $\Phi_{ij}(0) = \delta_{ij}$. Since we have $y_i(0) = A(1, 1, 1)$ for $A_i(t)$ if the fundamental parameters are chosen in a minimal way and since $F_j(t) \sim M_{1/2}$, the trilinear coupling constants for the interactions of scalar fields are given by

$$A_i(t) = e_i(t)A + f_i(t)M_{1/2}. \quad (8)$$

These solutions for $A_i(t)$ must be substituted into the expressions on the right-hand sides of the renormalization-group equations for the scalar-particle masses, the functions $F_i(t)$ involving terms proportional

to A^2 , $AM_{1/2}$, and $M_{1/2}^2$. Considering that, in the case being considered, $y_i(0) = m_0^2(1, 1, 1, 1, 1)$, we can represent the required solution for $m_i^2(t)$ as

$$m_i^2(t) = a_i(t)m_0^2 + b_i(t)M_{1/2}^2 + c_i(t)AM_{1/2} + d_i(t)A^2. \quad (9)$$

The functions $e_i(t)$, $f_i(t)$, $a_i(t)$, $b_i(t)$, $c_i(t)$, and $d_i(t)$, which determine the evolution of $A_i(t)$ and $m_i^2(t)$, remain unknown, since an analytic solution to the full set of renormalization-group equations within the NMSSM is unavailable. These functions greatly depend on the choice of values for the Yukawa coupling constants at the Grand Unification scale M_X . At the electroweak scale $t = t_0$, relations (8) and (9) specify the parameters $A_i(t_0)$ and $m_i^2(t_0)$ of a soft breakdown of supersymmetry as functions of their initial values at the Grand Unification scale.

The results of our numerical analysis, which are presented in the table, indicate that, with increasing

$$Y_i(0), \text{ where } Y_t(t) = \left(\frac{h_t(t)}{4\pi}\right)^2, \quad Y_\lambda(t) = \left(\frac{\lambda(t)}{4\pi}\right)^2,$$

$$\text{and } Y_\kappa(t) = \left(\frac{\kappa(t)}{4\pi}\right)^2, \text{ the functions } e_i(t_0), c_i(t_0),$$

and $d_i(t_0)$ decrease and tend to zero in the limit $Y_i(0) \rightarrow \infty$, relations (8) and (9) becoming much simpler in this limit. Instead of the squares of the scalar-particle masses, it is convenient to consider their linear combinations

$$\mathfrak{M}_i^2(t) = m_2^2(t) + m_Q^2(t) + m_U^2(t), \quad (10)$$

$$\mathfrak{M}_\lambda^2(t) = m_1^2(t) + m_2^2(t) + m_Y^2(t),$$

$$\mathfrak{M}_\kappa^2(t) = 3m_Y^2(t)$$

in analyzing the set of renormalization-group equations. In the case of universal boundary conditions, the solutions to the differential equations for $\mathfrak{M}_i^2(t)$ can be represented in the same form as the solutions for $m_i^2(t)$ [see Eq. (9)]; that is,

$$\mathfrak{M}_i^2(t) = 3\tilde{a}_i(t)m_0^2 + \tilde{b}_i(t)M_{1/2}^2 + \tilde{c}_i(t)AM_{1/2} + \tilde{d}_i(t)A^2. \quad (11)$$

Since the homogeneous equations for $A_i(t)$ and $\mathfrak{M}_i^2(t)$ have the same form, the functions $\tilde{a}_i(t)$ and $e_i(t)$ coincide; in the limit of strong Yukawa coupling, the m_0^2 dependence disappears in the combinations (10) of the scalar-particle masses as the solutions to the renormalization-group equations for the Yukawa coupling constants approach quasifixed points. This behavior of the solutions implies that $A_i(t)$ and $\mathfrak{M}_i^2(t)$ corresponding to $Y_i(0) \gg \tilde{a}_i(0)$ also approach quasifixed points. As was shown in [19], two quasifixed points of the renormalization-group equations

Values of the functions $e_i(t_0)$, $f_i(t_0)$, $a_i(t_0)$, $b_i(t_0)$, $c_i(t_0)$, and $d_i(t_0)$ versus the choice of $\kappa^2(0)$, $\lambda^2(0)$, and $h_t^2(0)$

$\kappa^2(0)$	0	0	0	0	0	4	10	10
$\lambda^2(0)$	2	4	10	10	10	4	10	10
$h_t^2(0)$	10	10	10	4	2	10	10	4
$e_t(t_0)$	0.0011	0.0024	0.0082	0.0310	0.0651	0.0070	0.0102	0.0308
$e_\lambda(t_0)$	0.2127	0.1192	0.0260	-0.0227	-0.0544	0.0661	0.0113	-0.0232
$e_\kappa(t_0)$	0.5066	0.3451	0.1804	0.0774	-0.0062	0.0430	-0.0136	-0.0528
$f_t(t_0)$	1.7196	1.7406	1.7698	1.8352	1.9272	1.7254	1.7489	1.8119
$f_\lambda(t_0)$	-0.4414	-0.4295	-0.4161	-0.3976	-0.3722	-0.4386	-0.4262	-0.4046
$f_\kappa(t_0)$	0.0173	0.0195	0.0175	-0.0069	-0.0422	0.0232	0.0273	0.0138
$a_1(t_0)$	0.7533	0.6725	0.5902	0.5387	0.4969	0.7632	0.6882	0.6247
$a_2(t_0)$	-0.6217	-0.6601	-0.6927	-0.6842	-0.6539	-0.6079	-0.6406	-0.6415
$a_y(t_0)$	0.5066	0.3451	0.1804	0.0774	-0.0062	0.0430	-0.0136	-0.0528
$a_Q(t_0)$	0.5417	0.5558	0.5724	0.5924	0.6164	0.5430	0.5571	0.5779
$a_U(t_0)$	0.0833	0.1116	0.1448	0.1847	0.2328	0.0859	0.1141	0.1558
$b_1(t_0)$	0.5557	0.5665	0.5761	0.5757	0.5703	0.5538	0.5627	0.5646
$b_2(t_0)$	-3.0399	-3.0070	-2.9664	-2.9044	-2.8175	-3.0352	-3.0014	-2.9402
$b_y(t_0)$	0.0724	0.0939	0.1131	0.1122	0.1015	0.0695	0.0907	0.1004
$b_Q(t_0)$	5.3129	5.3202	5.3305	5.3514	5.3821	5.3150	5.3234	5.3432
$b_U(t_0)$	3.6951	3.7099	3.7305	3.7722	3.8336	3.6995	3.7162	3.7557
$c_1(t_0)$	0.0034	0.0036	0.0040	0.0087	0.0145	0.0024	0.0034	0.0080
$c_2(t_0)$	-0.0085	-0.0096	-0.0165	-0.0543	-0.1080	-0.0159	-0.0197	-0.0549
$c_y(t_0)$	0.0068	0.0072	0.0079	0.0173	0.0290	0.0052	0.0056	0.0127
$c_Q(t_0)$	-0.0040	-0.0044	-0.0068	-0.0210	-0.0409	-0.0061	-0.0077	-0.0210
$c_U(t_0)$	-0.0079	-0.0088	-0.0137	-0.0420	-0.0817	-0.0122	-0.0154	-0.0419
$d_1(t_0)$	-0.0186	-0.0144	-0.0055	-0.0008	0.0023	-0.0063	-0.0029	-0.0010
$d_2(t_0)$	-0.0143	-0.0114	-0.0069	-0.0122	-0.0217	-0.0076	-0.0062	-0.0129
$d_y(t_0)$	-0.0372	-0.0288	-0.0109	-0.0016	0.0045	-0.0196	-0.0034	0.0044
$d_Q(t_0)$	0.0014	0.0010	-0.0005	-0.0038	-0.0080	-0.0004	-0.0011	-0.0039
$d_U(t_0)$	0.0029	0.0020	-0.0010	-0.0076	-0.0160	-0.0008	-0.0022	-0.0079
$\tilde{a}_t(t_0)$	0.0033	0.0073	0.0245	0.0929	0.1953	0.0210	0.0305	0.0923
$\tilde{a}_\lambda(t_0)$	0.6382	0.3575	0.0779	-0.0680	-0.1631	0.1983	0.0340	-0.0695
$\tilde{a}_\kappa(t_0)$	1.5199	1.0352	0.5411	0.2323	-0.0185	0.1290	-0.0407	-0.1583
$\tilde{b}_t(t_0)$	5.9680	6.0231	6.0947	6.2192	6.3981	5.9794	6.0382	6.1588
$\tilde{b}_\lambda(t_0)$	-2.4118	-2.3466	-2.2771	-2.2165	-2.1457	-2.4119	-2.3479	-2.2752
$\tilde{b}_\kappa(t_0)$	0.2172	0.2817	0.3394	0.3367	0.3045	0.2085	0.2722	0.3011
$\tilde{c}_t(t_0)$	-0.0204	-0.0228	-0.0370	-0.1173	-0.2306	-0.0342	-0.0427	-0.1178
$\tilde{c}_\lambda(t_0)$	0.0017	0.0012	-0.0047	-0.0283	-0.0645	-0.0083	-0.0107	-0.0342
$\tilde{c}_\kappa(t_0)$	0.0204	0.0216	0.0238	0.0520	0.0870	0.0156	0.0166	0.0380
$\tilde{d}_t(t_0)$	-0.0099	-0.0084	-0.0084	-0.0235	0.0457	-0.0088	-0.0095	-0.0247
$\tilde{d}_\lambda(t_0)$	-0.0700	-0.0547	-0.0233	-0.0146	-0.0150	-0.0334	-0.0125	-0.0096
$\tilde{d}_\kappa(t_0)$	-0.1115	-0.0865	-0.0327	-0.0049	0.0135	-0.0587	-0.0103	0.0132

within the NMSSM are of greatest interest from the physical point of view. Of these, one corresponds to the boundary conditions $Y_t(0) = Y_\lambda(0) \gg \tilde{\alpha}_i(0)$ and $Y_\kappa(0) = 0$ for the Yukawa coupling constants. The fixed points calculated for the parameters of a soft breakdown of supersymmetry by using these values of the Yukawa coupling constants are

$$\rho_{A_t}^{\text{QFP}}(t_0) \approx 1.77, \quad \rho_{\mathfrak{M}_t^2}^{\text{QFP}}(t_0) \approx 6.09, \quad (12)$$

$$\rho_{A_\lambda}^{\text{QFP}}(t_0) \approx -0.42, \quad \rho_{\mathfrak{M}_\lambda^2}^{\text{QFP}}(t_0) \approx -2.28,$$

where $\rho_{A_i}(t) = A_i(t)/M_{1/2}$ and $\rho_{\mathfrak{M}_i^2}(t) = \mathfrak{M}_i^2(t)/M_{1/2}^2$. Since the coupling constant κ for the self-interaction of neutral scalar fields is small in the case being considered, $A_\kappa(t)$ and $\mathfrak{M}_\kappa^2(t)$ do not approach the quasifixed point. Nonetheless, the

spectrum of SuSy particles is virtually independent of the trilinear coupling constant A_κ since $\kappa \rightarrow 0$.

In just the same way, one can determine the position of the other quasifixed point for $A_i(t)$ and $\mathfrak{M}_i^2(t)$, that which corresponds to $R_{\lambda 0} = 3/4$ and $R_{\kappa 0} = 3/8$. The results are

$$\rho_{A_t}^{\text{QFP}}(t_0) \approx 1.73, \quad \rho_{A_\lambda}^{\text{QFP}}(t_0) \approx -0.43, \quad (13)$$

$$\rho_{A_\kappa}^{\text{QFP}}(t_0) \approx 0.033, \quad \rho_{\mathfrak{M}_t^2}^{\text{QFP}}(t_0) \approx 6.02,$$

$$\rho_{\mathfrak{M}_\lambda^2}^{\text{QFP}}(t_0) \approx -2.34, \quad \rho_{\mathfrak{M}_\kappa^2}^{\text{QFP}}(t_0) \approx 0.29,$$

where $R_{\lambda 0} = Y_\lambda(0)/Y_t(0)$ and $R_{\kappa 0} = Y_\kappa(0)/Y_t(0)$. It should be noted that, in the vicinities of quasifixed points, we have $\rho_{\mathfrak{M}_\lambda^2}^{\text{QFP}}(t_0) < 0$. Negative values of $\mathfrak{M}_\lambda^2(t_0)$ lead to a negative value of the parameter

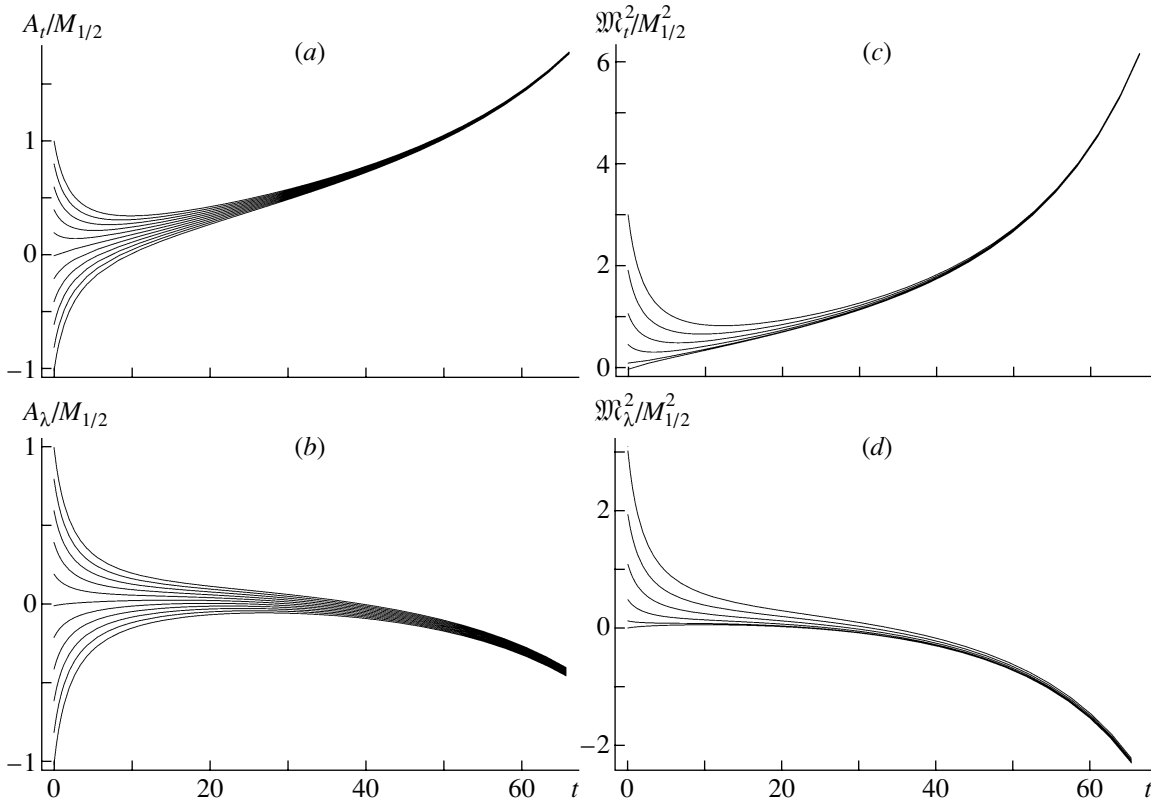


Fig. 1. Behavior of the solutions $A_t(t)$, $A_\lambda(t)$, $\mathfrak{M}_t^2(t)$, and $\mathfrak{M}_\lambda^2(t)$ to the renormalization-group equations within the NMSSM at $\kappa^2 = 0$ and $\lambda^2(0) = h_t^2(0) = 10$ for universal boundary conditions versus t . The parameters A and m_0^2 are varied in the ranges $-M_{1/2} \leq A \leq M_{1/2}$ and $0 \leq m_0^2 \leq M_{1/2}^2$, respectively.

$m_2^2(t_0)$ in the potential of interaction of Higgs fields (see table). In other words, an elegant mechanism that is responsible for a radiative violation of $SU(2) \times U(1)$ symmetry and which does not require introducing tachyons in the spectrum of the theory from the outset survives in the regime of strong Yukawa coupling within the NMSSM. This mechanism of gauge-symmetry breaking was first discussed in [30] by considering the example of the minimal SuSy model.

The evolution of the constants of a soft breakdown of supersymmetry, $A_i(t)$ and $\mathfrak{M}_i^2(t)$, is illustrated in Figs. 1 and 2 for $Y_t(0), Y_\lambda(0) \gg \tilde{\alpha}(0)$ and $Y_\kappa = 0$, as well as for $Y_\kappa(0) \gg \tilde{\alpha}(0)$. Although the ratio $A/M_{1/2}$ is varied between -1 and 1 , with the scalar-particle mass m_0^2 lying in the range $0 \leq m_0^2 \leq M_{1/2}^2$, solutions to the renormalization-group equations are focused in a narrow interval at low energies. However, $A_\kappa(t)$ and $\mathfrak{M}_\kappa^2(t)$ are concentrated near zero, since the neutral field Y is not renormalized by gauge interactions; therefore, they remain dependent on the initial conditions (see also table). The values of $A_t(t_0)$ and $\mathfrak{M}_t^2(t_0)$

show the weakest dependence on A and m_0^2 , because the former are renormalized by strong interactions.

By using the fact that $\mathfrak{M}_t^2(t)$ as determined for the case of universal boundary conditions is virtually independent of m_0^2 , we can predict $a_i(t_0)$ values near the quasifixed points. The results are

$$\begin{aligned}
 & 1) R_{\lambda 0} = 1, \quad R_{\kappa 0} = 0, \quad (14) \\
 & a_y(t_0) = a_u(t_0) = \frac{1}{7}, \quad a_1(t_0) = a_q(t_0) = \frac{4}{7}, \\
 & a_2(t_0) = -\frac{5}{7}; \\
 & 2) R_{\lambda 0} = 3/4, \quad R_{\kappa 0} = 3/8, \\
 & a_y(t_0) = 0, \quad a_1(t_0) = -a_2(t_0) = \frac{2}{3}, \quad a_q(t_0) = \frac{5}{9}, \\
 & a_u(t_0) = \frac{1}{9}.
 \end{aligned}$$

To do this, it was necessary to consider specific combinations of the scalar-particle masses, such as $m_U^2 - 2m_Q^2$, $m_Q^2 + m_U^2 - m_2^2 + m_1^2$, and $m_y^2 - 2m_1^2$ (at $\kappa = 0$), that are not renormalized by Yukawa interactions. As a result, the dependence of the above combinations of the scalar-particle masses on m_0^2 at the

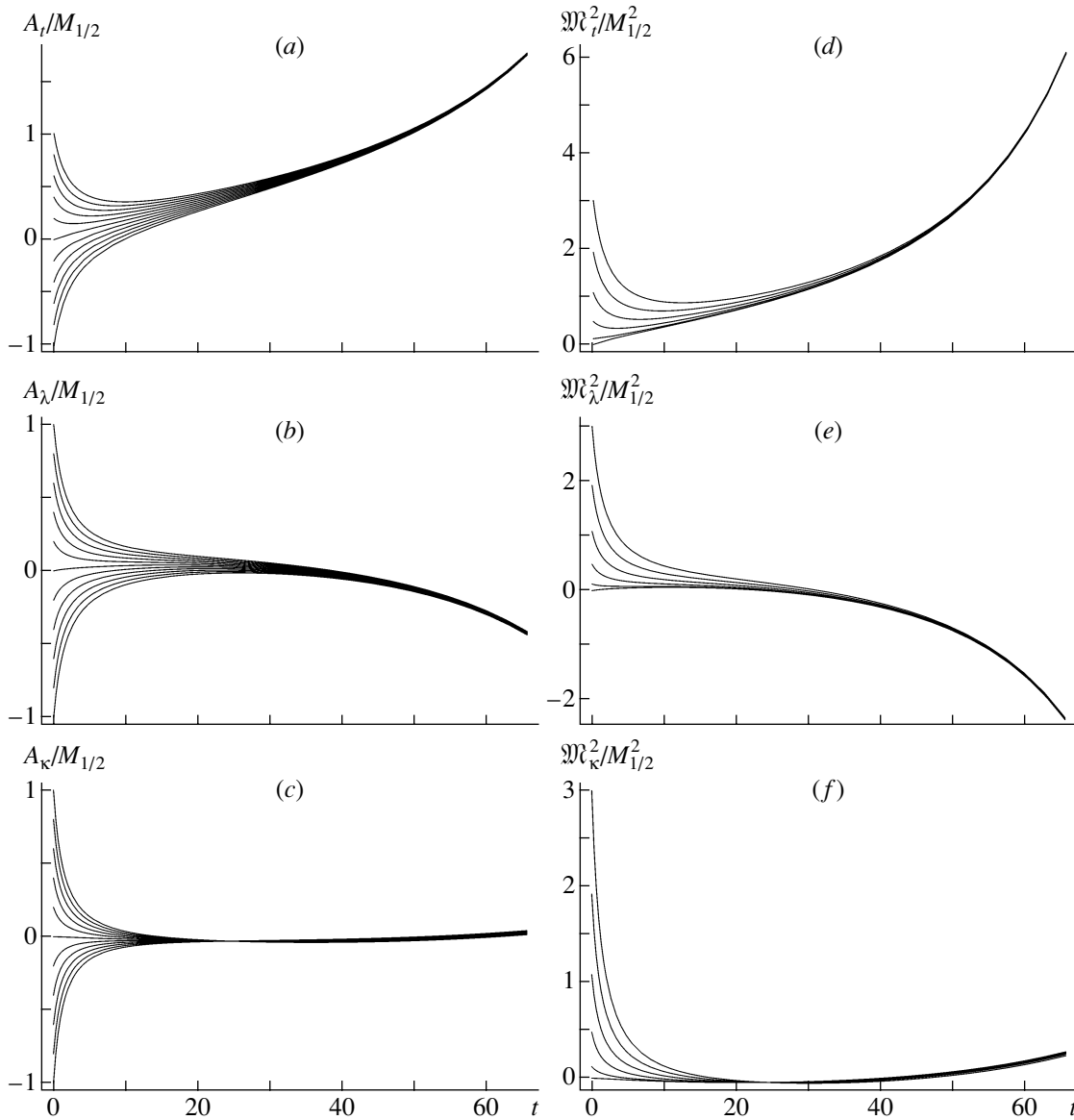


Fig. 2. Evolution of $A_i(t)$, $A_\lambda(t)$, $A_\kappa(t)$, $\mathfrak{M}_i^2(t)$, $\mathfrak{M}_\lambda^2(t)$, and $\mathfrak{M}_\kappa^2(t)$ from $t = 0$ to $t = t_0$ at $h_i^2(0) = \lambda^2(0) = \kappa^2(0) = 10$ for universal boundary conditions. The parameters A and m_0^2 are varied within the same limits as in Fig. 1.

electroweak scale is identical to that at the Grand Unification scale. The data in the table show that the predictions in (14) agree fairly well with the results of numerical calculations.

3. STRAIGHT LINES AND PLANES IN THE SPACE OF PARAMETERS OF A SOFT BREAKDOWN OF SUPERSYMMETRY

By considering the example of an exact analytic solution at $Y_\lambda = 0$, we can see how the A and m_0^2 dependence of the parameters of a soft breakdown of supersymmetry disappears. From this point, our

analysis of solutions to renormalization-group equations for $A_i(t)$ and $\mathfrak{M}_i^2(t)$ will not be restricted to the case of universal boundary conditions; that is, $A_i(0)$ and $\mathfrak{M}_i^2(0)$ will be considered as independent boundary values. In the case being considered, the full set of renormalization-group equations within the NMSSM can be partitioned into two subsets—of these, one coincides with the set of renormalization-group equations within the MSSM, while the other describes the evolution of $Y_\kappa(t)$, $A_\kappa(t)$, and $\mathfrak{M}_\kappa^2(t)$. For $Y_\lambda = 0$, the evolution of $A_i(t)$ and $\mathfrak{M}_i^2(t)$ is determined by relations (5). For the other two parameters $A_\kappa(t)$ and $\mathfrak{M}_\kappa^2(t)$ of a soft breakdown of supersymmetry, which correspond to the Yukawa coupling

constant κ , we obtain

$$A_\kappa(t) = A_\kappa(0)\epsilon_\kappa(t), \tag{15}$$

$$\mathfrak{M}_\kappa^2(t) = \mathfrak{M}_\kappa^2(0)\epsilon_\kappa(t) - A_\kappa^2(0)\epsilon_\kappa(t)(1 - \epsilon_\kappa(t)),$$

where $\epsilon_\kappa(t) = Y_\kappa(t)/Y_\kappa(0) = 1/(1 + 6Y_\kappa(0)t)$. With increasing $Y_\kappa(0)$ and $Y_t(0)$, the values of the Yukawa coupling constants at the electroweak scale approach the quasifixed point, while solutions to the renormalization-group equations for the parameters of a soft breakdown of supersymmetry are attracted to the straight lines $A_t = 1.67M_{1/2}$ and $A_\kappa = 0$ in the (A_t, A_κ) plane and to the straight lines $\mathfrak{M}_t^2 = 5.49M_{1/2}^2$ and $\mathfrak{M}_\kappa^2 = 0$ in the $(\mathfrak{M}_t^2, \mathfrak{M}_\kappa^2)$ plane. The dependence on the boundary values $A_i(0)$ and $\mathfrak{M}_i^2(0)$ disappears only in the limit $Y_i(0) \rightarrow \infty$, which corresponds to a quasifixed point in the (ρ_t, ρ_κ) plane.

At nonzero values of Y_λ , it is possible to construct, on the basis of an approximate solution for the Yukawa coupling constants within the NMSSM [19], approximate solutions to the renormalization-group equations for the parameters of a soft breakdown of supersymmetry. Near the quasifixed points given by (12) and (13), these solutions describe the evolution of $A_t(t)$ and $\mathfrak{M}_t^2(t)$ to a fairly high precision (about 1 percent). The relative deviations of the approximate solutions from numerical ones are significantly greater for $A_\lambda(t)$ and $\mathfrak{M}_\lambda^2(t)$. At the electroweak scale, the relative error here is as large as 20 to 30 percent near quasifixed points. Finally, the approximate solutions for the parameters of a soft breakdown of supersymmetry that correspond to the Yukawa coupling constant κ are characterized by the poorest accuracy, providing only a qualitative description of the behavior of the numerical solutions. Our results lead to the conclusion that the relative deviation of the approximate solution being studied from the precise numerical solution decreases with increasing contribution of gauge interactions to the renormalization of the corresponding parameter of a soft breakdown of supersymmetry.

Approximate solutions to the renormalization-group equations within the NMSSM for the trilinear coupling constants and the combination (10) of the scalar-particle masses are presented in the Appendix. In the regime of strong Yukawa coupling at $A_i(0) = A$ and $\mathfrak{M}_i^2(0) = 3m_0^2$, the dependence of these solutions on the initial conditions vanishes in proportion to $1/Y_i(0)$. Disregarding $O(1/Y_i(0))$ terms, we find, for nonuniversal boundary conditions, that

$$\begin{aligned} \begin{pmatrix} A_t(t) \\ \mathfrak{M}_t^2(t) \end{pmatrix} &\approx \frac{R_{\lambda 0}F_\lambda(t)}{6F_t(t) + 2R_{\lambda 0}F_\lambda(t)} \\ &\times \begin{pmatrix} A_t(0) - A_\lambda(0) \\ \mathfrak{M}_t^2(0) - \mathfrak{M}_\lambda^2(0) \end{pmatrix} + \dots, \end{aligned} \tag{16}$$

$$\begin{aligned} \begin{pmatrix} A_\lambda(t) \\ \mathfrak{M}_\lambda^2(t) \end{pmatrix} &\approx \frac{3F_t(t)}{6F_t(t) + 2R_{\lambda 0}F_\lambda(t)} \\ &\times \begin{pmatrix} A_\lambda(0) - A_t(0) \\ \mathfrak{M}_\lambda^2(0) - \mathfrak{M}_t^2(0) \end{pmatrix} \\ &+ \frac{2R_{\kappa 0}t}{6R_{\lambda 0}F_\lambda(t) + 6R_{\kappa 0}t} \begin{pmatrix} A_\lambda(0) - A_\kappa(0) \\ \mathfrak{M}_\lambda^2(0) - \mathfrak{M}_\kappa^2(0) \end{pmatrix} + \dots, \\ \begin{pmatrix} A_\kappa(t) \\ \mathfrak{M}_\kappa^2(t) \end{pmatrix} &\approx \frac{6R_{\lambda 0}F_\lambda(t)}{6R_{\lambda 0}F_\lambda(t) + 6R_{\kappa 0}t} \\ &\times \begin{pmatrix} A_\kappa(0) - A_\lambda(0) \\ \mathfrak{M}_\kappa^2(0) - \mathfrak{M}_\lambda^2(0) \end{pmatrix} + \dots \end{aligned}$$

In Eqs. (16), we discarded terms proportional to $M_{1/2}, M_{1/2}^2, A_i(0)M_{1/2}$, and $A_i(0)A_j(0)$. The explicit expressions for the functions $F_i(t)$ are presented in the Appendix [see Eq. (A.2)]. From the results that we obtained, it follows that, in the case of nonuniversal boundary conditions, the approximate solutions to the renormalization-group equations for $A_i(t)$ and $\mathfrak{M}_i^2(t)$ remain dependent on the difference of the values of these constants at the Grand Unification scale. At the same time, the linear combinations

$$\begin{aligned} 9F_t(t)A_t(t) + 3R_{\lambda 0}F_\lambda(t)A_\lambda(t) \\ + R_{\kappa 0}tA_\kappa(t) &= \text{const}, \\ 9F_t(t)\mathfrak{M}_t^2(t) + 3R_{\lambda 0}F_\lambda(t)\mathfrak{M}_\lambda^2(t) \\ + R_{\kappa 0}t\mathfrak{M}_\kappa^2(t) &= \text{const}' \end{aligned} \tag{17}$$

of the parameters undergo virtually no changes in response to variations of $A_i(0)$ in the first combination and of $\mathfrak{M}_i^2(0)$ in the second combination. At the electroweak scale ($t = t_0$), relations (17) specify straight lines (at $Y_\kappa = 0$) and planes (at $Y_\kappa(0) \gg \tilde{\alpha}(0)$) in the space of the parameters of a soft breakdown of supersymmetry. In the regime of strong Yukawa coupling, the approximate solutions to the renormalization-group equations are attracted to these straight lines and planes.

The results of our numerical analysis, which are illustrated in Fig. 3, indicate that, in the vicinity of the infrared fixed point at $Y_\kappa = 0$, solutions to the renormalization-group equations at the electroweak scale are indeed concentrated near some straight lines for the case where the simulation was performed by using boundary conditions uniformly distributed in the (A_t, A_λ) and the $(\mathfrak{M}_t^2, \mathfrak{M}_\lambda^2)$ plane. The strength with which these solutions are attracted to them grows with increasing $Y_i(0)$. The equations for the lines being considered can be obtained by fitting the numerical results displayed in Fig. 3. This yields

$$\begin{aligned} A_t + 0.147(0.121)A_\lambda &= 1.70M_{1/2}, \\ \mathfrak{M}_t^2 + 0.147(0.121)\mathfrak{M}_\lambda^2 &= 5.76M_{1/2}^2. \end{aligned} \tag{18}$$

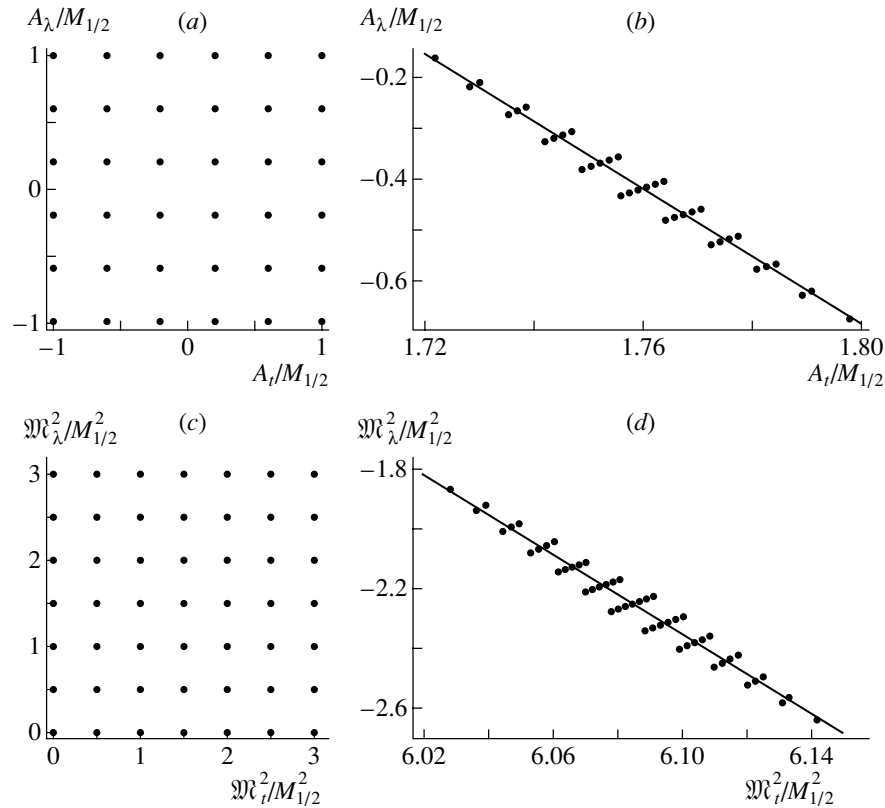


Fig. 3. (a, c) Boundary conditions imposed on the renormalization-group equations within the NMSSM and distributed uniformly in the $(A_t/M_{1/2}, A_\lambda/M_{1/2})$ and $(\mathfrak{M}_t^2/M_{1/2}^2, \mathfrak{M}_\lambda^2/M_{1/2}^2)$ planes and (b, d) corresponding parameter values at the electroweak scale for $\kappa^2 = 0$ and $h_i^2(0) = \lambda^2(0) = 20$. The quantities $\mathfrak{M}_t^2(t_0)$ and $\mathfrak{M}_\lambda^2(t_0)$ were calculated at $A_t(0) = A_\lambda(0) = 0$. The straight lines in Figs. 3b and 3d were constructed by fitting the values of $(A_t(t_0), A_\lambda(t_0))$ and $(\mathfrak{M}_t^2(t_0), \mathfrak{M}_\lambda^2(t_0))$, respectively.

For $Y_\kappa(0) \gg \tilde{\alpha}(0)$, solutions to the renormalization-group equations are grouped near planes in the space of the parameters of a soft breakdown of supersymmetry $[(A_t, A_\lambda, A_\kappa) \text{ and } (\mathfrak{M}_t^2, \mathfrak{M}_\lambda^2, \mathfrak{M}_\kappa^2)]$ (see Figs. 4, 5):

$$\begin{aligned}
 & A_t + 0.128(0.091)A_\lambda \\
 & + 0.022(0.0105)A_\kappa = 1.68M_{1/2}, \\
 & \mathfrak{M}_t^2 + 0.128(0.091)\mathfrak{M}_\lambda^2 + \\
 & + 0.022(0.0105)\mathfrak{M}_\kappa^2 = 5.77M_{1/2}^2.
 \end{aligned} \tag{19}$$

In (18) and (19), the predictions for the coefficients of A_λ , A_κ , \mathfrak{M}_λ^2 and \mathfrak{M}_κ^2 according to the calculations at $R_{\lambda 0} = 1$ and $R_{\kappa 0} = 0$ and at $R_{\lambda 0} = 3/4$ and $R_{\kappa 0} = 3/8$ on the basis of the approximate solutions (16) and (17) to the renormalization-group equations within the NMSSM in the regime of strong Yukawa coupling are given in parentheses. It can be seen from Fig. 4 that, as the values of the Yukawa coupling constants at the Grand Unification scale are increased, the areas of the surfaces near which the solutions $A_i(t)$ and $\mathfrak{M}_i^2(t)$ are concentrated shrink in one of

the directions, with the result that, at $Y_i(0) \sim 1$, the solutions to the renormalization-group equations are attracted to one of the straight lines belonging to these surfaces.

Thus, the approximate solutions presented in this study lead to qualitatively correct results. However, an analysis of numerical solutions to the renormalization-group equations revealed that, with increasing $Y_i(0)$, only in the regime of infrared quasifixed points (that is, at $R_{\lambda 0} = 1$ and $R_{\kappa 0} = 0$ or at $R_{\lambda 0} = 3/4$ and $R_{\kappa 0} = 3/8$) do $e_i(t_0)$ and $\tilde{a}_i(t_0)$ decrease in proportion to $1/Y_i(0)$. Otherwise, the dependence on A and m_0^2 disappears much more slowly with increasing values of the Yukawa coupling constants at the Grand Unification scale—specifically, in proportion to $\left(\frac{1}{Y_i(0)}\right)^\delta$, where $\delta < 1$ (for example, $\delta = 0.35 - 0.4$ at $\kappa = 0$). In the case of nonuniversal boundary conditions, only when solutions to the renormalization-group equations approach quasifixed points are these solutions attracted to the fixed lines and surfaces in the space of the parameters

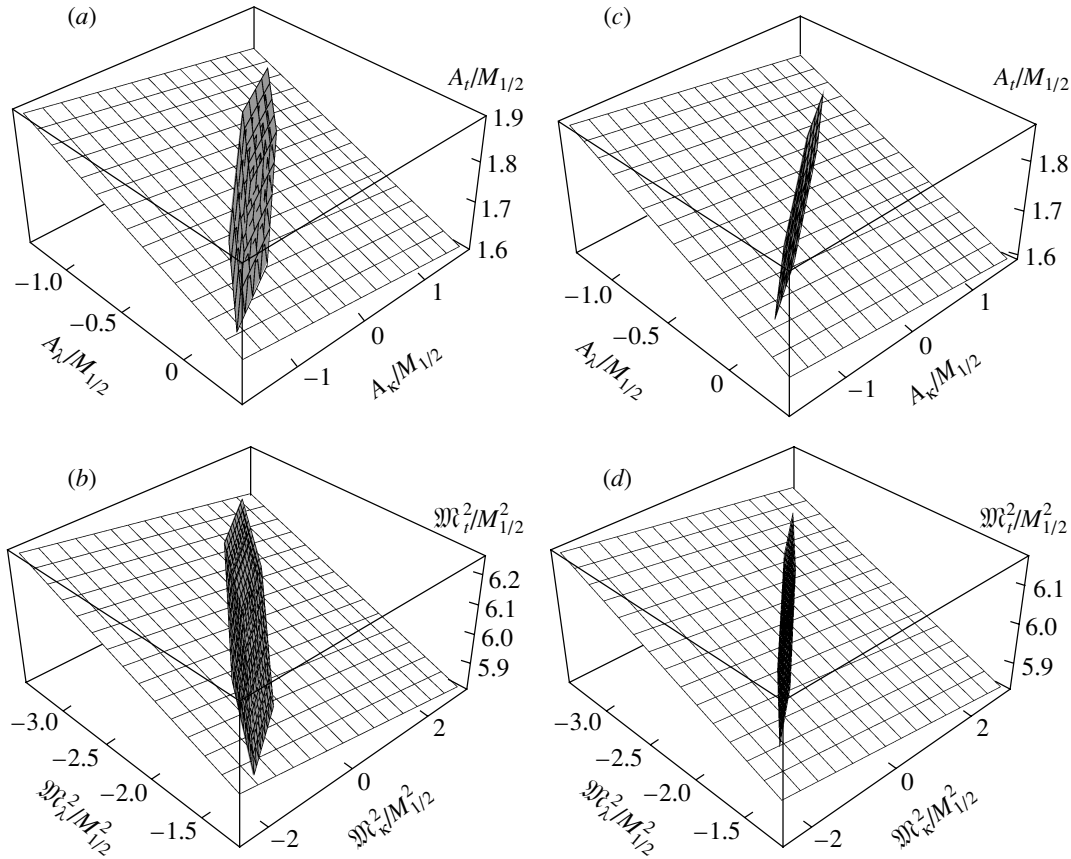


Fig. 4. Planes in the parameter spaces (a, c) $(A_t/M_{1/2}, A_\lambda/M_{1/2}, A_\kappa/M_{1/2})$ and (b, d) $(\mathfrak{M}_t^2/M_{1/2}^2, \mathfrak{M}_\lambda^2/M_{1/2}^2, \mathfrak{M}_\kappa^2/M_{1/2}^2)$. The shaded parts of the planes correspond to the regions near which the solutions for (a, b) $h_t^2(0) = 16$, $\lambda^2(0) = 12$, and $\kappa^2(0) = 6$ and (c, d) $h_t^2(0) = 32$, $\lambda^2(0) = 24$, and $\kappa^2(0) = 12$ are concentrated, the initial values $A_i(0)$ and $\mathfrak{M}_i^2(0)$ being uniformly distributed over the ranges $-M_{1/2} \leq A_i \leq M_{1/2}$ and $0 \leq \mathfrak{M}_i^2(0) \leq 3M_{1/2}^2$, respectively.

of a soft breakdown of supersymmetry; in the limit $Y_i(0) \rightarrow \infty$, the parameters $A_i(t)$ and $\mathfrak{M}_i^2(t)$ cease to be dependent on the boundary conditions, in contradiction with the results presented in (16). Finally, we note that, by using approximate solutions to the renormalization-group equations within the NMSSM, it is impossible to explain the emergence of those lines in the $(A_t, A_\lambda, A_\kappa)$ and $(\mathfrak{M}_t^2, \mathfrak{M}_\lambda^2, \mathfrak{M}_\kappa^2)$ spaces to which solutions of the equations in question are attracted when all three Yukawa coupling constants are $Y_i(0) \sim 1$.

4. ANALYSIS OF SOLUTIONS TO THE RENORMALIZATION-GROUP EQUATIONS NEAR QUASIFIXED POINTS

That, in the regime of strong Yukawa coupling, quasifixed points, lines, and surfaces appear in the space spanned by the parameters of a soft breakdown of supersymmetry is explained by fast changes in the Yukawa coupling constants at the initial stage. In

view of this, the entire scale from M_X to M_t^{pole} can be partitioned into two unequal intervals. Within the initial stage corresponding to $M_X \geq q \geq q_1 \sim 10^{12}$ GeV, the Yukawa coupling constants are significantly greater than the gauge coupling constants and decrease fast with increasing t . In this region, the evolution of all fundamental parameters of a soft breakdown of supersymmetry is determined by $Y_i(t)$, so that all gauge coupling constants $\tilde{\alpha}_i(t)$ can be disregarded for a first approximation. At the initial stage of evolution, the one-loop renormalization-group equations for $Y_i(t)$ can then be represented in the form

$$\frac{dY_i(t)}{dt} = -Y_i(t) \left(\sum_j c_{ij} Y_j(t) \right), \quad (20)$$

where $c_{ij} \geq 0$. If the set of Eqs. (20) has a fixed point, all the Yukawa coupling constants are proportional to each other in the vicinity of this point. In analyzing Eqs. (20), it is therefore convenient to introduce the

additional constant Y_0 satisfying the equation

$$\frac{dY_0(t)}{dt} = -Y_0^2(t)$$

and to investigate, instead of $Y_i(t)$, the ratio $r_i(t) = Y_i(t)/Y_0(t)$. The fixed point of the renormalization-group Eqs. (20) is then determined by solving the set of linear algebraic equations

$$\sum_j (c_{ij}r_j^0 - \delta_{ij}) = 0. \quad (21)$$

Linearizing the set of renormalization-group Eqs. (20) near the fixed point $r_i(t) = r_i^0(1 + \theta_i(t))$, we obtain

$$\left\{ \begin{array}{l} \frac{d\theta_i}{dz} = \sum_j c_{ij}r_j^0\theta_j, \\ \frac{dA_i}{dz} = \sum_j (c_{ij}r_j^0A_j + c_{ij}r_j^0\theta_jA_j), \\ \frac{d\mathfrak{M}_i^2}{dz} = \sum_j (c_{ij}r_j^0(\mathfrak{M}_j^2 + A_j^2) + c_{ij}r_j^0\theta_j(\mathfrak{M}_j^2 + A_j^2)), \end{array} \right\}, \quad (22)$$

where $z = \ln_0(t)/Y_0(0) = -\ln(1 + Y_0t)$. A general solution to this set of linear differential equations at $\theta_i = 0$ has the form

$$\begin{aligned} A_i(z) &= \sum_k \alpha_k u_{ik} e^{\lambda_k z}, \\ \mathfrak{M}_i^2(z) &= \sum_k \beta_k u_{ik} e^{\lambda_k z} \\ &+ \sum_{k,n} \lambda_k e^{\lambda_k z} u_{ik} u_{kn}^{-1} \int_0^z A_n^2(y) e^{-\lambda_n y} dy, \end{aligned} \quad (23)$$

where λ_k are the eigenvalues of the matrix $c_{ij}r_j^0$, u_{ik} is the eigenvector corresponding to the eigenvalue λ_k , and α_k and β_k are constants of integration that are expressed in terms of $A_i(0)$ and $\mathfrak{M}_i^2(0)$. It should be noted that all eigenvalues λ_k are positive. They are determined by solving the characteristic equation $\det(c_{ij}r_j^0 - \lambda'\delta_{ij}) = 0$.

From Eq. (21), it follows that, at $\lambda' = 1$, one of the columns of the matrix $(c_{ij}r_j^0 - \delta_{ij})$ is a linear combination of all other columns of this matrix; hence, its determinant is identically equal to zero. This means that the value of $\lambda_0 = 1$ is a root of the characteristic equation. The eigenvector $u_{i0} = (1, 1 \dots 1)$ corresponds to this eigenvalue. As a rule, all other roots of the characteristic equation are less than unity. With increasing t , the dependence of solutions (23) on the boundary conditions at the Grand Unification scale becomes weaker. At $q \sim 10^{12} - 10^{13}$ GeV, in which case the Yukawa coupling constants are on the same order of magnitude as the gauge coupling constants,

the values of $A_i(z)$ and $\mathfrak{M}_i^2(z)$ at this scale that are calculated by formulas (23) should be treated as new boundary values for the full set of renormalization-group equations within the NMSSM, which is presented in the Appendix.

In the case where only the t -quark Yukawa coupling constant is nonzero, the set of differential Eqs. (20) for the Yukawa coupling constants reduces to one equation; as a result, the full nonlinearized set of renormalization-group equations can be solved exactly in the limit $\tilde{\alpha}_i \rightarrow 0$. The results are given by

$$Y_t(t) = \frac{Y_t(0)}{1 + 6Y_t(0)t}, \quad A_t(t) = A_t(0)\epsilon_t(t), \quad (24)$$

$$\mathfrak{M}_t^2(t) = \mathfrak{M}_t^2(0)\epsilon_t(t) - A_t^2(0)\epsilon_t(t)(1 - \epsilon_t(t)),$$

where $\epsilon_t(t) = Y_t(t)/Y_t(0)$. The solution in (24) coincides in form with solution (23) to the above linearized set of differential equations. Formally, it can be obtained by setting $M_{1/2} = 0$ and $E(t) = 1$ in the exact solution to the NMSSM renormalization-group equations that is given by (4) and (5). A comparison of the analytic solution (24) in the regime of strong Yukawa coupling with the exact solution to the renormalization-group equations within the minimal SuSy model reveals that, as the result of the evolution of $A_t(t)$ and $\mathfrak{M}_t^2(t)$ from the scale $q_1 \sim 10^{12}$ GeV to the electroweak scale, there arises, in addition to $\epsilon_t(t)$, an extra factor $1/E(t)$ in front of $A_t(0)$ and $\mathfrak{M}_t^2(0)$ in Eqs. (5). This new factor is independent of the initial conditions for the t -quark Yukawa coupling constant at the Grand Unification scale.

From relations (23), it follows that an expansion of solutions to the renormalization-group equations in powers of the small parameter $\epsilon_t(t)$ —this expansion emerges in the regime of strong Yukawa coupling within the MSSM—is also valid in more involved models. At the electroweak scale, solution (23) to the renormalization-group equations can be represented as

$$\begin{pmatrix} A_i(t) \\ \mathfrak{M}_i^2(t) \end{pmatrix} = \sum_k u_{ik} v_{ik}(t) \begin{pmatrix} \alpha_k \\ \beta_k \end{pmatrix} (\epsilon_t(t))^{\lambda_k} + \dots, \quad (25)$$

where the quantities $v_{ik}(t)$ are weakly dependent on the Yukawa coupling constants at the Grand Unification scale and $\epsilon_t(t) = Y_t(t)/Y_t(0)$. In expression (25), we have discarded terms proportional to $M_{1/2}, M_{1/2}^2, A_i M_{1/2}$, and A_i^2 . The extra factors $v_{ik}(t)$ appear upon renormalizing the parameters of a soft breakdown of supersymmetry from $q \sim 10^{12} - 10^{13}$ GeV to $q \sim m_t$. At $\kappa = 0$, there exists, in addition to $\lambda_0 = 1$ and $u_{i0} = (1, 1)$, yet another eigenvalue $\lambda_1 = 3/7$ and the corresponding eigenvector $u_{i1} = (1, -3)$, whose components specify (A_t, A_λ)

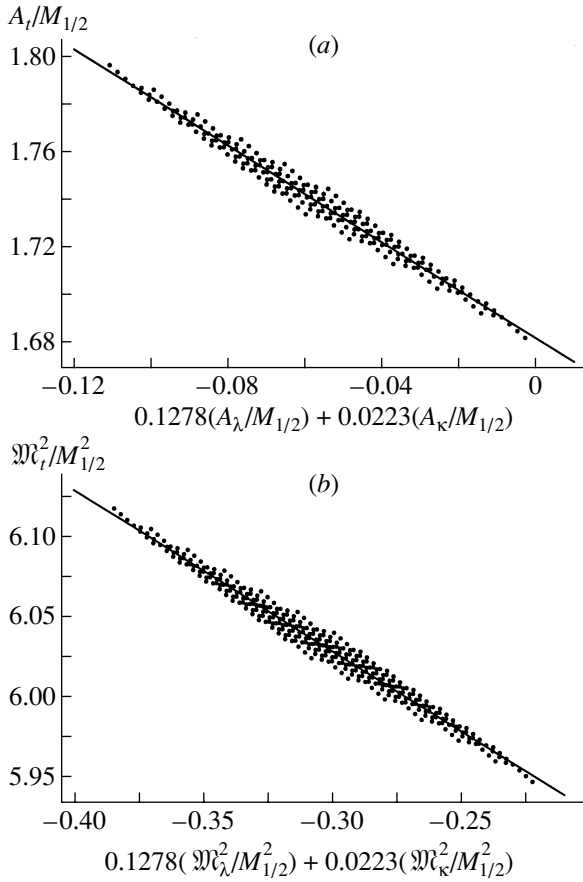


Fig. 5. Set of points lying in the (a) $(0.1278(A_\lambda/M_{1/2}) + 0.0223(A_\kappa/M_{1/2}), A_t/M_{1/2})$ and (b) $(0.1278(\mathfrak{M}_\lambda^2/M_{1/2}^2) + 0.0223(\mathfrak{M}_\kappa^2/M_{1/2}^2), \mathfrak{M}_t^2/M_{1/2}^2)$ planes and corresponding to the values of the parameters of a soft breakdown of supersymmetry at the electroweak scale for $h_t^2(0) = 32$, $\lambda^2(0) = 24$, and $\kappa^2(0) = 12$ and for a uniform distribution of the boundary conditions in the parameter spaces $(A_t, A_\lambda, A_\kappa)$ and $(\mathfrak{M}_t^2, \mathfrak{M}_\lambda^2, \mathfrak{M}_\kappa^2)$. The initial values $A_i(0)$ and $\mathfrak{M}_i^2(0)$ were varied within the ranges $-M_{1/2} \leq A_i(0) \leq M_{1/2}$ and $0 \leq \mathfrak{M}_i^2(0) \leq 3M_{1/2}^2$, respectively. The straight lines in Figs. 5a and 5b correspond to the planes in Figs. 4c and 4d.

and $(\mathfrak{M}_t^2, \mathfrak{M}_\lambda^2)$. With increasing $Y_t(0) = Y_\lambda(0)$, the dependence on α_0 and β_0 becomes weaker and the solutions at $t = t_0$ are concentrated near the straight lines $(A_t(\alpha_1), A_\lambda(\alpha_1))$ and $(\mathfrak{M}_t^2(\beta_1), \mathfrak{M}_\lambda^2(\beta_1))$. In order to obtain the equations for these straight lines, it is necessary to set $A_\lambda(0) = -3A_t(0)$ and $\mathfrak{M}_\lambda^2(0) = -3\mathfrak{M}_t^2(0)$ at the Grand Unification scale. At the electroweak scale, there then arise a relation between $A_t(t_0)$ and $A_\lambda(t_0)$ and a relation between $\mathfrak{M}_t^2(t_0)$ and $\mathfrak{M}_\lambda^2(t_0)$:

$$\begin{aligned} A_t + 0.137A_\lambda &= 1.70M_{1/2}, \\ \mathfrak{M}_t^2 + 0.137\mathfrak{M}_\lambda^2 &= 5.76M_{1/2}^2. \end{aligned} \tag{26}$$

These relations agree well with the results obtained above and presented in (18). Moreover, the equations deduced for the straight lines at $Y_i(0) \sim 1$ by fitting the results of the numerical calculations nearly coincide with those in (26).

When the Yukawa coupling constant κ is nonzero, the matrix $c_{ij}r_j^0$ has three eigenvalues. One of these is $\lambda_0 = 1$, while the other two are $\lambda_1 = \frac{3 + \sqrt{5}}{9} \approx 0.58$ and $\lambda_2 = \frac{3 - \sqrt{5}}{9} \approx 0.085$. The corresponding eigenvectors u_{i1} and u_{i2} , which specify $(A_t, A_\lambda, A_\kappa)$ and $(\mathfrak{M}_t^2, \mathfrak{M}_\lambda^2, \mathfrak{M}_\kappa^2)$ are given by

$$\begin{aligned} u_{i1} &= \begin{pmatrix} -\frac{1}{24}(1 + \sqrt{5}) \\ \frac{\sqrt{5}}{6} \\ 1 \end{pmatrix}, \\ u_{i2} &= \begin{pmatrix} \frac{1}{24}(\sqrt{5} - 1) \\ -\frac{\sqrt{5}}{6} \\ 1 \end{pmatrix}. \end{aligned} \tag{27}$$

An increase in $Y_\lambda(0) = 2Y_\kappa(0) = \frac{3}{4}Y_t(0)$ leads to the following: first, the dependence of $A_i(t)$ and $\mathfrak{M}_i^2(t)$ on α_0 and β_0 disappears, which leads to the emergence of planes in the space spanned by the parameters of a soft breakdown of supersymmetry,

$$\begin{aligned} A_t + 0.103A_\lambda + 0.0124A_\kappa &= 1.69M_{1/2}, \\ \mathfrak{M}_t^2 + 0.103\mathfrak{M}_\lambda^2 + 0.0124\mathfrak{M}_\kappa^2 &= 5.78M_{1/2}^2; \end{aligned} \tag{28}$$

after that, the dependence on α_1 and β_1 becomes weaker at $Y_i(0) \sim 1$. This means that, with increasing initial values of the Yukawa coupling constants, solutions to the renormalization-group equations are grouped near some straight lines, and we can indeed see precisely this pattern in Figs. 4 and 5. All equations presented here for the straight lines and planes in the \mathfrak{M}_i^2 space were obtained at $A_i(0) = 0$.

From relations (26) and (28), it follows that $A_t(t_0)$ and $\mathfrak{M}_t^2(t_0)$ are virtually independent of the initial conditions; that is, the straight lines and planes are orthogonal to the A_t and \mathfrak{M}_t^2 axes. On the other hand, the $A_\kappa(t_0)$ and $\mathfrak{M}_\kappa^2(t_0)$ values that correspond to the Yukawa self-interaction constant Y for the neutral fields are fully determined by the boundary conditions for the parameters of a soft breakdown of supersymmetry. For this reason, the planes in the $(A_t, A_\lambda, A_\kappa)$ and $(\mathfrak{M}_t^2, \mathfrak{M}_\lambda^2, \mathfrak{M}_\kappa^2)$ spaces are virtually parallel to the A_κ and \mathfrak{M}_κ^2 axes.

In the case of nonuniversal boundary conditions, the parameters of a soft breakdown of supersymmetry as functions of $A_i(0)$ and $\mathfrak{M}_i^2(0)$ in the regime of strong Yukawa coupling are determined by

$(\epsilon_t(t))^{\lambda_{\min}}$ [see Eq. (25)], where λ_{\min} is the smallest eigenvalue of the matrix $c_{ij}r_j^0$ and $\epsilon_t(t_0) \sim 1/h_t^2(0)$. If the values of all $A_i(0)$ and all $\mathfrak{M}_i^2(0)$ coincide, a solution to the linearized set of differential Eqs. (22) at $\theta_i \neq 0$ can be represented in the form

$$\begin{cases} \theta_i(z) = \sum_k \gamma_k u_{ik} e^{\lambda_k z}, \\ A_i(z) = A(0) \left(e^z + (e^z - 1) \frac{d\theta_i(z)}{dz} \right), \\ \mathfrak{M}_i^2(z) = \mathfrak{M}^2(0) \left(e^z + (e^z - 1) \frac{d\theta_i(z)}{dz} \right) \\ + A^2(0) (e^z - 1) \\ \times \left(e^z + \frac{1}{2} (e^z + 1) \frac{d\theta_i(z)}{dz} + (e^z - 1) \frac{d^2\theta_i(z)}{dz^2} \right), \end{cases} \quad (29)$$

where γ_k are constants of integration. In the stable-fixed-point regime, where all θ_i are equal to zero, the evolution of $A_i(t)$ and $\mathfrak{M}_i^2(t)$ is identical to that within the MSSM [see Eqs. (24)]. In the limit being considered, the dependence on $A(0)$ and $\mathfrak{M}^2(0)$ dies out fast, in proportion to $Y_t(t)/Y_t(0)$, and the parameters $A_i(t)$ and $\mathfrak{M}_i^2(t)$ approach the fixed point. Since $\theta_i \sim e^{\lambda_{\min} z}$ for $z \rightarrow -\infty$, the dependence of the parameters of a soft breakdown of supersymmetry on the initial conditions is determined by $(\epsilon_t(t))^{\lambda_{\min}}$ in all other cases—that is, by the strength with which the quasifixed point attracts the solutions to the renormalization-group equations for the Yukawa coupling constants in the limiting case of $Y_i(0) \gg \alpha_i(0)$. As a rule, λ_{\min} is significantly less than unity; for example, $\lambda_{\min} = 3/7 \approx 0.43$ at $\kappa = 0$ and $\lambda_{\min} \approx 0.085$ at nonzero κ . This is the reason why, in the regime of strong Yukawa coupling, the dependence on A and m_0^2 dies out at a rate much lower than that which is predicted by approximate solutions. Nonetheless, expressions (23)–(25) and (29) for $A_i(t)$ and $\mathfrak{M}_i^2(t)$ tend to zero in the limit $Y_i(0) \rightarrow \infty$; for this reason, the $A_i(0)$ and $\mathfrak{M}_i^2(0)$ dependence of the solutions being studied disappears completely.

5. CONCLUSION

An increase in the Yukawa coupling constants at the Grand Unification scale results in that, for $Y_t(t)$, $Y_\lambda(t)$, and $Y_\kappa(t)$, the solutions to the renormalization-group equations within the NMSSM are attracted to infrared quasifixed points. We have shown that, as $Y_i(t)$ approach these points, the corresponding solutions for the trilinear coupling constants $A_i(t)$ characterizing scalar fields and for the combinations $\mathfrak{M}_i^2(t)$ of the scalar-particle masses [see Eqs. (10)] cease to be dependent on their initial values at the

scale M_X and, in the limit $Y_i(0) \rightarrow \infty$, also approach the fixed points in the space spanned by the parameters of a soft breakdown of supersymmetry. Since the set of differential equations for $A_i(t)$ and $m_i^2(t)$ is linear, the A , $M_{1/2}$, and m_0^2 dependence of the parameters of a soft breakdown of supersymmetry at the electroweak scale can be explicitly obtained for universal boundary conditions. It turns out that, near the quasifixed points, all $A_i(t)$ and all $\mathfrak{M}_i^2(t)$ are proportional to $M_{1/2}$ and $M_{1/2}^2$, respectively. Thus, we have shown that, in the parameter-space region considered here, the solutions to the renormalization-group equations for the trilinear coupling constants and for some combinations of the scalar-particle masses are focused in a narrow interval within the infrared region. Since the neutral scalar field Y is not renormalized by gauge interactions, $A_\kappa(t)$ and $\mathfrak{M}_\kappa^2(t)$ are concentrated near zero; therefore, they are still dependent on the initial conditions. The parameters $A_t(t_0)$ and $\mathfrak{M}_t^2(t_0)$ show the weakest dependence on A and m_0^2 because these parameters are renormalized by strong interactions. By considering that the quantities $\mathfrak{M}_i^2(t_0)$ are virtually independent of the boundary conditions, we have calculated, near the quasifixed points, the values of $a_i(t_0)$, which determine the m_0^2 dependence of the scalar-particle masses at the electroweak scale.

In the general case of nonuniversal boundary conditions, the solutions to the renormalization-group equations within the NMSSM for $A_i(t)$ and $\mathfrak{M}_i^2(t)$ are grouped near some straight lines and planes in the space spanned by the parameters of a soft breakdown of supersymmetry. Moving along these lines and surfaces as $Y_i(0)$ is increased, the trilinear coupling constants and the above combinations of the scalar-particle masses approach quasifixed points. The formation of the straight lines and planes can be traced by considering the examples of an exact (at $Y_\lambda = 0$) and an approximate (for $Y_\lambda \neq 0$) solution. Although the approximate solution for the parameters of a soft breakdown of supersymmetry in a nonminimal SuSy model (this solution has been obtained here for the first time) describes the evolution of $A_\kappa(t)$ and $\mathfrak{M}_\kappa^2(t)$ very poorly, it leads to qualitatively correct results.

However, our analysis of the behavior of solutions to the renormalization-group equations within the NMSSM in the regime of strong Yukawa coupling has revealed that the $A_i(0)$ and $\mathfrak{M}_i^2(0)$ dependence of the trilinear coupling constants and the above combinations of the scalar-particle masses dies out quite slowly, in proportion to $(\epsilon_t(t))^{\lambda_{\min}}$, where $\epsilon_t(t) = Y_t(t)/Y_t(0)$ and λ_{\min} is the minimal eigenvalue of the matrix $c_{ij}r_j^0$. As a rule, λ_{\min} is positive and much less

than unity. For example, $\lambda_{\min} = 3/7$ at $Y_\kappa = 0$ and $\lambda_{\min} \approx 0.085$ at $Y_\kappa \neq 0$. The above is invalid only for the solutions $A_i(t)$ and $\mathfrak{M}_i^2(t)$ that correspond to universal boundary conditions for the parameters of a soft breakdown of supersymmetry and to the initial values of $R_{\lambda 0} = 1$, $R_{\kappa 0} = 0$ and $R_{\lambda 0} = 3/4$, $R_{\kappa 0} = 3/8$ for the Yukawa coupling constants at the Grand Unification scale. They correspond to quasifixed points of the renormalization-group equations for $Y_i(t)$. As the Yukawa coupling constants are increased, such solutions are attracted to infrared quasifixed points in proportion to $\epsilon_t(t)$.

It is precisely because of the inequality $\lambda_{\min} \ll 1$ that straight lines in the $(A_t, A_\lambda, A_\kappa)$ and $(\mathfrak{M}_t^2, \mathfrak{M}_\lambda^2, \mathfrak{M}_\kappa^2)$ spaces, rather than infrared quasifixed points, play a key role in the analysis of the behavior of solutions for $A_i(t)$ and $\mathfrak{M}_i^2(t)$ in the case where $Y_t(0), Y_\lambda(0), Y_\kappa(0) \sim 1$. In the space spanned by the parameters of a soft breakdown of supersymmetry, these straight lines lie in the planes near which $A_i(t)$ and $\mathfrak{M}_i^2(t)$ are grouped in the regime of strong Yukawa coupling at the electroweak scale. A method has been proposed in the present study for deriving equations that describe the straight lines and planes being discussed. The straight lines and planes that were obtained by using this method or by fitting the results of our numerical calculations are nearly orthogonal to the A_t and \mathfrak{M}_t^2 axes. This is because the constants $A_t(t_0)$ and $\mathfrak{M}_t^2(t_0)$ are virtually independent of the initial conditions at the scale M_X . On the other hand, the parameters $A_\kappa(t_0)$ and $\mathfrak{M}_\kappa^2(t_0)$ are determined, to a considerable extent, by the boundary conditions at the scale M_X . At $R_{\lambda 0} = 3/4$ and $R_{\kappa 0} = 3/8$, the planes in the $(A_t, A_\lambda, A_\kappa)$ and $(\mathfrak{M}_t^2, \mathfrak{M}_\lambda^2, \mathfrak{M}_\kappa^2)$ spaces are therefore parallel to the A_κ and \mathfrak{M}_κ^2 axes.

Within the NMSSM involving a minimal set of fundamental parameters, we have been unfortunately unable to construct, at $Y_i(0) \gg \alpha_i(0)$, a self-consistent solution that, on one hand, would lead to a heavy spectrum of SuSy particles and which, on the other hand, would make it possible to obtain, for the lightest Higgs boson, a mass value greater than that in the MSSM. In order to obtain such a solution, it is necessary to modify the nonminimal SuSy model. In the near future, we plan to investigate the spectrum of the superpartners of observable particles and Higgs bosons within the simplest modification of the NMSSM such that it leads to a self-consistent solution in the regime of strong Yukawa coupling.

ACKNOWLEDGMENTS

We are grateful to M.I. Vysotsky, D.I. Kazakov, and K.A. Ter-Martirosyan for stimulating questions

and for enlightening discussions and comments. R.B. Nevzorov is indebted to Istituto Nazionale di Fisica Nucleare (Sezione di Ferrara, Italy) for the kind hospitality extended to him.

This work was supported by the Russian Foundation for Basic Research (RFBR), project nos. 98-02-17372, 98-02-17453, 00-15-96786, and 00-15-96562.

APPENDIX 1

Set of Renormalization Group Equations within the NMSSM and Its Approximate Solution

The full set of one-loop renormalization-group equations within the NMSSM can be represented in the form [28]

$$\begin{aligned}
 \frac{d\tilde{\alpha}_i}{dt} &= -b_i \tilde{\alpha}_i^2, \\
 \frac{dY_t}{dt} &= -Y_t(Y_\lambda + 6Y_t - \frac{16}{3}\tilde{\alpha}_3 - 3\tilde{\alpha}_2 - \frac{13}{15}\tilde{\alpha}_1), \\
 \frac{dY_\lambda}{dt} &= -Y_\lambda(4Y_\lambda + 2Y_\kappa + 3Y_t - 3\tilde{\alpha}_2 - \frac{3}{5}\tilde{\alpha}_1), \\
 \frac{dY_\kappa}{dt} &= -6Y_\kappa(Y_\lambda + Y_\kappa), \\
 \frac{dM_i}{dt} &= -b_i \tilde{\alpha}_i M_i, \\
 \frac{dA_t}{dt} &= -Y_\lambda A_\lambda - 6Y_t A_t + \frac{16}{3}\tilde{\alpha}_3 M_3 \\
 &\quad + 3\tilde{\alpha}_2 M_2 + \frac{13}{15}\tilde{\alpha}_1 M_1, \\
 \frac{dA_\lambda}{dt} &= -4Y_\lambda A_\lambda - 2Y_\kappa A_\kappa - 3Y_t A_t \\
 &\quad + 3\tilde{\alpha}_2 M_2 + \frac{3}{5}\tilde{\alpha}_1 M_1, \\
 \frac{dA_\kappa}{dt} &= -6Y_\lambda A_\lambda - 6Y_\kappa A_\kappa, \quad (A.1) \\
 \frac{dm_1^2}{dt} &= -Y_\lambda(m_1^2 + m_2^2 + m_y^2 + A_\lambda^2) \\
 &\quad + 3\tilde{\alpha}_2 M_2^2 + \frac{3}{5}\tilde{\alpha}_1 M_1^2, \\
 \frac{dm_2^2}{dt} &= -Y_\lambda(m_1^2 + m_2^2 + m_y^2 + A_\lambda^2) \\
 &\quad - 3Y_t(m_2^2 + m_U^2 + m_Q^2 + A_t^2) \\
 &\quad + 3\tilde{\alpha}_2 M_2^2 + \frac{3}{5}\tilde{\alpha}_1 M_1^2, \\
 \frac{dm_y^2}{dt} &= -2Y_\lambda(m_1^2 + m_2^2 + m_y^2 + A_\lambda^2) \\
 &\quad - 2Y_\kappa(3m_y^2 + A_\kappa^2), \\
 \frac{dm_U^2}{dt} &= -2Y_t(m_2^2 + m_U^2 + m_Q^2 + A_t^2)
 \end{aligned}$$

$$\begin{aligned}
 & + \frac{16}{3} \tilde{\alpha}_3 M_3^2 + \frac{16}{15} \tilde{\alpha}_1 M_1^2, \\
 \frac{dm_Q^2}{dt} = & -Y_t(m_2^2 + m_U^2 + m_Q^2 + A_t^2) + \frac{16}{3} \tilde{\alpha}_3 M_3^2 \\
 & + 3\tilde{\alpha}_2 M_2^2 + \frac{1}{15} \tilde{\alpha}_1 M_1^2,
 \end{aligned}$$

where the index i runs through the natural values from 1 to 3, $b_1 = 33/5$, $b_2 = 1$, $b_3 = -3$, $\tilde{\alpha}_i(t) = \alpha_i(t)/(4\pi) = (g_i(t)/(4\pi))^2$, $Y_t(t) = (h_t(t)/(4\pi))^2$, $Y_\lambda(t) = (\lambda(t)/(4\pi))^2$, and $Y_\kappa(t) = (\kappa(t)/(4\pi))^2$. The variable t is defined in a conventional way; that is, $t = \ln(M_X^2/q^2)$, where $M_X = 3 \times 10^{16}$ GeV. On the right-hand sides of the differential Eqs. (A.1), we have discarded terms proportional to the Yukawa coupling constants Y_b and Y_τ , because their contribution is negligibly small at $\tan\beta \sim 1$. For the Yukawa and gauge coupling constants, the set of two-loop renormalization-group equations within the

NMSSM is presented in [29]. Using the results obtained from an analysis of renormalizations of various types of constants in SuSy theories [31] and taking into account the two-loop equations for the Yukawa and the gauge coupling constants, one can easily obtain the relevant renormalization-group equations describing the evolution of the parameters of a soft breakdown of supersymmetry. Moreover, the full set of two-loop renormalization-group equations within the NMSSM can be obtained directly from the results presented in [32].

Although an exact analytic solution to the set of one-loop renormalization-group equations (A.1) within the NMSSM is not known at present, an approximate solution for the parameters of a soft breakdown of supersymmetry can be constructed on the basis of the following approximate solution for the Yukawa coupling constants [19]:

$$\begin{aligned}
 Y_t(t) &= \frac{Y_t(0)E_t(t)}{(1 + 6Y_t(0)F_t(t))^{1/2}(1 + 6Y_t(0)F_t(t) + 2Y_\lambda(0)F_\lambda(t))^{1/2}}, \\
 Y_\lambda(t) &= \frac{Y_\lambda(0)E_\lambda(t)}{(1 + 6Y_t(0)F_t(t) + 2Y_\lambda(0)F_\lambda(t))^{1/2}(1 + 6Y_\lambda(0)F_\lambda(t))^{1/6}} \\
 &\quad \times \frac{1}{(1 + 6Y_\lambda(0)F_\lambda(t) + 6Y_\kappa(0)t)^{1/3}}, \\
 Y_\kappa(t) &= \frac{Y_\kappa(0)}{(1 + 6Y_\lambda(0)F_\lambda(t) + 6Y_\kappa(0)t)}, \tag{A.2}
 \end{aligned}$$

$$E_t(t) = \left[\frac{\tilde{\alpha}_3(t)}{\tilde{\alpha}(0)} \right]^{16/9} \left[\frac{\tilde{\alpha}_2(t)}{\tilde{\alpha}(0)} \right]^{-3} \left[\frac{\tilde{\alpha}_1(t)}{\tilde{\alpha}(0)} \right]^{-13/99}, \quad F_t(t) = \int_0^t E(t') dt',$$

$$E_\lambda(t) = \left[\frac{\tilde{\alpha}_2(t)}{\tilde{\alpha}(0)} \right]^{-3} \left[\frac{\tilde{\alpha}_1(t)}{\tilde{\alpha}(0)} \right]^{-1/11}, \quad F_\lambda(t) = \int_0^t E_\lambda(t') dt', \quad \tilde{\alpha}_i(t) = \frac{\tilde{\alpha}(0)}{1 + b_i \tilde{\alpha}(0)t}.$$

To do this, it is necessary to replace the quantities $\tilde{\alpha}_i$ and Y_i in the approximate solution (A.2) by $\tilde{\alpha}'_i$ and Y'_i ,

$$\tilde{\alpha}'_i = \tilde{\alpha}_i (1 + M_i \eta + \bar{M}_i \bar{\eta} + 2M_i \bar{M}_i \eta \bar{\eta}), \tag{A.3}$$

$$Y'_i = Y_i (1 + A_i \eta + \bar{A}_i \bar{\eta} + 2A_i \bar{A}_i \eta \bar{\eta} + \mathfrak{M}_i^2 \eta \bar{\eta}),$$

$$\eta = \theta^2, \quad \bar{\eta} = \bar{\theta}^2,$$

where θ are Grassmann variables, and to construct an expansion in η . This method for deducing solutions made it possible to simplify considerably the expressions for $A_t(t)$ and $\mathfrak{M}_t^2(t)$ within the MSSM at $\tan\beta \sim 1$ [33] and to obtain and analyze approximate solutions for the parameters of a soft breakdown of supersymmetry within the MSSM for $\tan\beta \gg 1$ [34].

In the most general case of nonuniversal boundary conditions, we have

$$A_i(t) = \sum_j e_{ij}(t) A_j(0) + f_i(t) M_{1/2}, \tag{A.4}$$

$$\begin{aligned}
 \mathfrak{M}_i^2(t) &= \sum_j (\tilde{a}_{ij}(t) \mathfrak{M}_j^2(0) + \tilde{c}_{ij}(t) A_j(0) M_{1/2}) \\
 &\quad + \sum_{jk} \tilde{d}_{ijk}(t) A_j(0) A_k(0) + \tilde{b}_i(t) M_{1/2}^2,
 \end{aligned}$$

where $e_{ij}(t) = \tilde{a}_{ij}(t)$, since the homogeneous equations for $A_i(t)$ and $\mathfrak{M}_i^2(t)$ coincide, and where the functions $e_{ij}(t)$, $\tilde{a}_{ij}(t)$, $f_i(t)$, $\tilde{b}_i(t)$, $\tilde{c}_{ij}(t)$, and $\tilde{d}_{ijk}(t)$ are expressed in terms of the partial derivatives

of the Yukawa coupling constants as

$$\begin{aligned}
 e_{ij}(t) &= Y_j(0) \frac{\partial \ln Y_i(t)}{\partial Y_j(0)}, \\
 f_i(t) &= \tilde{\alpha}(0) \frac{\partial \ln Y_i(t)}{\partial \tilde{\alpha}(0)}, \\
 \tilde{b}_i(t) &= \frac{\partial}{\partial \tilde{\alpha}(0)} \left[\tilde{\alpha}^2(0) \frac{\partial \ln Y_i(t)}{\partial \tilde{\alpha}(0)} \right] \\
 &= f_i(t) + \tilde{\alpha}(0) \frac{\partial f_i(t)}{\partial \tilde{\alpha}(0)}, \\
 \tilde{c}_{ij}(t) &= 2\tilde{\alpha}(0) \frac{\partial}{\partial \tilde{\alpha}(0)} \left[Y_j(0) \frac{\partial \ln Y_i(t)}{\partial Y_j(0)} \right] \\
 &= 2\tilde{\alpha}(0) \frac{\partial e_{ij}(t)}{\partial \tilde{\alpha}(0)}, \\
 \tilde{d}_{ijk}(t) &= \tilde{d}_{ikj}(t) = Y_k(0) \frac{\partial}{\partial Y_k(0)} \\
 &\times \left[Y_j(0) \frac{\partial \ln Y_i(t)}{\partial Y_j(0)} \right] = Y_k(0) \frac{\partial e_{ij}(t)}{\partial Y_k(0)}.
 \end{aligned} \tag{A.5}$$

Substituting the above approximate solutions for the Yukawa coupling constants within the NMSSM into (A.5), we obtain

$$\begin{aligned}
 e_{\lambda\lambda}(t) &= 1 - \frac{2Y_\lambda(0)F_\lambda(t)}{1 + 6Y_\lambda(0)F_\lambda(t) + 6Y_\kappa(0)t} \\
 &\quad - \frac{Y_\lambda(0)F_\lambda(t)}{1 + 6Y_\lambda(0)F_\lambda(t)} \\
 &\quad - \frac{Y_\lambda(0)F_\lambda(t)}{1 + 6Y_t(0)F_t(t) + 2Y_\lambda(0)F_\lambda(t)}, \\
 e_{\lambda\kappa}(t) &= -\frac{2Y_\kappa(0)t}{1 + 6Y_\lambda(0)F_\lambda(t) + 6Y_\kappa(0)t},
 \end{aligned}$$

$$\begin{aligned}
 e_{\lambda t}(t) &= -\frac{3Y_t(0)F_t(t)}{1 + 6Y_t(0)F_t(t) + 2Y_\lambda(0)F_\lambda(t)}, \\
 e_{\kappa\lambda}(t) &= -\frac{6Y_\lambda(0)F_\lambda(t)}{1 + 6Y_\lambda(0)F_\lambda(t) + 6Y_\kappa(0)t}, \\
 e_{\kappa\kappa}(t) &= 1 - \frac{6Y_\kappa(0)t}{1 + 6Y_\lambda(0)F_\lambda(t) + 6Y_\kappa(0)t} \\
 e_{\kappa t}(t) &= e_{t\kappa}(t) = 0, \\
 e_{t\lambda}(t) &= -\frac{Y_\lambda(0)F_\lambda(t)}{1 + 6Y_t(0)F_t(t) + 2Y_\lambda(0)F_\lambda(t)}, \\
 e_{tt}(t) &= 1 - \frac{3Y_t(0)F_t(t)}{1 + 6Y_t(0)F_t(t)} \\
 &\quad - \frac{3Y_t(0)F_t(t)}{1 + 6Y_t(0)F_t(t) + 2Y_\lambda(0)F_\lambda(t)}; \\
 f_\lambda(t) &= \frac{tE'_\lambda(t)}{E_\lambda(t)} - \frac{Y_\lambda(0)(tE_\lambda(t) - F_\lambda(t))}{1 + 6Y_\lambda(0)F_\lambda(t)} \\
 &\quad - \frac{2Y_\lambda(0)(tE_\lambda(t) - F_\lambda(t))}{1 + 6Y_\lambda(0)F_\lambda(t) + 6Y_\kappa(0)t}
 \end{aligned}$$

$$\begin{aligned}
 & - \frac{3Y_t(0)(tE_t(t) - F_t(t)) + Y_\lambda(0)(tE_\lambda(t) - F_\lambda(t))}{1 + 6Y_t(0)F_t(t) + 2Y_\lambda(0)F_\lambda(t)}, \\
 f_\kappa(t) &= -\frac{6Y_\lambda(0)(tE_\lambda(t) - F_\lambda(t))}{1 + 6Y_\lambda(0)F_\lambda(t) + 6Y_\kappa(0)t}, \\
 f_t(t) &= \frac{tE'_t(t)}{E_t(t)} - \frac{3Y_t(0)(tE_t(t) - F_t(t))}{1 + 6Y_t(0)F_t(t)} \\
 & - \frac{3Y_t(0)(tE_t(t) - F_t(t)) + Y_\lambda(0)(tE_\lambda(t) - F_\lambda(t))}{1 + 6Y_t(0)F_t(t) + 2Y_\lambda(0)F_\lambda(t)},
 \end{aligned}$$

$$\begin{aligned}
 \tilde{b}_\lambda(t) &= \frac{d}{dt} \left(t^2 \frac{E'_\lambda(t)}{E_\lambda(t)} \right) - \frac{Y_\lambda(0)t^2 E'_\lambda(t)}{1 + 6Y_\lambda(0)F_\lambda(t)} + \frac{6Y_\lambda^2(0)(tE_\lambda(t) - F_\lambda(t))^2}{(1 + 6Y_\lambda(0)F_\lambda(t))^2} \\
 &\quad - \frac{3Y_t(0)t^2 E'_t(t) + Y_\lambda(0)t^2 E'_\lambda(t)}{1 + 6Y_t(0)F_t(t) + 2Y_\lambda(0)F_\lambda(t)} - \frac{2Y_\lambda(0)t^2 E'_\lambda(t)}{1 + 6Y_\lambda(0)F_\lambda(t) + 6Y_\kappa(0)t} \\
 &+ \frac{2(3Y_t(0)(tE_t(t) - F_t(t)) + Y_\lambda(0)(tE_\lambda(t) - F_\lambda(t)))^2}{(1 + 6Y_t(0)F_t(t) + 2Y_\lambda(0)F_\lambda(t))^2} + \frac{12Y_\lambda^2(0)(tE_\lambda(t) - F_\lambda(t))^2}{(1 + 6Y_\lambda(0)F_\lambda(t) + 6Y_\kappa(0)t)^2}, \\
 \tilde{b}_\kappa(t) &= -\frac{6Y_\lambda(0)t^2 E'_\lambda(t)}{1 + 6Y_\lambda(0)F_\lambda(t) + 6Y_\kappa(0)t} + \frac{36Y_\lambda^2(0)(tE_\lambda(t) - F_\lambda(t))^2}{(1 + 6Y_\lambda(0)F_\lambda(t) + 6Y_\kappa(0)t)^2}, \\
 \tilde{b}_t(t) &= \frac{d}{dt} \left(t^2 \frac{E'_t(t)}{E_t(t)} \right) - \frac{3Y_t(0)t^2 E'_t(t)}{1 + 6Y_t(0)F_t(t)} + \frac{18Y_t^2(0)(tE_t(t) - F_t(t))^2}{(1 + 6Y_t(0)F_t(t))^2} \\
 &+ \frac{2(3Y_t(0)(tE_t(t) - F_t(t)) + Y_\lambda(0)(tE_\lambda(t) - F_\lambda(t)))^2}{(1 + 6Y_t(0)F_t(t) + 2Y_\lambda(0)F_\lambda(t))^2} - \frac{3Y_t(0)t^2 E'_t(t) + Y_\lambda(0)t^2 E'_\lambda(t)}{1 + 6Y_t(0)F_t(t) + 2Y_\lambda(0)F_\lambda(t)}.
 \end{aligned} \tag{A.6}$$

$$\tilde{c}_{\lambda\lambda}(t) = -\frac{4Y_\lambda(0)(tE_\lambda(t) - F_\lambda(t))(1 + 6Y_\kappa(0)t)}{(1 + 6Y_\lambda(0)F_\lambda(t) + 6Y_\kappa(0)t)^2} - \frac{2Y_\lambda(0)(tE_\lambda(t) - F_\lambda(t))}{(1 + 6Y_\lambda(0)F_\lambda(t))^2}$$

$$\begin{aligned}
 & + 12 \frac{Y_t(0)Y_\lambda(0)F_\lambda(t)(tE_t(t) - F_t(t))}{(1 + 6Y_t(0)F_t(t) + 2Y_\lambda(0)F_\lambda(t))^2} \\
 & - 2 \frac{Y_\lambda(0)(tE_\lambda(t) - F_\lambda(t))(1 + 6Y_t(0)F_t(t))}{(1 + 6Y_t(0)F_t(t) + 2Y_\lambda(0)F_\lambda(t))^2}, \\
 \tilde{c}_{\lambda\kappa}(t) & = \frac{24Y_\kappa(0)Y_\lambda(0)(tE_\lambda(t) - F_\lambda(t))t}{(1 + 6Y_\lambda(0)F_\lambda(t) + 6Y_\kappa(0)t)^2}, \\
 \tilde{c}_{\lambda t}(t) & = 12 \frac{Y_t(0)Y_\lambda(0)F_t(t)(tE_\lambda(t) - F_\lambda(t))}{(1 + 6Y_t(0)F_t(t) + 2Y_\lambda(0)F_\lambda(t))^2} \\
 & - 6 \frac{Y_t(0)(tE_t(t) - F_t(t))(1 + 2Y_\lambda(0)F_\lambda(t))}{(1 + 6Y_t(0)F_t(t) + 2Y_\lambda(0)F_\lambda(t))^2}, \\
 \tilde{c}_{\kappa\lambda}(t) & = -12 \frac{Y_\lambda(0)(tE_\lambda(t) - F_\lambda(t))(1 + 6Y_\kappa(0)t)}{(1 + 6Y_\lambda(0)F_\lambda(t) + 6Y_\kappa(0)t)^2}, \\
 \tilde{c}_{\kappa\kappa}(t) & = \frac{72Y_\kappa(0)Y_\lambda(0)(tE_\lambda(t) - F_\lambda(t))t}{(1 + 6Y_\lambda(0)F_\lambda(t) + 6Y_\kappa(0)t)^2}, \\
 & \tilde{c}_{\kappa t}(t) = \tilde{c}_{t\kappa}(t) = 0, \\
 \tilde{c}_{t\lambda}(t) & = 12 \frac{Y_t(0)Y_\lambda(0)F_\lambda(t)(tE_t(t) - F_t(t))}{(1 + 6Y_t(0)F_t(t) + 2Y_\lambda(0)F_\lambda(t))^2} \\
 & - 2 \frac{Y_\lambda(0)(tE_\lambda(t) - F_\lambda(t))(1 + 6Y_t(0)F_t(t))}{(1 + 6Y_t(0)F_t(t) + 2Y_\lambda(0)F_\lambda(t))^2}, \\
 \tilde{c}_{tt}(t) & = -\frac{6Y_t(0)(tE_t(t) - F_t(t))}{(1 + 6Y_t(0)F_t(t))^2} \\
 & + 12 \frac{Y_t(0)Y_\lambda(0)F_t(t)(tE_\lambda(t) - F_\lambda(t))}{(1 + 6Y_t(0)F_t(t) + 2Y_\lambda(0)F_\lambda(t))^2} \\
 & - 6 \frac{Y_t(0)(tE_t(t) - F_t(t))(1 + 2Y_\lambda(0)F_\lambda(t))}{(1 + 6Y_t(0)F_t(t) + 2Y_\lambda(0)F_\lambda(t))^2}; \\
 \tilde{d}_{\lambda\lambda\lambda}(t) & = -\frac{2Y_\lambda(0)F_\lambda(t)(1 + 6Y_\kappa(0)t)}{(1 + 6Y_\lambda(0)F_\lambda(t) + 6Y_\kappa(0)t)^2} \\
 & - \frac{Y_\lambda(0)F_\lambda(t)}{(1 + 6Y_\lambda(0)F_\lambda(t))^2} \\
 & - \frac{Y_\lambda(0)F_\lambda(t)(1 + 6Y_t(0)F_t(t))}{(1 + 6Y_t(0)F_t(t) + 2Y_\lambda(0)F_\lambda(t))^2}, \\
 \tilde{d}_{\lambda\lambda\kappa}(t) & = \tilde{d}_{\lambda\kappa\lambda}(t) \\
 & = \frac{12Y_\kappa(0)Y_\lambda(0)tF_\lambda(t)}{(1 + 6Y_\lambda(0)F_\lambda(t) + 6Y_\kappa(0)t)^2}, \\
 \tilde{d}_{\lambda\lambda t}(t) & = \tilde{d}_{\lambda t\lambda}(t) \\
 & = \frac{6Y_t(0)Y_\lambda(0)F_t(t)F_\lambda(t)}{(1 + 6Y_t(0)F_t(t) + 2Y_\lambda(0)F_\lambda(t))^2}, \\
 \tilde{d}_{\lambda\kappa\kappa}(t) & = -\frac{2Y_\kappa(0)t(1 + 6Y_\lambda(0)F_\lambda(t))}{(1 + 6Y_\lambda(0)F_\lambda(t) + 6Y_\kappa(0)t)^2}, \\
 \tilde{d}_{\lambda t t}(t) & = -\frac{3Y_t(0)F_t(t)(1 + 2Y_\lambda(0)F_\lambda(t))}{(1 + 6Y_t(0)F_t(t) + 2Y_\lambda(0)F_\lambda(t))^2},
 \end{aligned}$$

$$\begin{aligned}
 \tilde{d}_{\kappa\lambda\lambda}(t) & = -\frac{6Y_\lambda(0)F_\lambda(t)(1 + 6Y_\kappa(0)t)}{(1 + 6Y_\lambda(0)F_\lambda(t) + 6Y_\kappa(0)t)^2}, \\
 \tilde{d}_{\kappa\lambda\kappa}(t) & = \tilde{d}_{\kappa\kappa\lambda}(t) = \frac{36Y_\lambda(0)Y_\kappa(0)F_\lambda(t)t}{(1 + 6Y_\lambda(0)F_\lambda(t) + 6Y_\kappa(0)t)^2}, \\
 \tilde{d}_{\kappa\kappa\kappa}(t) & = -\frac{6Y_\kappa(0)t(1 + 6Y_\lambda(0)F_\lambda(t))}{(1 + 6Y_\lambda(0)F_\lambda(t) + Y_\kappa(0)t)^2}, \\
 \tilde{d}_{t\lambda\lambda}(t) & = -\frac{Y_\lambda(0)F_\lambda(t)(1 + 6Y_t(0)F_t(t))}{(1 + 6Y_t(0)F_t(t) + 2Y_\lambda(0)F_\lambda(t))^2}, \\
 \tilde{d}_{t\lambda t}(t) & = \tilde{d}_{t t\lambda}(t) \\
 & = \frac{6Y_t(0)Y_\lambda(0)F_t(t)F_\lambda(t)}{(1 + 6Y_t(0)F_t(t) + 2Y_\lambda(0)F_\lambda(t))^2}, \\
 \tilde{d}_{t t t}(t) & = -\frac{3Y_t(0)F_t(t)}{(1 + 6Y_t(0)F_t(t))^2} \\
 & - \frac{3Y_t(0)F_t(t)(1 + 2Y_\lambda(0)F_\lambda(t))}{(1 + 6Y_t(0)F_t(t) + 2Y_\lambda(0)F_\lambda(t))^2}, \\
 \tilde{d}_{\lambda\kappa t}(t) & = \tilde{d}_{\lambda t\kappa}(t) = \tilde{d}_{\kappa\lambda t}(t) = \tilde{d}_{\kappa\kappa t}(t) \\
 & = \tilde{d}_{\kappa t\lambda}(t) = \tilde{d}_{\kappa t\kappa}(t) = 0, \\
 \tilde{d}_{\kappa t t}(t) & = \tilde{d}_{t\lambda\kappa}(t) = \tilde{d}_{t\kappa\lambda}(t) = \tilde{d}_{t\kappa\kappa}(t) \\
 & = \tilde{d}_{t\kappa t}(t) = \tilde{d}_{t t\kappa}(t) = 0.
 \end{aligned}$$

At $Y_\lambda(0) = 0$, the solution given by (A.2) and (A.6) coincides with the exact analytic solution to the set of renormalization-group equations (A.1). Summing the above expressions for $e_{ij}(t)$, $\tilde{c}_{ij}(t)$, and $\tilde{d}_{ijk}(t)$,

$$e_i(t) = \tilde{a}_i(t) = \sum_j e_{ij}(t),$$

$$\tilde{c}_i(t) = \sum_j \tilde{c}_{ij}(t), \quad \tilde{d}_i(t) = \sum_{jk} \tilde{d}_{ijk}(t),$$

we find the functions $e_i(t)$, $\tilde{c}_i(t)$, and $\tilde{d}_i(t)$, which determine the A , $M_{1/2}$, and m_0^2 dependence of the parameters of a soft breakdown of supersymmetry for the case of universal boundary conditions.

REFERENCES

1. E. Gildener and S. Weinberg, Phys. Rev. D **13**, 3333 (1976).
2. H. P. Nilles, Phys. Rep. **110**, 1 (1984); A. B. Lahanas and D. V. Nanopoulos, Phys. Rep. **145**, 1 (1987).
3. L. Hall, J. Lykken, and S. Weinberg, Phys. Rev. D **27**, 2359 (1983); S. K. Soni and H. A. Weldon, Phys. Lett. B **126B**, 215 (1983).
4. H. P. Nilles, M. Strednicki, and D. Wyler, Phys. Lett. B **120B**, 345 (1983).
5. L. Girardello and M. T. Grisaru, Nucl. Phys. B **194**, 65 (1982).
6. U. Amaldi, W. De Boer, and H. Fürstenu, Phys. Lett. B **260**, 447 (1991); P. Langacker and M. Luo, Phys. Rev. D **44**, 817 (1991); J. Ellis, S. Kelley, and D. V. Nanopoulos, Nucl. Phys. B **373**, 55 (1992).

7. H. Georgi and S. L. Glashow, Phys. Rev. Lett. **32**, 438 (1974).
8. L. E. Ibañez and C. Lopez, Phys. Lett. B **126B**, 54 (1983); Nucl. Phys. B **233**, 511 (1984); W. De Boer, R. Ehret, and D. I. Kazakov, Z. Phys. C **67**, 647 (1995).
9. C. T. Hill, Phys. Rev. D **24**, 691 (1981); C. T. Hill, C. N. Leung, and S. Rao, Nucl. Phys. B **262**, 517 (1985).
10. V. Barger, M. S. Berger, P. Ohmann, and R. J. N. Phillips, Phys. Lett. B **314**, 351 (1993); M. Carena, M. Olechowski, S. Pokorski, and C. E. M. Wagner, Nucl. Phys. B **419**, 213 (1994); W. A. Bardeen, M. Carena, S. Pokorski, and C. E. M. Wagner, Phys. Lett. B **320**, 110 (1994); M. Carena and C. E. M. Wagner, Nucl. Phys. B **452**, 45 (1995); S. A. Abel and B. C. Allanach, Phys. Lett. B **415**, 371 (1997); **431**, 339 (1998).
11. V. Barger, M. S. Berger, and P. Ohmann, Phys. Rev. D **49**, 4908 (1994).
12. G. K. Yeghiyan, M. Jurčišin, and D. I. Kazakov, Mod. Phys. Lett. A **14**, 601 (1999).
13. S. Codoban, M. Jurčišin, and D. Kazakov, hep-ph/9912504.
14. M. Carena, M. Olechowski, S. Pokorski, and C. E. M. Wagner, Nucl. Phys. B **426**, 269 (1994); M. Jurčišin and D. I. Kazakov, Mod. Phys. Lett. A **14**, 671 (1999).
15. J. A. Casas, J. R. Espinosa, and H. E. Haber, Nucl. Phys. B **526**, 3 (1998).
16. P. Igo-Kemenes, in *Proceedings of XXX International Conference on High-Energy Physics, Osaka, 2000* (in press).
17. P. Fayet, Nucl. Phys. B **90**, 104 (1975); M. I. Vysotskiĭ and K. A. Ter-Martirosyan, Zh. Éksp. Teor. Fiz. **90**, 838 (1986) [Sov. Phys. JETP **63**, 489 (1986)]; L. Durand and J. L. Lopez, Phys. Lett. B **217**, 463 (1989); L. Drees, Int. J. Mod. Phys. A **4**, 3635 (1989).
18. J. Ellis, J. F. Gunion, H. E. Haber, *et al.*, Phys. Rev. D **39**, 844 (1989).
19. R. B. Nevzorov and M. A. Trusov, Preprint No. 5, ITÉF (Institute of Theoretical and Experimental Physics, Moscow, 2000).
20. P. Binetruy and C. A. Savoy, Phys. Lett. B **277**, 453 (1992).
21. B. C. Allanach and S. F. King, Phys. Lett. B **407**, 124 (1997); I. Jack and D. R. T. Jones, Phys. Lett. B **443**, 177 (1998).
22. B. C. Allanach and S. F. King, Phys. Lett. B **328**, 360 (1994).
23. M. S. Chanowitz, J. Ellis, and M. K. Gaillard, Nucl. Phys. B **128**, 506 (1977); A. J. Buras, J. Ellis, M. K. Gaillard, and D. V. Nanopoulos, Nucl. Phys. B **135**, 66 (1978).
24. M. A. Diaz, T. A. Ter Veldius, and T. J. Weiler, Phys. Rev. D **54**, 5855 (1996); M. Masip, R. Muñoz-Tapia, and A. Pomarol, Phys. Rev. D **57**, 5340 (1998); G. K. Yeghiyan, Preprint No. 1532(5)-99, YER-PHI (1999); hep-ph/9904488; U. Ellwanger and C. Hugonie, hep-ph/9909260.
25. R. Barbieri, S. Ferrara, and C. Savoy, Phys. Lett. B **119B**, 343 (1982); A. H. Chamseddine, R. Arnowitt, and P. Nath, Phys. Rev. Lett. **49**, 970 (1982).
26. V. S. Kaplunovsky and J. Louis, Phys. Lett. B **306**, 269 (1993); A. Brignole, L. E. Ibañez, and C. Muñoz, Nucl. Phys. B **422**, 125 (1994); **436**, 747 (1995); K. Choi, H. B. Kim, and C. Muñoz, Phys. Rev. D **57**, 7521 (1998); A. Lukas, B. A. Ovrut, and D. Waldram, Phys. Rev. D **57**, 7529 (1998); T. Li, Phys. Rev. D **59**, 107902 (1999).
27. T. Elliott, S. F. King, and P. L. White, Phys. Lett. B **305**, 71 (1993); U. Ellwanger, M. Rausch de Traubenberg, and C. A. Savoy, Phys. Lett. B **315**, 331 (1993); T. Elliott, S. F. King, and P. L. White, Phys. Lett. B **351**, 213 (1995); U. Ellwanger, M. Rausch de Traubenberg, and C. A. Savoy, Nucl. Phys. B **492**, 21 (1997).
28. J.-P. Derendinger and C. A. Savoy, Nucl. Phys. B **237**, 307 (1984).
29. S. F. King and P. L. White, Phys. Rev. D **52**, 4183 (1995).
30. L. E. Ibañez and G. G. Ross, Phys. Lett. B **110B**, 215 (1982); J. Ellis, D. V. Nanopoulos, and K. Tamvakis, Phys. Lett. B **121B**, 123 (1983); L. E. Ibañez and C. Lopez, Phys. Lett. B **126B**, 54 (1983); C. Kounnas, A. B. Lahanas, D. V. Nanopoulos, and M. Quiros, Phys. Lett. B **132B**, 95 (1983).
31. L. V. Avdeev, D. I. Kazakov, and I. N. Kondrashuk, Nucl. Phys. B **510**, 289 (1998).
32. S. P. Martin and M. T. Vaughn, Phys. Rev. D **50**, 2282 (1994).
33. D. I. Kazakov, Phys. Lett. B **449**, 201 (1999).
34. S. Codoban and D. I. Kazakov, hep-ph/9906256.

Translated A. Isaakyan

ELEMENTARY PARTICLES AND FIELDS
Theory

Vacuum Effects in $(2 + 1)$ -Dimensional Topological Massive Gauge Theory

V. Ch. Zhukovsky and N. A. Peskov

Moscow State University, Vorob'evy gory, Moscow, 119899 Russia

Received April 3, 2000

Abstract—The one-loop effective potential within $(2 + 1)$ -dimensional topological massive gauge theory is calculated against the background of a constant non-Abelian field with allowance for quark and gluon contributions, and the results of this calculations are analyzed. The quantum-mechanical problem of quark motion in such a field is considered. Conditions are established under which this problem possesses supersymmetry properties. © 2001 MAIK “Nauka/Interperiodica”.

1. INTRODUCTION

In recent years, much attention has been given to studying a nontrivial structure of the vacuum in gauge theories. Among interesting results obtained along these lines, we would like to mention the well-known conclusion that, in QCD, fields squared have nonzero vacuum expectation values—that is, there is a so-called gluon condensate (see, for example, [1]). In view of this, the QCD vacuum differs significantly from the QED vacuum. At same time, we recall that, despite strenuous efforts, a consistent theory of the vacuum state in QCD has not yet been developed. A consideration of gluon- and quark-field interactions against the background of some classical gauge field (model gluon condensate), along with a calculation and an analysis of the one-loop effective potential against the background of a preset external field, is one of the approaches to studying the QCD vacuum.

At the same time, the discoveries made in the late 1970s and the early 1980s have thus far provoked keen interest in low-dimensional models of quantum field theory. Although these models are not fully realistic, they furnished very useful tools for studying quasi-one- and quasi-two-dimensional media. For example, there appeared, in 1979, the article of Su, Schrieffer, and Heeger [2], who studied linear polymer chains. A continual model of some polymer chains proved to be basically similar to one-dimensional models of quantum field theory that were studied previously. Thus, it would be incorrect to assert that low-dimensional theories are of purely academic interest. On the contrary, it has been presently revealed that there is a close relation between the predictions of low-dimensional quantum field theories and a number of unusual effects discovered experimentally in condensed-matter physics. Since the first observation of the integral quantum Hall effect in 1980 by

Klitzing *et al.* [3], models of quantum field theory in $(d = 2 + 1)$ -dimensional spacetime have become very popular.

In odd-dimensional gauge theories, the Lagrangian for a gauge field can be supplemented with a term that renders this field massive, a so-called topological Chern–Simons term. The analyses reported in the article of Deser, Jackiw, and Templeton [4], which was published in 1982, and in the article of Jackiw and Templeton [5], which appeared a year earlier, were among the pioneering studies devoted to $d = 3$ massive gauge fields. Since then, $(2 + 1)$ -dimensional theories have attracted attention not only because of their unusual properties—interest in massive gauge theories has been sparked by their ability to predict and to describe remarkable physical phenomena like the quantum Hall effect and high-temperature superconductivity. At the same time, a further investigation of the structure of $(2 + 1)$ -dimensional massive gauge theories is of interest in itself and also from the point of view of their connection with the topological properties of quantum field theory at $d = 4$, where the possibility of the emergence of structures similar to the Chern–Simons term is discussed. By way of example, we note the possible modification to $(3 + 1)$ -dimensional electrodynamics from [6]. This modification, which violates Lorentz invariance and parity, is based on introducing, in the QED Lagrangian, a Chern–Simons term that couples the dual electromagnetic tensor to the 4-vector.

A recent debate on the role of finite matter density in the dynamical generation of a Chern–Simons term (see, for example, [7, 8]) revealed that the problem of topological effects in gauge theories has not been exhausted. Investigation of radiative effects in three-dimensional theories [9, 10] demonstrated

the importance of the Chern–Simons term for regularizing the infrared divergence in evaluating higher loop diagrams against the background of an external field. Nevertheless, the question of whether the regularization procedure is applicable in $(d = 2 + 1)$ -dimensional space remains open—the result of the calculations depends on the regularization method used. It was in [4] where this ambiguity was noticed for the first time. Later on, attempts were made to find conditions under which one regularization procedure or another can be applied. In this connection, we would like to indicate that Kogan and Morozov [11] considered drawbacks of various regularization procedures and that, in studying the polarization operator, Babukhadia *et al.* [12] tried to modify the regularization procedure in such a way as to ensure the regularization-method independence of the quantity being studied.

In the present article, the one-loop contribution to the effective potential of a gauge field and that to the quark polarization operator in $(2 + 1)$ -dimensional space are considered against the background of a constant non-Abelian field (condensate) that represents an exact solution to the equations for the gauge field that involve the Chern–Simons term.

2. CONSTANT SOLUTIONS TO FIELD EQUATIONS

Within $(2 + 1)$ -dimensional $SU(2)$ gluodynamics, the Lagrangian for a massive gauge field has the form [4]

$$\mathcal{L} = -\frac{1}{4}F_{\mu\nu}^a F^{a\mu\nu} - \frac{\theta}{4}\varepsilon^{\mu\nu\alpha} \left(F_{\mu\nu}^a A_\alpha^a - \frac{g}{3}\varepsilon^{abc} A_\mu^a A_\nu^b A_\alpha^c \right), \quad (1)$$

where $A_\mu \equiv \tau^a A_\mu^a/2$ are the potentials of the gluon field, τ^a are the Pauli matrices in color space, and $F_{\mu\nu}^a = \partial_\mu A_\nu^a - \partial_\nu A_\mu^a + g\varepsilon^{abc} A_\mu^b A_\nu^c$ is the chromomagnetic-field strength. The coefficient θ of the last term—a Chern–Simons topological term—plays the role of the gauge-field mass and is referred to as a topological mass. In Abelian theory (electromagnetic interaction), the constant θ is not quantized; in general, it can depend on medium parameters (temperature, chemical potential, etc.). The situation is different in non-Abelian theories, where the requirement of gauge invariance under topologically nontrivial gauge transformations entails the quantization of θ [4]:

$$4\pi\frac{\theta}{g^2} = n, \quad n = 0, \pm 1, \pm 2, \dots \quad (2)$$

The reason is that, under the gauge transformations

$$A_\mu \rightarrow A_\mu^U = U^{-1}A_\mu U + \frac{i}{g}U^{-1}\partial_\mu U,$$

the action functional $I(A)$ does not remain constant—it changes by the quantity $\Delta I(A) = 8\pi^2\theta w(U)/g^2$, where

$$w(U) = \frac{1}{24\pi^2} \times \int dx \varepsilon^{\mu\nu\alpha} \text{tr}(\partial_\mu U U^{-1} \partial_\nu U U^{-1} \partial_\alpha U U^{-1}).$$

The quantity $w(U)$, referred to as the topological charge of the gauge transformation U , takes only integral values [13, 14]. It characterizes gauge transformations, breaking down their set into homotopically equivalent classes. The amplitudes of physical processes are determined in terms of an exponential of the action functional, $\exp\{iI(A)\}$. The requirement that this exponential be gauge invariant imposes the quantization condition (2) on the topological mass.

The equations for the gauge field are modified in the presence of the Chern–Simons term. In contrast to the Yang–Mills equations, they involve an extra term featuring a topological mass; that is,

$$D_\mu^{ac} F^{a\mu\beta} - \frac{\theta}{2}\varepsilon^{\beta\mu\nu} F_{\mu\nu}^c = 0, \quad (3)$$

where $D_\mu^{ac} = \delta^{ac}\partial_\mu - g\varepsilon^{abc}A_\mu^b$. A solution to this equation can be sought in the form of the spherically symmetric, coordinate-independent ansatz $A^{a\mu} \sim \delta^{a\mu}$, so that only those components of the non-Abelian potential are nonzero that have coincident group and coordinate indices.¹⁾ In this ansatz, four solutions satisfy Eq. (3). These are

$$A^{a\mu} = \frac{\theta}{2g}\delta^{a\mu}\chi_{\lambda\omega}^{(a)}, \quad (4)$$

where the dimensionless unit vector $\chi_{\lambda\omega}^{(a)} = (\lambda i, \lambda\omega i, \omega)$ determines the diagonal components and where the constants $\lambda = \pm 1$ and $\omega = \pm 1$, which parametrize the solution in question, take their values independently of each other. We note that a constant solution in the form of the above ansatz does not—and cannot—involve free parameters, since Eq. (3) is nonlinear and, moreover, is nonhomogeneous in the degree of the potential. A field of this type satisfies the relations

$$F_{\mu\nu}^a = -\frac{\theta}{2}\varepsilon_{\mu\nu\alpha} A^{a\alpha}, \quad A^{a\mu} A_\mu^b = \frac{\theta^2}{4g^2}\delta^{ab},$$

$$A^{a\mu} A^{a\nu} = \frac{\theta^2}{4g^2}g^{\mu\nu}.$$

¹⁾In the following, we assume that the index 3 of color space coincides with the index 0 of Minkowski space.

For the gauge field described by the Lagrangian in (1), the energy density E is determined as the component \mathcal{T}^{00} of the symmetrized energy–momentum tensor. The canonical energy–momentum tensor is symmetrized by adding, to it, the total divergence of the rank-3 tensor $T_{\alpha\mu\nu} = -A_\mu^a \left(F_{\alpha\nu}^a + \frac{\theta}{2} \varepsilon_{\alpha\nu\beta} A^{a\beta} \right)$, which is antisymmetric in the indices α and ν . By considering that the gauge field in question obeys Eq. (3), we can easily find that the symmetric tensor has the form

$$\begin{aligned} \mathcal{T}^{\mu\nu} &= T^{\mu\nu} + \partial_\alpha T^{\alpha\mu\nu} \\ &= F^{a\mu\alpha} F_\alpha^{a\nu} + \frac{1}{4} g^{\mu\nu} F_{\alpha\beta}^a F^{a\alpha\beta} \\ &= {}^*F^{a\mu} {}^*F^{a\nu} - \frac{1}{2} g^{\mu\nu} {}^*F_\alpha^a {}^*F^{a\alpha}, \end{aligned}$$

where the dual strength tensor ${}^*F_\mu^a = \frac{1}{2} \varepsilon_{\mu\alpha\beta} F^{a\alpha\beta}$ is a vector quantity in three-dimensional spacetime. For the solutions to the field equation (4) that were found in the present study, the symmetric energy–momentum tensor is given by

$$\mathcal{T}^{\mu\nu} = -\frac{\theta^4}{32g^2} g^{\mu\nu}.$$

A negative sign of the energy density means that the field energy is negative and that it decreases with increasing topological mass; at nonzero topological-mass values ($\theta \neq 0$), the energy of the solutions that we obtained is below the energy of the trivial solution $A_\mu = 0$. It should be noted that the quantity θ is not variable (it is preset).

Further, we consider the one-loop effective potential

$$V_{\text{eff}} = E + \mathcal{E}_G^{(1)} + \mathcal{E}_Q^{(1)},$$

taking into account the contributions both from the gluon ($\mathcal{E}_G^{(1)}$) and from the quark ($\mathcal{E}_Q^{(1)}$) loop. We first find the gluon contribution to the effective potential. We represent the total gluon field $\mathcal{A}^{a\mu}$ as the sum of the constant background field (4) and small quantum fluctuations $a^{a\mu}$; that is,

$$\mathcal{A}^{a\mu} = A^{a\mu} + a^{a\mu}.$$

In (2 + 1)-dimensional theory, gluons have only one transverse degree of freedom. In just the same way as in QED, gauge arbitrariness is removed by subjecting the field of gluon fluctuations to a gauge condition. This gauge fixing is achieved by supplementing the original Lagrangian with the additional term

$$\mathcal{L}_{\text{gf}} = -\frac{1}{2\xi} \left(D_\mu^{ab} a^{b\mu} \right)^2$$

in ξ gauge, where $\xi \geq 0$ is a gauge parameter and $D_\mu^{ab} = \delta^{ab} \partial_\mu - g \varepsilon^{acb} A_\mu^c$ is the covariant derivative defined with allowance for the background field. The contribution from unphysical gluon degrees of freedom is annihilated by the ghost fields $\bar{\eta}$ and η . Thus, the total Lagrangian for the gauge field can be written as

$$\begin{aligned} \mathcal{L} &= -\frac{1}{4} \mathcal{F}_{\mu\nu}^a \mathcal{F}^{a\mu\nu} \\ &\quad - \frac{\theta}{4} \varepsilon^{\mu\nu\alpha} \left(\mathcal{F}_{\mu\nu}^a \mathcal{A}_\alpha^a - \frac{g}{3} \varepsilon^{abc} \mathcal{A}_\mu^a \mathcal{A}_\nu^b \mathcal{A}_\alpha^c \right) \\ &\quad - \frac{1}{2\xi} \left(D_\mu^{ab} a^{b\mu} \right)^2 + \left(D_\mu^{ab} \bar{\eta}^b \right) \left(\nabla^{ca\mu} \eta^c \right), \end{aligned}$$

where $\nabla_\mu^{ab} = \delta^{ab} \partial_\mu - g \varepsilon^{acb} A_\mu^c$ and $\mathcal{F}_{\mu\nu}^a$ is the total strength of the quantized and the nonquantized field. In order to analyze one-loop corrections, it is sufficient to consider the linearized equations for the ghost and gluon-fluctuation fields. This means that, in the Lagrangian that we obtained, it is sufficient to retain second-order terms in fluctuations.

By choosing $\xi = 1$ (Feynman gauge), we obtain the Lagrangian for fluctuations against the background of the external field preset in the form (4):

$$\begin{aligned} \mathcal{L}(a_\mu^b | A_\mu^b) &= \mathcal{L}(a_\mu^b) - \frac{1}{2} (\partial_\mu a^{b\mu})^2 - \frac{\theta^2}{4} (a^{b\mu})^2 \quad (5) \\ &\quad + g \varepsilon^{abc} A_\mu^a f^{b\mu\nu} a_\nu^c - g \varepsilon^{abc} A_\mu^c a^{b\mu} \partial_\nu a^{a\nu}. \end{aligned}$$

Here, the first term on the right-hand side is the Lagrangian in the form (1), defined on the manifold of fluctuation fields; it also depends on the strength tensor of the non-Abelian gauge fluctuation field $f_{\mu\nu}^b$.

In this case, the energy spectrum of gluons is determined by the equation

$$\begin{aligned} &\det \left[\delta^{ac} g^{\mu\nu} (p^2 + \theta^2/2) - i\theta \delta^{ac} \varepsilon^{\alpha\mu\nu} p_\alpha \right. \\ &\quad \left. - 2ig \varepsilon^{abc} \left(A^{b\nu} p^\mu + A^{b\mu} p^\nu - g^{\mu\nu} A_\alpha^b p^\alpha \right) \right] = 0. \end{aligned}$$

This equation specifies nine branches of the energy spectrum, ε_i ($i = 1, \dots, 9$):

$$p^2 = \lambda_i \theta^2/2, \quad p^2 = \varepsilon_i^2 - \mathbf{p}^2.$$

It turns out that $\lambda_{1,2} = 3 \pm 2\sqrt{2}$ and $\lambda_{3,4} = 5 \pm 2\sqrt{6}$ and that $\lambda_5 = \dots = \lambda_9 = -1$ correspond to the fivefold-degenerate branch of the tachyon-mode spectrum.

3. BOSON LOOPS

The one-loop correction to the energy of the background gauge field is given by

$$\tilde{\mathcal{E}}_G^{(1)} = \frac{1}{2} \sum_{\mathbf{p}, i} \varepsilon_i(\mathbf{p}) = \frac{1}{2} \sum [\mathbf{p}^2 + \lambda_i \theta^2 / 2]^{1/2}. \quad (6)$$

We note that this definition of $\tilde{\mathcal{E}}_G^{(1)}$ takes into account all degrees of freedom, including unphysical ones. In considering the field over the entire coordinate space and in calculating its volume density, the sum appearing in the last expression must be replaced by an integral as $\sum_{\mathbf{p}, i} \rightarrow (2\pi)^{-2} \int d\mathbf{p} \sum_i$. In addition, it is implied in expression (6) that the real and the imaginary part of the one-loop correction $\tilde{\mathcal{E}}_G^{(1)}$ are defined as (see, for example, [14])

$$\begin{aligned} \text{Re } \tilde{\mathcal{E}}_G^{(1)} &= \frac{1}{2} \sum_{\varepsilon_i^2 > 0} [\varepsilon_i^2(\mathbf{p})]^{1/2}, \\ \text{Im } \tilde{\mathcal{E}}_G^{(1)} &= -\frac{1}{2} \sum_{\varepsilon_i^2 < 0} |\varepsilon_i^2(\mathbf{p})|^{1/2}. \end{aligned}$$

The imaginary part proves to be finite and can be represented as (with allowance for degeneracy)

$$\begin{aligned} \text{Im } \tilde{\mathcal{E}}_G^{(1)} &= -\frac{5}{2(2\pi)^2} \\ &\times \int_{|\mathbf{p}|=0}^{\theta/\sqrt{2}} \sqrt{\theta^2/2 - \mathbf{p}^2} d\mathbf{p} = -\frac{5}{24\sqrt{2}\pi} |\theta|^3. \end{aligned}$$

As to the real part of the energy correction, it appears to be divergent. By means of the dimensional-regularization procedure, we can recast it into the form

$$\text{Re } \tilde{\mathcal{E}}_G^{(1)\text{reg}} = \mu^{2\epsilon} \frac{1}{2} \sum_{\mathbf{p}, i} [\mathbf{p}^2 + \lambda_i \theta^2 / 2]^{1/2-\epsilon}, \quad (7)$$

where μ is an arbitrary constant having dimensions of mass. In order to transform the last integral, we make use of the proper-time representation. Assuming that $\epsilon > 1/2$, we rewrite expression (7) in the form

$$\begin{aligned} \text{Re } \tilde{\mathcal{E}}_G^{(1)\text{reg}} &= \frac{\mu^{2\epsilon}}{2(2\pi)^2} \frac{1}{\Gamma(\epsilon - 1/2)} \int_0^\infty \frac{ds}{s^{3/2-\epsilon}} \\ &\times \left\{ \int d\mathbf{p} \sum_{i=1}^4 e^{-s(\mathbf{p}^2 + \lambda_i \theta^2 / 2)} \right. \\ &\left. + 5 \int_{|\mathbf{p}|=\theta/\sqrt{2}}^\infty d\mathbf{p} e^{-s(\mathbf{p}^2 - \theta^2 / 2)} \right\}. \end{aligned}$$

By performing integration with respect to the two-dimensional momentum, we obtain

$$\begin{aligned} \text{Re } \tilde{\mathcal{E}}_G^{(1)\text{reg}} &= \frac{\mu^{2\epsilon}}{8\pi\Gamma(\epsilon - 1/2)} \\ &\times \int_0^\infty \frac{ds}{s^{5/2-\epsilon}} \left\{ 5 + \sum_{i=1}^4 e^{-s\lambda_i \theta^2 / 2} \right\}. \end{aligned}$$

That part of $\text{Re } \tilde{\mathcal{E}}_G^{(1)\text{reg}}$ which is divergent in the ultraviolet limit ($s \rightarrow 0$) is contained in the expression

$$\begin{aligned} \text{Re } \tilde{\mathcal{E}}_G^{(1)\text{div}} &= \frac{\mu^{2\epsilon}}{8\pi\Gamma(\epsilon - 1/2)} \\ &\times \int_0^\infty \frac{ds}{s^{5/2-\epsilon}} \left\{ 5 + \sum_{i=1}^4 (1 - s\lambda_i \theta^2 / 2) \right\}. \end{aligned} \quad (8)$$

In the limit $\epsilon \rightarrow 0$, the renormalized energy that is determined by the difference $\text{Re } \tilde{\mathcal{E}}_G^{(1)\text{ren}} \equiv \text{Re } \tilde{\mathcal{E}}_G^{(1)\text{reg}} - \text{Re } \tilde{\mathcal{E}}_G^{(1)\text{div}}$ is finite and can be reduced to a form where it is sufficient to evaluate some Γ functions. Thus, we eventually obtain the real part of the effective potential of the gauge field:

$$\text{Re } \tilde{\mathcal{E}}_G^{(1)} = -\frac{|\theta|^3}{4\pi} \left(3\sqrt{\frac{3}{2}} + \frac{5}{3} \right).$$

Here, we have omitted the index “reg.” It should be noted that, in implementing the dimensional-regularization procedure, integrals similar to those in (8) are usually set to zero [15]. This is precisely the reason why we can state that the divergent part of the effective potential at $d = 3$ vanishes (that is, $\text{Re } \tilde{\mathcal{E}}_G^{(1)\text{div}} = 0$) and that the bare masses and coupling constants are not renormalized. This is consistent with the fact that gauge field theories are superrenormalizable in three-dimensional spacetime [5, 16]. We note that the prescription for eliminating divergences in our problem is markedly different from that at $d = 4$. In the last case, naive subtractions of ultraviolet divergences introduce an infrared divergence in the limit of integration for $s \rightarrow \infty$, with the result that it becomes necessary to apply a nontrivial procedure for subtracting such divergences (renormalization program).

We also note that the branches of the gluon energy spectrum that include tachyon modes do not contribute to the real part of the correction in (6).

It is now necessary to get rid of the contribution from unphysical degrees of freedom of the gluon field. For this purpose, we consider the contribution of ghosts. The equations of motion for the ghosts have the form

$$(D^2)^{ba} \eta^b = 0,$$

where $(D^2)^{ba} = D_{\mu}^{ac} D^{bc\mu}$. These equations make it possible to derive the energy spectrum of ghosts, which is determined from the condition

$$\det \left[(p^2 - \theta^2/2)\delta^{ab} \right] = 0.$$

This yields three branches of the ghost energy:

$$\varepsilon_{\text{gh } i}^2 = \mathbf{p}^2 + \theta^2/2, \quad i = 1, 2, 3.$$

The ghost contribution to the effective potential is determined by the relation

$$\mathcal{E}_{G \text{ unphys}}^{(1)} = - \sum_{\mathbf{p}, i} \varepsilon_{\text{gh } i}(\mathbf{p}),$$

where a minus sign in front of the sum is due to the fact that ghosts are fermions. In just the same way as in the case of gluons, all branches of the ghost spectrum $\varepsilon_{\text{gh } i}$ contribute only to the real part of the effective potential. We have

$$\begin{aligned} \text{Re } \mathcal{E}_{G \text{ unphys}}^{(1)\text{reg}} &= -\mu^{2\epsilon} \sum_{i, \mathbf{p}} [\mathbf{p}^2 + \theta^2/2]^{1/2-\epsilon} \\ &= -\frac{\mu^{2\epsilon}}{(2\pi)^2} \int d\mathbf{p} \frac{1}{\Gamma(\epsilon - 1/2)} \int_0^{\infty} \frac{ds}{s^{3/2-\epsilon}} \cdot 3e^{-s(\mathbf{p}^2 + \theta^2/2)}. \end{aligned}$$

A further calculation yields

$$\text{Re } \mathcal{E}_{G \text{ unphys}}^{(1)} = \frac{1}{4\sqrt{2}\pi} |\theta|^3.$$

Since the contribution of the ghost fields cancels that from unphysical gluon degrees of freedom, the one-loop contribution from physical gluons assumes the form

$$\mathcal{E}_G^{(1)} = \tilde{\mathcal{E}}_G^{(1)} + \tilde{\mathcal{E}}_{G \text{ unphys}}^{(1)}.$$

Thus, we conclude that, at $d = 3$, the contribution from the boson sector to the effective potential can be represented as

$$\begin{aligned} V_{\text{eff}} &\equiv E + \text{Re } \mathcal{E}_G^{(1)} \\ &= -\frac{\theta^4}{32g^2} - \frac{|\theta|^3}{4\pi} \left(\frac{3\sqrt{3}-1}{\sqrt{2}} + \frac{5}{3} \right), \\ \text{Im } \mathcal{E}_G^{(1)} &= -\frac{5}{24\sqrt{2}\pi} |\theta|^3. \end{aligned}$$

We note that general theory furnishes no hints as to how one must deal with tachyon modes; therefore, one has to invoke ad hoc assumptions to specify the imaginary part of the radiative correction associated with gluons and ghosts—in particular, an assignment for the sign of the imaginary part is precisely an assumption of this type. The presence of tachyon modes indicates that the background field (4) is not a classically stable solution and that the corresponding

vacuum is unstable. The problem of finding stable solutions is still of importance in contemporary theoretical physics of gauge fields. Instability of the bosonic vacuum of topologically massive gauge theory was partly investigated, for example, in [17].

It should be recalled that, in non-Abelian theory, the topological mass θ is quantized; therefore, the result presented here is valid only for sufficiently large values of θ . The quantization condition (2) for the gauge-field mass makes it possible to estimate quantities obtained for various values of the integer n , which quantizes the mass. The energy of the gauge field specified by Eq. (4), $E \sim g^6 n^4$, and the one-loop gluon-induced correction to it, $\mathcal{E}_G^{(1)} \sim g^6 n^3$, are on the same order of magnitude if n is about unity (this in turn indicates that θ is small in perturbation theory). For small n , it is therefore insufficient to consider only one-loop effects in calculating the effective potential—higher loops must be taken into account.

4. FERMION LOOPS

It is also of interest to consider the fermion contribution to the effective potential. For the γ matrices in $(2 + 1)$ -dimensional space, we choose the representation $\gamma^0 = \sigma^3$ and $\gamma^{1,2} = i\sigma^{1,2}$, where σ^i are the Pauli matrices. We then also have the relation $\gamma^\mu \gamma^\nu = g^{\mu\nu} - i\varepsilon^{\mu\nu\alpha} \gamma_\alpha$. The energy spectrum of quarks in the external field (4) is determined by the Dirac equation

$$\left[(i\hat{\partial} - m) + \frac{1}{2} g\tau^a A_\mu^a \gamma^\mu \right] \psi(x) = 0, \quad (9)$$

where $\hat{\partial} \equiv \partial_\mu \gamma^\mu$.

Within this formulation of the problem, two quark states corresponding to different colors in the fundamental representation of the $SU(2)$ group are possible. At $d = 3$, spinors are two-component quantities describing only two degrees of freedom of the “particle–antiparticle” type, so that the spin coefficients and the sign of energy are tightly related to each other. The choice of one of the two possible polarization states of a spinor particle is related to its mass. The reason is that the mass term $m\bar{\psi}\psi$ appearing in the Lagrangian is noninvariant under the \mathcal{P} reflections $x \rightarrow -x$ and $y \rightarrow y$ (the simultaneous reflection of two coordinates is equivalent to a rotation). Only the combined operation of \mathcal{P} reflection and the reversal $m \rightarrow -m$ of the sign of the mass leaves the Lagrangian unchanged [4, 18]. Therefore, it is natural to introduce, in the particle rest frame, the spin matrix for two-dimensional fermions in the form $\Sigma = (\text{sgn } m)\gamma^0/2$; since γ^0 is simultaneously the matrix of the sign of energy, opposite-sign spin states correspond to positive- and negative-energy states. We note that \mathcal{T} reflection will also be accompanied

by the reversal of the sign of the mass term. The mass term in the gauge-field Lagrangian (1) behaves similarly under space and time inversion. The combined \mathcal{PT} transformation leaves the total Lagrangian unchanged.

Solving Eq. (9), we obtain two branches of the energy spectrum of quarks in the external field (4). Specifically, we have

$$\varepsilon_i^2 = \mathbf{p}^2 + m_{\text{eff } i}^2,$$

where $m_{\text{eff } 1}^2 = (m - \tilde{\theta})^2$ and $m_{\text{eff } 2}^2 = (m - \tilde{\theta})(m + 3\tilde{\theta})$ are the effective quark masses and $\tilde{\theta} = \theta/4$. The two branches of energy coincide if $m = \tilde{\theta}$, which corresponds to zero effective quark mass in this field ($m_{\text{eff } 1} = m_{\text{eff } 2} = 0$). It should be noted that, for $-\tilde{\theta} - 2|\tilde{\theta}| < m < -\tilde{\theta} + 2|\tilde{\theta}|$, the quark spectrum involves tachyon modes, since $\varepsilon_2^2 < 0$ for some momentum values.

The two branches of the energy spectrum correspond to two quantum numbers characterizing the eigenvalues of the operator

$$J = \tilde{\theta}^{-1} g A^\mu p_\mu - \omega \gamma^0 \tau^3 (p_\mu \gamma^\mu - m + \tilde{\theta}). \quad (10)$$

By representing solutions to Eq. (9) in the form of plane waves,

$$\psi_s(x) = (2\pi)^{-1} \exp(-i\varepsilon_s t + i\mathbf{p} \cdot \mathbf{x}) \Psi_s,$$

where $s = 1, 2$ and Ψ_s are the constant spinors, which are eigenspinors for the Dirac Hamiltonian that correspond to the eigenvalues ε_s , we can prove fulfillment of the equality

$$J\Psi_s = (-1)^s (\tilde{\theta} - m) \Psi_s.$$

We note that the right-hand side of the last equation vanishes at $m = \tilde{\theta}$; not only do the two branches of energy coincide in this case, $\varepsilon_1 = \varepsilon_2$, but the quark states then become identical, $\Psi_1 = \Psi_2$.

In this connection, the following comment is in order. Solution (4) to Eqs. (3) exemplifies field configurations in which the motion appears to be a combination of motions in color (intrinsic index “ a ”), configuration, and spinor spaces (space index “ μ ”) [19, 20]. This in turn makes it possible to relate spin and isospin transformations (see, for example, [21]). There then appears the possibility of introducing a new conserved quantity—combined spin—that generalizes the concept of spin and isospin. The combined spin describes the system of two spins, the isotopic spin associated with color-symmetry group $SU(2)_c$ and the conventional spin in $d = (2 + 1)$ -dimensional space. The latter is described by the simplest rank-1 spinor representation $\text{Spin}(1) \sim SU(2)$. In this case, the operator J is thus the combined-spin operator. It then turns out (see above) that the relationship between the quark mass and the effective

gluon mass determines the multiplet character of the quark state with respect to the combined spin. If $m \neq \tilde{\theta}$, the quark state is characterized by two eigenvalues of the operator J —that is, it is a doublet. The special case where $m = \tilde{\theta}$ and where the combined spin is zero corresponds to a singlet state. The operator J can then be represented in the form

$$J = \tilde{\tau}^3 \varepsilon^{ij} p_i (\tilde{\tau}_j - \sigma_j),$$

where we have introduced the color matrices $\tilde{\tau}^a = (\tilde{\tau}^1, \tilde{\tau}^2, \tilde{\tau}^3) = (\lambda\tau^1, \lambda\omega\tau^2, \omega\tau^3)$, which satisfy the relation identical to that for the isospin matrices, $\tilde{\tau}^a \tilde{\tau}^b = \delta^{ab} + i\varepsilon^{abc} \tilde{\tau}^c$.

These conclusions are based not only on the relation between the intrinsic and the space indices of the external-field configuration (4) but also on the fact that the spinor group and the $SU(2)_c$ group have the same structure. We note also that, for topologically nonlinear systems, the case where the intrinsic index “ a ” is related to the space index “ μ ” in the potential A_μ^a is common rather than exceptional.

The one-loop fermion contribution to the vacuum energy is given by

$$\begin{aligned} \mathcal{E}_Q^{(1)} &= \text{Re } \mathcal{E}_Q^{(1)} + i\text{Im } \mathcal{E}_Q^{(1)} \quad (11) \\ &= - \sum_{\varepsilon_s^2(\mathbf{p}) > 0} \varepsilon_s(\mathbf{p}) - i \sum_{\varepsilon_s^2(\mathbf{p}) < 0} |\varepsilon_s(\mathbf{p})|. \end{aligned}$$

Thus, its real part has the form

$$\text{Re } \mathcal{E}_Q^{(1)} = -\frac{1}{(2\pi)^2} \int d\mathbf{p} \varepsilon_1 - \frac{1}{(2\pi)^2} \int_{|\mathbf{p}|=p_*}^{\infty} d\mathbf{p} \varepsilon_2,$$

where $p_* = [-m_{\text{eff } 2}^2]^{1/2} \Theta(-m_{\text{eff } 2}^2)$ is the lowest momentum at which there does not arise tachyon modes in the energy spectrum of quarks. The Heaviside step function is defined in such a way that $\Theta(x) = 1$ for $x > 0$ and $\Theta(x) = 0$ for $x \leq 0$. A regularization and an isolation of the finite part in $\text{Re } \mathcal{E}_Q^{(1)}$ are performed on the basis of the scheme identical to that used to determine the real part of expression (6). The sign in front of the real part in (11) is negative because quarks obey Fermi statistics. The calculations show that the fermion contribution to the effective potential has the form

$$\begin{aligned} \text{Re } \mathcal{E}_Q^{(1)} &= \frac{1}{6\pi} \{ |m_{\text{eff } 1}|^3 - |m|^3 \\ &\quad + \Theta(m_{\text{eff } 2}^2) [|m_{\text{eff } 2}|^3 - |m|^3] \}. \end{aligned}$$

In calculating this quantity, we performed a standard renormalization, so that $\text{Re } \mathcal{E}_Q^{(1)} = 0$ in the absence of

an external field ($\tilde{\theta} = 0$). In particular, the result in the limiting case of zero quark mass ($m \rightarrow 0$) is

$$\text{Re } \mathcal{E}_Q^{(1)} = \frac{|\tilde{\theta}|^3}{6\pi}.$$

In just the same way as in the case of gluons, the imaginary part is finite and nonzero only if there are tachyon modes in the quark spectrum. The eventual expression for the imaginary part has the simple form

$$\begin{aligned} & \text{Im } \mathcal{E}_Q^{(1)} \\ &= -\frac{1}{6\pi} |(m - \tilde{\theta})(m + 3\tilde{\theta})|^{3/2} \Theta(4\tilde{\theta}^2 - (m + \tilde{\theta})^2). \end{aligned}$$

In the limit of massless quarks, we have

$$\text{Im } \mathcal{E}_Q^{(1)} = -\frac{\sqrt{3}|\tilde{\theta}|^3}{2\pi}.$$

The presence of tachyon modes in the spectrum of quarks and gluons generates an imaginary part in the energy of vacuum fluctuations, whence it follows that the state in question is unstable. We note that the inclusion of additional factors, such as the boundary conditions, the finiteness of the region where the fields are localized, finite temperatures, and higher loops, could stabilize configurations similar to those considered above. It is important to note that, because the topological mass is a preset parameter of the original Hamiltonian—it characterizes the gauge-field mass—and not a variable parameter, the general character of the effective potential does not seem to require that the system descend to states having indefinitely large θ values.

5. SHIFT OF THE QUARK ENERGY

It is of interest to consider the radiative shift of the quark energy in the external field (4). The propagators for quarks and gluons in this field have been found. The quark Green's function is determined from the equation

$$[\gamma^\mu (i\partial_\mu + gA_\mu) - m]S(x, y) = \delta(x - y).$$

Solving this equation with a constant potential $A^{a\mu}$ specified by Eq. (4) and going over to the momentum representation, we obtain

$$\begin{aligned} S(p) &= [(p^2 - m_{\text{eff}1}^2)(p^2 - m_{\text{eff}2}^2)]^{-1} \\ &\times \left\{ [p^2 - (m - \tilde{\theta})^2][\gamma^\mu (p_\mu + gA_\mu) + m] \right. \\ &\left. - 2(\gamma^\mu p_\mu + m - \tilde{\theta})[gA^\nu p_\nu + \tilde{\theta}(m - \tilde{\theta})] \right\}. \end{aligned}$$

The propagator for gluon-field fluctuations in the classical external gluon field (4) is determined by the form (5) of the Lagrangian. In view of this, the gluon propagator takes the form

$$D_{\mu\nu}^{ab} = \delta^{ab} g_{\mu\nu} \left[\frac{1}{2\mathcal{E}} + \frac{\mathcal{E}}{2\alpha} \right]$$

$$\begin{aligned} & -\frac{4g^2}{\theta^2} A_\mu^a A_\nu^b \left[\frac{1}{3\mathcal{E}} - \frac{\mathcal{E}}{3\beta} \right] + \frac{4g^2}{\theta^2} A_\nu^a A_\mu^b \left[\frac{1}{2\mathcal{E}} - \frac{\mathcal{E}}{2\alpha} \right] \\ & + \frac{16g^2\mathcal{E}}{\theta^2\alpha\beta} F_{\mu\alpha}^a F_{\nu\beta}^b p^\alpha p^\beta + \frac{8ig^2}{\theta^2\beta} (F_{\mu\alpha}^a A_\nu^b \\ & - F_{\nu\alpha}^b A_\mu^a) p^\alpha + \frac{16ig^2}{\theta^3\alpha} \varepsilon^{\alpha\beta\gamma} F_{\mu\alpha}^a F_{\nu\beta}^b p_\gamma, \end{aligned}$$

where $\mathcal{E} = p^2 + \theta^2/2$, $\alpha = \mathcal{E}^2 - 4\theta^2 p^2$, and $\beta = \mathcal{E}^2 - 6\theta^2 p^2$.

The situation where $m = \tilde{\theta}$ is of greatest interest. Not only do the effective quark masses vanish in this case, but the quark state then corresponds to zero eigenvalue of the operator J under the condition $m_{\text{eff}1} = m_{\text{eff}2} = 0$. We recall that, by virtue of the choice of form for an external field, the isospin is tightly related to the ordinary spin. Thus, additional constraints are imposed on the Dirac equation, with the result that the number of states that describe the spin and the isospin is further restricted.

The solution in (4) to the Dirac equation in an external field must obviously represent the plane wave $\psi(x) = (2\pi)^{-1} \exp(-i\varepsilon t + i\mathbf{p} \cdot \mathbf{x})u(p)$, where $u(p)$ is a constant spinor. Solving the Dirac equation, we obtain

$$u(p) = \psi_\tau \psi_\sigma = \frac{1}{2} \begin{pmatrix} \kappa\lambda \\ e^{-i\omega\phi} \end{pmatrix}_\tau \begin{pmatrix} e^{i\phi} \\ \kappa \end{pmatrix}_\sigma. \quad (12)$$

This expression is valid for a nonzero quark momentum \mathbf{p} . The values of $\kappa = \pm 1$ represent the sign of energy ($\varepsilon \equiv p_0 = \kappa|\mathbf{p}|$), while the phase ϕ is determined by the relations $p^2 \pm ip^1 = |\mathbf{p}|e^{\pm i\phi}$. The spinor ψ_τ describes the color state of the quark, and ψ_σ characterizes its spin state. Each of the spinors ψ_τ and ψ_σ is an eigenspinor of the operators T and S , respectively, which are given by

$$T = \frac{i}{|\mathbf{p}|} \tilde{\tau}^3 \mathbf{p} \cdot \tilde{\boldsymbol{\tau}}, \quad S = \frac{1}{|\mathbf{p}|} \gamma^0 \mathbf{p} \cdot \boldsymbol{\gamma},$$

where the matrices $\tilde{\tau}^a$ were determined above. The quantity κ (sign of energy) is an eigenvalue of these operators; that is,

$$T\psi_\tau = \kappa\psi_\tau, \quad S\psi_\sigma = \kappa\psi_\sigma.$$

We note that a state vector appearing to be a simultaneous eigenvector of the operators T and S is a solution to Eq. (9) only if the product of the corresponding eigenvalues is equal to unity (otherwise—for an arbitrary eigenvector of the two operators that corresponds to arbitrary eigenvalues—this is not so).

It should be noted that, for one value of κ , the Dirac equation has only one solution—that is, the quark state becomes singlet with respect to the combined spin J . This is also tightly related to the fact that the external-field potential (4) is not real-valued (it

follows that, in this field, the quark Hamiltonian is not Hermitian).

The one-loop correction to the quark energy is given by

$$\Delta\varepsilon = -\frac{i}{T} \iint d^3x d^3x' \bar{\psi}_k(x) M_{kl}(x, x') \psi_l(x'),$$

where $iM_{kl}(x, y) = -ig^2\gamma^\mu(\tau^a/2)_{kn} S_{nm}(x, y) \times \gamma^\nu(\tau^b/2)_{ml} D_{\mu\nu}^{ab}(x, y)$ is the one-loop polarization operator. We can easily find these quantities in the momentum representation. The result is

$$\begin{aligned} \Delta\varepsilon &= \bar{u}_k(p) iM_{kl}(p) u_l(p), \\ iM_{kl}(p) &= ig^2\gamma^\mu(\tau^a/2)_{kn} \\ &\times \int d^3k S_{nm}(p-k) \gamma^\nu(\tau^b/2)_{ml} D_{\mu\nu}^{ab}(k). \end{aligned}$$

For a radiative correction, a conventional procedure consists in a renormalization by subtracting, from the unrenormalized expression for the quantity $\Delta\varepsilon$, its zero-field value. However, the expression that we obtained is convergent, so that it does not require the subtraction of the field-free term.

Thus, the polarization operator assumes the form

$$\begin{aligned} iM(p) &= ig^2 \frac{\pi^2 \sqrt{2}}{|\theta|} \left[-b_1 \theta + \frac{5}{9} \left(\frac{2}{\theta} g A^\mu + \frac{1}{2} \gamma^\mu \right) p_\mu \right. \\ &\quad \left. - g A^\mu \gamma^\nu (b_2 g_{\mu\nu} - b_3 \theta^{-2} p_\mu p_\nu) \right], \end{aligned}$$

where b_i , $i = 1, 2, 3$, are constant coefficients whose specific values are

$$\begin{aligned} b_1 &= \frac{5}{6} - \frac{i}{12} (3\sqrt{2} + 4\sqrt{3}), \\ b_2 &= \frac{10}{9} + \frac{i}{9} (8\sqrt{3} + 9\sqrt{2}), \\ b_3 &= \frac{4}{45} - \frac{4\sqrt{3}i}{15}. \end{aligned}$$

The operator $i\gamma^0 M$ is a perturbation of the original Hamiltonian for a Dirac particle. We note that, in the space spanned by the basis vectors $u_{\pm\kappa}(p)$ (12), which is the space of solutions to the Dirac equation, the unperturbed Hamiltonian is a Hermitian operator by virtue of the fact that there are no tachyon modes in the spectrum (that is, the spectrum is real-valued). This basis is not complete, however, in the space of solution representations (where the Hamiltonian is no longer a Hermitian operator), but, in the case of $m = \tilde{\theta}$ —and this is the case of our prime concern—it singles out the space of singlets with respect to the operator J defined in Eq. (10). Moreover, the polarization operator also appears to be Hermitian for the two solutions in (12) that correspond to opposite signs κ of energy. Thus, we may assume that the

perturbation does not drive the quark out of the singlet state. For this reason, the perturbed quark state can be represented only in the form of a linear combination of the orthonormalized state vectors $u_{+\kappa}(p)$ and $u_{-\kappa}(p)$. In calculating the radiative correction $\Delta\varepsilon$ to the energy, special attention must be given to the fact that the quark Hamiltonian in the external field (4) is non-Hermitian, and it is therefore necessary, in taking expectation values, to make the substitution $iM \rightarrow iM - gA_\mu\gamma^\mu + gA_\mu^+\gamma^\mu$, whereupon a correct application of perturbation theory is ensured. What motivates this prescription is that the Dirac conjugate spinor satisfies the Dirac equation featuring the Hermitian conjugate potential A_μ^+ rather than the potential A_μ chosen for an external field (for real-valued potentials, this prescription is obviously unnecessary). The conjugate potential can be obtained by means of the simple substitution $\lambda \rightarrow -\lambda$.

In order to obtain the expression for $\Delta\varepsilon$, it only remains to take the expectation value of the polarization operator over the state in (12). This leads to the identity

$$\Delta\varepsilon = \frac{5\pi^2\sqrt{2}}{18} ig^2 |\theta|^{-1} (p_0 - \kappa|\mathbf{p}|) \equiv 0.$$

It should be noted that this result is valid for any nonzero value of the momentum $\mathbf{p} = (p^1, p^2)$. Thus, the fermions remain massless in the one-loop approximation as well.

6. SUPERSYMMETRIC SOLUTIONS

That fermions effectively remain massless even in the one-loop approximation implies the presence of some symmetry in the problem. Indeed, the results that we obtained suggest supersymmetric properties of fermion states in the external field (4), provided that $m = \tilde{\theta}$.

The minimal superalgebra representation that is ensured by two supercharges Q_1 and Q_2 and the supersymmetric Hamiltonians H_S (see, for example, [22]) includes both commutation and anticommutation relations; that is,

$$\begin{aligned} H_S &= Q_1^2 = Q_2^2, \quad [H_S, Q_i] = 0, \\ \{Q_i, Q_j\} &= 2\delta_{ij} H_S, \quad i, j = 1, 2. \end{aligned}$$

The quark Hamiltonian in the external field (4) can be represented in the form

$$\begin{aligned} H &= ip^1\gamma^2 - ip^2\gamma^1 + \tilde{\theta}(\gamma^0 - \omega\tau^3) \\ &\quad - \lambda\tilde{\theta}(\tau^1\gamma^2 - \omega\tau^2\gamma^1). \end{aligned}$$

The supersymmetry of the problem is manifested in that the squared Dirac Hamiltonian $H_S = H^2$, which can be represented as

$$H_S = \mathbf{p}^2 + 2\tilde{\theta} [i\lambda(p^1\tau^1 + \omega p^2\tau^2)]$$

$$-i\omega\tau^3(p^1\gamma^2 - p^2\gamma^1)],$$

forms a superalgebra together with the (two) supercharges

$$Q_1 = \left[\sqrt{2}\gamma^0 - \frac{i\lambda\omega\tilde{\theta}}{|\mathbf{p}|} \right] \mathbf{p} \cdot \boldsymbol{\gamma} - \frac{\omega\tilde{\theta}}{|\mathbf{p}|} \gamma^0 \tau^3 (\omega p^1 \tau^1 + p^2 \tau^2) + \frac{1}{|\mathbf{p}|} (\omega p^1 \tau^1 + p^2 \tau^2) \mathbf{p} \cdot \boldsymbol{\gamma},$$

$$Q_2 = \left[\frac{i\omega\sqrt{2}}{|\mathbf{p}|} + \frac{\lambda\tilde{\theta}}{\mathbf{p}^2} \gamma^0 \right] (\omega p^1 \tau^1 + p^2 \tau^2) \mathbf{p} \cdot \boldsymbol{\gamma} + i\tilde{\theta} \tau^3 + i\omega\gamma^0 \mathbf{p} \cdot \boldsymbol{\gamma}.$$

It is interesting to note that the Hamiltonian H_S can be recast into the form

$$H_S = \mathbf{p}^2 - 2\tilde{\theta}J,$$

where J is the operator defined by expression (10). Under the condition $m = \tilde{\theta}$, this operator is nilpotent, $J^2 = 0$.

The quark ground state, where the momentum is zero ($\mathbf{p} = 0$)—we note that $p^0 = 0$ in this case—requires a dedicated consideration. It is then straightforward to solve the relevant Dirac equation (9). A general solution for a constant spinor has the form

$$u(p=0) = \frac{c_1}{2} \begin{pmatrix} 1 \\ 0 \end{pmatrix}_\tau \begin{pmatrix} \omega + 1 \\ \omega - 1 \end{pmatrix}_\sigma \quad (13)$$

$$+ \frac{c_2}{2} \begin{pmatrix} 0 \\ 1 \end{pmatrix}_\tau \begin{pmatrix} \omega - 1 \\ \omega + 1 \end{pmatrix}_\sigma + \frac{c_3}{\sqrt{8}}$$

$$\times \left[\begin{pmatrix} 1 \\ 0 \end{pmatrix}_\tau \begin{pmatrix} \omega - 1 \\ \omega + 1 \end{pmatrix}_\sigma + \lambda \begin{pmatrix} 0 \\ 1 \end{pmatrix}_\tau \begin{pmatrix} \omega + 1 \\ \omega - 1 \end{pmatrix}_\sigma \right],$$

where arbitrary constant coefficients c_i are related by the normalization condition.

In order to demonstrate the supersymmetric properties of the Dirac equation for the quark ground state being considered ($p^0 = 0$ under the condition $m = \tilde{\theta}$), we require fulfillment of the additional condition $gA^0\gamma^0\psi = m\psi$. This in turn means that $\sigma^3\tau^3\psi = \omega\psi$. We note that the third term in (13) does not satisfy this requirement, the first two terms being eigenvectors of the operator $\sigma^3\tau^3$. Under these conditions, the Dirac equation assumes the form

$$-(\gamma^1\nabla^1 + \gamma^2\nabla^2)\psi_0 = 0.$$

Let us introduce the operators

$$b^\pm = (2i)^{-1}(\gamma^1 \pm i\gamma^2),$$

which are combinations of γ matrices (see, for example, [23]) and which play the role of anticommuting

fermion operators (creation and annihilation operator). Hence, the Dirac operator $D = \gamma^\mu(p_\mu + gA_\mu) - m$ can be represented in the form

$$D = Q_+ + Q_-,$$

where the operators on the right-hand side, which are the generators of supersymmetric transformations, are given by $Q_+ = 2b^+\nabla_u$ and $Q_- = 2b^-\bar{\nabla}_u$ and possess the nilpotency property. Here, we have used the following notation: $\nabla_u = \partial_u - igA_u$, $\bar{\nabla}_u = \bar{\partial}_u - ig\bar{A}_u$, $\partial_u = \frac{1}{2}(\partial_1 - i\partial_2)$, $\bar{\partial}_u = \frac{1}{2}(\partial_1 + i\partial_2)$, and so on. The above properties of the operators Q_+ and Q_- suggest the form of the simplest Hamiltonian H_S invariant under transformations generated by these operators [22]. For such a Hamiltonian for a supersymmetric quantum-mechanical system, one can consider the squared Dirac operator (see also [23])

$$H_S = (D^2) = \{Q_+, Q_-\}, \quad Q_\pm^2 = 0, \quad [H_S, Q_\pm] = 0.$$

We set $\psi_0 = \psi_\tau\psi_\sigma$, where ψ_τ refers to a color (boson) state and ψ_σ describes a spin (fermion) state. The ground state is determined the equality $H_S\psi_0 = 0$, which entails

$$Q_+\psi_0 = 0, \quad Q_-\psi_0 = 0.$$

Let us consider the first of these equalities, which is equivalent to $b^+\nabla_u\psi_0 = 0$. We assume that $\psi_\sigma = |0\rangle_\sigma$, in which case we have $b^+\psi_\sigma = |1\rangle_\sigma$; therefore, $\nabla_u\psi_\tau = 0$ ($|0\rangle_\sigma$ and $|1\rangle_\sigma$ are fermion states). The relation $\partial_{1,2}\psi_0 = 0$ holds for the ground state being considered, whence it follows that

$$(\tau^1 - i\omega\tau^2)\psi_\tau = 0.$$

If, in particular, $\omega = +1$, we find for $\sigma^3\psi_\sigma = -\psi_\sigma$ that $\tau^3\psi_\tau = -\psi_\tau$ and $(\tau_1 - i\tau_2)\psi_\tau = 0$ (we recall that $\tau^3\sigma^3 = \omega = +1$). It follows that $\psi_\tau = |0\rangle_\tau$. We can now clearly see that the first two terms in (13) describe supersymmetric quark states in the external field specified by the potential (4).

ACKNOWLEDGMENTS

We are grateful to A.V. Borisov for stimulating discussions on the problems treated in our study. We also acknowledge the enlightening comments of Prof. M. Mueller-Preusker and Prof. D. Ebert. N.A. Peskov is indebted to them for the kind hospitality extended to him during his stay at the Humboldt University in Berlin.

This work was supported in part by the Deutsche Forschungsgemeinschaft (project no. DFG436RUS113/477).

REFERENCES

1. M. B. Voloshin and K. A. Ter-Martirosyan, *Theory of Gauge Interactions of Elementary Particles* (Énergoatomizdat, Moscow, 1984).
2. W. P. Su, J. R. Schrieffer, and A. J. Heeger, *Phys. Rev. Lett.* **42**, 1698 (1979).
3. K. von Klitzing, G. Dorda, and M. Pepper, *Phys. Rev. Lett.* **45**, 494 (1980).
4. S. Deser, R. Jackiw, and S. Templeton, *Ann. Phys. (N.Y.)* **140**, 372 (1982).
5. R. Jackiw and S. Templeton, *Phys. Rev. D* **23**, 2291 (1981).
6. S. M. Carroll, G. B. Field, and R. Jackiw, *Phys. Rev. D* **41**, 1231 (1990).
7. V. Zeitlin, hep-th/9612225; hep-th/9701100.
8. A. N. Sissakian, O. Yu. Shevchenko, and S. B. Solganik, hep-th/9608159; hep-th/9612140.
9. K. V. Zhukovskii and P. A. Éminov, *Izv. Vyssh. Uchebn. Zaved., Fiz.*, No. 5, 61 (1995); K. V. Zhukovskii and P. A. Éminov, *Phys. Lett. B* **359**, 155 (1995); K. V. Zhukovsky and P. A. Éminov, *Yad. Fiz.* **59**, 1265 (1996) [*Phys. At. Nucl.* **59**, 1208 (1996)]; A. V. Borisov and K. V. Zhukovskii, *Vestn. Mosk. Univ., Ser. 3: Fiz., Astron.*, No. 1, 74 (1997).
10. V. Ch. Zhukovsky, N. A. Peskov, and A. Yu. Afinogenov, *Yad. Fiz.* **61**, 1514 (1998) [*Phys. At. Nucl.* **61**, 1408 (1998)].
11. Ya. I. Kogan and A. Yu. Morozov, *Yad. Fiz.* **41**, 1080 (1985) [*Sov. J. Nucl. Phys.* **41**, 693 (1985)].
12. L. R. Babukhadia, N. A. Kiknadze, and A. A. Khe-lashvili, *Yad. Fiz.* **58**, 1718 (1995) [*Phys. At. Nucl.* **58**, 1619 (1995)].
13. R. Jackiw, *Rev. Mod. Phys.* **52**, 661 (1980).
14. A. A. Sokolov, I. M. Ternov, V. Ch. Zhukovskii, and A. V. Borisov, *Gauge Fields* (Mosk. Gos. Univ., Moscow, 1986).
15. L. D. Faddeev and A. A. Slavnov, *Gauge Fields: Introduction to Quantum Theory* (Nauka, Moscow, 1988; Addison-Wesley, Redwood City, 1990); H. D. Trottier, *Phys. Rev. D* **44**, 464 (1991).
16. S. Templeton, *Phys. Rev. D* **24**, 3134 (1981).
17. Ya. I. Kogan, *Pis'ma Zh. Éksp. Teor. Fiz.* **51**, 496 (1990) [*JETP Lett.* **51**, 560 (1990)]; Ya. I. Kogan and I. V. Polyubin, *Phys. Lett. B* **252**, 237 (1990).
18. S. Deser, R. Jackiw, and S. Templeton, *Phys. Rev. Lett.* **48**, 975 (1982).
19. R. Jackiw and C. Rebbi, *Phys. Rev. D* **13**, 3398 (1976).
20. P. Hasenfratz and G. 't Hooft, *Phys. Rev. Lett.* **36**, 1119 (1976).
21. R. Rajaraman, *Solitons and Instantons: An Introduction to Solitons and Instantons in Quantum Field Theory* (North-Holland, Amsterdam, 1982; Mir, Moscow, 1985).
22. L. É. Gendenshtein and I. V. Krive, *Usp. Fiz. Nauk* **146**, 553 (1985) [*Sov. Phys. Usp.* **28**, 645 (1985)]; I. M. Ternov, V. Ch. Zhukovskii, and A. V. Borisov, *Quantum Processes in Strong External Fields* (Mosk. Gos. Univ., Moscow, 1989); V. Ch. Zhukovskii, *Zh. Éksp. Teor. Fiz.* **90**, 1137 (1986) [*Sov. Phys. JETP* **63**, 663 (1986)]; F. Cooper, A. Khare, and U. Sukhatme, hep-th/9405029.
23. F. Cooper, A. Khare, R. Musto, and A. Wipf, *Ann. Phys. (N.Y.)* **187**, 1 (1988).

Translated by A. Isaakyan